P. V. Timbadiya
P. L. Patel
Vijay P. Singh
Bandita Barman   *Editors*

Fluid Mechanics and Hydraulics

Proceedings of 26th International
Conference on Hydraulics, Water
Resources and Coastal Engineering
(HYDRO 2021)

Springer

Lecture Notes in Civil Engineering

Volume 314

Lecture Notes in Civil Engineering (LNCE) publishes the latest developments in Civil Engineering—quickly, informally and in top quality. Though original research reported in proceedings and post-proceedings represents the core of LNCE, edited volumes of exceptionally high quality and interest may also be considered for publication. Volumes published in LNCE embrace all aspects and subfields of, as well as new challenges in, Civil Engineering. Topics in the series include:

- Construction and Structural Mechanics
- Building Materials
- Concrete, Steel and Timber Structures
- Geotechnical Engineering
- Earthquake Engineering
- Coastal Engineering
- Ocean and Offshore Engineering; Ships and Floating Structures
- Hydraulics, Hydrology and Water Resources Engineering
- Environmental Engineering and Sustainability
- Structural Health and Monitoring
- Surveying and Geographical Information Systems
- Indoor Environments
- Transportation and Traffic
- Risk Analysis
- Safety and Security

To submit a proposal or request further information, please contact the appropriate Springer Editor:

- Pierpaolo Riva at pierpaolo.riva@springer.com (Europe and Americas);
- Swati Meherishi at swati.meherishi@springer.com (Asia—except China, Australia, and New Zealand);
- Wayne Hu at wayne.hu@springer.com (China).

All books in the series now indexed by Scopus and EI Compendex database!

P. V. Timbadiya · P. L. Patel · Vijay P. Singh ·
Bandita Barman

Editors

Fluid Mechanics
and Hydraulics

Proceedings of 26th International Conference
on Hydraulics, Water Resources and Coastal
Engineering (HYDRO 2021)

Springer

Editors
P. V. Timbadiya
Department of Civil Engineering
Sardar Vallabhbhai National Institute
of Technology
Surat, India

P. L. Patel
Department of Civil Engineering
Sardar Vallabhbhai National Institute
of Technology
Surat, India

Vijay P. Singh
Department of Biological and
Agricultural Engineering
Zachry Department of Civil
and Environmental Engineering
Texas A&M University
College Station, TX, USA

Bandita Barman
Department of Civil Engineering
Indian Institute of Technology
(Indian School of Mines) Dhanbad
Dhanbad, India

Preface

Fluid mechanics is a branch of mechanics to study fluid behaviour at rest and in motion. The impact of forces exerted by the fluid on stationary and moving objects is of significant importance in practical situations. Such forces in a fluid system are defined through the fundamental laws of nature. The governing equations of conservation of mass, momentum and energy are fundamental to addressing and solving fluid mechanics problems. These equations are often solved through different numerical techniques that simulate the flow behaviour in closed and open channels. The governing equations can also be used to solve both rigid and mobile bed channel problems. Both computational and experimental studies are useful for understanding flow behaviour in real engineering problems. This branch also has many applications in hydraulics, including jet propulsion, hydraulic jump, hydropower, aggradation and degradation in rivers, flow–vegetation interaction, flow–structure interaction, sediment transport and contaminant transport in rivers.

This book covers several engineering problems pertaining to the field of fluid mechanics and hydraulics. The studies related to open channel flow, turbulent flow characteristics, the role of vegetation, sediment transport, incipient motion and bridge pier scouring are presented first in this book. The numerical modelling of different physical processes in closed conduit and open channels is included in this book. The application of the finite difference method and other CFD models to solve field problems is also added in this book. The problems presented include shallow water flow, multistage pumps, fate and transport of contaminants, to name a few. This book also covers some studies on empirical relationships in hydraulics, the application of machine learning tools, river meandering and morphological changes. A few studies demonstrate the applications of remote sensing and Geographical Information System (GIS) to analyse the morphological changes in the river. The studies on water pollution, water quality and its modelling also contribute to this book. One of the presented studies shows the environmental impact assessment of water resources projects. In addition, a few studies on the transport of pollutants in surface water and groundwater and a review study on pollution release due to sediment erosion in a riverbed are also included in this book. This book will help the readers to gain an

overview of various fluid mechanics and hydraulics problems and their application through various experimental, numerical, case studies and review articles.

Surat, India	P. V. Timbadiya
Surat, India	P. L. Patel
College Station, TX, USA	Vijay P. Singh
Dhanbad, India	Bandita Barman

Acknowledgements

Contents

Shivani Pandey, Satanand Mishra, Vijay Kumar Dwivedi,
Tanmay Sardar, Archana Singh, and Hari Narayan Bhargav

About the Editors

P. V. Timbadiya is an Associate Professor in the Water Resources Engineering section, Department of Civil Engineering, Sardar Vallabhbhai National Institute of Technology (SVNIT), Surat, India. He secured his doctoral degree and post-graduation in Water Resources Engineering from SVNIT Surat in 2012 and 2004, respectively. He has guided three Doctoral Thesis and 29 Master's Dissertations. He has more than 110 research papers to his credit, including 25 articles in peer-reviewed journals. He served as Dean (Alumni and Resources Generation), and currently serving as Sectional Head, Water Resources Engineering Section at SVNIT. He played an instrumental role in setting up infrastructure facilities in the Centre of Excellence on 'Water Resources and Flood Management' such as the Experimental Hydraulics Lab, Computational Hydraulics Lab, Water Circulation System, and others. He is appointed as 'National Consultant' for Kalpsar Project by Narmada, Water Resources, Water Supply and Kalpsar Department of Government of Gujarat, India. He received 'Prof. R. J. Garde Research Award' for the year 2020 by the Indian Society for Hydraulics. He has awarded DST-SERB Core Research Grant for the project on 'Local Scouring around tandem and staggered bridge piers on Non-uniform mobile bed' in the year 2021. He is active in various professional bodies and organized numerous conferences, workshops, and short-term training programmes in his academic career.

P. L. Patel is a Professor of Hydraulics and Water Resources in the Department of Civil Engineering, Sardar Vallabhbhai National Institute of Technology (SVNIT), Surat, India. He served as the Deputy Director of SVNIT. He also worked as a Reader in the Civil Engineering Department at Delhi College of Engineering (now DTU) from 1999–2007. He served as an Assistant Executive Engineer in Border Roads Organization (BRO) from 1995–1999. He did his bachelor's in Civil Engineering from Government Engineering College, India and then pursued his Master's and Doctoral degrees in Civil Engineering from the then University of Roorkee, now Indian Institute of Technology Roorkee, India. He has published more than 220 papers in peer-reviewed journals and conferences of repute. He has guided 12 Doctoral Thesis and 47 Master's Dissertation so far. He has also served in various

academic positions in SVNIT Surat, such as Dean (Academics), Head of Civil Engineering Department, Dean (Research and Consultancy), Dean (PG), etc. He was also instrumental in setting up a Centre of Excellence (CoE) on 'Water Resources and Flood Management' in the Institute through a research grant from World Bank-sponsored TEQIP-II. He is a recipient of visiting International Fellowship (VIF-2017) 2017 for attending the ASCE EWRI Congress-2017 in Sacramento, California, USA. He is active in various professional bodies and organized numerous conferences, workshops, and short-term training programmes in his academic career.

Vijay P. Singh is a University Distinguished Professor, a Regents Professor, and Caroline and William N. Lehrer Distinguished Chair in Water Engineering at Texas A&M University. He received his B.S., M.S., Ph.D., and D.Sc. in engineering. He is a registered professional engineer, a registered professional hydrologist, and an Honorary Diplomate of ASCE-AAWRE. He is a Distinguished Member of ASCE, a Distinguished Fellow of AGGS, an Honorary Member of AWRA, and a Fellow of EWRI-ASCE, IAH, ISAE, IWRS, and IASWC. He has published extensively in the areas of hydrology, irrigation engineering, hydraulics, groundwater, water quality, and water resources (more than 1320 journal articles, 31 textbooks, 75 edited reference books, 110 book chapters, and 315 conference papers). He has received over 95 national and international awards, including three honorary doctorates. He is a member of 11 international science/engineering academies. He has served as President of the American Institute of Hydrology (AIH), Chair of the Watershed Council of the American Society of Civil Engineers and is currently President of the American Academy of Water Resources Engineers. He has served/serves as Editor-in-Chief of 3 journals and two book series and serves on editorial boards of more than 25 journals and three book series. His Google Scholar citations include 64073, h-index: 115, and I10-index: 903.

Bandita Barman is presently working as an Assistant Professor in the Department of Civil Engineering at the Indian Institute of Technology (Indian School of Mines) Dhanbad, India since July 2021. She previously worked as an Assistant Professor at Sardar Vallabhbhai National Institute of Technology (SVNIT), Surat, India from October 2019-July 2021. She worked as a Postdoctoral Research Fellow in the School of Water Resources and Hydropower Engineering, Wuhan University, China from February 2019 to September 2019. She is a recipient of the Key Funded Post-doctoral Fellowship from Wuhan University, China. She completed her Ph.D. in Civil Engineering with a specialization in Water Resources Engineering and Management from Indian Institute of Technology (IIT) Guwahati in August 2018. She has authored twenty research publications, including seven articles in peer-reviewed high-impact factor journals and one book chapters. Her research interests are fluvial hydraulics, sediment transport, modelling and simulation of fluvial processes, and river sediment mining.

Effect of Emergent Rigid Vegetation on Flow Properties in an Open Channel

J. R. Khuntia, K. Devi, B. S. Das, K. K. Khatua, and S. Jena

Abstract The flow characteristics in open channels with emerging rigid vegetation are discussed in this paper. By strengthening ecosystem sustainability and restoration, vegetation can be actively exploited as a tool for flood management. Vegetation growing in channels irregularly raises the hydraulic resistance, which can result in energy loss and reduced conveyance capacity. The results of the earlier experiments have been thoroughly investigated regarding the flow resistance produced by uniformly distributed vegetation stems. The vegetation consists of emergent rigid rods replicating stem of a tree. Velocities were measured using 3D acoustic Doppler velocimeters (ADV), with both downward facing and upward facing probes. The magnitude of the longitudinal velocities was found to decrease significantly behind the vegetative stem. Due to the presence of turbulence, the transverse and vertical velocities were high. According to the findings, vegetation density, stem diameter, vegetation length and flow depth all affect resistance. Additionally, it has been seen that as vegetation density increased, the flow rate reduced. The relationships between friction factor (f) and Manning's coefficient (n) with the independent non-dimensional geometric and roughness parameters have been demonstrated. Experimental data sets of NITR and past researchers have been taken for developing a new mathematical relationship for roughness in terms of non-dimensional parameters.

J. R. Khuntia (✉) · K. Devi
Department of Civil Engineering, Chaitanya Bharathi Institute of Technology (A), Hyderabad 500075, India
e-mail: jnanaranjan444@gmail.com; jnanaranjan_civil@cbit.ac.in

K. Devi
e-mail: kamalinidevi1@gmail.com; kamalinidevi_civil@cbit.ac.in

B. S. Das
Department of Civil Engineering, National Institute of Technology Patna, Patna 800005, India
e-mail: bsd.nitrkl@gmail.com; bsd.ce@nitp.ac.in

K. K. Khatua · S. Jena
Department of Civil Engineering, National Institute of Technology Rourkela, Rourkela 769008, India
e-mail: kkkhatua@nitrkl.ac.in

S. Jena
e-mail: sjena@nitrkl.ac.in

1

The mathematical expression has been proved to match well with the experimental data sets and found to be better as compared to that of the conventional equations.

Keywords Open channel · Flow resistance · Friction factor · Manning's coefficient · Rigid vegetation

1 Introduction

In main channels, floodplains and wetland water areas, vegetation like grasses, bushes and mangroves often grow. They increase the shear stress at the channel bed which further increases the hydraulic resistance. As a result, the carrying capacity of an open channel flow is diminished which causes better sediment deposition and restricts the potential of flow. Vegetation plays a crucial role in the movement of sediments and regulation of ecosystems in coastal and riverine areas. Therefore, the presence of vegetation is essential for the restoration of riverine ecosystems. Ecological, morphological, hydrological, and water quality considerations are just a few of the multifarious factors that contribute to the overall restoration process [1]. Analyzing the hydrodynamics of naturally occurring rivers with vegetation is challenging and difficult. However, vegetation affects flow resistance from a hydraulic perspective and reduces the likelihood of flooding. Depending on the flow depth, vegetation may be emergent or submerged. Emergent vegetation is defined as having the rest of its stems above the water's surface and flowing water up to a certain height of the stem.

The type and density of the vegetation, together with the depth and speed of the flow, all affect how the river behaves when it passes through vegetation. Due to the bending of streamlines driven on by the vegetation, the Manning's n roughness or Darcy–Weisbach friction factor can change with the area of mean channel velocity [2]. Additionally, vegetation prevents erosion by connecting soil with roots, decreasing runoff velocity, reducing flux, absorbing the impact of raindrops (i.e., reducing dislodging) and shielding the soil from the sun's and wind's effects (i.e., preventing drying) [3]. The properties of mean flow and turbulence for both rigid and flexible vegetation were examined by Tsujimoto et al. [4]. Vegetation can create complex two-dimensional currents, eddies, and stagnation zones, which can increase friction and obstruct the flow. This type of vegetation-induced turbulence can make it difficult to analyze and understand the hydrodynamics of rivers [5]. Meijer and Van Velzen [6] used steel rods as well as natural reeds for their experiments. Nepf [7] created and evaluated a physical model that predicts the diffusion, vegetation drags and turbulence intensity within emergent vegetation. Under emergent and submerged scenarios, Stone and Shen [8] studied the hydraulic resistance of flow and simulated with cylindrical stems. Ghisalberti and Nepf [9] employed a typical eelgrass meadow model. They claimed that the various vegetation concentrations had an impact on the hydraulic conditions, such as the turbulence patterns and vertex characteristics. Flow with emergent vegetation, the velocity profile is influenced by changes in the density and the orientation of vegetation [10].

The objective of this present paper is to extend the study of emergent vegetation, i.e., effect of flow resistance and drag coefficient with different flow depth and vegetation density. A mathematical model is developed between drag coefficient (C_D) and friction factor (f), Manning's coefficient (n), Reynolds number (Re) and vegetation density (λ). The variation of C_D against D/s, Re_d, Re_h, Fr and λ has been analyzed for model development.

2　Theoretical Analysis

2.1　Drag Coefficient

The drag force (F_D) per fluid mass due to vegetation can be formulated as (Thom [11])

$$F_D = \frac{1}{2}\rho A C_D U^2 \tag{1}$$

where ρ is the density of water, U is the mean velocity of uniform flow, A projected area to the flow and C_D is drag coefficient.

2.2　Vegetation Density

The number and spacing between the rods is based upon the vegetation density (λ). Non-dimensional vegetation density is the product of number of vegetation and area of each stem/rod.

$$\text{Density,}\quad \lambda(\%) = \frac{N\pi D^2}{4} \tag{2}$$

where D is rod/stem diameter (m), N is total number of vegetation per unit area (m^{-2}).

2.3　Reynolds Number

Two different Reynolds numbers have been used for this study, i.e., Reynolds number considering the diameter of the stem as characteristic length (Re_d) and Reynolds number considering the flow depth as characteristic length (Re_h).

$$\text{Mathematically}: \text{Re}_d = \frac{UD}{\nu} \text{ and } \text{Re}_h = \frac{Uh}{\nu} \tag{3}$$

where h is depth of flow (m), ν is kinematic viscosity (m^2/s).

2.4 Froude Number

Froude number for each flow depth is defined as:

$$\text{Fr} = \frac{U}{\sqrt{gh}} \tag{4}$$

3 Experimental Setup and Procedures

Experiments were conducted in a recirculating rectangular tilting flume of length 12 m, 0.6 m width and a maximum depth of 0.6 m with longitudinal slope 0.001 at Hydraulic Engineering laboratory of NIT Rourkela. The tilting flume is made of mild steel frame with glass wall at the test reach section. The details of experimentation are in Khuntia [12]; Khuntia et al. [13–16]. Some experimental data sets are also collected from Panigrahi [17] for flow modeling. The layout of the experimental setup used in the present study is shown in Fig. 1. Table 1 shows the geometrical details of the experimental channel section of NITR.

In the present study, cylindrical iron rods of diameter 6.5 mm are used as replica of vegetation (tree) stems. The rods are drilled into the plywood and filled the holes with adhesives to make it watertight for which water will not seep through the holes. The staggered pattern of rods with spacing in each row and column was 10 cm. The
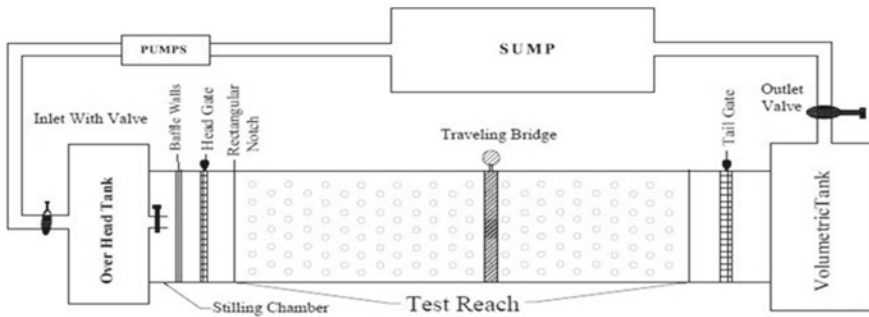
Fig. 1 Layout of experimental setup, NITR

Table 1 Geometrical details of the experimental channel section of NITR

Sl. No.	Particulars	Specifications
1	Channel and geometry type	Straight and rectangular
2	Channel bottom and top width (B)	0.6 m
3	Depth of the flume	0.75 m
4	Longitudinal slope (S)	0.001
5	Length of the flume	12 m
6	Test reach length	10 m
7	Type of bed surface	Rigid cylindrical emergent vegetation

staggered arrangement of vegetation and arrangement of rigid rods in experimental flume are shown in Fig. 2 and Fig. 3, respectively.

In this study, the important parameters were measured in experimentation, i.e., bed slope, depth of flow, velocity and discharge. To measure the bed slope of the channel, the water is to be ponded by closing the tail gate. Then, the point gauge of least count 0.01 mm was used to measure the depth of water at the two end points along the centre-line of the test reach. The slope of the channel was found by dividing the different in depth of water at two ends to length between two ends. After the measurement, the longitudinal slope or bed slope was found as 0.001. The bed slope was kept constant throughout the experiments. Depth of flow in the channel was measured using a point

Fig. 2 Staggered arrangement of vegetation
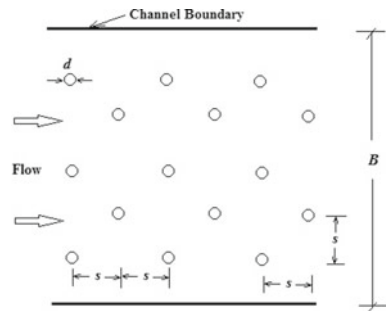
Fig. 3 Arrangement of rigid rods as emergent vegetation

Table 2 Geometric features of vegetation used in NITR channel

Sl. No.	Particulars	Specifications
1	Type and shape	Emergent rigid and cylindrical
2	Stem diameter (d)	0.0065 m
3	Stem length (l)	0.1 m
4	Spacing each side	0.1 m
5	Number of stems	76/m^2
6	Test reach length	10 m $\times$ 0.6 m

gauge fitted with traveling bridge. Local velocities were measured by using three-dimensional 16 MHz micro-ADV (acoustic Doppler velocimeter) at several locations along and across the pre-defined channel sections. The micro-ADV holder was also attached to the traveling bridge on the other side of the point gauge. The discharges were measured using volumetric tank at downstream end of the flume. A vertical piezometer with water table indicator of least count 0.1 cm fitted to the volumetric tank which helps to measure the constant rise of water in it. For this purpose, the passing way of water from volumetric tank to underground sump has been closed by valve. The time of rise in water level in the piezometer is recorded by a stopwatch. The volume of water is the product of volumetric tank area and height of 1 cm water rise in the piezometer. Finally, the discharge is calculated by dividing the volume of water to the time required (in second) for the rise of 1 cm of a particular flow depth. The discharge is thus computed for every experimental run through time rise method. Table 2 shows the geometric features of vegetation used in NITR channel.

4 Longitudinal Velocity Profiles

Velocity profiles generally follow the log law profile in case of no vegetation. The effect of bed friction on the shape of the profile is only important near the bed surface where the profile decreases to zero (Stone and Shen [8]).

Velocity at different longitudinal distances along the flow direction was measured by ADV and pitot tube (i.e., where ADV is not accessible) for each experimental run in the rigid vegetated open channel under emergent cases. Velocities were measured at every 0.1 h interval where h is the flow depth. These measured values of velocities were plotted as velocity profiles and is shown in Fig. 4.

From Fig. 4, it is observed that the velocity profiles are mostly uniform over each depth of flow. The magnitude of the velocity is increased with increase in depth of the flow. From experimental data of NITR series, the variations of drag coefficient (C_D) with non-dimensional parameters (i.e., Re_d, Re_h, Fr, f, n) have been plotted in Fig. 5.

From Fig. 5, it has been observed that drag coefficient (C_D) increases with increase in Reynolds number based on stem diameter (Re_d) and Froude number (Fr). But, drag
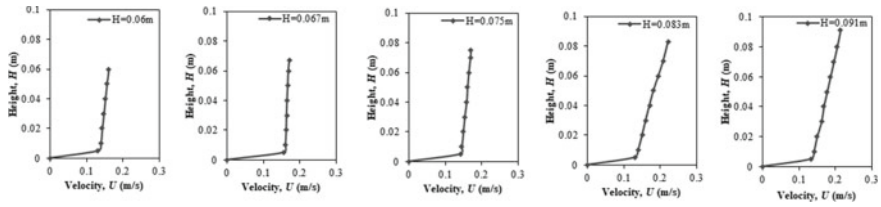
Fig. 4 Longitudinal velocity profiles of different flow depths (NITR series)

coefficient (C_D) decreases with increase in Reynolds number based on flow depth (Re_h), friction factor (f) and Manning's roughness coefficient (n).

5   Model Development

Drag coefficient (C_D) is an important parameter for every experimental study with vegetation. So, this paper tries to develop a multi-variable regression model by taking some important non-dimensional parameters so that it will help to find out the drag coefficient. For this present model, C_D is taken as dependent parameter and D/s, Re_d, Re_h, Fr and λ are taken as independent parameters. The variations of C_D against D/s, Re_d, Re_h, Fr and λ have been analyzed for model development.

5.1   Multi-variable Regression Analysis

In this present study, a number of possible single regression models considering different one-to-one relationship (e.g., exponential, power, linear or logarithmic) between dependent parameter and independent parameters were tested. Based on a criterion, the selection of best regression models was achieved with the highest coefficient of determination (R^2) values. Five preferred input independent variables have been used for this study since each variable was controlling the drag coefficient. Multi-variable regression analysis compiles these five independent variables to model the dependent variable. Finally, through multi-linear regression analysis, a model has been derived with high coefficient of determination.

The independent variables were determined by using the cross-sectional geometric non-dimensional parameters (D/s and λ) and hydraulic non-dimensional parameters (Re_d, Re_h and Fr). Then, the plot between independent parameters with the dependent parameter has been plotted. From those plots, the relationship of each independent parameter with dependent parameter with high regression coefficient (i.e., $R^2 \approx 0.92$–0.99) has been selected for regression analysis is shown in Fig. 5. Table 3 presents geometric and hydraulic parameters used in this study.
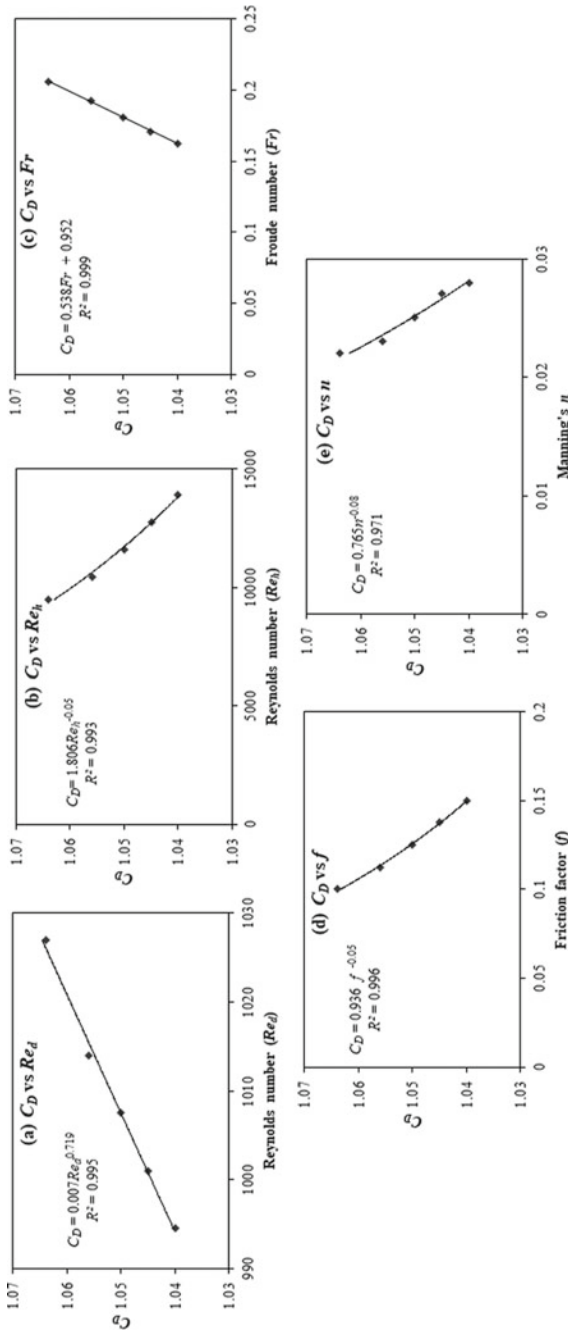
Fig. 5 Plot between drag coefficient (C_D) and influencing parameters of NITR series **a** C_D versus Re_d **b** C_D versus Re_h **c** C_D versus Fr **d** C_D versus f **e** C_D versus n

Table 3 Geometric and hydraulic parameters used in this study

Series	D (m)	s (−)	D/s (−)	Re_d (−)	Re_h (−)	Fr (−)	λ (%)
NITR	0.0065	0.01	0.65	994–1027	9480–13,923	0.162−0.206	0.25
Kothyari et al. [18]	0.01	0.091	0.109	4000	240,000	0.165	0.25
Thomson et al. [19] S1	0.025	0.223	0.112	14,152	183,245	1.285	0.28
Thomson et al. [14] S2	0.025	0.135	0.185	26,054	285,547	1.45	0.3
Stone and Shen [8] S1	0.0121	0.1446	0.0837	542–7301	5301–71,289	0.039−0.522	2.2
Stone and Shen [8] S2	0.0121	0.1448	0.0835	1338–9762	13,067–95,317	0.096−0.698	6.1
Stone and Shen [8] S3	0.00635	0.023	0.276	741–2341	16,706–91,269	0.118−0.669	0.55
Stone and Shen [8] S4	0.00318	0.019	0.167	647–2692	12,637–52,561	0.092−0.385	0.55
Ishikawa et al. [20] S1	0.004	0.0316	0.126	2137.188	22,546	0.209	0.29
Ishikawa et al. [20] S2	0.0064	0.0632	0.101	3454.811	35,648	0.65	0.26
Tsujimoto et al. [4]	0.0015	0.002	0.75	153–634	10,191–42,388	0.103−0.429	0.44
Fenzl [21] S1	0.00238	0.0024	0.992	647–1127	5096–8872	0.146−0.254	0.81
Fenzl [21] S2	0.00238	0.0047	0.506	668–1773	5259–13,964	0.150−0.399	0.2
Fenzl [21] S3	0.00238	0.0071	0.335	855–2692	6730–21,194	0.196−0.606	0.09
Fenzl [21] S4	0.00238	0.0094	0.253	1043–2044	8219–16,096	0.235−0.460	0.05

In the present study, only one bed slope, a single value of roughness parameter having a fixed value of vegetation height, thickness, distribution pattern, spacing and density are considered. The dependency of drag coefficient on the above-mentioned parameter is expressed as

$$C_D = f_n(\mathrm{Re}_d, \mathrm{Re}_h, Fr, D/s, \lambda)$$

The developed relationships of drag coefficient (C_D) are found to be in the power form with high value of coefficient determination (R^2) against Re_d, Re_h, Fr and D/s. Also, the developed relationship of drag coefficient (C_D) is found to be in the exponential form against λ. The graphical relationship of the relationship is presented in Fig. 6.

It is observed that at lower vegetal density drag coefficient (C_D) decreases with increase in both Reynolds numbers (i.e., Re_d and Re_h) and increases with increase in Froude number. But, in case of higher vegetation density, C_D increases with increase in both Reynolds numbers (i.e., Re_d and Re_h) and Froude numbers. It is also observed that C_D increases with increase in D/s and decreases with increase in vegetation density at all values of Froude number. From Fig. 6, it is observed that values of R^2 from single regression of C_D with each independent parameters are very high which indicates that the developed model can work satisfactorily for evaluation of C_D by using multi-variable regression analysis.

Finally, the multi-variable regression model for drag coefficient has been developed as:

$$\begin{aligned}
C_D = {}& 3.375 + 0.217 {D\big/_s}^{0.063} + 2.35\mathrm{Re}_d^{-0.03} + 0.998\mathrm{Re}_h^{-0.03} \\
& - 2.339\mathrm{Fr}^{-0.03} - 2.709e^{-0.01\lambda}
\end{aligned} \tag{5}$$

6 Results and Discussions

In this paper, three conventional models, i.e., Ishikawa et al. [20], Kothyari et al. [18] and Cheng [22], are used to compare with the present model. To check the efficacy of the present model, error analysis has been performed. The different parameters of error analysis, i.e., mean absolute deviation (MAD), mean absolute percentage error (MAPE) and root mean square error (RMSE), have been calculated as per given Eqs. (6)–(8) respectively.

$$\mathrm{MAD} = \frac{1}{n} \sum |(C_\mathrm{D})_{\mathrm{Predicted}} - (C_\mathrm{D})_{\mathrm{Observed}}| \tag{6}$$

$$\mathrm{MAPE} = \frac{1}{n} \sum \left| \frac{(C_\mathrm{D})_{\mathrm{Predicted}} - (C_\mathrm{D})_{\mathrm{Observed}}}{(C_\mathrm{D})_{\mathrm{Observed}}} \right| \times 100 \tag{7}$$

$$\mathrm{RMSE} = \sqrt{\frac{1}{n} \sum \frac{(C_\mathrm{D})_{\mathrm{Predicted}} - (C_\mathrm{D})_{\mathrm{Observed}}}{(C_\mathrm{D})_{\mathrm{Observed}}}} \tag{8}$$
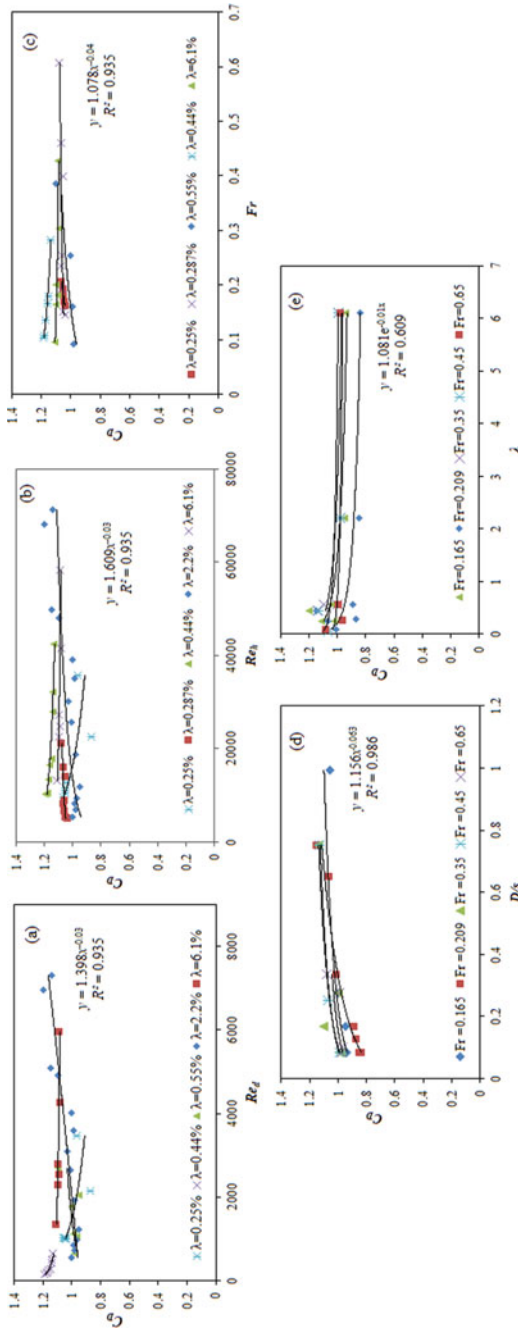
Fig. 6 Plot between drag coefficient (C_D) and non-dimensional parameters **a** C_D versus Re_d **b** C_D versus Re_h **c** C_D versus Fr **d** C_D versus D/s **e** C_D versus λ

Table 4 MAD, MAPE and RMSE results of different models used in this study

Models	MAD	MAPE (%)	RMSE
Ishikawa et al. [20]	0.25	20.80	0.27
Kothyari et al. [18]	1.28	122.16	1.19
Cheng [22]	2.17	226.74	8.89
Present model	0.04	3.48	0.05

From error analysis, it is observed that the present model is more efficient to predict drag coefficient than the previous models. From Table 4, it is found that the present model performs well with less error as compared to Ishikawa et al. [20], Kothyari et al. [18] and Cheng [22] models. The errors of MAD, MAPE and RMSE for present model are 0.04, 3.48% and 0.05, respectively which is less as compared to other conventional models.

7 Conclusions

Flow resistance is the most important hydraulic parameter of vegetated open channel flow. The various flow resistances like drag coefficient (C_D), Manning's roughness coefficient (n) and Darcy–Weisbach friction factor (f) are found to be more in vegetated open channel as compared to non-vegetated open channel.

The following conclusions are derived from the present study:

- The trend of the curves of the drag coefficient are expressed as power functions against Re_d, Re_h, Fr and D/s and exponential function against λ. It is observed that at lower vegetal density drag coefficient (C_D) decreases with increase in both Reynolds numbers (i.e., Re_d and Re_h) and increases with increase in Froude number. But, in case of higher vegetation density, C_D increases with increase in both Reynolds numbers (i.e., Re_d and Re_h) and Froude number. It is also observed that C_D increases with increase of ratio D/s and C_D decreases with increase in vegetation density at all values of Froude number.
- Regression-based multi-variable model has been developed to predict the drag coefficient relating to Reynolds number (considering the stem diameter as characteristics length), Reynolds number (considering the flow depth as characteristics length), Froude number, Manning's n and vegetation density under emergent rigid vegetation conditions. The model performed well with less error as compared to previous researchers' models.
- The different errors of MAD, MAPE and RMSE for present model are 0.04, 3.48% and 0.05, respectively, which is less as compared to other conventional models
- Additional research is desirable to validate the applicability of the rigid vegetation model developed in this study to flexible vegetation conditions.

References

1. Brookes A, Shields Jr FD (1996) River channel restoration: guiding principles for sustainable projects, Wiley
2. Fathi-Moghadam M (2006) Effects of land slope and flow depth on retarding flow in non-submerge vegetated lands. J Agronomy 5(3):536–540
3. Goldman SJ, Jackson K (1986) Erosion and sediment control handbook, McGraw-Hill Education
4. Tsujimoto T, Kitamura T, Okada T (1991) Turbulent structure of flow over rigid vegetation-covered bed in open channels. KHL Progressive Report 1
5. Furukawa K, Wolanski E, Mueller H (1997) Currents and sediment transport in mangrove forests. Estuar Coast Shelf Sci 44(3):301–310
6. Meijer DG, Van Velzen EH (1999) Prototype-scale flume experiments on hydraulic roughness of submerged vegetation. In: Conference proceedings of the 28th international IAHR conference, Graz
7. Nepf HM (1999) Drag, turbulence, and diffusion in flow through emergent vegetation. Water Resour Res 35(2):479–489
8. Stone BM, Shen HT (2002) Hydraulic resistance of flow in channels with cylindrical roughness. J Hydraul Eng 128(5):500–506
9. Ghisalberti M, Nepf HM (2002) Mixing layers and coherent structures in vegetated aquatic flows. J Geophys Res Oceans 107(C2)
10. Dorcheh SAM (2007) Effect of rigid vegetation on the velocity, turbulence, and wave structure in open channel flows. Ph.D. Dissertation, Cardiff University, United Kingdom
11. Thom AS (1975) Momentum, mass and heat exchange of plant communities. Veget Atmos 57–109
12. Khuntia JR (2016) Effect of secondary current on flow prediction in an open channel flow, M. Tech dissertation, National Institute of Technology Rourkela, India
13. Khuntia JR, Devi K, Khatua KK (2016) Variation of local friction factor in an open channel flow. Indian J Sci Technol 9(46):1–6
14. Khuntia JR, Devi K, Proust S, Khatua KK (2018) Depth-averaged velocity and bed shear stress in unsteady open channel flow over rough bed. In: River flow 2018: 9th international conference on fluvial hydraulics, vol 40, issue no 05071, pp 1–8
15. Khuntia JR, Devi K, Khatua KK (2018) Prediction of depth-averaged velocity in an open channel flow. Appl Water Sci 8(6):1–14
16. Khuntia JR, Devi K, Khatua KK (2021) Turbulence characteristics in a rough open channel under unsteady flow conditions. ISH J Hydraul Eng 27(sup1):354–365
17. Panigrahi K (2015) Experimental study of flow through rigid vegetation in open channel. M. Tech (R) dissertation, National Institute of Technology, Rourkela, India
18. Kothyari UC, Hayashi K, Hashimoto H (2009) Drag coefficient of unsubmerged rigid vegetation stems in open channel flows. J Hydraul Res 47(6):691–699
19. Thompson AM, Wilson BN, Hustrulid T (2003) Instrumentation to measure drag on idealized vegetal elements in overland flow. Trans ASAE 46(2):295
20. Ishikawa Y, Mizuhara K, Ashida M (2000) Drag force on multiple rows of cylinders in an open channel. Grant-in-aid research project report, Kyushu Univ., Fukuoka, Japan

21. Fenzl RN (1962) Hydraulic resistance of broad shallow vegetated channels. Ph.D. Dissertation, University of California, Davis, California, USA
22. Cheng NS (2012) Calculation of drag coefficient for arrays of emergent circular cylinders with pseudo fluid model. J Hydraul Eng 139(6):602–611

Double-averaged Turbulence Characteristics Over Hemispherical Rough Bed

Jaynata Shounda and Krishnendu Barman

Abstract This study characterized the double-averaged (time and space) turbulence parameters and local flow distributions through the experimental measurement over fully submerged artificially made hemispherical rough bed. Three different directional components of velocity data were collected by 3D micro-acoustic Doppler velocimeter (ADV) with a Reynolds number 62000. The changes of spatially averaged mean velocity profiles into specific flow layers on this rough bed were discussed corresponding with the smooth bed data. In the bottom wall region, double-averaged negative velocity components indicate the flow separation and strong recirculation zone. However, results from the double-averaged turbulent-kinetic-energy (TKE) flux and form-induced TKE flux were shown the upward and downward TKE transport throughout the flow depth. Also, TKE budgets terms turbulence production, diffusion and dissipation attain their peaks at the interfacial sub-layer of this rough bed flow. The production and dissipation rates of TKE have reached their maximum points at just above the lower extremity of form-induced sub-layer and within the interfacial sub-layer, respectively. The interfacial sub-layer has been treated as the losing zone of TKE pressure energy distribution and the zone of turbulence spreading. Moreover, the lower boundary of form-induced sub-layer shows as the energy access region.

Keywords Turbulence · Double-averaged · Form-induced sub-layer · Turbulent-kinetic-energy budget

J. Shounda (✉) · K. Barman
Department of Applied Mathematics With Oceanology and Computer Programming, Vidyasagar University, Midnapore, West Bengal 721102, India
e-mail: shoundajayanta40@gmail.com

K. Barman
e-mail: krishnendubarman07@gmail.com

1   Introduction

Open channel flow phenomenon over the hemispherical roughened bed is an important topic in hydraulic research. The various types of natural roughened objects are the causes of turbulence near the bed. The fundamental target of river hydrology is to analyze the stream-flow properties over armor layer roughness. Naturally, rock objects are the obstruction to the movement of water in streambed. To understand the flow biota interaction, classifications of flow layers, flow types, transportation of suspended sediment over various rough obstacle bed conditions and the highly heterogeneous 3D flow field over riverbed, the double-averaging method (DAM) are one of the most helpful tools in hydraulic research. To overcome the simple 2D assumptions problem, DAM is used taking into account the averaging over a certain area parallel to rough bed in addition to the averaging over time. The detailed explanation of this study can found in such following studies [1, 4–6, 9–12]. Importance of few spatially averaged flow parameters such as viscous drag, form-induced stresses and form-drag was discussed in the above-mentioned papers. For understanding of turbulence phenomenon over a gravel bed, it is necessary to discuss the third-order moments such as TKE flux and TKE budget. It has a significant application to analyze the study about transportation of sediment or containment diffusion. Over two k-type bed roughness conditions, Krogstadt and Antonia [7] concluded that the non-dimensional height $y/\delta \approx 0.04$ treated as the high-energy production zone compared to diffusion rate, but there were no significant effect showing for dissipation rate. Mignot et al. [8] experimented a TKE-related DA-study over one layer of broad crested stones. They observed that in between roughness crest, i.e., within interfacial sub-layer, maximum negativity of TKE flux arises and budget terms showing their maximum effect above the roughness crest. An experiment over a crested gravel-sediment roughened bed was also done by Mignot et al. [9]. They showed that maximum TKE diffusion and TKE production initiated at near roughness crest region and proved experimentally that total DA TKE production is half of that production of S-shaped class. After applying the downward seepage, the turbulence increased with higher TKE production, less TKE diffusion and less TKE dissipation and was also observed in a recent sediment-transportation study [3].

This present work illustrates the behavior of turbulence characteristics in a hemispherical rough bed flows for relative spacing $p/r = 6$ where p is the pitch length and $r \ (= 1.4 \text{ cm})$ is the height of the hemisphere. At first, we parameterized the velocity profile along stream-wise direction which also compared with the plane-bed normalized double-averaged velocity data. A polynomial function of the DA velocity profile for rough bed is fitted. The purpose of this work is to discuss about the turbulent kinetic energy (TKE)-related terms, such as primary TKE flux, form-induced TKE flux along longitudinal and wall-normal direction. Further, TKE-budget has also discussed by using graphical representation against normalized height (z/h) where z = measuring height and h = flow depth.

2 Experimentation and Measurement Technique

The experiments of hemispherical rough bed for relative spacing ($p/r = 6$) were conducted in the Department of Aerospace Engineering and Applied Mechanics at the fluid mechanics and hydraulics laboratory (FMHL), Indian Institute of Engineering Science and Technology (IIEST), Shibpur, Howrah, India. To get time-averaging flow components an acoustic Doppler velocimeter (ADV) is placed 11 m from the water source end of this straight tilting flume of 18.3 m length, 0.9 m broad and 0.9 m deep with a fixed slope 0.00025. A glassy side walls having 4 m length were fitted in the flume to visualize the noises of flow. A vertical turbine pump with capacity 0.3 m^3 sec^{-1} is used to supply of water in a fixed rate into the flume. At first, the data were recorded in 22 different heights in smooth bed with uniform flow for a particular position by using ADV at the distance 11 m from the upstream inlet. The spacing cases of pitch-to-height ratio $p/r = 6$ are usually known as k-type ratio, where $p =$ central distance of two hemispheres and $r =$ hemispherical radius (2.8 cm).

Three different directional velocity data at every selecting point were recorded for 3 min by SonTek 16 MHz micro-ADV with constant sampling frequency 40 Hz within a sampling space 0.09 cm^3, similar to Barman et al. [2]. There are 36 symmetrical measuring locations for this spacing as shown in Fig. 1c. Entire experiment was conducted for a fixed flow-depth, $h = 20$ cm and depth average velocity, $U_m = 29$ cm/s. Using the standard logarithmic law, the friction velocity or shear velocity, u_* ($= 1.38$ cm/s) for smooth bed was calculated by Deshpande and Kumar [3] (Table 1).

3 Methodology

In this present study, the right-handed coordinate system is introduced. Here, flow component parallel to rough bed (u), transverse velocity component (v) and bottom normal velocity component (w) is oriented along x-, y- and z-axis, respectively. Therefore, the instantaneous velocity components (u, v, w) in the (x, y, z) directions can be expressed in tensor notation as follows

$$u_i(x, y, z, t) = \bar{u}_i(x, y, z) + u_i'(x, y, z, t), \ \bar{u}_i = \frac{1}{n} \sum_{j=1}^{n} u_j \qquad (1)$$

where $\bar{u}_i$ is the time averaged velocity components and u_i' is the corresponding velocity fluctuations. But, when the double averaging concept are introduced, then the temporally averaged velocity distributions are written as the combination of spatial mean and spatial disturbance
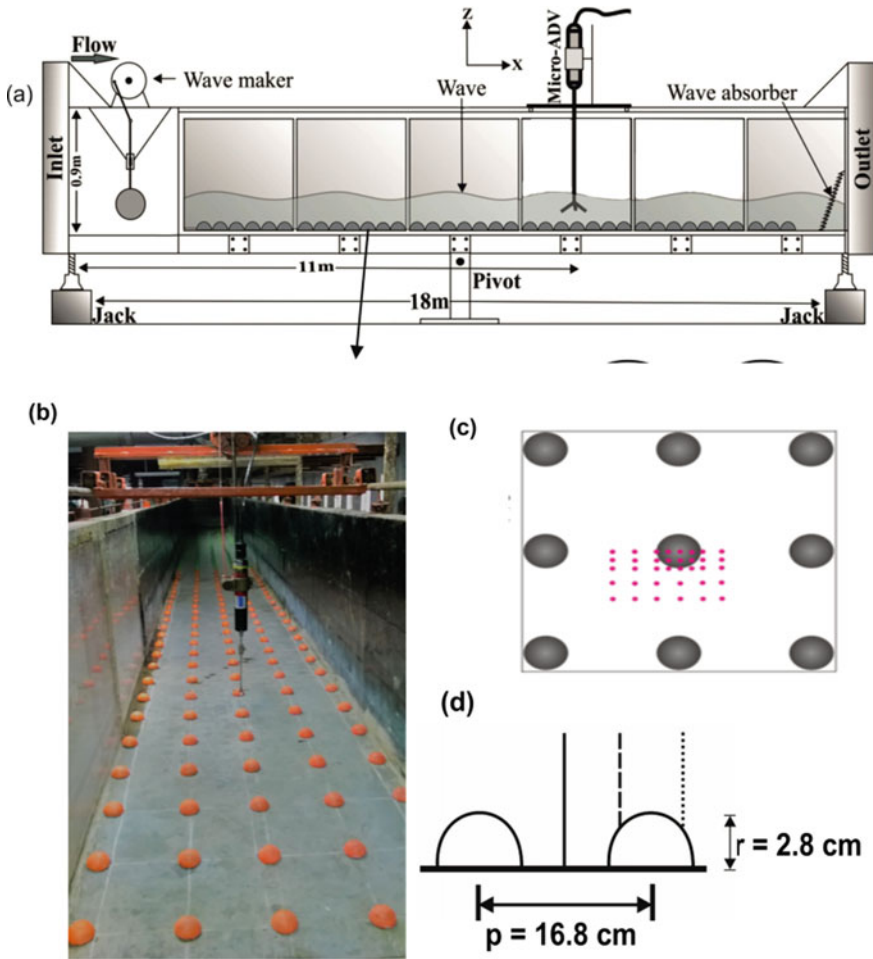
Fig. 1 a Experimental setup; **b–d** schematic diagram for the top view of *d*-type (*p/r* = 6) and measuring points

Table 1 Details experimental parameters

Experimental parameters	
Depth-averaged flow velocity, U_m (cm/s)	29.0
Mean flow depth, h (cm)	20.0
Flow Reynolds number, $R_e = U_m h/\upsilon$	62×10^3
Froude number, Fr	0.22
Friction velocity for flat-surface, u_* (cm/s)	1.38
Friction velocity for rough bed, u_* (cm/s)	2.25

$$\bar{u}_i(x, y, z) = \langle \bar{u}_i \rangle(z) + \tilde{u}_i(x, y, z), \ \langle \bar{u}_i \rangle = \frac{1}{n} \sum_{j=1}^{n} \bar{u}_j \qquad (2)$$

where $\langle \bar{u}_i \rangle$ is the spatial mean and fluctuation of spatial component is $\tilde{u}_i$. Third-order primary and form-induced moments terms can be calculated by the following formula

$$\left. \begin{aligned} \langle uvw \rangle &= \frac{1}{m} \sum_{j=1}^{m} (u_j - \bar{u}_j)(v_j - \bar{v}_j)(w_j - \bar{w}_j) \\ \langle \tilde{u}\tilde{v}\tilde{w} \rangle &= \frac{1}{m} \sum_{i=1}^{m} (\bar{u}_j - \langle u_j \rangle)(\bar{v}_j - \langle v_j \rangle)(\bar{w}_j - \langle w_j \rangle) \end{aligned} \right\} \qquad (3)$$

In case of turbulent kinetic energy budget, the summation of four terms, such as turbulent dissipation (ε), diffusion of energy (t_D, t_F), diffusion of pressure energy (p_D) and viscous diffusion (v_D) under the uniform flow condition, is balanced by the production term (t_P) Mignot et al. [8].

$$\underbrace{-\langle u'w' \rangle \frac{\partial \langle u' \rangle}{\partial z}}_{\text{production}(t_P)} = \underbrace{\langle \varepsilon \rangle}_{\text{dissipation}} + \underbrace{\frac{\partial \langle f_{\text{kw}} \rangle}{\partial z}}_{t_D} + \underbrace{\frac{\partial \langle f_{\tilde{k}\tilde{w}} \rangle}{\partial z}}_{t_F} + \underbrace{\frac{1}{\rho} \frac{\partial \langle \overline{p'w'} \rangle}{\partial z}}_{\text{pressure}(p_D)} - \underbrace{v \frac{\partial^2 \langle k \rangle}{\partial z^2}}_{\text{viscous}(v_D)} \qquad (4)$$

$$\underbrace{\phantom{\frac{\partial \langle f_{\text{kw}} \rangle}{\partial z} + \frac{\partial \langle f_{\tilde{k}\tilde{w}} \rangle}{\partial z}}}_{\text{TKE(diffusion)}}$$

where ρ, v and p' are fluid density, kinematic viscosity and pressure fluctuations. Again, f_{kw}, $f_{\tilde{k}\tilde{w}}$ are the upward directional primary and form-induced kinetic energy fluxes and k is the kinetic energy along z-direction. These relevant terms can be calculated by the following procedure

$$\left. \begin{aligned} \langle f_{\text{kw}'} \rangle &= \frac{1}{2} \left(\langle u'u'w' \rangle + \langle v'v'w' \rangle + \langle w'w'w' \rangle \right); \\ \langle f_{\tilde{k}\tilde{w}} \rangle &= \frac{1}{2} \left(\langle \tilde{u}\tilde{u}\tilde{w} \rangle + \langle \tilde{v}\tilde{v}\tilde{w} \rangle + \langle \tilde{w}\tilde{w}\tilde{w} \rangle \right); \\ \langle k \rangle &= \frac{1}{2} \left(u'^2 + v'^2 + w'^2 \right) \end{aligned} \right\} \qquad (5)$$

Further, stream-wise primary and form-induced TKE fluxes are defined as

$$\left. \begin{aligned} \langle f_{\text{ku}'} \rangle &= \frac{1}{2} \left(\langle u'u'u' \rangle + \langle v'v'u' \rangle + \langle w'w'u' \rangle \right) \\ \langle f_{\tilde{k}\tilde{u}} \rangle &= \frac{1}{2} \left(\langle \tilde{u}\tilde{u}\tilde{u} \rangle + \langle \tilde{v}\tilde{v}\tilde{u} \rangle + \langle \tilde{w}\tilde{w}\tilde{u} \rangle \right) \end{aligned} \right\} \qquad (6)$$

Deshpande and Kumar and Krogstadt and Antonia [3, 7] illustrated the formula for dissipation rate ($\langle \varepsilon \rangle$) for an uniform flow over a roughened bed

$$\langle \varepsilon \rangle = \frac{15\upsilon}{\langle \overline{u} \rangle^2} \left(\left\langle \sqrt{\overline{\frac{\partial u'}{\partial t}}} \right\rangle \right)^2 \tag{7}$$

The diffusion rate of pressure energy (p_D) can be formulated from Eq. (4) as

$$p_D = t_P - \langle \varepsilon \rangle - t_D - t_F \tag{8}$$

4   Results and Discussions

4.1   DA-velocity Distribution

It is seen from Fig. 2a–c that the normalized double-averaged velocity profiles ($U = \langle \overline{u} \rangle / u^*$, $V = \langle \overline{v} \rangle / u^*$ and $W = \langle \overline{w} \rangle / u^*$) change significantly due to the presence of hemispherical obstacles up to the form-induced sub-layer ($z/h = 0.3$), and thereafter, these profiles are quite similar to that of the flat rigid surface at the roughness free layer. The significance of some negative velocities near the bed region is the causes of recirculation and flow separation. However, it is shown in Fig. 2b, c that there is less significant flow effect in transverse and bottom-normal directions.

In between the non-dimensional height $z/h < 0.18$, the DA velocity profiles are approximately matched by a cubic polynomial function as follows

$$U(t) = -0.09t^3 - 1.5t^2 + 6t + 6.4 \tag{9a}$$

For the form-induced sub-layer ($0.18 < z/h < 0.29$), it follows a linear polynomial function as

$$U(t) = -1.4t^2 + 3.8t + 18 \tag{9b}$$

while for the rest of the region the DA downward velocity follows the linear model such as

$$U(t) = 0.25t + 21 \tag{9c}$$

From Fig. 3, it is shown the lower intersecting point of U-curve with vertical axis is below the origin for the relative spacing $p/r = 6$ which signifies the recirculation corresponding to negative velocity. Above the roughness zone, the linear law of DA velocity data implies the zone of less turbulence. It is concluded that this model is very helpful to analyze the idea of DA flow field over hemispherical roughened bed (Fig. 4).

Fig. 2 a–c represents the normalized spatially averaged velocity components ($U = \langle \overline{u} \rangle / u^*$, $V = \langle \overline{v} \rangle / u^*$ and $W = \langle \overline{w} \rangle / u^*$) over hemispherical rough beds
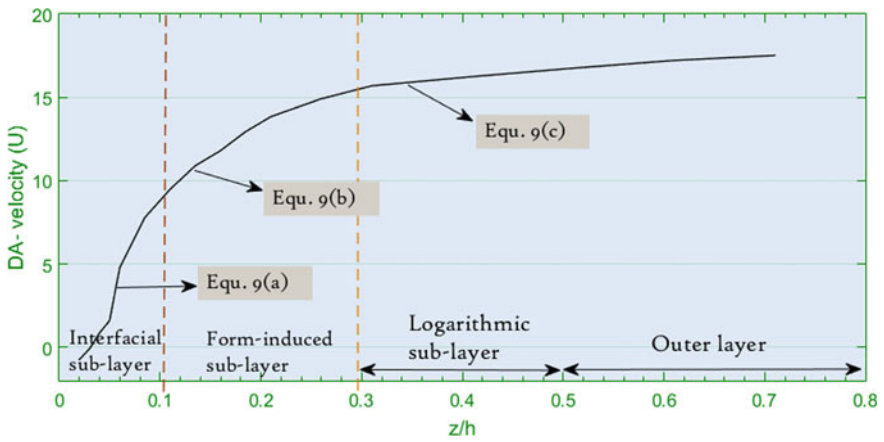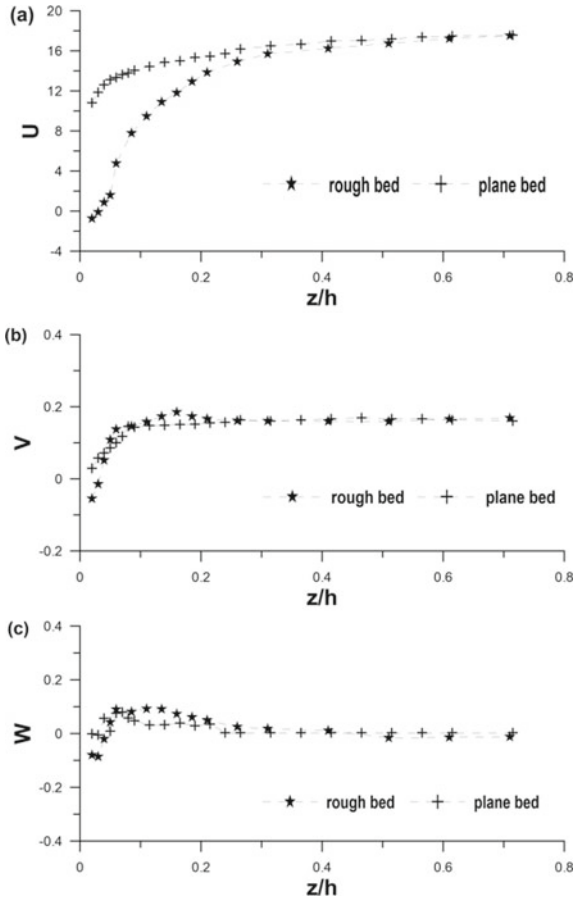
Fig. 3 Represents the model generated curve of spatially averaged velocity profiles for $p/r = 6$
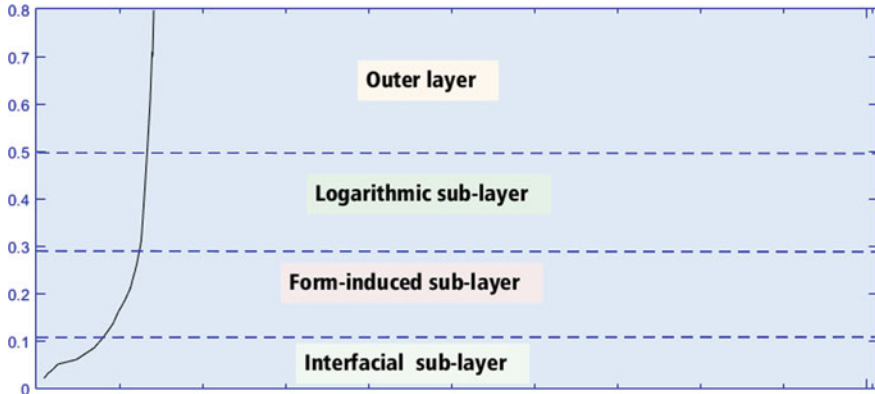
Fig. 4 Specific flow layers corresponding to flume height

4.2 TKE Flux

The longitudinal and upward directional primary TKE flux and form-induced TKE flux can be normalized by shear velocity as

$$\left.\begin{aligned} k_u = \langle f_{\text{ku}'}\rangle/u^{*3}, \, k_w = \langle f_{\text{kw}'}\rangle/u^{*3} \\ k_u^+ = \langle f_{\tilde{k}\tilde{u}}\rangle/u^{*3}, \, k_w^+ = \langle f_{\tilde{k}\tilde{w}}\rangle/u^{*3} \end{aligned}\right\} \tag{10}$$

Figure 5 represents the stream-wise and upward directional vertical profiles of non-dimensional primary TKE flux (k_u, k_w) and form-induced TKE flux $\left(k_u^+, k_w^+\right)$ against the flow-depth ratio z/h. The corresponding fluxes $\left(k_{up}, k_{wp}\right)$ profile with respect to plane bed experimental data is also represented in Fig. 5a.

The k_u profile starts with some positive values up to $z/h \approx 0.213$; thereafter, it becomes negatively decreasing to middle of logarithmic sub-layer. In between interfacial sub-layer, the peak values of k_u signifies the stream-wise flux transmitted downward in below the hemispherical tops. The negative values of k_u indicated that the upstream directional TKE transportation above the roughness layer. The stream-wise TKE flux transported in downstream direction was also observed by Mignot et al. [9]. Here, it is also showing that the starting some k_w-values are negative in between the interfacial sub-layer, and for rest of the region, it is positively increasing up to $z/h \approx 0.27$, and then, it is decreasing up to free surface. At the height $z/h \approx 0.064$, the highest negative k_w-values implies the normal flux transported strongly in upward direction, whereas for $z/h \approx 0.264$ it is showing strong normal flux transportation along downward direction. There is no significance change observed for the plan bed corresponding profile. Form-induced TKE flux along downward k_u^+ is initially observed as positively increasing to attaining a peak values at $z/h \approx 0.091$, and then, it decreases to zero values at middle-most form-induced sub-layer. After that, this profile negatively decreases up to the flow-depth $z/h \approx 0.412$ in between

Fig. 5 Horizontal representation of DA TKE flux along stream-wise and bottom-normal direction **a** primary kinetic energy fluxes; **b** form-induced kinetic energy fluxes
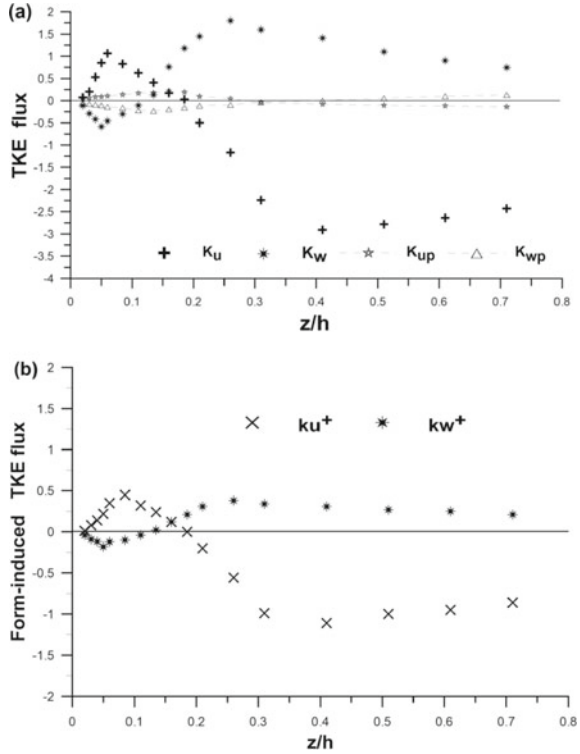
the logarithmic sub-layer, and then, it is quite increasing through free surface. All negative values of k_w^+ occur for the layer $0 < z/h < 1.421$, and for rest of the layers, this profile shows all positive values. It can be concluded that the strong transportation effect of k_u^+ and k_w^+ along upward direction is noticing at just above the interfacial sub-layer and just below the lower extremity of the form-induced sub-layer. Again, in the middle-most region of interfacial sub-layer and just above the lower-extremity of logarithmic sub-layer, these two characteristics shows their maximum effect along downward direction.

4.3 TKE-Budget

The ADV data also helps to analyze the estimation of TKE budget terms which have already been defined in Eq. (4). Due to presence of high Reynolds number, the viscous diffusion rate (v_D) is negligible. To transform the remaining terms into non-dimensional form, h/u^{*3} used as multiplier (Deshpande and Kumar [3]), and finally, the terms become:

$$T_P = \frac{t_P h}{u^{*3}}; \ E_D = \frac{\langle \varepsilon \rangle h}{u^{*3}}; \ T_D = \frac{(t_D + t_F)h}{u^{*3}}; \ P_D = \frac{p_D h}{u^{*3}} \tag{11}$$

All of these four budget terms are presenting graphically in Fig. 5 against the normalized height z/h. From Fig. 6a, it is shown that the trending of T_P-profile for relative spacing $p/r = 6$ and plane bed is quite similar. The highest peak values of T_P are attained at the flow-depth $z/h \approx 0.150$; i.e., this layer treated as the energy source region. Basically, this is the region where the flows of energy transported from temporal averaged flow to velocity fluctuations. In the upper layer of this above-mentioned flow-depth, the decreasing profile of production rate implies the efficiency of energy production is decreasing with increased flow-depth up to free surface. The plotting of non-dimensional dissipation rate in Fig. 6b represents that the conservation of internal energy increases from bottom region and attaining the maximum strength at the layer $z/h \approx 0.064$. Again, this energy conservation decreases along with increasing flow-depth up to just below the lower extremity of logarithmic sub-layer. The diffusion rate presentation in Fig. 6c is also looking as periodic trend with non-uniform period. The first negativity zone is occurring at $0 < z/h < 0.072$, , and above the form-induced sub-layer, there is second negativity field which is noticed, whereas for the region between the above-mentioned space is shown as positive diffusion field. So, it is concluded that the interfacial sub-layer and above the form-induced sub-layer there are less-spreading zone of turbulence, but here form-induced sub-layer is treated as zone of creation of turbulence effect. The pressure energy diffusion (P_D) rates are negatively decreasing up to attain the negative maximum value at $z/h \approx 0.14$ and after that it is increased for rest of the layer. The positive P_D-values start from the upper boundary of form-induced sub-layer, and maximum effect of pressure energy conservation is showing for the logarithmic layer. All of the cases, it is observed that there is not too much effect relevant to plane bed TKE budget-characteristics compared with the relative spacing data of $p/r = 6$.

5 Conclusions

The main focus of this work is to investigate the changes of turbulence properties against depth. This experiment has been completed under the uniform flow condition over hemispherical rough bed, and the relevant has been calculated by DAM. The resulting output of spacing case $p/r = 6$ has also been compared with corresponding plane-bed experimental DA data with vertical representation against flow-depth ratio z/h. Some of the important findings are as follows:

i.   It has noticed that the normalized double-averaged velocity profiles changes rapidly up to the form-induced sub-layer ($z/h = 0.3$) and above this layer the curve coincides with the smooth-bed velocity profile through the free surface. Some negative velocities in between interfacial sub-layer create recirculation and flow separation. The flow effects in transverse and normal directions are

Fig. 6 Vertical representation of turbulent kinetic energy budget terms **a** production rate (T_P) **b** dissipation rate (E_D) **c** diffusion rate (T_D) **d** pressure energy diffusion (P_D)
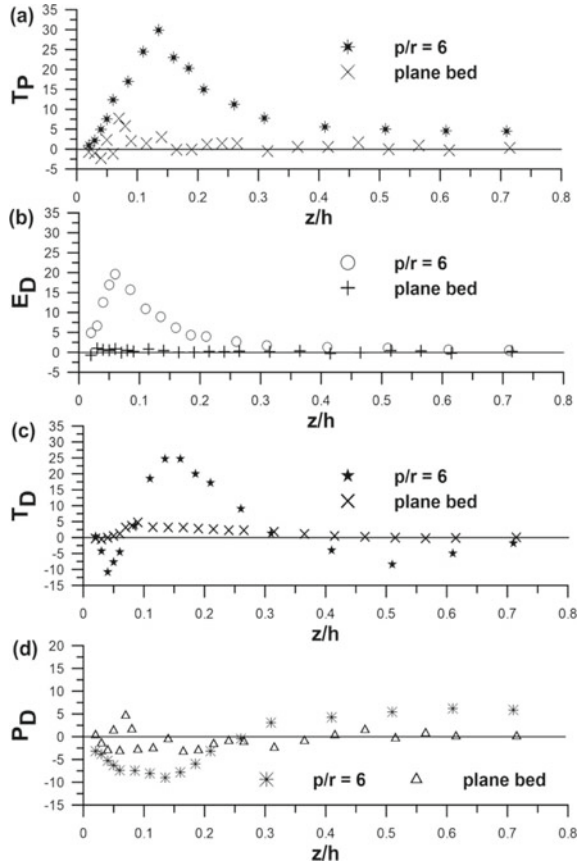
not considerable. A model of polynomial fitting also shows for this DA velocity data for different three zones.

ii. The maximum strength of stream-wise TKE flux directed to downward direction is occurring in interfacial sub-layer corresponds to peak positive k_u-value. The upstream directional TKE transportation also shows at just above the roughness layer caused by the peak negative value of k_u. At the height $z/h \approx 0.064$, the normal flux is transported strongly in upward direction, whereas it is strongly directed in downward at the depth ratio $z/h \approx 0.264$. There is no significance change is observing for the plan bed corresponding profile.

iii. Two zones are noticing for the strong transportation effect of k_u^+ and k_w^+ along upward direction such as at just above the interfacial sub-layer and just below the lower extremity of the form-induced sub-layer. Again, middle-layer of the interfacial sub-layer and just above the lower extremity of logarithmic sub-layer is also treated as the maximum downward effect zone corresponding to k_u^+ and k_w^+, respectively.

iv. The strengthened energy source region is observed at the flow-depth $z/h \approx$ 0.150 corresponding to highest peak values of T_P. The conservation of internal energy increases from bottom region and attains the maximum strength at the layer $z/h \approx 0.064$. The interfacial sub-layer and above the form-induced sub-layer are the less-spreading zone of turbulence, whereas form-induced sub-layer is considering as zone of turbulence creation. The positive P_D-values start from the upper boundary of form-induced sub-layer and maximum effect of pressure energy conservation is showing for the logarithmic layer.

References

1. Aberle J, Nikora V, Henning M, Ettmer B, Hentschel B (2010) Statistical characterization of bed roughness due to bed forms: a field study in the Elbe River at Aken, Germany. Water Resour Res 46:1–11

2. Barman K, Roy S, Debnath K (2018) Wave-current generated turbulence over hemisphere bottom roughness. Estuarine Coastal Shelf Sci 202:1–17

3. Deshpande V, Kumar B (2015) Turbullent flow structures in alluvial channels with curved cross-sections of downward seepage. Earth Surf Proc Land 41:1073–1087

4. Ferreira RML, Ferreira LM, Ricardo AM, Franca MJ (2010) Impacts of sand transport on flow variables and dissolved oxygen in gravel-bed streams suitable for salmonid spawning. River Res Appl 26:414–438

5. Ferreira RML, Ferreira LM, Ricardo AM, Franca MJ, Leal GAB, Cardoso AH (2012) Flow over rough mobile beds: Friction factor and vertical distribution of the longitudinal mean velocity. Water Resour Res 48:1–14

6. Gime´nez-Curto LA, Corniero-Lera MA (2002) Flow characteristics in the interfacial shear layer between a fluid and a granular bed. J Geophys Res 101(C9):20,745–20,758

7. Krogstadt PA, Antonia RA (1999) Surface roughness effects in turbulent boundary layers. Experimentsin Fluids Springer 27:450–460

8. Mignot E, Barthelemy E, Hurther D (2008) Turbulent kinetic energy budget in gravel-bed channel flow. Inst Geophys Polish Acad Sci 56(3):601–613

9. Mignot E, Barthelemy E, Hurther D (2009) Double-averaging analysis and local flow characterization of near-bed turbulence in gravel-bed channel flows. J Fluid Mech 618:279–303

10. Nikora V, Goring D, McEwan I, Griffiths G (2001) Spatially averaged open-channel flow over rough bed. J Hydraul Eng 127(2):123–133

11. Nikora V, McEwan I, McLean S, Coleman S, Pokrajac D, Walters R (2007) Double averaging concept for rough bed open-channel and overland flows: theoretical background. J Hydraul Eng 133(8):873–883

12. Papadopoulos K, Nikora V, Cameron S, Stewart M, Gibbins C (2019) Spatially-averaged flows over mobile rough beds: equations for the second order velocity moments. J Hydraul Res 58(1):133–151

13. Papadopoulos K, Nikora V, Vowinckel B, Cameron S, Jain R, Stewart M, Gibbins C, Fröhlich J (2019) Double-averaged kinetic energy budgets in flows over mobile granular beds: insights from DNS data analysis. J Hydraul Res 58(4):653–672

Quantification of Wake Vortices Around Tandem Piers on Rigid Bed Channel

L. N. Pasupuleti, P. V. Timbadiya, and P. L. Patel

Abstract The current study focused on the strengths of wake vortices diffuse from pier boundary through velocity power spectra at 5, 30, and 50% of flow depth for piers arranged in tandem configuration. The experimental investigations were carried using the instantaneous 3D velocity measurements, undertaken using 16 MHz micro down looking Acoustic Doppler Velocimeter (ADV) at different grids along with flow depth for single and tandem piers. The measurements around two piers having the same diameter (separated by longitudinal distance $2d$) ($d = 8.8$ cm) at different levels of flow depth have been carried out and made comparison with a single pier on rigid bed condition under same flow conditions. The analysis of velocity power spectra is used to identify the inference of wake vortices of one pier over others in tandem arrangement vis-à-vis a single pier. The results reveal that the strengths of wake vortices are decreased by 2.5 times at level 5% of flow depth for the front tandem pier than that of a single pier. These strengths are increased while moving away from the bed in both cases. Further, the Strouhal number (St) of single and tandem piers are 0.15 and 0.11, respectively. It can be seen that, for a single pier case, at each level, the velocity power spectra are distinguished. Whereas for tandem piers, the maximum strengths are distributed among the piers and resulted in lower peaks. The study concluded that a significant decrease of wake vortices between tandem piers might lead to the occurrence of minimum scour around the tandem rear pier.

Keywords Tandem arrangement · Wake vortices · Velocity power spectra · Strouhal number

L. N. Pasupuleti (✉)
Department of Civil Engineering, Aditya Engineering College, Surampalem, India
e-mail: laxmiraagini@gmail.com

P. V. Timbadiya · P. L. Patel
Department of Civil Engineering, Sardar Vallabhbhai National Institute of Technology, Surat, India
e-mail: pvtimbadiya@ced.ac.in

P. L. Patel
e-mail: plpatel@ced.ac.in

1 Introduction

For safe design of the bridge pier, it is necessary to understand the mechanism of horseshoe vortex and wake vortices which are prime responsible for formation of local scour around the pier. The understanding of such vortices formed around the piers, around closely spaced bridge piers will be different from single pier [1], wherein, the turbulence behind the front piers of parallel pier arrangements is different form turbulence behind single pier under identical flow conditions. Moreover, the studies on flow characterization around the piers, particularly, piers arranged in tandem and staggered configuration is one of the active topics in coastal engineering. In past, few studies were focused on turbulence characterization around tandem piers. Wherein [2] found, turbulence kinetic energy, turbulence intensities and Reynolds shear stresses were decreased behind the front pier in tandem arrangement ($S/d = 3$, where, S was the center-to-center spacing, d is diameter of the pier) in comparison to single pier using Acoustic Doppler Velocimeter (ADV) on rigid beds. The effect of skew angles ($\theta = 0°, 30°, 45°, 60°, 90°$) on local scour with respect to flow direction around tandem piers ($S/d = 2$) was investigated by [3, 4]. They found, at 45°, the maximum scour depths occurred at both the piers and suggested 30° is the best alignment for rear pier position in tandem configuration. Keshavarzi et al. [5] explored Reynolds shear stresses, turbulence intensities, and turbulence kinetic energy and around tandem piers ($S/d = 2.5$) using Particle Image Velocimeter (PIV). They found, large turbulence was produced behind the front pier vis-à-vis single pier. Vijayasree et al. [6] explored flow characterization around single, tandem, and oblong piers using ADV. They concluded, turbulence kinetic energy, Reynolds shear stress, and turbulence intensities are significantly decreased behind the oblong pier vis-à-vis tandem front and isolated pier. Few studies [7–15] were focused on turbulence fields around the single pier and identified strong turbulence behind the pier.

Extensive experimentations were undertaken on scour around single pier to estimate the scour depth. The studies focused on turbulence fields around the closely spaced tandem piers and shown the best alignments of rear pier position. However, the vortices formed around the tandem piers, particularly in the wake regions of both front and rear piers are scarce in the literature. The limited availability of studies on quantification of wake vortices around tandem piers, motivated the authors to carry the present study. The objective of the present study is to quantify the strengths of wake vortices shed from the pier boundary through velocity power spectra at 5, 30, and 50% for a given flow depth in both front and rear pier of tandem arrangement, and compared the same with single pier under identical flows.

2 Materials and Methods

2.1 Experimental Set-Up

A recirculation sediment transport flume (15 m long, 0.89 m wide, and 0.6 m height) was used to carry out the experiments, situated at Advance Hydraulics Laboratory in the department of Civil Engineering, Sardar Vallabhbhai National Institute of Technology, Surat, Gujarat, India, plan and elevation of flume is shown in Fig. 1 [16]. A 8.0 m long glass sided walls were fixed for clear view of flow. To allow the smooth flow over the working section of 6 m, 2 honey comb cages separated by 1.0 m are placed at the inlet. The flow depth over the working section will be maintained by tail gate, which is situated at the outlet of the flume. The steady uniform flow over the working section will be maintained through SCADA system.
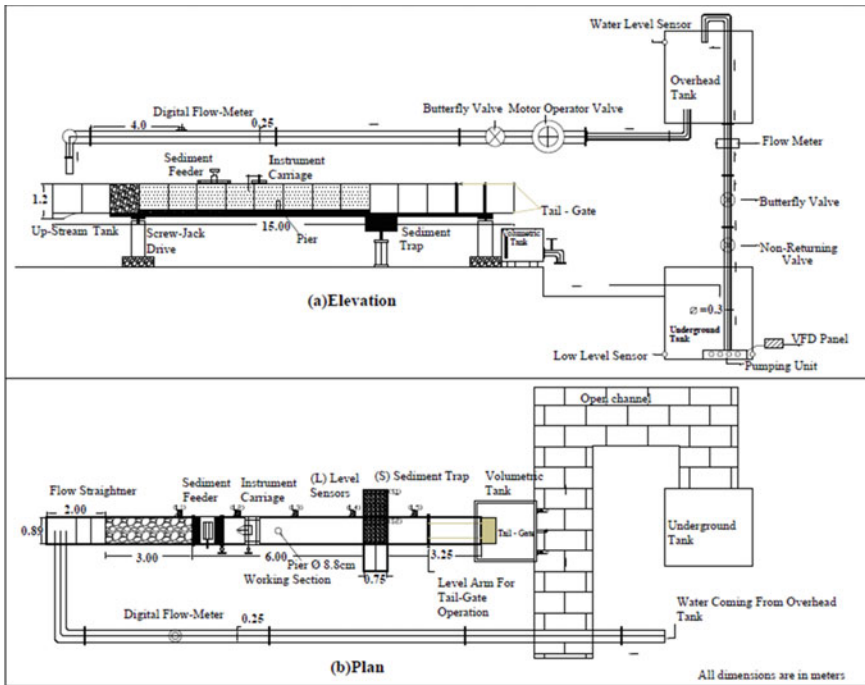
Fig. 1 Schematic of experimental set-up **a** elevation, **b** plan

Table 1 Flow conditions used in the experimentation

Discharge (m³/s)	Flow depth (Z_0) (m)	Flow Reynolds No., Re (10^4)	Mean approaching flow velocity (U) (m/s)	Diameter of pier (m) (d)	Longitudinal slope (10^{-4})
0.022	0.105	2.47	0.235	0.088	3.8

2.2   Instrumentation and Data Collection

In current study, experiments were performed over the rigid bed, wherein a single pier (d = 8.8 cm) was glued over the channel bottom, positioned at 8.0 m from the inlet. The flow conditions (see Table 1) were maintained constant during all the experiments. The instantaneous 3D velocity measurements, undertaken using 16 MHz micro down looking Acoustic Doppler Velocimeter (ADV) was used to collect three-dimensional velocities around the pier at different grids (see Fig. 2). Here, u, v, w in X, Y, Z directions are expressed as $u = \bar{u} + u'$, $v = \bar{v} + v'$, $w = \bar{w} + w'$, where $\bar{u}$, $\bar{v}$, $\bar{w}$ are time-averaged velocities, and u', v', w' are fluctuating components in X, Y, Z directions. Here, X is longitudinal, Y is transverse, and Z is vertical flow direction. After the collection of data around single pier, the pumps were stopped and flume was allowed to drain. The rear pier was positioned at S/d = 2, here, S, center-to-center spacing, and collected the three-dimensional velocity data around front and rear piers under identical flow conditions (Fig. 3b). The collected raw data were processed to remove the noise, and velocity signals were de-spiked using a phase space threshold de-spiking technique (Fig. 4). Similar technique was adopted in the previous studies [17–19] for de-spiking the velocities. The detrended de-spiked signals need to check on Kolmogorov's scale for successful capturing of inertial subrange. The three-dimensional velocity profile plotted on Z/Z_0 v/s U^+, V^+, W^+, (see Fig. 5). Here, $U^+ = \bar{u}/U$, $V^+ = \frac{\bar{v}}{U}$, and $W^+ = \bar{w}/U$. From Fig. 5, it depicts, measured velocity profile U^+ at 1.0 m distance from the upstream pier follows the log law up to flow depth of 5.5 cm from the channel bottom. On other hand, the variation of V^+ and W^+ are nearer to zero. This can be ascertained that flow was developed in the working section.

3   Results and Discussion

In current study, the power spectra analysis was carried to quantify the wake vortices defused from pier boundary in single and tandem piers, shown in Fig. 6 and Fig. 7, respectively. Here, the velocity power spectra were computed at different levels, 5% (Z = 0.525 cm), 30% (Z = 3.15 cm), and 50% (Z = 5.25 cm) of flow depth using detrended velocity signals with the help of the Fast Fourier Transform (FFT) packages available in the Origin-2019b. Here, the computed spectra was multiplied
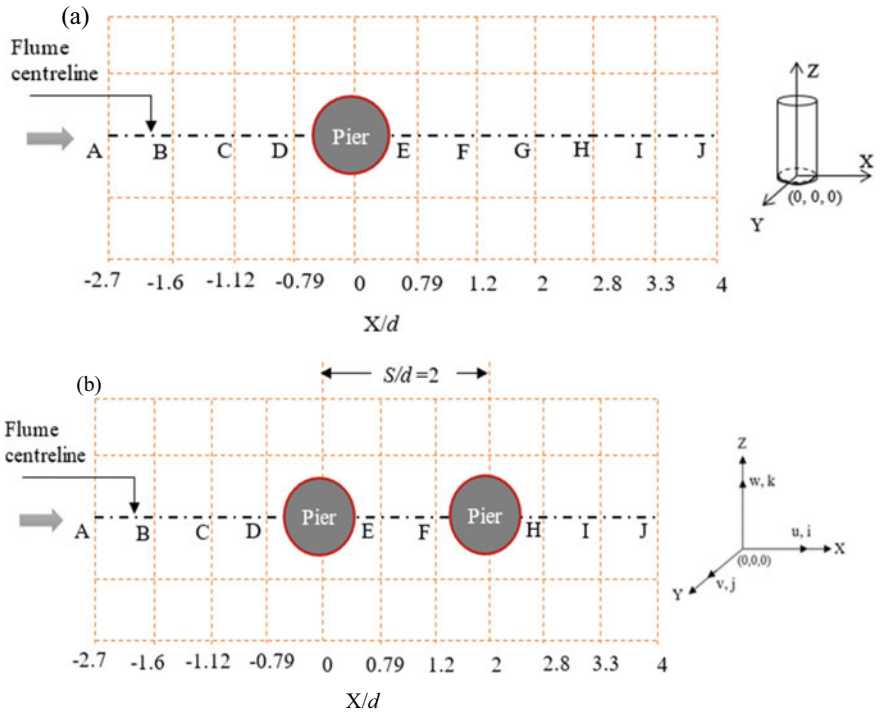
Fig. 2 Schematic of ADV data collection for **a** single pier and **b** tandem piers
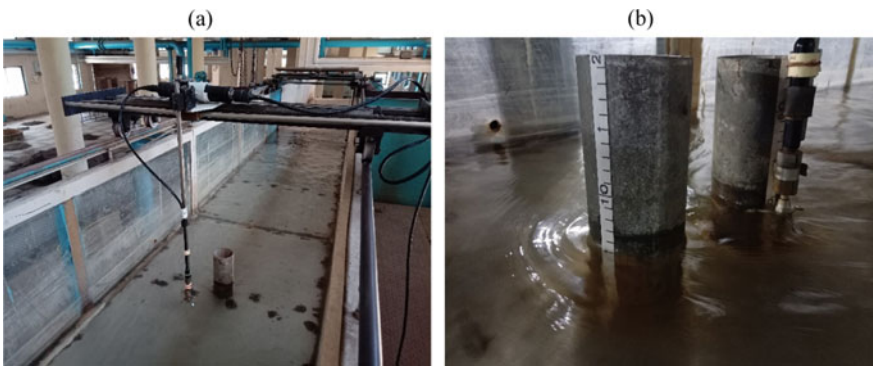
Fig. 3 Photographs of ADV data collection for **a** single pier and **b** tandem piers
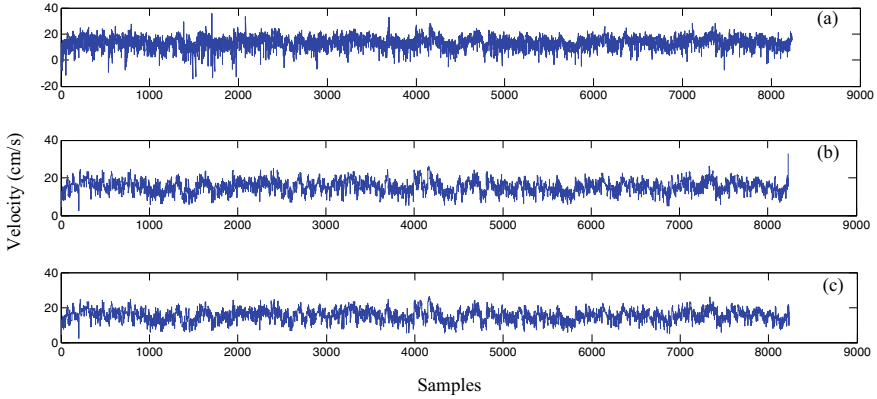
Fig. 4 **a** Sample time series of velocity measurement **b** cubic interpolated time series after removal of noise contamination **c** de-spiked and cubic interpolate time series
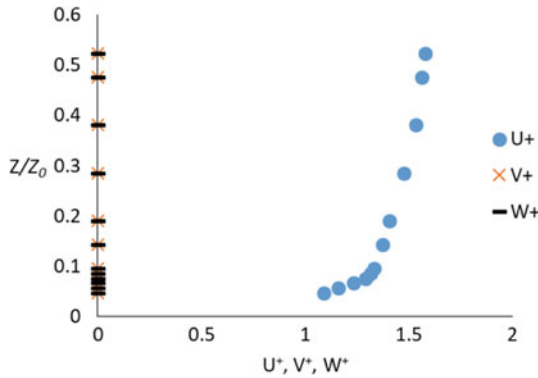
Fig. 5 Velocity distribution over rigid bed at 1 m upstream of single pier

with corresponding frequency [$f.P_u(f)$, $f.P_v(f)$, and $f.P_w(f)$ (cm^2/s^2)] to present the spectra in variance preserve form for streamwise, transverse, and vertical velocity components, respectively. To quantify the strength of wake vortices behind the piers of single and tandem arrangements, the Strouhal number (St) is computed using St $= fd/U$, where f is the dominant vortex shedding frequency, d is the diameter of pier, U is the approaching mean flow velocity [2, 17, 19]. From Figs. 6 and 7, it can be seen that the dominant component is transversal velocity component ($f.P_v(f)$) in the wake regions of single and tandem piers (for locations, refer, Fig. 2). Whereas other two velocity components (streamwise and vertical) are shown weak strengths at corresponding locations.

The velocity power spectra reveals, the strength of wake vortices is significantly decreased at front tandem pier vis-à-vis single pier. It is observed that the transversal component is 2.5 times higher for single pier as compared to front tandem pier.
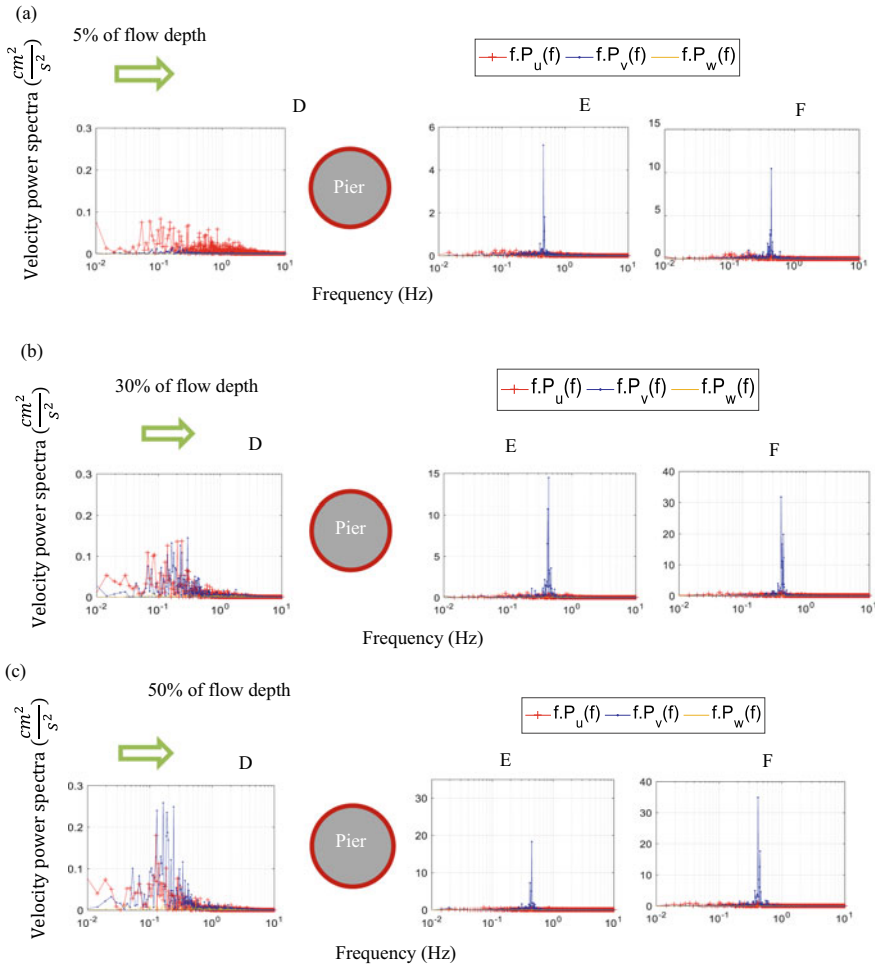
Fig. 6 Velocity power spectra at flow depths **a** 5%, **b** 30%, and **c** 50%, at flume centerline around the single pier

Further, these strengths are increased with level while moving away from the bed. The maximum strengths are seen at 50% ($Z = 5.25$ cm) and minimum are observed at 5% ($Z = 0.525$ cm) for single and tandem piers. Further, the Strouhal number reveals, the large size eddies are formed behind the single pier with St $= 0.15$ as compared to front tandem pier (St $= 0.11$). It can be seen; the size of eddy is increased by 35% behind the single pier vis-à-vis front tandem pier. The eddies of small size cause high-frequency fluctuations, whereas larger eddies cause small-frequency fluctuations [20]. The high frequency of all three components of velocity fluctuation in downstream of the front pier in single and tandem arrangements indicated the presence of smaller eddies in the region. It is to be noted that large size of the eddy is governed by the size of the
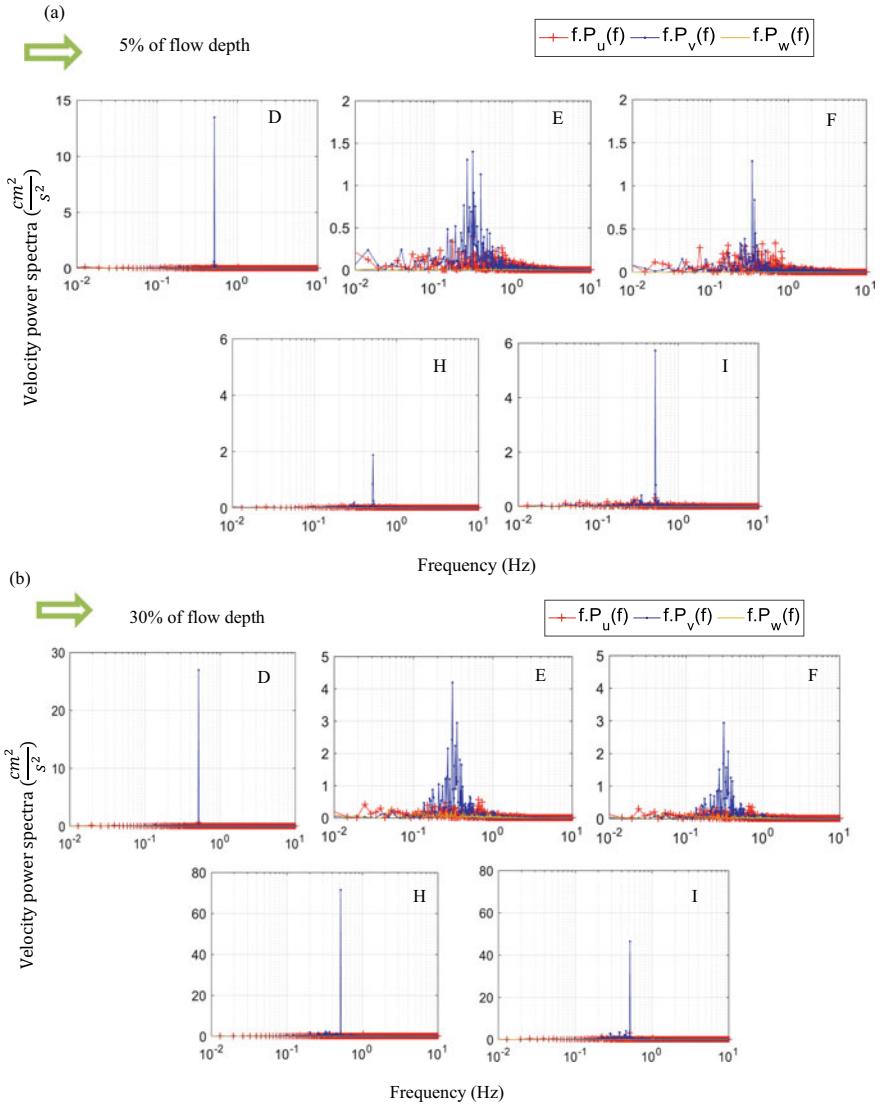
Fig. 7 Velocity power spectra at flow depths **a** 5%, **b** 30%, and **c** 50%, at flume centerline around the tandem pier

flow depth itself, whereas the smallest size of the eddy is determined by viscosity, and it decreases with an increase in average velocity of flow [21]. The comparisons of spectra in the front pier and rear pier of tandem arrangement depicted, the strengths are increased significantly as compared to the front pier, as and when the fluid particles reached to rear pier. Due to the significant decrease in strength of wake vortices between tandem piers, results to have a minimum scour around the tandem rear pier.
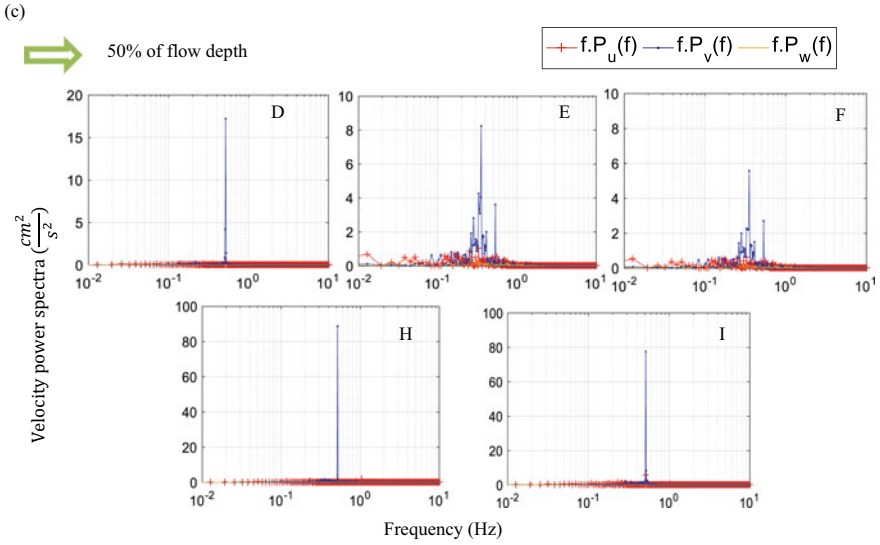
Fig. 7 (continued)

4 Conclusions

The following conclusions are drawn from the current study:

- The wake vortex strength has been found 2.5 times higher in single pier than front tandem pier. These strengths are increased with level and found maximum at 50% ($Z/Z_0 = 0.5$) in single and tandem piers.
- Transversal velocity component is dominant one, and other two velocity components (streamwise and vertical) are shown weak spectra in the wake regions of single, front, and rear piers of tandem arrangement.
- The Strouhal number, St is 0.15 and 0.11 for single and front tandem pier, respectively. It reveals, the large size eddies are formed behind the single pier vis-à-vis front tandem pier. Due to the significant decrease of wake vortex strength between tandem piers might lead to the occurrence of minimum scour around the tandem rear pier.

References

1. Zhou K, Duan JG, Bombardelli FA (2020) Experimental and theoretical study of local scour around three-pier group. J Hydraul Eng 146(10):04020069
2. Ataie-Ashtiani B, Aslani-Kordkandi A (2013) Flow field around single and tandem piers. Flow Turbul Combust 90(3):471–490
3. Memar S, Zounemat-Kermani M, Beheshti A A, De Cesare G, Schleiss AJ (2018) Investigation of local scour around tandem piers for different skew-angles. E3S Web Conf 40:03008
4. Hannah CR (1978) Scour at pile groups. Research Report 28–3, University of Canterbury, Christchurch, New Zealand
5. Keshavarzi A, Ball J, Khabbaz H, Shrestha CK, Zahedani MR (2018) Experimental study of flow structure around two in-line bridge piers. Proc Inst Civ Eng Water Manage 171(6):311–327
6. Vijayasree BA, Eldho TI, Mazumder BS (2019) Turbulence statistics of flow causing scour around circular and oblong piers. J Hydraul Res 57(6):1–14
7. Dargahi B (1989) The turbulent flow field around a circular cylinder. Exp Fluids 8:1–12
8. Graf WH, Istiarto I (2002) Flow pattern in the scour hole around a cylinder. J Hydraul Res 40(1):13–20
9. Muzzammil M, Gangadhariah T (2003) The mean characteristics of horseshoe vortex at a cylindrical pier. J Hydraul Res 41(3):285–297
10. Kirkil G, Constastantinescu G, Ettema R (2008) Coherent structures in the flow field around a circular cylinder with scour hole. J Hydraul Eng 134(5):572–587
11. Dey S, Raikar RV (2007) Characteristics of horseshoe vortex in developing scour holes at piers. J Hydraul Eng 133(4):399–413
12. Kumar A, Kothyari UC (2012) Three-dimensional flow characteristics within the scour hole around circular uniform and compound piers. J Hydraul Eng 138(5):420–429
13. Ataie-Ashtiani B, Aslani-Kordkandi A (2012) Flow field around side-by-side piers with and without a scour hole. Europ J Mech Fluids 36:152–166
14. Graf WH, Yulistiyanto B (1998) Experiments on flow around a cylinder: the velocity and vorticity fields. J Hydraul Res 36(4):637–653
15. Gautam P, Eldho TI, Mazumder BS, Behera MR (2019) Experimental study of flow and turbulence characteristics around simple and complex piers using PIV. Exp Thermal Fluid Sci 100:193–206
16. Pasupuleti LN, Timbadiya PV, Patel PL (2020) Bed level variations around the submerged tandem piers in sand beds. ISH J Hydraul Eng 28(1):149–157
17. Sarkar K, Chakraborty C, Mazumder BS (2016) Variations of bed elevations due to turbulence around submerged cylinder in sand beds. Environ Fluid Mech 16(3):659–693
18. Pasupuleti LN, Timbadiya PV, Patel PL (2021a) Vorticity fields around a pier on rigid and mobile bed channels. ISH J Hydraul Eng 1–10
19. Pasupuleti LN, Timbadiya PV, Patel PL (2021) Flow field measurements around isolated, staggered, and tandem piers on a rigid bed channel. Int J Civ Eng 20:569–586
20. Garde RJ (1994) Turbulent flow. New Age International Limited. New Delhi
21. Garde RJ (2005) River morphology. New Age International Publishers, New Delhi

Evaluation of Selected Bed Load Transport Equation for Different Representative Sediment Sizes in Mountain Rivers

Vipinkumar Yadav and Sanjaykumar M. Yadav

Abstract Bed load transport is a significant phenomenon in natural streams. The size of sediment moving with the flow varies in size and mode of travel accordingly. The flow characteristics varies much in plains and mountain terrain. The bed size composition in mountain rivers is dominated by cobbles and gravels with coarse sand. The large sediments move as bed load and continuously cause the changes in bed profile. Therefore, the bed load transport is important parameter in design of hydraulic structures in mountain areas. The size of sediment moving as bed load depends largely on flow velocity and bed shear stresses. Many empirical relations were suggested by various researchers to estimate the bed load transport rate in the open channel flow. Many of these relations were based on laboratory simulations. The validity of these equations is inconsistent for varying site conditions and need much calibration through field measurements. In present study, the bed load was measured along with other related hydraulic parameters like flow velocity, flow depth, and bed load concentration. The grain size distribution was analyzed to obtain mean sediment size and other representative diameters. Einstein and Brown (1950) bed load equation was tested to observe the variation in prediction of bed load transport rate using the different representative sediment sizes. Statistical measures were used to assess the performance variation.

Keywords Bed load transport · Empirical equations · Sediment size · Mountain river · Field measurement

V. Yadav (✉) · S. M. Yadav
Department of Civil Engineering, Sardar Vallabhbhai National Institute of Technology Surat, Surat 395007, India
e-mail: vkygecs@gmail.com

S. M. Yadav
e-mail: smy@ced.svnit.ac.in

1 Introduction

Sediment transport is an important process in open channels. The natural alluvial channels inherently consist of loose alluvium, which moves along with the flow of water under favorable condition. Bed load is a significant contributor of total load transported in a mountain river. The measurement and estimation of sediment transport in a river at different locations is necessary for effective design of various hydraulic structures like culver, bridge, and dam. Sediment flow also affects the morphology of a river. With changing pattern of erosion and deposition of sediment in the flow, the river changes its course and becomes braided. The extent of such changes depends on many factors like size and distribution of sediments in bed and boundaries, the quantity and velocity of flow discharge, the cross-sectional capacity, etc. The continuous deposition of sediment by the river at any point may lead to severe reduction in channel carrying capacity leading to overflow at higher discharge and thus causing flooding in adjacent areas. The rivers bring sediment from upper catchment during rainfall and may deposit these at downstream obstructions.

Mountain streams are characterized by higher flow rates with less discharge. The bed of such rivers generally have high slope and bed consists of large rocks, boulders, and cobbles. Under favorable conditions the bed sediment start moving with the flow and get deposited at some downstream point, with another such movement under next favorable condition called incipient motion condition. The incipient conditions do not remain fixed for any size of sediment, and they may vary due to the dynamic combination of flow rate, sediment size, orientation of sediment, hiding and sheltering, vegetation, local slope, etc. "Bedload transport is known to be a highly fluctuating temporal phenomenon, even under constant (mean) flow conditions, as a consequence of stochasticity in bedform migration, grain sorting, hysteresis or sediment supply" [1]. The empirical equations used for predicting bed load have varied success for mountain rivers. Many of these existing bed load equations originated from theoretical understanding or experimentation in controlled laboratory environment. While testing on real field rivers, such equations have not been able to predict bed load transport rates with good accuracy, indicating the need of further research in this area based on field observations. Reliable prediction of bed load transport rate with good accuracy is still not achieved [2].

Because of the influence of the hiding factor, the results obtained, particularly in gravel bed rivers, are less reliable than those obtained in sand bed rivers [3]. "In a non-uniform mixture, the relative size effect tends to increase the transport rate of larger grains and decrease the transport rate of smaller grains. The extent of the relative size impact, and hence the transport rate of particular sizes within a mixture, will be influenced by the mixture's composition, which can alter during transport and in relation to the change in flow and sediment supply. The distribution of grain sizes available for transport must be taken into account in a quantitative model for mixed-size transport" [4]. The uniform bed load transport equations developed by various researchers are based on some single representative sediment size taken as dominant size for calculating the sediment transport in a given river. Though less

accurate than non-uniform sediment transport equations which considers the relative presence of different sediment size in motion, the uniform sediment transport equations are much simpler and gives relatively good prediction. However, for accurate prediction of prevailing sediment transport in any river for the purpose of hydrologic or hydraulic planning, it is desirable to test and calibrate existing uniform and non-uniform sediment transport equations based on the field measured data. In India, the measured field data for bed load transport is lacking by a great measure.

In the present study, performance of some uniform bed load equations has been tested for different representative size of bed load sediments moving in the Ver River based on field measured geometric, hydraulic, and sediment data.

2 Materials and Methods

2.1 Study Area and Data Collection

2.1.1 Ver River

"The Ver stream originates from the Khoramba Mountain and meets the Tapi River in its downstream. The bed load has been measured at Ver stream located near the Godavadi village in Mandvi region Surat, India (21.258731 °N, 73.219994 °E). The stream bed is made up of sand, gravel, and cobble. The flow depth at the site is around 0.50–1.2 m [1]. Figure 1 shows the satellite view of the study reach with extent of cross-sections on both sides of the culvert and Fig. 2 shows the field view of Ver stream during monsoon.

2.1.2 Data Collection

Field measurements were done at eight cross-sections of Ver stream at selected site (Fig. 3). Five cross-sections were taken u/s of causeway and three sections were selected d/s of it. Figure 2 shows points of cross-sections where the hydraulic parameters, such as flow depth, velocity, and sediment parameter, bed load were measured simultaneously at every cross-section. Bed load was measured by USGS-modified HS bed load sampler. The slope of channel bed was measured between each cross-section using dumpy level and staff [1].

The bed load samples were collected from August 24 2016 to September 29 2016. Three methods are suggested for systematic collection of the sample, i.e., single equal width increment (SEWI), multiple equal width increment (MEWI), and unequal width increment (UWI) method [5]. In the present study, UWI method of bed load measurement has been used as the selected river reach consists of highly undulated bed surface and the distance between two sampling points varies due to changes in cross-section width at selected points [1].
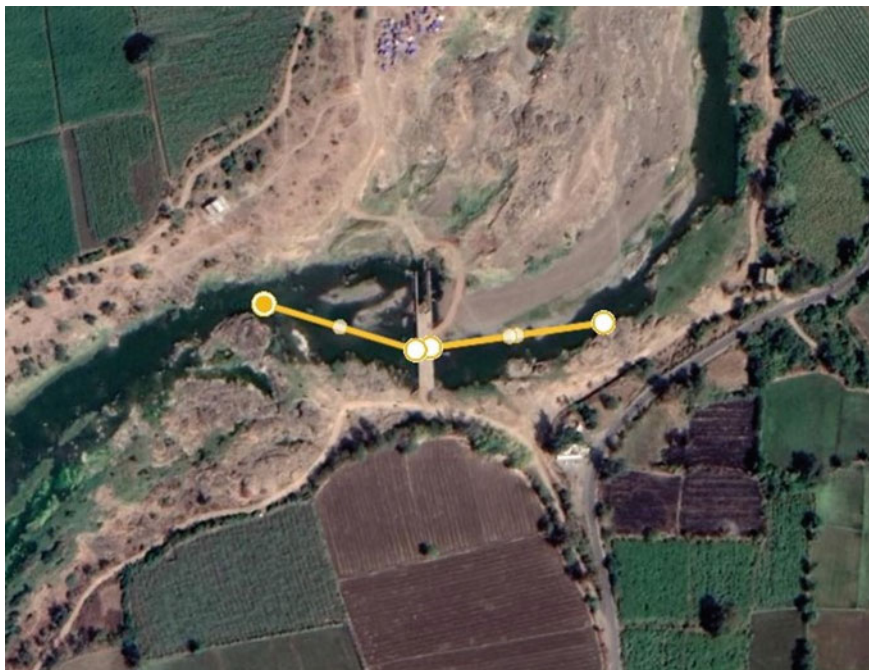
Fig. 1 Satellite view of study reach of Ver River with end points of sections

Fig. 2 Field view of Ver River during monsoon [1]
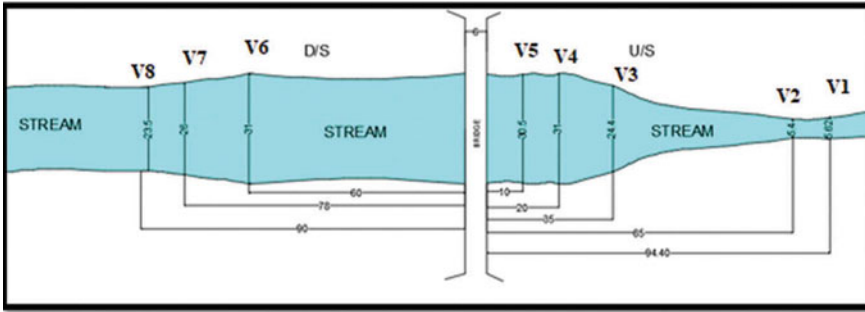
Fig. 3 Cross-sections along study reach of Ver River

The sampling time was kept 10 min. The velocity of flow was measured in m/s by using a propeller type current meter. To measure channel bed slope, two cross-sections were selected and water surface along cross-section was measured. The slope value with respect to central axis was measured by dividing the difference of water surface measured at cross-section with the distance between two cross-sections [1]. A summary of observed hydraulic and sediment parameters is given in Table 1.

Table 2 presents the various sediment size within the distribution of sediment samples collected at selected cross-sections [1].

For quick comparison, the lateral variation of bed load (g/s/m) at cross-section V1 (u/s) and V8 (d/s), approximately 90 m from reference point is shown in Fig. 4a and b. The grain size distribution at these sections is shown in Fig. 5a and b and the corresponding velocity distribution is shown in Fig. 6a and b, respectively.

The observed bed load measurements were checked against the bed load predicted using different bed load equations.

3 Bed Load Transport by Existing Bed Load Equations

There are many bed load equations developed on the basis of different theoretical concepts like shear stress, stream power, probability, dimensional equality, etc. In addition to conceptual equations, empirical equations based on the laboratory experiments and field measurements were also proposed by different researchers. The applicability and suitability of these equations vary from case to case and the uncertainty in dynamic combination of factors responsible for bed load transport, often necessitates extensive exercise of calibration of the selected equations based on the field observations.

Although some bed load equations have been developed for a given range of sediment size, these equations may give better prediction for sediment size in adjacent range also. Therefore, it becomes logical to evaluate a better performing robust bed load equation for a site rather then testing many bed load equations for calibration.

Table 1

42 — V. Yadav and S. M. Yadav

Table 1 Summary of measured hydraulic and sediment parameters [1]

Cross-section		V1	V2	V3	V4	V5	V6	V7	V8
Location		94.4 u/s	65 u/s	35 u/s	20 u/s	10 u/s	60 d/s	78 d/s	90 d/s
Slope	(m/m)	0.0007	0.0007	0.0007	0.0007	0.0007	0.0007	0.0007	0.0007
Width	(m)	5.62	5.4	24.4	31	30.5	31	26	23.5
Area	(m²)	3.05	2.77	10.6	12.76	9.6	8.44	13.59	10.63
Hydraulic depth	(m)	0.543	0.513	0.435	0.412	0.315	0.272	0.523	0.452
Wetted perimeter	(m)	5.95	5.73	24.64	31.05	30.51	31.02	26.09	23.57
Hydraulic radius	(m)	0.513	0.483	0.43	0.411	0.315	0.272	0.521	0.451
Mean flow velocity	(m/s)	0.459	0.414	0.546	0.635	0.613	0.792	0.741	0.567
Discharge per unit width	(m²/s)	0.249	0.212	0.237	0.262	0.193	0.216	0.387	0.257
Measured Bed load transport rate	(ton/day)	0.457	0.47	4.456	9.847	14.302	12.146	15.603	4.948

Table 2 Average particle size (mm) of observed bed load at different sections

Cross-section	D16	D35	D40	D50	D84	D90
V1	1.7	3.2	3.85	5	11.5	13
V2	1.35	2	2.4	3.3	9	12.5
V3	0.7425	1.45	1.575	1.9	5.85	7
V4	1.0975	1.8225	2.05	2.7225	8.2725	10.2
V5	1.175	1.85	2.05	2.65	7.7	9.5
V6	0.4375	1.015	1.18	1.6	5.9	8.5
V7	0.7675	1.425	1.575	1.95	6.275	8
V8	0.81	1.5225	1.695	2.675	7.7975	9.775
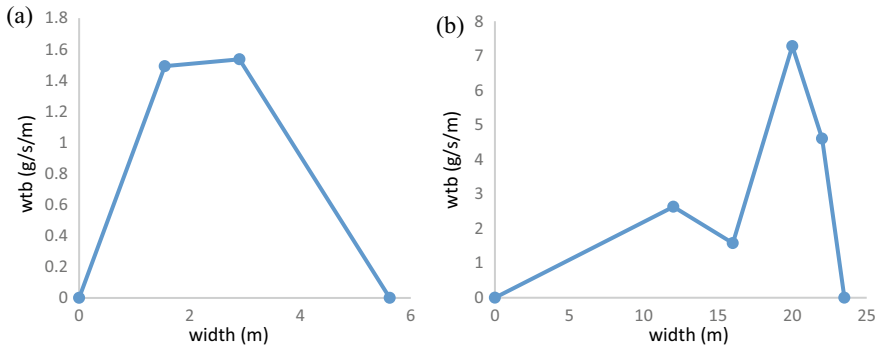
Fig. 4 Variation of bed load at cross-section **a** V1 (u/s) and **b** V8 (d/s)
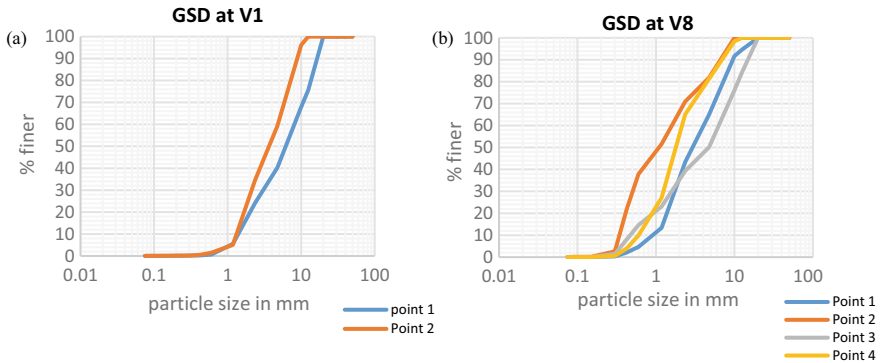
Fig. 5 Grain size distributions at cross-sections **a** V1 (u/s) and **b** V8 (d/s)
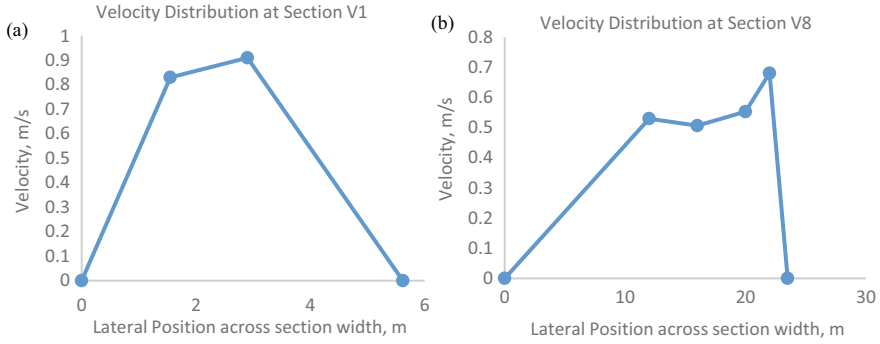
Fig. 6 Velocity distribution at cross-section **a** V1 (u/s) and **b** V8 (d/s)

For the present analysis, performance of Einstein and Brown [6] equation has been evaluated taking different characteristic sediment size from the sampled grain size distribution.

The Einstein approach for bed load prediction which is based on probabilistic approach was modified by Brown. The equations can be rewritten as Eq. (1).

$$q_{sv} = q_* x F_1 x \sqrt{\left[\left(\frac{\gamma_s}{\gamma} - 1\right) x g x D_{50}^3\right]} \tag{1}$$

$$F_1 = \left[\frac{2}{3} + \frac{36 * \vartheta^2}{\left(\frac{\gamma_s}{\gamma} - 1\right) * g * D_{50}^3}\right]^{0.5} - \left[\frac{36 * \vartheta^2}{\left(\frac{\gamma_s}{\gamma} - 1\right) * g * D_{50}^3}\right]^{0.5}$$

$$q_* = 2.15 \exp\left(\frac{-0.391}{\tau_*}\right)$$

$$q_* = 40 * \tau_*^3 \text{ When } \tau_* < 0.09$$

$$\tau_* = \frac{\gamma * R * S}{(\gamma_s - \gamma) * D_{50}}$$

q_{sv} is the bed load discharge in volume per unit width, (m^3/s/m); q_* is the dimensionless volumetric bed load transport rate per unit width; F_1 is parameter of fall velocity; D_{50} is median sediment diameter, (m); τ_* is Shields number; γ and γ_s are specific weight of fluid and specific weight of sediment respectively, (N/m^3); ϑ is kinematic viscosity; R is hydraulic radius, (m); S is channel slope, (m/m) [1].

4 Results and Discussion

The equation of Einstein and Brown has given much better result overall for D84 size as characteristic sediment size. Beside Discrepancy Ratio (DR), Mean Absolute Percentage Error (MAPE), Root Mean Squared Error (RMSE), Scatter Index (SI), and BIAS were calculated and compared. These statistical measures are calculated as given by Eqs. (2)–(5) [1, 7, 8].

$$\text{MAPE} = \frac{100}{n} \sum_{i=1}^{n} \text{mod}\left[\frac{(\text{BL}_P - \text{BL}_O)}{\text{BL}_O}\right] \tag{2}$$

$$\text{RMSE} = \sqrt{\frac{\sum_{i=1}^{n}(\text{BL}_P - \text{BL}_O)^2}{n}} \tag{3}$$

$$\text{SI} = \frac{\sqrt{\frac{1}{n}\sum_{i=1}^{n}\left((\text{BL}_P - \overline{\text{BL}_P}) - (\text{BL}_O - \overline{\text{BL}_O})\right)^2}}{\frac{1}{n}\sum_{i=1}^{n}\text{BL}_O} \tag{4}$$

$$\text{BIAS} = \frac{\sum_{i=1}^{n}(\text{BL}_P - \text{BL}_O)}{n} \tag{5}$$

where BL_P and $\overline{\text{BL}_P}$ are predicted bed load and mean predicted bed load, BL_O and $\overline{\text{BL}_O}$ are observed and mean observed bed load and 'n' is total number of observations.

In the present study, the prediction of bed load transport rate is close to observed bed load rate as indicated by various statistical measures like DR, Standard deviation, BIAS, RMSE, MAPE, SI. The summary of statistical measures is given in Table 3.

The plots of predicted vs observed bed load transport rate (tons/day) for different sediment size are given in Fig. 7a–f.

Table 3 Summary of statistical measures for all sections

Statistical measure	D16	D35	D40	D50	D84	D90
Average DR	35.71	13.95	9.85	4.07	0.61	0.44
Std deviation	47.34	17.30	12.21	3.98	3.74	3.89
RMSE	283.74	114.36	96.74	35.12	10.01	8.06
MAPE	3941.01	1494.36	1081.12	317.24	-13.76	-37.52
BIAS	198.80	80.17	64.77	18.81	-0.95	-2.92
SI	298.13	120.77	102.10	36.77	10.29	8.33
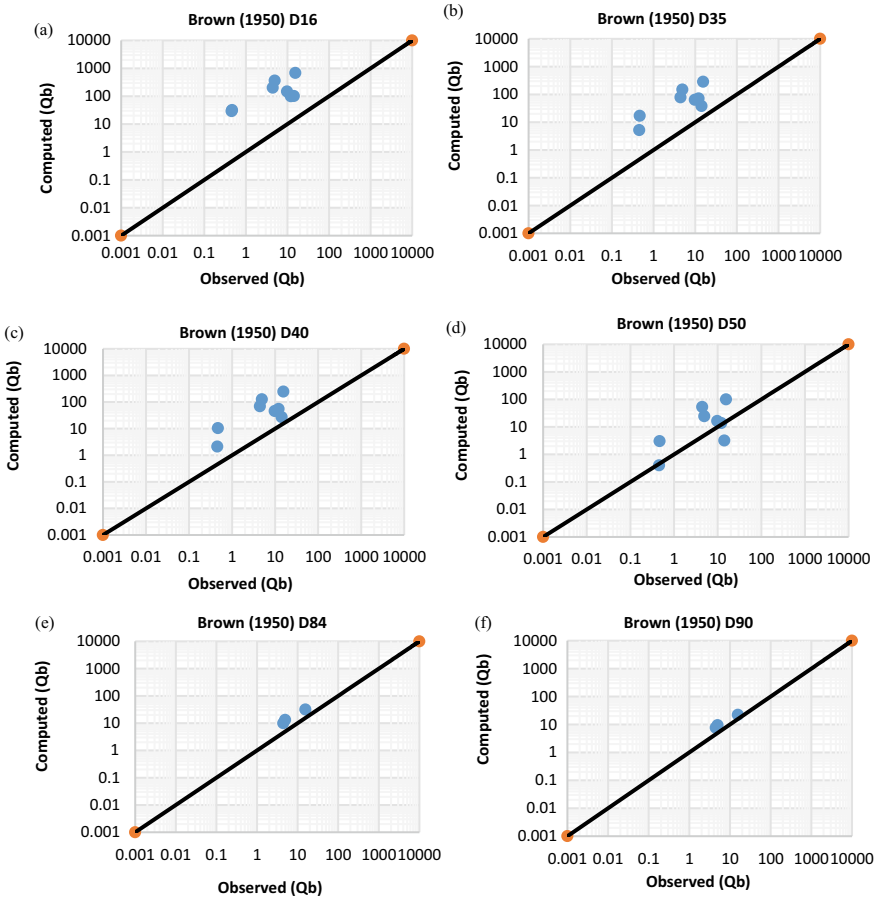
Fig. 7 Plots of Predicted vs Observed bed load rate (tons/day) for **a** D16 **b** D35 **c** D40 **d** D50 **e** D84 **f** D90

5   Conclusions

The following conclusions can be drawn from the present study:

 (i)   Although bed load equation is generally developed for a particular range of sediment size, it can still give better prediction in adjacent range of sediment size.
 (ii) The Einstein and Brown (1950) gives better prediction for D84 instead of D50.
 (iii) Any bed load equation when used for a site has to be calibrated using field measurements for accurate prediction of bed load transport rate.
 (iv) The sediment size varies greatly along the different reaches of a mountain river and the same equation may not be able to perform better in different reaches owing to variation in sediment size, and may necessitate more trials with different bed load equations.
 (v)   The same bed load equation may not perform well spatially and temporally for the same reach.

References

1. Yadav SM, Yadav VK, Gilitwala A (2019) Evaluation of bed load equations using field measured bed load and bed material load. ISH, J Hydraul Eng. https://doi.org/10.1080/09715010.2019.1594417
2. Bunte K, Abt SR, Potyondy JP, Ryan SE (2004) Measurement of coarse gravel and cobble transport using portable bedload traps. J Hydraul Eng 130(9):879–893. https://doi.org/10.1061/(ASCE)0733-9429(2004)130:9(879)
3. Guo J (2002) Hunter rouse and shields diagram. Adv Hydraul Water Eng 1 and 2:1096–1098. https://doi.org/10.1142/9789812776969_0200
4. Wilcock PR, Kenworthy ST (2002) A two-fraction model for the transport of sand/gravel mixtures. Water Resour Res 38(10):1194. https://doi.org/10.1029/2001WR000684
5. Pourhosein M, Afzalimehr H, Singh VP, Dehghani AA (2015) Evaluation of bed load in a gravel-bed river. Int J Hydraul Eng 4(3):70–79
6. Brown CB (1950) Sediment Transportation. Eng Hydraul Wiley NY 12:769–857
7. Najafzadeh M, Movahed FS, Sarkamaryan S (2017) NF-GMDH based self-organized systems to predict bridge pier scour depth under debris flow effects. Mar Georesour Geotechnol. https://doi.org/10.1080/1064119X.2017.1355944
8. Najafzadeh M, Movahed FS (2018) GMDH-GEP to predict free span expansion rates below pipelines under waves. Mar Georesour Geotechnol. https://doi.org/10.1080/1064119X.2018.1443355

The Experimental Analysis of Incipient Motion Condition of Nonuniform Sediment

Deepali Rahul Kulkarni and Anand Bhalerao

Abstract Rivers are important geological agents for erosion, transportation and deposition. In rivers, sediment transport is a very critical and complex phenomenon as far as Civil Engineering problems are concerned. Some of the problems are land erosion, soil conservation, silting of reservoir, floods, meandering of rivers, local scour, stable channel, etc. To understand sediment transport very thoroughly one need to understand the incipient motion of the sediment and sediment properties. The studies carried previously shows that the incipient motion condition of particle influenced by the particle size only. This research paper emphasizes on the experimental findings of slope dependency on incipient motion condition of nonuniform sediment. The nine sand samples of non-cohesive nonuniform sediment were prepared with different gradation and used in this experiment. The experiments were carried in the 10 m long, 0.30 m wide and 0.45 m deep tilting flume. The flume slope adjusted as per the decided slopes 0.001–0.0035. In the center of the flume the test section of 1.0-m long, 0.30-m-wide and 0.10-m deep was provided for placing the sediment sample. Critical shear stress was computed for various samples and various flow conditions. The critical shear stress was ranged between 0.04 and 0.08 N/m^2. The effect of various parameters on incipient motion condition of nonuniform sediment was studied with the help of experimental data. The relationship of slope and critical shear stress of nonuniform sediment at incipient motion was studied.

Keywords Nonuniform sediment · Incipient motion condition · Critical shear stress · Slope

D. R. Kulkarni (✉)
Bharati Vidyapeeth (Deemed to Be University) College of Engineering, Pune, Maharashtra 411046, India
e-mail: drkulkarni@bvucoep.edu.in

A. Bhalerao
Central University of Rajasthan, Ajmer, Rajasthan 305817, India

49

1 Introduction

Incipient motion condition for sediments is well explained by many investigators in last ten decades. It's always very important to describe incipient motion condition of sediment for stable channel design, forecast of bed level changes, design and maintenance of hydraulic structures, etc. The condition of incipient motion is well described by critical shear stress. Computation of critical shear stress at incipient condition is very crucial for nonuniform sediment. As natural stream bed may consist of nonuniform sediments and the behavior of bed consisting of nonuniform sediments is completely different than that of uniform sediments. In last few decades many researchers like Egiazaroff [1], Ashida and Michiue [2], Hayashi [3], Parker and Klingeman [4], Wilcock and Southard [5], Patel and Ranga Raju [6], Ashworth and Ferguson [7], Kuhnle [8], Wu and Wang [9], Shvidechenko et al. [10], Wilcock and Kenworthy [11], Achanta Ramkrishna Rao [12], Sarkar et al. [13], Lamb [14], Patel et al. [15], Tingjje (2015), Patel [16], Kumar and Kulkarni [17], Deokare and Kulkarni [18] have worked on the incipient motion condition of nonuniform sediment. All investigators put forwarded their own analysis with considering various parameters.

As stated by Sarkar et al. [13] the critical shear stress of any size fraction in nonuniform sediment composition of bed material is influenced by other sizes due to hiding and exposure effect. It is seen that the finer particles are covered by coarser particles and need higher shear stress to start movement and coarser particles in mixture are moved at lower shear stress due to increased exposure. Several investigators proposed relationships of CTS of a particular size fraction. Patel et al. [15] mentioned that the relative variation of the critical value of dimensionless bed shear stress for different grain size d_i within a mixture is largely controlled by their relative size with respect to a central value of the grain size distribution.

Patel et al. [15] have analyzed the data from previous investigators to check the predictors for CTS of representative sizes in the nonuniform sediment mixture. They found that the following Eqs. (1) and (2) are suitable to compute CTS of particular size fraction of unimodal and weekly bimodal sediment mixtures.

$$\frac{\tau_{*ci}}{\tau_{*c\sigma}} = \left[\frac{d_i}{d_\sigma}\right]^{-0.96} \tag{1}$$

$$\tau_{*c\sigma} = 0.0465(M)^{0.546} \tag{2}$$

Though a lot of investigation carried in last few decades in predicting the CTS of particular size in the sediment mixture but considerable uncertainty prevails in the predictors. In the present study, the efforts have been made to propose new relation for computing CTS of particular size fraction of wide range of sediment mixtures. The dimensional analysis is used to decide the factors affecting the critical shear stress of sediment mixture.

$$\frac{\tau_{0c}}{A^{1/2}\gamma_f} = f\left[\frac{y}{A^{1/2}}, \frac{\gamma_s}{\gamma_f}, S, \frac{P}{A^{1/2}}, \frac{d_i}{A^{1/2}}, \frac{d_a}{A^{1/2}}, \frac{Q}{VA}, \sigma_g\right] \tag{3}$$

2 Experimental Setup and Methodology

2.1 Bed Material

The sample used in the experimentation is natural sand having 2600 kN/m^3 density. The sand sieved into different size fractions. Then the required sample prepared by mixing the sand with proper proportion to get the required gradation. The grain size distribution of all mixes used in the present study shown and their characteristics summarized in Table 1.

Following geometric parameters will be computed in this study for the research work:

$$d_a = \frac{1}{100} \sum \Delta p_i d_i \tag{4a}$$

$$\log d_g = \frac{1}{100} \sum \Delta p_i \log d_i \tag{4b}$$

$$\sigma_g = \sqrt{\left(\frac{d84}{d16}\right)} \tag{4c}$$

$$d\sigma = d_g * \sigma_g \tag{4d}$$

where

Table 1 Properties of bed material used in the present study

Bed material	d_a (mm)	d_g (mm)	d_{50} (mm)	σ_g
R1	0.750	0.602	0.89	2.38
R3	0.707	0.502	0.67	2.738
R5	0.809	0.539	0.68	3.43
V1	1.380	1.173	1.50	2.41
V2	1.799	1.492	2.55	2.75
V3	1.437	1.261	2.48	3.07
T1	1.76	1.505	1.63	2.8
T2	1.481	1.232	1.495	3.5
T3	2.116	1.629	2.36	4.2
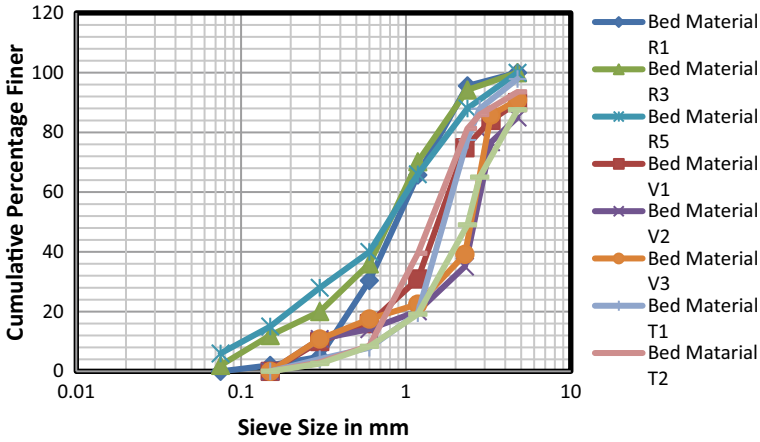
Fig. 1 Grain size distribution curve for bed material used in the present study

d_a = arithmetic mean size, d_g = geometric mean size, d_{50} = median size of sediment bed material (it is considered that the size of particle such that 50% of the material is finer than this size), σ_g = geometric std. deviation, Δp_i = percentage of weight corresponding to size di, d_{84} = particle size such that 84% of particles are finer than this size, d_{16} = particle size such that 16% of particles are finer than this size.

The variety and gradation of sediment combinations have been decided on such that the coarse nonuniform sediment to be had in alluvial rivers of India consisting of Ganga, Brahmaputra, etc. The gradation is shown in the following figure which is used in the present study (Fig. 1).

2.2 Methodology

For every sediment kind as a minimum six runs with unique hydraulic situations were accomplished withinside the present study. For every run, sand pattern became positioned withinside the check segment of tilting flume with predetermined slope to the bed. The steady intensity of waft became maintained all through every run. A very low discharge was allowed into the flume at first, in order that the sediment bed will become completely saturated. After filling with water the run started out through steadily increasing flow to the desired value. The tailgate was adjusted whilst essential to hold the uniform flow in the flume. With unique slopes, numbers of runs had been being finished with the flow various among a totally low one with nearly no sediment transport and one that actions extensive part of the bed material. An overall 18 runs had been finished in the experiment. The length of single run became governed through the sediment transport rate and varied among 1–3.5 h. Care to be

taken to hold the uniform flow and that steady rate of sediment transport situation was attained. After attainment of steady transport rate sediment was collected. Collected sediment then dried, weighted and sieved to get the fractional transport rate.

2.3 Experimental Procedure

The experiments had been done in a straight 10 m lengthy tilting flume having width of 0.30 m and depth of 0.45 m. The facets of channel had been made of acrylic sheet to keep smoothness and therefore fending off the impact of facet wall. Water was allowed to flow easily from the upstream reservoir through pipes positioned on the inlet. Water was recirculated centrifugal pump. The flow rate was managed through the assist of a valve connected to the inlet pipe. A tailgate is hooked up on the downstream end of the channel. For a specific water discharge, if the tailgate is raised, it will increase the water level and vice versa. A calibrated V notch is hooked up at the acute downstream of the release channel to measure the release of every run. The water level and bed level had been measured with the assist of calibrated pointer gauges. The point velocity was measured with the assist of calibrated pigmy type current meter. The sediment was trapped on the downstream end of the tilting flume. The sediments was gathered, dried and sieved once more to get the gradation of transported material. The information became gathered after which analyzed in line with the requirements. The experimental information is compared with the existing relationships. Figure 2 shows the experimental setup for the present study.

3 Result and Discussion

Table 2 shows the experimental data for present study. The critical shear stress (CTS) for individual particle in the mixture is calculated by Reference Transport Method (RTM) suggested by Parker et al. [19]. In this method the CTS is estimated from fitted relationship of the dimensionless bed load parameter W_i^* and the dimensionless grain shear stress τ'_{*i} as the shear stress corresponding to $W_i^* = 0.002$ where in

$$W_i^* = \frac{i_B q_B (G-1)}{i_b \gamma_s \sqrt{g(R_b' S)^3}} \tag{5}$$

where
   i_B, i_b – proportions of size fraction d_i in the transported material and the sediment bed, respectively,
   q_B – total bed load transport rate per unit width by weight, γ_s – unit weight of sediment,
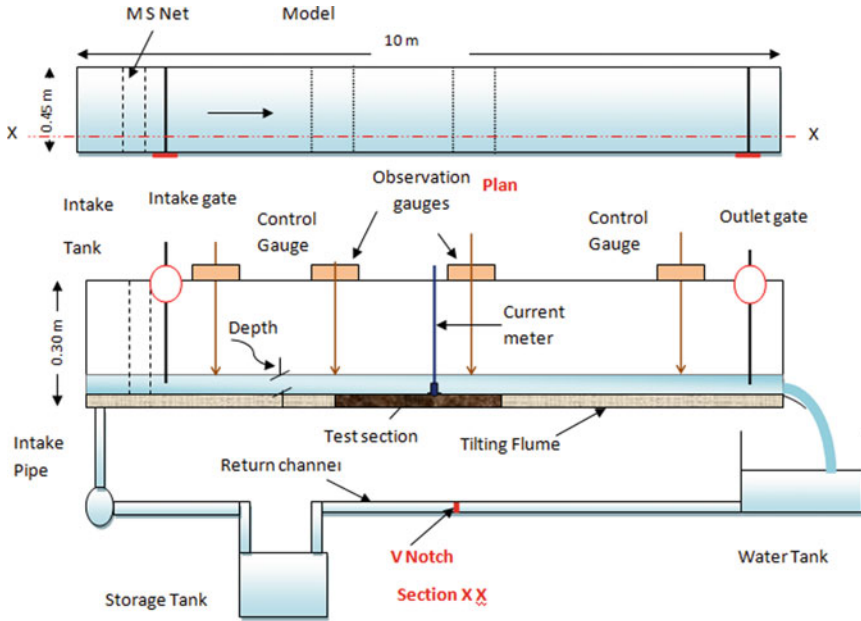
Fig. 2 Experimental setup

γ_f – unit weight of water, G – relative density of sediment, g – gravitational acceleration,

R_b' – hydraulic radius corresponding to grain resistance, S – Longitudinal slope of channel.

The dimensionless grain shear stress τ'_{*i} is defined as:

$$\tau'_{*i} = \frac{\tau_0'}{\Delta\gamma_s d_i} \tag{6}$$

In which, $\Delta\gamma_s = \gamma_s - \gamma_f$ and τ_0' is the grain shear stress which can be computed by using equation:

$$\tau_0' = \gamma_f R_b' S \tag{7}$$

where

R_b' is corrected hydraulic radius corresponding to grain resistance.

Here the hydraulic radius corresponding to grain resistance, R_b' can be obtained from:

$$U = \frac{1}{n'} (R_b')^{\frac{2}{3}} S^{\frac{1}{2}} \tag{8}$$

Table 2 Hydraulic parameters observed in the present study (given table for only 18 runs)

Run no.	Total run time (h)	Bed material	Average discharge (Q) m^3/s	Depth of flow (d) (m)	Average slope (S)	Velocity of flow m/s	Sediment collected after each Run (Kg)
1	1.15	R1	0.006421	0.10	0.0015	1.422	0.350
2	1.30	R1	0.00792	0.12	0.0015	1.688	0.237
3	2.00	R1	0.01075	0.15	0.0015	2.388	0.208
4	1.20	R1	0.0072115	0.10	0.002	1.602	0.212
5	1.45	R1	0.008795	0.12	0.002	1.954	0.200
6	2.05	R1	0.012546	0.15	0.002	2.788	0.148
7	1.00	R3	0.007361	0.10	0.0015	1.6357	0.359
8	1.15	R3	0.010759	0.12	0.0015	2.391	0.251
9	1.30	R3	0.014499	0.15	0.0015	3.221	0.218
10	1.10	R3	0.0063549	0.10	0.002	1.4122	0.221
11	1.20	R3	0.0105708	0.12	0.002	2.335	0.189
12	1.30	R3	0.013393	0.15	0.002	2.9362	0.200
13	1.00	R5	0.005612	0.10	0.0015	1.2471	0.322
14	1.15	R5	0.009271	0.12	0.0015	2.0602	0.213
15	1.30	R5	0.01575	0.15	0.0015	3.501	0.190
16	1.15	R5	0.005631	0.10	0.002	1.363	0.211
17	1.30	R5	0.010659	0.12	0.002	2.368	0.198
18	1.45	R5	0.01433	0.15	0.002	3.184	0.211S

In which n' = Manning's roughness coefficient corresponding to grain resistance and it can be computed using Strickler's equation:

$$n' = \frac{(d_{65})^{1/6}}{24.0}, \text{ in SI units} \tag{9}$$

where d_{65} is the size of particle such that 65% of the sample is finer than this size

A typical plot of W_i^* and τ'_{*i} for computing dimensionless critical shear stress of individual fractions in case of sediment mixture is shown in Fig. 3.

From the above graph the critical shear stress for each and every individual particle (τ_{*ci}) fraction is computed and tabulated for further analysis (Table 3).

Various investigators have proposed the relationship for CTS of a specific size fraction in a sediment mixture as a ratio of dimensionless CTS of this size to the dimensionless CTS of a few representative sizes as a characteristic of their representative size ratios.

Egiazaroff [1], Ashida and Michiue [2], Hayashi et al. [3] have given the relationship based on the representative size ratios. These relations are as follows:

Egiazaroff [1]

Fig. 3 Variation of W_i^*
With τ_{*i}' for bed material V1
and particle size $d_i =$
2.73 mm

Bed Material
V1, d_i = 2.73
mm
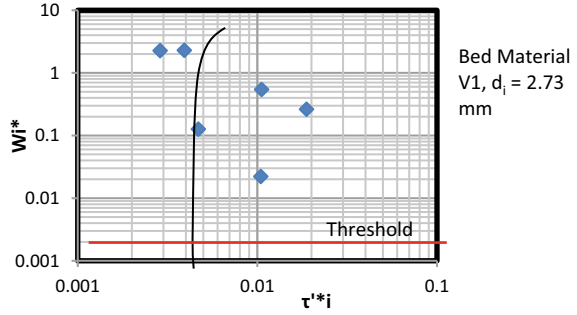
Table 3 CTS values for few
bed materials used in the
present study

	Values of τ_{*ci}		
d_i	Bed material R1	Bed material R2	Bed material R3
3.348	0.080	0.071	0.085
1.669	0.140	0.155	0.170
0.841	0.220	0.280	0.320
0.424	0.051	0.059	0.850
0.212	0.820	0.152	0.188
0.106	0.190	0.230	0.320

$$\frac{\tau_{*ci}}{\tau_{*ca}} = \left(\frac{\log 19}{\log 19^{d_i}/d_a} \right)^2 \tag{10}$$

where d_a is arithmetic mean size

τ_{*ca} is dimensionless critical shear stress for arithmetic mean size.

Ashida and Michiue [2]

$$\frac{\tau_{*ci}}{\tau_{*ca}} = 0.85 \left(\frac{d_i}{d_a} \right)^{-1} \tag{11}$$

Hayashi et al. [3]

$$\frac{\tau_{*ci}}{\tau_{*ca}} = \left(\frac{d_i}{d_a} \right)^{-1} \quad \text{for} \frac{d_i}{d_a} < 1.0 \tag{12a}$$

$$\frac{\tau_{*ci}}{\tau_{*ca}} = \left(\frac{\log 8}{\log 8^{d_i}/d_a} \right)^{-1} \quad \text{for} \frac{d_i}{d_a} > 1.0 \tag{12b}$$

Fig. 4 Comparison of present study data with previous equations
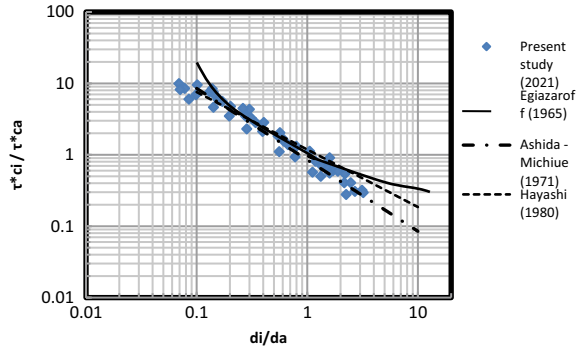
After computing CTS for individual fraction and CTS for mean size fraction, the plot of $\frac{\tau_{*ci}}{\tau_{*ca}}$ and $\frac{d_i}{d_a}$ for present study experimental data and data from previous study are plotted.

The above Fig. 4 shows the plot of $\frac{\tau_{*ci}}{\tau_{*ca}}$ and $\frac{d_i}{d_a}$ in which the experimental as well as Eqs. (10), (11) and (12) are plotted. The plot above shows that the experimental data is well aligned with the previous data provided by Ashida and Michiue [2].

4 Development of New Relation

The experimental data from the present study is used to form a new relationship to define CTS of a particular size fraction in a sediment mixture as ratio of dimensionless CTS of this size (τ_{*ci}) to dimensionless CTS of some representative size (it may be τ_{*ca}, τ_{*c50} or $\tau_{*c\sigma}$) as a function of their representative size ratio. Egiazaroff [1], Ashida and Michiue [2] and Hayashi et al. [3] have expressed $\frac{\tau_{*ci}}{\tau_{*ca}}$ as a function of $\frac{d_i}{d_a}$ as given in Eqs. (10), (11) and (12). arithmetic mean diameter (d_a) is the parameter used to define the non-dimensional CTS for nonuniform bed material.

Parkar et al. [19], and Shvidchenko et al. [10] have given the relationship based on the median size (d_{50}). Patel and Ranga Raju [6] have introduced empirical relation based on the geometric mean size (d_{σ}). Taking the clues from the literature the new relation will be presented for computation of non-dimensional CTS based on the representative sizes. Here median size (d_{50}) of the bed material is used to describe the non-dimensional CTS. Median size of the bed material is defined as the size of the particle such that 50% sample by weight is finer than this size. This size is extracted from the particle size distribution curve whereas the arithmetic mean size and geometric mean size are the statistically computed by using formulae (4a), (4b) and (4d). It will be more logical to use median size of the particle. Therefore, relation for non-dimensional CTS will be defined based on median size in the present study.

Fig. 5 Variation of τ_{*ci}/τ_{*c50} with d_i/d_{50} for experimental values from present study
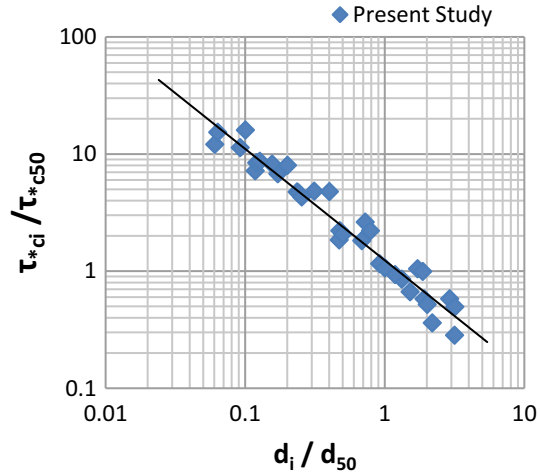
4.1 Relation Based on Median Size 'd_{50}'

Using RTM method, τ_{*ci} and τ_{*c50} values were computed. The values of $\frac{\tau_{*ci}}{\tau_{*c50}}$ are plotted against the ratio $\frac{d_i}{d_{50}}$ as shown in Fig. 5.

From Fig. 5, following equation is proposed based on the experimental data.

$$\frac{\tau_{*ci}}{\tau_{*c50}} = 1.237\left(\frac{d_i}{d_{50}}\right)^{-0.95} \tag{13}$$

4.2 Other Sources Data Used for Validation of the New Relation

The data such as arithmetic mean diameter (d_a), median size (d_{50}), geometric standard deviation (σ_g) are used from the composition of bed material from previous investigators, i.e., Patel and Ranga Raju [6], Sarkar et al [13], Wilcock and Southard [5], 13White and Day [20] and Misri [21] for the assessment of proposed relation by the author.

The values of $\frac{\tau_{*ci}}{\tau_{*c50}}$ have been computed by using Eq. (13). These values then have compared with the observed data by the respective authors. The validation of proposed relationship may be evaluated by preparing a plot of Computed $\frac{\tau_{*ci}}{\tau_{*c50}}$ and Observed $\frac{\tau_{*ci}}{\tau_{*c50}}$.

From Fig. 6 it is discovered that maximum data points are found within $\pm\,20\%$ error range and few data points lie between $+\,20\%$ and $+\,30\%$ error band on the said plot except few points from the author DAY—A data set.
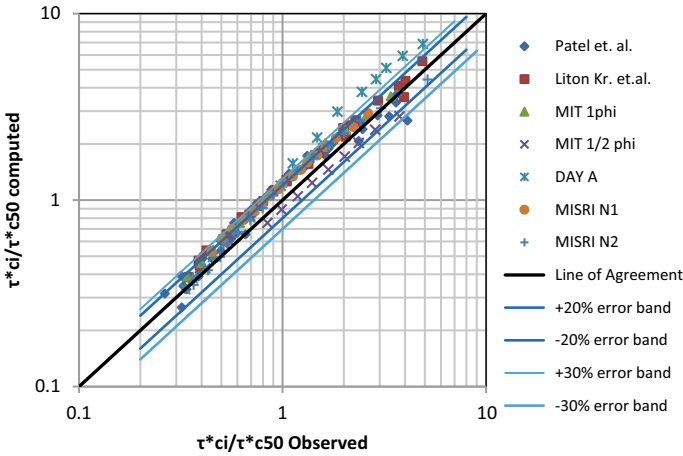
Fig. 6 Comparison of observed and computed τ_{*ci}/τ_{*c50}

One more aspect to be discussed with previous points is the effect of slope on critical shear stress of particle. As per Eq. (3), dimensional analysis shows that critical shear stress of representative size has effect of bed slope. Following graph shows that the variation of τ_{*c50} with bed slope.

The graph in Fig. 7 shows that increase in the critical shear stress for median size increase with the slope. A best fit line to all the data (in a least squared method) is shown in Fig. 7 and is given by:

$$\tau_{*c50} = 0.729 S^{0.542} \tag{14}$$

where S is the bed slope

CTS of median size particle can be computed for the known bed slope by using Eq. (14).

5 Conclusion

From analysis of experimental data sets along with those available from earlier investigations, the following conclusions can be carried out. The existing relationships for calculations of critical shear stress of nonuniform sediment mixture have been checked with the experimental data sets compared with the Egiazaroff [1], Ashida and Michiue [2] and Hayashi et al. [3]. It has been found that the experimental data is well within the range. The new relations have been developed for the non-dimensional critical shear stress of different fractions in sediment mixture as per given in Eq. (13). The relation has been verified with the data from other sources. Figure 6 shows the agreement of the data with the proposed equation except few data points from
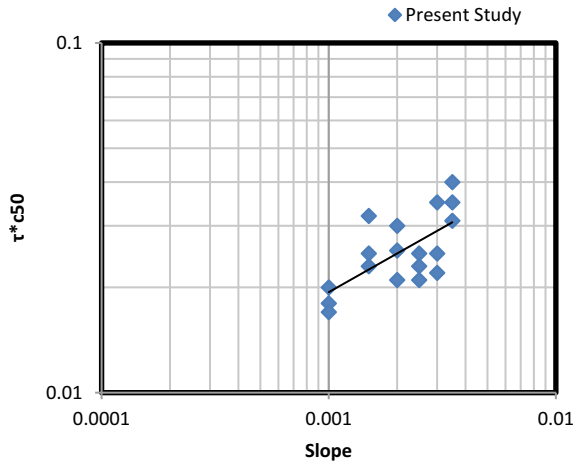
Fig. 7 Variation of τ_{*c50} with slope

DAY—A data set. The relation has resulted in a satisfactory output. If the median size of a sediment mixture is known then their non-dimensional critical shear stress for the respective representative size can be computed with this equation. Along with the size of the particle the slope also have the influence on the critical shear stress of nonuniform sediment. As per the results shown in Fig. 7, τ_{*c50} increases with increase in the bed slope. Initially particles may move with increase in slope however moved particles may be shielded by courser particles. Those lumped particles may require more shear stress to move together. As mentioned by Michael Lamb et al. [14] the other processes such as wall drag, friction angle, bed morphology may have influence on the mobility of the particle.

References

1. Egiazaroff LV (1965) Calculation of nonuniform sediment concentrations. J Hydraul Div SCE 94(4):225–247
2. Ashida K, Miohuje M (1971) An investigation of river bed degradation downstream of a dam. In: Proceedings of 14th IAHR congress, vol 3. International Association for Hydraulic Research Paris C30-1-C30-9
3. Hayashi T, Ozaki S, Ichibashi T (1980) Study of bed load transport of sediment mixture. In: Proceedings of the 24th Japanese conference on hydraulics, pp 35–43

4. Parker G, Klingeman PC (1982) On why gravel bed streams are paved. Water Resour Res 18(5):1409–1423
5. Wilcock PR, Southard JB (1988) Experimental study of incipient motion in mixed-size sediment. Water Resour Res 24(7):1137–1151
6. Patel PL, Ranga Raju KG (1996) Fractionwise calculation of bed load transport. J Hydraul Res 34(3):363–379
7. Ashworth PJ, Ferguson RI (1989) Size-selective entrainemnt of bed load in gravel bed stream, Water Resour Res 28(2):411–425
8. Kuhnle RA (1993) Fluvial transport of sand and gravel mixtures with bimodal size distributions. Sed Geol 85:17–24
9. Wu W, Wang SS, Jia Y (2001) Non uniform sediment transport in alluvial rivers. J Hydraul Res 38(6):427–434
10. Shvidchenko AB, Pender G, Hoey TB (2001) Critical shear stress for incipient motion of sand/gravel streambeds. Water Resour Res 37(8):2773–2783
11. Wilcock PR, Kenworthy ST (2002) A two-fraction model for the transport of sand/gravel mixtures. Water Resour Res 38(10):12-1–12-12
12. Rao AR (2004) Incipient motion of hypothetical stram beds-part 2: critical shear approach. ISH J Hydraul Eng 10(2):94–106
13. Sarkar LK, Hossaain MM, Haque MA (2007) Incipient motion of different size fractions in nonuniform sediement of smaller grain sizes. ISH J Hydraul Eng 13(2):66–92
14. Lamb M, Dietrich W, Venditti J (2008) J Geophys Res 113(F02008):1–20
15. Patel PL et al (2009) Critical tractive stress of representative sizes in nonuniform sediments ISH. J Hydraul Eng (15)3:40–50
16. Patel SB, Patel PL, Porey PD (2014) Estimation of fractional critical tractive stress from fractional bed load transport measirements of unimodal and bimodal sediments. Measur 47:393–400
17. Kumar R, Kulkarni D (2017) Experimental study of incipient motion condition for non-uniform sediment. Inter J Civ Eng Technol 8(6):218–224
18. Deokare V, Kulkarni D, Talegaonkar SD (2019). Computaion of critical shear stress for non -uniform sediment. Inter J Recent Technol Eng 8(3):1402–1406
19. Parker G, Klingeman PC, Mclean DG (1982) Bed load and size distribution in paved gravel-bed streams. J Hydraul Div ASCE 108(4):544–571
20. White WR, Day TJ (1982) Transport of graded gravel bed material gravel-bed rivers
21. Misri RL (1981) Partial bed load transport of coarse nonuniform sediment. Ph.D. Thesis Submitted in Fulfillment of the Requirements for the Degree of Doctor of Philosophy, University Of Roorkee, Roorkee, India
22. Bagnold RA (1966) An approach to the sediment transport problem from general physics. U.S. Geological Survey Professional Paper 422-J
23. Bridge JS, Bennett SJ (1992) A model for the entrainment and transport of sediment grains of mixed sizes. Shap Densit Water Resour Res 28(2):337–363
24. Garde RJ, Ranga Raju KG (1985) Mechanics of sediment transportation and alluvial stream problems, 2nd edn. Wiley Eastern Limited, New Delhi, India
25. Kuhnle RA (1994) Incipient motion of sand-gravel sediment mixtures. J Hydraul Eng ASCE 119(12):1400–1415
26. Kramer H (1935) Sand mixtures and sand movement in fluvial models trans. ASCE 100:798–838
27. Misri RL, Garde RJ, Ranga Raju KG (1983) Experiments on bed load transport of nonuniform sands and gravels. In: Proceedings of the 2nd international symposium on river sedimentation, Nanjing
28. Qin YY (1980) Incipient motion of nonuniform sediment. J Sediment Res L (Resume Publication) (In Chinese)
29. Patel PL (1995) Initiation of motion and bed load transport of nonuniform sediments. Ph.D. Thesis Submitted in fulfillment of the Requirements for the Degree of Doctor of Philosophy, University Of Roorkee, India

30. Patel SB et al (2015) Fractional bed load transport model for nonuniform unimodal and bimodal sediments. J Hydro Environ Res 9:104–119
31. Samaga BR, Ranga Raju KG, Garde RJ (1986) Bed load transport of sediment mixtures. J Hydraul Res ASCE 112(11):1003–1017
32. Shvidchenko AB, Pender G (2008) Flume study of the effect of relative depth on incipient motion of coarse uniform sediments. Water Resour Res 36(2):619–628
33. Hey RD, Bathurst JC, Throne CR (eds), John Wiley And Sons, London, UK
34. Wilberg PL, Smith JD (1987) Calculations of the critical shear stress for motion of uniform and heterogeneous sediments. Water Resour Res 23(8):1471–1480
35. Wilcock PR (1988) Methods for estimating the critical shear stress of individual fractions in mixed-size sediment. Water Resour Res 24(7):1127–1135
36. Wilcock PR (1993) Critical shear stress of natural sediments. J Hydraul Eng ASCE 119(4):491–505
37. Wilcock PR (1992) Experimental investigation of effect of mixture properties on transport dynamics, dynamics of gravel-bed rivers. In: Billi P, Hey RD, Thorne CR, Tacconi P (Eds), John Wiley And Sons, New York, pp 109–139
38. Shields A (1936) Anwendung Der Ahnlichkeits-Mechanik Und Der Turbulenzforschung Auf Die Geschiebebewegung. Preussische Ver Uchsan Talt Fur Wa Serbau Und Schiffbau, Berlin
39. Rouse HFR (1939) An analysis of sediment transportation in the light of fluid turbulence. U.S. Department of Agriculture Oil Conservat Ion Erviee, Scs-Tr-25
40. Kramer (1935) Sand mixture nad sand movement in fluvial models. Transaction A.S.C.E. 100
41. Sediment Tran Porlation Mechanics; Initiation Of Motion; Progress Report Of The Task Committee On Preparation Of Sedimentation Manual; Journal Of Hydraulics Division Proc. A.S.C.E. March 1966
42. Studies Of River bed Material And Their Movement With Special Reference To The Lower Mi Si Ippi River. Paper 1 0.17, .5. Waterway Experiment Station, Vick Burg, Mis Issippi (1935)
43. Paintal AS, The Probabili Ti Haraeteristie of Bed Load Transport In Alluvial Channels. This Submitted To The University of Minne Ota, Minneapolis. In Partial Fulfillment of The Requirements For The Degree Of Doctor Of Philosophy.
44. Einstein HA (1942) Formulae for the transportation of bed load. Transaction, A.S.C.E. 107
45. Kau Ske AA (1947) Movement of sediment as bed load in rivers transaction. Am Geophys Union 0.4
46. White M (1940) The equilibrium of grains on the bed of a strcam. Roy Soc (A), Proce, p 174
47. Huange T, Lu Y, Lu Y (2015) Incipient motion and bed load transport of non-uniform sediment. In: E - Proceedings of 36th IAHR World Congress

Local Scour Near Sluice Gate in Clay–Sand Mixtures

T. Divya, A. Sarkar, and S. N. Kuiry

Abstract Local scour near the hydraulic structures is a practical problem of engineering design. The foundation can be damaged due to excessive scour, which may lead to the failure of the structure. One such problem is the local scour in the vicinity of a sluice gate due to the formation of the water jet. Scour downstream of the sluice gate due to submerged jet has been well understood experimentally in cohesionless sediments. However, in the real life, the riverbed materials are not necessarily cohesionless. There are chances that it can be a mixture of cohesive and non-cohesive soils. The experiments were conducted for different proportions of clay–sand mixture in a laboratory flume. In each experiment, clay proportions were varied as 0, 15, 20, 25, 30, 35, and 40 percent by total weight of sediment mixture while other parameters were kept constant. Scour processes, parameters of maximum scour were presented. An attempt was made to propose the equation for maximum scour depth in clay–sand mixture bed by using dimensional analysis.

Keywords Clay–sand mixtures · Scour · Sluice gate · Wall jet · Sediments

1 Introduction

Local scour of the mobile sediment beds downstream of hydraulic structures is a problem of practical importance. The foundation can be undermined due to excessive scour, leading to the failure of the structure. When a jet of water issues through sluice gate over a sediment bed, the local shear stress increases that exceed the critical

T. Divya (✉) · S. N. Kuiry
Department of Civil Engineering, Indian Institute of Technology Madras, Surat 600036, India
e-mail: divyathokala01@gmail.com

S. N. Kuiry
e-mail: snkuiry@civil.iitm.ac.in

A. Sarkar
Department of Civil Engineering, Indian Institute of Technology Bhubaneshwar, Bhubaneshwar 752050, India
e-mail: asarkar@iitbbs.ac.in

shear stress for incipient motion, which results in local scour downstream of the sluice gate [1]. Scour downstream of the sluice gate due to a submerged jet has been well-investigated experimentally due to its applicability in the design of hydraulic structures. Much work has been done on scour due to plane jets of cohesionless soil by [1–7]. Rajaratnam [3] and Rajaratnam and Macdougall [2] investigated the scour characteristics due to plane wall jet in sand bed using dimensional analysis. Hassan and Narayanan [4], Chatterjee et al. [1], and Dey and Sarkar [6] investigated the scour caused by wall jets issuing from the sluice gate for different lengths of the apron, sluice gate openings, and efflux velocities. Kells et al. [5] studied the effect of grain size on scour. Dey and Sarkar [6, 8] studied scour characteristics and similarity of scour profiles. Melville and Lim [7] investigated the factors influencing the scour and proposed equation for maximum scour depth. However, in the actual scenario, the riverbed material is not only sand but also a mixture of cohesive and non-cohesive soils [9]. Few investigations are available on scour by plane wall jets in cohesive soils [10–12]. Hamidifar and Omid [13], Rustiati et al. [14] studied the scour in clay–sand mixtures. They conducted experiments in clay–sand mixtures and concluded that increase of clay content significantly reduces the scour. Kho et al. [15] were seen an increment in the scour with increase of clay content. Very recently Jain et al. [16] Lodhi et al. [17] have studied the influence of cohesion on scour in clay–sand-gravel mixtures. It was seen in both the studies that the scour depth decreases drastically with the increase of percentage of clay from 10 to 50%.

In this context, it can be said that the research on scour due to horizontal wall jets over clay–sand mixtures beds is more emphasized to decide the clay behavior while scouring. In this paper, the experimental investigation of local scour in clay–sand mixture due to a 2D submerged horizontal wall jet issuing from a sluice opening is investigated. Observations of scour were made with respect to clay content. A simple relation for maximum scour depth is proposed based on dimensional analysis.

2 Materials and Methods

2.1 Flume Setup

Experiments were performed in a flume of dimensions 10m × 0.4m × 0.8 m. The schematic of the experimental setup is shown in Fig. 1. A sluice gate was used to produce a 2D horizontal submerged wall jet. The sluice gate opening was kept to 2.5 cm for all the runs. Apron length was kept zero. A sediment recess of 0.12 m deep and 1 m long was constructed in the middle of the flume at the downstream of sluice-gate. Tailwater depth in the flume was adjusted using a tailgate at the downstream end of the flume. The water supply into the flume was regulated using a valve. A flow meter was used to measure the discharge entering the flume. Flow depths were measured using a point gauge with an accuracy of ± 0.1 mm installed on a rail system over the side walls of the flume.
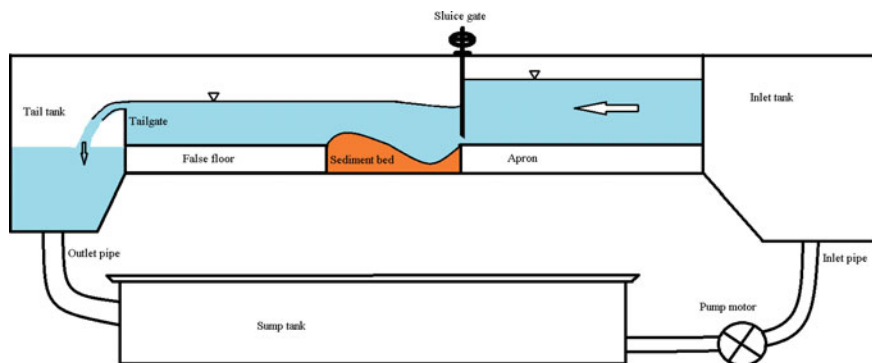
Fig. 1 Schematic side view of experimental setup (not to scale)

2.2 Sediment Bed Preparation

River sand and Kaolinite clay were used as sediments and their properties were tested as per Indian standard methods. The different properties of sediments found are listed in Table 1.

The median sizes of sand and clay were determined by sieve analysis and hydrometer analysis, respectively. The particle size of sand was determined by using sieve analysis, whereas hydrometer analysis was used for clay. Sediment beds were prepared by mixing water with clay and sand in the required proportions. The mixture was kept covered over 16 h to ensure the uniform distribution of moisture. The mixture was placed near the apron in three layers of approximately 0.04 m. Each layer was uniformly compacted throughout using the modified proctor hammer of weight 4.89 kg by with a free fall of 450 mm. The extra portion was trimmed off and leveled to a plain surface. Before starting of each run, the density, water content of the were determined for the compacted bed. A Hardson soil sampler was used to determine the bulk density with diameter of 5.4 cm and height 6 cm. The same soil

Table 1 Sediment properties

Property	Sand	Kaolinite
Median size, d_{50} (mm)	0.519	0.012
Geometric standard deviation, σ_g	1.78	–
Specific gravity, G	2.57	2.4
Plastic limit, PL (%)	–	32
Liquid limit, LL (%)	–	46
Plasticity Index, PI (%)	–	14
OMC (%)	–	31
$\gamma_{d\max}$ ($\kappa N/\mu^3$)	–	14.2

sample was used to determine the water content using the oven-dry method to ensure the water added while mixing process.

2.3 Experimental Schemes

Initially, the flume is filled with the water that will avoid undesirable erosion due to sudden non-uniform jet. A tailgate was operated to maintain a desired tailwater depth. The water was slowly issued to the flume to a desired discharge value. As soon as the flow reached the sluice gate, the bed geometry started changing, and the scour was initiated near the edge of the apron. The profiles of scour were drawn on a transparent graph sheet that is attached to the flume with glass wall at different times. The scour profiles were overserved to be two-dimensional. After 9 h of the scour initiation, the change in maximum scour depth was noticed to be insignificant. Therefore, the experiments were run for period of 12 h. Table 2 presents the observed experimental flow conditions, and maximum scour depths. The nomenclature KISxx represents xx% of kaolinite clay in sand.

3 Results and Discussions

3.1 Evolution of Scour

During the scour process, the qualitative observations were made visually. When the water issues through sluice opening, the conversion of potential energy to kinetic energy takes place, a part of this energy gets dissipated on the apron through the hydraulic jump, and the other part causes the flow separation at the edge of the apron due to which sediment particles lift up. The scour initiation was observed at the edge of the apron, where the jet's action created a hole. Cohesionless bed achieved 90% of maximum scour depth after 1 h; but in clay–sand mixtures, it was observed between 3 and 6 h.

3.2 Equilibrium Bed Profiles

Figure 2a–d shows the quasi-equilibrium bathymetry of equilibrium scour profiles. It is well known that the scour profiles are two-dimensional in cohesionless sediments across the width of the flume ([4–6, 18]), which is also seen in the present study (Fig. 2a). Scour profiles in clay–sand sediments are also observed to be two-dimensional for clay content range used. Dune height formed is not very uniform

Table 2 Experimental data

Run no.	Soil type	$w\%$	d (g/cc)	γ (g/cc)	τ (N/cm^2)	Q (L/s)	U_o (m/s)	$F_{r,jet}$	T_w (cm)	h (cm)	y_{meq} (cm)
1	Sand	–	1.608	1.907	0.8	5.64	0.56	1.08	11.0	12.1	9.30
2	KIS15	10.08	1.347	1.609	1.33	5.38	0.54	1.07	11.1	12.2	10.15
3	KIS20	9.53	1.586	1.892	4.13	5.38	0.54	1.08	11.0	12.0	9.98
4	KIS25	9.69	1.579	1.936	11.4	5.22	0.52	1.08	11.0	11.9	11.08
5	KIS30	11.63	1.522	1.601	6.33	5.36	0.53	1.08	11.0	12.0	11.00
6	KIS35	10.97	1.586	1.921	4.20	5.28	0.53	1.08	11.1	12.3	11.45
7	KIS40	11.85	1.926	2.190	4.33	5.35	0.53	1.07	11.1	12.3	11.86
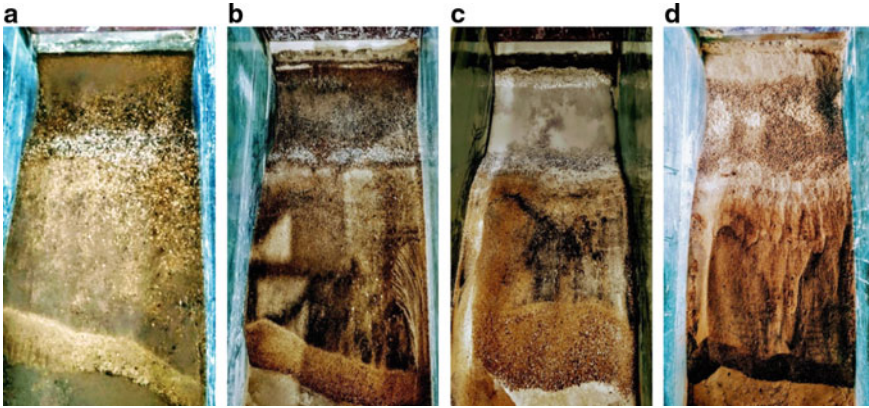
Fig. 2 Equilibrium scour profiles **a** sand **b** KIS15 **c** KIS25 **d** KIS40

across the width. However, the scour behavior after 40% clay is not investigated herein.

3.3 Effect of Clay Properties on Scour

Figure 3 shows the effect of clay content (cc) on dimensionless maximum equilibrium scour depth ($\hat{y}_{me}$). A linear behavior was seen in scour depth with the increment of clay proportion in the present study (Fig. 3a), which was similar to the observation of Kho et al. [15] for the case of bridge pier in clay–sand mixtures of kaolinite clay (Fig. 3b). It was explained that the lattice structure of the clay expands, and bonds between the clay particles breakdown with passage of time in the water, that causes dispersion. Hamidifar and Omid [19] carried similar study downstream of an apron for clay–sand mixtures using kaolinite clay. Their study reported that up to 15% of clay, the scour depth increases, then decreases subsequently (Fig. 3c). It was seen that at 40% clay, reduction in maximum scour depth is 80% at equilibrium compared to cohesionless sediments. It was said that the initial increment of scour depth for low percentages of clay is due to the lubrication effect of clay particles. The clay plates break and move farther due to dispersion, which increases scour. The linear regression equations obtained for the present study as well as for Kho et al. [15] and Hamidifar and Omid [19] study, respectively, are

$$\hat{y}_{me} = 0.026\text{CC} + 3.67 \qquad (1)$$

$$\hat{y}_{me} = 0.031\text{CC} + 1.53 \qquad (2)$$
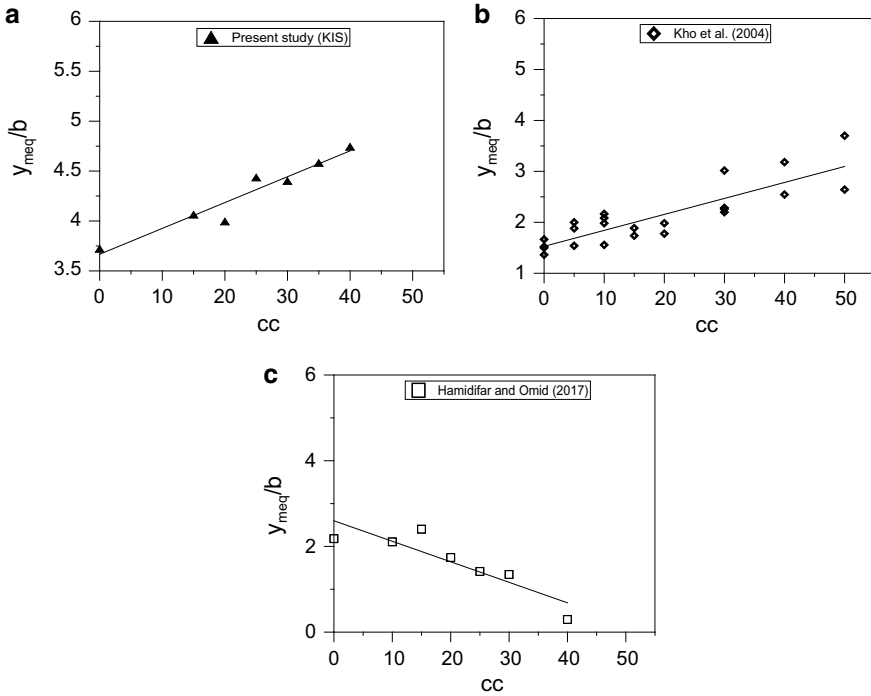
Fig. 3 Variation of dimensionless maximum equilibrium scour depth with clay content **a** present study **b** Kho et al. [15] and **c** Hamidifar and Omid [19]

The coefficients of determinations (R^2) 0.93 and 0.74 are given in Eqs. (1) and (2), respectively. However, the data points are minimal in the present study. Ansari et al. [20] observed that there is no resistance to scour up to 20% clay in which cohesion and clay particles are easily washed away. The results in the present study were coinciding with Kho et al. [15] observations but they were contradicting the observations made by Hamidifar and Omid [19]. However, for lower clay contents near to 20% overall behavior of clay is same. We cannot justify the behavior of clay in these ranges as the sand content dominates. The properties of clay play a different role in eroding the bed. Numerous properties can characterize the behavior of scour in sediments with cohesive soils. The bonding between the particles can vary depending on clay mineral present and it increases with the plasticity of clay ([18, 19]). Erosion of clay particles is less in case of clay with low sodium absorption ratio [23]. The high cation exchange capacity of clay possesses high cohesion [24]. Also, the increase in salinity levels increases erosion rates [25]. Further investigation is required to relate these parameters with scour.

3.4   Time Variation of Scour Depth

The maximum scour depth is considered to be affected by the following independent variables

$$y_m = f(U_0, cc, T_w, b, d_{50}, \rho, \rho_s, \tau_b, g, \mu, w, t) \tag{3}$$

Here, y_m is maximum scour depth, U_0 is velocity of jet coming from sluice opening, cc is clay content, T_w is tailwater depth, b is sluice gate opening, d_{50} median size of sediment, r is density of water, r_s is sediment density, t_b is bed shear stress, g is acceleration due to gravity, w is initial water content, μ dynamic viscosity of water, and t is time.

Applying Buckingham π-theorem with repeating variables as b, U_0, and r, the following set of dimensionless parameters are obtained.

$$\hat{y}_m = \left(\frac{L}{b}, \frac{T_w}{b}, \frac{d_{50}}{b}, \frac{\tau_b}{\rho U_0^2}, \frac{1}{F_r^2}, \frac{\rho_s}{\rho}, \frac{1}{R_e}, cc, w, \hat{t} \right) \tag{4}$$

where F_r is jet Froude number, R_e is jet Reynolds number. Since the parameters L, T_w, b, and w were kept constant, the terms L/b, T_w/b, and w are eliminated. The median size is dominated by sand, and the effect of clay size is ignored considering the constant size of sediment. As the same size of sand is used for all the runs, the term d_{50} is eliminated. Also, from the analysis there is no correlation found between shear, clay content, and scour depth. The bed shear variation with time is unknown after issuing the flow, and the effect of shear stress is neglected for the present study. F_r is maintained constant. The effect of r_s is negligible as uniform compaction was given for all the runs. R_e, effect is negligible for turbulent flows in open channels and is eliminated. The final equation reduced to

$$\frac{y_m}{b} = (cc, \hat{t}) \tag{5}$$

Nonlinear regression analysis is performed using the experimental data to obtain the time variation of maximum scour depth. Equation (5) yields the following relation for non-dimensional maximum scour depth for the present study.

$$\hat{y}_m = 0.57cc^{0.22}\hat{t}^{0.27} \quad 15 \le cc \le 40 \tag{6}$$

R^2 value of 0.76 obtained for Eq. (6). Figure 4 shows the line of agreement between the observed and predicted data. The standard error of 0.69 obtained for Eq. (6). Therefore, the above equation can satisfactorily describe the experimental data. The influence of clay content alone is considered from 15 to 40% for the given flow conditions. The scour prediction equations generally yield conservative estimates. Thus, Eq. (6) can be used for the estimation of time variation of scour depth for given flow conditions and properties of sediments applied.

Fig. 4 Comparison of maximum scour depth observed and calculated using Eq. (6)
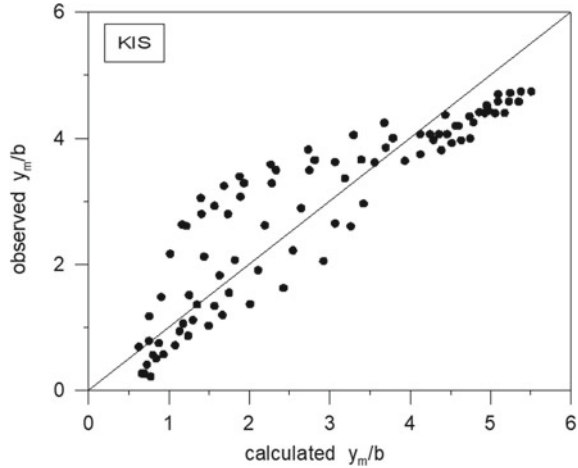
4 Conclusions

The experiments on scour producing by a submerged plane wall jet in clay–sand mixtures downstream of a sluice gate were performed using various clay contents (varied from 15 to 40%) using kaolinite clay as a mixture with sand. The presence of clay considerably influences the magnitude of scour. The following conclusions are drawn from the analysis of the results of the present study:

- For clay–sand mixtures, erosion characteristics differ in several ways in comparison with cohesionless sediments. However, for clay contents near to or around 20%, the properties of scour are similar in comparison with non-cohesive soils.
- The scour profiles obtained are two-dimensional for both cohesionless soils and clay–sand mixtures.
- The presence of clay can increase or decrease the scour depth depending on chemical reaction of the clay property with water. The variation of maximum scour depth with clay content was seen which is agreeing the results of Kho et al. [15] study but contradicting the results of Hamidifar and Omid [19] case. The attention is more emphasized on chemical properties of clay which plays very important role.
- The equation based on the dimensional analysis to determine the temporal variation of scour depth in two clay minerals is proposed to have a general understanding of clay behavior, although it is valid for the provided features of soil and flow conditions.
- However, it is recommended that experiments need to be conducted in natural clays obtained from the fields. The electrochemical properties and mineralogical composition affecting the scour in cohesive soils require greater attention.

Notations

b	Sluice opening size.
cc	Clay percentage.
d_{50}	Median size of sediment.
F_j	Jet Froude number.
Q	Discharge.
t	Time.
T_w	Tailwater depth.
h	Upstream water depth.
U_o	Mean jet velocity at vena contracta.
y	Vertical dimension of scour at time t.
y_m	Maximum scour depth at time t.
y_{me}	Maximum scour depth at semi-equilibrium state.
$\hat{y}_{me}$	y_{me}/b.
$\hat{y}_m$	y_m/b.

References

1. Chatterjee SS, Ghosh SN, Chatterjee M (1994) Local scour due to submerged horizontal jet. J Hydraul Eng 120:973–992. https://doi.org/10.1061/(asce)0733-9429(1994)120:8(973)
2. Rajaratnam N, Macdougall RK (1983) Erosion by plane wall jets. J Hydraul Eng 109:1061–1064
3. Rajaratnam N (1981) Erosion by plane turbulent jets. J Hydraul Res Res V 19:277–305. https://doi.org/10.1080/00221688109499508
4. Hassan NMKN, Narayanan R (1985) Local scour downstream of an apron. J Hydraul Eng 111:1371–1385. https://doi.org/10.1061/(ASCE)0733-9429(1985)111:11(1371)
5. Kells JA, Balachandar R, Hagel KP (2001) Effect of grain size on local channel scour below a sluice gate. Can J Civ Eng 28:440–451. https://doi.org/10.1139/cjce-28-3-440
6. Dey S, Sarkar A (2006) Scour downstream of an apron due to submerged horizontal jets. J Hydraul Eng 132:246–257. https://doi.org/10.1061/(ASCE)0733-9429(2006)132:3(246)
7. Melville BW, Lim SY (2014) Scour caused by 2D horizontal jets. J Hydraul Eng 140:149–155. https://doi.org/10.1061/(ASCE)HY.1943-7900.0000807
8. Dey S, Sarkar A (2008) Characteristics of submerged jets in evolving scour hole downstream of an apron. J Eng Mech 134:927–936. https://doi.org/10.1061/(asce)0733-9399(2008)134:11(927)
9. Kothyari UC, Jain RK (2008) Influence of cohesion on the incipient motion condition of sediment mixtures. Water Resour Res 44:1–15. https://doi.org/10.1029/2007WR006326
10. Kuti EO, Yen CL (1976) L'affouillement des sols cohésifs. J Hydraul Res 14:195–206. https://doi.org/10.1080/00221687609499667
11. Dey S, Westrich B (2003) Hydraulics of submerged jet subject to change in cohesive bed geometry. J Hydraul Eng 129:44–53. https://doi.org/10.1061/(asce)0733-9429(2003)129:1(44)
12. Mazurek KA, Rajaratnam N, Sego DC (2003) Affouillement d'un sol cohésif par des jets de paroi turbulents plans immergés. J Hydraul Res 41:195–206. https://doi.org/10.1080/00221680309499961
13. Hamidifar H, Omid MH, Nasrabadi M (2011) Scour downstream of a rough rigid apron. World Appl Sci J 14:1169–1178

14. Rustiati NB, Dermawan V, Rispiningtati R, Limantara LM (2017) The influence of sandy clay bed material to local scour behaviour. J Water L Dev 35:193–202. https://doi.org/10.1515/jwld-2017-0084
15. Kho KT, Valentine E, Glendinning S (2004) An experimental study of local scour around circular bridge piers in cohesive soils. Civ Eng 1–8
16. Jain R, Lodhi AS, Oliveto G, Pandey M (2021) Influence of Cohesion on scour at Piers founded in clay–sand–gravel mixtures. J Irrig Drain Eng 147:1–13. https://doi.org/10.1061/(asce)ir.1943-4774.0001616
17. Lodhi AS, Jain RK, Sharma PK, Karna N (2021) Influence of cohesion on scour at wake of partially submerged spur dikes in cohesive sediment mixtures. ISH J Hydraul Eng 27:123–134. https://doi.org/10.1080/09715010.2018.1525325
18. Balachandar R, Kells JA (1997) Local channel in scour in uniformly graded sediments: the time-scale problem. Can J Civ Eng 24:799–807. https://doi.org/10.1139/cjce-24-5-799
19. Hamidifar H, Omid MH (2017) Local scour of cohesive beds downstream of a rigid apron. Can J Civ Eng 44:935–944. https://doi.org/10.1139/cjce-2016-0398
20. Ansari SA, Kothyari UC, Ranga Raju KG (2002) Influence of cohesion on scour around bridge piers. J Hydraul Res 40:717–729. https://doi.org/10.1080/00221680209499918
21. Ansari SA, Kothyari UC, Ranga Raju KG (2003) Influence of cohesion on scour under submerged circular vertical jets. J Hydraul Eng 129:1014–1019. https://doi.org/10.1061/(ASCE)0733-9429(2003)129:12(1014)
22. Link O, Klischies K, Montalva G, Dey S (2013) Effects of bed compaction on scour at piers in sand-clay mixtures. J Hydraul Eng 139:1013–1019. https://doi.org/10.1061/(ASCE)HY.1943-7900.0000762
23. Middleton HE (1930) Properties of soils which influence soil erosion. US Dept Agric
24. Sonia Devi Y, Barbhuiya AK (2017) Bridge pier scour in cohesive soil: a review. Sadhana—Acad Proc Eng Sci 42:1803–1819. https://doi.org/10.1007/s12046-017-0698-5
25. Neave M, Rayburg S (2006) Salinity and erosion: a preliminary investigation of soil erosion on a salinized hillslope. IAHS-AISH Publ 531–539

Bridge Pier Scour Depth Prediction Model—A Review

A. Baranwal, B. S. Das, and A. Choudhary

Abstract The study of scouring around bridge piers is essential for the safe and economical design of bridges over river channels. The term scouring is a natural process by which particles around periphery of pier get eroded with the flowing water and is removed over a certain depth resulting in the creation of a scour hole around the bridge pier. The process of scouring occurred due to obstruction of flow in the river caused a formation of horseshoe vortices around the piers due to this vortices sediment around the pier get eroded and flow out with the water. Scouring has the potential to threaten the stability of bridge pier foundations. Clear water scouring (CWS) condition occurred when the shear stress of the bed sediments equals to the critical stress after that scouring of bed sediment is not happened and live bed scour (LBS) condition exits till scour depth varies continuously as sediment inflow and outflow from scour hole. In these conditions, scour depth around the pier continuously changes but equilibrium scour depth (ESD) remains same. To minimize the scouring, previous researchers performed experiments around bridge piers for different sizes, shapes, and different hydraulic conditions. In this review paper, all the available ESD predicting equation and different shape factors for various shapes and sizes of pier are collected from the previous literature for the prediction of scour depth.

Keywords Local scour · Clear water scouring (CWS) · Live bed scouring (LBS) · Scour depth

A. Baranwal (✉) · B. S. Das · A. Choudhary
Department of Civil Engineering, National Institute of Technology, Patna 800005, India
e-mail: anubhavnitp18@gmail.com

B. S. Das
e-mail: bsd.ce@nitp.ac.in

A. Choudhary
e-mail: amandeepc.pg19.ce@nitp.ac.in

1 Introduction

Scouring is the flowing out of bed materials in the flow field around an obstruction such as bridge pier and abutment. Nowadays, scouring is also considering an important parameter in the design and analysis of hydraulic structures. Muzzammil [1] reported that horseshoe vortex which is created due to obstruction of the cylindrical bridge piers is the primary causes of scouring around it. Dey and Raikar [2] performed study to calculate the characteristics of horseshoe vortex which play a significant role for developing the scour hole as shown in Fig. 1. During the experiment, the flow characteristics are measured with the help of acoustic Doppler velocimeter (ADV) at the different intermediate scour depth. It is finally concluded that flow and turbulence intensity of horseshoe vortex are the reasonably similar for the developing the scour depth. Mazumdar et al. [3] explained that when flow passes around the bridge pier there are separation of three-dimensional flow phenomena occurred, and due to the pier obstruction, two types of vortices are generated as horseshoe vortex at upstream bottom side of pier and wake vortex at the downstream side of the pier by the river flow. An increased of bottom shear stress is taking placed due to the formation of horseshoe vortex at that point, and hence, the local sediment is starting moving with the flow. This causes a development of scour hole taking placed at downstream side of the pier which change the flow pattern of the river due to reducing of the local shear stress. Scouring process and the total depth of scour are totally depend on the flow characteristics, pier shape, pier size, and river bed material. The major scour force is the dominant vortex on the upstream side of the pier, and it creates a scour hole around the pier when it removes bed sediment from bottom of the upstream side of the pier. The intensity of the vortices at the bottom of the pier reduces as the scour hole becomes deeper, and eventually a state of equilibrium is established. Whenever the shear stress caused by the vortices is equal to the critical shear stress of the sediment, then CWS condition occurred and after that bed material is not scoured and when the amount of sediment inflow equal to the amount of sediment outflow from the scour hole, then a LBS equilibrium state occurs. The scour depth varies in these conditions, but the average scour depth remains constant. The horseshoe vortices have more impact on the upstream sides of a pier, whereas wake vortices play a large role on the downstream side, as seen in Fig. 2. It is formed along the surface of the pier, then separated from both sides of pier, and continued towards downstream side. The wake vortex which is generated due to the flow separation caused by the pier obstruction. It is responsible to carry bed sediment towards downstream side of the pier. Intensity and size of the wake vortex are varying with the pier shape and pier size. The dissipation of wake vortex occurred rapidly towards the downstream side of the pier [4].
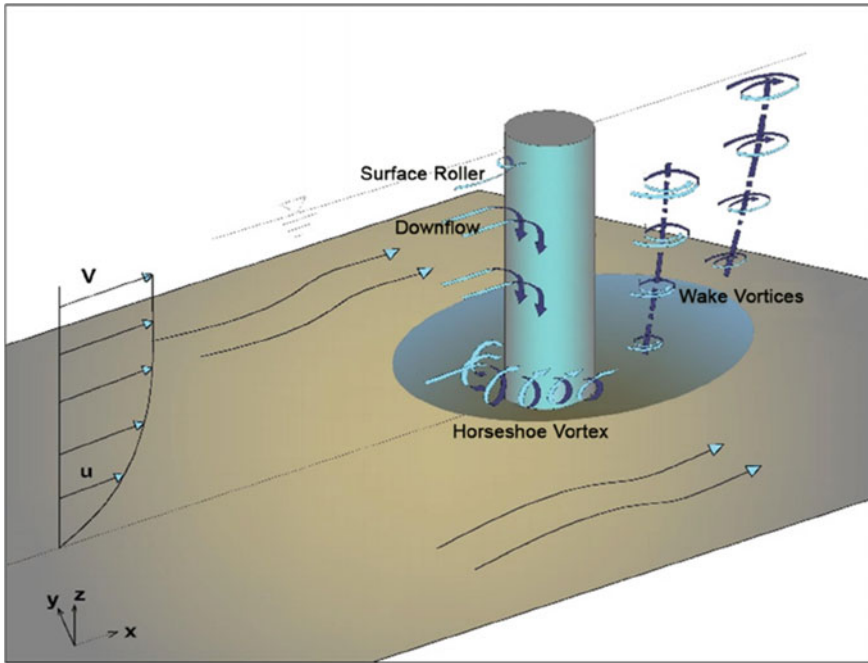
Fig. 1 Schematic diagram of horseshoe vortex on the *u/s* side of the pier [5]

Fig. 2 A depiction of wake vortices which form at the top surface of pier and moved towards downstream side [6]
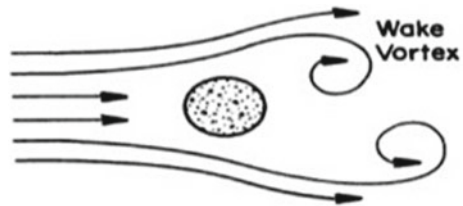
2 Main Causes of Bridge Collapse

In New Zealand, the problem of scouring is reasons on an average every year one bridge collapsed [7]. Arneson et al. [8] given performed a study with Federal Highway Administration (FHWA) and reported that 383 bridges were collapsed due to scouring in which 25% of damage of pier and 75% of damage of abutment as shown in Fig. 3. It is submitted a detailed report to the National Roads Board (NRB) of New Zealand, mentioned that total 108 bridges collapsed during 1960–1984 of which 29 were the failure due to abutment scour. Macky [9] also submitted report to the Department of Scientific and Industrial (DSIR) of New Zealand and mentioned that about 50% of total expenditure was expensed for bridge maintenance and repair work, out of which 70% was made for repairing of abutment scour.
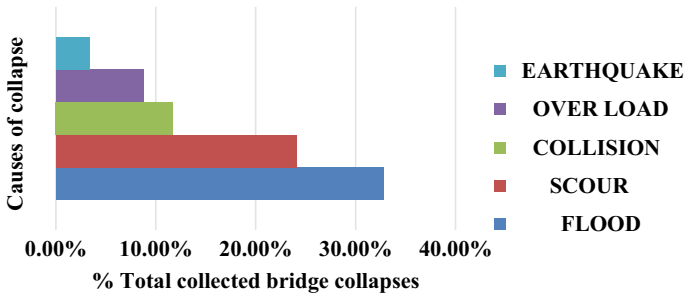
Fig. 3 Main causes of bridge collapse [10]

Local scour around bridge foundations such as piers and abutments are a typical cause of bridge failures. Local scour erodes the sediments surrounding the piers, reducing the lateral capacity of bridge pier foundations [11].

3   Type of Bridge Scour

Generally, total scouring can be classified into three main forms, namely general scouring, constriction scouring, and local scouring.

The total scour at a bridge pier can be categorized as one or several scour types, as shown in Fig. 4. General scour occurs in aggrading and degrading types of river channels due to changes in discharge or changes in the sediment quantity due to the absence of obstacles in the channel. Constriction scour occurs whenever the cross-sectional area of the channel is reduced due to the construction of structures such as bridge piers and abutments in the channel, the flow velocity of the channel increases, and increased shear stresses overcome the threshold shear stress of the bed, mobilizing the sediments in the channel [12]. Individual bridge piers and abutments are subject to local scouring. The induced downward flow at the upstream end of bridge piers causes localized deterioration in the structure [13]. The scour hole has a tendency to reduce the stiffness of the foundation system of bridges and can cause bridge piers to fail without warning. Sumer et al. [14] reported that deformation of flow fields around obstacles usually increases local bed shear stress and turbulent intensity, leading to an increase in sediment transport. Ghorbani and Karimi [15] investigated scouring around bridge piers at flooded river and observer that as particle size of river sediment increased, the depth of local scour decreased so scouring is also influenced by bed surfaces and fine sand bed level scouring would be more comparative. Guo [16] has done a studied-on pier scouring in CWS condition for mix sediment condition and it is observed that scour depth around the bridge pier is the results from sediment interactions of flow structures. The flow structure interaction was responsible for generating horse vortices at the foot of the pier playing an important role for ESD. Whenever area of flow blockage is increased then ESD is also
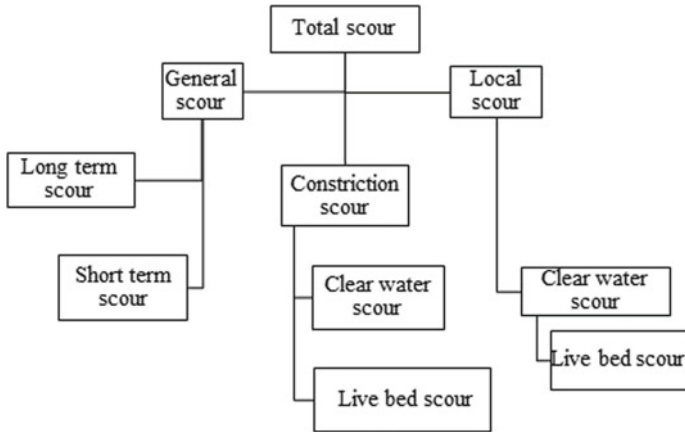
Fig. 4 Hierarchy of the classification of total scour

increased and it decreased with nonuniform sediment. To model scour depth, many researchers have been used regression analysis, numerical modelling, and various soft computing techniques such as ANN, ANFIS, GEP, SVM, and M5 Tree. Choudhary [17] developed two scour depth models for bridge pier using ANFIS and GEP for CWS and LBS and explained that the ANFIS model shows the good accuracy compared to other existing model provided by various researchers. The R^2 value was found to be greater than 0.90, and MAPE value was found to be less than 10% for both CWS and LBS conditions. Both models have been recommended for the scour depth modelling due to its robustness and better accuracy.

4 Development of the Scour Depth on the Basis of Time Passage

It is mentioned that under LBS condition (where sediment is generally in motion), rapid growth of scour depths results in the flow reaching ESD soon while fluctuating about the ESD. An equilibrium CWS depth is asymptotically achieved for a much longer time than LBS conditions.

5 Factors Influencing Scour Depth

Flow velocity (v), flow depth (y), pier width (b), pier length (l), and angle of attack (θ) are the important parameters which affect scouring phenomena.

6   Bridge Scour Prediction

Over the past few decades, bridge researchers and engineers have concluded that bridge pier and abutment scour are influenced by many factors such as the dynamic hydraulic properties of the flow, geometry of the channel, shape of the bridge piers, size of pier, abutments and different bed material. Prediction of scour depth around bridge piers using exiting information during or prior to flood events is critical for avoiding bridge collapse and potential loss of life. The practice of scour prediction can be divided into two categories: (a) utilizing empirical equations to predict scour depth around bridge piers; (b) using soft computing methods such as ANN, ANFIS, SVM, and GEP to predict bridge scour [18, 19]. It is worth noting that both the real time and final scour depths can be forecasted.

7   Prediction of Equilibrium Scour Depth (ESD) of Different Shapes of Pier

The ability to predict ESD is required for the cost-effective and safe design of bridge network elements. An underestimation of the scour depth results in a shallow bridge foundation, while an overestimation of the scour depth results in an uneconomical design [20, 21]. Design flow conditions are chosen to predict the ESD. The ESD or CWS under steady flow must be determined on a continual basis such as [22–28].

Breusers et al. [25] proposed an Eq. (1) to calculate the ESD:

$$y_{se} = 1.35 \, K_i b^{0.7} y^{0.3} \tag{1}$$

where y_{se} is the ESD, K_i (correction of pier shape) $= 1.0$ for circular pier, $b =$ pier width, $y =$ flow depth

Colorado State University (CSU) [29] is a prediction of ESD equation as published in the literature were used to, and it can be predicting the ESD for different geometry of the pier. CSU formulas can be written as shown in Eq. (2).

$$\frac{y_{se}}{b} = 2K_1 K_2 K_3 K_4 \left(\frac{y}{b}\right)^{0.35} F_r^{0.43} \tag{2}$$

where F_r is Froude no., $v =$ flow velocity, $g =$ gravitational acceleration, and constant $K_1 =$ correction of pier shape which is a function of pier (length/width), $K_2 =$ correction of approach flow attack angle ($K_2 = 1$ for regular approach flow), $K_3 =$ correction of bed form ($K_3 = 1$ for Clear water with flatbed), and $K_4 =$ correction of sediment mixtures ($K_4 =$ for uniform sediment). For all the shapes of piers in CWS and sediment mixtures, the CSU Eq. (3) becomes

$$y_{se} = 2K_1 y^{0.35} b^{0.65} F_r^{0.43} \tag{3}$$

Correction of pier shape (K_1) is also termed as shape factors (K_{sh}) of pier. The value of shape factor for uniform piers (piers having constant section throughout their depth) Melville and Coleman [7] has been proposed with the help of several investigators, including [30–33]. Shape factor is calculated as the ratio of scour depth measured for a non-circular shape to the scour depth for a circular shape for $l/b = 4$ where l and b are the length and width of pier [7].

$$K_{sh} = \frac{y_{se}(\text{non - circular})}{y_{se}(\text{circular})} \tag{4}$$

where y_{se} (non-circular) and y_{se} (circular) are the ESD for non-circular and circular shape of piers.

8 A Brief Summary of Scour Depth Modelling Equation

Following are the brief summary of scour depth modelling equation which is collected from the literature;

Laursen [22] proposed Eq. (5) for prediction of total scour depth

$$\frac{d_s}{y} = 1.35\left(\frac{b}{y}\right)^{0.70} \tag{5}$$

Neill [23] proposed a model to predict the scour depth Eq. (6)

$$\frac{d_s}{b} = 1.35\left(\frac{y}{b}\right)^{0.30} \tag{6}$$

Breusers [34] has given Eq. (7) for estimation of ESD

$$\frac{d_s}{y} = 1.4\left(\frac{b}{y}\right) \tag{7}$$

Shen et al. [35] developed Eq. (8) for estimation of ESD

$$\frac{d_s}{y} = 11.0(\text{Fr})^2 \tag{8}$$

Shen et al. [24] obtained Eq. (9) for estimation of ESD

$$\frac{d_s}{y} = 3.4(\text{Fr})^{.67}\left(\frac{b}{y}\right)^{0.67} \tag{9}$$

Coleman [36] has been provided Eq. (10) for estimation of ESD

$$\frac{d_s}{y} = 1.39(\text{Fr})^{0.2}\left(\frac{b}{y}\right)^{0.9} \tag{10}$$

Colorado State University (CSU) [29] developed Eq. (11) for scour depth estimation, and it is best suited for experimental data

$$\frac{d_s}{y} = 2.2(\text{Fr})^{0.43}\left(\frac{b}{y}\right)^{0.65} \tag{11}$$

Kothyari et al. [37] developed Eq. (12) for scour depth for LBS and CWS

$$\frac{d_s}{b} = 0.88\left(\frac{b}{d_{50}}\right)^{0.67}\left(\frac{y}{d_{50}}\right)^{0.4}(\beta)^{-0.3} \tag{12}$$

where $\beta = (B - b)/B$ and B—channel width

Richardson and Davis [4] have been modified HEC-18 equation for prediction of scour depth which is actually derived from Colorado State University equation. The Federal Highway Administration (FHWA) actually developed this equation by laboratory test data.

$$\frac{y_s}{y_1} = 2.0K_1K_2K_3\left(\frac{a}{y_1}\right)^{0.65}\left(F_{r_1}\right)^{0.43} \tag{13}$$

$$K_2 = \left(\cos\theta + \frac{L}{a}\sin\right)^{0.65} \tag{14}$$

$$F_{r_1} = \frac{V_1}{(gy_1)^{1/2}} \tag{15}$$

where K_1 and K_3—pier shape factor, and θ—angle of attack of the flow.

Sheppard et al. [38] proposed Eq. (16) using dimensionless analysis for scour depth model

$$\frac{d_s}{b} = 2.5f_1\left(\frac{y}{b}\right)f_2\left(\frac{U}{U_C}\right)f_3\left(\frac{b}{d_{50}}\right) \tag{16}$$

where

$$f_1\left(\frac{y}{b}\right) = \tanh\left(\frac{b}{d_{50}}\right)^{0.4} \tag{17}$$

$$f_2\left(\frac{U}{U_C}\right) = 1 - 1.175\left[\ln\left(\frac{U}{U_C}\right)\right]^2 \tag{18}$$

$$f_3\left(\frac{b}{d_{50}}\right) = \left[\left(\frac{\left(\frac{b}{d_{50}}\right)}{0.4\left(\frac{b}{d_{50}}\right)^{1.2} + 10.6\left(\frac{b}{d_{50}}\right)^{-0.13}}\right)\right] \tag{19}$$

where U—approach mean velocity, U_c—critical velocity, and d_{50}—mean diameter of sediment

Kim et al. [39] proposed Eq. (20) for estimation of ESD under equilibrium scour condition

$$\frac{d_s}{y} = 0.69\left(\frac{b}{y}\right)^{0.35}\left(\frac{d_{50}}{y}\right)^{-0.10}\sigma^{0.39}\mathrm{Fr}^{0.56} \tag{20}$$

Pandey et al. [40] provided Eq. (21) for the scour depth modelling

$$\frac{d_s}{y} = 0.987\left(F_{d_{50}}\right)^{-0.302}\left(\frac{y}{b}\right)^{-0.566}\left(\frac{b}{d_{50}}\right)^{0.079} \tag{21}$$

where $F_{d_{50}}$—particle Froude number.

Rathor and Manekar [41] gave Eq. (22) for gene expressing programming model to calculate the ESD by using field along with laboratory data.

$$\frac{d_s}{y} = \mathrm{EP}_1 + \mathrm{EP}_2 + \mathrm{EP}_3 \tag{22}$$

where $\mathrm{EP}_1 = \frac{b}{b+1.6y}$, $\mathrm{EP}_2 = \frac{bV}{y}\left(\frac{1}{b+U}\right)$ and $\mathrm{EP}_3 = \frac{b}{y\left\{\left(\frac{34.12y}{F_{rd}}\right)+2\sigma_g\right\}}$.

9 Collection of Data for Clear Water Scouring (CWS) and Live Bed Scouring (LBS)

Choudary [17] has been collected data from different research papers. A total of 655 datasets out of which 442 and 213 datasets are for CWS and LBS, respectively. The details of datasets and their ranges have been shown for both conditions in Tables 1 and 2.

10 Error Analysis of Exiting Models

To check the strength of the aforementioned models, error analysis has been performed in terms of mean absolute percentage error (MAPE), root mean square error (RMSE), coefficient of determination (R^2), Nash–Sutcliffe coefficient (E) and index of agreement (I_d) [54, 55]. The results of error analysis are presented in Tables 3

Table 1 Different parameters range for CWS condition collected from literature [17]

S. No.	Authors	b/y	d_{50}/y	u/u_c	σ	F_r
1	Chabert and Engeldinger [31]	0.143–1.5	0.0007–0.0300	0.536–0.976	1.3–1.3	0.097–0.597
2	Shen et al. [24]	0.713–1.299	0.0011–0.0020	0.533–0.882	1.4–1.4	0.103–0.213
3	Ettema [42]	0.166–0.166	0.0009–0.0068	0.949–0.952	1.3–4.6	0.144–0.394
4	Jain and Fischer [43]	0.498–0.994	0.0244–0.0244	0.808–1.0	1.3–1.3	0.499–0.618
5	Ettema [44]	0.048–2.399	0.0003–0.1070	0.444–1.0	1.1–1.3	0.068–0.879
6	Chee [45]	0.509–0.509	0.0038–0.0038	0.852–0.852	1.2–1.2	0.231–0.231
7	Chiew [46]	0.151–0.265	0.0014–0.0152	0.795–0.977	1.2–4.3	0.170–0.480
8	Yanmaz and Altinbilek [27]	0.285–1.486	0.0062–0.0237	0.447–0.737	1.1–1.3	0.230–0.234
9	Dey et al. [47]	1.140–2.165	0.0052–0.0165	0.744–1.0	1.3–1.4	0.291–0.374
10	Graf (1995) [48]	0.431–0.647	0.0090–0.0123	0.922–0.926	1.3–1.3	0.404–0.448
11	Melville [49]	0.079–1.665	0.0039–0.0075	0.438–0.820	1.3–1.3	0.124–0.267
12	Melville and Chiew [28]	0.190–1.0	0.0048–0.0136	0.415–0.904	1.3–1.3	0.122–0.382
13	Sheppard et al. [38]	0.090–1.634	0.0001–0.0052	0.689–0.909	1.2–1.5	0.072–0.276
14	Sheppard and Miller [50]	0.310–0.362	0.0005–0.0019	0.560–0.870	1.3–1.3	0.084–0.180
15	Ettema et al. [51]	0.064–0.406	0.0010–0.0010	0.858–0.858	1.3–1.3	0.147–0.147
16	Pandey et al. (2018) [40]	0.400–1.459	0.0024–0.1259	0.220–0.970	1.12–1.23	0.220–0.970
17	Pandey et al. [52]	0.471–1.350	0.0250–0.0856	0.708–0.984	1.51–1.88	0.433–0.713
18	Pandey et al. [53]	0.550–1.350	0.0395–0.0474	0.660–0.940	1.38–1.38	0.424–0.553

and 4. In Table 3, error analysis of different approaches for CWS using normalized data is depicted, in which Shen et al. [35] give high MAPE value of 394.23% and Choudhary [17] model provides MAPE error less than 10%. In Table 4, error analysis of different approaches for LBS using normalized data is shown, in which Shen et al. [35] give high MAPE value of 240.01% and Choudhary [17] gives the least error that is 5.29%, respectively.

Table 2 Different parameters range for LBS condition collected from literature [17]

S. No.	Authors	b/y	d_{50}/y	u/u_c	σ	F_r
1	Chabert and Engeldinger [31]	0.214–1.0	0.0015–0.0052	1.029–1.309	1.3–1.3	0.189–0.378
2	Shen et al. [24]	0.568–1.500	0.0006–0.0026	1.033–3.941	1.4–2.2	0.198–0.951
3	Jain and Fischer [43]	0.206–0.994	0.0024–0.0244	1.025–4.690	1.3–1.3	0.499–1.498
4	Chee [45]	0.509–1.021	0.0024–0.0140	1.114–4.298	1.2–1.3	0.302–1.213
5	Chiew [46]	0.085–0.412	0.0013–0.0152	1.007–3.101	1.2–5.5	0.178–0.881
6	Sheppard et al. [38]	0.250–1.668	0.0001–0.0012	1.088–1.190	1.5–1.5	0.115–0.223
7	Sheppard and Miller [50]	0.355–0.757	0.0006–0.0028	1.386–5.360	1.3–1.3	0.299–1.260

Table 3 Error analysis of existing equations for clear water scouring using normalized data [17]

Existing equations	MAPE	RMSE	R^2	E	I_d
Choudhary [17]-ANFIS model	9.39	0.05	0.96	0.94	0.98
Choudhary [17]-GEP model	21.37	0.07	0.88	0.86	0.94
Shen et al. [35]	394.23	0.39	0.01	-6.53	0.20
Shen et al. [24]	65.68	0.07	0.81	0.77	0.92
CSU [29]	54.02	0.06	0.88	0.79	0.92
Kim et al. [39]	99.94	0.18	0.39	-0.70	-0.98
Pandey et al. [56]	96.70	0.20	0.54	-0.96	0.69

Table 4 Error analysis of different approaches for LBS condition using normalized data [17]

Existing equations	MAPE	RMSE	R^2	E	I_d
Choudhary [17]-ANFIS model	5.29	0.05	0.95	0.95	0.98
Choudhary [17]-GEP model	15.31	0.07	0.90	0.90	0.96
Laursen and Toch [32]	81.45	0.38	0.01	−2.43	−2.96
Breusers [34]	71.24	0.35	1.97	−1.90	−2.72
Shen et al. [35]	240.01	0.87	0.05	−17.19	0.06
Shen et al. [24]	68.16	0.30	0.01	−1.18	−1.64
Coleman [36]	75.46	0.36	0.0005	−2.12	−3.29

11 Conclusions

In this paper, three main topics relevant to bridge pier scouring have been presented: (1) The mechanism of scour taking place at the pier foundation level; (2) different available modelling equations in the literature for prediction of scour depth around piers; and (3) the developed ANFIS model for CWS condition and LBS condition showing the good accuracy with the observed scour depth ratio obtained from laboratory and field experiments. Moreover, this review paper addressed the complex issue of scouring which quantifies the uncertainty associated with the pier scour estimate.

References

1. Muzzammil M (2003) Characteristics of horseshoe vortex at cylindrical bridge pier models. Ph.D. Thesis, Department of Civil Engineering, Indian Institute of Technology, Kanpur, India
2. Dey S, Raikar R (2007) Characteristics of horseshoe vortex in developing scour holes. J Hydraul Eng 133(4):399–413
3. Mazumdar A, Das R, Das S (2014) Scour mechanism around piers at clear water equilibrium condition. Int J Adv Eng Res Develop 2348–6406
4. Richardson EV, Davis SR (2001) Evaluating Scour at Bridges Report. Hydraulic Engineering Circular No. 18, NHI 01–001 (HEC-18), Federal Highway Administration, US Department of Transportation, Washington, DC, USA
5. Akhlaghi E, Babarsad MS, Derikvand E, Abedini M (2019) Assessment the effects of different parameters to rate scour around single piers and pile groups: a review. Arch Comput Meth Eng 26(1):1–15
6. Akan AO (2006) Open channel hydraulics. Amsterdam, The Netherlands, Elsevier BV
7. Melville BW, Coleman SE (2000) Bridge scour. Water Resources Publications, LLC, Colorado, USA
8. Arneson LA, Zevenbergen LW, Lagasse PF, Clopper PE (2012) Evaluating scour at bridges (No. FHWA-HIF-12-003). National Highway Institute (US)
9. Macky GH (1990) Survey of road expenditure due to scour. CR-90-09, Department of Scientific and Industrial Research, Hydrology Centre, Christchurch, New Zealand
10. Imhof D (2004) Risk assessment of existing bridge structures. PhD Thesis, University of Cambridge, UK
11. Rambabu M, Rao SN, Sundar V (2003) Current-induced scour around a vertical pile in cohesive soil. J Ocean Eng 30(7):893–920
12. Briaud et al (1999) Prediction of scour rate in cohesive soils at bridge piers. J Geotech Geo-Environ Eng 559(4):237–246
13. Hamill G, Ryan D (2000) Designing for protection against propeller scour in harbours. In: 4th International conference on hydrodynamics.
14. Sumer BM, Chu LHC, Cheng NS, Fredsoe J (2003) Influence of turbulence on bed load sediments transport. J Hydraul Res 129(8):585–596
15. Ghorbani B, Karimi A (2007) A comparison of single and double submerged vanes effect on the scour occurring at a cylindrical pier. In: Proceedings of 6th conference of hydraulic, pp 4–6
16. Guo J (2012) Pier scour in clear water for sediment mixtures. J Hydraul Res 50(1):18–27
17. Choudhary A (2021) Modelling of local scour depth at bridge pier using ANFIS and GEP. M.Tech Dissertation, NIT Patna, India
18. Nil, Baranwal A, Das BS (2023) Clear water and live bed scour depth modelling around bridge pier using support vector machine. Can J Civ Eng (inPress)

19. Nil, Baranwal A, Das BS (2023) Live bed scour depth modelling around bridge pier using Support Vector Machine, River Flow 2022, 11th International Conference on Fluvial Hydraulics (in Press)
20. Ting FC, Briaud JL, Chen HC, Gudavalli R, Perugu S, Wei G (2001) Flume tests for scour in clay at circular piers. J Hydraul Eng 127(11):969–978
21. Baranwal A, Das BS, Setia B (2023) A comparative study of scour around various shaped bridge pier. Eng Res Express 5:015052
22. Laursen EM (1963) An analysis of relief bridge scour. J Hydraul Div 89(3):93–118
23. Neill CR (1964) River bed scour: a review. Res. Council of Alberta, Bridge Engineers, Contract No. 281, Calgary, Alberta, Canada
24. Shen HW, Schneider VR, Karaki S (1969) Local scour around bridge piers. J Hydraul Div 14(3):120–153
25. Breusers HNC, Nicollet G, Shen HW (1977) Local scour around cylindrical piers. J Hydraul Res IAHR 15(3):211–252
26. Raudkivi AJ, Ettema R (1983) Clear-water scour at cylindrical piers. J Hydraul Eng 109(3):338–350
27. Yanmaz AM, Altinbilek HDGA (1991) Study of time-dependent local scour around bridge piers. J Hydraul Eng 117(10):1247–1268
28. Melville BW, Chiew YM (1999) Time scale for local scour at bridge piers. J Hydraul Eng 125(1):59–65
29. Colorado State University (1975) Highways in the river environment. Hydraulic and Environmental Design Considerations, The Federal Highway Administration, U.S. Department of Transportation, Washington, DC, USA
30. Tison LJ (1940) Scour around bridge piers in rivers. Annales Des Travaux Publics De Beligique 41(6):813–871
31. Chabert J, Engeldinger P (1956) Study of scour around bridge piers. Rep. Prepared for the Laboratoire National d'Hydraulique
32. Laursen EM, Toch A (1956) Scour around bridge piers and abutments (vol 4). Iowa Highway Research Board, Ames, IA
33. Garde RJ, Subramanya K, Nambudripad KD (1961) Study of scour around spur-dikes. J Hydraul Div 87(6):23–37
34. Breusers HNC (1965) Scour around drilling platforms. Bull Hydraul Res 19
35. Shen HW, Schneider VR, Karaki S (1966) Mechanics of local scour. Institute for Applied Technology, US Dept. of Commerce, National Bureau of Standards USA
36. Coleman NL (1971) Analyzing laboratory measurements of scour at cylindrical piers in sand beds. Hydraul Res Its Impact Environ Proc 3:307–313
37. Kothyari UC, Garde RCJ, Ranga Raju KG (1992) Temporal variation of scour around circular bridge piers. J Hydraul Eng 118(8):1091–1106
38. Sheppard DM, Odeh M, Glasser T (2004) Large scale clear-water local pier scours experiments. J Hydraul Eng 130(10):957–963
39. Kim I, Fard MY, Chattopadhyay A (2015) Investigation of a bridge pier scour prediction model for safe design and inspection. J Bridg Eng 20(6):04014088
40. Pandey M, Sharma PK, Ahmad Z, Karna N (2018) Maximum scour depth around bridge pier in gravel bed streams. Nat Hazards 91(2):819–836
41. Rathod P, Manekar VL (2020) Gene expression programming to predict local scour using laboratory and field data. ISH J Hydraul Eng 41(3):1–9
42. Ettema R (1976) Influence of bed material gradation on local scour. University of Auckland
43. Jain SC, Fischer EE (1979) Scour around circular bridge piers at high Froude numbers. FHWA-RD-79-104 Final Report
44. Ettema R (1980) "Scour at bridge piers." Rep. No. 216, School of Engineering., University of Auckland, Auckland, New Zealand
45. Chee RKW (1982) Live-bed scour at bridge piers. Auckland University, New Zealand, Publication of, p 290

46. Chiew YM (1984) Local scour at bridge piers. Auckland University, New Zealand, Publication of

47. Dey S, Bose SK, Sastry GL (1995) Clear water scour at circular piers: a model. J Hydraul Eng 121(12):869–876

48. Graf WH (1995) "Local scour around piers." Annu. Rep., Laboratoire de Recherches Hydrauliques, Ecole Polytechnique Federale de Lausanne, Lausanne, Switzerland, B.33.1–B.33.8

49. Melville BW (1997) Pier and abutment scour: integrated approach. J Hydraul Eng 123(2):125–136

50. Sheppard DM, Miller W (2006) Live-bed local pier scour experiments. J Hydraul Eng ASCE 132(7):635–642

51. Ettema R, Kirkil G, Muste M (2006) Similitude of large-scale turbulence in experiments on local scour at cylinders. J Hydraul Eng 132(1):33–40

52. Pandey M, Zakwan M, Khan MA, Bhave S (2020) Development of scour around a circular pier and its modelling using genetic algorithm. Water Supp 20(8):3358–3367

53. Pandey M, Zakwan M, Sharma PK, Ahmad Z (2020) Multiple linear regression and genetic algorithm approaches to predict temporal scour depth near circular pier in non-cohesive sediment. ISH J Hydraul Eng 26(1):96–103

54. Das BS, Khatua KK (2018) Flow resistance in a compound channel with diverging and converging floodplains. J Hydraul Eng 144(8):04018051

55. Das BS, Khatua KK, Devi K (2016) Prediction of energy loss in compound channels having enlarging floodplains. River Flow-2016. Edited by G. Constantinescu, M. Garcia, and D. Hanes. CRC Press, New York, 65–71

56. Pandey M, Ahmad Z, Sharma PK (2016) Estimation of maximum scour depth near a spur dike. Can J Civ Eng 43(3):270–278

Analysis of Scour Depth Around a Bridge Pier Using HEC-RAS Modeling Tool—A Case Study

Biswajit Dalal and Subhrajyoti Deb

Abstract Bridges are significant structures that require a large investment to construct, and it is necessary to protect these structures by constant monitoring and maintenance. In this study, we have used HEC-RAS programming tool to develop a scour model for evaluating the maximum local scour depth around bridge piers from the observed data from 1980 to 2010 of the Subhas bridge in Tripura, India. Calibration of our model is performed using different empirical scouring models where it is found that the computed scour depth from HEC-RAS program is in line with other models like CSU, Larras, and Ahmed. Dimensionless analysis is also performed to find the variation of scour depth with flow depth, Froude number, angle of attack, and contraction ratio. An increase in scour depth with increase in pier diameter is observed in this study. Overall, the HEC-RAS modeling tool performed well to predict local scour around piers, and the present study found that the bridge piers are safe against the scouring.

Keywords Bridge piers · Contraction scour · Local scour · Scour depth · HEC-RAS

1 Introduction

Bridges play an important role for connecting highway and railway networks. Bridge safety and serviceability have long been major considerations in the practice and profession of civil engineering [1]. When water flows through a bridge, in that case scour can be defined in such a way that it is nothing but the erosive action of the running water, when it excavates the sediment from the bed or banks of the river bed, due to the interaction of the structures, such as bridge pier, abutments on the flowing water [2]. The main characteristic features of the flow is a relatively large secondary vortex flow within the scour hole and skewed velocity distributions along the circumference of the pier [3]. In alluvial stream continuous transportation of

B. Dalal (✉) · S. Deb

Department of Civil Engineering, ICFAI University Tripura, Tripura 799210, India

e-mail: biswajitdalal.official@gmail.com
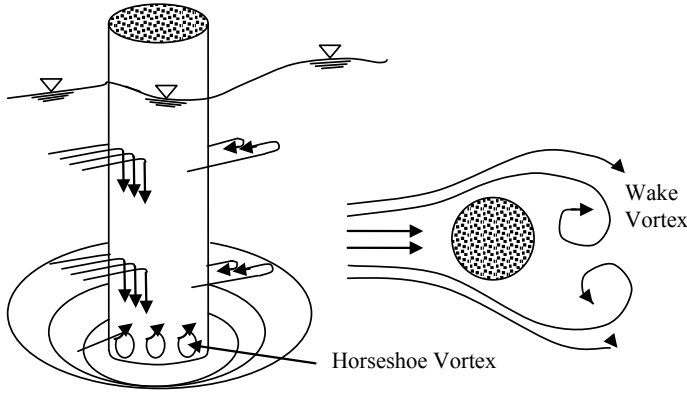
Fig. 1 Schematic sketch of vortex system at circular bridge pier

sediment can be seen as a geomorphological process. If something disrupts this sediment transportation process by constructing barrages, dams etc., it may cause a long-term changes in the stream bed evaluation [4]. Due to the continuous sediment transportation if it deposits in the reach length and due to the deposition if river bed increases then it is called aggradations and in an opposite way, due to the erosion if sediment bed decreased day by day then it is called degradation. But, in total scour aggradations does not have any contribution [5]. In 1930 Lacey's regime formula was developed with a very limited field data in the Ganga River considering waterway ranged between 3.6 and 2 km [6]. The study revealed that the width of waterway has affects on the abutment scour and the contraction scour. Another study suggested that the angle of attack is also a significant factor which affects scour depth around a bridge pier [7]. The separation of the upstream incoming boundary layer and the development near the bottom of necklace-like vertical formations are known as horseshoe vortices, which stretch around the pier and bend over its upstream portion as a result of pier. If the upstream flow is turbulent, these vortices are highly variable in time [8]. The schematic diagram of vortex system at circular pier is shown below in Fig. 1.

2 Theoretical Background

Maximum pier scour depths may be predicted using the Colorado State University (CSU) equation for both live-bed and clear-water pier scour. The scour depth (y_s) is estimated as follows:

$$y_s = 2.0 K_1 K_2 K_3 K_4 a^{0.65} y_1^{0.35} \mathrm{Fr}_1^{0.43} \tag{1}$$

where K_1 = shape factor, K_2 = angle of attack factor, K_3 = bed slope factor, K_4 = bed material factor, y_1 = depth measured at upstream side of the pier in meter, a = Width of piers in meter, and Fr_1 = Froude number. All the flow distribution output for the cross section is taken at the just upstream side of the pier.

A local pier scour equation developed by Dr. David Froehlich has been added to the HEC-RAS software as an alternative to the CSU equation (Froehlich 1991).

Dr. David Froehlich introduced another model as an alternative to the CSU equation (Froehlich 1991; FHWA 1996). The Froehlich model is an established model to estimate local scour around a pier, and it is given by:

$$y_s = 0.32\phi (a')^{0.62} y_1^{0.47} Fr_1^{0.22} D_{50}^{-0.09} + a \tag{2}$$

where y_1 = depth measured at upstream side of the pier in meter, Fr_1 = Froude number, a' = width of the pier in the direction of the flow in meter, and ϕ = Shape factor.

The algorithms of CSU (Eq. 1) as well as Froehlich (Eq. 2) are inbuilt in the HEC-RAS modelling tool. So a non-dimensional analysis is done directly from the output data which are produced by the HEC-RAS.

3   Calibrated Models

In the present study, scour model developed by HEC RAS tool is compared with some other scour equations. Scour depth (y_{sp}) is estimated as follows:

$$\text{Ahmad (1953)} \quad y_{sp} = K q^{2/3} - y_0 \tag{3}$$

where y_0 = flow depth at the upstream of pier or abutment excluding local scour; K = Flow parameter which depends upon size and shape of the piers, width of the abutments, angle of attack, the approach velocity and the boundary conditions [9].

$$\text{Blench-Inglis (1949)} \quad y_{sp} = 1.8 b^{0.25} q^{0.5} \left(\frac{y_0}{V_0^2} \right)^{0.25} - y_0 \tag{4}$$

where b = pier width, q = flow rate per unit width in the upstream side of the river, y_0 = bed factor, and V_0 = approach velocity in the upstream side of the river.

$$\text{Colorado State University(1975)} \quad y_{sp} = 2.0 y_0 K_1 K_2 \left(\frac{b}{y_0} \right)^{0.65} Fr^{0.43} \tag{5}$$

where K_1 = a model parameter which depends upon the shape of the bridge piers, K_2 = a model parameter which depends upon the ratio of the pier length to pier width, y_0 = bed factor, b = the angle of the approach flow referenced to the bridge

pier, and Fr = Froude number.

$$\text{Froehlich (1988)} \quad y_{\text{sp}} = 0.32 b \phi \left(\frac{b'}{b}\right)^{0.62} \left(\frac{y_0}{b}\right)^{0.46} \text{Fr}_0^{0.2} \left(\frac{b}{d_{50}}\right)^{0.08} \quad (6)$$

Here, b = pier width parallel to the flowing water, b' = a parameter which depends upon the shape of the pier, ϕ = angle of approach measured in degrees, Fr = Froude number, and d_{50} = grain size in mm.

$$\text{Inglis-Poona (1949)} \quad y_{\text{sp}} = 1.73 b \left(\frac{y_0}{b}\right)^{0.78} - y_0 \quad (7)$$

$$\text{Larras (1963)} \quad y_{\text{sp}} = 1.42 K_{s2} b^{0.75} \quad (8)$$

where y_0 = flow depth in the upstream of the pier, K_{S2} = a model parameter which depends the shape of the pier, and b = pier width.

$$\text{Shen-Maza (1964)} \quad y_{\text{sp}} = 3.4 \text{Fr}^{0.67} \quad (9)$$

where Fr = Froude number.

4 Data Collection

The study area is located near Udaipur in Tripura over Gomati River. The latitude and longitude of Udaipur are 23°31′ N and 91°31′ E, respectively. This bridge is connecting Assam-Agartala Nation Highway No- 8.

Thirty year's peak discharge data for Gomati River is collected from Gomati Barrage Subdivision under Water Resource Division, Udaipur, and some other data also collected from this division. These data include section of the bridge at various intervals, HFL, LBL, water depth, etc. These data are arranged from the year 1980 to 2010. The graphical representation of the data is shown in Fig. 2. It is shown that the maximum peak discharge over thirty years was occurred during the year 1980 to 2010.

Sediment sample was collected from the bridge site using the auger. Dry sieve analysis is carried for Gomati River sediment sample and plotted in the graph as shown in Fig. 3a and d_{50} value is calculated for analysis of scour in HEC-RAS modeling tool [10]. In the present study, scouring due to flood has been computed.
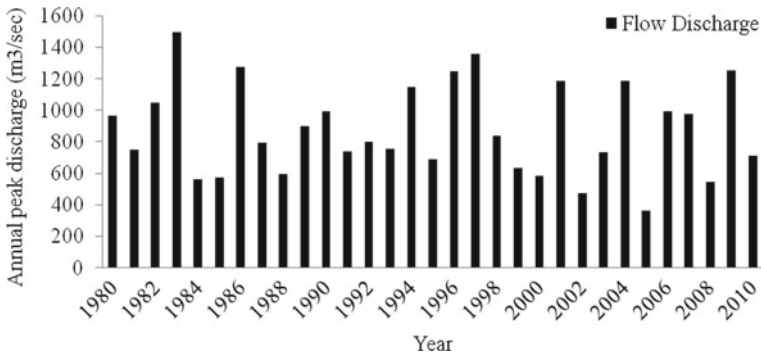
Fig. 2 Peak discharge data of Gomati River for the period 1980–2010

5 Model Development in HEC-RAS

HEC-RAS is a good tool to estimate the local scour and mobile bad computation [11]. In this study, one bridge pier scour model is developed using the HEC-RAS [version 5.0] tool for Subhas Setu over Gomati River. Two conditions have been applied. One is full waterway condition, and another is 30% restricted waterway condition. Calibration and validation of this model also have done. Geomantic data of Subhas Setu is entered into the HEC-RAS software. The interface of HEC-RAS is shown in the Fig. 3b.

6 Results and Discussion

6.1 Computation of Scour Depth

Scour depends on many factors like discharge, velocity of flow, water level, angle of attack, pier diameter, etc. [12]. Present study is considering only discharge, pier diameter, and angle of attack as variable. Angle of attack varies from 0° to 15° and pier diameter varies from 1 to 5 m. Scour profile is examined for both the conditions. One is full stretch waterway, and another is 30% restricted waterway. Table 1 shows all the value of scour which is generated in HEC-RAS modeling tool for both conditions.

From the above table, it is clear that the scour in river bed increases with the increase of pier diameter as well as angle of attack. The graphical representation between pier diameter and scour depth at different angle of attack for Subhas Setu is shown in Fig. 4
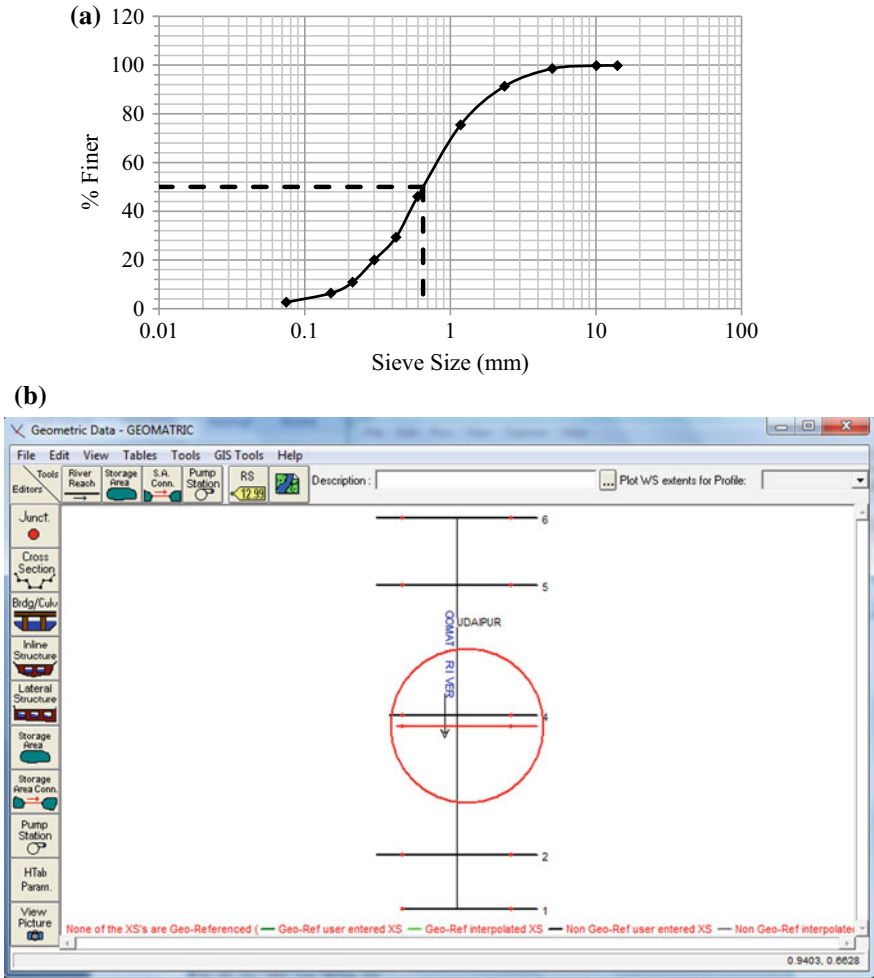
Fig. 3 **a** Particle size distribution for the sediment sample of Gomati River. **b** HEC RAS interface of the Subhas Setu on Gomati River

6.2 Calibration of Scour Depth

There are many other models of scour prediction. Nowaday's, HEC-RAS is using all worldwide to find the scour depth. It is more acceptable than the other models [13]. There is a scope of comparing scour depth computed by HEC-RAS tool with other scour models [14]. In the present study, one statistical analysis is done based on the scour depth. Considering HEC-RAS model as a standard, one bar chart is plotted shows which models are under estimated and which are over estimated among the seven scour models with respect to HEC-RAS as shown in Fig. 5

Table 1 Variation of scour depth of Subhas Setu

.Types of flow	Angle of attack (°)	Scour in pier (m)				
		0.5	1	1.5	2	2.5
Full stretch 80 m	0	1.68	2.64	3.50	4.14	4.78
	3	2.31	3.22	4.02	4.60	5.22
	6	2.84	3.78	4.51	5.05	5.65
	9	3.33	4.25	4.97	5.46	6.03
	12	3.79	4.70	5.39	5.88	6.41
	15	4.19	5.12	5.81	6.21	6.75
Contraction scour (m)		0.36	0.47	0.58	0.69	0.81
Abutment scour (m)		0	0	0	0	0
Effective flow 56 m	0	2.20	3.10	4.15	4.85	5.60
	3	3.02	3.78	4.78	5.39	6.11
	6	3.73	4.43	5.36	5.92	6.61
	9	4.37	4.99	5.90	6.41	6.06
	12	4.96	5.59	6.40	6.89	7.51
	15	5.49	6.01	6.90	7.28	7.90
Contraction scour (m)		2.67	2.99	3.39	3.60	3.80
Abutment scour (m)		0	0	0	0	0

6.3 Statistical Analysis

After giving input of all these discharge data in HEC-RAS, scour depths are found for all the discharges and the variation regarding the discharge. Graph between discharge and scour depth for Subhas Setu on Gomati River is shown in Fig. 6. On these graphs, one trend line is drawn. The correlation between the discharge and scour depth is shown on the graph.

6.4 Dimensionless Analysis

The dimensionless grouping approach is used to get the factors impacting the local scour depth around bridge piers. To explain the fluctuation of these dimensionless groups with the local scour, data from the HEC-RAS model is used.

Scour depends on many factors. One of them is flow depth. All the variables are makes to dimensionless by dividing with the pier diameter [3]. In the Fig. 7, it shows the comparison between scour depth and flow depth. It shows that the scour depth increases with the increase in flow depth. The influence of approach velocity is studied by examining the effect of pier's Froude number with local scour depth [15]. Figure 8 shows this variation.

Fig. 4 Variation in scour depth with pier diameter for different angle of attack for Gomati River: **a** full waterway and **b** Restricted waterway

(a)

(b)
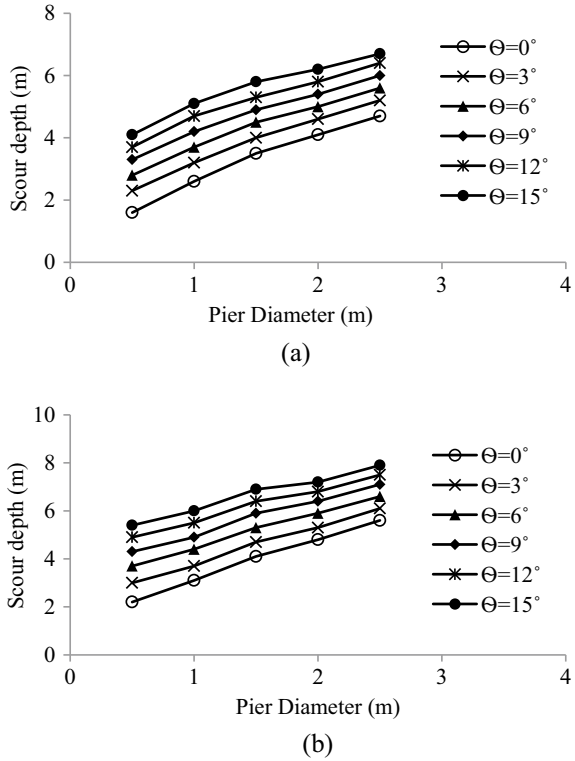
Fig. 5 Overestimated and underestimated scour models with respect to HEC-RAS model
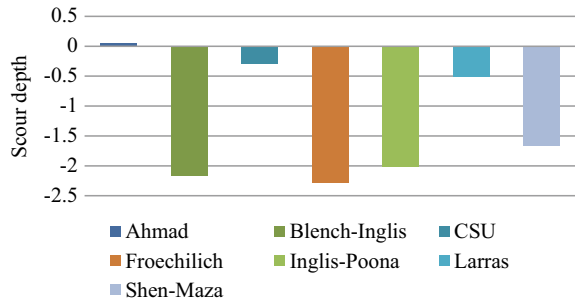
In the present study, it is observed that the scour depth increased by 54.02% when the angle of attack was increased from 0° to 15° (Fig. 9). It is being confirmed that the angle of attack directly can affect the scour depth around bridge piers.

In the present study, it is also observed that the scour depth is affected by the numbers of pier used and the shape of the piers. Generally, the numbers of pier used and the shape of the piers are represented by a coefficient termed as contraction ratio (C_R). The effect of contraction ratio on the local scour depth is shown in Fig. 10.
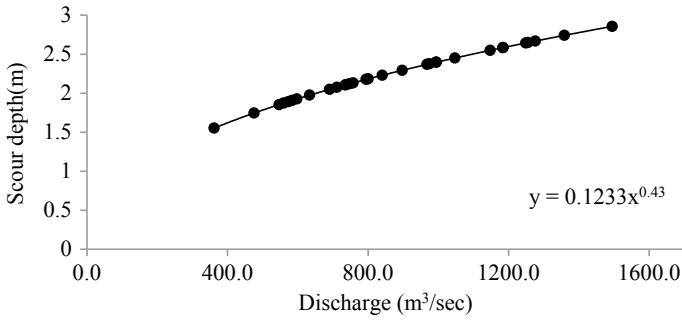
Fig. 6 Variation of scour depth with discharge in Gomati River

$y = 0.1233x^{0.43}$
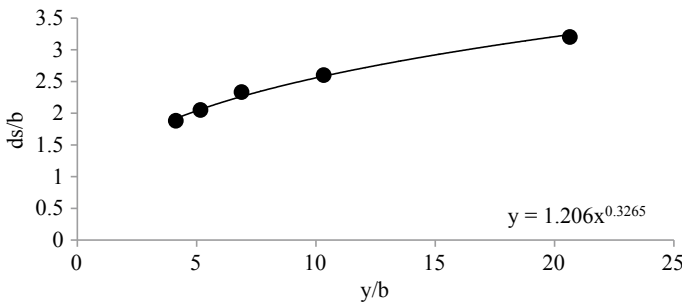
Fig. 7 Variation of scour with flow depth in Gomati River

$y = 1.206x^{0.3265}$
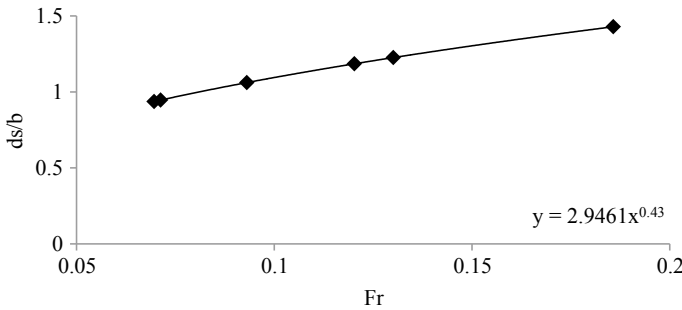
Fig. 8 Variation of scour with Froude number in Gomati River

$y = 2.9461x^{0.43}$

6.5 Correlation Analysis

There have been several strategies created for performing regression analysis. Linear regression and ordinary least squares regression are both parametric approaches. Correlation is a linear relationship measure. If the relationship is not linear, the
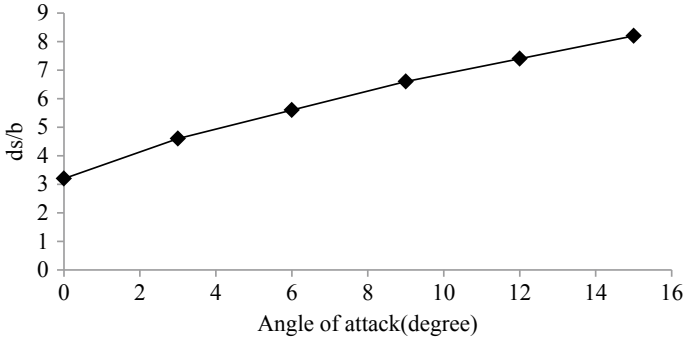
Fig. 9 Variation of scour with angle of attack in Gomati River
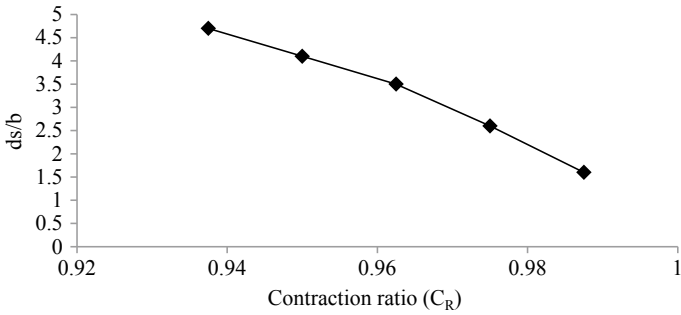
Fig. 10 Variation of scour with contraction ratio in Gomati River

correlation coefficient is not an adequate statistic to measure their link, and if the relationship is linear, the correlation coefficient is close to one. Correlations between HEC RAS scour depth and other seven models are done. The correlation factor for seven equations is shown in Table 2.

Table 2 Correlation factor

S. No.	Equation	Correlation factor
1	CSU	0.9975
2	Larras	0.9951
3	Ahmed	0.9961
4	Blench-Inglis	0.8905
5	Shen-Maza	0.9241
6	Inglis-Poona	0.9182
7	Froechlich	0.8739

7 Conclusion

Scour depth analysis is necessary for study of river morphology and the safety and stability of bridge piers on a river. In the present study, we have estimated scour depth using HEC RAS modeling tool and also compared it with seven different other empirical models. Some of the major observations after the result and analysis are listed below:

1. In the present study, it was found that an increase in the angle of attack resulted in the increase in the scour depth. Also, it was observable that the scour depth increased with the increase of pier diameter.
2. On the contrary, scour depth of the selected bridge piers increases when the width of the cross-section of the river decreases.
3. Scour depth computed by HEC-RAS modeling tool is similar with (a) CSU (1975), (b) Ahmed (1953), and (c) Larras (1963), and correlation between all these models and the computed scour depth from HEC-RAS model is strongly correlated with CSU (1975) model.
4. With the increase of discharge, local scour depth also increases. As well as with the increase of flow depth, Froude number local scour depth increases; on the other hand, scour depth decreases with the increase in contraction ratio of river.

References

1. Kothyari UC (2007) Indian practice on estimation of scour around bridge piers—a comment. Sadhana 32(Part 3):187–197
2. Ghorbani B (2008) A field study of scour at bridge piers in flood plain rivers. Turkish J Eng Sci 32, Paper No. 189–199
3. Dey S, Bose SK, Sastry GLN (1995) Clear water scour at circular piers: a model. J Hydraulic Eng 121(12), Paper No. 5642
4. Beg M (2013) Predictive competence of existing bridge pier scour depth predictors. Eur Int J Sci Technol 2(1):161–178
5. Smith SP (1994) Preliminary procedure to predict bridge scour in bedrock. Technical Report No. Cdot-R-Sd-94-14
6. Majumder S K and Kumar Y (2011) Estimation of scour in bridge piers on alluvial non-cohesive soil by different methods. Adviser, ICT Pvt. Ltd
7. Tiwari H, Sharma N, Simegn AA (2012) Bridge Scour by HEC-RAS model: a case study over Ganga bridge. Recent Trends Civil Eng Technol 2:1–8
8. Lue JY, Shi ZZ, Hong JH, Lee JJ, Raikar RV (2011) Temporal variation of scour depth at non-uniform cylindrical piers. J Hydraulic Eng 137(1)

9. Mueller DS, Miller RL, Wilson JT (1994) Historical and potential scour around bridge piers and abutments of selected stream crossings in Indiana. U.S. Geological Survey. Water-Resources Investigations Report 93-4066
10. Setia B (1997) Scour around bridge piers: mechanism and prediction. PhD Thesis in IIT, Kanpur
11. Gibson S, Brunner G, Piper D S and Jensen M (2006) Sediment transport computation with HEC-RAS. In: Proceedings of the eighth federal interagency sedimentation conference, Reno, NV, USA
12. Elsebaie IH (2013) An experimental study of local scour around circular bridge pier in sand soil. Int J Civil Environ Eng IJCEE-IJENS 13(01)
13. Khassaf SI, Shakir SS (2013) Modeling of local scour around Al-Kufa bridge piers. Int J Adv Res IJOAR .ORG 1(8). Online: ISSN 2320
14. Haghiabi AH, Zaredehdasht S (2012) Evaluation of HEC-RAS ability in erosion and sediment transport forecasting. World Appl Sci J 17:1490–1497
15. Ting FCK, Briaud JL, Chen HC, Gudavalli R, Perugu S, Wei G (2002) Flume tests for scour in clay at circular piers. J Hydraulic Eng 127(11), Paper No. 18247

Numerical Investigation of Secondary Flow Structures in a Gravel Bed Asymmetric Compound Channel

S. Sahoo, K. Devi, J. R. Khuntia, and K. K. Khatua

Abstract The efficiency of a water management system is determined largely based on its water conveyance capacity through canals. Any reduction in this capacity may result in consumers not getting sufficient water resources. Amongst many factors affecting the conveyance capacity of an open channel, one of the most significant impacts is the generation of secondary currents. The secondary flow cells are generated due to the lateral and vertical component of flow velocities. There have been many experimental and analytical investigation performed to understand the effect of secondary flow cells. However, to overcome such rigorous and time-consuming experimental procedures, numerical simulations can be applied using computational fluid dynamics (CFD). In this present study, numerical simulations have been performed to understand the impact of secondary current cells in an asymmetric compound channel. Amongst many turbulence models available in ANSYS Fluent software package, k-ω turbulence model has been selected because of its capability to provide good results with less computing resources. The numerically simulated results are validated with theoretical models. It has been observed that the numerical results confirmed well with the theoretical models. Three types of vortices, namely longitudinal vortex, free surface vortex, and bottom vortex are observed in the channel cross-section. As the flow depth increases, the vortices are shifted towards the interface of main channel and flood plain and also, they are decreased with increase of relative depth, which clearly agrees with theoretical studies. This study will be helpful

S. Sahoo (✉) · K. K. Khatua
Department of Civil Engineering, National Institute of Technology, Rourkela 769008, India
e-mail: sarjatisahoo1991@gmail.com

K. K. Khatua
e-mail: kkkhatua@nitrkl.ac.in

K. Devi · J. R. Khuntia
Department of Civil Engineering, Chaitanya Bharathi Institute of Technology (A), Hyderabad, Telangana 500075, India
e-mail: kamalinidevi1@gmail.com; kamalinidevi_civil@cbit.ac.in

J. R. Khuntia
e-mail: jnanaranjan444@gmail.com; jnanaranjan_civil@cbit.ac.in

to the hydraulic engineers and researchers working on the conveyance capacity of channels.

Keywords Secondary flow cells · ANSYS fluent · k-ω turbulence model

1 Introduction

Water conveyance in the rivers and channels is either of simple geometry or of compound section geometry. The flow in rivers or man-made canals is often turbulent and three dimensional. This flow comprises of two flow components, primary and secondary flow. The primary flow is along the flow direction, and secondary flow is the resultant of the flow along the lateral and transverse flow [1, 2]. These secondary flows influence the primary mean flow producing a 3-D flow structure. Another cause of generation of secondary flow may be the turbulence anisotropy of normal Reynolds stresses [3]. The maximum velocity appears beneath the free surface because of this secondary current generation within the channel. This is called the dip phenomena [3]. So, it is very important to know the behaviour of secondary currents develop at the interaction zones of a compound channel and how they affect the whole flow process, discharge capacity, velocity distribution, boundary shear distribution, and other flow parameters. Many experimental and numerical studies have been undertaken to better understand secondary flow phenomena. Liao and Knight [4] proposed three suitable hand calculation formulae to forecast the conveyance capacity in prismatic compound channels of both symmetric and asymmetric type configuration. They applied their formulae to evaluate the depth-averaged velocity, boundary shear stress, and discharge and discovered that the predicted results agreed well with the experimental results. Moreta et al. [5] developed an expression to quantify the momentum transfer at the interaction zones and validated their expression with other experimental results as well as with FCF channels. Considering the momentum transfer between the flood plain and the main channel, a new model to forecast the conveyance capacity of compound channels was presented by Khatua et al. [6]. Townsend [7], Knight et al. [8, 9], Wormleaton and Merrett [10], Devi and Khatua [11], and Sahoo et al. [12] all made note of the fact that at a shallow depth of the floodplain, the high velocity difference between main channel and floodplain cause a strong shear layer and a lateral momentum transfer across the interface. The impact of the lateral transfer of momentum on the unsteady flow prediction was noted by Khuntia et al. [13], Nezu and Nakagawa [14], Stephenson and Kolovopoulos [15] and Abida and Townsend [16].

Recently, there has been a very rapid increase in computing power, encouraging the use of computational fluid dynamics (CFD) modelling to carry out comprehensive research on turbulence in free surface flows without first undergoing the traditional rigorous laboratory experiments or difficult field studies. This is a better substitute for the expensive and time-consuming procedures of the experimental or field study. The three-dimensional numerical simulations also provide clear insight on the complex

flow process of compound channels in terms of pictures resulted from the simulations [17]. Numerous validation investigations revealed that the CFD models are also capable of making reasonable predictions about the key traits of various pattern flows [18-21].

In this present study, the experimental results on compound channels of [22] have been considered for the analysis and comparison purpose for the new results obtained from the numerical simulations. The experiments of [22] are performed on an asymmetric compound channel situated inside the Hydraulics laboratory of Civil Engineering Department, NIT Rourkela. For the experiments, small gravels are used as roughness material on the flood plain to achieve a differential roughness condition as the main channel is constructed of cement concrete. For numerical simulation, ANSYS Fluent software has been used in this study. To perform a simulation, two things should be considered, namely accuracy and computational resources. From the available turbulence models, k-omega model has been chosen for its reasonable accuracy and less use of computational power and resources.

2 Theoretical Analysis

2.1 Primary and Secondary Flows

When it comes to three-dimensional turbulent flow, the primary flow and secondary flow are frequently regarded as the two flow components. Secondary flow runs counter clockwise to the major flow direction, which is parallel to the flow direction. The secondary flow, also known as secondary currents, is usually a minor component in comparison to the primary flow. Secondary flows might be of two different forms. One is brought on by changes in planform curvature and cross-sectional geometry, and the other is brought on by fluctuations in turbulent velocity. Because of the anisotropy of the normal Reynolds stresses during turbulence, secondary flows may form in straight open channels [3]. No channel curvature is necessary to produce these secondary flows, which are frequently described as turbulence-driven secondary currents. Secondary currents in rectangular channels, both wide and narrow, are schematically depicted in Fig. 1.

Compound open channels have more intricate flow fields because of the significant interaction that arises between the flows in the main channel and on the floodplains [23]. According to Ervine et al. [24], the secondary flow is important because of the 3D mixing; as a result, the development of secondary cells dominates the flow mechanisms. It is discovered that the geometry of the channel influences the pattern and placement of these cells, and that the strength of these cells depends on the flow depth in the floodplain [25]. Figure 2 illustrates the complex flow process in a compound channel.

(a) Wide channel   (b) narrow channel
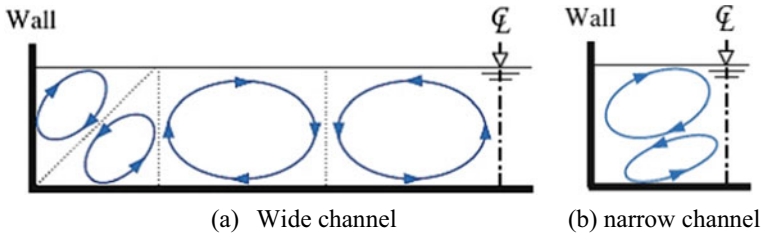
Fig. 1 Schematics showing open channels (rectangular) with secondary currents [1]
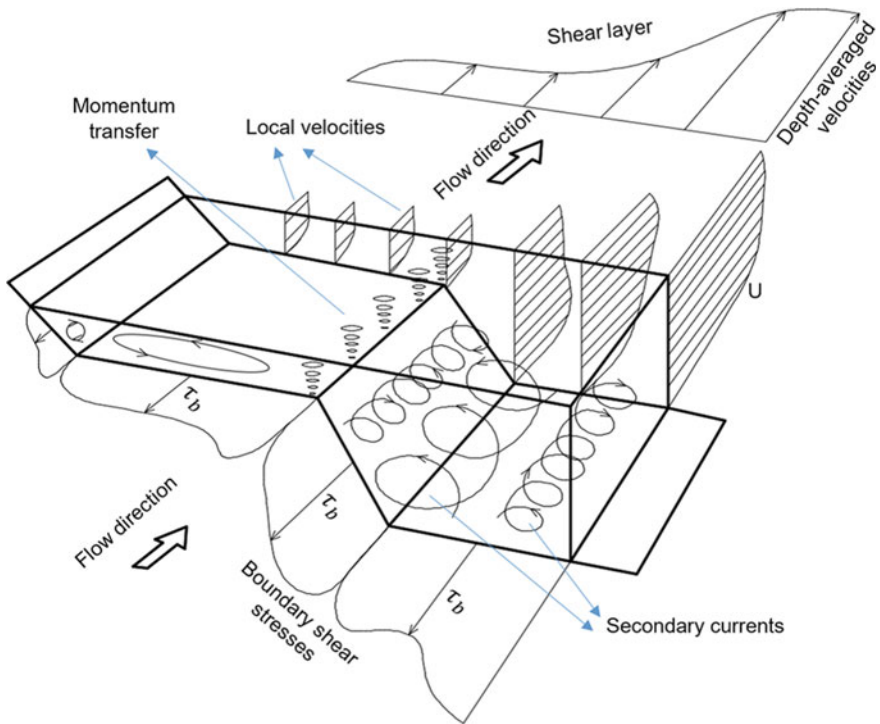
Fig. 2 Turbulent flow structure in compound channel [23]

2.2 Applications of Computational Fluid Dynamics (CFD) for Numerical Modelling

The Navier-Stokes (N-S) equations, which are established on the principles of conservation of mass and momentum within a moving fluid, must be solved in order to employ computational fluid dynamics (CFD) for numerical modelling. For the turbulent flow of an incompressible Newtonian fluid, the Navier-Stokes equations are as follows:

Equation of continuity (the conservation of mass),

$$\frac{\partial u_i}{\partial x_i} = 0 \tag{1}$$

Momentum equation (the conservation of momentum),

$$\frac{\partial u_i}{\partial t} + \frac{\partial}{\partial x_j}\left(u_i u_j\right) = -\frac{1}{\rho}\frac{\partial p}{\partial x_i} + \frac{1}{\rho}\frac{\partial \tau_{ij}}{\partial x_i} \tag{2}$$

2.3 The Standard k-ω Model

The turbulent frequency ($\omega = \varepsilon/k$) and the turbulent kinetic energy (k) transport equations are both solved by the k-model. Then, using the eddy viscosity idea, the stress tensor is calculated. The -equation was first put forth by Kolmogorov [26], who used the same physical justifications and dimensional reasons that were used to derive the -equation. However, Wilcox [27] presented the modern iteration of the k-ω model, which assumes the formulations listed below [28]:

$$\frac{\partial k}{\partial t} + U_j \frac{\partial k}{\partial x_j} = v_t\left(\frac{\partial U_i}{\partial x_j} + \frac{\partial U_j}{\partial x_i}\right)\frac{\partial U_i}{\partial x_j} - \beta^* k\omega + \frac{\partial}{\partial x_j}\left[(v + \sigma^* v_t)\frac{\partial k}{\partial x_j}\right] \tag{3}$$

$$\frac{\partial \omega}{\partial t} + U_j \frac{\partial \omega}{\partial x_j} = \alpha\frac{\omega}{k}v_t\left(\frac{\partial U_i}{\partial x_j} + \frac{\partial U_j}{\partial x_i}\right)\frac{\partial U_i}{\partial x_j} - \beta\omega^2 + \frac{\partial}{\partial x_j}\left[(v + \sigma v_t)\frac{\partial \omega}{\partial x_j}\right] \tag{4}$$

$$v_t = \frac{k}{\omega} \tag{5}$$

$$\alpha = \frac{5}{9}, \beta = \frac{5}{40}, \beta^* = \frac{9}{100}, \sigma = \frac{1}{2}, \sigma^* = \frac{1}{2} \tag{6}$$

2.4 The SST k-ω Model

Menter [29] created the Shear Stress Transport (SST) variation of the basic k-model. To use the k-ω turbulence model in the inner region of the boundary layer and the k-ε turbulence model in the free shear flow, the model blends the two. The Wilcox model next to the wall and the k-ε model in the free stream are both activated by the blending function F_1. This ensures that the correct model is used across the entire flow field:

- For flow modelling in the near boundary region, the k-ω model works well.
- The k-ε model works well for predicting flow behaviour away from the boundary.

These features improve the accuracy and reliability of the SST k-ω model for a broader range of flows. The main and auxiliary equations of the SST k-ω model are presented below:

- Turbulent Kinetic Energy

$$\frac{\partial k}{\partial t} + U_j \frac{\partial k}{\partial x_j} = P_k - \beta^* k\omega + \frac{\partial}{\partial x_j}\left[(v + \sigma_k v_T)\frac{\partial k}{\partial x_j}\right] \tag{7}$$

- Specific Dissipation Rate

$$\frac{\partial \omega}{\partial t} + U_j \frac{\partial \omega}{\partial x_j} = \alpha S^2 - \beta\omega^2 + \frac{\partial}{\partial x_j}\left[(v + \sigma_\omega v_t)\frac{\partial \omega}{\partial x_j}\right]$$
$$+ 2(1 - F_1)\sigma_{\omega^2}\frac{1}{\omega}\frac{\partial k}{\partial x_i}\frac{\partial \omega}{\partial x_i} \tag{8}$$

- F_1 (Blending Function)

$$F_1 = \tanh\left\{\left\{\min\left[\max\left(\frac{\sqrt{k}}{\beta^*\omega\mathcal{Y}}, \frac{500v}{\mathcal{Y}^2\omega}\right), \frac{4\sigma_{\omega^2}k}{CD_{k\omega}\mathcal{Y}^2}\right]\right\}^4\right\} \tag{9}$$

- Kinematic Eddy Viscosity

$$v_t = \frac{a_1 k}{\max(a_1\omega, SF_2)} \tag{10}$$

- F_2 (Second Blending Function)

$$F_2 = \tanh\left[\left[\max\left(\frac{2\sqrt{k}}{\beta^*\omega\mathcal{Y}}, \frac{500v}{\mathcal{Y}^2\omega}\right)\right]^2\right] \tag{11}$$

- PK (Production Limiter)

$$P_k = \min\left(\tau_{ij}\frac{\partial U_i}{\partial x_j}, 10\beta^* k\omega\right) \tag{12}$$

3 Methodology

3.1 Application of ANSYS Fluent for Simulation

The ANSYS Fluent (2021 R1) is used to solve the above-mentioned equations and simulate the compound channel flow. In the current work, the experimental channel of [22] has been used to simulate various flow depths. The detailed experimental procedure is explained in [22]. The experiments are performed on an asymmetrical compound channel in which the flood plain is covered with small gravels having the roughness value as 0.02. The hydraulic properties for the asymmetric compound channel are presented in Table 1.

For the present work, ANSYS Fluent (2021 R1) is used to simulate to visualize the secondary flow structures in an asymmetric compound channel. A screen shot from the Fluent software showing all the components of the package is presented in Fig. 3. The post-processor component has the ability to process and show simulation results. The stages of process of Fluent software are shown in Fig. 4.

Table 1 Hydraulic properties for the asymmetric compound channel

Material		Flow depth, h (m)	Relative depth (d_r)	Area of flow a, (m^2)	Wetted perimeter, p (m)	Discharge, q (m^3/s)	Mean velocity, u_m (m/s)	Bed slope, s_o
Main channel	Flood plain							
Cement concrete trowel finish (n = 0.01)	Small gravel @size 7-20 mm (n = 0.020)	0.14	0.214	0.079	1.355	0.040	0.505	0.001
		0.145	0.241	0.086	1.369	0.043	0.503	
		0.156	0.295	0.099	1.399	0.054	0.545	
		0.16	0.313	0.105	1.411	0.060	0.578	
		0.17	0.353	0.118	1.439	0.069	0.586	
		0.176	0.375	0.126	1.456	0.077	0.613	
		0.181	0.392	0.132	1.470	0.082	0.620	

Fig. 3 Components of the fluent software

Fluid Flow (Fluent)
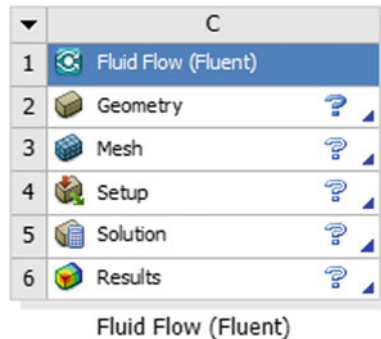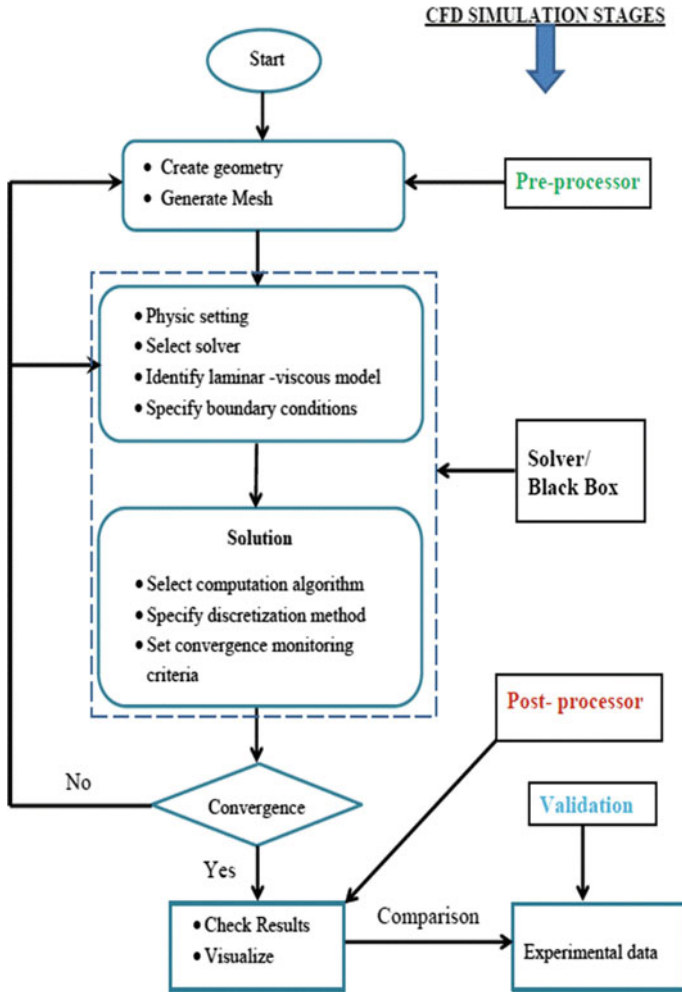
Fig. 4 Stages of process of fluent package

Amongst many available turbulence models, the SST *k-omega* model has been selected for the present study for its advantages as discussed in the previous section.

3.2 Constructing the Geometry

For the successful simulation, the geometry of the channel should be constructed carefully. Design modeller package was used for creating geometry for each flow
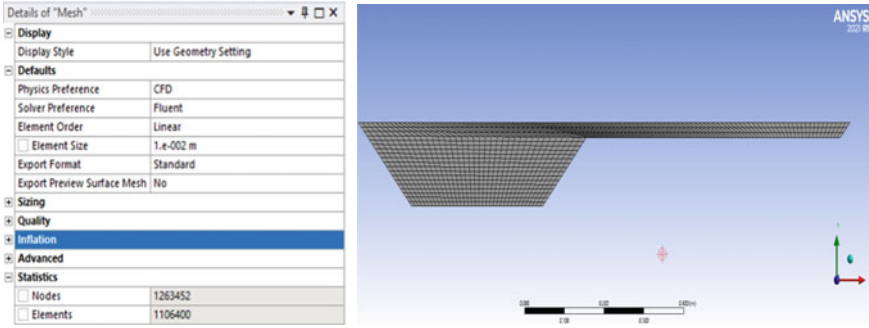
Fig. 5 Details of mesh for flow depth 14 cm and cross-sectional view of the channel after meshing

depth. X-direction, Y-direction, and Z-direction were chosen as width, depth, and length of the channel, respectively.

3.3 Generating the Mesh

The geometry is divided into smaller units known as cells for the mesh production process. In all simulations, rectangular cells with an element size of 0.02 m were employed to create meshes. Figure 5 presents the cross-sectional view of the channel and the mesh details for a flow depth of 14 cm.

3.4 Defining the Boundary Conditions

To fully describe the physical properties of the flow area and to specify the properties of domain surfaces, boundary conditions must be applied to all of the computational domain's boundaries. The effort of selecting a complex turbulence model could collapse if the boundary conditions are not applied correctly [17]. The boundary conditions applied were No-slip for all the walls (main channel and flood plain) and Free-Slip Wall with Zero Gradient for Turbulent Kinetic Energy (k) for the free surface.

(a) **Inlet**: The inlet was kept as pressure inlet, by providing the free surface level as 0.14 m and mean velocity as 0.505 m/s. same procedure was followed for all flow depths.
(b) **Outlet**: A pressure outlet has been applied and the free surface level was kept at 0.14 m. same procedure was followed for all flow depths.
(c) **Wall**: For the channel walls a no slip boundary condition has been adopted, which specifies that the velocity of all fluid particles close to the wall of the boundary will assume the velocity of the wall.

After providing all the boundary and initial conditions, a proper turbulence model is applied. In this study, the SST $k\text{-}\omega$ model has been chosen.

4 Results and Discussions

4.1 Secondary Flow Structures

The secondary current vectors which are the resultant of lateral and transverse direction velocity components are calculated by using the equation:

$$V_r = \sqrt{V^2 + W^2} \tag{13}$$

where V is the velocity component in lateral direction, and W is the velocity component in vertical direction.

The secondary flow structure for both the roughness cases is presented in Fig. 6.

5 Conclusions

Numerical simulations for the asymmetrical compound channels have been performed using the ANSYS Fluent CFD software. The results of the secondary flow structures at the junctions of its subsections are presented. Evaluation of the depth averaged velocities for different flow depth of such channels are compared with the previous experimental results. Following conclusions are derived from the present numerical simulations of compound channels:

- Higher values of secondary velocity are found at the lower flow depths of a compound channel. The secondary flow velocities are seen to be directed towards flood plain region of higher flow depth cases.
- The number of secondary currents cells are found to decrease with increase of flow depths. Another observation is also made that the secondary current cells move towards the intersection region of main channel and flood plain as the flow depth increases.
- As the flow depth increases in a compound channel, it behaves like a simple channel at higher flow depths. That means there will not be any trace of secondary flow cells.
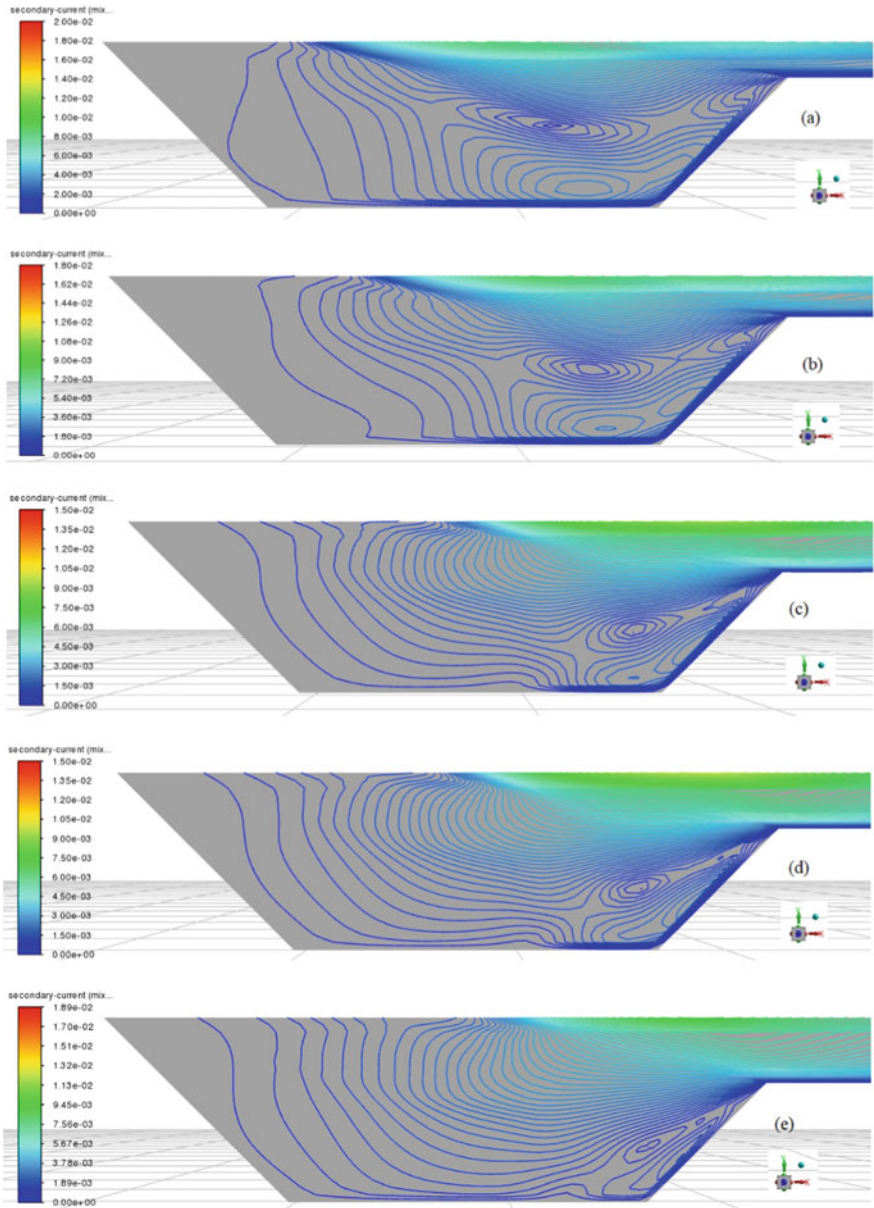
Fig. 6 Secondary flow structures for different flow depths (small gravel case) using ANSYS fluent: **a** 14 cm, **b** 14.5 cm, **c** 15.6 cm, **d** 16 cm, **e** 17 cm, **f** 17.6 cm, **g** 18.1 cm
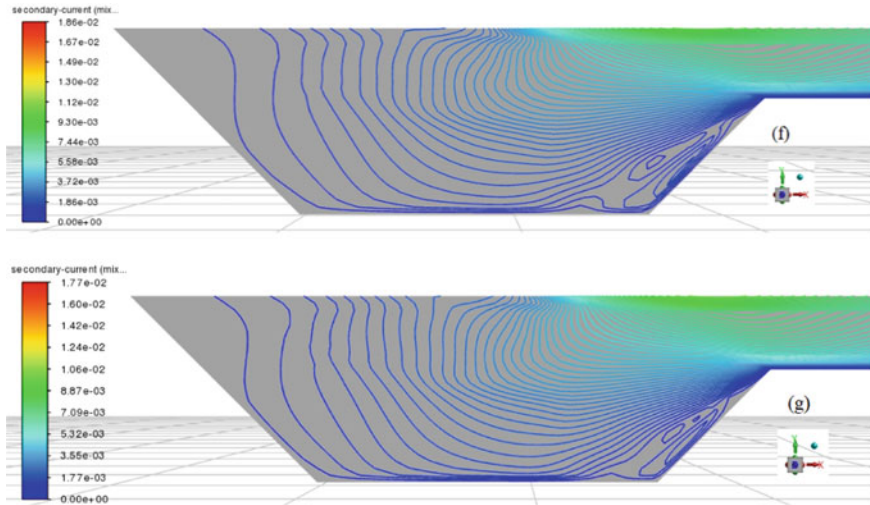
Fig. 6 (continued)

References

1. Alawadi WAAK (2019) Velocity distribution prediction in rectangular and compound channels under smooth and rough flow conditions. Doctoral dissertation, University of Salford
2. Khuntia JR (2016) Effect of secondary current on flow prediction in an open channel flow, M.Tech dissertation, NIT Rourkela, India
3. Tominaga A, Nezu I, Ezaki K, Nakagawa H (1989) Three-dimensional turbulent structure in straight open channel flows. J Hydraul Res 27(1):149–173
4. Liao H, Knight DW (2007) Analytic stage-discharge formulas for flow in straight prismatic channels. J Hydraul Eng 133(10):1111–1122
5. Moreta PJ, Martin-Vide JP (2010) Apparent friction coefficient in straight compound channels. J Hydraul Res 48(2):169–177
6. Khatua KK, Patra KC, Mohanty PK (2012) Stage-discharge prediction for straight and smooth compound channels with wide floodplains. J Hydraul Eng 138(1):93–99
7. Townsend RD (1967) An investigation of turbulence characteristics in a river model of complex cross-section. J Inst Civ Eng, 155–175
8. Knight DW, Demetriou JD (1983) Flood plain and main channel flow interaction. J Hydraul Eng 109(8):1073–1092
9. Knight DW, Sellin RHJ (1987) The SERC flood channel facility. J Inst Water Environ Manage 1(2):198–204
10. Wormleaton PR, Merrett D (1990) An improved method of calculation of steady uniform flow in prismatic main/flood channel plain sections. J Hydr Res 28:157–174
11. Devi K, Khatua KK (2019) Discharge prediction in asymmetric compound channels. J Hydro-Environ Res 23:25–39
12. Sahoo S, Khuntia JR, Devi K, Khatua KK (2022) Energy and momentum correction coefficients in compound open channel flow. River Hydraul: Hydraul Water Resour Coast Eng 2:309–320
13. Khuntia JR, Devi K, Khatua KK (2021) Turbulence characteristics in a rough open channel under unsteady flow conditions. ISH J Hydraul Eng 27(sup1): 354–365
14. Nezu I, Nakagawa H (1993) Basic structure of turbulence in unsteady open channel flows. In: Proceedings of 9th international symposium on turbulent shear flows, Kyoto, Japan, pp 7.1.1–7.1.6

15. Stephenson D, Kolovopoulos P (1990) Effects of momentum transfer in compound channels. J Hydraul Eng 116(12):1512–1522
16. Abida H, Townsend R (1992) A numerical model for routing floods through compound channels. In: Hydrocomp' 92, Proceedings of the international conference on interaction of computational methods and measurements in hydraulics and hydrology, Budapest, Hungary, pp 115–122
17. Bates PD, Lane SN, Ferguson RI (eds) (2005) Computational fluid dynamics: applications in environmental hydraulics. Wiley
18. Jing H, Guo Y, Li C, Zhang J (2009) Three-dimensional numerical simulation of compound meandering open channel flow by the Reynolds stress model. Int J Numer Meth Fluids 59(8):927–943
19. Sharifipour M, Bonakdari H, Zaji AH, Shamshirband S (2015) Numerical investigation of flow field and flowmeter accuracy in open-channel junctions. Eng Appl Comput Fluid Mech 9(1):280–290
20. Wu Y, Liu Z, Chen Y, Li M (2018) Investigation of velocity distribution and turbulence characteristics in subcritical circular open channel flows using a modified Reynolds stress model. J Hydro-environ Res 19:68–77
21. Asnaashari A, Akhtari AA, Dehghani AA, Bonakdari H (2016) Experimental and numerical investigation of the flow field in the gradual transition of rectangular to trapezoidal open channels. Eng Appl Comput Fluid Mech 10(1):272–282
22. Sahoo S (2017) A modified coherence method for flow prediction in a compound channel. MTech dissertation
23. Shiono K, Knight DW (1991) Turbulent open-channel flows with variable depth across the channel. J Fluid Mech 222:617–646
24. Ervine DA, Babaeyan-Koopaei K, Sellin RH (2000) Two-dimensional solution for straight and meandering overbank flows. J Hydraul Eng 126(9):653–669
25. Devi K (2018) Flow modelling in straight compound channels with symmetrical, asymmetrical and unsymmetrical floodplains. Doctoral dissertation
26. Kolmogorov AN (1942) Equations of motion of an incompressible turbulent fluid. Izv Akad Nauk SSSR Ser Phys 6(6):56–58
27. Wilcox DC (1988) Reassessment of the scale-determining equation for advanced turbulence models. AIAA J 26(11):1299–1310
28. ANSYS A (2013) Version 15.0; ANSYS. Inc., Canonsburg, PA, USA November
29. Menter FR (2002) Two-equation eddy-viscosity turbulence models for engineering applications. AIAA J 40(2):254–266

Numerical Solution of Two-Dimensional Shallow Water Flow with Finite Difference Scheme

Ashishkumar Koradia and Bandita Barman

Abstract In this study, Saint-Venant equations (SVEs) are solved numerically using MacCormack finite-difference scheme. Derivation of 2D Saint-Venant continuity and momentum equations is presented using the finite difference method. For the discretization of SVEs, MacCormack Predictor-Corrector Scheme is utilized. In both space and time, it is 2nd-order accurate. The Saint-Venant equations for 2D flow is solved for the computation of hydraulic jump in a straight channel with the addition of artificial viscosity term to MacCormack Predictor-Corrector Scheme for reducing numerical oscillations. Results show that this scheme easily captures hydraulic jump near upstream (within 3 m of channel span) without numerical oscillation. The results of the numerical experiment show that the MacCormack Predictor-Correction Scheme is working well with the 2D numerical experiment of hydraulic jump in a straight channel.

Keywords Numerical modelling · FDM · MacCormack predictor-correction scheme · Artificial viscosity

1 Introduction

Flood is a natural disaster, which causes the loss of livestock, human beings, destruction to the infrastructure, and the agricultural lands [1]. The main causes of flood occurrences are increasing urbanization without proper design or planning which turn to be more runoff rate, weather parameters like prolonged rainfall, which increase

A. Koradia (✉)
Department of Civil Engineering, Sardar Vallabhbhai National Institute of Technology Surat, Surat 395007, India
e-mail: koradia_ak@wr.iitr.ac.in

B. Barman
Department of Civil Engineering, Indian Institute of Technology (Indian School of Mines), Dhanbad, India
e-mail: bandita@iitism.ac.in

surface runoff and reduce adequate river capacity due to urbanization. It is very necessary to know the nature of floods in rivers or channels for saving human lives and infrastructure using early disaster management. For that in the early day's methods used for this is only predict the daily discharge at one fixed cross-section of the channel which is inappropriate for early disaster management [2]. To overcome the above-stated problem, nowadays, mainly physical and numerical based models are used very effectively to solve these types of problems. Toombes and Chanson [3] stated that it is economical to use a numerical based model instead of a physical-based model if the current problem can be solved effectively by numerical based model and added that it is very complex and difficult to solve the real-life problem without use of the numerical method.

To govern different flow conditions like surface flow, subsurface flow, and coupled flows, mathematical models are very useful. For such a flow condition, various studies were done on flood modeling. de Saint-Venant [4] was proposed dynamic flood wave propagation equations for the 1D applications and which are known as SVEs and they are widely used to calculate velocity, depth, and the flow rate over the surface. For 2D surface flow conditions, SVEs are obtained from the Navier-Stokes Equations (NSEs), and this equation is known as Shallow Water Equations (SWEs) [5]. SWEs are derived from the principles of mass and momentum conservation. These equations are frequently employed in the case of unsteady free surface flow (hydrodynamic flow). These equations belong to the family of first-order hyperbolic partial differential equations, and cannot be solved using analytical methods. As a result, various numerical approaches must be used for these sorts of equations. SWEs are solved using several numerical methods. Finite difference method (FDM), finite volume method (FVM), and finite element method (FEM) [6–8] are well known for the solution of shallow water hydrodynamic equation. From these three methods, FDM is the oldest one. It is used extensively because it is relatively easy to implement, efficiently computing linear algebra, and easy to program. John and Anderson [9] stated that the use of FDM for SWEs is led to dissipation and dispersion errors because of its truncated terms and it required proper treatment for that. To reduce dissipation and dispersion errors, [10] suggested an excellent numerical scheme for solutions of SWEs, which is a Finite Difference Explicit MacCormack Predictor-Corrector Scheme. Due to its shock capturing nature, it is widely used for smoothly capture high discontinuity like bore wave, hydraulic jump, etc., in river flow.

The advantage of this technique is that it leaves a smooth area for a large gradient relatively undisturbed. In this technique, the extra term adds after the traditional MacCormack method for finding depth, velocity, and runoff rate at new time steps. In this technique, to control the dissipation, a regulating coefficient is used which is computed using the hit and trial approach. The extreme value of this regulating-coefficient shows extreme diffusion of results, which lead to spurious oscillations in solution. Overcome this problem, an additional term as "corrector step" added after the old (traditional) MacCormack Predictor-Corrector Scheme, which easily controls the spurious oscillations [12]. After used this model for a different test case, they concluded that this model obtained very smooth results as compare to the traditional one.

Objective of study is to perform numerical experiment for hydraulic jump in straight channel using MacCormack Predictor-Corrector Scheme with Artificial Viscosity term.

2 Materials and Methods

2.1 Governing Equations

The 2D SVEs are used to monitor surface flow. The conservations of mass and momentum approach was used to obtain these equations [11]. The following are the governing equations for surface flow:

$$\frac{\partial h}{\partial t} + \frac{\partial (hu)}{\partial x} + \frac{\partial (hv)}{\partial y} = 0 \tag{1}$$

$$\frac{\partial (hu)}{\partial t} + \frac{\partial \left(hu^2 + \frac{gh^2}{2} \right)}{\partial x} + \frac{\partial (huv)}{\partial y} = gh(S_{0x} - S_{fx}) \tag{2}$$

$$\frac{\partial (hu)}{\partial t} + \frac{\partial (huv)}{\partial x} + \frac{\partial \left(hv^2 + \frac{gh^2}{2} \right)}{\partial y} = gh(S_{0y} - S_{fy}) \tag{3}$$

The continuity equation is Eq. (1), and the momentum equations for the x and y directions are Eqs. (2–3). Now writing 2D SWEs in matrix form as shown by [11].

$$U_t + E_x + F_y + S = 0 \tag{4}$$

where

$$U_t = \left\{ \begin{array}{c} h \\ hu \\ hv \end{array} \right\}, E_x = \left\{ \begin{array}{c} hu \\ hu^2 + \frac{gh^2}{2} \\ huv \end{array} \right\}, F_y = \left\{ \begin{array}{c} hv \\ huv \\ hv^2 + \frac{gh^2}{2} \end{array} \right\}$$

$$\text{and } S = \left\{ \begin{array}{c} 0 \\ -gh(S_{0x} - S_{fx}) \\ -gh(S_{0y} - S_{fy}) \end{array} \right\}$$

The friction slopes S_{fx} and S_{fy} are obtained from Manning's formula as [11]:

$$S_{fx} = \frac{n^2 \times u \times \sqrt{(u^2 + v^2)}}{h^{\frac{3}{4}}} \text{ and } S_{fy} = \frac{n^2 \times u \times \sqrt{(u^2 + v^2)}}{h^{\frac{3}{4}}} \tag{5}$$

There are no closed-form solutions to the governing Eq. (4) since it is a set of 1st-order nonlinear hyperbolic PDEs. So, these equations are numerically solved.

2.2 MacCromack Discretization Technique

MacCormack's discretization approach is a variant of the Lax-Wendroff Method, although it is considerably easier to apply [9]. Both approaches are explicit FDM with second-order spatial and temporal accuracy. The discretization procedure of the Lax-Wendroff approach is simple, but the algebra computation is time-consuming, with the second time derivatives accounting for the majority of the long algebra [9]. Fortunately, all of this algebra is shortcut; this is achieved by MacCormack process. MacCormack [10] applying this method first. It is the simplest to comprehend and program. Furthermore, for many fluid flow applications, the results obtained by using MacCormack approach are perfectly appropriate. The method of MacCormack is illustrated here for these reasons and will be used for the applications. The use of this technique is a two-step hyperbolic equation method: a predictor step that is followed by a corrector step [9].

2.2.1 Discretization of 2-D Saint-Venant Equations

For 2D surface flow, the governing equations are [11]:

$$\frac{\partial h}{\partial t} = -\left(h \frac{\partial u}{\partial x} + h \frac{\partial v}{\partial y} \right) \tag{6}$$

$$\frac{\partial u}{\partial t} = -\left(\frac{\partial u^2}{\partial x} + g \frac{\partial h}{\partial x} + u \frac{\partial v}{\partial y} + g(S_{fx} - S_{ox}) \right) \tag{7}$$

$$\frac{\partial v}{\partial t} = -\left(v \frac{\partial u}{\partial x} + g \frac{\partial h}{\partial y} + \frac{\partial v^2}{\partial y} + g(S_{fy} - S_{oy}) \right) \tag{8}$$

Predictor Step:

The spatial derivatives on the right-hand side are replaced by forward differences in Eqs. (6), (7), and (8). Which is show in Eqs. (9), (10) and (11), respectively [9].

$$\left(\frac{\partial h}{\partial t} \right)_{i,j}^{t} = -\left(h_{i,j}^{t} \frac{u_{i+1,j}^{t} - u_{i,j}^{t}}{\Delta x} + h_{i,j}^{t} \frac{u_{i,j+1}^{t} - u_{i,j}^{t}}{\Delta y} \right) \tag{9}$$

$$\left(\frac{\partial u}{\partial t} \right)_{i,\ j}^{t} = -\left(2u_{i,j}^{t} \frac{u_{i+1,j}^{t} - u_{i,j}^{t}}{\Delta x} + g \frac{h_{i+1,j}^{t} - h_{i,j}^{t}}{\Delta x} \right.$$

$$+u_{i,j}^t \frac{v_{i,j+1}^t - v_{i,j}^t}{\Delta y} + g(S_{fx(i,j)}^t - S_{ox(i,j)}^t) \bigg) \tag{10}$$

$$\left(\frac{\partial v}{\partial t}\right)_{i,\,j}^t = -\left(2v_{i,j}^t \frac{u_{ij+1}^t - u_{i,j}^t}{\Delta y} + g\frac{h_{i,j+1}^t - h_{i,j}^t}{\Delta y}\right.$$

$$\left.+v_{i,j}^t \frac{u_{i+1,j}^t - u_{i,j}^t}{\Delta x} + g(S_{fy(i,j)}^t - S_{oy(i,j)}^t)\right) \tag{11}$$

In Eqs. (12), (13) and (14), for initial value problem, variables at time t, i.e., the right-hand side are known value. So, the predicted value of $(\overline{h})^{t+\Delta t}$, $(\overline{u})^{t+\Delta t}$ and $(\overline{v})^{t+\Delta t}$, can be calculated as below [9]:

$$\overline{h}_{i,j}^{t+\Delta t} = h_{i,j}^t + \left(\frac{\partial h}{\partial t}\right)_{i,j}^t \Delta t \tag{12}$$

$$\overline{u}_{i,j}^{t+\Delta t} = u_{i,j}^t + \left(\frac{\partial u}{\partial t}\right)_{i,j}^t \Delta t \tag{13}$$

$$\overline{v}_{i,j}^{t+\Delta t} = v_{i,j}^t + \left(\frac{\partial v}{\partial t}\right)_{i,j}^t \Delta t \tag{14}$$

$(\overline{h})^{t+\Delta t}$, $(\overline{u})^{t+\Delta t}$ and $(\overline{v})^{t+\Delta t}$ are only predicted value of height and velocity in x and y-direction. It is only first order accurate since Eqs. (12), (13) and (14) contains only the 1st-order term in Taylor Series.

Corrector Step:

In this step, first obtain a predicted value of the time derivative at time $+\Delta t$, $\left(\overline{\frac{\partial h}{\partial t}}\right)_{i,j}^{t+\Delta t}$, $\left(\overline{\frac{\partial u}{\partial t}}\right)_{i,j}^{t+\Delta t}$ and $\left(\overline{\frac{\partial v}{\partial t}}\right)_{i,j}^{t+\Delta t}$; here we use the predicted values from the predictor step as known values in the RHS. In Eqs. (12), (13) and (14), the spatial derivatives are replaced with rearward differences. Equations (15), (16) and (17), respectively, represent corrector step [9].

$$\left(\overline{\frac{\partial h}{\partial t}}\right)_{i,j}^{t+\Delta t} = -\left(\overline{h}_{i,j}^{t+\Delta t} \frac{\overline{u}_{i,j}^{t+\Delta t} - \overline{u}_{i-1,j}^{t+\Delta t}}{\Delta x} + \overline{h}_{i,j}^{t+\Delta t} \frac{\overline{u}_{i,j}^{t+\Delta t} - \overline{u}_{i,j-1}^{t+\Delta t}}{\Delta y}\right) \tag{15}$$

$$\left(\overline{\frac{\partial u}{\partial t}}\right)_{i,j}^{t+\Delta t} = -\left(2\overline{u}_{i,j}^{t+\Delta t} \frac{\overline{u}_{i,j}^{t+\Delta t} - \overline{u}_{i-1,j}^{t+\Delta t}}{\Delta x} + g\frac{\overline{h}_{i,j}^{t+\Delta t} - \overline{h}_{i-1,j}^{t+\Delta t}}{\Delta x}\right.$$

$$\left.+ u_{i,j}^{t+\Delta t} \frac{\overline{v}_{i,j}^{t+\Delta t} - \overline{v}_{i,j-1}^{t+\Delta t}}{\Delta y} + g(S_{fx(i,j)}^{t+\Delta t} - S_{ox(i,j)}^{t+\Delta t})\right) \tag{16}$$

$$\left(\overline{\frac{\partial v}{\partial t}}\right)_{i,j}^{t+\Delta t} = -\left(2\overline{v}_{i,j}^{t+\Delta t}\frac{\overline{u}_{i,j}^{t+\Delta t} - \overline{u}_{i,j-1}^{t+\Delta t}}{\Delta y} + g\frac{\overline{h}_{i,j}^{t+\Delta t} - \overline{h}_{i,j-1}^{t+\Delta t}}{\Delta y}\right.$$
$$\left. + \overline{v}_{i,j}^{t+\Delta t}\frac{\overline{u}_{i,j}^{t+\Delta t} - \overline{u}_{i-1,j}^{t+\Delta t}}{\Delta x} + g(S_{fy(i,j)}^{t+\Delta t} - S_{oy(i,j)}^{t+\Delta t})\right) \tag{17}$$

Final Step:

The arithmetic mean is used to calculate the average value of the time derivative of height and velocity in the x and y directions, as illustrated in Eqs. (18), (19) and (20), respectively [9].

$$\left(\frac{\partial h}{\partial t}\right)_{av} = \frac{1}{2}\left(\left(\frac{\partial h}{\partial t}\right)_{i,j}^{t} + \left(\overline{\frac{\partial h}{\partial t}}\right)_{i,j}^{t+\Delta t}\right) \tag{18}$$

$$\left(\frac{\partial u}{\partial t}\right)_{av} = \frac{1}{2}\left(\left(\frac{\partial u}{\partial t}\right)_{i,j}^{t} + \left(\overline{\frac{\partial u}{\partial t}}\right)_{i,j}^{t+\Delta t}\right) \tag{19}$$

$$\left(\frac{\partial v}{\partial t}\right)_{av} = \frac{1}{2}\left(\left(\frac{\partial v}{\partial t}\right)_{i,j}^{t} + \left(\overline{\frac{\partial v}{\partial t}}\right)_{i,j}^{t+\Delta t}\right) \tag{20}$$

The final, "corrected" value of height and velocity in x and y-direction at time $t + \Delta t$ are shown in Eqs. (21), (22), and (23), respectively [9].

$$h_{i,j}^{t+\Delta t} = h_{i,j}^{t} + \left(\frac{\partial h}{\partial t}\right)_{av}\Delta t \tag{21}$$

$$u_{i,j}^{t+\Delta t} = u_{i,j}^{t} + \left(\frac{\partial u}{\partial t}\right)_{av}\Delta t \tag{22}$$

$$v_{i,j}^{t+\Delta t} = v_{i,j}^{t} + \left(\frac{\partial v}{\partial t}\right)_{av}\Delta t \tag{23}$$

2.3 Artificial Viscosity

Normally, for Courant number less than one, 2nd-order FDM generate numerical oscillations. This is due to truncation error and diffusive properties of scheme. So, it is necessary to remove such numerical oscillation for smooth flow. Such condition addition of Artificial Viscosity term required to overcome such problem. This term was used successfully in different application with MacCormack's technique by

many researchers. The governing flow equations for 2D unsteady flow are as below:

$$\frac{\partial U}{\partial t} = -\frac{\partial E}{\partial x} - \frac{\partial F}{\partial y} + S \tag{24}$$

In this governing equation, a small amount of artificial viscosity is added in each time step of solution vector U [9]:

$$S_{i,j}^t = \frac{C_x \left| p_{i+1,j}^t - 2p_{i,j}^t + p_{i-1,j}^t \right|}{p_{i+1,j}^t + 2p_{i,j}^t + p_{i-1,j}^t} \left(U_{i+1,j}^t - 2U_{i,j}^t + U_{i-1,j}^t \right)$$

$$+ \frac{C_y \left| p_{i,j+1}^t - 2p_{i,j}^t + p_{i,j-1}^t \right|}{p_{i,j+1}^t + 2p_{i,j}^t + p_{i,j-1}^t} \left(U_{i,j+1}^t - 2U_{i,j}^t + U_{i,j-1}^t \right) \tag{25}$$

In Eq. (25), C_x and C_y are two freely defined parameters with typical values ranging from 0.01 to 0.3. In the Eq. (25), U indicates the various elements of the solutions vector, each taken in independently. S is assessed in the predictor step using the known quantities at the moment, while in the corrector step, the values on the right-hand side of Eq. (25) are the anticipated values, with $S_{i,j}^t$ and it is represent by $\overline{S}_{i,j}^{t+\Delta t}$ [9].

$$\overline{S}_{i,j}^{t+\Delta t} = \frac{C_x \left| \overline{p}_{i+1,j}^{t+\Delta t} - 2\overline{p}_{i,j}^{t+\Delta t} + \overline{p}_{i-1,j}^{t+\Delta t} \right|}{\overline{p}_{i+1,j}^{t+\Delta t} + 2\overline{p}_{i,j}^{t+\Delta t} + \overline{p}_{i-1,j}^{t+\Delta t}} \left(\overline{U}_{i+1,j}^{t+\Delta t} - 2\overline{U}_{i,j}^{t+\Delta t} + \overline{U}_{i-1,j}^{t+\Delta t} \right)$$

$$+ \frac{C_y \left| \overline{p}_{i,j+1}^{t+\Delta t} - 2\overline{p}_{i,j}^{t+\Delta t} + \overline{p}_{i,j-1}^{t+\Delta t} \right|}{\overline{p}_{i,j+1}^t + 2\overline{p}_{i,j}^t + \overline{p}_{i,j-1}^t} \left(\overline{U}_{i,j+1}^{t+\Delta t} - 2\overline{U}_{i,j}^{t+\Delta t} + \overline{U}_{i,j-1}^{t+\Delta t} \right) \tag{26}$$

The artificial viscosity term calculated from Eqs. (25) and (26) are added as extra term in predictor step (for predictor value of h, u, and) of MacCormack technique at time step $t + \Delta t$ [9].

$$\overline{h}_{i,j}^{t+\Delta t} = h_{i,j}^t + \left(\frac{\partial h}{\partial t} \right)_{i,j}^t \Delta t + S_{i,j}^t \tag{27}$$

$$\overline{u}_{i,j}^{t+\Delta t} = u_{i,j}^t + \left(\frac{\partial u}{\partial t} \right)_{i,j}^t \Delta t + S_{i,j}^t \tag{28}$$

$$\overline{v}_{i,j}^{t+\Delta t} = v_{i,j}^t + \left(\frac{\partial v}{\partial t} \right)_{i,j}^t \Delta t + S_{i,j}^t \tag{29}$$

At time $t + \Delta t$, as an extra term of artificial viscosity calculated from Eq. (26) is added in to the corrected values of h, u and v in corrector step [9].

Table 1 Number of boundary conditions required in open boundary problem

	Subcritical flow		Supercritical Flow	
	Upstream	Downstream	Upstream	Downstream
1D simulation	1	1	2	0
2D simulation	2	1	3	0

$$h_{i,j}^{t+\Delta t} = h_{i,j}^t + \left(\frac{\partial h}{\partial t}\right)_{av} \Delta t + \overline{S}_{i,j}^{t+\Delta t} \tag{30}$$

$$u_{i,j}^{t+\Delta t} = u_{i,j}^t + \left(\frac{\partial u}{\partial t}\right)_{av} \Delta t + \overline{S}_{i,j}^{t+\Delta t} \tag{31}$$

$$v_{i,j}^{t+\Delta t} = v_{i,j}^t + \left(\frac{\partial v}{\partial t}\right)_{av} \Delta t + \overline{S}_{i,j}^{t+\Delta t} \tag{32}$$

2.4 Initial and Boundary Conditions

The number of boundary conditions is determined by the Froude number or whether the flow is described as subcritical or supercritical [13] (Table 1).

2.5 Stability Condition

For the time marching problem, stability depends on Courant–Friedrichs–Lewy (CFL) condition [9].

$$\max\left(\frac{(u + \sqrt{gh})\Delta t}{\Delta x}\right) \le 1, \max\left(\frac{(v + \sqrt{gh})\Delta t}{\Delta y}\right) \le 1 \tag{33}$$

The spatial grid spacing, flow velocity, and celerity are defining computation time interval, and it will change significantly in computation. Thus, it is necessary to control size of this computational time interval for stability of scheme.

2.6 Governing Equation of Hydraulic Jump

$$\frac{y_2}{y_1} = \frac{1}{2}\left(-1 + \sqrt{1 + 8Fr_1^2}\right) \tag{34}$$

Here y_1 and y_2 are upstream and downstream flow depth immediately after and before of the jump, respectively, and Fr_1 is Froude number at upstream [14].

3 Results and Discussion

The present MacCormack Predictor-Corrector Scheme is used to represent numerical experiment for h hydraulic jump.

3.1 Numerical Experiment for Hydraulic Jump

The present MacCormack model is also applied to study the unsteady flow behavior of hydraulic jump in straight channel(flume). Various parameters considered for numerical experiment are taken from [15]. The details of the experiment, as well as their results, are presented here. The jump was allowed to form in the first 3 m of the glassed flume by controlling the depth at the downstream end. Table 2 lists the various test parameters.

The normal component of velocity is set to zero at the side walls. At the upstream boundary, U-velocity and depth are fixed, while V-velocity is zero. The flow depth is fixed, and the U and V velocities at the downstream boundary are extrapolated

Table 2 Various parameters for hydraulic jump in straight channel

Name	Unit	Value
Total length of flume (l)	m	14
Total width of flume (w)	m	0.46
Acceleration due to gravity (g)	m/s^2	9.81
Manning roughness coefficient (n)	s/m$^{1/3}$	0.016
Bed slope (s_b)	m/m	0
Interval in x-direction (Δx)	m	0.28
Interval in y-direction (Δy)	m	0.0575
Grid points	–	50 × 8
Total time (t_{max})	S	100
Time interval (Δt)	s	0.02
Total time steps (k_{max})	–	5001
Upstream depth	M	0.043
Upstream velocity	m/s	2.737
Downstream depth	m	0.222
Froude number	–	4.23
Courant–Friedrichs–Lewy (CFL)	–	0.8

from the interior nodes. The results have been presented in Fig. 1. Also, it observed that depth of flow after hydraulic jump (subcritical flow condition) obtained by governing equation of hydraulic jump and from numerical experiment are 0.236 and 0.222 m, respectively, which is differ by 5.93%. From the result, it is cleared that the MacCormack method is capable to capture the hydraulic jump in an open channel.

(a)

(b)
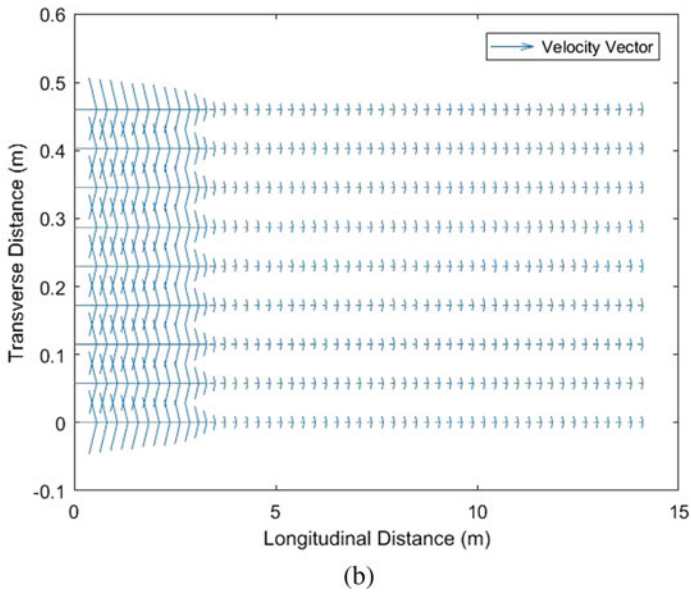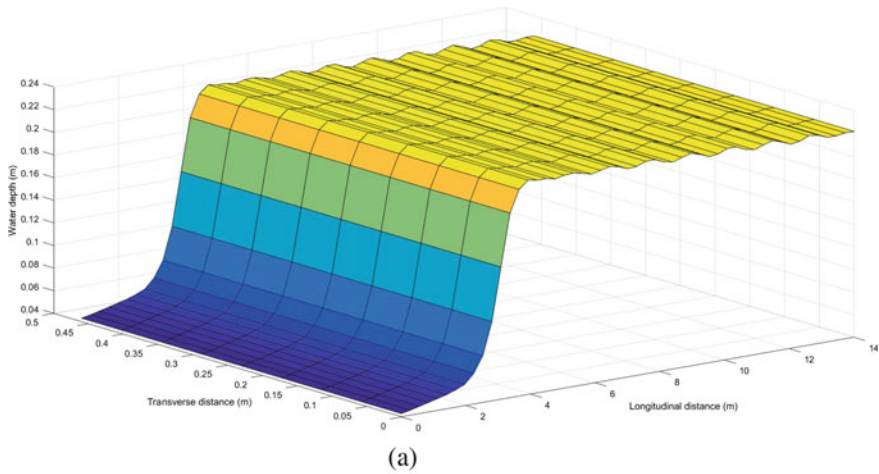
Fig. 1 Hydraulic jump: **a** water surface elevation **b** velocity vector profile

4 Conclusions

(i) The Saint-Venant Equations for 2D flow is solved for the computation of hydraulic jump in straight channel with addition of Artificial Viscosity term to MacCormack Predictor-Corrector Scheme for reduce numerical oscillations. From results it is clarifying that this scheme easy capture hydraulic jump near upstream (within 3 m of channel span) without numerical oscillation.

(ii) Also, it observed that depth of flow after hydraulic jump (subcritical flow condition) obtained by governing equation of hydraulic jump and from numerical experiment are 0.236 m and 0.222 m, respectively which is differ by 5.93%.

(iii) The results of the numerical experiments show that, the MacCormack Predictor-Correction Scheme works well with 2D numerical experiment of hydraulic jump.

References

1. Mujumdar P (2001) Flood wave propagation. Resonance 6(5):66–73. https://doi.org/10.1007/BF02839085
2. Zheleznyak I, Byshovets L (1975) A mathematical model of flood waves moving along a cascade of reservoirs on a large river. Appl Math Mod Hydrol Water Resour Syst
3. Toombes L, Chanson H (2011) Numerical limitations of hydraulic models. In: Proceedings of the 34th world congress of the international association for hydro-environment research and engineering: 33rd hydrology and water resources symposium and 10th conference on hydraulics in water engineering. Engineers Australia, p 2322
4. de Saint-Venant B (1871) Theory of unsteady water flow, with application to river floods and to propagation of tides in river channels. French Acad Sci 73:148–154
5. Dawson C, Mirabito C (2008) The shallow water equations. University of Texas, Austin, p 29
6. Ming H, Chu C (2000) Two-dimensional shallow water flows simulation using TVD-MacCormack scheme. J Hydraul Res 38(2):123–131. https://doi.org/10.1080/00221680009498347
7. Brufau P, Vázquez-Cendón M, García-Navarro P (2002) A numerical model for the flooding and drying of irregular domains. Int J Numer Meth Fluids 39(3):247–275. https://doi.org/10.1002/fld.285
8. Liang D, Falconer R, Lin B (2006) Comparison between TVD-MacCormack and ADI-type solvers of the shallow water equations. Adv Water Resour 29(12):1833–1845. https://doi.org/10.1016/j.advwatres.2006.01.005
9. John D, Anderson J (1995) Computational fluid dynamics: the basics with applications. Mech Eng Ser
10. MacCormack RW (1969) AIAA hypervelocity impact conference. AIAA paper, pp 69–354
11. Chaudhry M (2008) Two-dimensional flow. Open-Channel Flow, pp 407–452
12. Tsakiris G, Bellos V (2014) A numerical model for two-dimensional flood routing in complex terrains. Water Resour Manage 28(5):1277–1291
13. Garcia R, Kahawita R (1986) Numerical solution of the St. Venant equations with the MacCormack finite-difference scheme. Int J Num Meth Fluids 6(5):259–274. https://doi.org/10.1002/fld.1650060502
14. Chippada S, Ramaswamy B, Wheeler M (1994) Numerical simulation of hydraulic jump. Int J Numer Meth Eng 37(8):1381–1397. https://doi.org/10.1002/nme.1620370807

15. Baghlani A, Talebbeydokhti N, Abedini M (2008) A shock-capturing model based on flux-vector splitting method in boundary-fitted curvilinear coordinates. Appl Math Model 32(3):249–266. https://doi.org/10.1016/j.apm.2006.11.012

Modeling of Conical Central Baffle Flumes Using CFD

Ankur Kapoor, Aniruddha D. Ghare, and Sujith Nair

Abstract A CFD-based simulation study on the Conical Central Baffle Flume (CCBF) is presented in this paper. A CCBF consists of a cone-shaped obstruction positioned vertically at the center of an open channel. Computational Fluid Dynamics (CFD) is a tool to mathematically model a physical phenomenon, numerically analyze and solve the system involving fluid flows. Flow-3D® was used to perform CFD-based three-dimensional numerical simulations of Conical Central Baffle Flumes in rectangular channels. Flow-3D® is a suite of CFD software that provides accurate simulation results because to its simple and effective mesh creation technique and accuracy in capturing free surfaces. A CFD model is developed which replicated the system over which experiments were conducted in laboratory. By comparing the centerline water surface profile of the simulation and experiment flows for the identical discharge and flow parameters, the CFD model developed in Flow-3D® is validated. The comparison shows that the simulation profile, to a great extent, resembles the experimental profile. The simulation flow depths are used to predict discharge using the discharge prediction model for CCBFs with a maximum absolute relative error of 6.02% and mean absolute error of 3.30%. Based on the investigation, the use of the CFD-based numerical analysis is recommended in flow measurement studies using the portable central baffle flumes to recognize the flow patterns and fluid behavior under specific flow conditions. CFD is a useful technique for spotting trends or relative differences linked to changes in the installation, even if it cannot replace a laboratory calibration.

Keywords Conical CBF · Flow measurement · Numerical simulations · CFD · Open channels

A. Kapoor (✉)
Department of Civil Engineering, G H Raisoni Institute of Engineering and Technology, Nagpur 440028, India
e-mail: ankurkapoor06@yahoo.com

A. D. Ghare · S. Nair
Department of Civil Engineering, Visvesvaraya National Institute of Technology, Nagpur 440010, India

1 Introduction

Measurement of continuous flows in open channels is essential for optimal water use and proper scheduling for agriculture. The increasing stress and scarcity of water demands a device capable of registering discharge at the desired location and time in an open channel. Such a device will also be of great use even for the metering of water and subsequent billing. Many flow measurement devices have been developed. In open channels, continuous flows are often measured using hydraulic devices that provide a certain stage–discharge relationship. Flume is one such type of hydraulic device usually used in open channels. Various critical depth flumes have been developed and implemented for flow measurement in open channel. The critical depth flumes are generally of fixed type meaning, and the flumes offer measurement of flow at the point of its installation in the channel. The flumes are either constructed by channel side convergence while constructing the channel or fabricated using a metal sheet and fixed at the selected location in the channel. Venturi flume, Parshall flume, cutthroat flume, standing wave flume, etc., are the few fixed type flumes being used for flow measurement in open channels. Though the Venturi and cutthroat flumes are easy to install, the Parshall and standing wave flumes pose certain difficulties as the floor of the flume and the channel are not at the same level. The fixed flumes often tend to settle with time, which needs to be regularly checked for the flume's proper functioning. The accumulation of sediments near the upstream or throat of the flume and the growth of vegetation with time in unlined channels also affect the precision of measurement. Another limitation of the traditional fixed flumes is the inability of a flume to be used at multiple locations since they do not have any movable parts. Since the flume's main objective is to reduce the flow area to cause the occurrence of the critical flow section, which helps to create a unique stage–discharge relationship, it would be helpful to have a low-cost temporary construction to confine the flow area wherever and whenever needed. Such a portable device was first proposed by Hager [4]. The device, then referred to as a mobile Venturi flume, consists of a cylinder placed centrally in a horizontal channel. The availability and streamlined design of the cylinder led to its selection as the obstruction. Hager [3] also developed a variant of the mobile Venturi flume specially designed for circular channels for direct flow measurement by mounting a cylinder at the entrance of the channel having diameter less than that of the circular channel. Hager [3, 4] proposed discharge equations based on the critical energy concept and also provided reference charts between the dimensionless terms consisting of discharge and energy head. The equations related upstream head and discharge in terms of the cylinder and channel geometry.

Samani et al. [9] replaced the graphical approach presented by Hager [3] with a computer model for flow measurement using the circular flume. The objective of the computer model was to calibrate the flume of any size without the need for extensive laboratory experiments. Samani and Magallanez [8] extended the computer model studies for use in trapezoidal channels. The computer model to define the flow through the flume followed the conventional energy and Froude number equations. The governing equations were based on the assumptions of a leveled flume and no

energy loss between the upstream and critical section. The study also considered the occurrence of critical flow at the smallest cross-section between the pipe and the channel, which was assumed to be at the center of the flume, and therefore, the critical cross-sectional area was calculated accordingly. Ghare et al. [2] experimentally calibrated the cylindrical flume for use in trapezoidal channels having side slopes ranging from 0.50 H:1 V to 2 H:1 V. The experimental calibration of a measuring device is always based on a limited set of geometric and flow conditions. It is difficult to consider all the possible variations occurring on the field during practical application of the flume, in the physical experiments. The cost of establishing an experimental setup is another factor that often limits the possible change. Excessive manufacturing cost and the challenge of obtaining laboratory data result in the use of CFD to recognize the flow patterns and fluid behavior under specific flow conditions.

Recent advances in hydrodynamics have resulted in the application of numerical analysis based on CFD in flow measurement studies. The use of CFD-based numerical simulation in mobile flumes was investigated by Li et al. [7]. The flow pattern of three cylindrical flumes designed for usage in U-shaped channels was investigated numerically using Flow-3D® software [1]. By comparing the centerline water surface profile of the simulation and physical experiment, the created CFD model was proven to be accurate. One such portable flow measuring device proposed by Kapoor et al. [6] has been investigated using CFD-based numerical model studies in the present study.

2   Conical Central Baffle Flume (CCBF)

The device proposed by Kapoor et al. [6] consists of a cone-shaped baffle (obstruction) placed at the center of a rectangular channel, referred as the Conical Central Baffle Flume (Fig. 1).

An analytical discharge prediction model (Eq. 1) for the conical flume was developed by Kapoor et al. [6], which was based on energy concept and calibrated using
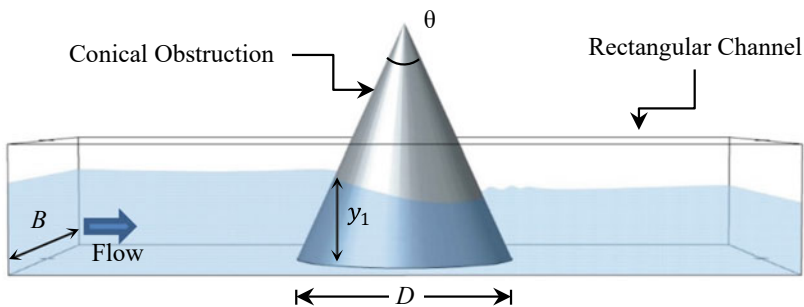
Fig. 1 Conical Central Baffle Flume [6]

laboratory experiments.

$$Q = C_d \sqrt{\frac{\left(B_c\, y_c + m\, y_c{}^2\right)^3 g}{B_c + 2m y_c}} \tag{1}$$

in which $B_c = B - D$ (contracted width) and $m = \tan\frac{\theta}{2}$

The discharge correction factor (C_d) was expressed (Eq. 2) in terms of upstream head (y_1) and contracted channel width (B_c) to correct the unrealistic assumptions of uniform velocity distribution and streamline curvature.

$$C_d = 1.1\left(\frac{y_1}{B_c}\right)^{0.135} \tag{2}$$

The critical flow depth, assumed at the central section of the flume, was expressed as the function of upstream flow depth (y_1) as

$$y_c = \frac{\left(b^2 + 40m\, B_c\, y_1\right)^{1/2} - b}{10m} \tag{3}$$

in which $b = 3B_c - 4m y_1$

The proposed discharge prediction model by Kapoor et al. [6] was calibrated using experimental data collected on flumes (Table 1) having different bed widths (B) and cone diameters (D) such that the contraction ratio (D/B) varies from 0.60 to 0.92. The experiments were performed for different discharges such that the dimensionless discharge ($Q_m/B^{\frac{5}{2}} g^{\frac{1}{2}}$) varies between 0.037 and 0.232. The sole physical measurement performed at the cone face after positioning it in the center of the channel is the upstream flow depth (y_1). The proposed model (Eq. 1) predicted discharge with a maximum absolute error of 8.19% and an average absolute error of 4.24%.

In the present study, the CFD-based numerical simulation studies have been conducted on the CCBF proposed by Kapoor et al. [6]. The primary objective of this study is to develop a CFD model for the CCBF and validate it by comparing the simulation results with the experimental data [6]. The validation would ascertain the use of CFD-based numerical analysis in flow measurement studies using the portable central baffle flumes.

Table 1 Dimensions of the tested CCBFs [6]

CCBF	B (m)	D (m)	θ
CCBF-1	0.60	0.360	23.00°
CCBF-2	0.30	0.275	07.63°
CCBF-3	0.30	0.200	30.00°
CCBF-4	0.10	0.080	15.84°
CCBF-5	0.10	0.075	14.77°

3 CFD Simulations

CFD simulations require numerical solutions to the equations controlling fluid flow. Since, water which is a Newtonian fluid is flowing through the flume, the fluid flow could be described by the continuity and momentum conservation equation (Navier–Stokes equations).

For incompressible flows, the mass continuity of the fluid motion is represented in the Cartesian coordinate system as follows:

$$\frac{\partial u}{\partial x} + \frac{\partial v}{\partial y} + \frac{\partial w}{\partial z} = 0 \tag{4}$$

where u, v, and w are the fluid velocity components in the x, y, and z directions.

The Navier–Stokes equations or momentum conservation equations for three-dimensional flows in the Cartesian coordinate system are represented as

$$\rho\left(\frac{\partial u}{\partial t} + u\frac{\partial u}{\partial x} + v\frac{\partial u}{\partial y} + w\frac{\partial u}{\partial z}\right) = -\frac{\partial p}{\partial x} + \rho g_x + \mu\left(\frac{\partial^2 u}{\partial x^2} + \frac{\partial^2 u}{\partial y^2} + \frac{\partial^2 u}{\partial z^2}\right) \tag{5}$$

$$\rho\left(\frac{\partial v}{\partial t} + u\frac{\partial v}{\partial x} + v\frac{\partial v}{\partial y} + w\frac{\partial v}{\partial z}\right) = -\frac{\partial p}{\partial y} + \rho g_y + \mu\left(\frac{\partial^2 v}{\partial x^2} + \frac{\partial^2 v}{\partial y^2} + \frac{\partial^2 v}{\partial z^2}\right) \tag{6}$$

$$\rho\left(\frac{\partial w}{\partial t} + u\frac{\partial w}{\partial x} + v\frac{\partial w}{\partial y} + w\frac{\partial w}{\partial z}\right) = -\frac{\partial p}{\partial z} + \rho g_z$$
$$+ \mu\left(\frac{\partial^2 w}{\partial x^2} + \frac{\partial^2 w}{\partial y^2} + \frac{\partial^2 w}{\partial z^2}\right) \tag{7}$$

where ρ is the density of the fluid, ρ is the pressure, μ is the fluid viscosity, and g_x, g_y, and g_z are the components of body acceleration, whereas u, v, and w are the fluid velocities in the x, y, and z directions, respectively.

The numerical simulations were performed using FLOW-3D® [1] with a one-phase fluid model, free surface interface, and incompressible flow conditions. For free surface modeling, Flow-3D® relies on the Solution Algorithm (SOLA) developed by Hirt and Nichols [5] and the extremely accurate True Volume of Fluid (TruVOF) approach. This method tracks the interface between liquid and gas within the mesh using fluid fraction, ranging from 0 to 1. The novel Fractional Area Volume Obstacle Representation (FAVOR™) meshing technique is used by Flow-3D®. The method allows the construction of simple structured rectangular grids, which makes the mesh easy to generate without affecting the numerical accuracy of the simulation.

In Flow-3D®, a basic simulation model of the CCBF was created that reproduced the experimental flume. The dimensions of the Conical Central Baffle Flumes in rectangular channel are mentioned in Table 1. The CCBF geometry (Fig. 2) was prepared using predefined geometries in Flow-3D®.
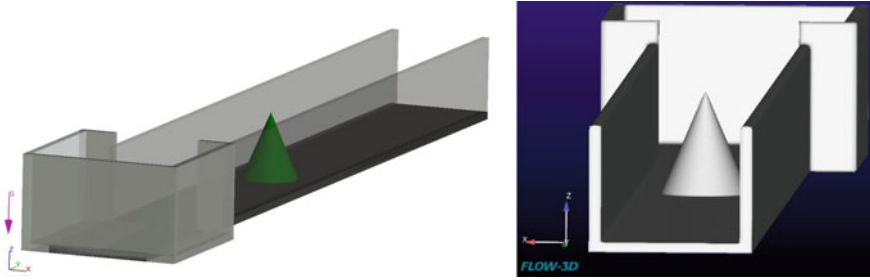
Fig. 2 CCBF geometry prepared in Flow-3D®

The flume geometry was defined using simple structured rectangular mesh which covered the computational domain. Mesh block-1 having 30 mm cell size was generated for the u/s reservoir and the channel. To more precisely capture the flow properties in the area of the obstruction, a finer mesh block-2 with 10 mm resolution was layered within mesh block-1. The boundary conditions specified to the mesh blocks are shown in Fig. 3 in which 'S' denotes *Symmetry*, 'W' denotes *Wall* and 'O' *denotes* Output boundary condition. The RNG k-turbulence model, which is frequently used for external flows with complex geometries in CFD applications, was enabled to simulate the turbulence in the flow. The simulations were conducted until steady-state conditions were reached.

The validation using CFD simulations is performed in two steps. Comparing the water surface profiles of the simulation and experiment flows for the identical discharge and flow parameters is the first step in validating the simulation model setup. After validating the simulated model, the proposed discharge prediction model (Eq. 1) is verified. Similar discharge values to those used in the experiment trials were used in the simulations. The dimensionless discharge $\left(Q^* = \frac{Q}{B^{5/2}g^{1/2}}\right)$ of the experimental runs was found to vary between 0.037 and 0.232.

4 Validation of CFD Model Setup

It is important to first validate the model setup created in the Flow-3D® so that the same can be used for further validation of the discharge prediction model (Eq. 1) and also to perform further simulations for an extended range of flow parameters in the future studies. In the present study, the simulation problem setup is validated by comparing the simulation flow profile with the experimental one for the same discharge. Since the experimental flow depths were recorded along the centerline of the channel therefore, the comparison at various locations was also made along the centerline of the channel by plotting both the water surface profiles for the same discharge values. The comparison of the water surface profiles for CCBF-1 with discharge 42 L per second (lps) is shown in Fig. 4. Similar graphs were plotted

Mesh block-1
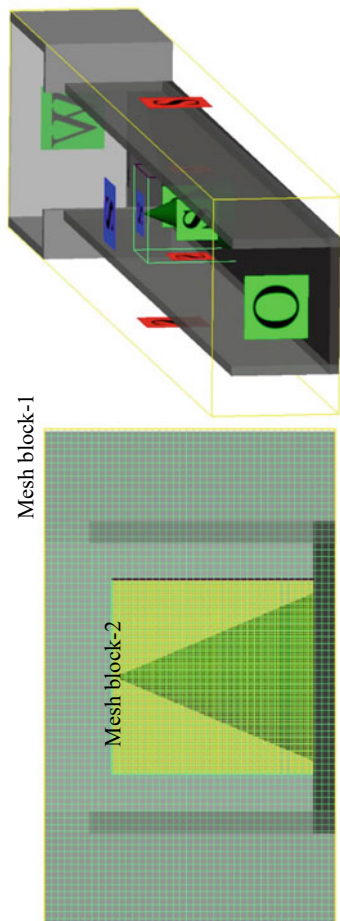
Mesh block-2

Fig. 3 Mesh blocks and mesh boundary conditions
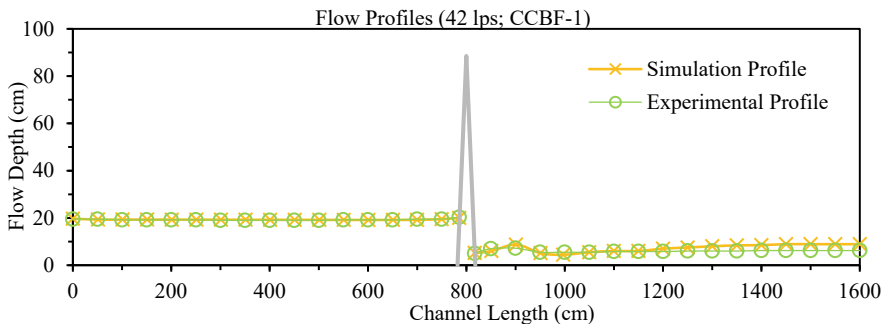
Fig. 4 Flow profile comparison

for all CCBFs and discharges. The comparison reveals that the simulation profile, to a great extent, resembles the experimental profile with an average difference of 2.5% between the two flow profiles. Additionally, comparisons are made between the measured experimental flow depths at the cone face (y_1) for a discharge Q for all the Conical Central Baffle Flumes and the simulation results. The maximum difference between the experimental and simulation flow depths at the cone face (y_1) is found to be 5.81% with a mean value of 2.71%.

Additionally, to comparing the upstream flow depths, the ratio of the simulated flow depth downstream and upstream of the obstacle has also been determined for all of the simulations. This ratio is consistent throughout all simulations and is within the experimentally measured submergence limit range of 0.44 to 0.73 [6]. The comparison of the flow profiles and the simulation submergence ratios certifies the use of created simulation model setup.

5 Validation of Discharge Model Using CFD

Since the simulation and experimental flow profiles closely resembles each other, the simulated upstream depth (y_1) can be used to validate the discharge prediction model developed by Kapoor et al. [6]. The first step toward the model validation is to calculate the critical depth of flow (y_c) using Eq. (3). The equation for the critical depth has been developed assuming that the critical conditions prevail at the central section of the obstruction, observed in the flow direction. Therefore, the calculated critical flow depths (y_c) are compared with the simulation flow depths at the center of the conical obstruction (y_{center}) for all the simulations. It is found that the maximum difference between y_c calculated using Eq. (3) and y_{center} is 4.82% with an absolute mean value of 2.97%.

Thereafter, the calculated y_c has been used to predict discharge using the discharge Eq. (1) for all the simulations and compared with the true discharge values. More than 90% accuracy is obtained in the discharge estimated using discharge Eq. (1) for

simulations on the CCBF placed in a rectangular channel (Table 2). The maximum absolute error was found to be 6.02% with an absolute mean value of 3.30%. This shows that the experimentally calibrated discharge Eq. (1) developed by Kapoor et al. [6] works well even on the simulation data and that the CFD-based numerical simulations can be used to ascertain the applicability of the model for more such combinations of flow and geometry parameters.

It is worth mentioning at this stage that the discharge Eq. (1) when applied on the same data based on which it was calibrated gave a maximum error of 8.19% with a mean value of 4.24%; however, the error values were significantly reduced when applied on the simulation data. In addition to this, the percentage observations giving less than 5% error in discharge prediction were 53% in case of experimental

Table 2 Discharge calculations for simulation data

CCBF#	y_1 (cm) [Simulation]	y_c (cm) (Eq. 3)	C_d (Eq. 2)	Q (lps) (Eq. 1)	Q_m (lps)	Error (%) $\left\lvert \frac{[6]-[5]}{[6]} \right\rvert$	Dimensionless discharge (Q^*)
[1]	[2]	[3]	[4]	[5]	[6]	[7]	[8]
CCBF-1	16.97	11.64	1.050	32.95	32.00	2.96	0.037
	19.99	14.00	1.073	43.75	42.00	4.17	0.048
	22.42	16.03	1.090	53.45	52.00	2.79	0.059
CCBF-2	10.37	07.50	1.105	07.49	07.20	4.01	0.047
	11.55	08.50	1.122	09.10	08.80	3.37	0.057
	12.49	09.20	1.134	10.49	10.00	4.89	0.065
	13.00	09.40	1.140	11.29	10.80	4.49	0.070
	14.00	10.30	1.151	12.93	13.00	0.52	0.084
CCBF-3	18.10	13.20	1.437	06.29	06.20	1.48	0.040
	18.99	13.90	1.446	06.89	07.20	4.28	0.046
	23.50	17.50	1.489	10.38	10.00	3.84	0.065
	25.00	18.70	1.501	11.72	11.80	0.69	0.076
	26.50	19.50	1.513	13.14	13.00	1.10	0.084
CCBF-4	07.08	05.20	1.305	01.12	01.06	6.02	0.107
	08.01	06.00	1.327	01.42	01.36	4.58	0.137
	08.61	06.50	1.340	01.63	01.56	4.80	0.157
	09.38	07.00	1.355	01.93	01.86	3.85	0.188
	10.27	07.70	1.372	02.31	02.30	0.37	0.232
CCBF-5	07.25	05.10	1.270	01.33	01.28	3.90	0.129
	07.83	05.82	1.283	01.53	01.48	3.62	0.149
	08.03	05.95	1.288	01.61	01.57	2.37	0.158
	08.47	06.20	1.297	01.78	01.72	3.24	0.174
	08.92	06.60	1.306	01.96	01.87	4.66	0.189

Fig. 5 Frequency distribution of errors associated with experimental and simulation data
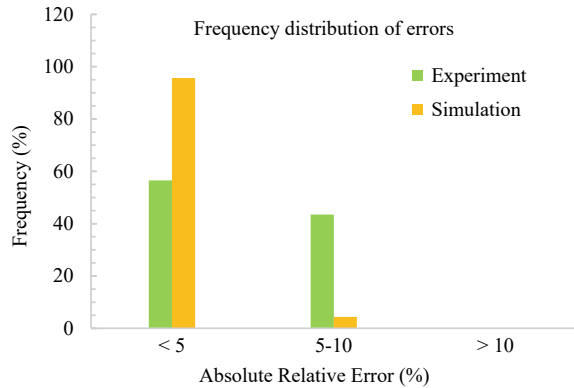
data, whereas the same were found to be nearly 96% in case of simulation data. The frequency distribution of relative absolute errors in discharge prediction associated with both experimental and simulation data is shown in Fig. 5.

6   Conclusions

The Conical Central Baffle Flume has been investigated using CFD. Flow-3D$^®$ has been used to perform the numerical simulations. The simulations were performed for those CCBFs and discharges over which the actual experiments were conducted. Therefore, the CFD model was validated using the experimental data by comparing the simulation and experimental flow profiles. The simulation flow profiles resemble the experimental profiles validating the CFD model. The average difference between the experimental and simulation flow depths at the cone face (y_1) is found to be 2.71%. The upstream flow depths (y_1) were used to calculate the critical depths (y_c) and compared with the simulation flow depths at the center (y_{center}). The calculated y_c was then used to predict discharge using the discharge Eq. (1) for all the simulations and compared with the actual discharge values. The average absolute error in discharge prediction was found to be 3.30%. Additionally, the ratio of the downstream and upstream simulation flow depths was found to lie between 0.44 and 0.73, which corresponds to the submergence limit recorded during experiments. Based on the comparisons between y_c and y_{center}, , it can be concluded that as long as the submergence is less than 73%, the proposed equation for critical depth (Eq. 3) may estimate y_c at the center with an accuracy of over 95%. Moreover, it has been discovered that when the submergence ratio is less than 0.73, the discharge estimated using discharge Eq. (1) for simulations on the CCBF placed in a rectangular channel is more than 90% accurate. The results of the present study define the accuracy and capability of CFD to capture actual flow scenarios. The CFD model can be used to simulate flow through CCBFs for an extended range of flow parameters in the future studies.

References

1. FLOW-3D® Version 12.0 [Computer software] (2019) Santa Fe, NM: Flow Science, Inc. https://www.flow3d.com
2. Ghare AD, Kapoor A, Badar AM (2020) Cylindrical central baffle flume for flow measurements in open channels. J Irrig Drain, ASCE 146(9):06020007. https://doi.org/10.1061/(ASCE)IR.1943-4774.0001499
3. Hager WH (1988) Mobile flume for circular channel. J Irrig Drain, ASCE 114(3):520–534. https://doi.org/10.1061/(ASCE)0733-9437(1988)114:3(520)
4. Hager WH (1985) Modified venturi channel. J Irrig Drain, ASCE 111(1):19–35. https://doi.org/10.1061/(ASCE)0733-9437(1985)111:1(19)
5. Hirth C, Nichols B (1981) Volume of fluid (VOF) method for the dynamics of free boundaries. J Comput Phys 39(1):201–225
6. Kapoor A, Ghare AD, Vasudeo AD, Badar AM (2019) Channel flow measurement using portable conical central baffle. J Irrig Drain, ASCE 145(11):06019010. https://doi.org/10.1061/(ASCE)IR.1943-4774.0001427
7. Li X, Jin L, Bernie AE, Yang Z, Wang W, He W, Wang Y (2020) Influence of the structure of cylindrical mobile flumes on hydraulic performance characteristics in U-shaped channels. Flow Meas Instrum 72. https://doi.org/10.1016/j.flowmeasinst.2020.101708
8. Samani Z, Magallanez H (1993) Measuring water in trapezoidal canals. J Irrig Drain, ASCE 119(1):181–186. https://doi.org/10.1061/(ASCE)0733-9437(1993)119:1(181)
9. Samani Z, Jorat S, Yousaf M (1991) Hydraulic characteristics of a circular flume. J Irrig Drain, ASCE 117(4):558–566. https://doi.org/10.1061/(ASCE)0733-9437(1991)117:4(558)

Numerical Simulation of Pressure Flow Due to Vertical Contraction on a Rigid Bed

Sofi Aamir Majid and Shivam Tripathi

Abstract Flow in open channels is characterized by a constant pressure boundary. However, near a local obstruction, for example a bridge pier, the flow field is modified. Vertical contraction of flow may occur during extreme floods when a bridge gets submerged. In the vertical contraction, atmospheric flow transits to the pressure flow resulting in curved streamlines and formation of a stagnation zone under the bridge. Further, a recirculation zone is created at the downstream end of the bridge that increases the bed shear stresses. The present study investigates the role of independent variables, namely approach flow velocity, amount of contraction, and the length of the bridge on the dimensions of the stagnation and recirculation zones. The flow is simulated on an open-source platform, OpenFOAM, using InterFoam, a popular solver for simulating open channel flows. Due to the computational constraints, two-dimensional flow is simulated. The results show that the depth of the stagnation zone under the bridge increases with the approach velocity and shows no dependence on the length and opening of the bridge. The length of the recirculation zone increases with the decrease in the bridge opening and increases with increase in approach velocity. Besides, the depth of stagnation zone starts to increase from the upstream end of the contraction and attains a maximum inside the contraction. These findings can be useful in estimating the magnitude and location of pressure flow scour due to vertical contraction at bridges.

Keywords Bridges · Vertical contraction · Pressure flow scour · Stagnation zone · Recirculation zone

S. A. Majid (✉) · S. Tripathi
Department of Civil Engineering, Indian Institute of Technology Kanpur, Kanpur 208016, India
e-mail: aamirm@iitk.ac.in

S. Tripathi
e-mail: shiva@iitk.ac.in

1 Introduction

The flow in open channels is driven by gravity and is characterized by a free surface where a constant pressure exists. The design of bridges for the maximum scour depth at the pier or abutment site is usually based on the assumption that the flow under bridge will always pass as an open channel flow [1]. However, in extreme floods, the water level may rise above the bottom bridge chord and the flow under the bridge transits from free surface to pressure flow due to vertical contraction of flow. In some cases, the bridge may be completely submerged. The recent trends in climate change increase the possibility of bridge submergence. The existence of pressure flow inside the contraction can increase the scour on already eroded bed or might initiate scour on previously uneroded bed. A limited number of studies have addressed the issue of pressure flow scour due to vertical contraction. Most of such studies have been restricted to the development of statistical models based on laboratory experiments to predict the pressure flow scour [2–4].

Figure 1 shows the definition of vertical contraction. The approach flow of depth H_a and average velocity of V_a are subjected to a vertical contraction due to a bridge of length L. The total bridge opening available for the flow at bridge site is H_b. The depth averaged velocity of the flow velocity inside the contraction changes to V_b and is related to V_a as $V_b = (H_a/H_b)V_a$. The increased flow velocity can increase the scouring potential of the flow.

The problem of vertical contraction scour has not been extensively investigated using computation fluid dynamics models. In fact, only a few studies have been conducted to simulate the pressure flow scour [5]. The mechanism of vertical contraction scour can be better understood if the velocity field inside and close the vertical contraction is investigated. Shan et al. studied the flow field inside the contraction using particle image velocimetry and computational fluid dynamics [6]. They reported that a stagnation zone is formed inside the bridge opening. The stagnation zone decreases the vertical flow passage further. A statistical model was developed to estimate the maximum stagnation depth as a function of flow properties and the contraction geometry. The developed model was then incorporated in the pressure flow scour model to improve the performance of the model to predict the pressure flow scour. Carnacina et al. studied the flow dynamics close to a pier in vertical contraction. They reported that a boundary layer is developed under the bridge [7]. They also reported that the shear stresses are increased significantly in the vicinity of

Fig. 1 Schematic of vertical contraction
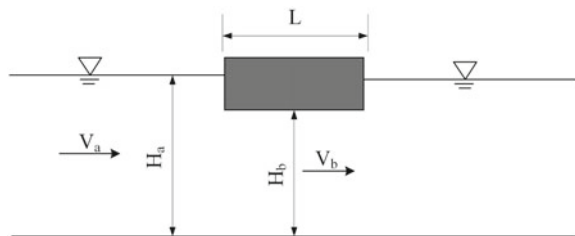
pier in pressure flow as compared to the open channel flow. They found a significant increase in the pier scour in pressure flow conditions as compared to the open channel conditions.

Kara et al. conducted a large eddy simulation (LES) of pressure flow over a rigid bed [8]. The bridge was completely submerged, and an abutment was also simulated. They reported a significant increase in the turbulent kinetic energy (TKE) downstream of the contraction. They attributed it to the fact that the water plunged downward at the downstream end of the contraction. Yoon et al. studied the flow dynamics close to an abutment in pressure flow conditions [9]. They reported that an additional acceleration is imparted close to the abutment in pressure flow conditions which increase the scour. In the present study, a rigid bed simulation of pressure flow is conducted to study the flow characteristics inside and close to the vertical contraction.

2 Materials and Methods

2.1 Numerical Model

To simulate the pressure flow due to vertical contraction, two-dimensional Navier–Stokes (NS) equations are solved. We have assumed an infinite lateral dimension (wide channel assumption) in which there are no significant lateral effects. The flow is solved in the longitudinal (flow) direction and the vertical direction. The NS equation can be stated in the vector form as Eq. (1) and coupled with the continuity equation (Eq. 2) form a closed set of equations to obtain the solution for the flow velocity components and pressure. In the present study, a two-phase flow is simulated, i.e., the fluid is assumed to be composed of water and air. Thus, an additional equation needs to be solved for the transport of the phase fraction (Eq. 3). In Eq. (1), U is the velocity vector, μ_t is the turbulent viscosity and is primarily a function of the flow rather than fluid. p is the pressure and g is the acceleration due to gravity.

$$\frac{\partial(\rho U)}{\partial t} + \nabla.(\rho U U) - \nabla \cdot \left((\mu + \mu_t)\left(\frac{1}{2}\left(\nabla U + \nabla U^T\right)\right)\right) = -\nabla p + \rho g \quad (1)$$

$$\nabla \cdot U = 0 \quad (2)$$

$$\frac{\partial \alpha}{\partial t} + \nabla \cdot (U\alpha) = 0 \quad (3)$$

μ and ρ are the dynamic viscosity and the density of fluid and are obtained as weighted mean of the fractions of air and water, respectively, (Eqs. 4 and 5). α is the phase fraction of water, ρ_1, ρ_2, μ_1 and μ_2 are the density of water and air, and dynamic viscosity of water and air, respectively.

$$\rho = \alpha\rho_1 + (1 - \alpha)\rho_2 \tag{4}$$

$$\mu = \alpha\mu_1 + (1 - \alpha)\mu_2 \tag{5}$$

The preceding set of equations is numerically closed by using the $k - \omega$ SST (shear stress transport) turbulence model for the estimation of turbulent viscosity, μ_t. The model was proposed by Menter and accounts for the shear stress transport in the estimation of turbulent viscosity [10]. Roulund et al. reported that $k - \omega$ SST turbulence model performed most consistently in the estimation of shear stresses in the stagnation regions [11]. In the $k - \omega$ SST turbulence model, two equations are solved, one for the generation of the turbulent kinetic energy (k equation) (Eq. 6) and other for the specific dissipation of the turbulence kinetic energy (ω equation) (Eq. 7).

$$\frac{\partial(\rho k)}{\partial t} + \nabla \cdot (\rho U k) = P_k - \beta^* k\omega + \nabla \cdot [(\mu + \sigma_k \mu_t)\nabla k] \tag{6}$$

$$\frac{\partial(\rho \omega)}{\partial t} + \nabla \cdot (\rho U \omega) = \alpha\rho S^2 - \beta\rho\omega^2 + \nabla \cdot [(\mu + \sigma_\omega \mu_t)\nabla\omega]$$
$$+ 2(1 - F_1)\rho\sigma_{w2}\frac{1}{\omega}\nabla k \cdot \nabla\omega \tag{7}$$

In the Eq. (7), the blending function F_1 is given as

$$F_1 = \tanh\left[\left[\min\left[\max\left(\frac{\sqrt{k}}{\beta^*\omega y}, \frac{500\nu}{y^2\omega}\right), \frac{4\rho\sigma_{\omega 2}k}{CD_{k\omega}y^2}\right]\right]^4\right] \tag{8}$$

where $CD_{k\omega}$ is given by Eq. (9) and y is the distance to the nearest wall.

$$CD_{k\omega} = \max\left(2\rho\sigma_{\omega 2}\frac{1}{\omega}\nabla k \cdot \nabla\omega, 10^{-10}\right) \tag{9}$$

The kinematic viscosity, $\nu_t = \mu_t/\rho$, is then estimated as

$$\nu_t = \frac{a_1 k}{\max(a_1\omega, SF_2)} \tag{10}$$

In Eq. (10), S is the strain rate tensor given as $S = 1/2(\nabla U + \nabla U^T)$, and F_2 is the second blending function defined by Eq. (11).

$$F_2 = \tanh\left[\left[\max\left(\frac{2\sqrt{k}}{\beta^*\omega y}, \frac{500\nu}{y^2\omega}\right)\right]^2\right] \tag{11}$$

Table 1 Constants used in $k - \omega$ SST turbulence model

β^*	α_1	β_1	σ_{k1}	$\sigma_{\omega1}$	α_2	β_2	σ_{k2}	$\sigma_{\omega2}$	a_1
0.09	5/9	3/40	0.85	0.5	0.44	0.0828	1	0.856	0.31

The P_k term used in the k equation (Eq. 6) limits the production of turbulence in stagnation regions and is given as Eq. (12).

$$P_k = \min\left(\mu_t \nabla U \left(\nabla U + \nabla U^T\right), 10\beta^* \rho k \omega\right) \tag{12}$$

The other model constants in the Eqs. (1–12) are listed in Table 1.

Equations (1–12) are solved in the OpenFOAM environment. Pressure implicit with splitting of operators (PISO) [12] algorithm is used to solve the continuity and momentum equation. InterFoam, a popular solver in OpenFOAM for solving the two-phase flows, is employed. The stability of solution of NS equations heavily relies upon the time step chosen and to overcome such limitation, a dynamic time stepping is chosen such that the courant number, $C_n = |U|\Delta t / \Delta x$, is always less than 1. Each simulation is run for a time of 300 s to allow the flow to develop completely, and after 300 s the sampling for the velocity and shear stresses is done.

2.2 Boundary Conditions

The above equations are solved in two dimensions for a geometry shown in Fig. 2. A rectangular prismatic two-dimensional channel is employed to conduct the computations. Since a two-phase flow is simulated, the vertical dimension of the channel is kept sufficiently larger than the expected water flow depth in the channel to accommodate the air in the space above. As the flow is driven by the gravity, a downstream weir is placed to adjust the water depth in the channel. The vertical contraction is placed sufficiently downstream of the inlet to allow the flow to develop before reaching the contraction. A fine mesh of length 7 m and height 0.2 m is generated having approximately 4500 cells in the longitudinal direction and 200 cells in vertical direction. A non-uniform cell sizing is adopted to make the cell dimensions even smaller in the vicinity and inside of the contraction. The mesh close to the contraction is shown in Fig. 2.

The standard boundary conditions are adopted for the pressure and velocity fields. For the piezometric pressure field ($p - \rho g h$), zero gradient boundary condition is specified except at the top where a constant boundary condition is adopted. For the velocity field, inlet discharge is specified due to variable height inlet. The discharge is calculated based on the expected flow depth and the required averaged flow velocity. Zero gradient boundary conditions are specified for the velocity at the outlet. For the bottom and the bridge, no slip boundary condition is used, and for the top (atmosphere), zero gradient boundary condition is used.

Fig. 2 Numerical setup and
the mesh close to the
contraction
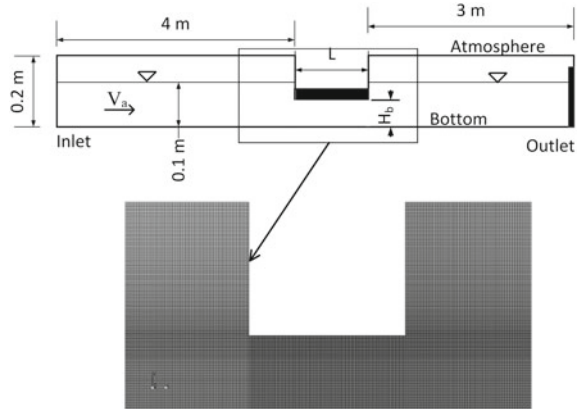
The boundary conditions for k and ω have been adopted from Roulund et al. [11]. The inlet value of k has been calculated assuming that the turbulence intensity in the flow is 5%. The entire TKE field is initialized assuming the same turbulence intensity of 5%. For the phase fraction, α, a variable height inlet with upper and lower bounds as 1 and 0 is used. For all other patches, including outlet, bottom, atmosphere, and bridge, a zero gradient boundary condition is used for α.

3   Results and Discussions

3.1   Numerical Experiments

Five simulation experiments were conducted to see the effects of approach flow velocity, V_a, bridge length, L, and bridge opening, H_b. The experiments included one free surface flow simulation to find the appropriate height of the weir to adjust the flow depth. The channel bed is smooth and the approach flow depth, $H_a = 0.1$, is kept constant for all experiments. Table 2 describes the four pressure flow simulation experiments. The L1H1V1 is assumed to be a base experiment, and the variables are varied from this base case. In each simulation, one variable is changed from the base case, and the corresponding change in the flow field is observed.

Table 2 Description of numerical simulation experiments

Experiment	L1H1V1	L1H1V2	L1H2V1	L2H1V1
V_a(m/s)	0.20	0.30	0.20	0.20
L(m)	0.15	0.15	0.15	0.25
H_b(m)	0.072	0.072	0.060	0.072

Fig. 3 Comparison of
simulated velocity profile
with log law velocity profile
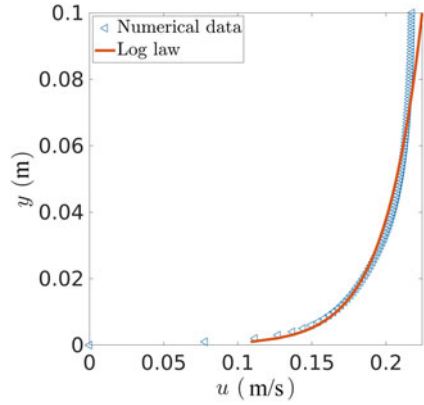
3.2 Velocity Field

The validation of the generated numerical data for open channel flow case is compared with the open channel flow velocity model (Fig. 3). It can be observed that the simulated velocity profile agrees well with the log law. For details on the log law (law of the wall), readers are referred to Han et al. [13]. Besides, InterFoam has been thoroughly evaluated in the literature [14].

As discussed earlier, the velocity increases as the flow enters inside the contraction. The contour plot of longitudinal velocity is shown in Fig. 4, for L1H1V1 experiment. In addition to increased longitudinal velocity, significant vertical velocity components are also generated at the upstream end of the contraction and the downstream of the contraction. The flow gets contracted at the entrance of the bridge and a stagnation zone starts to develop. The flow is contracted further by the development of this stagnation zone. After some distance, the stagnation zone attains a maximum and starts to decay toward the downstream end of the contraction. At the downstream of the contraction, another stagnation zone with a significant amount of flow recirculation is observed. A small stagnation zone is also observed just before the contraction. It can also be inferred from Fig. 4 that the magnitude of velocity gradients under the bridge is more than the gradients close to bottom of the channel. This observation indicates to production of large turbulent shear stresses under the bridge.

3.3 Turbulent Shear Stress

The color plot of turbulent shear stresses is shown in Fig. 5. It can be observed that a strong region of turbulent shear stresses is generated under the bridge. This can be attributed to flow disturbance at the entrance of the contraction. Besides, it can be inferred that the increased shear stresses are majorly resisted by the bridge than
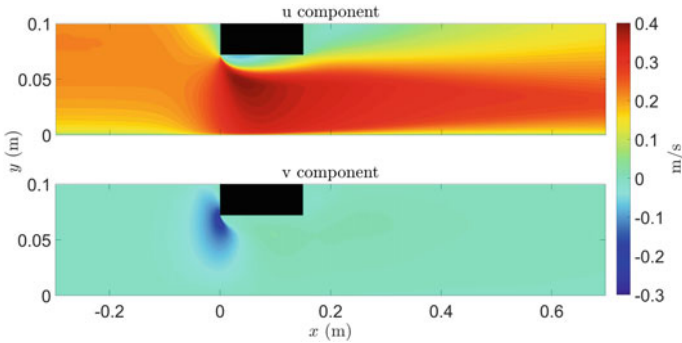
Fig. 4 Color plot of longitudinal and vertical velocity components in L1H1V1. The black rectangle represents the bridge (vertical contraction)
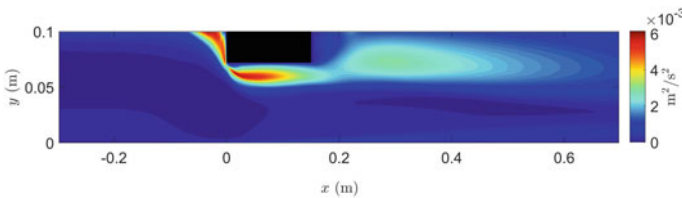
Fig. 5 Color plot of shear stresses in L1H1V1

the bottom of the channel. Further, significant shear stresses are generated in the recirculation zone downstream of the contraction due to flow expansion.

3.4 Stagnation and Recirculation Zones

The stagnation zone inside the contraction is considered as the most important feature of the pressure flow scour phenomenon [6]. In this subsection, the dependence of the stagnation and recirculation zones is studied quantitatively as well as qualitatively. We define the stagnation zone as the region from the top in which the cumulative discharge passed is zero. The cumulative discharge, Q_h, up to a height, h, (Fig. 6) from the top is obtained by the integration of the longitudinal (x) velocity component, u, as Eq. (13).

$$Q_h = \int_{H_a-h}^{H_a} u\,dy \qquad (13)$$

Figure 6 shows the stagnation zones observed in the four pressure flow experiments. The streamlines are also plotted. The stagnation zones are the regions bounded

Fig. 6 Stagnation zones and the streamlines observed in the numerical simulations
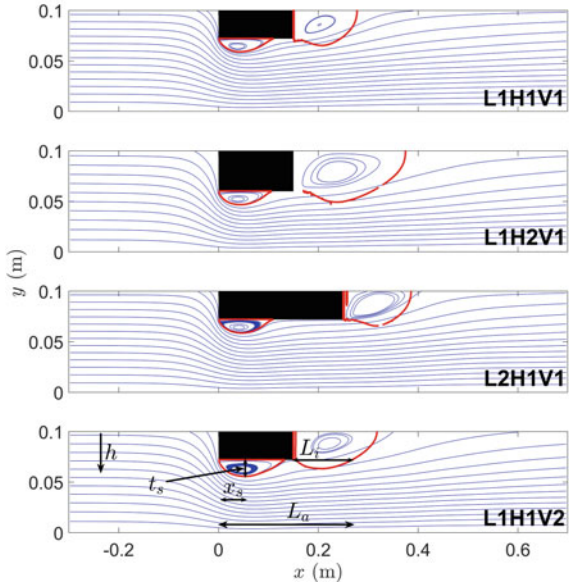
by red curves. It can be observed that the streamlines are curved at the entrance of the contraction which leads to the development of stagnation zone under the bridge. A small recirculation is also observed under the bridge. The shape of the stagnation zone under the bridge is semi-elliptical. It starts to develop at the entrance, attains a maximum, and then starts to decay. At the exit of the contraction, a recirculation zone is formed, and a significant recirculation is observed. This recirculation zone increases the apparent length of the contraction.

Table 3 summarizes the features of the stagnation and recirculation zones. In the table, t_s and x_s are the magnitude and location of the maximum depth of the stagnation observed inside the contraction, respectively, and L_i and L_a are the apparent increase and total length of the contraction due to recirculation of the flow, respectively (Fig. 6). It can be observed in Fig. 6 and Table 3 that t_s and x_s are independent of the bridge opening H_b and the length of the contraction L and depends on the approach flow velocity V_a. The length of the recirculation zone downstream of the contraction, L_i, seems to depend on the bridge opening H_b and the approach flow velocity, V_a, and shows less dependence on the length of the contraction, L.

Table 3 Summary of the stagnation and recirculation zones observed in simulations (cm)

	L1H1V1	L1H2V1	L2H1V1	L1H1V2
t_s	1.3	1.33	1.33	1.63
x_s	4.25	4.3	4.55	5.35
L_i	9.4	15.70	10.0	11.7
L_a	24.4	30.70	25.0	26.7

4   Conclusions

In this study, two-dimensional NS equations are solved coupled with $k - \omega$ SST turbulence closure. The model can predict the flow structures in the pressure flow due to vertical contraction. The vertical contraction accelerates the flow due to the decrease in the passage of the flow under the bridge. The vertical flow passage is further contracted due to the stagnation zone under the bridge. It is observed that the stagnation zone under the bridge shows more dependence on the approach flow than the geometry of the contraction. Significant vertical flow components are observed at the entrance of the contraction due to vertical blockage of the flow. Regions of high shear stresses are observed under the bridge, and shear stresses produced close to the bed inside the contraction are smaller than those produced near the bridge. Stagnation and recirculation zones are created inside and downstream of the contraction. These regions are formed due to the contraction and expansion of the streamlines, respectively. The apparent increase in the length of the bridge due to recirculation of the flow downstream of the contraction is found to be more dependent on the bridge opening as compared to other variables. The study can be extended to investigate the effects of total bridge submergence, when a part of flow passes over the bridge, on the stagnation and recirculation zones.

References

1. Carnacina I, Pagliara S, Leonardi N (2019) Bridge pier scour under pressure flow conditions. River Res Appl 35(7):844–854
2. Arneson LA (1997) The effect of pressure-flow on local scour in bridge openings. Ph.D. thesis, Department of Civil Engineering, Colorado State University
3. Lyn DA (2008) Pressure-flow scour: a reexamination of the HEC-18 equation. J Hydraul Eng 134(7):1015–1020
4. Umbrell ER, Young GK, Stein SM, Jones JS (1998) Clear-water contraction scour under bridges in pressure flow. J Hydraul Eng 124(2):236–240
5. Majid SA, Tripathi S (2021) Three-dimensional numerical simulation of pressure-flow scour. In: Water security and sustainability. Springer, Singapore, pp 11–16
6. Shan H, Zhaoding Xie CB, Suaznabar O, Steven Lottes JS, Kerenyi K (2012) Submerged flow bridge scour under clear water conditions. Publication No. FHWA-HRT-12-034. Federal Highway Administration, Washington DC
7. Carnacina I, Leonardi N, Pagliara S (2019) Characteristics of flow structure around cylindrical bridge piers in pressure-flow conditions. Wat (Switzerland) 11(11):2240
8. Kara S, Stoesser T, Sturm TW, Mulahasan S (2015) Flow dynamics through a submerged bridge opening with overtopping. J Hydraul Res 53(2):186–195
9. Yoon KS, Lee SO, Hong SH (2019) Time-averaged turbulent velocity flow field through the various bridge contractions during large flooding. Wat (Switzerland) 11(1):143
10. Menter FR (1994) Two-equation eddy-viscosity turbulence models for engineering applications. AIAA J 32(8):1598–1605

11. Roulund A, Sumer BM, Fredsøe J, Michelsen J (2005) Numerical and experimental investigation of flow and scour around a circular pile. J Fluid Mech 534:351–401
12. Issa RI (1986) Solution of the implicitly discretized fluid flow equations by operator-splitting. J Comput Phys 62(1):40–65
13. Han Y, Yang SQ, Sivakumar M, Qiu LC (2017) Investigation of velocity distribution in open channel flows based on conditional average of turbulent structures. Mathematical Problems in Engineering
14. Deshpande SS, Anumolu L, Trujillo MF (2012) Evaluating the performance of the two-phase flow solver interFoam. Comput Sci Discov 5(1):014016

Calibration of Conventional Type Current Meters at Various Submergence Level—A Case Study

R. B. Deogade, H. R. Khandagale, and Milankumar Someshwara

Abstract It is crucial to estimate discharges for the management and distribution of water assets. Within a gauging section, local velocities are measured by a rotating element and a stationary type current meter. A Rating Trolley is used to validate or calibrate these instruments as per IS 13371 /ISO 3455. In India, the vertical axis cup type is the most widely used as conventional type current meter. Considering the stream environment and flow conditions, it is crucial that the correct techniques, instrumentation are used for measuring water velocity. It is essential to establish a relationship between rotational speed of current meter and Rating Trolley velocity through the experimental setup. At Central Water and Power Research Station (CWPRS), Pune, the Current Meter Rating Trolley (CMRT) consists of electronic drive and speed control system and an onboard automated data acquisition and processing system to achieve speed range of 0.01 m/s to 7.5 m/s, with uncertainties in calibration process within 0.1% of 95% of confidence level. The instrument needs calibration/performance testing which is mounted on CMRT by rigid rod suspension. The CMRT then drives at different speeds, and the velocity of fluid movement may be determined from the sensing of signals emitted through the rotation of the rotor by using data acquisition system. This paper presents a comparison of calibration at different submergence level from the water surface using conventional type current meters. A comparison is carried out by suspended the current meters below and above the recommended submerges level. At a higher submergence level with increasing towing speed, there is separation of flow behind rod profile, causing decreasing in angular velocity. At lower submergence level with increasing towing speed, a water surface influence is observed on the current meter.

Keywords Cup type current meter · Rating tank · Water submergence level · Current meter Rating Trolley · Calibration of current meter · Propeller type current meter

R. B. Deogade (✉) · H. R. Khandagale · M. Someshwara
Central Water and Power Research Station, Khadakwasla, Pune, Maharashtra 411024, India
e-mail: deogade_rb@cwprs.gov.in

1   Introduction

The exact estimation of stream is a necessity for water resources planning, pollution prevention and flood control. There are various methods and instruments for estimating stream rates in open channels. At gauging stations, local velocities are measured by conventional rotating element and non-rotating element current meters. Periodic calibration required being a mechanical current meters which are calibrated in existing infrastructure of straight open tank which is internationally accepted procedure as specified in the ISO 3455 [1] and IS13371 [2]. It is mandatory to check performance of the current meter before using for measurements by establishing a relationship between its rotational speed and fluid velocity [3]. The IS 13371 mandates recalibration of current meters after 300 hours of use or yearly which is prior. For estimation of stream velocity, variety of instruments are utilized, most regularly are the conventional rotating type current meters.

2   Calibration/Performance Testing of Current Meters

Accuracy of speed measurements largely depends on precision of calibration. To accomplish accuracy in calibration, extraordinary facilities and expertise are required. The ideal way to calibrate a current meter by rigid rod suspension and tow it in stagnant water at known pre-defined speeds of Rating Trolley. The significant parts of this framework are a straight open tank of sufficient length and uniform cross segment, a Rating Trolley moving on two equal rails precisely lined up with the length of the tank and the equipment for measuring parameters required during calibration.

The pre-defined speed of Rating Trolley and the revolutions of rotating element type current meter are measured instantaneously, and these two parameters are interpreted by one or two equations which helps to calculate measured velocities [4].

3   Working Principle of Rotating Type Current Meter

The rotating element of a current meter is driven by the fluid at an angular velocity which is proportional to local velocity of the fluid at the point of immersion. The axis of the rotating element may be at right angles, or it may be parallel to the direction of flow. The conventional current meters are of two general types, the conical cup type with vertical axis and the propeller type with horizontal axis of rotation. A rotor of cup type current meter is constructed out of a conical cup, or curved vanes attached at equal intervals around the perimeter which will rotate when placed in the fluid flow. A rotor of propeller type current meter is an assembly consist of a number of

angled vanes attached at equal intervals around the perimeter of a hub or two or more helical screw blades formed around a hub. The rotor speed is measured using a signal device (time counter/direct velocity counter or both) attached to the current meter.

The relationship between the velocity of the water and rate of revolutions of current meter for various velocities is established experimentally by the following formula:

$v = a + (b \times R)$ [1]

where v = velocity in m/s a and b = constant determined for each equation.

R = the number of Revolutions Per Second (RPS) of the current meters.

4 Current Meter Calibration Facility at CWPRS

CWPRS has a rating tank of 228 m long, 3.66 m wide and 2.13 m deep. Figure 1 shows CMRT facility. The Rating Trolley is moved on the two equal straight steel rails 4.267 m apart and driven by electric servomotors. The capacity to the driving engines of the Rating Trolley is taken care of by 440 V, 50 Hz overhead covered shrouded bus conductor framework. The Rating Trolley is operated with fully automated through Programmable Logic Controller (PLC) system by incorporating precise electronic drive to achieve speed range of 0.01 m/s to 7.5 m/s, real time on board computerized data acquisition and processing system on Supervisory Control and Data Acquisition (SCADA). The uncertainties in measurements of calibration parameters are within 0.1% at 95% confidence level. Provision of optical encoder is made on the distance measuring wheel of the Rating Trolley for precise measurement of distance covered by Rating Trolley during calibration process. Data acquisition software acquires simultaneous data for distance covered by Rating Trolley, travel time, hence speed and pulse output of each current meter under test during each calibration run [4].

Fig. 1 Current meter rating facility at CWPRS

5 Main Types of Current Meters Consider for Experiment

The rotating cup and propeller type current meters are shown in Figs. 2 and 3.

6 Experimental Setup

During calibration, the current meters are rigidly suspended from the rear side of the Rating Trolley. For the test, the current meters were submerged as per ISO 3455–2007 [1] recommended level, i.e., twice the diameter of rotor for axial-flow current meter and one and half times the height of rotor for cup type current meter i.e., 25 cm approximately from surface water level for cup type and propeller type current meters as shown in Fig. 4. Figures 5 and 6 show calibration at immersion depth of 35 cm and 15 cm, respectively.

Fig. 2 Current meter—cup type

Fig. 3 Current meter—propeller type
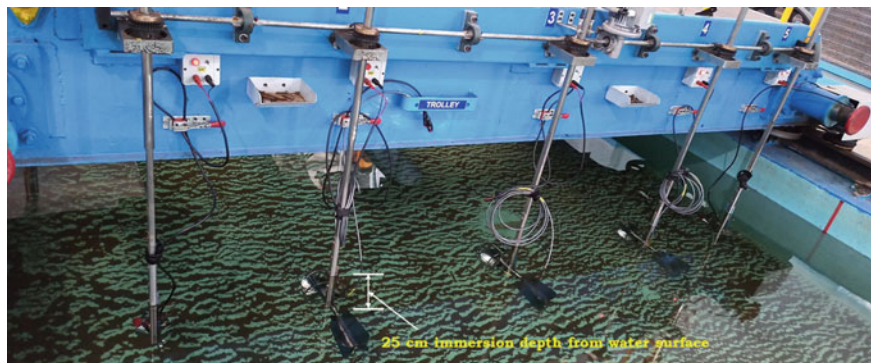
Fig. 4 Immersion depth at 25 cm

Fig. 5 Immersion depth at 35 cm
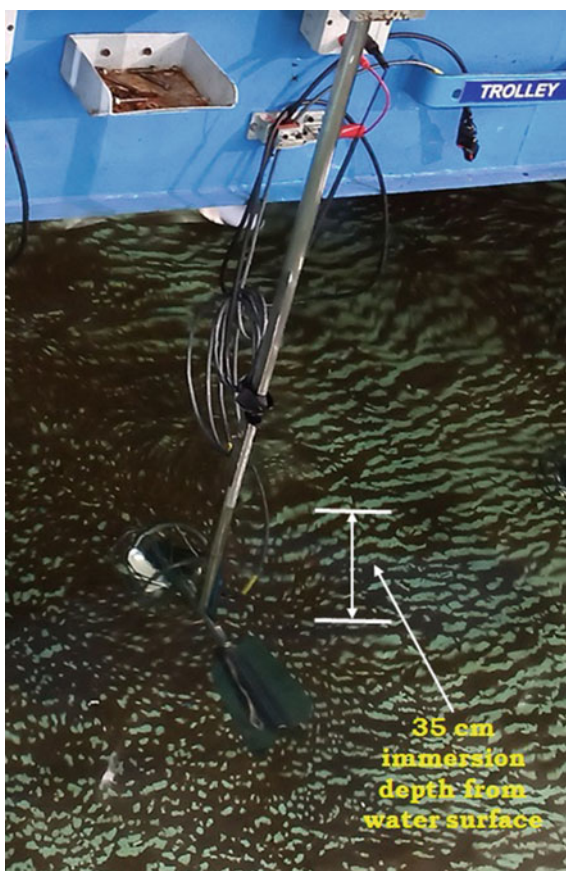
Fig. 6 Immersion depth at
15 cm

7 Test Procedure

During the calibration, the following procedure was adopted;

a. Checked for rotations of current meters were logged.
b. In tailor-made programme input the predefined 12 Rating Trolley velocities (VT) in the range of 0.15 m/s to 4.0 m/s and corresponding number of rotations.
c. Intially ensured that while moving the Rating Trolley in the range of 0.05 m/s to 0.1 m/s it captured the threshold velocity.
d. When the Rating Trolley runs for the pre-defined velocities, then acquired the given number of rotation for each velocity and collected the data for entire range.
e. After the calibration, the result of the current meter is expressed in the form of the best fit calibration curve.
f. Establish the relation between the Rating Trolley Velocity (VT) and acquired datafrom the current meter in the form of equation.

Table 1 Test results for cup type current meters, Sr. No. 139 at various immersion depths

VT m/s	RPS @ 11 cm depth	RPS @ 15 cm depth	RPS @ 25 cm depth	RPS @ 35 cm depth	RPS @ 42 cm depth
0.901	1.31	1.28	1.26	1.31	1.24
1.001	1.46	1.40	1.41	1.45	1.40
1.201	1.75	1.68	1.69	1.76	1.71
1.501	2.19	2.10	2.13	2.20	2.13
1.701	2.48	2.39	2.43	2.47	2.41
2.001	3.02	2.98	2.88	2.92	2.86
2.300	3.44	3.44	3.34	3.44	3.46
2.602	3.92	3.88	3.75	3.93	3.93
2.803	3.98	4.05	4.06	4.22	4.21
3.003	4.17	4.18	4.30	4.42	4.23
3.500	5.01	6.47	4.98	4.96	5.08
4.001	5.88	7.60	5.67	5.84	5.91

g. Repeated the calibration procedure (a) to (f) for the various depths immersion of current meters.

8   Test Results

Experiments were carried out for two cup and three propeller type current meters at various immersion depth viz. 11 cm, 15 cm, 25 cm, 35 cm and 42 cm from water surface. The revolutions per second (RPS) of each current meter at various water depth with different trolley velocity (VT) is shown in Tables 1, 2, 3, 4, 5, and 6 shows the calibration equations at different depth immersion. Figures 7, 8, 9, 10 and 11 show graphical representation.

Table 2 Test results for cup type current meters, Sr. No. 121 at various immersion depths

VT m/s	RPS @ 11 cm depth	RPS @ 15 cm depth	RPS @ 25 cm depth	RPS @ 35 cm depth	RPS @ 42 cm depth
0.901	1.26	1.31	1.27	1.27	1.22
1.001	1.39	1.38	1.41	1.42	1.39
1.201	1.70	1.53	1.68	1.68	1.68
1.502	2.11	1.92	2.08	2.10	2.10
1.701	2.38	2.27	2.38	2.38	2.37
2.001	2.85	2.80	2.79	2.79	2.76
2.303	3.28	3.21	3.18	3.27	3.20
2.602	3.71	3.78	3.56	3.68	3.59
2.803	3.78	3.91	3.84	4.00	3.86
3.002	4.03	4.20	4.09	4.16	4.03
3.500	4.82	5.07	4.74	4.73	4.81
4.001	5.49	5.75	5.38	5.42	5.60

Table 3 Test results for propeller type current meters, Sr. No. 202111-15/02 at various immersion depths

VT m/s	RPS @ 11 cm depth	RPS @ 15 cm depth	RPS @ 25 cm depth	RPS @ 35 cm depth	RPS @ 42 cm depth
0.901	1.17	1.13	1.17	1.10	1.06
1.001	1.29	1.25	1.30	1.22	1.21
1.201	1.57	1.52	1.57	1.49	1.50
1.502	1.92	1.92	1.97	1.88	1.91
1.701	2.18	2.18	2.23	2.12	2.17
2.001	2.51	2.60	2.63	2.48	2.58
2.302	2.87	3.01	3.00	2.86	2.93
2.602	3.22	3.41	3.34	3.23	3.30
2.802	3.32	3.57	3.56	3.47	3.58
3.003	3.51	3.70	3.78	3.62	3.69
3.500	4.18	4.29	4.33	4.15	4.23
4.002	4.79	4.93	4.88	4.78	4.85

Table 4 Test results for propeller type current meters, Sr. No. 202111-16/02 at various immersion depths

VT m/s	RPS @ 11 cm depth	RPS @ 15 cm depth	RPS @ 25 cm depth	RPS @ 35 cm depth	RPS @ 42 cm depth
0.901	0.97	0.94	1.15	1.10	1.02
1.001	1.12	1.08	1.28	1.24	1.17
1.201	1.41	1.40	1.53	1.51	1.45
1.502	1.87	1.82	1.96	1.93	1.78
1.701	2.16	2.09	2.21	2.19	2.05
2.002	2.63	2.56	2.59	2.58	2.45
2.302	3.04	2.94	3.01	3.04	2.94
2.602	3.45	3.25	3.41	3.44	3.30
2.802	3.47	3.39	3.66	3.71	3.56
3.002	3.66	3.65	3.90	3.85	3.64
3.500	4.44	4.24	4.54	4.48	4.28
4.001	5.15	4.78	5.15	5.18	5.10

Table 5 Test results for propeller type current meters, Sr. No. 202111-16/01 at various immersion depths

VT m/s	RPS @ 11 cm depth	RPS @ 15 cm depth	RPS @ 25 cm depth	RPS @ 35 cm depth	RPS @ 42 cm depth
0.901	1.18	1.10	1.19	1.14	1.14
1.001	1.30	1.21	1.32	1.29	1.29
1.201	1.58	1.46	1.59	1.57	1.58
1.502	1.99	1.82	1.99	1.99	1.98
1.701	2.26	2.07	2.28	2.27	2.24
2.001	2.72	2.69	2.68	2.67	2.64
2.302	3.10	3.07	3.11	3.10	3.06
2.602	3.50	3.47	3.51	3.44	3.43
2.802	3.55	3.61	3.79	3.70	3.68
3.003	3.80	3.58	4.01	3.78	3.90
3.500	4.594	4.695	4.619	4.559	4.587
4.001	5.199	5.263	5.216	4.894	5.164

Table 6 Equations of current meters after calibration at different depth of immersion

Type and sr. no	Immersion depth @ 11 cm	Depth @ 15 cm	Depth @ 25 cm	Depth @ 35 cm	Depth @ 42 cm
Cup and 139	$R \leq 2.3281$	$R \leq 4.4313$	$R \leq 3.9301$	For all values of R	For all values of R
	$V = -0.0016 + 0.6875R$	$V = 0.0255 + 0.6872R$	$V = 0.0497 + 0.6782R$	$V = -0.0159 + 0.6867R$	$V = 0.0636 + 0.6694R$
	$R \geq 2.3281$	$R \geq 4.4313$	$R \geq 3.9301$		
	$V = -0.0313 + 0.6936R$	$V = 1.9908 + 0.255R$	$V = -0.1326 + 0.7277R$		
Cup and 121	$R \leq 2.5361$	$R \leq 2.2554$	$R \leq 2.7632$	$R \leq 4.0173$	$R \leq 4.3362$
	$V = 0.0241 + 0.6988R$	$V = -0.1223 + 0.8219R$	$V = -0.0131 + 0.7224R$	$V = 0.0094 + 0.707R$	$V = -0.0333 + 0.7393R$
	$R \geq 2.5361$	$R \geq 2.2554$	$R \geq 2.7632$	$R \geq 4.0173$	$R \geq 4.3362$
	$V = -0.0879 + 0.743R$	$V = 0.1942 + 0.6595R$	$V = -0.149 + 0.7715R$	$V = -0.5309 + 0.8415R$	$V = 0.4403 + 0.6355R$
Propeller and 202,111-15/02	$R \leq 2.079$	$R \leq 2.6854$	$R \leq 2.6563$	$R \leq 2.5279$	$R \leq 2.5055$
	$V = -0.028 + 0.7932R$	$V = 0.0675 + 0.7456R$	$V = 0.0064 + 0.7614R$	$V = 0.0204 + 0.7963R$	$V = 0.1243 + 0.7255R$
	$R \geq 2.079$	$R \geq 2.6854$	$R = 2.6563$	$R \geq 2.5279$	$R \geq 2.5055$
	$V = -0.1874 + 0.8777R$	$V = -0.3364 + 0.8854R$	$V = -0.3958 + 0.901R$	$V = -0.2315 + 0.8878R$	$V = -0.2451 + 0.873R$
Propeller and 202,111-16/01	$R \leq 2.2347$	For all values of R	$R \leq 3.8592$	$R \leq 2.7373$	$R \leq 2.6968$
	$V = 0.0322 + 0.7408R$	$V = 0.1088 + 0.7454R$	$V = 0.0276 + 0.7353R$	$V = 0.0743 + 0.7191R$	$V = 0.0522 + 0.7354R$
	$R \geq 2.2347$		$R \geq 3.8582$	$R \geq 2.7373$	$R \geq 2.6968$
	$V = -0.0515 + 0.7745R$		$V = -0.368 + 0.8378R$	$V = -0.3244 + 0.8554R$	$V = -0.0862 + 0.7838R$
Propeller and 202,111-16/02	$R \leq 2.3017$	$R \leq 2.4036$	$R \leq 3.7107$	$R \leq 2.3017$	$R \leq 2.9018$
	$V = 0.2572 + 0.6655R$	$V = 0.2531 + 0.6861R$	$V = 0.0289 + 0.7585R$	$V = 0.2572 + 0.6655R$	$V = 0.1045 + 0.7267R$
	$R \geq 2.3017$	$R \geq 2.4036$	$R \geq 3.7107$	$R \geq 2.3017$	$R \geq 2.9018$
	$V = -0.0187 + 0.7854R$	$V = -0.1787 + 0.8657R$	$V = -0.1503 + 0.8068R$	$V = -0.0187 + 0.7854R$	$V = -0.0816 + 0.7923R$

R = Revolution per second (RPS) and V = Velocity in m/s
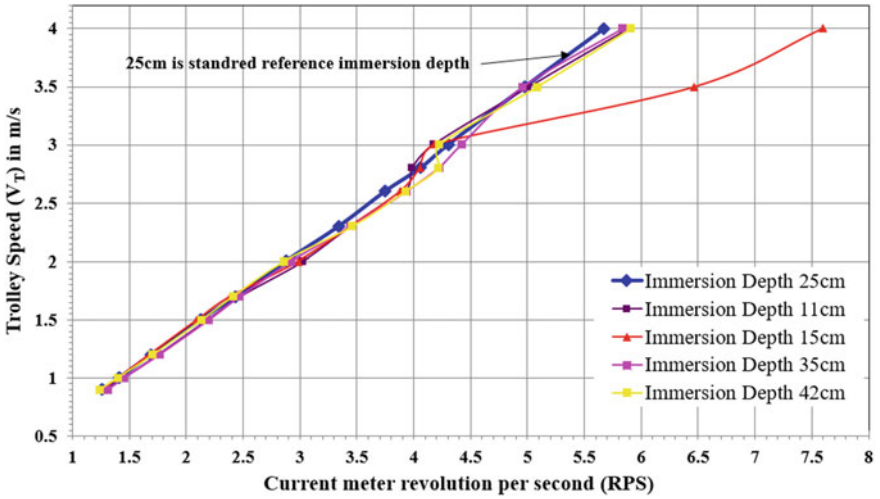
Fig. 7 Trolley speed versus RPS for cup current meter, Sr. No. 139 at various immersion depths
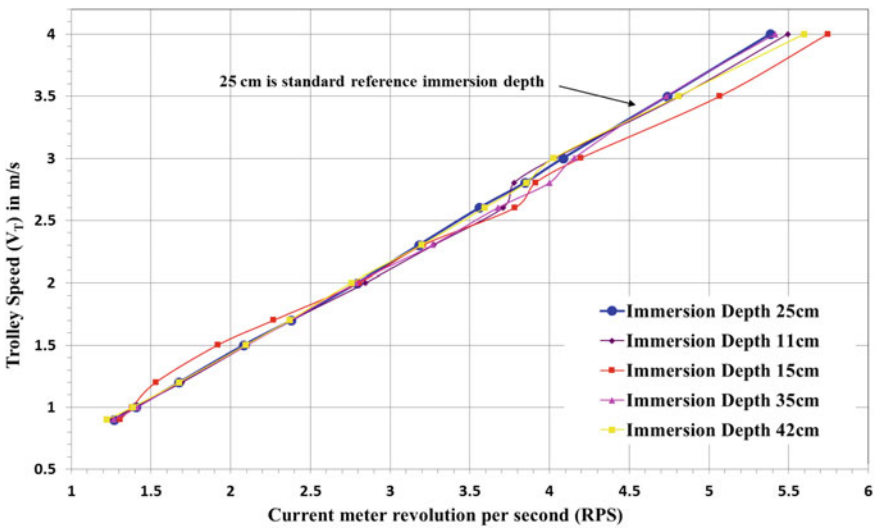
Fig. 8 Trolley speed versus RPS for cup current meter, Sr. No. 121 at various immersion depths
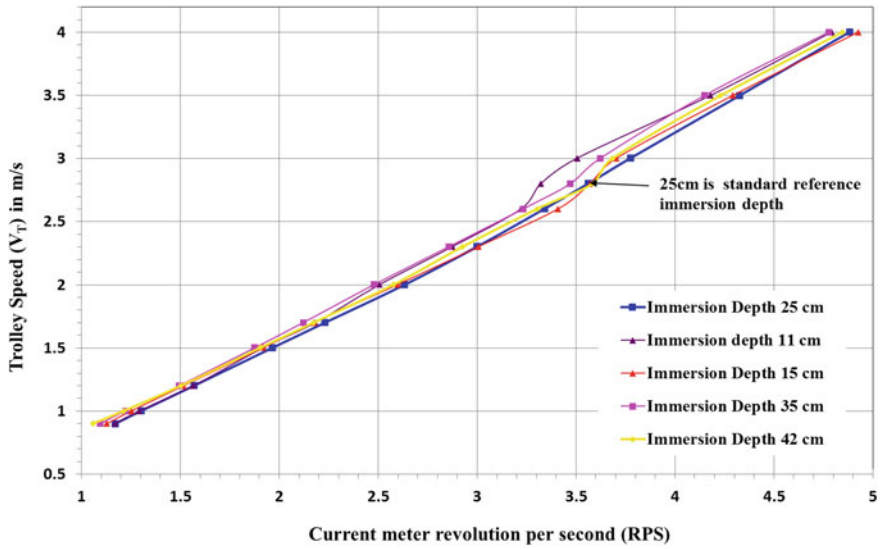
Fig. 9 Trolley speed versus RPS for propeller current meter, Sr. No. 202111-15/02 at various immersion depths
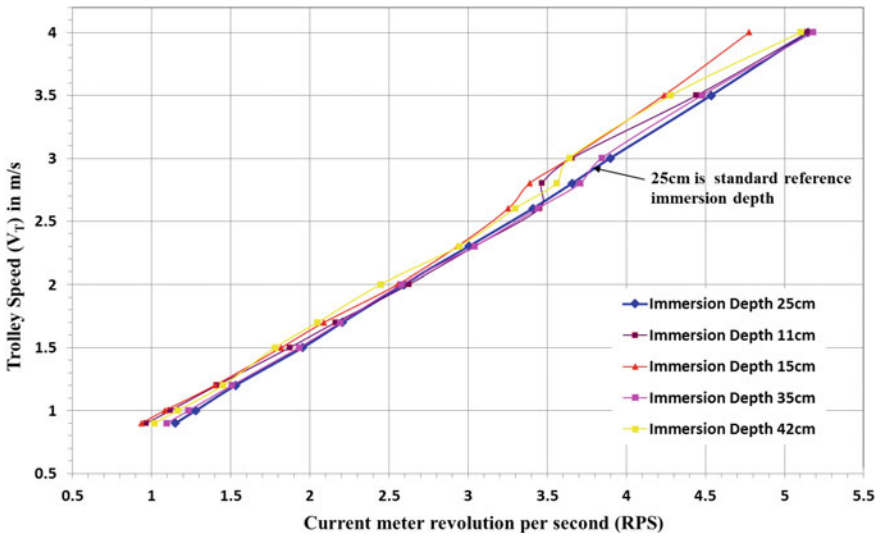
Fig. 10 Trolley speed versus RPS of propeller current meter, Sr. No. 202111-16/02 at various immersion depths
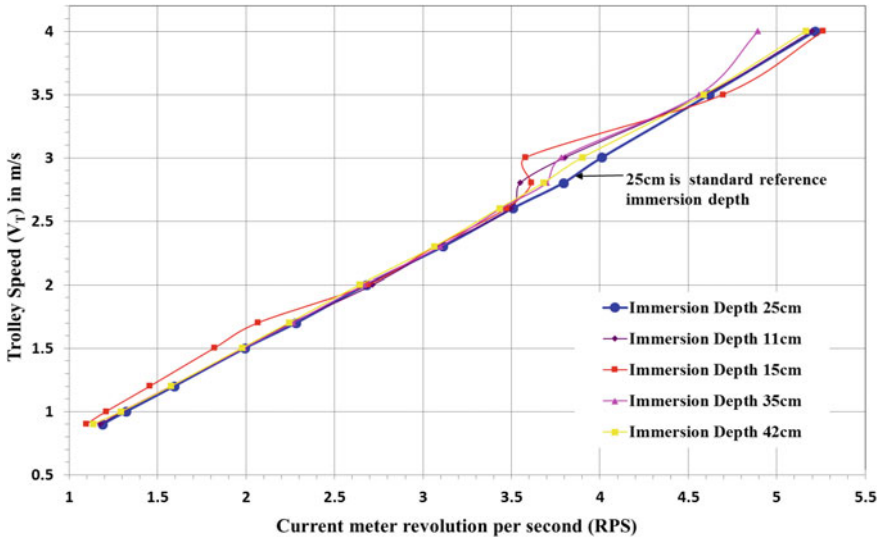
Fig. 11 Trolley speed versus RPS of propeller current meter, Sr. No. 202111-16/01 at various immersion depths

9   Conclusions

The subsequent conclusions are derived from the foregoing study:

- At a lower immersion depth of 11 cm and 15 cm and for the Rating Trolley speed more than 2.0 m/s, the Revolutions Per Second (RPS) captured by current meters are deviated from 10.72 to −34.00% against the standard immersion depth of 25 cm.
- At a higher immersion depth of 35 cm and 42 cm and for the Rating Trolley speed more than 2.0 m/s, the Revolutions Per Second (RPS) captured by current meters are deviated from 6.667% to −4.80% against the standard immersion depth of 25 cm.
- Hence, to achieve better result considering accuracy of measurement, then it is recommended that the current meter should be deployed at standard depth during measurement.

References

1. ISO 3455–2007, Liquid flow measurement in open channels—calibration of rotating—element current meters in straight open tanks
2. IS 13371:2014, Code of practice for calibration (Rating) of rotating element current meters in open tank
3. Gupta RP, Bhonde KG, Khandagale HR (2016) Testing and calibration of contact free radar type discharge sensor—a case study. In: National Conference on Water resource and Hydropower, University of Petroleum & Energy Studies, Dehradun
4. Gupta R.P, Bhonde KG, Khandagale HR, Milankumar S (2019) Comparison of velocity data for acoustic doppler current profiler and conventional type current meters using rating trolley—a case study. In: ISH—Hydro 2019 International Conference, Osmania University

Different Modeling Approaches in Increasing Efficiency of Raceway Pond

Sweety Rajput, B. S. Das, and Anil Kumar Sharma

Abstract The open-closed looped raceway pond is one of the best energy-saving options that can meet several requirements like energy and nutritional reclamation, wastewater treatment, and biomass cultivation for biofuel production. At present, raceway pond (RP) is widely used for producing biofuel using microalgae as feedstock. The wide use of this technique is because of its low maintenance and construction cost, and its simplicity in operation. Therefore, the hydrodynamic study of RP can be helpful to increase the productivity of the pond. The hydrodynamic features like depth of flow, shear stress, and velocity of the fluid play an important role in increasing the efficacy of the pond. The geometric property such as aspect ratio, the pattern of the paddlewheel, deflectors use, sump, and baffles also affect its flow pattern. In past decades, computational fluid dynamics (CFD) has gained attention in expressing a wide range of parameters even in multiphase flow with a high degree of accuracy in raceway ponds. Various numerical simulations using ANSYS (Fluent) have been suggested by many authors in existing RPS's hydrodynamics. Therefore, this review focuses on providing the various numerical optimizing approaches in existing raceway ponds and suggests the best performance of the model under known conditions using different decision variables. A comprehensive review of up-to-date research on various numerical approaches will be done placing special attention on various geometries of raceway pond, flow patterns, and recalling all experimental studies. Based on the current state of the art, several research gaps will be recognized and possible future directions will be proposed.

Keywords Raceway pond · Numerical approach · ANSYS (Fluent) · CFD · Hydrodynamic

S. Rajput (✉) · B. S. Das · A. K. Sharma
Department of Civil Engineering, National Institute of Technology Patna, Patna 800005, India
e-mail: sweetyrajput113@gmail.com

B. S. Das
e-mail: bsd.ce@nitp.ac.in

A. K. Sharma
e-mail: aks.ce@nitp.ac.in

1 Introduction

Microalgae are widely used for biodiesel production, thus utilizing CO_2 during the photosynthesis process and resulting in reducing greenhouse gas emissions [1, 2]. The raceway pond (RP) is a shallow artificial pond used for the cultivation of algae, and sometimes also used in the treatment of wastewater. This RP is a closed-circuit open channel either rectangular or oval in which paddlewheels are installed to make water flow continuous in the circuit. The raceway ponds utilize the CO_2 and make free use of solar energy for the growth of microalgae [3, 4]. The raceway pond consists of a paddlewheel which is widely used for mixing nutrients. The paddlewheel also helps to transport CO_2 and O_2 within cells of algae. By increasing paddlewheel rotating speed, mixing efficiency can be increased, but it requires more electricity. Also, agitation velocity should be more than 0.1 m/s to reduce the chance of settling of algae cells in RPs [5, 6]. Setting a large-scale experimental setup of RPs is expensive and needs more time to construct. But advancement in numerical simulation techniques provides access for researchers to compute various parameters based on an experiment with less time and expense. Many paddlewheels geometry was designed for minimizing energy losses in RPs and investigating hydrodynamic properties such as velocity field, shear stress, and dead zones [7, 8]. Similarly, Xu et al. [9] investigated the flow field during mixing in RPs. In the current scenario, the CFD is widely used to optimize various parameters of RP to increase its efficiency. A configuration like a bend, dead zone, and dimension have been simulated by CFD, and the result showed very promising agreement with the experimental data. In the majority of research on RWP, energy efficiency and flow velocity were the main parameters to be considered. In the present study, the focus is given to reviewing all the mathematical and numerical models that have been used to simulate the raceway pond and paddlewheel to obtain the optimum design. All experimental models have been reported from the current state art to deduce the best model for the raceway pond.

2 Numerical Modeling

In marine engineering, various studies have been conducted by many authors using numerical modeling to evaluate the performance of raceway ponds. Various suggestions have been given in the field of computational fluid mechanics which has been used as a tool to solve the mathematical equation for predicting the nature of flow in raceway ponds. Sompech et al. [10] suggested that CFD can be used to identify the dead zone in various modifications of raceway ponds which can be energy efficient to operate. It was proposed that if the velocity of flow is less than 0.1 m/s which is considered the dead zone. Figure 1 shows the comparison of the dead zone of three different configurations of RP which include standard configuration, three end baffled configuration of RP, and RP with three baffle deflectors at each end and dumbbell-shaped end of central divider baffle which is a modified version of RP.
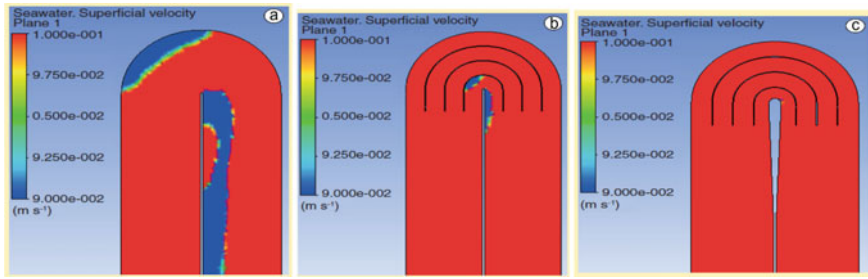
Fig. 1 Representation of dead zones in three different configuration of raceway pond. **a** Standard configuration, **b** Three end baffle, and **c** Modified configuration [10]

The different models of RP simulated using the k-ε model showed that Fig. 1c is not having any dead zone at the velocity of 0.15 m/s. As seen from Fig. 1a, b, with a velocity of 0.14 m/s, both have the dead zone of 14.2% and 0.9%, respectively. Liffman et al. [8] proposed various methods to minimize the kinetic energy losses and flow separation at sharp bends. The result showed that designing the bend can minimize energy losses by 87% as compared to traditional design. Prussi et al. [11] proposed the three-dimensional CFD simulation using the volume of flow approach to investigate the flow trajectories of algal cells. Musgrove et al. [12] use the standard k-ε turbulence model to reduce the head loss, and area of the dead zone and evaluate the shear stress in the carbonation sump. Many authors [13–15] have used turbulent kinetic energy (k) and dissipation rate (ε) as represented in Eqs. (1) and (2).

$$\frac{\partial \rho \varepsilon}{\partial t} + \frac{\partial \rho U_j \varepsilon}{\partial x_j} = \frac{\partial}{\partial x_j}\left[\left(\mu + \frac{\mu_t}{\sigma_\varepsilon}\right)\frac{\partial \varepsilon}{\partial x_j}\right] + T_k - \rho \varepsilon + T_{kb} \tag{1}$$

$$\frac{\partial \rho \varepsilon}{\partial t} + \frac{\partial \rho U_j \varepsilon}{\partial x_j} = \frac{\partial}{\partial x_j}\left[\left(\mu + \frac{\mu_t}{\sigma_\varepsilon}\right)\frac{\partial \varepsilon}{\partial x_j}\right] + \frac{\varepsilon}{k}(C_{\varepsilon 1} T_k = C_{\varepsilon 2}\rho\varepsilon + C_{\varepsilon 1} T_{\varepsilon b}) \tag{2}$$

where T_k represents the turbulence generation due to viscous forces, T_{kb} and $T_{\varepsilon b}$ denote the generation of turbulence kinetic energy from buoyancy forces, ρ is fluid density (kg/m^3), ε is dissipation rate (m^2/s^3), and k is kinetic energy. The model assumes that the turbulence viscosity (μ_t) is related to the kinetic energy and dissipation rate as shown in Eq. (3).

$$\mu_t = \frac{C_\mu \rho k^2}{\varepsilon} \tag{3}$$

In the model, $\sigma_k = 1$ and $\sigma_\varepsilon = 1.3$ are the Prandtl numbers for kinetic energy and dissipation rate, where $C_{\varepsilon 1} = 1.44$, $C_{\varepsilon 2} = 1.92$, and $C_\mu = 0.09$ [16, 17].

Amini et al. [18] proposed the RNG k-ε turbulence model to simulate a flow raceway pond using a paddlewheel. It was suggested that the RNG k-ε model is suitable even at a high Reynolds number and can be used to obtain a solution for

complex geometries. Huang et al. [19] suggested that coupling sloping baffles and flow deflectors has more possibility of increasing the growth of microalgae along with less power utility. Huang et al. [20] again proposed an Eulerian two-phase model for an airlift system in airlift-driven sloping raceway ponds (ALSRWPs). In the study, the turbulent flow behavior was described using the standard k-ε model. Yang et al. [21] compute the algal cell motion using chute baffles. The result suggested that the use of up-down chute baffles can reduce the l/D cycle (light/dark) periods and therefore, increase the growth rate of algae. Shetty and Modak [22] suggested ICEM CFD for simulating raceway geometry. It was suggested that the k-ω SST turbulence model provides a better result and is a better choice for modeling flow using delta wings. Zeng et al. [23] simulates the paddlewheels geometry, i.e., the traditional paddlewheels and other in which paddlewheel blades are inclined at some angles. The CFD simulation was used and concluded that 15° inclination of blade angles is best for mixing in RPs. It was proposed the use of the LES turbulence model for simulation which is described in Eq. (4) and was suggested that LES is a more accurate method than the standard k-ε model for determining flow behavior.

$$\frac{\partial}{\partial t}(pU_i) + \frac{\partial}{\partial x_j}\big(pU_iU_j\big) = -\frac{\partial p}{\partial x_i} + \left[\mu\left(\frac{\partial U_i}{\partial x_j} + \frac{\partial U_j}{\partial x_j} - \frac{2}{3}\delta_{ij}\frac{\partial U_t}{\partial x_t}\right)\right]$$
$$-\frac{\partial \tau_{ij}}{\partial x_j} \tag{4}$$

Sawant et al. [24] proposed CFD simulation using various modifications in RPs geometry with various mixing speeds, with and without gas sparging. The finite volume approach and k-ε model were used and concluded that increasing the mixing speed resulted in reducing the dead zone at the pond bottom. Lima et al. [25] proposed ANSYS CFX19 software for simulation of flow in RPs, and the result showed that vertical circulation is generally observed at curves and has minimum effect in inclined walls. Table 1 lists the summary of all software and CFD code used by various authors to optimize the various turbulent characteristics of the raceway pond.

3 Empirical Modeling

A large number of experiments have been performed by various researchers to obtain the optimized geometry of the raceway pond to increase its effectiveness. This review listed all the experimental geometries of raceway pond set by various researchers which have been mentioned in Table 2.

Table 1 Summary of CFD code and software used to simulate the raceway pond parameters

S. no.	Authors	Purpose	Software	Model used
1	Voleti [26]	CFD model was developed to study the hydrodynamics of modified RWP	MATLAB, ANSYS CFX 14.0	Standard k-ε model
2	Hreiz et al. [27]	To determine the vortex flow field in x and y directions	ANSYS ICEM, ANSYS (Fluent)15.0	VOF, RNG k-ε model
3	Xu et al. [9]	To determine the path line and flow pattern in RP	ANSYS (Fluent)	Standard k-ω model
4	Shetty and Modak [22]	To determine the effect of inclination of paddlewheel blades on raceway pond efficiency	ANSYS ICEM 12.0, ANSYS CFX 12.0	k–ω model, RANS
5	Pirasaci et al. [28]	To compute the flow field in RPs and to trace the path of particles generated by light attenuation	ANSYS15	RANS, VOF, k-ε model
6	Amini et al. [18]	To determine the light transfer efficiency and hydrodynamic performance of the pond	ANSYS (Fluent), MATLAB	RNG k-ε model
7	Sawant et al. [24]	To determine the hydrodynamic performance in different modifications in RP	ANSYS CFX	standard k-ε model
8	Lima et al. [25]	To determine the multi-parametric performance of RP	ANSYS CFX 19	k–ε model, RANS

3.1 Raceway Pond Geometry

Raceway pond has been proved to be an efficient method for the growth of microalgae. Many authors have suggested various geometry of raceway ponds to increase the efficiency of RPs. Sompech et al. [10] simulate RP of 5000 m^2 having a central divider of the thickness of 0.1 m. The configuration computed includes a traditional pattern which includes a horizontal dividing wall without flow deflectors, the island configuration to eliminate dead zone, and a semicircular flow deflector for achieving a uniform flow pattern in all bends. The study compared all three configurations and concludes that the configuration with three baffle deflectors is superior to other

Table 2 List of raceway pond geometry

S. no	Length (m)	Width (m)	Depth (m)	Velocity of flow (m/s)	Author
1	626.72	8	3.95	0.1	Weissman et al. [6]
2	20–50	2–5	0.4–0.8	0.20–0.40	Li et al. [29]
3	3.2	1.5	1	0.25	Voleti [26]
4	10.5	0.7	1	0.3	Liffman et al. [8]
5	3.2	1.5	1	0.1–0.65	Liffman et al. [8]
6	57	4.1	0.25	–	Liffman et al. [8]
7	0.8	0.2	0.08	0.012–0.02	Hreiz et al. [27]
8	2	0.6	0.35	0.01–0.018	Cheng et al. [30]
9	0.7	0.2	0.2	0.017–0.03	Yang et al. [21]
10	10	2	1	0.2	Shetty and Modak [22]
11	3.9	0.65	0.6	0.1–0.3	Ranganathan et al. [31]
12	4.04	0.88	0.05	0–0.2	Sawant et al. [24]
13	50	1	0.15–2	0.27	Pandey and Premalatha [32]
14	10	0.8	0.3	0.23	Pirasaci et al. [28]
15	1.4	0.35	0.5	0.1–0.3	Amini et al. [18]
16	30	3	0.9	0.058	Kusmayadi et al. [33]
17	30.2	3.0	0.9	0.058	Kusmayadi et al. [33]
18	9.57	0.77	0.6	0.2–0.4	Lima et al. [25]

modifications. Voleti [26] proposed RP in which the channel was separated by a divider connected by two 180° curves at both sides with a radius of 0.44 m. It was suggested dead zones are visualized near the curve close to the divider. Liffman et al. [8] proposed six bends geometry and compared it with conventional width/depth bend. It was suggested that opting for energy utility can be minimized to 60% by opting for narrow, medium, or wide box design. Ali et al. [34] suggested that aspect ratio (AR) is a dimensionless number and can be used to study the geometrical effect in RPs.

$$\text{Aspect Ratio(AR)} = \frac{\text{Channel Width}}{\text{Channel Depth}} = \frac{W}{d} \tag{5}$$

The study considered three ARs (5, 10, and 15) with varying paddlewheel rotating speed, water depth, and several algal cells at the inlet to study the effect of ARs in the mixing process. It was suggested that small AR is most acceptable in RPs for algae growth and also helps in better distribution of nutrients and light. Huang et al. [19] modifies four geometries of RPs, i.e., RWP-I (conventional raceway), RWP-II (RP including two semicircular flow deflectors at bend), RWP-III (four sloping baffles at pond bottom), and RWP-IV (RP fitted with both sloping baffle and semicircular flow deflector). The sloping baffle length was 45 cm, width 10 cm, and slope 30°. The

Fig. 2 Representation of shear stress for different pond velocities and sizes [7]
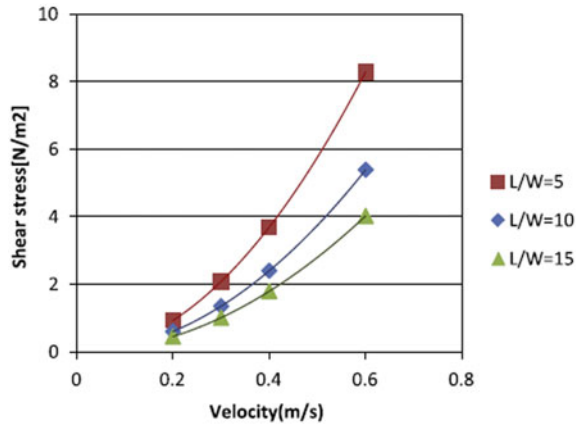
result concluded that energy consumption can be reduced and pond efficiency can be increased by using RWP-IV. Sawant et al. [24] experimented on RWP of volume 4.5 m³ in which division of tank was done by a central baffle of dimension 1.9 m x 1 m × 0.2 m. The mixing was introduced by an HF impeller including three blades of a diameter of 0.45 m. In the study, he optimized the design of RP for the length/width ratio of the column and flow characteristics of three different (length/width ratio) L/W (i.e., 5, 10, and 15). The result showed that the L/W ratio should be 10 or more than 10 to maintain a uniform velocity of flow in RP. Lima et al. [25] design the RP and evaluate the hydrodynamic characteristic based on velocity uniformity and energy consumption. The result suggested that vertical circulation was observed near the bends and has no effect on the inclined walls. Figure 2 shows how pond velocity and different sizes affect shear stress. The shear stress is directly proportional to V^2; hence, from the figure, it can be deduced that if the ratio L/W is low, then shear stress is high [7].

4 Mixing Performance

4.1 Paddlewheel

Mixing in a raceway pond is generally introduced by a paddlewheel. By optimizing the paddlewheel, the efficiency of the raceway pond can be increased. Therefore, many studies have been proposed to understand the mixing efficiency of RPs. Peterson et al. [35] conducted a study on paddlewheel and propeller aspirators to understand the mixing efficiency in RP and found that paddlewheels provide reasonably good circulation around the pond edge as compared to propeller aspirators. Sompech et al. [10] studied a mixing system in RP in which a paddlewheel was located at the mid-section of RP. Huang et al. [19] proposed the use of eight bladed
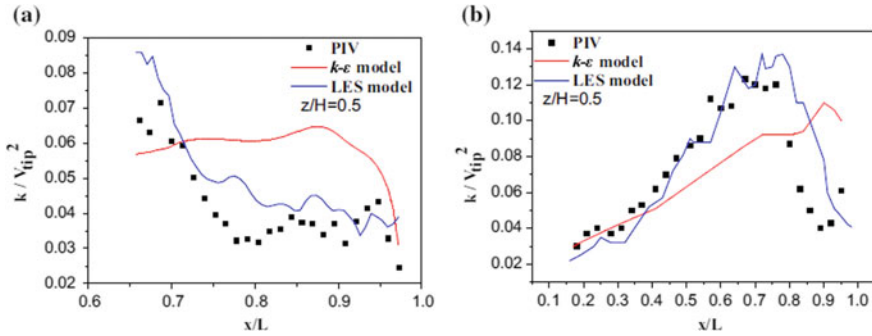
Fig. 3 Comparison of PIV, LES, and k-ε model of simulation, **a** k/v^2_{tip} result in plane-1 **b**. k/v^2_{tip} result in plane-2 [23]

paddlewheel installed at one side of channel. The result while comparing the geometry of the raceway pond with different paddlewheel speeds concludes that the average flow velocity in RP installed with two semicircular flow deflectors was increased by 29% when the speed of the paddlewheel was increased to 20 rpm. Zeng et al. [23] conducted a study of paddlewheel having six blades installed at a height of 0.35 m in RP. For simulation of turbulent kinetic energy, k-ε and LES model was used. The result concludes that RP fitted with paddlewheel of blade inclination 15° has a high-velocity region and attains better mixing with less power consumption as compared to conventional RP fitted with paddlewheel. The result also showed that 15° inclination of paddlewheel in RP design has less area of the dead zone. Figure 3 showed the comparison of the k-ε and LES model of simulation for turbulence kinetic energy (TKE) distribution. It was observed that k/v^2_{tip} decreases with the increase in paddlewheel distance in Fig. 3a. In Fig. 3b, the peak at x/L reaches 0.8, therefore, it is evident that the LES model predicts a better result than a k-ε model where k/v^2_{tip} is dimensionless TKE by the square of tip velocity. Chen et al. [36] proposed a study to understand the impact of the rotational speed of paddlewheel and flow deflector baffles in RWP. The result showed that by increasing the rotation speed of the paddlewheel ranging from 5 to 12 rpm the light/dark cycle decreased in RP. Also, installing flow deflector baffles to increase the L/D ratio for microalgae. Kusmayadi et al. [33] suggested in their study that many authors have simulated AR and different velocities as well as shear stress. It was concluded that AR greater than 10 provides a better result for attaining uniform velocity and shear stress.

4.2 Vortex Generators

Godfrey [37] proposed that mixing performance in raceway ponds can be improved using delta wing vortex generators. Voleti [26] develops a raceway model to operate a paddlewheel with a delta wing. The six-bladed paddlewheel is used for mixing in

RP. The delta wing of an equilateral triangle-shaped, with an angle of attack (α) 30°, was submerged in RP which was held at 3.17 m above the RP bed. The delta wing was placed in the opposite direction of the paddlewheel. The delta wing was placed closed to bend to understand the effect of bend on vertical mixing. The relationship used to compare the mixing with and without the delta wing is represented by Eq. (4); where U_A is the average vertical velocity, U_p is the vertical velocity at each point of the grid, and X is the number of grid points, V_A is average stream velocity at section.

$$U_A = \frac{\left(\sum_{i=1}^{p} |U_p|\right)}{X} \tag{6}$$

$$\text{VMI} = 100\% \, \frac{U_A}{V_A} \tag{7}$$

It was, suggested that because of strong vortices, the dissipation rate is more near delta wings. Pandey et al. [32] proposed the concept of vertical mixing index to analyze the position of paddlewheel in RPs. CFD was used as an analytical tool, and ANSYS (Fluent) is used for modeling, meshing, simulation, and post-processing. It was, suggested that for proper mixing the VMI should be in the range of 20%–50% which shows that at the bottom surface of RP there is an availability of a positive flow gradient. Shetty et al. [22] conducted a study on delta wing effectiveness for better vertical mixing in RP. Later various geometry of delta wing which includes an angle of attack (α) and the number of wings was optimized using the k-ω model. Also, study on the efficacy of deflectors for resolving the issue of dead zones near the bend was done. The result showed that dead zones are reduced at the bend and there is a uniform velocity of flow along the pond and also clear that dead zone formation takes place in the zone near the bend where velocity is almost zero. It was, suggested that $\alpha = 30°$ is proved to be more efficient and two delta wings placed on each side of baffles gives better result in improving the mixing for RP. Deflectors are very effective in solving the issue of dead zones at bends.

5   Sediment Condition

Few studies have been conducted to understand the behavior of water flow and sediment transport in RP. Huggins et al. [38] use CFD for the simulation of water flow and sediment transport in RP. An experiment was conducted to evaluate the distribution of solids in which particle density was assumed as 1150 kg/m³. The particle size was in the range of 692, 532, 350, 204, 61, and 35 µm. The result showed that for the largest particle the percentage of solid removed was 100% and 54.9%, 0.9%, and 0.1% for the remaining smallest size particle, respectively. Huggins et al. [39] performed similar studies on modification of RP, where modification was done by adding a new baffle design and adding/removing two wires at the sides of

the quiescent zone. It was found that the particle settling rate increased from 81.8 to 91.1% for unmodified and modified RP.

6   Result and Discussion

The various data collected from different studies has been showing that the geometry of RPs is an important aspect of the efficient working of raceway ponds. From various studies, it has been suggested that the dead zone formation can be prevented by using three flow deflector baffles at every end in the conventional model of RP. The baffle has the potential to reduce energy consumption also. The study also suggested that the island configuration of RP can prevent dead zone but the average velocity in the channel should be at least 0.18 m/s. Various studies in CFD showed that vertical mixing in the RP model can be increased by using a series of delta wings. To reduce power consumption by paddlewheel, the velocity of the water can be lowered by using delta wings. The delta wing with an angle of attack of 30° proves to be efficient in generating high vertical mixing with less power consumption. Experimental studies showed that because of strong vortices generated by delta wings dissipation rates are higher near to delta wing. The length of the raceway pond as deduced from Table 1 varies from 0.7 m to 626.62 m. Similarly, width and depth vary from 0.2–8 m to 0.05–3.95 m, respectively. The velocity of 0.3 m/s is widely used in the simulation of RP. This dimension can be used for the simulation of a raceway pond. But it was suggested from an experimental study that RP more than 50 m in length is not a feasible option assuming that a larger number of smaller tanks, compared with fewer tanks of larger dimensions, permits more flexible operational, and maintenance conditions such as variation among raceways of cultivated culture, growing stage, flow condition, periodic drainage for cleaning and scheduled harvesting of algae. From Table 2, it is very evident that most of the study was done using the k-ε turbulence model, although it provides a better result in most of the cases. Some studies showed that LES is more accurate than the k-ε model as shown in Fig. 3. The experimental and simulation result showed that the combination of the sloping baffle and flow deflector in RP has huge potential to increase the productivity of RP with less power consumption. To increase the flashing light, effect the RP was modified with flow deflector and wing baffle and the result proves that by optimizing the flow deflector there is a decrease in the dead zone by 60.42% in RP. It was suggested that RP with large AR values is not suitable for algae cultivation because of low water temperature. From various simulations performed by various authors, it was suggested that a blade angle of 15° provides better mixing using a paddlewheel in RP. The simulation result showed that most of the energy dissipation occurs at end of the central baffle. The modification in the shape of central baffles can minimize pressure drop in RP.

7 Conclusion

From the present study, it has been deduced that a raceway pond is the most economical and viable solution for the production of microalgae. From many experimental observations, it has been observed that shear stress is higher at bottom of RP. Modification of various geometries of RP was tested and simulated using CFD to understand the particle settling rate (PSR) potential in RP. Although numerical simulation of flow in RP provides great potential to set various operational parameters before construction and helps to avoid all trial and error methods. Apart from all geometry simulations, the model of RP with 180° bends proves to be efficient in terms of reducing the average dark cycle and maintaining the helical flow pattern in RP. The delta wings are having potential to make circulation in algae cells to the pond bottom and therefore, provide maximum exposure to sunlight. The efficiency of RP can be increased by optimizing its geometry, algal cell distribution, paddlewheel geometry, and AR. In RP, the heat transfer is dependent on various factors like AR, depth of water, rotating speed of paddlewheel, wind speed, humidity, and soil characteristics. From mathematical modeling, it was deduced that the k-ε and k-ω model was widely used for modeling in many studies and the k-ω model had a very promising result as compared to the k-ε model. From the various study, it was concluded that the effective way of increasing the performance of a raceway pond is providing the paddlewheel near to bend and placing the baffles at bends which significantly reduce the dead zone and minimize power consumption also.

8 Future Prospect

Future studies need to be focused on turbulence models like the Reynold stress model (RSM), and SST model as only one type of model has been studied in most of the cases, i.e., the k-ε model. Further, modification in the model of RP based on particle settling velocity distribution has some potential to understand the basis of erosion and sedimentation in the tank. Many experimental factors like depth, flow speed, and harvesting period in increasing the efficiency of RP still need to be studied. Further, studies on increasing the use of RP by combining it with wastewater treatment plants can be a possibility among advancements. There is more potential for optimizing the various parameter of the delta wing for vortex formation like the width of the channel, shape of the delta wing, and angle of attack. The further potential of future work is there in optimizing the bend geometry, sparger design, and location to increase the efficiency of RP. Although CFD is an efficient tool for simulating the hydrodynamics of PR, still some studies have the potential in understanding the functioning of an efficient raceway pond which includes light penetration, mass transfer, and biological kinetics.

References

1. Keffer JE, Kleinheinz GT (2002) Use of Chlorella vulgaris for CO(2) mitigation in a photobioreactor. J Ind Microbiol Biotechnology 5:275–280
2. Li Q, Du W, Liu D (2008) Perspectives of microbial oils for biodiesel production. Appl Microbiol Biotechnology 80:749–756
3. Borowitzka MA (1999) Pharmaceuticals and agrochemicals from microalgae.CRC Press
4. Oswald WJ (1988) Micro-algae and waste-water treatment. In: Borowitzka MA, Borowitzka LJ (eds) Micro-algal Biotechnology. Cambridge University Press
5. Vonshak A, Abeliovich A, Boussiba S, Arad S, Richmond A (1982) Production of Spirulina biomass: effects of environmental factors and population density. Biomass 2:175–185
6. Weissman JC, Goebel RP, Benemann JR (1988) Photobioreactor design: mixing, carbon utilization and oxygen accumulation. Biotechnol Bioeng 31:336–344
7. Hadiyanto H, Elmore S, Gerven TV, Stankiewicz A (2013) Hydrodynamic evaluations in high rate algae pond (HRAP) design. Chem Eng J 217:231–239
8. Liffman K, Paterson DA, Liovic P, Bandopadhayay P (2013) Comparing the energy efficiency of different high-rate algal raceway pond designs using computational fluid dynamics. Chem Eng Res Des 91(2):221–226
9. Xu B, Li P, Waller P (2014) Study of the flow mixing in a novel ARID raceway for algae production. Renew Energy 62:249–257
10. Sompech K, Chisti Y, Srinophakun T (2012) Design of raceway ponds for producing microalgae. Biofuels 3(4):387–397
11. Prussi M, Buffi M, Casini D, Chiaramonti D, Martelli F, Carnevale M, Tredici MR, Rodolfi L (2014) Experimental and numerical investigations of mixing in raceway ponds for algae cultivation. Biomass Bioenerg 67:390–400
12. Musgrove E, Heaven S (2015) Investigating the hydrodynamic performance of carbonation sumps in High Rate Algal Pond (HRAP) raceways using computational fluid dynamics (CFD). University of Southampton, UK, PhD Thesis
13. Das BS, Khatua KK (2018) Numerical method to compute water surface profile for converging compound channel. Arab J Sci Eng 43(10):5349–5364
14. Das BS, Devi K, Proust S, Khatua KK (2018) Flow distribution in diverging compound channels using improved independent subsection method. In: River flow 2018: 9th International conference on fluvial hydraulics, vol 40, Issue no 05068, pp 8
15. Das L, Khatua KK, Das BS (2022) Experimental and numerical analyses of boundary shear stress in non-prismatic compound channel. River Hydraul Hydraul Water Res Coastal Eng 2:37–58
16. Hafez KA, Elsamni QA, Zakaria KY (2011) Numerical investigation of the fully developed turbulent flow over a moving wavy wall using k–e turbulence model. Alex Eng J 50(2):145–162
17. Rodi W (1993) Turbulence models and their application in hydraulics—a state of the art reviews. International Association for Hydraulic Research, 21–29
18. Amini H, Hashemisohi A, Wang L, Shahbazi A, Bikdash M, Dukka KC, Yuan W (2016) Numerical and experimental investigation of hydrodynamics and light transfer in open raceway ponds at various algal cell concentrations and medium depths. Chem Eng Sci 156:11–23
19. Huang J, Qu X, Wan M, Ying J, Li Y, Zhu F, Wang J, Shen G, Chen J, Li W (2015) Investigation on the performance of raceway ponds with internal structures by the means of CFD simulations and experiments. J Algal Res 10:64–71
20. Huang J, Yang Q, Chen J, Wan M, Ying J, Fan F, Wang J, Li W, Li Y (2016) Design and optimization of a novel airlift-driven sloping raceway pond with numerical and practical experiments. Algal Res 20:164–171
21. Yang Z, Cheng J, Ye Q, Liu J, Zhou J, Cen K (2016) Decrease in light/dark cycle of microalgal cells with computational fluid dynamics simulation to improve microalgal growth in a raceway pond. Biores Technol 220:352–359
22. Shetty YK, Modak JM (2016) Effect Of Delta Wings and Deflectors to Improve the Production in Algal. Int J Res in Eng Tech 05:2321–7308

23. Zeng FX, Huang JK, Meng C, Zhu FC, Chen JP, Li YG (2016) Investigation on novel raceway pond with inclined paddle wheels through simulation and microalgae culture experiments. Bioprocess Biosyst Eng 39(1):169–180
24. Sawant SS, Khadamkar HP, Mathpati CS, Pandit R, Lali AM (2017) Computational and experimental studies of high depth algal raceway pond photobioreactor. Renew Energy 118:152–159
25. Lima A, Marinho B, Morais T (2020) Hydrodynamic analysis of flow in raceway ponds for algae cultivation under versatile conditions. Aquacult Int 29(5):1–17
26. Voleti RS (2012) Experimental studies of vertical mixing in an open channel raceway for algae biofuel production. Utah State University, Department of Mechanical and Aerospace Engineering
27. Hreiz R, Sialve B, Morchain J, Escudié R, Guiraud P (2014) Experimental and numerical investigation of hydrodynamics in raceway reactors used for algaculture. Chem Eng J 250:230–239
28. Pirasaci T, Manisali AY, Dogaris I, Philippidis G, Sunol AK (2017) Hydrodynamic design of an enclosed Horizontal BioReactor (HBR) for algae cultivation. Algal Res 28:57–65
29. Li Y, Horsman M, Wu N, Lan CQ, Dubois CN (2008) Biofuels from microalgae. Biotech Prog 24(4):815–820
30. Cheng J, Yang Z, Ye Q, Zhou J, Cen K (2015) Enhanced flashing light effect with up-down chute baffles to improve microalgal growth in a raceway pond. Bioresour Technol 190:29–35
31. Ranganathan P, Amal JC, Savithri S, Haridas A (2017) Experimental and modeling of Arthrospira platensis cultivation in open raceway ponds. Bioresour Technol 242:197–205
32. Pandey P, Premalatha M (2017) Design and analysis of flow velocity distribution inside a raceway pond using computational fluid dynamics. Bioprocess Biosyst Eng 40:439–450
33. Kusmayadi A, Suyono KA, Nagarajan D, Chang JS, Yen HW (2020) Application of computational fluid dynamics (CFD) on the raceway design for the cultivation of microalgae: a review. J Ind Microbiol Biotechnol 47(4–5):373–382
34. Ali H, Cheema TA, Yoon HS, Do Y, Park C (2015) Numerical prediction of algae cell mixing feature in raceway ponds using particle tracing methods. J Biotechnol Bioeng 112(2):297–307
35. Peterson EL, Jonathan A, Lal H, Wadhwa C (2000) CFD modeling pond dynamic processes. Aquacult Eng 23:61–93
36. Chen Z, Zhang X, Jiang Z, Chen X, He H, Zhang X (2016) Light/dark cycle of microalgae cells in raceway ponds: effects of paddlewheel rotational speeds and baffles installation. Biores Technol 219:387–391
37. Godfrey AH (2012) An investigation into delta wing Vortex generators as a means of increasing algae biofuel raceway vertical mixing including an analysis of the resulting turbulence characteristics. All Graduate Theses and Dissertations. https://digitalcommons.usu.edu/etd/1338
38. Huggins DL, Piedrahita RH, Rumsey T (2004) Analysis of sediment transport modeling using computational fluid dynamics (CFD) for aquaculture raceways. Aquacult Eng 31:277–293
39. Huggins DL, Piedrahita RH, Rumsey T (2005) Use of computational fluid dynamics (CFD) for aquaculture raceway design to increase settling effectiveness. Aquacult Eng 33:167–180

Numerical Simulation to Study the Influence of Number of Vanes of Diffuser on Performance of Multistage Pump

Deepak Prajapat, Ruchi Khare, and Shyam N. Shukla

Abstract Pumps acquire a large amount of the world's electricity consumption, and multistage pumps are often used for high head requirements and have a large application in the domestic and industrial water supply. Therefore, performance enhancement of multistage pumps is very beneficial not only for the economy but also for energy saving. The multistage pump consists of an inlet pipe, impellers, diffusers, return channel, casing, and outlet pipe. The performance of multistage pumps depends upon so many factors, and the number of vanes in a diffuser is one of them. Since little literature is available about the multistage pumps with no clear guidelines available for the selection of the number of vanes in the diffuser. Therefore, evaluation of the performance of multistage pump by evaluating the number of vanes in the diffuser seems quite beneficial. In this paper, an attempt is made to evaluate the number of vanes of diffuser in multistage pump using Computational Fluid Dynamics (CFD). The best combination of impeller and diffuser vanes is ascertained.

Keywords Multistage pumps · CFD · Diffuser · Number of vanes · Ansys CFX

1 Introduction

In this era of the industrial revolution and fast-forward moving world, fluid supply with a high head is a really important task for various applications. Multistage pumps are becoming very common for such high head fluid supplies. The multistage pump is a kind of turbo-machinery that falls under the category of centrifugal pumps. The multistage pump consists of few impellers mounted on the same shaft coupled in a series connection for achieving a higher head. It is mostly used for firefighting, boiler

D. Prajapat (✉) · R. Khare
Maulana Azad National Institute of Technology, Bhopal 462003, India
e-mail: deepak.prajapat.sdbg@gmail.com

S. N. Shukla
MIT Academy of Engineering, Pune 412105, India
e-mail: shyam.shukla@mitaoe.ac.in

water feeding, and dewatering of mines. Among all essential components, diffuser is an important component [1].

The performance characteristics of a multistage pump including the head, brake horsepower, and efficiency highly depend on the diffuser design. For the better performance of multistage pump design parameters of diffuser such as the number of vanes, inlet vane angle and outlet vane angles should be well optimized.

Earlier we had only experimental test methods for performance evaluation after the 1980s computer revolution taking place and increasing computational power made Computational Fluid dynamics (CFD) an effective and reliable tool for such types of fluid machinery and complex flow phenomenon study [5]. Currently, there are many commercial CFD codes available such as Ansys CFX, Ansys Fluent, OpenFOAM, Powerflow & Comsol.

Roche et al. [3] investigated numerically multistage pump with 7, 8, and 12 vanes diffuser in the first stage only and concluded little variation in brake horsepower. A similar numerical study with two stages was carried out by Pawar and Khare [2]. Tan et al. [6] studied the effect of vane angle, vane thickness, and the number of vanes of radial diffuser for a single-stage centrifugal pump. And many more researchers also evaluated numerically and experimentally such as wang et al. [7] and Roclawski et al. [4].

The main objective of this work is to understand various flow parameters inside the multistage pump and observe the effect of the number of vanes on the pump performance. In this work, CFD simulation is carried out with radial diffuser having 8, 9, and 10 number of vanes. We have simulated two stages of a radial centrifugal multistage pump. Creo Parametric is used for geometry preparation, for meshing ICEM CFD and Ansys CFX solver is used for RANS equation solution. The analysis is conducted at a constant speed and for four different discharges.

2 Modeling and Simulation

The following steps (Fig. 1) are involved in this CFD simulation of the multistage pump:

The simulation of multistage pump geometry (Fig. 2) of different components was prepared using Creo Parametric software and exported in ".iges" format to ICEM CFD for meshing. Dimensions and other parameters are given in Table 1.

Three diffusers with different vane numbers 8, 9, and 10 are prepared separately, and meshing is completed. A mesh independence test is also performed, and a proper meshing set is selected based on the lowest percentage variation in head and efficiency as compared to the previous coarse meshing set. Five different global element scale factors 1, 0.95, 0.9, 0.85, and 0.83 are investigated, and 0.85 is selected for further analysis as the variation between 0.85 and 0.83 is found negligible. Unstructured mesh is used with a prism layer around the impeller vanes.
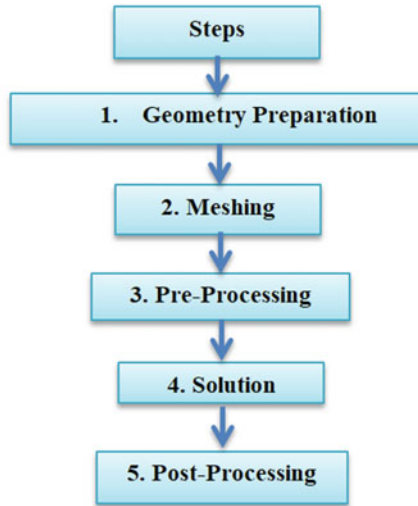
Fig. 1 Steps involved in simulation
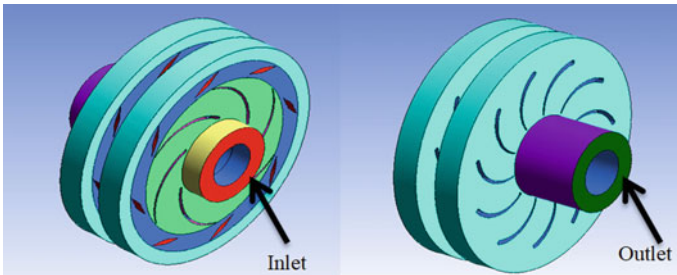
Fig. 2 Pump geometry

After finalizing mesh size meshing of each component of the two-stage multistage pump is prepared and exported in ".cfx5" file format to CFX-Pre. Mesh information is given in Table 2.

After meshing, pre-processing is done in CFX-Pre where a frozen rotor interface is used to differentiate between rotating and stationary domains with automatic pitch change. Impeller rotational speed is kept as 1900 rpm. Four different discharges 400, 464, 525, and 630 m^3/h and water at 25°C as a working fluid are used.

A suitable physical time scale and convergence of the solution are ensured. In Ansys CFX, solver solution is obtained, and then various outputs are obtained from CFD-Post which is described in the "Results and Discussion" section.

Table 1 Geometric details

Component	Parameter	Value	Unit
Impeller	Inlet radius	97.5	mm
	Outlet radius	206	mm
	Inlet vane angle	40	degree
	Outlet vane angle	20	degree
	Width	23	mm
	Number of vanes	6	Nos
	Speed of rotation	1900	rpm
Diffuser	Inlet radius	206	mm
	Outlet radius	251	mm
	Inlet vane angle	5	degree
	Outlet vane angle	25	degree
	Width	23	mm
	Number of vanes	8, 9, and 10	Nos
Return channel	Inlet radius	251	mm
	Outlet radius	287.25	mm
	Width	35	mm
	Number of guide vanes	11	Nos

Table 2 Mesh details

Number of vanes in diffuser	Number of nodes	Number of elements	Number of tetrahedron
8	746,646	3,709,375	3,614,695
9	748,532	3,717,513	3,622,813
10	750,274	3,724,659	3,639,979

3 Results and Discussion

As mentioned previously, the main objective of this work is to understand various flow parameters inside the multistage pump and observe the effect of the number of vanes on the pump performance. In this analysis, all three diffuser vanes are simulated with four different discharges, and various graphs in terms of pressure contours, streamlines, and performance characteristics are plotted.

3.1 Pressure Contours

Static pressure contours for all three diffuser vanes at the best efficiency point (BEP) (i.e., 525m3/h) are shown below. These pressure contours depict that number of vanes affects the pressure distribution in the diffuser channel (Fig. 3).

3.2 Streamline Patterns

Streamline patterns for different cases at BEP are shown below. These streamlines show smooth flow through pump channels, as little variation can be seen in streamline patterns as the number of vanes changes (Fig. 4).

3.3 H–Q Characteristic

In the head–discharge characteristic, no significant effect of the number of vanes on the head can be seen in Fig. 6. At all discharges, the head has almost similar for all three vanes. There is a slight variation of the head at off-design points while at best efficiency point it is the same.

3.4 η–Q Characteristic

Efficiency is affected by the number of vanes as shown in Fig. 5. 9 vanes diffuser has significant lead at 400 and 464m3/h (off-design points). The other two vanes have almost identical efficiency plots. It means that at off-design points there is an effect of the number of vanes while at the best efficiency point and higher discharge, there is little variation (Fig. 6).

4 Conclusion

The following conclusions could be drawn from the current study:

- This study replicated that number of vanes of the diffuser has a slight influence on the performance of the multistage pump.
- 9 vanes diffuser has slightly higher efficiency compared to the other two vanes. The reason behind this could be an odd–even selection of the number of vanes in the diffuser (9 vanes) and impeller (6 vanes). Therefore, 6 impeller vanes with 9 diffuser vanes are found as the best combination.

Fig. 3 Static pressure contours **a** 8 vanes diffuser, **b** 9 vanes diffuser, and **c** 10 vanes diffuser
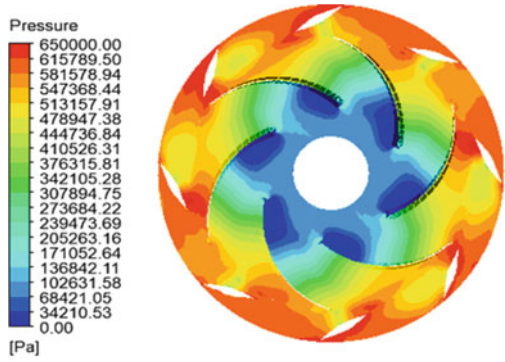
Pressure Difference ΔP=1114904 Pa
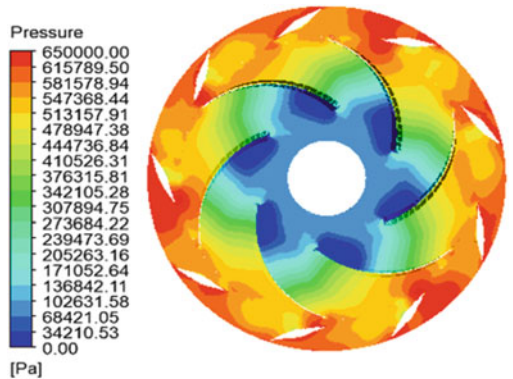
Pressure Difference ΔP=1103286 Pa
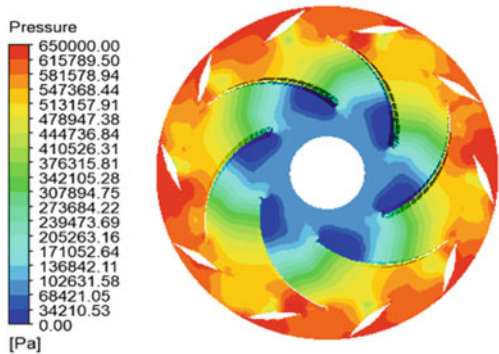
Pressure Difference ΔP=1201149 Pa

Fig. 4 Streamline patterns **a** 8 vanes diffuser, **b** 9 vanes diffuser, and **c** 10 vanes diffuser
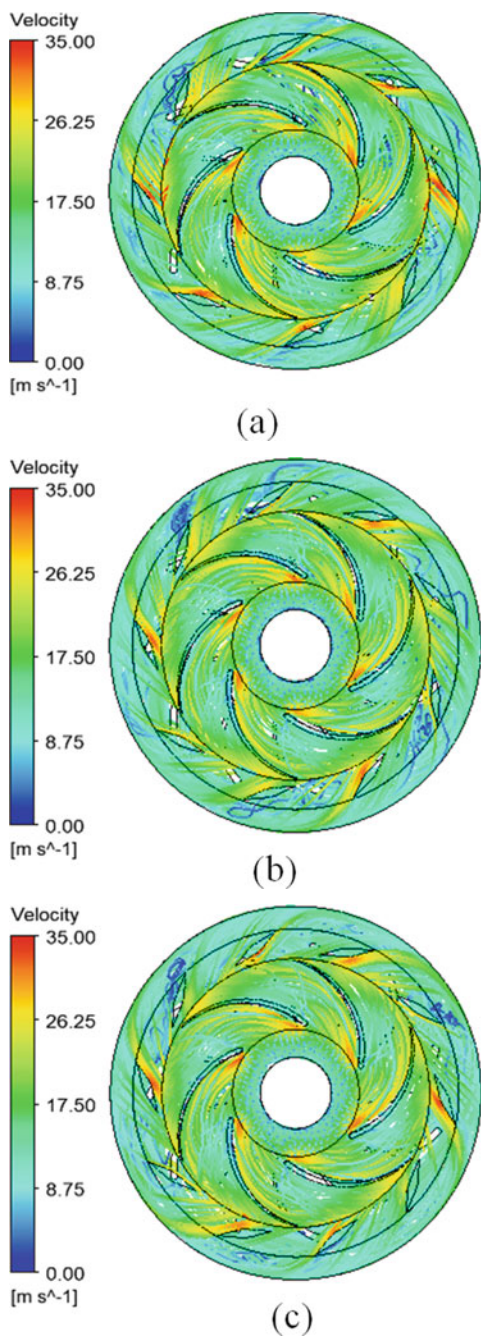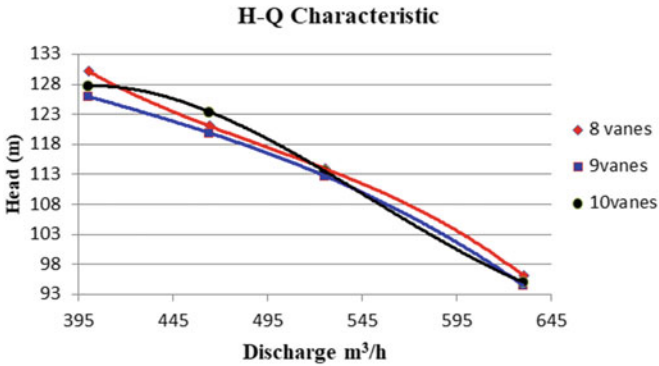
Fig. 5 H–Q characteristic
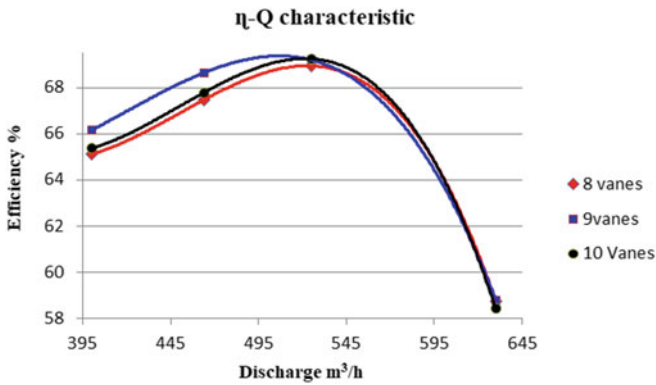
Fig. 6 η-Q characteristic

- The number of vanes in the diffuser also has a little impact on pressure distribution and streamline pattern in the flow passage of the multistage pump.
- The relative position of impeller vanes and diffuser vanes also affects the performance parameters of the pump.

References

1. Gülich JF (2008) Centrifugal pumps, vol 2. Springer, Berlin
2. Pawar A, Khare R (2020) Design of multistage centrifugal pump and performance analysis using CFD. In: Proceedings of the 8th International and 47th National Conference on Fluid Mechanics and Fluid Power (FMFP)
3. Roche-Carrier L, DitubaNgoma G, Ghie W (2013) Numerical Investigation of a first stage of a multistage centrifugal pump: impeller, diffuser with return vanes, and casing. International Scholarly Research Notices

4. Roclawski H, Hellmann DH (2006) Numerical simulation of a radial multistage centrifugal pump. In: 44th AIAA Aerospace Sciences Meeting and Exhibit
5. Shah SR, Jain SV, Patel RN, Lakhera VJ (2013) CFD for centrifugal pumps: a review of the state-of-the-art. Procedia Eng 51:715–720
6. Tan MG, He XH, Liu HL, Dong L, Wu XF (2016) Design and analysis of a radial diffuser in a single-stage centrifugal pump. Eng Appl Comp Fluid Mech 10(1):500–511
7. Wang C, Shi W, Wang X, Jiang X, Yang Y, Li W, Zhou L (2017) Optimal design of multistage centrifugal pump based on the combined energy loss model and computational fluid dynamics. Appl Energy 187:10–26

Numerical Modelling of Transport and Fate of Chromium (VI) in Sub-surface Porous Media

Shreya Ganguly and Sayantan Ganguly

Abstract Chromium (VI) is used in major industries like stainless steel production, electroplating, leather tanning and textile dye synthesis. If Cr (VI) is disposed without any proper treatment, it might leach into the soil and pollute the groundwater. Chromium (VI) is a known carcinogen and is thus extremely harmful if consumed. The present study numerically models the transport and fate of chromium (VI) leached from a stainless steel plant located in the Rupnagar District, Punjab, for a period of 20 years using COMSOL Multiphysics simulation software. A contaminant transport model is developed including the processes of advection, dispersion and sorption. A uniform recharge through precipitation is considered from the topmost layer of the soil profile in the study. The numerical model is validated using standard analytical solutions of the advection–dispersion equation.

Keywords Chromium (VI) · Contaminant transport · Numerical modelling · Advection–dispersion–sorption equation · COMSOL multiphysics

1 Introduction

Chromium is released into the environment through various industrial sources like steel and alloy production, electroplating, leather tanning and dye synthesis [1].

Disclaimer: The presentation of material and details in maps used in this chapter does not imply the expression of any opinion whatsoever on the part of the Publisher or Author concerning the legal status of any country, area or territory or of its authorities, or concerning the delimitation of its borders. The depiction and use of boundaries, geographic names and related data shown on maps and included in lists, tables, documents, and databases in this chapter are not warranted to be error free nor do they necessarily imply official endorsement or acceptance by the Publisher or Author.

S. Ganguly · S. Ganguly (✉)
Department of Civil Engineering, Indian Institute of Technology Ropar, Rupnagar, Punjab 140001, India
e-mail: sayantan.ganguly@iitrpr.ac.in

S. Ganguly
e-mail: shreya.19cez0011@iitrpr.ac.in

189

Chromium exists as Cr (III) and Cr (VI) in nature and has different physical and chemical characteristics including toxicity, reactivity and mobility [2]. The trivalent chromium is an important element for living beings while the hexavalent chromium is carcinogenic, toxic (more than 500 times of Cr(III) in aqueous solution), non-biodegradable and is responsible for liver and kidney damage when consumed [3]. According to WHO, the permissible limit of Cr (VI) in drinking water is 0.05 parts per million (ppm) [4]. The toxic properties of Cr (VI) may arise due to its strong oxidative potential and free diffusion across cell membranes. Cr (VI) may present in the forms of chromate (CrO_4^{2-}), hydrogen chromate ($HCrO_4^{-}$) and dichromate ($Cr_2O_7^{2-}$) depending on the concentration and pH of the solution [3]. Due to several health adversities and high solubility, Cr (VI) poses a serious environmental threat and needs to be reduced to its stable form Cr (III) for its remediation. Therefore, it is essential to study the transport and fate of Cr (VI) through soil and water to assess the water quality changes and the extent of contamination that it might cause over time. The transport phenomena include the processes of advection, dispersion and sorption. These processes are governed by the soil and aquifer characteristics like pH, moisture content, hydraulic conductivity, recharge by precipitation, the presence of minerals in soil media and microbial activities [2]. The presence of ferrous ion, sulphide and organic complexes in soil can reduce Cr (VI) naturally [4]. Even microorganisms reduce Cr (VI) to Cr (III) via enzymatic processes during degradation of organic matters. Therefore, both abiotic and biotic processes affect the fate and transport of Cr (VI) in the environment [5].

In this study, the transport of Cr (VI) was evaluated through various layers of soil at a field site in Rupnagar District, Punjab, using COMSOL multiphysics software. COMSOL uses finite element method to derive the numerical solution of the governing partial differential equations. The finite element method is primarily based on the discretization of the modelling domain into smaller and simpler sub-domains called elements. The solution is obtained by assembling and solving a set of equations over all the elements of the model. In this study, the governing equations include: (1) the continuity (conservation of mass) equation, (2) equation of velocity of fluid flow (momentum conservation) and (3) convection–diffusion equation [6]. The physics applied in the study are Darcy's law in porous media and transport of dilute species in porous media. Both scanning electron microscopy (SEM) and energy dispersive X-ray spectroscopy (EDS) analysis were performed on the topsoil of the study area to obtain the surface morphology and chemical composition of the ambient soil particles which are integral in estimating their adsorption efficiencies to remove Cr (VI) naturally.

2   Materials and Methods

2.1   Numerical Simulation Technique

The study demonstrates the application of COMSOL multiphysics software to esti-
mate steady-state sub-surface groundwater flow along with solute transport along a
vertical cross section of an unconfined aquifer (Fig. 1). For validation purpose, a thin
strip of an unconfined aquifer is considered and the results obtained are compared
analytically using the 1D advection–diffusion equation (Fig. 2). Discretization of the
domain is conducted by using very fine free triangular mesh.

In COMSOL, fluid motion is calculated using Darcy's law where pressure is the
dependent variable and the velocity field is determined by the structure of the porous
medium, pressure gradient and the fluid viscosity. The equations used in COMSOL
to determine the fluid flow are as follows:

$$\nabla.(\rho \underline{u}) = Q_m \qquad\qquad (1)$$
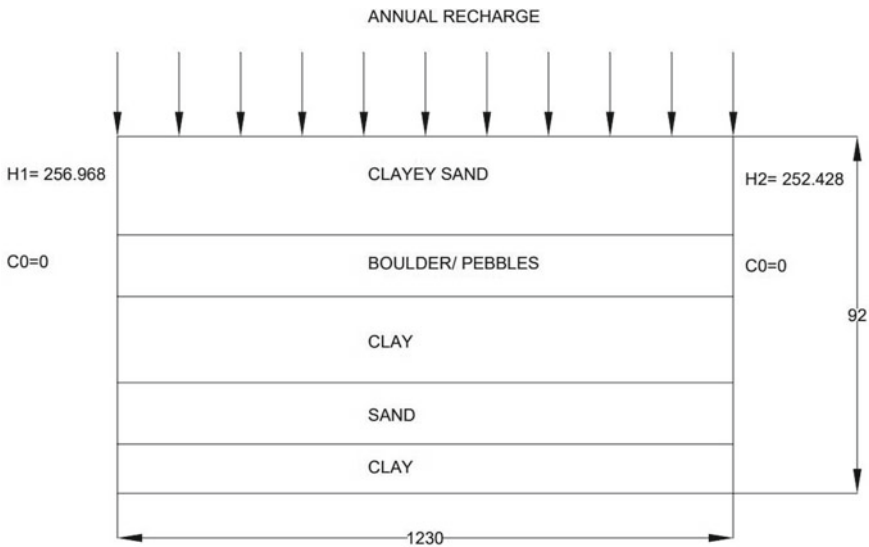
Fig. 1   Schematic diagram of the porous media domain with vertical recharge
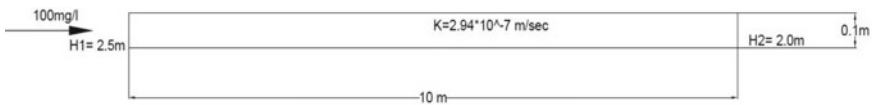
Fig. 2   Schematic diagram of the thin section of an unconfined aquifer with Cr (VI) transport
through the x-direction

$$\underline{u} = -\frac{\kappa}{\mu}\nabla P \tag{2}$$

$$-n.\rho\underline{u} = 0 \tag{3}$$

where $\underline{u}$ is the two-dimensional velocity vector, ρ is the density of fluid, Q_m is the rate of recharge to water table per unit volume of aquifer, κ is the permeability, μ is the dynamic viscosity of the fluid, P is the hydrodynamic pressure and n is the normal velocity vector, respectively. No flow condition is maintained at the boundary CD while a constant annual recharge is maintained at the boundary AB. The boundary conditions and initial conditions associated with Eqs. (1) and (2) are as follows:

$$\text{At,} \quad X = 0, \ H = H_1 \tag{4}$$

$$\text{At,} \quad X = L, \ H = H_2 \tag{5}$$

$$P = 0, \quad \text{at } X = L_x \tag{6}$$

$$v = 0 \ \text{at } Y = 0 \tag{7}$$

$$v = 0 \ \text{at } Y = L_y \tag{8}$$

In COMSOL, *the transport of diluted species in porous media* interface is used in this study to determine the transport of Cr (VI) plume for a period of 20 years. The transport mechanisms used are mass transport in porous media and convection. The flow in a saturated porous media is given by the equation:

$$\frac{\partial(\varepsilon_p c_i)}{\partial t} + \frac{\partial(\rho c_{p,i})}{\partial t} + \underline{u}.\nabla c_i = \nabla.[(D_{D,i} + D_{e,i})]\nabla_{c,i}] + R_i + S_i \tag{9}$$

where ε_p is the porosity of the media, c_i (mol/m^3) is the concentration of species i, ρ is the dry bulk density (kg/m^3), D_D is the dispersion of species i (m^2/s), D_e is the effective diffusion of species i (m^2/s), u is the velocity field and t is the time, respectively. In the right-hand side of the equation, R_i represents reaction rate expression for the species i (mol/(m^3·s)) and S_i is the source or the sink term. The boundary conditions associated with this study are:

$$c = 0 \ \text{at } x = 0 \tag{10}$$

$$\frac{\partial c}{\partial x} = 0 \ \text{at } x = L_x \tag{11}$$

$$\frac{\partial c}{\partial y} = 0 \text{ at } y = 0 \tag{12}$$

$$\frac{\partial c}{\partial y} = 0 \text{ at } y = L_y \tag{13}$$

For the analytical calculations, the following 1D advection–dispersion equation for solute transport in porous media is used:

$$D\frac{\partial^2 C}{\partial x^2} - V\frac{\partial C}{\partial x} = \frac{\partial C}{\partial t} \tag{14}$$

The solution of the governing equation is given by Ogata with the following initial and boundary conditions:

Initial condition:

$$C(x,0) = 0 \, x \geq 0 \tag{15}$$

Boundary conditions:

$$C(0,t) = C_0 \, t \geq 0 \tag{16}$$

$$C(\propto,0) = 0 \, t \geq 0 \tag{17}$$

$$C(x,t) = \frac{C_0}{2}\left[\mathrm{erfc}\left(\frac{x-vt}{2\sqrt{D_L t}}\right) + \exp\left(\frac{vx}{D_L}\right) \times \mathrm{erfc}\left(\frac{x+vt}{2\sqrt{D_L t}}\right)\right] \tag{18}$$

where C_0 is the initial concentration of Cr (VI), C is the concentration of Cr (VI) at any time, D_L is longitudinal coefficient of hydrodynamic dispersion, L is the co-ordinate direction of the flowline, x is the distance from the point of injection of the solute, v is the linear groundwater velocity and t denotes the time of travel of the solute over a certain area.

2.2 Study Area and Data Source

2.2.1 Study Area Domain

The study area originates from the IIT Ropar main campus (area $= 113{,}160$ m^2) with latitude 30°57′58.36″ N and longitude 076°28′19.68″ E, extending 1230 m towards a sewage treatment plant located at latitude 30°58′12.18″ N and longitude 076°27′32.82″ E. It is assumed that Cr (VI) is leaking from a stainless steel plant located at 300 m from the main campus. Cr (VI) being highly soluble is leaching through the ground and is contaminating the various soil layers and the groundwater
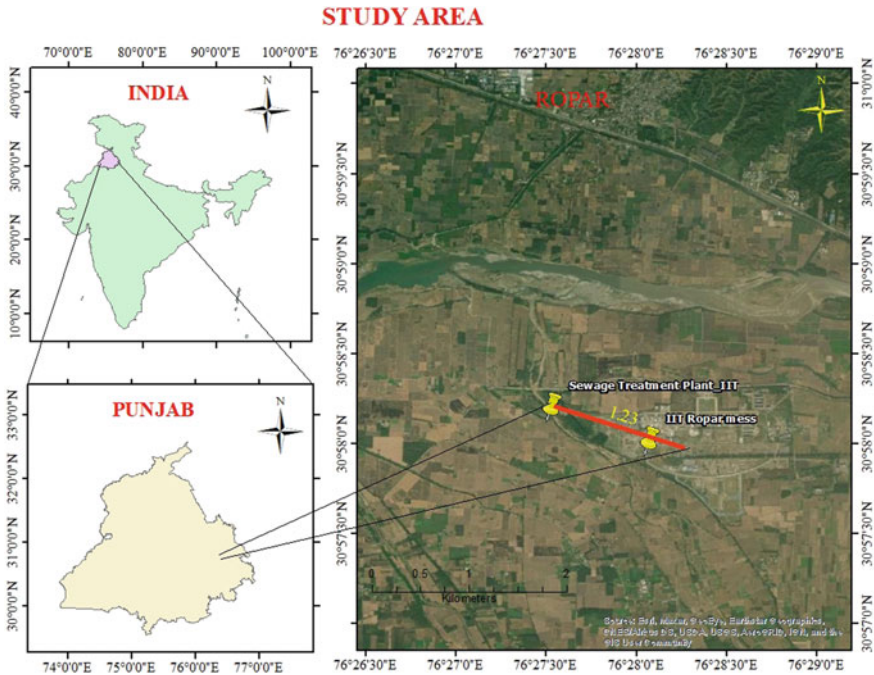
Fig. 3 Index map of study area

located at a very shallow depth from the surface. A constant recharge by precipitation of 10.56 m/year is considered in the topmost layer of the vertical section of the soil profile.

2.2.2 Data Collection

The soil profile was obtained from the piezometer drilling data at the IIT Ropar campus site. The hydraulic heads are calculated by measuring the piezometers located at both the boundaries while the elevation of the domain is measured by using a portable GPS metre (Fig. 3).

2.2.3 Selection of Input Parameters

The input parameters were selected based on the data obtained for the study. It is considered that 300 mg/l of Cr (VI) is leaching from a steel plant for a period of 20 years continuously. For the validation model, the concentration of Cr (VI) was considered to be 100 mg/l for a domain of area 1 m^2 having clayey soil with a hydraulic conductivity of 2.94×10^{-7} m/s. The transport of Cr (VI) was evaluated for

a period of 10 years, and the concentrations at 2 m and 4 m distances were determined, respectively. The remaining input parameters are given in Tables 1 and 2. No sorption effects have been considered in the model owing to negligible concentration of iron and manganese.

Table 1 Input parameters for the 2D domain

Parameters	Symbol	Value	Unit
Width of domain	W	1230	m
Height of domain	H	92	m
Density of fluid	ρ	1000	kg/m^3
Effective Porosity of clayey sand	μ_{CS}	0.24	–
Effective porosity of boulders	μ_B	0.41	–
Effective Porosity of sand	μ_S	0.30	–
Hydraulic conductivity of clayey sand	K_{CS}	5.05×10^{-5}	m/s
Hydraulic conductivity of boulders	K_B	2.94×10^{-3}	m/s
Hydraulic conductivity of sand	K_s	2.94×10^{-4}	m/s
Annual recharge	U_0	10.56	m/year
Hydraulic head at left boundary	H_1	256.968	m
Hydraulic head at right boundary	H_2	252.428	m
Diffusion coefficient of Cr (VI)	D_D	1.05×10^{-9}	m^2/s
Longitudinal dispersivity	α_L	1	m
Transverse dispersivity	α_T	0.1	m
Initial concentration	C_0	0	mol/m^3
Cr (VI) concentration entering the domain	C	5.76	mol/m^3

Table 2 Input parameters for the validation model

Parameters	Symbol	Value	Unit
Width of domain	W	10	m
Height of domain	H	0.1	m
Density of fluid	ρ	1000	kg/m^3
Effective porosity of domain	μ	0.32	–
Hydraulic conductivity of domain	K	$2.94 * 10^{-7}$	m/s
Hydraulic head at left boundary	H_1	2.5	m
Hydraulic head at right boundary	H_2	2	m
Diffusion coefficient of Cr (VI) in domain	D_D	10^{-9}	m^2/s
Longitudinal dispersivity	α_L	10	m
Transverse dispersivity	α_T	2	m
Initial concentration of Cr (VI)	C_0	0	mol/m^3
Cr (VI) concentration entering the domain	C	1.92	mol/m^3
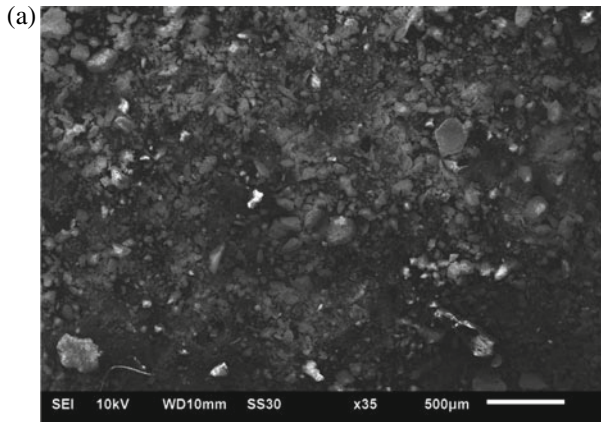
Fig. 4 **a** Surface morphology of topsoil observed in scanning electron microscopy. **b** Selection of sites on the sample for performing chemical composition analysis. **c** EDS spectrum of topsoil

3 Results and Discussion

3.1 SEM and EDS Study

The SEM and EDS analysis performed on the topsoil shows the surface morphology of the soil particles and their chemical composition, respectively. We observed that both clay and sand particles primarily constitute the soil. Figure 4a shows that the structures of the soil particles are irregular and flaky tending to agglomeration. The chemical composition (Table 3 and Fig. 4c) showed the existence of oxygen and sodium to be 50% and 13% approximately. Iron was available in trace amounts (less than 2%) indicating negligible adsorption sites for efficient Cr (VI) attenuation. As we observe in Table 3 and Fig. 4c, trace amounts of silicon and calcium are also present in the soil. The carbon concentration came from the tape used in the study. Therefore, it can be assumed that negligible/no adsorption is taking place in the topsoil or in the successive sand layers during the Cr (VI) transport. Hence, Cr (VI) may travel freely without any hindrance and further pollute the groundwater table located at shallow depth.

3.2 Numerical and Analytical Results from the Validation Model

Successively, the numerical simulation was performed for the validation model and its results were compared with the analytical results obtained from the advection–diffusion equation. The hydraulic heads and the concentration of Cr (VI) at 2 m, 4 m,

(b)

Date	Time	HV [kV]	Mag	WD [mm]
25/11/2021	12:01:44	10.0 keV	35x	10.0 mm

Fig. 4 (continued)

(c)
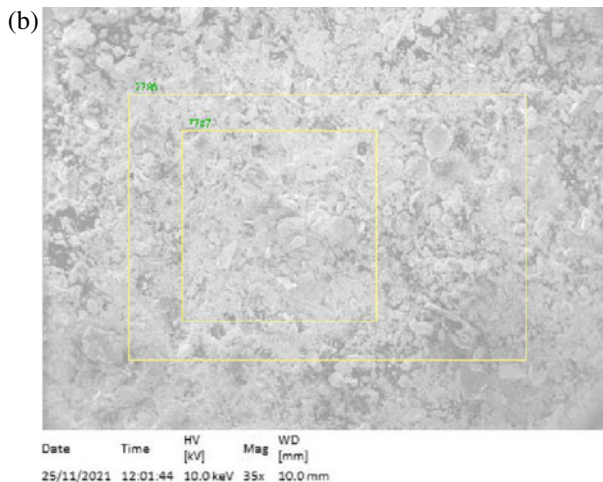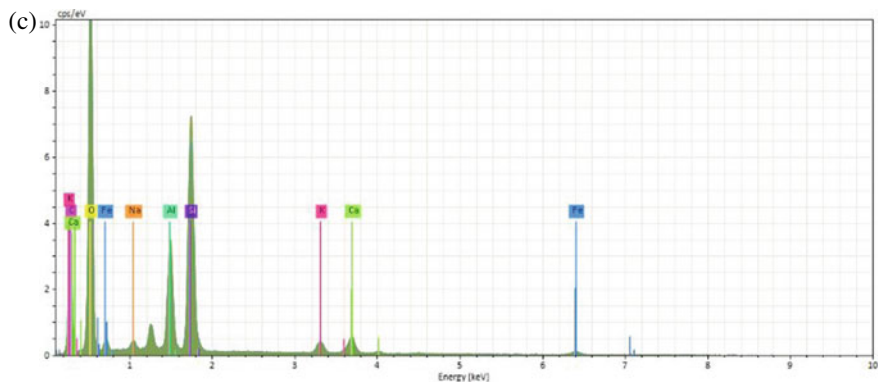
Fig. 4 (continued)

Table 3 Atomic concentration [%] of the topsoil

Spectrum	C	O	Na	Al	Si	K	Ca	Fe
7786	29.06	49.91	12.45	0.546	3.70	0.92	1.66	1.73
7787	23.39	52.45	15.19	0.58	3.82	0.94	1.69	1.94
Mean	26.22	51.18	13.82	0.57	3.76	0.93	1.68	1.84
Sigma	4.01	1.80	1.94	0.01	0.09	0.01	0.03	0.14
Sigma mean	2.84	1.27	1.37	0.01	0.06	0.01	0.02	0.10
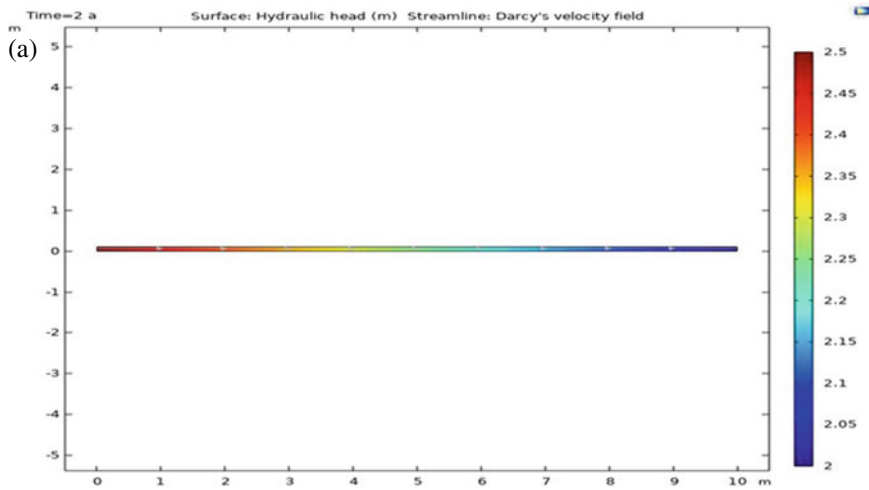
Fig. 5 **a** Hydraulic head results. **b** Change of concentration with increase in distance. **c** Concentration versus time graph obtained both numerically and analytically for a distance of 2 m. **d** Concentration versus time graph obtained both numerically and analytically for a distance of 4 m

6 m, 8 m and 10 m for a period of 10 years were obtained numerically. It was seen that with the increase in time, the concentration tend to reach a steady state. After 8 years, it reached the steady state completely; i.e. there was no change of concentration of Cr (VI) with time (Fig. 5a and b). Figure 5c and d depicts the change in concentration of Cr (VI) with time obtained both numerically and analytically for a distance of 2 m and 4 m, respectively. It can be observed that the graphs seem to match when the concentrations tend to reach a steady state.

3.3   Results Obtained from the 2D Domain

The results obtained (Fig. 6a–m) show the change in hydraulic heads and transport of Cr (VI) in porous sub-surface media with time, respectively. We observe that within a year the pollutant plume travelled a distance of 22 m from the ground surface. It dispersed towards the left boundary owing to the head difference and natural groundwater flow. The infiltration was rapid due to the presence of sand and gravel layers. Later, as the plume travelled through the clay layers, the dispersion slightly seized. The presence of iron compounds or microorganisms in the soil prevents the movement of the plume slightly owing to sorption and decay. Cr (VI) being extremely reactive gets chemically adsorbed on the surfaces of the particles or converted into Cr (III) by the microorganisms present naturally in the soil. But with the passage of time, the adsorption sites are filled, and thus, the plume resumes its path. Thus we see that at the end of 20 years, the plume travelled 77 m from the top layer.

(b)
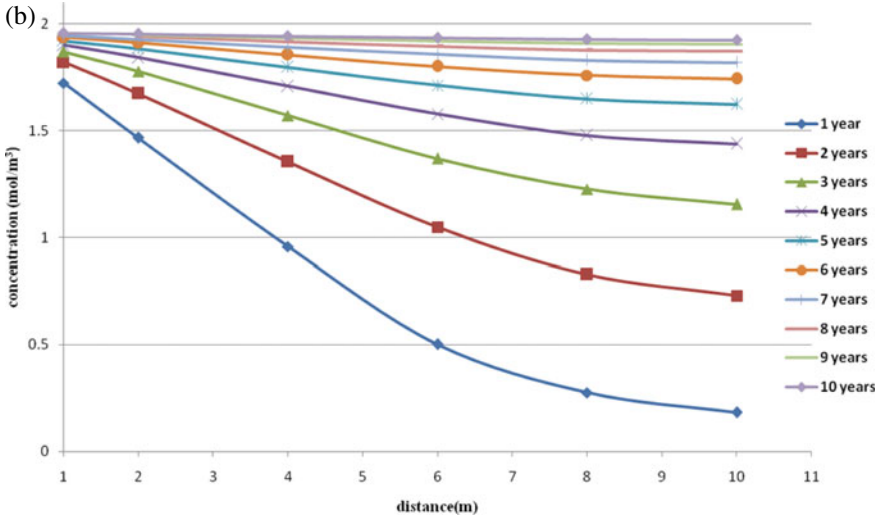
Fig. 5 (continued)

Fig. 5 (continued)

(c)
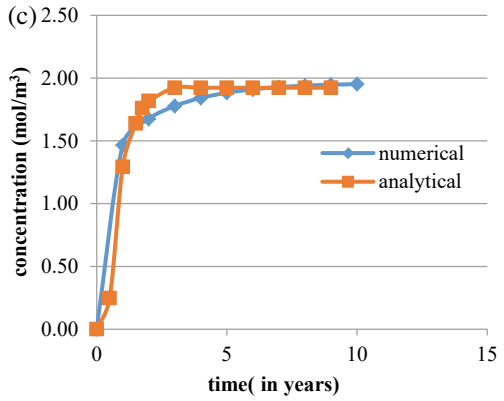
Fig. 5 (continued)

(d)
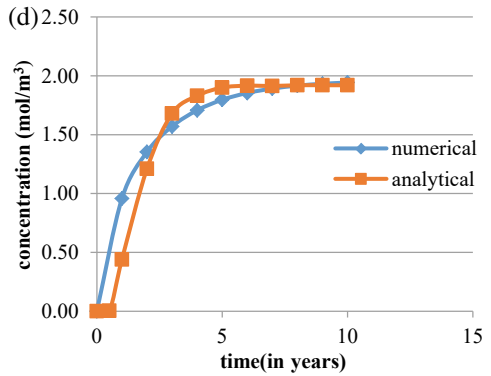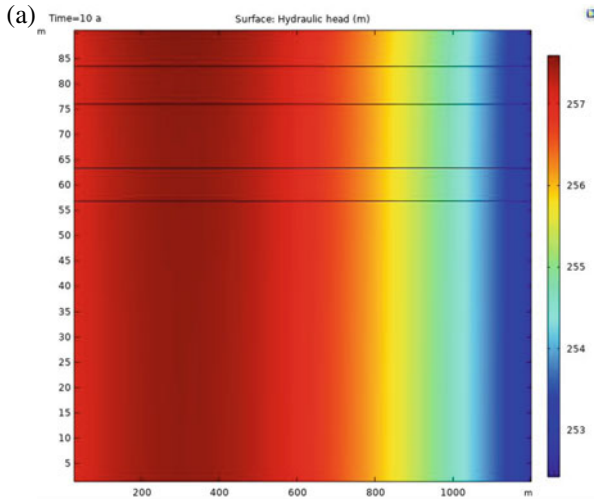
Fig. 6 **a** Distribution of hydraulic head. Transient spread of Cr (VI) plume of **b** 4 months, **c** 7 months, **d** 1 year, **e** 3 years, **f** 6 years, **g** 9 years, **h** 12 years, **i** 15 years, **j** 17 years, **k** 18 years, **l** 19 years, **m** 20 years

Similar work conducted on silty sand soil shows that 50 ml/l concentration of Cr (VI) travelled through the soil column of depth 30 m with constant flow rate of 1.2 ml/min and reached the first 10 cm depth in 15 min; for the greater depths, the travel time increased due to the sorption of Cr (VI) by the soil column [7].

4 Conclusions

The following conclusions are derived from the foregoing study:

1. The hydraulic conductivity of the soil profile affects the transport of the plume. The presence of clay layers increases the time of travel but cannot prevent it.
2. The sand layers increased the infiltration rate and thus can contaminate the water table if it is present at shallow depth.
3. The direction of transport of the plume depends on the hydraulic gradient and hydrodynamic dispersion.
4. Adsorption can be a major factor in controlling the transport of Cr (VI).
5. The presence of microorganisms in soil can convert Cr (VI) into Cr (III) which is harmless and biodegradable.
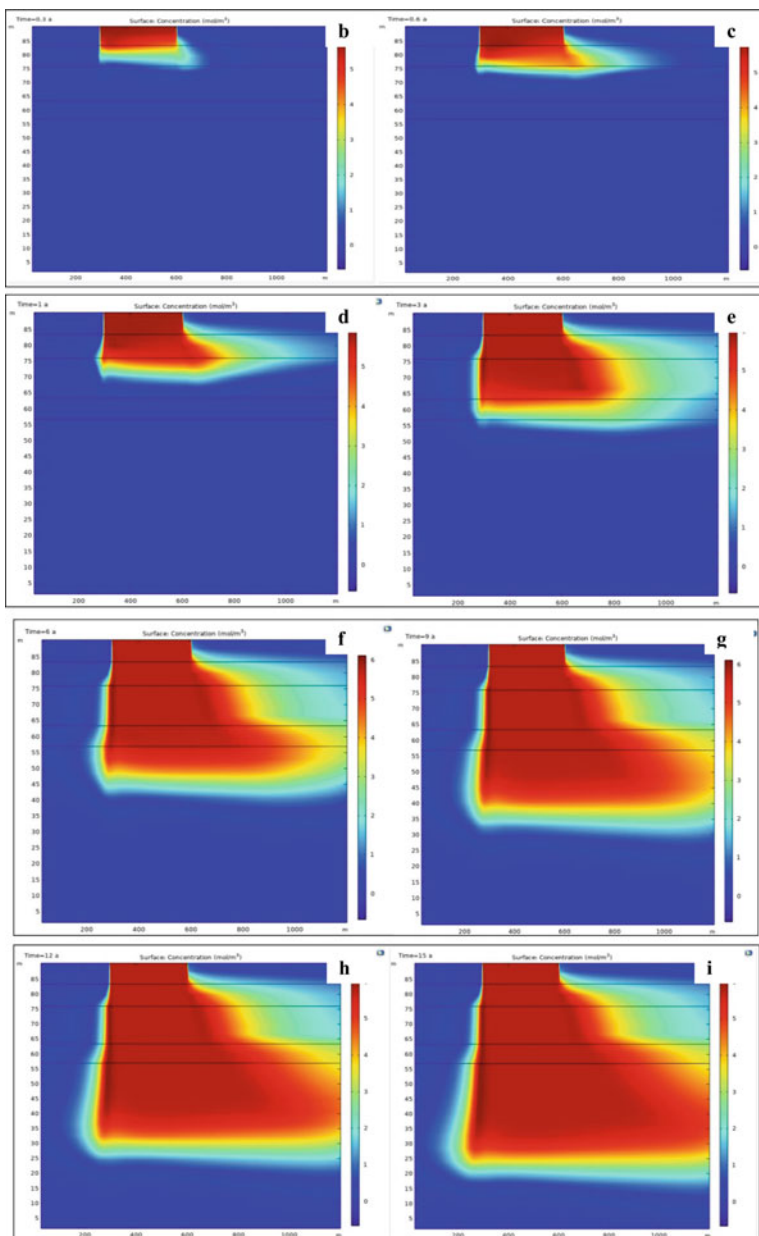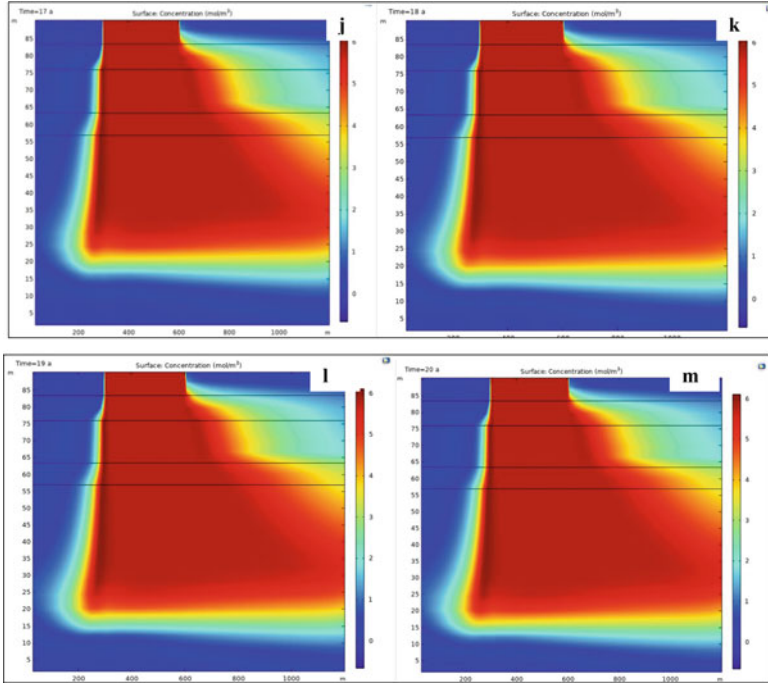
Fig. 6 (continued)

Fig. 6 (continued)

References

1. Ye T, Li H, Wang ZH, Huang R, Yu Y, Yang Z, Gao C, Xie C (2019) Transport and fate of hexavalent chromium in slag–soil system. Environmental Earth Sciences 78:239
2. Liu Y, Li Y, Hu Y, Mostofa KMG, Li S, Liu Z (2019) Adsorption characteristics and transport behavior of Cr (VI) in shallow aquifers surrounding a chromium ore processing residue (COPR) dumpsite. J Chem, 4932837
3. Kan CC, Ibe AH, Rivera KKP, Arazo RO (2017) Hexavalent chromium removal from aqueous solution by adsorbents synthesized from groundwater treatment residuals. Sustain Environ Res, 163–171
4. Wang S, Choi JH (2013) Simulating fate and transport of chromium in saturated sediments. Appl Math Model, 102–111
5. Ghiasi B, Niksokhan MH, Mazdeh AM (2020) Co-transport of chromium (VI) and bentonite colloidal particles in water- saturated porous media: effect of colloid concentration, sand gradation, and flow velocity. J Contaminant Hydrol. S0169-7722(20)30271-0

6. Kumar A, Pramanik S, Mishra M (2016) COMSOL Multiphysics® modeling Darcian and non-Darcian porous media. In: Journal conference in Bangalore
7. Khan AA, Muthukrishnan M Wang, Guha, BK (2010) Sorption and transport modeling of hexavalent chromium on soil media. J Hazardous Mater, 444–454

Effect of Valve Closure Schedule on Peak Pressure in Pressurised Conduit Under Transient Condition Using Method of Characteristics

V. M. Rana and H. M. Patel

Abstract Hydroelectric power station is the most economical unit for generating electricity for the nation. High head hydropower plant needs construction of a safe water conveyance system to withstand high-pressure surge. The conveyance system of the high head hydropower plant consists of a long tunnel and penstock. Pressure transients are likely to occur in such a conveyance system when there is a change in turbine discharge. Such conditions become highly critical under sudden closure of turbines. The effect of turbine discharge changes can be simulated in a simplified manner as valve closure. In this paper, an attempt has been made to study water mass oscillation in long tunnel under various closure schedules of valve placed downstream of long horizontal pipe. The upstream boundary condition is considered as a constant head boundary. The study basically focused on the use of method of characteristics for solving equation of continuity and equation of momentum for unsteady state flow. The valve closure schedules are assumed to have two stage closures with linear discharge reduction. The entire length of pipe is divided into various sections and pressures and discharges are found at all the nodes. The pressure variations at key locations in the conveyance system are plotted for different valve closure schedules. The various strategies of valve closures are attempted for evaluation of the peak pressure at key locations. It was observed that the strategy involving reduction in valve closure rate in the second stage significantly restricted the rise in peak pressure.

Keywords Hydropower · Transient flow · Method of characteristics

V. M. Rana (✉) · H. M. Patel
Faculty of Technology and Engineering, The M. S. University of Baroda, Vadodara 390001, India
e-mail: vijayrana-ced@msubaroda.ac.in

H. M. Patel
e-mail: hmpatel-ced@msubaroda.ac.in

1 Introduction

Hydropower stations use hydraulic turbines to convert energy possessed by flowing water into electricity. Such a source is one way of electrical generation from renewable potential sources. Usually, a hydropower plant is made up of the reservoir, water tunnel, surge tank, penstock, and turbine. Various turbine operations such as load acceptance, load rejection, and combination conditions produce transients in hydropower station, which are directly related to the safety of the whole hydropower station and local power transmission grid, even resulting in substantial damage and human loss in some cases. This issue attracts many researchers and engineers, due to its complexity and importance in practice. The effect of different parameters such as friction loss coefficient, length, cross-sectional area, and operation of turbine valve on unsteady state transient flow was analysed and investigated by different researchers [3]. The system of nonlinear ordinary differential equations of flow in hydropower system was numerically solved and manipulated in different way by different researchers. Franc [2] had suggested the use of finite element solution for mass oscillations in hydropower conveyance system on sudden valve opening. In the present study, the main objective is to develop continuity and momentum equations for unsteady state flow occurring due to turbine valve closure. The upstream boundary condition is considered as constant head of water in the reservoir. The study basically focused on application of method of characteristics for solving governing equations for unsteady state flow for simple Reservoir-Pipe model.

2 Materials and Methods

2.1 Reservoir-Pipe Model

The Reservoir-Pipe is very simple type of hydraulic model equipped with control valve at end. The unsteady state flow can be achieved in such type of model by operating end valve at different speed of closure. The present model is composed of two different diameter of pipe connected in series. The upstream boundary condition is consisting of constant static head observed in reservoir, and the downstream boundary condition is pressure head observed at valve end.

2.2 Data for Model Study

One large reservoir with two number of pipes connected in series at lower end is considered for study. The steady stage discharge through reservoir is 1 m^3/sec. The axis of pipe is considered as datum level for measurement of pressure head. The static water level observed in reservoir is 67.70 m, and the total time for simulation

(a) Layout of Study Problem

(b) Discretisation of Pipe for MOC
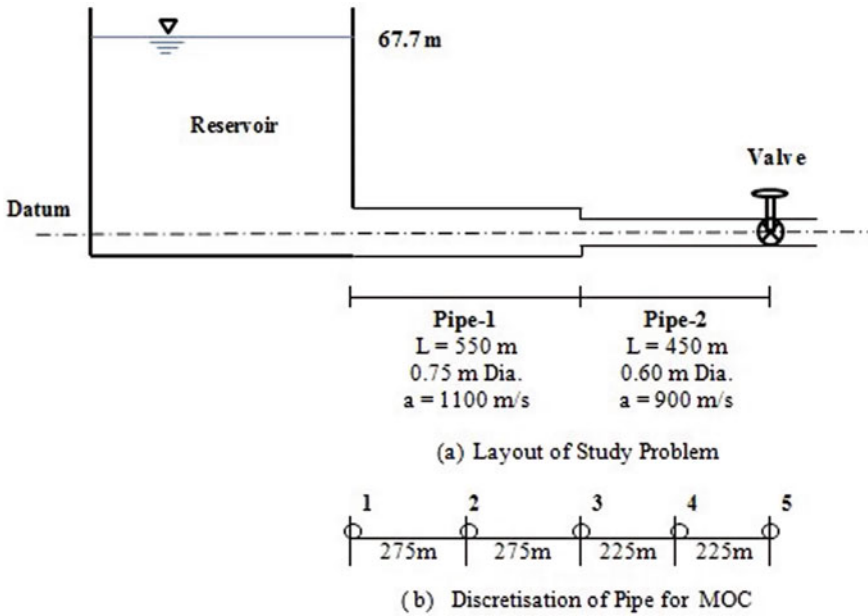
Fig. 1 Reservoir-pipe model

computation is 10 s. The total number of nods considered for study is 5. The total valve operating time is 6 s.

The length of pipe 1 is 550 m. The diameter of pipe 1 is 0.75 m. The pressure wave velocity for pipe 1 is 1100 m/sec. The friction factor for pipe 1 is 0.010. Similarly, the length of pipe 2 is 450 m. The diameter of pipe 2 is 0.60 m. The pressure wave velocity for pipe 2 is 900 m/sec. The friction factor for pipe 2 is 0.012 (Fig. 1).

2.3 Method of Characteristics

In this study, the mathematical model for hydraulic flow is formulated by using the basic governing equations of flow. These governing differential equations are derived by applying the principles of continuity and the momentum to a small differential element of the liquid flowing between reservoir and control valve with a specific control volume concept [1].

Referring to Fig. 2 for *x-t* plane, let the conditions at time $t =$ to be known at initial point. We can compute the unknown conditions at to $+\Delta t$ at another point. In x-t plane, it is a case of positive characteristics line AP and similarly for negative characteristics line BP. Q is discharge and H is pressure head at a point, and f is friction factor. A is cross-sectional area of flow, g is acceleration due to gravity, and a is pressure wave velocity.

Fig. 2 Excitation at
upstream and downstream
ends
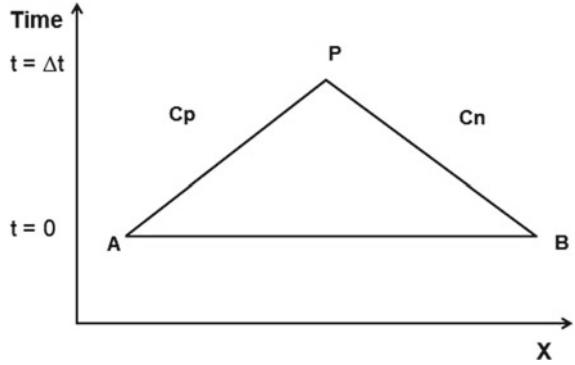
We can write

$$Q_P = C_P - C_a H_P \qquad (1)$$

We can write

$$Q_P = C_n + C_a H_P$$

where

Positive characteristic equation,

$$C_P = Q_A + gA\left(\frac{1}{a}\right)H_A - \frac{f\,\Delta t\,Q_A|Q_A|}{2AD} \qquad (2)$$

Negative characteristic equation,

$$C_n = Q_B - gA\left(\frac{1}{a}\right)H_B - \frac{f\,\Delta t\,Q_B|Q_B|}{2AD} \qquad (3)$$

and

$$C_a = gA\left(\frac{1}{a}\right) \qquad (4)$$

and solving for Q_p, we get,

$$Q_p = 0.50\left(-C_v + \sqrt{C_v^2 + 4C_pC_v^2}\right) \tag{5}$$

where

$$C_v = (\tau Q_o)^2/(C_a H_o) \tag{6}$$

Here, parameter τ is Tau, a variable coefficient corresponding to valve opening or closing, at which the flow through the valve is Q_o under a head H_o. Tau is a variable coefficient which depends on time t of valve opening or closing.

3   Results and Discussions

The six different operation conditions were considered by changing speed of valve closing. Tau value is obtained from Tau verses time curve for different valve closing. The simulation results were obtained which are described in following charts (Figs. 3, 4, 5, 6, 7, 8, 9, and 10; Table 1).

For Case-1, it is observed that, highest value of pressure observed is 245.47 m at 5.5 s and lowest value of pressure observed is −100.80 m at 7.5 s. This is the worst condition of pressure variation showing extreme high value and extreme low value for the values recorded under all the cases. The lowest value of pressure is found to be below cavitation limit. This indicates that cavitation will occur under this closure condition. It is not preferable for safe operation of hydropower plant. The theory of continuity equation suggests that under cavitation phenomena, the governing equation is not valid, and hence, the simulation results obtained after beginning of cavitation are to be ignored.
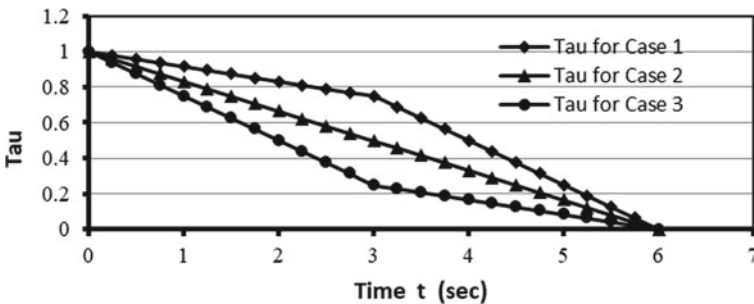
Fig. 3   Valve closing strategy for cases-1, 2, and 3
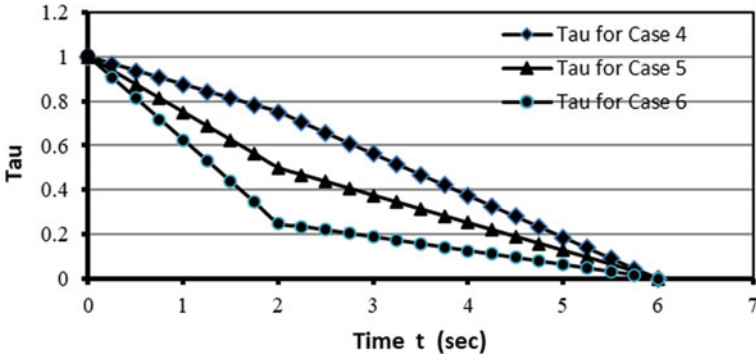
Fig. 4 Valve closing strategy for cases-4, 5, and 6
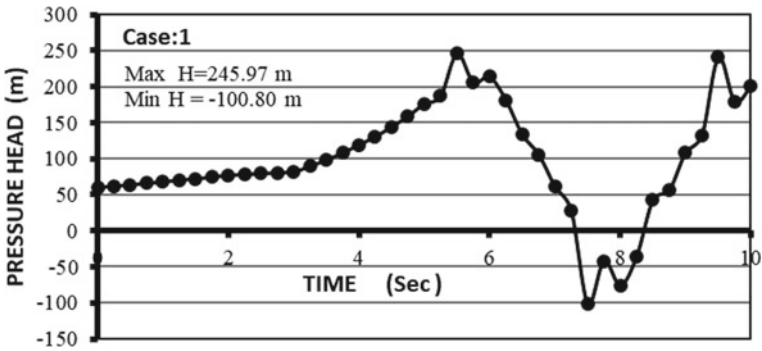
Fig. 5 Pressure head variation due to valve closure for case-1
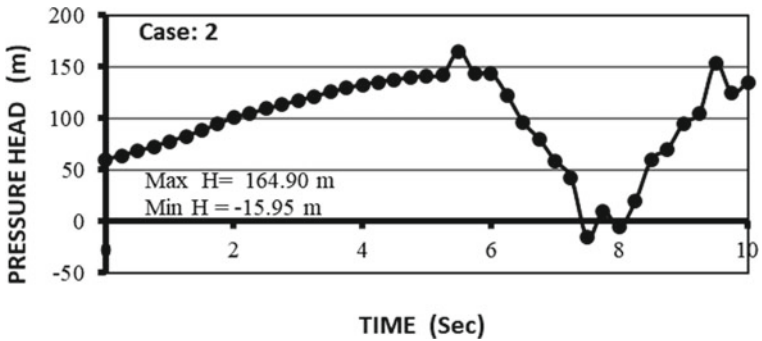
Fig. 6 Pressure head variation due to valve closure for case-2
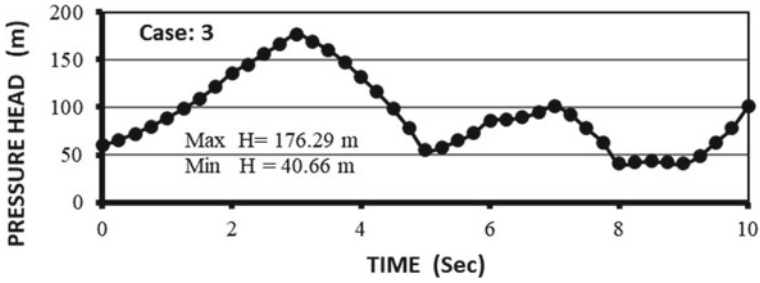
Fig. 7 Pressure head variation due to valve closure for case-3
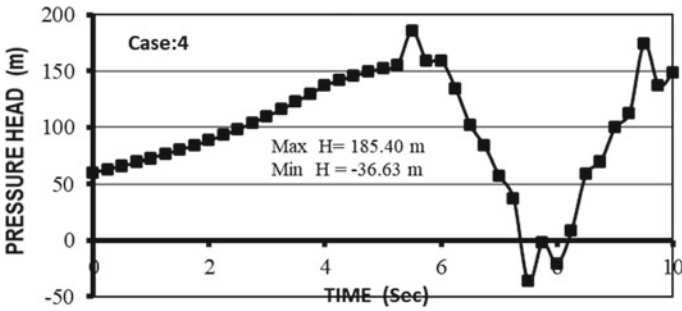
Fig. 8 Pressure head variation due to valve closure for case-4
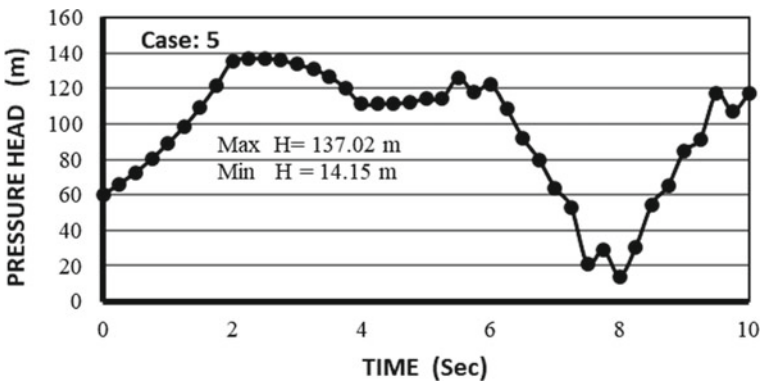
Fig. 9 Pressure head variation due to valve closure for case-5

For Case-2, the peak value of pressure is observed as 164.90 m at 5.5 s and lowest value of pressure is observed as −15.95 m at 7.5 s. The range of pressure variation is relatively narrow as compared to Case-1, but shows chances of cavitation. It is a better valve closure condition as compared to Case-1.
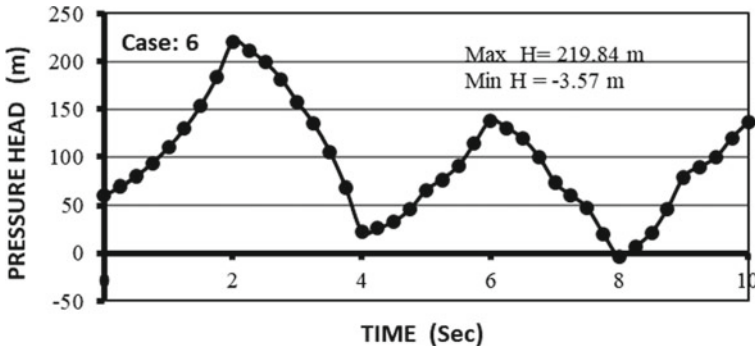
Fig. 10 Pressure head variation due to valve closure for case-6

Table 1 Pressure head variation at valve due to closure

Case	Maximum head (m)	Minimum head (m)	Remarks
Case-1	245.97	−100.80	Cavitation, high pressure
Case-2	164.90	−15.95	Cavitation
Case-3	176.29	40.66	No cavitation
Case-4	185.40	−36.63	Cavitation
Case-5	**137.02**	**14.15**	No cavitation, moderate pressure
Case-6	219.84	−3.57	High pressure

Bold values *indicate the best operational strategy among all cases*

When we study the results obtained under Case-3, we can notice that, highest value of pressure observed is 176.29 m at 3 s and lowest value of pressure observed is 40.66 m at 9 s. The range of pressure variation is relatively narrow as compared to Case-1, hence, it is a better valve closure condition as compared to Case-1. Similarly for Case-4 and Case-5, the pressure variation range is narrow as compared to Case-1, but chances of cavitation are there.

The simulation of condition under Case-5, it is observed that, highest value of pressure is 137.02 m at 2.5 s and lowest value of pressure is 14.15 m at 8 s. The range of pressure variation is relatively narrow as compared to all cases, and there is no chance of cavitation. It is the best valve closure condition among the all the cases.

4 Conclusions

The following conclusions are derived from the foregoing study:

- Total six valve closure strategies are studied for same closure time 6 s. The maximum and minimum pressure values found at valve end to be different depending upon the pattern of valve closure.
- The minimum high-pressure value is observed at valve end for Case-5, in which the closure is carried out rapidly for first two seconds, and then, the rate of closure rate is reduced in subsequent time range of 4 s, till the complete closure is achieved at 6 s.
- If the initial rate of closure is lower (Cases-1, 2, 4), the pressure at the valve drops to negative values, which results in cavitation in the pipe.
- When cavitation occurs, the governing equations are not valid, and hence, the results of simulated values are not meaningful.
- The method of characteristics is found to be very fast and precise in evaluating valve closing schedule under unsteady state flow condition.

References

1. Chaudhry MH (1987) Applied hydraulic transients, 2nd edn. Van Nostrand Reinhold, New York
2. Franc PW (1996) Finite element solution for mass oscillations in a surge tank on sudden valve opening. Elsevier Adv Eng Software 26(1996):185–187
3. Ramadan AM, Mustafa H (2013) Surge tank design considerations for controlling water hammer effects at hydro-electric power plants. University Bull Al-Mergib Univ 15(3):147–160

Improving the Khosla Method of Estimating Subsurface Flow Properties in Hydraulic Design Using MODFLOW

Rath Prayas, K. K. Khatua, and K. C. Patra

Abstract The Khosla theory of flow nets has stood the test of time. It has been in use for designing the hydraulic structure for nearly a century by estimating the seepage properties like the pressure heads, seepage discharge, and exit gradient. In this method, flow nets, comprising equipotential lines and streamlines, are implemented to predict the movement of the water below the hydraulic structure to estimate the various seepage properties. The major limitation of the method lies in the important assumption of homogeneity and isotropy in the foundation of the soil. In this paper, we have aimed to address this limitation by using a commonly used finite difference groundwater flow model MODFLOW. We have created a 2D theoretical barrage model and tested for the various seepage properties in different hydrogeological conditions including anisotropy and different thickness of the saturated zone below the structure. The results showed that by increasing the anisotropy, the exit gradient increased manifold. When the depth increases, the exit gradient and discharge increases up to a certain limit, upon further increasing the depth, there was minimal effect on the exit gradient. The results shall help us to evaluate the uncertainty in estimating the seepage properties and improve the Khosla method in designing the hydraulic structures.

Keywords Khosla method · Hydraulic structure · Seepage · Exit gradient · Anisotropy · MODFLOW

R. Prayas (✉)
Department of Civil Engineering, University of Wyoming, Laramie, WY, USA
e-mail: prath1@uwyo.edu

K. K. Khatua · K. C. Patra
Department of Civil Engineering, NIT, Rourkela, India
e-mail: 513ce1030@nitrkl.ac.in

K. C. Patra
e-mail: kcpatra@nitrkl.ac.in

1 Introduction

Hydraulic structures like dams and barrages have been in use to control the flow of water for flood control, recharging groundwater, store water for irrigation, and human consumption since time immemorial. Hydropower and industries also depend on these hydraulic structures for their water demand. In the last few decades, additional stress for water resources due to increase in population and climate change has resulted in higher need water storage and flood control structures. Also, in this span of time, a number of these hydraulic structures have failed. Studies and surveys of major failures in the last century have shown that piping is one of the major causes. Piping failure occurs when the seepage water has sufficient force to lift the soil at the downstream end of the structure resulting in progressive removal of the soil from beneath the foundation. This leads to subsidence of the structure. The force of the flow of the seepage depends on exit gradient that depends on properties of the subsurface flow. Thus, the need to study the subsurface flow beneath a hydraulic structure is of paramount importance. Over the last hundred years, engineers and scientists have studied the properties of seepage flow below these structures.

The theory of creep length [1] was introduced for the flow passing under hydraulic structures. The creep length was defined as the route of the first line of seepage which is in contact with the foundation of the hydraulic structure. Along the creep line, the hydraulic gradient is constant, and the energy loss is linearly proportional to the creep length. Hence, the uplift pressure distribution beneath the hydraulic structure is linear. It was discovered that there is difference between vertical and horizontal creep paths [2]. As a result, he introduced the weighted creep path theory. He added factors of 0.33 and 1 to the total horizontal and vertical lengths, respectively. A method based on flow nets [3] was established to estimate the pressure distribution and exit gradient. This method assumes the seepage flow which occurs in streamlines perpendicular to the equipotential heads. This method can be construed to be a special case of Darcian flow system, where heterogeneity and anisotropy are neglected. Khosla used complex power function to solve for the hydraulic heads (pressure) below the structures. Of all the three methods discussed, Khosla method is used extensively by hydraulic engineers in India. But the basic assumption of homogenous and isotropy in Khosla method can limit its applications. In the last few decades, various other computational methods to estimate flow through the porous media have been established. With increase in computational efficiency finite element [4–6], finite difference methods and isogeometric have been implemented to solve the flow system equations. MODFLOW is one such computer code that implements finite difference scheme to solve for groundwater flow problem. MODFLOW solves the following equation:

$$\frac{\partial}{\partial x}\left(K_x \frac{\partial h}{\partial x}\right) + \frac{\partial}{\partial y}\left(K_y \frac{\partial h}{\partial y}\right) + \frac{\partial}{\partial x}\left(K_z \frac{\partial h}{\partial z}\right) + Q_s' = \text{SS}\frac{\partial h}{\partial t} \tag{1}$$

where K_{xx}, K_{yy}, and K_{zz} are values of hydraulic conductivity along the x, y, and z coordinate axes, which are assumed to be parallel to the major axes of hydraulic conductivity (L/T); h is the potentiometric head (L), Q'_s is a volumetric flux per unit volume representing sources and sinks of water, with Q'_s being negative for flow out of the groundwater system, (T^{-1}); SS is the specific storage of the porous material (L^{-1}); and t is time (T).

2 Methods

In the present study, the seepage flow system is 2D and steady state with no sinks or sources. Hence, the terms in z direction, Q's, and the RHS term containing the time function in Eq. (1) are all reduced to zero. The model is implemented using MODFLOW NWT [7] in a Python environment using FloPy [8]. The MODFLOW NWT is the Newton–Raphson formulation of MODFLOW which handles drying and rewetting nonlinearities of the unconfined groundwater flow to allow more stable water table solutions than the previous versions [9]. The models were bounded by constant head boundaries on the vertical edges (i.e., flow divides) and the no flow boundary along the bottom (i.e., impermeable barrier) for all geometries (Fig. 1). The length of the hydraulic structure is b, the distance to the impermeable layer below is D, and the hydraulic conductivity of the flow system is in x- and y-directions which are denoted by K_x and K_y.

The whole domain is discretized into 5000 columns horizontally and 1000 rows vertically resulting in 50,000 cells. This fine scale of discretization helps us to avoid any errors due to grid sizes in estimating the seepage properties. The upstream head H is at 70 m and downstream head is set at 30 m. The width of the hydraulic structure (b) is set to be 40 m. The length of the domain L is 200 m. The base case thickness or depth to the impervious layer (D) is 25 m. The exit gradient is calculated from the output of heads calculated by MODFLOW at the different layers.

Fig. 1 Model domain and the schematization of the different parameters used
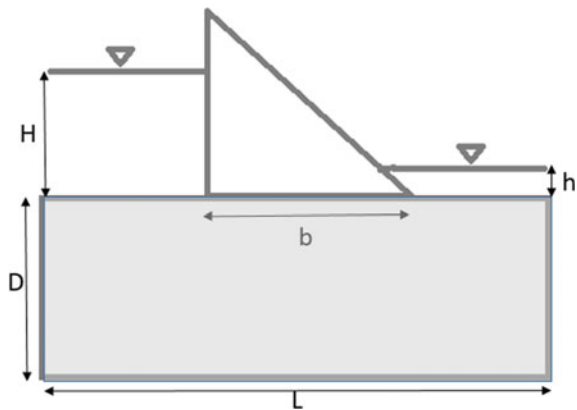
The model is tested with different thickness to length ratios (*D/L*) and anisotropies (K_y/K_x) to find the head distribution and upwards seepage discharge and exit gradient. The range of D/L tested is 0.025 to 2.5. And the range tested for anisotropies is 10^{-5} to 10^5.

3 Results

3.1 Effect of Thickness of the Saturated Layer

Figure 2 shows a simulation of the calculated heads with the structure. We evaluated the effect of the *D/L* by changing the values of *D*. We found that increasing the *D/L*, the head contours gradually became more distributed in the *x*-direction in the whole domain and the gradient along the y-direction became more noticeable (Fig. 3).
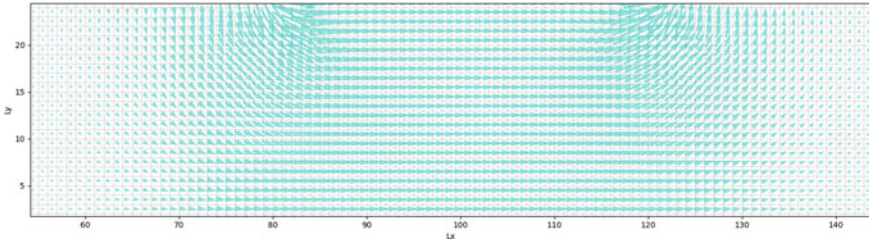
Fig. 2 Model cross section showing the direction of flow under the hydraulic structure. The cyan colored arrows are the flow vectors
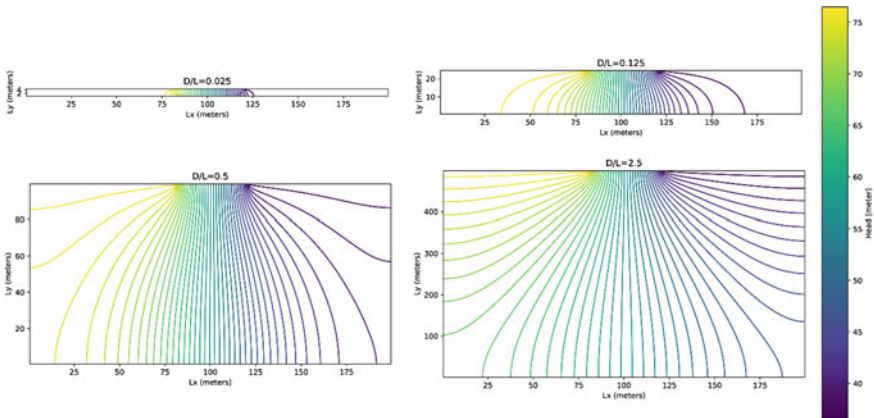
Fig. 3 Contour plot of head distribution under the hydraulic structure for different depths to length ratios
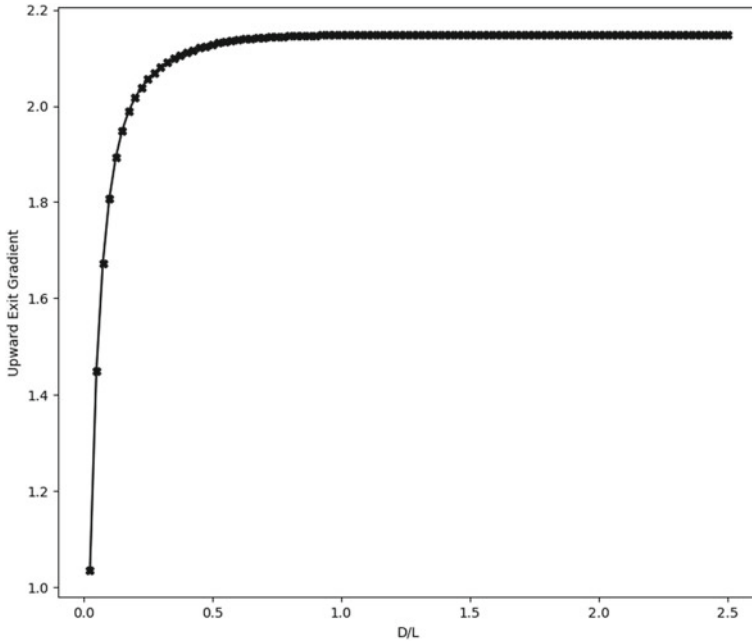
Fig. 4 Variation of upward exit gradient with change in thickness (*D*) of the saturated layer

The upward exit gradient thus increases with increase in the depth of the permeable layer. However, this increase is plateaued after a certain depth is reached (Fig. 4). Upon further increasing the depth, the exit gradient remains unaffected. Thus, the assumption of infinite thickness may affect the estimation of safe exit gradient by overestimating it for thinner saturated zones.

3.2 Effect of Anisotropy

Another main assumption of Khosla theory is the isotropic medium. We found that increasing the anisotropy, i.e., increasing the ratio of K_y/K_x increased the direction of flow in the y-direction (Fig. 5). Hence, the gradient in the upward direction decreases (Fig. 6). But the flow or the rate of specific discharge increased with increase in the anisotropy as the K_y increased (Fig. 7).
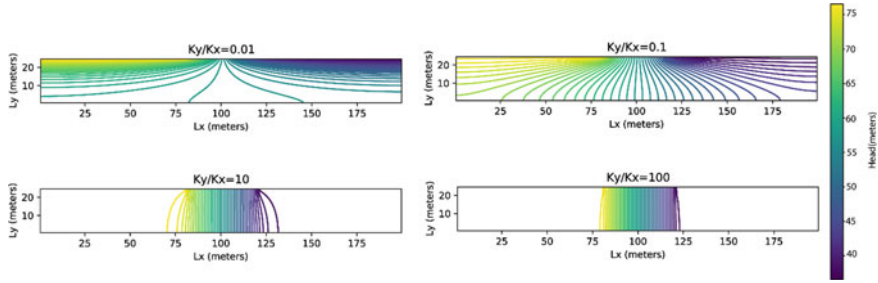
Fig. 5 Contour plot of head distribution under the hydraulic structure for different depths to length ratios
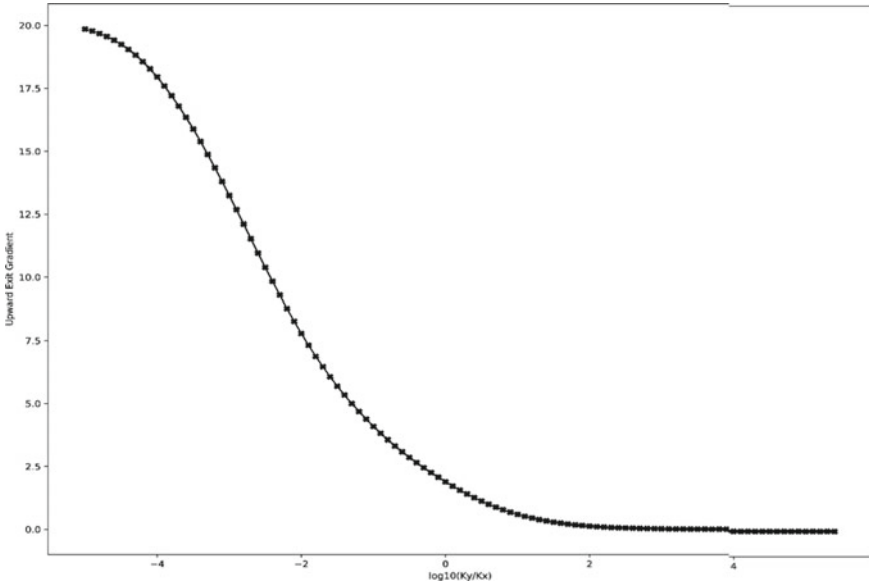
Fig. 6 Variation of upward exit gradient with change in anisotropy (K_y/K_x) of the saturated layer

4 Conclusions

The anisotropy and the thickness of the saturated layer affect the groundwater flow features. Hence, the underlying assumption of Khosla theory of flow nets may render its wide applicability in doubt especially when the anisotropy is high, or the thickness is low. We found at higher anisotropy, although the exit gradient is low, but the specific discharge (product of hydraulic conductivity and hydraulic gradient) increases. Hence, theoretically the consideration of exit gradient as the primary driver of discharge and hence the factor to be considered for safety should be treated with bit of doubt. For practical purposes, such high anisotropies may not be existing on
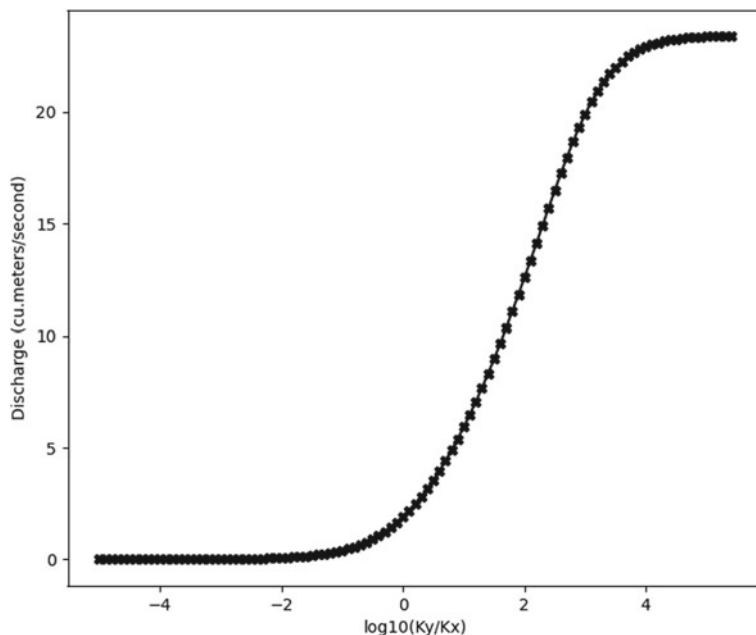
Fig. 7 Variation of specific discharge with change in anisotropy (K_y/K_x) of the saturated layer

riverbeds, but we should always be aware of these imitations while applying. This paper also shows how MODFLOW can be used to improve the Khosla theory and can be helpful for design. Future works will be done on the inclusion of cut-off walls in the present model and the effect of boundary conditions, i.e., *D/L*.

References

1. Bligh WG (1910) Dams, barrages and weirs on porous foundations. Eng News 64(26):708–710
2. Lane EW (1935) Security from under-seepage-masonry dams on earth foundations. Trans Am Soc Civ Eng 100(1):1235–1272
3. Khosla AN, Bose NK, Taylor EM, et al (1954). Design of Weirs on permeable foundations. Central Board of Irrigation, New Delhi.
4. Rasool HM, Al-Maliki LA, Al-Mamoori SK, Al-Ansari N (2021) Estimation of uplift pressure equation at key points under floor of hydraulic structures. Cogent Eng 8(1). https://doi.org/10.1080/23311916.2021.1917287
5. Ahmed AA, Bazaraa AS (2009) Three-dimensional analysis of seepage below and around hydraulic structures. J Hydrol Eng 14(3):243–247. https://doi.org/10.1061/(asce)1084-0699(2009)14:3(243)
6. Tokaldany EA, Shayan HK (2013) Uplift force, seepage, and exit gradient under diversion dams. Proc Inst Civ Eng Water Manage 166(8):452–462. https://doi.org/10.1680/wama.11.00084
7. Niswonger RG, Panday S, Ibaraki M (2011) MODFLOW-NWT, a Newton formulation for MODFLOW-2005: U.S. Geological Survey Techniques and Methods 6–A37. Groundwater Book 6, Section A, Modeling Techniques, Book *6-A37*, 44

8. Bakker M, Post V, Langevin CD, Hughes JD, White JT, Starn JJ, Fienen MN (2016) Scripting MODFLOW model development using Python and FloPy. Groundwater 54(5):733–739. https://doi.org/10.1111/gwat.12413

9. Hunt RJ, Feinstein DT (2012) MODFLOW-NWT: robust handling of dry cells using a Newton formulation of MODFLOW-2005. Ground Water 50(5):659–663. https://doi.org/10.1111/j.1745-6584.2012.00976.x

Estimation of Velocity Index for Flow Calculation in Open Channels Using Geometric and Hydraulic Characteristics

Pooja Patel, Rohan Kar, and Arindam Sarkar

Abstract The reliable estimation of discharge passing through a channel is highly dependent on the velocity distribution at a particular cross-section. However, the velocity measurement throughout the depth of a channel section is challenging for high flows. The velocity index or surface velocity ratio (SVR) method is a standard method of transforming surface velocity to mean velocity to estimate the discharge in an open channel, although previous studies suggested a constant value of SVR (≈ 0.85) to determine the mean velocity, which neglects the variability in velocity distribution at different channel sections due to the dip phenomenon. Therefore, the present study proposes a regression-based relationship between SVR, aspect ratio, and the relative roughness of a channel section to explain the inconsistency in velocity estimation. The proposed relationship is comparable with the observed data for field and laboratory cases. Moreover, the estimated discharge validates closely with observed values, and it shows the potential of this method in predicting the discharge in open channels.

Keywords Open channels · Surface velocity ratio · Aspect ratio · Discharge estimation

1 Introduction

The discharge estimation is of utmost importance for designing and analyzing different types of open channels. Discharge measurement using conventional equipment like the current meter is difficult during high flows due to several limitations such as site access, operator safety, and device stability. Therefore, the recent

P. Patel (✉) · R. Kar · A. Sarkar
School of Infrastructure, Indian Institute of Technology Bhubaneswar, Khordha 752050, India
e-mail: a20ce0901@iitbbs.ac.in

R. Kar
e-mail: rk49@iitbbs.ac.in

A. Sarkar
e-mail: asarkar@iitbbs.ac.in

studies showed the inclination toward developing more straightforward methods for discharge measurement, which use non-contact devices for flow velocity measurement [1, 2]. Another way to measure discharge is through surface flow velocity using floats [3]. The velocity index or surface velocity ratio (SVR) is one of such techniques which is used to transform surface flow velocity (u_s) to average flow velocity (u_m). It is a straightforward and quick technique requiring minimum effort and flows measurement equipment. However, it can be highly inaccurate because of the uncertainty in the value of SVR. Hence, the choice of SVR plays a vital role in the flow estimation of open channels. Considering the default value of SVR as 0.85 for all flow conditions gives an inaccurate flow approximation for unsteady flows [1, 4]. The value of SVR depends on the velocity profile at a particular section, influenced by the boundary roughness, channel characteristics (depth and width), and turbulence parameters [5]. Thus, it is required to establish a relationship between SVR and other channel or flow characteristics to eliminate its uncertainty.

The USBR report presented SVR as a unique function of water depth, which showed the increase in SVR with an increase in flow depth [6]. Further, Marjang and Merkley [3] also showed SVR variation with aspect ratio, flow depth, bed roughness, and bed slope. The SVR in Marjang and Merkley [3] was different when compared with values reported in USBR [6] for the same depth. Hence, it indicates that the values reported in USBR [6] are not suitable for all types of flow conditions and the other factors such as aspect ratio and roughness need to be considered in estimating SVR. Welber et al. [7] performed a similar study and showed the influence of relative roughness and the flow depth on SVR. Using laboratory data, Hundt [8] proposed a relationship between SVR and the gravel and cobble bed flow depth. However, it does not apply to the alluvial rivers where the bed mainly consists of sand particles. Moreover, the proposed relation used only laboratory data. Therefore, there is a need to develop a generalized relation incorporating other factors using field and experimental data.

Hence, the focus of the paper is to estimate the effect of the depth, channel roughness, and aspect ratio on the value of SVR using a wide range of field and laboratory data. Based on that, a relationship between SVR and factors significantly affecting it is developed. Further, the established relationship is used to calculate discharge for both field and laboratory datasets and finally compared with the observed flow for validation.

2 Study Area and Data Sources

This study uses field and laboratory datasets collected from past literature. The datasets comprise u_s, u_m, width (B), depth (h), bed slope (S), and roughness (in terms of mean size of bed particles, d_{50}) of the flow. The sources of the dataset and period are given in Table 1. The field data of the Mahanadi River (MR) at three stations (Kantamal, Tikarpara, and Kesinga) were procured from the Central Water Commission, Government of India (CWC). The CWC provided average flow velocity

Table 1 Sources and range of data used in the study

Sources		S	B/h	d_{50}/h
Laboratory data	Lyn [9]	–	4–4.6	0.002–0.004
	Coleman [10]	0.002	2–2.1	0.0006–0.002
	Larrarte [11]	0.0048	1.7–2.1	0.003–0.00048
	Vinukollu [12]	0.0001–0.048	1–22	0.0001–0.13
	Welber et al. [7]	0.00005–0.0075	3–130	0.0003–0.54
Field data (CWC)	Kantamal (2005, 2009)	0.0004–0.0006	75–104	0.10–0.70
	Kesinga (2005, 2009, 2010)	0.0006	89–107	0.006–0.03
	Tikarpara (2005, 2014, 2016)	0.0004–0.0005	63–103	0.03–0.09

S: Bed slope, B/h: Aspect ratio, d_{50}/h: Relative roughness, CWC: Central Water Commission, Government of India. The CWC datasets were collected for the respective stations during the period as indicated inside the parenthesis

by Manning's equation and maximum flow velocity using the current meter or float. The float measured maximum velocity is considered equivalent to surface velocity in this study. The MR data for all the stations in 2005 were used for validation purposes, whereas the remaining year's data were used to develop the relationship. In the absence of the d_{50} data for MR, Strickler's equation was used to convert the Manning's roughness coefficient (n) to d_{50}, as shown in Eq. (1), where d_{50} is in meters (m).

$$n = \frac{d_{50}^{1/6}}{21.1} \tag{1}$$

2.1 Surface Velocity Ratio Method

The discharge computation requires u_m (Eq. 2), which needs point velocity measurement along the depth at a channel section. However, u_m can be acquired if SVR and u_s are known, using Eq. 3.

$$Q = u_m A = SVR \times u_s \times A \tag{2}$$

$$SVR = \frac{u_m}{u_s} \tag{3}$$

where A is the cross-sectional area of a channel section. So, the prime concern in discharge computation using the above method is the choice of SVR. As mentioned

in previous studies, SVR depends on the geometric and hydraulic characteristics of the flow. However, the default value of SVR as 0.85 is widely utilized to transform u_s to u_m, leading to an inaccurate flow estimation. Therefore, based on past studies, four variables, B, d_{50}, h, and S, were considered to observe their influence on SVR. Thus, the dimensional analysis is performed to establish a functional relationship between SVR and the dimensionless variables. Next, the regression analysis of individual dimensionless variables was performed to check the correlation between the variable and SVR based on the coefficient of determination (R^2). The variables showing high correlation ($R^2 > 0.5$) were further considered to develop an expression of SVR using multilinear regression analysis. The developed relationship was further used to calculate SVR for other field and laboratory datasets. The computed SVR is substituted in Eq. (2) to calculate the discharge and eventually validated with the observed values.

3   Results and Discussions

3.1   Buckingham $\prod$ Theorem

Using the considered variables (B, d_{50}, h, and S), the SVR can be expressed as follows:

$$SVR = f(d_{50}, B, h, S) \tag{4}$$

By performing dimensional analysis using the Buckingham π theorem, the SVR can be represented as the function of three dimensionless variables as follows:

$$SVR = \varphi\left(\frac{d_{50}}{h}, \frac{B}{h}, S\right) \tag{5}$$

Further, the influence of these variables, aspect ratio (B/h), relative roughness (d_{50}/h), and bed slope (S) on SVR, is studied in the next section.

3.2   Effect of Aspect Ratio, Relative Roughness, and Bed Slope

The value of SVR published in USBR [6] for the surface velocity measured using float for different depths is shown in Fig. 1. The figure shows that SVR increases with the increase in flow depth, and SVR was assumed to be constant (≈ 0.8) for the flow depth > 0.6 m. However, the influence of other factors on SVR was not considered in USBR [6]. Further, Marjang and Merkley [3], Moramarco et al. [4], and Hauet

Fig. 1 USBR [6] published SVR corresponding to varying flow depth
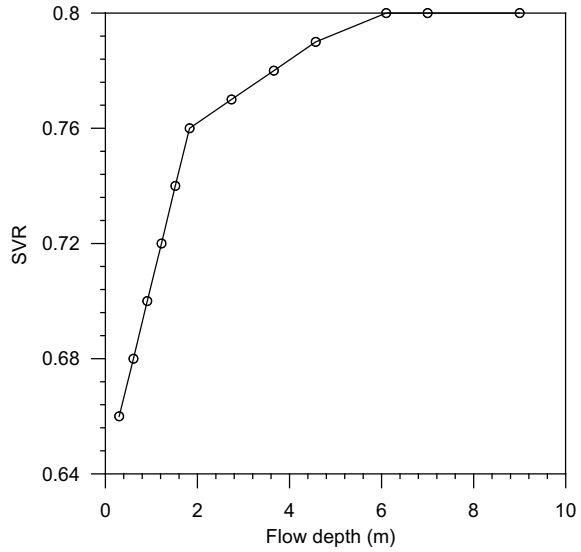
et al. [13] examined the effect of *B/h* on SVR and observed a decrease in SVR with an increase in *B/h*. A similar reduction in SVR with *B/h* is observed in the present study using different laboratory and field data (Fig. 2). It is also observed that it is physically valid and reasonable as SVR is tending toward 1 or may be greater than 1, indicating that the dip phenomenon is significant in that channel section. The dip phenomenon is significant in a narrow channel with a lower *B/h* (< 5) [14]. As a result, there is an increase in SVR with a decrease in *B/h*. Moreover, the single-fitted power function with R^2 equivalent to 0.61 shows a high correlation of *B/h* with SVR.

The dependence of SVR on d_{50}/h is explored using field and experimental data, as shown in Fig. 3, which shows that SVR has a good correlation ($R^2 = 0.68$) with the d_{50}/h. Marjang and Merkley [3] observed similar results: the SVR decreases with bed roughness. Thus, these studies support our findings that the SVR decreases with the rise in d_{50}/h. In addition to that, the dependence of SVR on longitudinal bed slope is shown in Fig. 4. However, it is seen that there is no such significant correlation ($R^2 <$ 0.5) between bed slope and SVR. Likewise, Marjang and Merkley [3] also mentioned that the longitudinal gradient has no considerable influence on SVR. Consequently, the bed slope was not further considered, and the other remaining variables (*B/h* and d_{50}/h) were taken up for multilinear regression analysis to develop an expression for SVR.
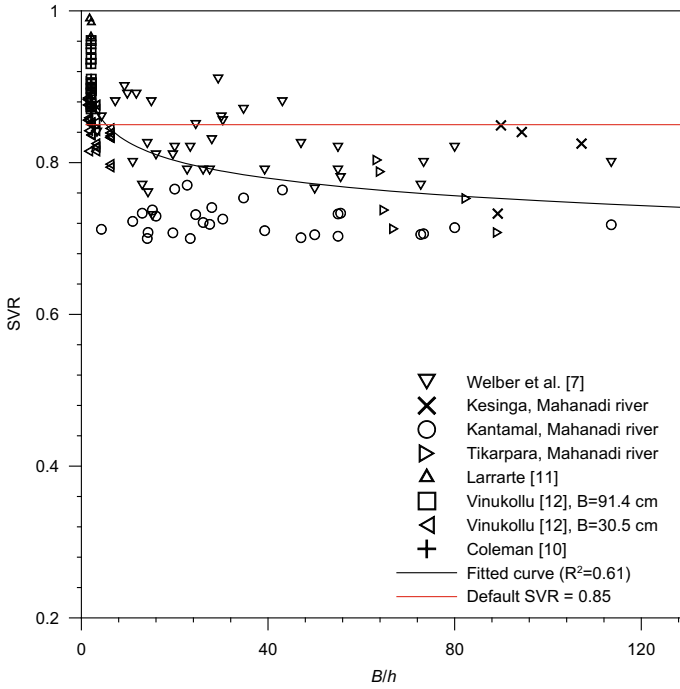
Fig. 2 Relationship between SVR and aspect ratio (*B/h*)

3.3 Multilinear Regression Analysis (MRA)

MRA is a statistical technique that uses self-explanatory variables to predict the dependent variable. The independent variables considered are d_{50}/h and B/h, whereas the dependent variable is SVR. Thus, the expression observed as a result of MRA is given as follows:

$$\text{SVR} = 0.87 - 0.212\,\frac{d_{50}}{h} - 0.001\,\frac{B}{h},\ \left(R^2 = 0.69,\ \ p\text{ - value} < 0.05\right) \quad (6)$$

The regression statistics of the proposed equation comprise R^2, and the probability value (*p*-value) is shown in Eq. (6). The obtained *p*-value of both variables is below the assumed significance level of 5%, which shows that both the independent variables are statistically significant and thus strongly related to SVR.
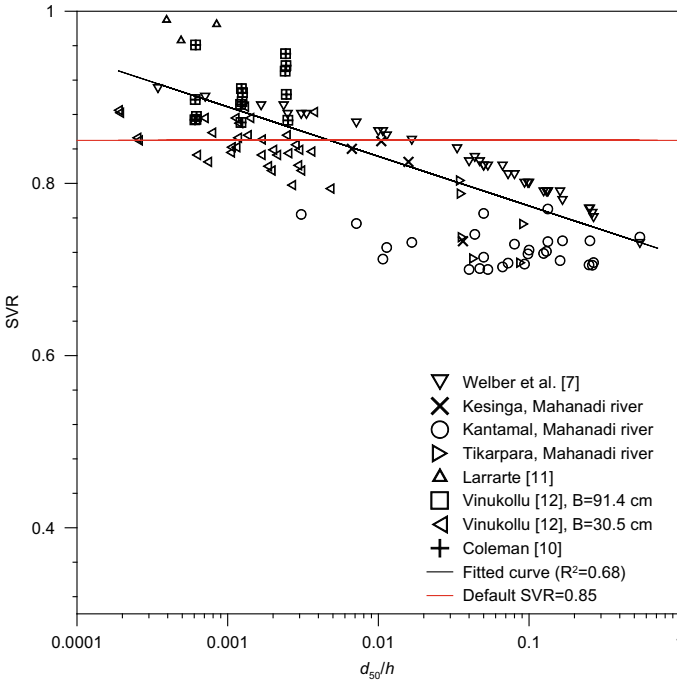
Fig. 3 Relationship between SVR and relative roughness (d_{50}/h)

3.4 Validation

The remaining data not used in developing the relationship was taken to validate the obtained model by comparing the calculated ($Q_{calculated}$) and observed discharges ($Q_{observed}$). The velocity data for the three stations of Mahanadi River (Tikarpara, Kesinga, and Kantamal) during 2005 was used for validation purposes. An experimental dataset [9] was also utilized for the same purpose. The calculated SVR (using Eq. 6) and the known cross-sectional area are substituted in Eq. (3) to obtain $Q_{calculated}$. The efficiency of the proposed model in simulating the discharge is assessed using the Nash–Sutcliffe efficiency coefficient (NSE), which varies from 0 to 1, with 1 being the perfect simulation. The NSE value shows how well the $Q_{calculated}$ versus $Q_{observed}$ plot fits the 1:1 line [15]. The value of NSE was computed using Eq. 7.

$$\text{NSE} = 1 - \frac{\sum (Q_{calculated} - Q_{observed})^2}{\sum (Q_{observed} - Q_{mean})^2} \tag{7}$$

where Q_{mean} is the mean of the observed discharge. Figures 5a, b show the $Q_{calculated}$ versus $Q_{observed}$ for the experimental and field data, respectively, along with their NSE values. The NSE value for all datasets is greater than 0.60, and for the field data, it
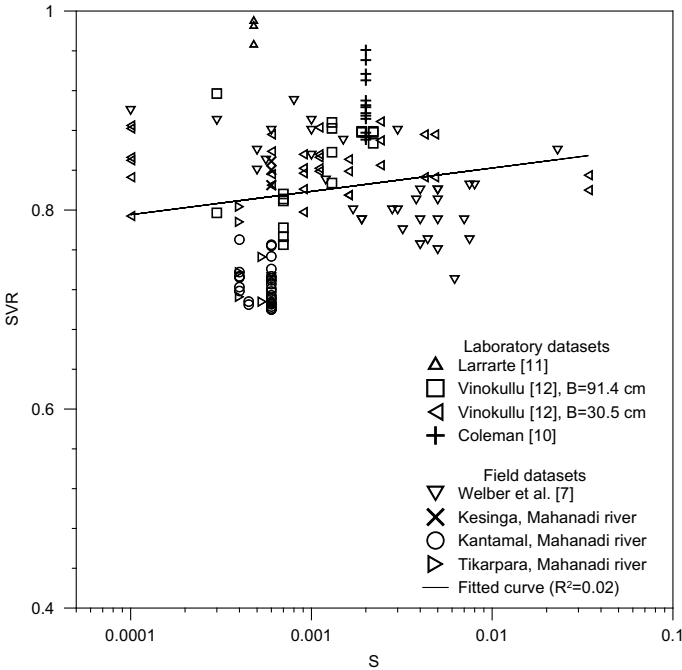
Fig. 4 Relationship between SVR and bed slope (S)

is high up to 0.99, which shows a good agreement between $Q_{calculated}$ and $Q_{observed}$. It indicates that the established relationship can be successfully utilized for the field and experimental study to determine the ungauged discharge with measured u_s and the cross-sectional area.

4 Conclusions

The following conclusions are derived from the current study:

- The use of the surface velocity ratio as 0.85 is highly inaccurate for flow calculation in open-channel flows.
- The value of the surface velocity ratio is strongly correlated with the relative roughness and aspect ratio of a channel section. However, the effect of bed slope on the velocity index is insignificant.
- The aspect ratio and relative roughness efficiently define the surface velocity ratio variations for all considered datasets. Thus, a relationship is proposed to determine surface velocity ratio as a function of aspect ratio and relative roughness, which reduces the uncertainty associated with surface velocity ratio due to secondary flow causing velocity dip phenomenon.
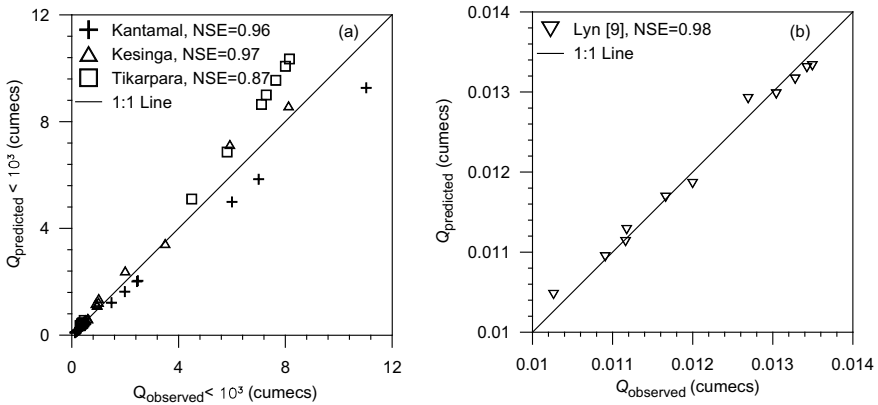
Fig. 5 Comparison of the calculated and observed discharge for validation using **a** CWC procured data at three gauging sites on the Mahanadi River (Kantamal, Kesinga, and Tikarpara) for 2005 and **b** Laboratory data from Lyn [9]

- The proposed relationship is validated using field and experimental data, which shows a high NSE of up to 0.98.
- Other factors, such as the wake effect and turbulence, influence the velocity distribution. Thus, the impact of such factors on the surface velocity ratio could be further explored.

References

1. Costa JE, Spicer KR, Cheng RT, Haeni FP, Melcher NB, Thurman EM, Plant WJ, Keller WC (2000) Measuring stream discharge by non-contact methods: a proof-of-concept experiment. Geophys Res Lett 27:553–556. https://doi.org/10.1029/1999GL006087
2. Costa JE, Cheng RT, Haeni FP, Melcher N, Spicer KR, Hayes E, Plant W, Hayes K, Teague C, Barrick D (2006) Use of radars to monitor stream discharge by non-contact methods. Wat Resources Res 42(7). https://doi.org/10.1029/2005WR004430
3. Marjang N, Merkley GP (2009) Surface velocity coefficients for application of the float method in rectangular and compound open channels. Irrig Sci 27(6):457–470. https://doi.org/10.1007/s00271-009-0162-3
4. Moramarco T, Barbetta S, Tarpanelli A (2017) From surface flow velocity measurements to discharge assessment by the entropy theory. Water (Switzerland) 9(2). https://doi.org/10.3390/w9020120
5. Smart GM, Biggs HJ (2020) Remote gauging of open channel flow: estimation of depth averaged velocity from surface velocity and turbulence. In River Flow 2020:1035–1044. https://doi.org/10.1201/b22619-145

6. USBR (1997) Water measurement manual. Water Resources Publications Inc., Highlands Ranch
7. Welber M, Le Coz J, Laronne JB, Zolezzi G, Zamler D, Dramais G, Hauet A, Salvaro M (2016) Field assessment of non-contact stream gauging using portable surface velocity radars (SVR). Water Resour Res 52(2):1108–1126. https://doi.org/10.1002/2015WR017906
8. Hundt S, Blasch K (2019) Laboratory assessment of alternative stream velocity measurement methods. PLoS ONE 14(9):e0222263. https://doi.org/10.1371/journal.pone.0222263
9. Lyn DA (1992) Turbulence characteristics of sediment-laden flows in open channels. J Hydraul Eng 118(7):971–988. https://doi.org/10.1061/(asce)0733-9429(1992)118:7(971)
10. Coleman NL (1986) Effects of suspended sediment on the open-channel velocity distribution. Water Resour Res 22(10):1377–1384. https://doi.org/10.1029/WR022i010p01377
11. Larrarte F (2006) Velocity fields within sewers: an experimental study. Flow Meas Instrum 17(5):282–290. https://doi.org/10.1016/j.flowmeasinst.2006.08.001
12. Vinukollu KR (2005) Open-channel velocity distribution analysis for calibration of float method in rectangular channels (Document No. 1426192) [Master's Dissertation, Utah State University]. ProQuest Dissertations Publishing
13. Hauet A, Morlot T, Daubagnan L (2018) Velocity profile and depth-averaged to surface velocity in natural streams: a review over a large sample of rivers. E3S Web of Conferences 40. https://doi.org/10.1051/e3sconf/20184006015
14. Subramanya K (2009) Flow in open channels, 3rd edn. Tata McGraw-Hill, New Delhi
15. Moriasi DN, Arnold JG, Van Liew MW, Bingner RL, Harmel RD, Veith TL (2007) Model evaluation guidelines for systematic quantification of accuracy in watershed simulations. Trans ASABE 50(3):885–900. https://doi.org/10.13031/2013.23153

Discharge Method to Estimate the Flow in Asymmetric Compound Open Channel

Sumit Kumar and Bhabani Shankar Das

Abstract During flood, the water from the main channel inundates the floodplain which is known as compound channels. Floodplains are at one or both sides of the main channel known as asymmetrical or symmetrical compound channel, respectively. Estimating the rate of flow in compound channel is an important factor in flood controlling projects. For estimating the rate of flow in compound channel, various traditional and modern methods have been discussed such as single-channel method (SCM), divided-channel method (DCM), Exchange Discharge Method (EDM), lateral distribution method (LDM), and Shiono–Knight method (SKM). Generally, these methods either have extensive computations or use numerical solution of differential equations. But, their efficiency for all compound channels with various hydraulic and geometric conditions may not be satisfied. In this study, the accuracy of the aforementioned methods has been compared for symmetric, asymmetric, and non-prismatic compound channels. Data are collected from the literatures from the present analysis. Error analysis has been performed to check the strength of different existing discharge estimation methods, and the best suitable method is recommended for the estimation of flow in compound channel.

Keywords Compound channels · Discharge method · Exchange discharge method (EDM) · Flood management basin

1 Introduction

Floods can damage living beings, lands, and structures, despite the fact that water is one of the most basic requirements for life to continue. Floods occur when the amount of water in river beds rapidly increases, typically as a result of persistent heavy rainfall and snow melts. The main bed is where the water flows in the stream before the flood, whereas the floodplains are where the water flows on the main bed margins along with the flood. A composite section channel is one that has both a

S. Kumar · B. S. Das (✉)

Department of Civil Engineering, National Institute of Technology Patna, Patna 800005, India

e-mail: bsd.ce@nitp.ac.in
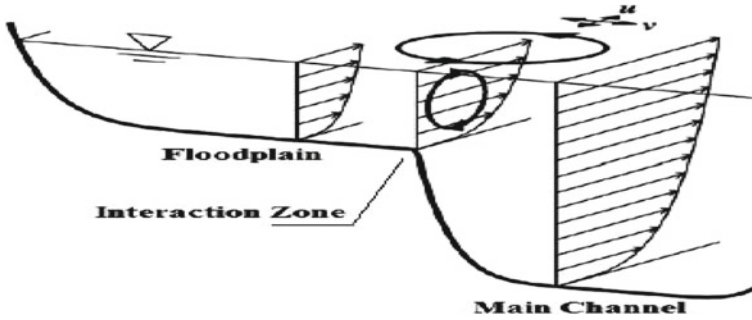
Fig. 1 Creation of turbulence in a compound channel segment [1]

main bed and a floodplain on one or both sides. While the flow of water in the main bed is influenced by a variety of factors, secondary currents formed between the floodplain and the main beds, as well as the accompanying momentum transfer, make understanding the movement in a composite section channel more difficult. River discharge is the most important criterion for hydroelectric generating plants, flood protection structures, water resource management, and drinking, use, and irrigation channels. In open-channel discharge calculations, the experimental Manning's and Chezy's equations are frequently used. While these equations generated inaccurate results for compound channels, they are used to derive one-dimensional modified equations. In channels with the compound section, turbulence is created by run of flow in both the main bed and the floodplain. The floodplain discharge is less than the main river discharge. Because of the velocity difference between the two beds, a slip layer occurs between the main channel and the floodplains. Vortexes form along the vertical and horizontal axes where two beds overlap in the interaction zone (Fig. 1). Because of the velocity difference between the two beds, a slip layer occurs between the main channel and the floodplains. Vortexes form along the vertical and horizontal axes where two beds overlap in the interaction zone (Fig. 1). This study compares the performance of different discharge computation methods that take or do not take into account the momentum transfer between the beds for various channel cross-sections and discharges.

2 Methodology

In compound channel, the following methods are generally used for calculation of discharge.

2.1 Single-Channel Method (SCM)

In order to calculate discharge in natural or artificial channels without velocity measurement, a range of experimental methods based on the calculation of the discharge by establishing a link between the water level and the discharge was carried out. Manning used the water level (h), the width of channel (B), the wetted perimeter (P), the roughness coefficient (n), and the bottom slope (S) as experimental variables.

$$U = \frac{1}{n} R^{2/3} S^{1/2} \tag{1}$$

In Eq. (1), U represents mean velocity, R represent hydraulic depth (wetted area/wetted perimeter). The Manning's equation, which is one of the most widely utilized equations for estimating flow in uniform open channel flows, is used in Eq. (2) by multiplying velocity and area.

$$Q = AU = \frac{1}{n} A R^{2/3} S^{1/2} = K S^{1/2} \tag{2}$$

Here, K is known as conveyance. The Manning's coefficient n varies with the type of bed material. While Eq. (2) gives a single manning coefficient, but in compound channel, primary bed and base materials are differ, so a common coefficient must be developed. The SCM method ignores momentum transfer between beds, which is impossible to account for in the case of non-uniform flow.

2.2 Divided-Channel Method (DCM)

In divided-channel method (DCM), cross-section of compound channel is split and considers the individual properties of each segment because in SCM method, a single value of Manning's coefficient is required.

$$Q = \sum Q_i = \sum A_i U_i = \sum \left(\frac{A_i}{n_i} R_i^{2/3} \right) S^{1/2} \tag{3}$$

In the DCM method, the cross-section of channel can be split into vertical, horizontal, or diagonal lines with imaginary lines.

2.3 Exchange Discharge Method (EDM)

The Exchange Discharge Method (EDM) was developed by enhancing the DCM method to accounting overall momentum transfer in compound channels' interaction

zone between the main channel and the floodplain. The Exchange Discharge Method (EDM) is developed with non-uniform flow in consideration [2, 3]. In this method, the momentum transfer across the surface is related to the velocity divergence between the beds.

The EDM method splits the section into sub-areas in the same way that the DCM method does, but the rectified conveyance (K_i) value is taken into account when calculating the discharge of the portions.

$$Q = \sum Q_i = \sum K_i^* S^{1/2} \tag{4}$$

where K_i^* is defined as:

$$K_i^* = \frac{K_i}{(1 + \chi_i)^{1/2}} \tag{5}$$

where χ_i is defined as:

$$\chi_1 = \frac{1}{gA_1} \left[\begin{array}{l} \psi^t(H - h_1) \left\{ \frac{R_2^{2/3}}{n_2} \left(\frac{1 + \chi_1}{1 + \chi_2} \right)^{1/2} - \frac{R_1^{2/3}}{n_1} \right\} \\ + \psi^t K_{21} \dfrac{dK_1}{dx} \end{array} \right] \cdot \left[\frac{R_1^{2/3}}{n_1} - \frac{R_2^{2/3}}{n_2} \left(\frac{1 + \chi_1}{1 + \chi_2} \right)^{1/2} \right] \tag{6}$$

$$\chi_2 = \frac{1}{gA_1} \left[\psi^t(H - h_1) \left\{ \frac{R_2^{2/3}}{n_2} \left(\frac{1 + \chi_1}{1 + \chi_2} \right)^{1/2} - \frac{R_1^{2/3}}{n_1} \right\} + \psi^g K_{12} \frac{dK_1}{dx} \right] \\ \cdot \left[\frac{R_2^{2/3}}{n_2} \left(\frac{1 + \chi_1}{1 + \chi_2} \right)^{1/2} - \frac{R_1^{2/3}}{n_1} \right] \left(\frac{1 + \chi_1}{1 + \chi_2} \right) \\ + \left[\psi^t(H - h_3) \left\{ \frac{R_2^{2/3}}{n_2} \left(\frac{1 + \chi_3}{1 + \chi_2} \right)^{1/2} - \frac{R_3^{2/3}}{n_3} \right\} + \psi^g K_{32} \frac{dK_3}{dx} \right] \\ \cdot \left[\frac{R_2^{2/3}}{n_2} \left(\frac{1 + \chi_3}{1 + \chi_2} \right)^{1/2} - \frac{R_3^{2/3}}{n_3} \right] \left(\frac{1 + \chi_3}{1 + \chi_2} \right) \tag{7}$$

$$\chi_3 = \frac{1}{gA_3} \left[\psi^t(H - h_3) \left\{ \frac{R_2^{2/3}}{n_2} \left(\frac{1 + \chi_3}{1 + \chi_2} \right)^{1/2} - \frac{R_3^{2/3}}{n_3} \right\} + \psi^g K_{23} \frac{dK_3}{dx} \right] \\ \cdot \left[\frac{R_3^{2/3}}{n_3} - \frac{R_2^{2/3}}{n_2} \left(\frac{1 + \chi_3}{1 + \chi_2} \right)^{1/2} \right] \tag{8}$$

In the above equations, Q is discharge, K is conveyance, S is slope of channel bed, g is gravity acceleration, A is area of part, H is height from main channel bed, h is height from bed bottom, n is Manning's coefficient, dx is longitudinal unit length throughout each abscissa, χ is the rate of friction losses to additional losses due to momentum transfer, and R is hydraulic mean depth.

2.4 Lateral Distribution Method (LDM)

The LDM is based on steady-state continuity and momentum depth-averaged equations of motion [2–5]. The following expression is produced by combining both equations and ignoring longitudinal derivatives:

$$\rho g S_0 Y - \frac{f}{8}\rho V^2 \sqrt{1 + \frac{1}{S^2}} + \frac{d}{dy}\left[\rho\lambda\sqrt{\frac{f}{8}}Y^2 V \frac{\partial V}{\partial y}\right] = 0 \tag{9}$$

where ρ = density of liquid; g = gravitational acceleration; Y = flow depth; f = Darcy's friction coefficient; V = depth-mean velocity; S = lateral bed slope; y = lateral coordinate; and λ = non-dimensional Boussinesq eddy viscosity.

2.5 Shiono–Knight Method (SKM)

The SKM approach solves the stream-wise depth-averaged momentum equation for stable uniform turbulent flow. The continuity equation in a prismatic open channel can be combined with the equation for the stream wise component of momentum in a steady uniform flow to give:

$$\rho\left[\frac{\partial UV}{\partial y} + \frac{\partial UW}{\partial z}\right] = \rho g S_0 + \frac{\partial}{\partial y}(-\overline{\rho uv}) + \frac{\partial}{\partial z}(-\overline{\rho uw}) \tag{10}$$

In the above Eq. (10), (U, V, W) are the mean velocity components in the x (stream wise), y (lateral), and z (normal to bed) directions, respectively; (u, v, w) are turbulent velocity fluctuations with respect to the mean, ρ is the density of fluid, g is the gravitational acceleration, and S0 is the slope of bed.

3 Data Source

Experimental data on asymmetric compound channels were gathered for this study from a variety of sources, as shown in Table 1.

Table 1 Geometrical and hydraulic characteristics for experimental compound channels included

Author, tested channel	Flow depth (H), cm	Relative depth (Dr)	Width (B), cm	Flood plain width (B_f), cm	Main channel width (B_m), cm	Sloped wall width (B_s), cm	Slope (S_o), m/m	Manning's coefficient of main channel (n_{mc})	Manning's coefficient of floodplain (n_{fp})
Gemici and Gemici [1]	4.6–10.4	0.41–0.654		15.0	19.0	–	0.003	0.014	0.013
Alawadi et al. [6], SRC-1	4.66	0.23	30.6	15.0	15.6	0	0.001	0.01	0.01
Alawadi et al. [6], SRC-2	5.61	0.36	30.6	15.0	15.6	0	0.001	0.01	0.01
Alawadi et al. [6], SRC-3	7.03	0.49	30.6	15.0	12.0	3.6	0.001	0.01	0.01
Alawadi et al. [6], STC-1	4.74	0.24	30.6	15.0	12.0	3.6	0.001	0.01	0.01
Alawadi et al. [6], STC-2	5.72	0.37	30.6	15.0	12.0	3.6	0.001	0.01	0.01
Alawadi et al. [6] STC-3	7.21	0.5	30.6	15.0	12.0	3.6	0.001	0.01	0.01
Alawadi et al. [6], LC-1	25.5	0.4	91.5	36.5	40.0	15.0	0.001	0.02	0.01
Alawadi et al. [6]), LC-2	31.2	0.51	91.5	36.5	40.0	15.0	0.002	0.02	0.01
Hamidifar et al. [7]	14.7–25.5	0.05–0.45	90	–	45.0	–	0.00088	–	–

4 Methodology

In compound channel, the following methods are generally used for calculation of discharge (Table 2).

5 Results and Discussions

The findings of several discharge prediction systems are summarized in Table 3. Absolute relative error (ARE), Normalized Root Mean Square Error (NRMSE), Mean Error (ME), Mean Absolute Error (MAE), and Mean Percentage Error (MPE) were used to assess the correctness of the estimated values. The RMSE, ME, MAE, and MPE (%) are calculated as follows.

$$\text{ARE} = \frac{Q_{\text{obs},i} - Q_{\text{model},i}}{Q_{\text{obs},i}} \times 100 \tag{11}$$

$$\text{NRMSE} = \frac{\sqrt{\frac{\sum_{i=1}^{n} \left(Q_{\text{model},i} - Q_{\text{obs},i}\right)^2}{n}}}{Q_{\text{obs},\max} - Q_{\text{obs},\min}} \tag{12}$$

$$\text{ME} = \frac{1}{n} \sum_{i=1}^{n} \left| \log_{10} \frac{K_{\text{model},i}}{K_{\text{obs},i}} \right| \tag{13}$$

$$\text{MAE} = \frac{1}{n} \sum_{i=1}^{n} \left| Q_{\text{model},i} - Q_{\text{obs},i} \right| \tag{14}$$

$$\text{MPE} = \frac{1}{n} \sum_{i=1}^{n} \left| \frac{\left| Q_{\text{model},i} - Q_{\text{obs},i} \right|}{Q_{\text{model},i}} \right| \times 100 \tag{15}$$

In the above equations, Q_{obs} and Q_{model} are the observed and predicted values of the channel discharge, i is the experimental run number, n is the number of data, and $Q_{\text{obs},\max}$ and $Q_{\text{obs},\min}$ refer to the maximum and minimum values of Q_{obs}, respectively.

6 Conclusions

In this study, different traditional and numerical methods for predicting rate of flow in an asymmetric compound channel are compared using experimental results. According to Gemici and Gemici [1], for the section and flow parameters employed

Table 2 Range of the variations of discharge for different methods

Author	Discharge (m³/s)					Remarks
	Q_{SCM}	Q_{DCM}	Q_{EDM}	Q_{COHM}	Q_{SKM}	
Gemici and Gemici [1]	0.00809–0.02553	0.00877–0.02657	0.00829–0.02562	–	–	When the main and flood channel side slopes are 90°
	0.00917–0.02524	0.01042–0.02658	0.00983–0.02564	–	–	When the main channel side slope 45° and flood channel side slopes 90°
Alawadi et al. [6], SRC-1	–	–	–	–	2.15×10^{-3}	SRC-1, SRC-2, and SRC-3 were undertaken in a small asymmetric rectangular compound channel, for which $B = 0.306$ m, $L = 12$ m, and $S_0 = 0.001$ m/m
Alawadi et al. [6], SRC-2	–			–	3.62×10^{-3}	
Alawadi et al. [6], SRC-3	–			–	5.73×10^{-3}	
Alawadi et al. [6], STC-1	–			–	1.91×10^{-3}	STC-1, STC-2, and STC-3 were performed using a trapezoidal compound channel whose width and slope are same as SRC
Alawadi et al. [6], STC-2	–			–	3.36×10^{-3}	
Alawadi et al. [6], STC-3	–			–	5.58×10^{-3}	
Alawadi et al. [6], LC-1	– –			–	129.96×10^{-3}	LC-1 and LC-2 are large asymmetric compound channel having width of 0.915 m and slope of 0.002 m/m
Alawadi et al. [6], LC-2	–			–	172.52×10^{-3}	
Hamidifar et al. [7]	$(18.6–66.1) \times 10^{-3}$	$(18.6–66.1) \times 10^{-3}$	$(18.6–66.1) \times 10^{-3}$	$(18.6–66.1) \times 10^{-3}$	$(18.6–66.1) \times 10^{-3}$	For smooth and rough floodplain

Table 3 Different discharge prediction systems' accuracy based on statistical indices

Author	Discharge prediction method	Error					Remark
		ARE	NRMSE	ME	MAE	MPE	
Gemici and Gemici [1]	SCM	7.43	–	–	–	–	When the main and flood channel side slopes are 90°
	DCM	2.32	–	–	–	–	
	EDM	6.42	–	–	–	–	
	SCM	6.96	–	–	–	–	When the main channel side slope is 45° and flood channel side slopes are 90°
	DCM	5.72	–	–	–	–	
	EDM	7.07	–	–	–	–	
Hamidifar et al. [7]	SCM	–	0.135	0.08	0.008	20.161	Smooth floodplain
	DCM-EH	–	0.104	0.058	0.006	14.417	
	DCM-ED	–	0.123	0.062	0.007	15.579	
	DCM-EV	–	0.116	0.052	0.006	12.835	
	DCM-IH	–	0.189	0.138	0.011	37.751	
	DCM-ID	–	0.228	0.154	0.013	42.676	
	DCM-IV	–	0.148	0.066	0.007	16.651	
	COHM	–	0.114	0.053	0.006	12.836	
	SKM	–	0.034	0.021	0.002	4.592	
	Most efficient method	–	SKM	SKM	SKM	SKM	
	SCM	–	0.08	0.061	0.005	15.12	Rough floodplain
	DCM-EH	–	0.099	0.054	0.005	13.589	
	DCM-ED	–	0.090	0.048	0.004	11.666	
	DCM-EV	–	0.056	0.031	0.003	7.242	
	DCM-IH	–	0.173	0.137	0.010	37.548	
	DCM-ID	–	0.182	0.138	0.009	37.304	
	DCM-IV	–	0.084	0.042	0.004	10.090	
	COHM	–	0.070	0.055	0.003	11.334	
	SKM	–	0.033	0.026	0.002	5.700	
	Most efficient method	–	SKM	SKM	SKM	SKM	

Where QSCM = rate of flow calculated by using the single-channel method, QDCM = rate of flow calculated by using the divided-channel method, QEDM = rate of flow calculated by using the Exchange Discharge Method, QCOHM = rate of flow calculated by using the coherence method, QSKM = rate of flow calculated by using the Shiono and Knight Method

in this investigation, DCM provided the best results, whereas EDM provided acceptable errors and SCM computed the rate of flow with significant errors. According to Alawadi et al. [6] and Hamidifar et al. [7], the SKM model is more accurate than the other models evaluated in this study, according to specific statistical performance indices on measured rate of flow such as NRMSE, ME, MAE, and MPE. Based on an overall evaluation of the percentage error of all the approaches evaluated in this research, the SKM can be recommended as the best discharge prediction method in asymmetric compound channels.

References

1. Gemici E, Gemici BT (2018) Computation methods of discharge in compound channels. Int J Nat Eng Sci 12(2):15–19
2. Das BS, Khatua KK, Devi K (2016) Prediction of energy loss in compound channels having enlarging floodplains. In: Constantinescu G, Garcia M, Hanes D (eds) River flow-2016. CRC Press, New York, pp 65–71
3. Das L, Khatua KK, Das BS (2022) Experimental and numerical analyses of boundary shear stress in non-prismatic compound channel. In: River hydraulics: hydraulics, water resources and coastal engineering, vol 2, pp 37–58
4. Das BS, Khatua KK (2018) Numerical method to compute water surface profile for converging compound channel. Arab J Sci Eng 43(10):5349–5364
5. Das BS, Devi K, Proust S, Khatua KK (2018) Flow distribution in diverging compound channels using improved independent subsection method. In: River flow 2018: 9th international conference on fluvial hydraulics, vol 40, article no 05068, p 8
6. Alawadi W, Al-Rekabi WS, Al-Aboodi AH (2018) Application of the Shiono and Knight Method in asymmetric compound channels with different side slopes of the internal wall. Appl Water Sci 8(1):1–10
7. Hamidifar H, Keshavarzi A, Omid MH (2016) Evaluation of 1-D and 2-D models for discharge prediction in straight compound channels with smooth and rough floodplain. Flow Meas Instrum 49:63–69
8. Ackers P (1993) Flow formulae for straight two-stage channels. J Hydraul Res 31(4):509–531
9. Das BS, Khatua KK (2019) Water surface profile computation for compound channel having diverging floodplains. ISH J Hydraulic Eng 25(3):336–349
10. Al-Khatib IA, Dweik AA, Gogus M (2012) Evaluation of separate channel methods for discharge computation in asymmetric compound channels. Flow Meas Instrum 24:19–25
11. Bousmar D, Zech Y (1999) Adequacy of one-dimensional flow modelling in compound channels near critical depth. In: Proceedings of the 28th IAHR Congress, Graz, Austria, pp 22–27
12. Conway P, O'Sullivan JJ, Lambert MF (2013) Stage–discharge prediction in straight compound channels using 3D numerical models. Proc Inst Civil Engineers-Water Manag 166(1):3–15
13. Devi K, Khatua KK (2017) Depth-averaged velocity and boundary shear stress prediction in asymmetric compound channels. Arab J Sci Eng 42(9):3849–3862
14. Shiono K, Knight DW (1988) Two dimensional analytical solution for a compound channel. Paper presented at 3rd International Symposium on Refined Flow Modeling and Turbulence Measurements. Int. Assoc. for Hydraul. Res., Tokyo
15. Shiono K, Knight D W (1989) Vertical and transverse measurements of Reynolds stress in a shear region of a compound channel. In: Proceedings of the Seventh International Symposium on Turbulent Shear Flows, Stanford University, USA, August 28, pp 1–28

16. Shiono K, Knight DW (1990) Mathematical models of flow in two or multi stage straight channels. In: Proceedings of Intenational Conference on River Flood Hydraulics, pp 229–238
17. Shiono K, Knight DW (1991) Turbulent open-channel flows with variable depth across the channel. J Fluid Mech 222:617–646

Analysis of River Bank Erosion–Accretion Process Using Geospatial approach—A Case Study of the Upper Segment of Yamuna River

R. Mittal, S. Said, and M. Beg

Abstract River bank erosion and accretion is one of the concerning intrinsic and dynamic phenomena of any alluvial river that initiates the migration process leading to loss of valuable land adjoining the floodplains. The present study quantifies the extent of bank erosion and accretion along the upper segment of Yamuna River by utilizing time series Landsat images of 40 years' duration (i.e., from 1979 to 2019 with time interval of 10 years). For analysis, the 180 km river segment spanning between Tajewala Barrage and the Wazirabad Barrage was divided into 18 fixed sections at equal intervals of 10 km (i.e., S1 to S18). Results exhibit a decreasing trend in the average areal extent of erosion and an increasing trend in the average areal accretion along both west bank and east bank during the entire assessment period when evaluated with respect to base year 1979. The maximum extent of erosion covering 1200 Ha along west bank was observed at section S10 during 1999 and the same section unveiled lowest erosion coverage of 58.77 Ha during 2019. Likewise, maximum accretion coverage of 1800 Ha was observed at section S6 during 2019 when evaluated with respect to 1979. Moreover, east bank depicted maximum erosion coverage of 1104.06 Ha at S2 during 2019 and maximum accretion coverage of 995.27 Ha at S4 during 1989 evaluated with respect to 1979. The analysis of results further testifies the river behavior as aggrading type and is passing through active accretion phase. The study outcomes can form the basis for setting up spatial guidelines for monitoring and assessing erosion and accretion trends in erodible river banks for sustainable planning and management.

Keywords Yamuna River · Tajewala Barrage · Wazirabad Barrage · Bank erosion and accretion · GIS framework

R. Mittal · S. Said (✉) · M. Beg
Department of Civil Engineering, Aligarh Muslim University (AMU), Aligarh, Uttar Pradesh 202002, India
e-mail: saif_said@rediffmail.com

1 Introduction

River bank erosion and accretion is a natural process of channel evolution which is mainly governed by anthropogenic activities that leads to significant alterations in the river regimes [1]. The process of bank erosion brings about critical implications for short- and long-term channel adaptations pertaining to plan-form changes in river geometry such as meandering, variation in sediment dynamics giving rise to channel braiding, loss of arable land and downstream sedimentation problems like riverine flooding, crop damage, etc. [2]. A better understanding of the mechanism of river bank erosion at spatiotemporal scales is imperative to tackle several geomorphic and river basin management issues [3, 4]. Anthropogenic activities like river bed sand mining, infrastructure development on floodplains, bank revetment, construction of reservoirs, and land use alterations have gradually but significantly changed the geomorphological dynamics of alluvial rivers [5–8]. As a result, channel stability is highly endangered [8]. Moreover, the channel experiences morphological adjustments so as to accommodate variations in flow discharge and sediment loads approaching from the upstream river section [9].

Studies involving river bank erosion analysis are generally carried out by employing either direct or indirect methods. The direct method relates to in situ field measurements in terms of areal extent of erosion coverage, magnitude of erosion, and changes in channel cross-section at selected point locations. The indirect method involves river analysis at spatial scales by utilizing archival as well as present data sources at different time spans. The spatial data sources can be in the form of conventional topographical maps, aerial photos, or satellite images. During the past two decades, satellite remote sensing (RS) coupled with Geographical Information System (GIS) technique has proven to be crucial toward providing precise and valuable information at spatiotemporal scales for creating geospatial database and carrying out river morphological studies [10, 11]. Furthermore, multi-temporal high-resolution satellite images provide synoptic coverage of the existing river configuration, shifting in river courses, formation of new channels and oxbow lakes, bank erosion and deposition, etc., that can be analyzed and mapped at different spatial scales [12, 13].

A large number of studies utilizing satellite images at different spatiotemporal, radiometric, and spectral resolutions have been conducted worldwide on river reaches with unstable and erodible banks and have been well documented in the published literature [14–20]. Baki et al. [21] investigated braided Jamuna River bank migration and island dynamics by utilizing LANDSAT MSS and TM images acquired from 1973 to 2003. It was observed that several critical river sections experiencing severe erosion and accretion along both the river banks. Hassan and Mahmud-ul-islam [22] utilized Landsat-TM-5 and Landsat 8 images of year 1989 and 2015 which were employed to identify alterations in land use practice, river bank erosion, and bar deposition in Chowhali Upazila, Sirajganj district of Bangladesh. Study revealed 1340 hectare within the study area to have been eroded, whereas 630 hectares were deposited as channel bar over a span of 26 years. Ait Mlouk et al. [23] estimated the

bank heights of Rdat River located in the southeast of Marrakech in Morocco, so as to evaluate the rate of contribution of river bank erosion to the river sediment load from 1984 to 2016 by utilizing Landsat images and the ALOS PALSAR elevation data. Binh et al. [24] developed a novel Spectral RB Erosion Detection (SRBED) technique and proposed Modified Automated Method for Extracting Rivers and Lakes (M-AMERL) a river bank change detection algorithm by utilizing Landsat data in the Vietnamese Mekong Delta. Results revealed an accelerated river bank erosion during 2008–2014, attributed to increased sand mining activities, construction of dams upstream, and a shift in the trend of tropical cyclones. The present study was undertaken with an objective to evaluate the spatiotemporal areal coverage of riverbank erosion and accretion along the upper segment of Yamuna River by utilizing Landsat images spanning over a period of 40 years (i.e., from 1979 to 2019 with time interval of 10 years). The objective was followed by generating erosion accretion maps in GIS framework and quantified the total and average river bank erosion accretion during the assessment period. The monitoring of river bank erosion and accretion spatiotemporal scales is crucial for sustainable management unstable floodplains.

2   Study Area and Data Source

2.1   Yamuna River (Upper Segment)

River Yamuna, the largest tributary of the river Ganges, originates from the Yamunotri glacier near Bandar Punch in the lower Himalayan ranges, traversing a total distance of 1376 km from origin to its confluence with river Ganges at Allahabad in Uttar Pradesh. On the basis of hydrological and ecological conditions, the entire length of Yamuna River has been categorized into five segments, namely, Himalayan segment (172 km), upper segment (224 km), Delhi segment (22 km), Eutriphicated segment (190 km), and the diluted segment (468 km) [25], and each segment amounts to varying degrees of erosion and accretion depending upon the physiography of the region and flow discharge in the river. In the Himalayan segment (from Yamunotri glacier to Tajewala Barrage), the problem of river bank erosion and accretion is controlled due to boulders and rocks confining the river valley but significant resulting in enormous sediment yield in the downstream due to high stream energy [26]. The remaining four segments lie in the alluvial plans and account for the channel planform alterations, such as bank line shifting, bank erosion, and sediment accretion, on account of typical alluvial characteristics [27]. At some sections, the rate of erosion and accretion is relatively less because of low stream energy of flow and sediment discharge, whereas some river sections witness relatively high rates of erosion and accretion owing to high stream energy and sediment loads. The present study area covers the upper segment of the Yamuna River, spanning between Tajewala (at present Hathni Kund) Barrage in Yamuna Nagar district of Haryana state and Wazirabad Barrage near Palla village bordering Delhi state, traversing a length of 224 km and
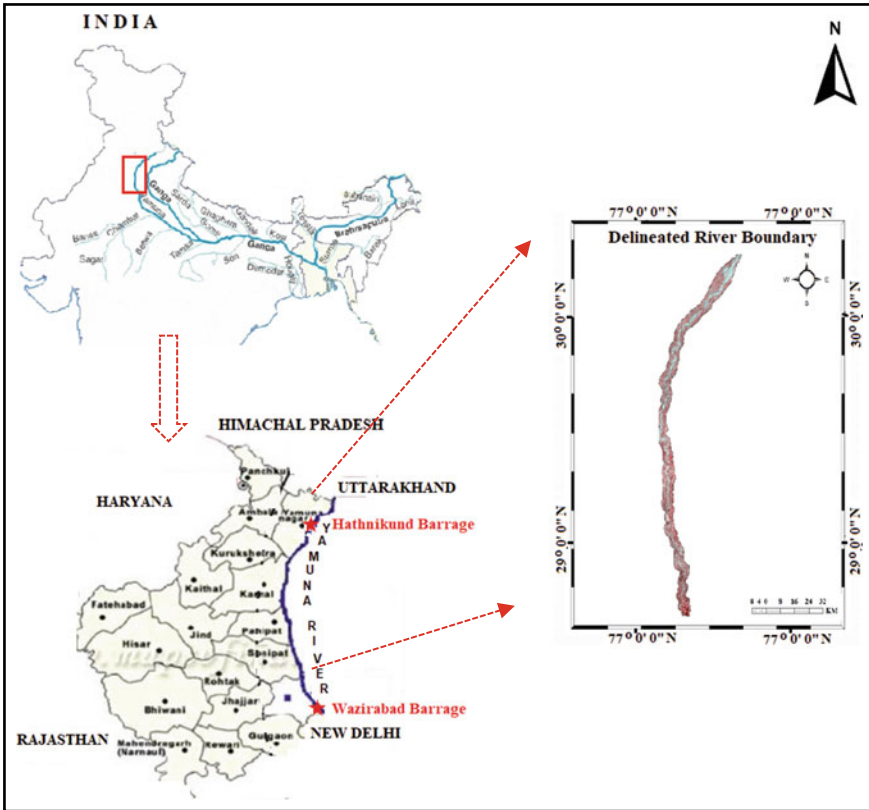
Fig. 1 Location map of the study area

confined within latitude 28.71° N to 30.31° N and longitude 78.23° E to 78.58° E (Fig. 1).

During the summer season, nearly 90% of inflow at Hathni Kund barrage is diverted to Western Yamuna canal and Eastern Yamuna canal for irrigation, thus leaving the river downstream in almost dry state. The river basin receives rainfall under the influence of southwest monsoon with maximum rainfall during June to September and a scanty winter rainfall. Temperatures are relatively moderate and range from 45 °C during summer (late May–June), to an average of 2°–9 °C during winters, and receive moderate-to-less rainfall during monsoon. The river bed comprising the upper segment is primarily sandy in texture and constitutes sand proportion in the range from 70.52 to 74.76%, silt 17.74 to 18.56%, and clay 7.35 to 11.55%. The region's economy is mainly governed by agriculture based on intensive cultivation and crop rotation with primary agricultural crops being wheat, rice, and sugarcane.

2.2 Data Used

To quantify the decadal spatiotemporal bank erosion and accretion process in the upper segment of Yamuna River, the study utilized a series of five moderate resolution Landsat images for the year 1979, 1989, 1999, 2009, and 2019 downloaded from the US Geological Survey (USGS) EarthExplorer portal. The details of satellite images used are provided in Table 1, and the mosaicked Landsat scenes covering the study area are shown in Fig. 2. The Landsat images were projected in the Universal Transverse Mercator (UTM) projection system with zone 43E and World Geodetic Survey 1984 (WGS84) datum.

Figure 3 illustrates the schematic workflow of methodology adopted in the present study to quantify the erosion and accretion process that has taken place in the upper segment of Yamuna River during the last four decades.

The individual band layers of Landsat images were stacked, resampled, subjected to quality enhancement and radiometric corrections so as to make the images free of inconsistencies and easily interpretable in ERDAS Imagine software. Radiometric corrections are necessary for change detection studies where temporal data are used

Table 1 Specifications of the satellite data used in the study

S. No.	Satellite	Sensor	Number of bands	Year of acquisition	Spatial resolution (m)	Source
1	Landsat 3	MSS	4	1979	60	USGS
2	Landsat 5	MSS	4	1989	30	USGS
3	Landsat 5	TM	7	1999	30	USGS
4	Landsat 5	TM	7	2009	30	USGS
5	Landsat 8	OLI/TIRS	11	2019	30	USGS

a	b	c	d	e
B 7: NIR (0.8-1.1 µm) B 6: NIR (0.7-0.8 µm) B 4: Visible (0.5-0.6 µm)	B 5: NIR (1.55-1.75 µm) B 4: NIR (0.76-0.9 µm) B 3: Visible (0.63-0.69 µm)	B 5: NIR (1.55-1.75 µm) B 4: NIR (0.76-0.9 µm) B 3: Visible (0.63-0.69 µm)	B 5: NIR (1.55-1.75 µm) B 4: NIR (0.76-0.9 µm) B 3: Visible (0.63-0.69 µm)	B 5: NIR (0.85-0.88 µm) B 4: Red (0.64-0.67 µm) B 3: Green (0.53-0.59 µm)
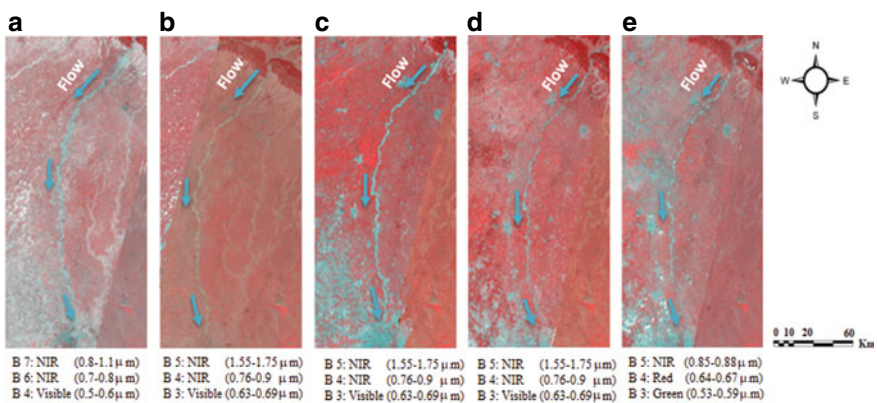
Fig. 2 Landsat images utilized in the study **a** 1979 Landsat 3 MSS **b** 1989 Landsat 5 MSS **c** 1999 Landsat-TM **d** 2009 Landsat-TM **e** 2019 Landsat-OLI/TIRS
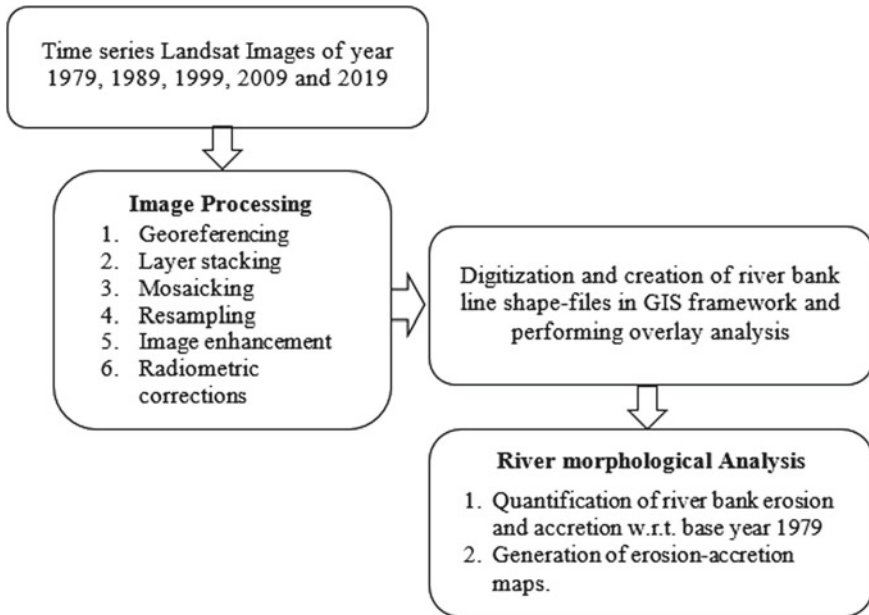
Fig. 3 Flow chart of methodology adopted in the study

so as to reduce inconsistencies inherent in the images due to variations in sun zenith angles. Therefore, radiometric normalization was performed before mosaicking the images by histogram equalization and matching to get uniform brightness levels and seamless boundaries between two or more images of the same year. All the selected images were acquired during the dry season when minimal haze and no clouds were present at the time of the survey, and therefore, no atmospheric correction was applied to the images. The bank lines (east and west) of the river segment for all assessment years were extracted via on-screen digitization in ArcGIS software and layers of polylines (vector) in shape file format were generated. The shape files were overlaid to generate the statistics of overall areal extent of erosion and accretion with respect to the earliest image under consideration as the base year (i.e., Landsat MSS 1979).

The erosion and accretion of the river banks were analyzed along 18 fixed sections at equal distance from north to south (i.e., S1 to S18). The results revealed the critical locations within each section where moderate-to-high erosion and accretion occurred during the assessment period and the areal extent of coverage is illustrated as spatially distributed erosion accretion maps. The remote sensing and a GIS-based approach utilized in the study unveiled substantial changes in the fluvial land form during the assessment years, resulting in significant inhabited land loss.

3 Results and Discussions

Based on visual interpretation of satellite images, river bank lines for the assessment years were digitized in GIS framework and overlaid to assess the extent of erosion and accretion along the study reach. The extent of river bank erosion and accretion was measured along 18 fixed sections with respect to the base year 1979, and results are presented in Table 2 and 3 and graphically illustrated as bar graphs in Figs. 4 and 5. Figure 6 exhibits maps of overlaid river bank lines depicting areal erosion and accretion for all assessment years with respect to the base year 1979.

Results in Table 2 reveal that the average areal extent of west bank erosion for all assessment years is relatively less when compared with the east bank erosion that quantified the maximum average extent of order 359.53 ha during 1989. Moreover, the maximum erosion extent of 1200 ha and 1150 ha was observed at section S10 along the west bank during 1999 and 1989, respectively, and the same section revealed

Table 2 River bank erosion during the assessment years with respect to base year 1979

Sections (km)		River bank erosion with respect to base year 1979 (ha)							
		1989		1999		2009		2019	
		West	East	West	East	West	East	West	East
S1	0–10	16.26	6.22	40.96	1.12	37.59	48.39	0.39	0.00
S2	10:20	247.98	1.30	40.59	2.01	280.17	3.09	214.69	0.50
S3	20–30	53.85	800.00	327.39	195.51	131.68	63.93	118.81	56.21
S4	30–40	1.31	995.27	14.26	551.70	2.48	764.88	2.48	315.83
S5	40–50	201.92	753.38	327.00	651.39	211.00	492.02	136.55	201.89
S6	50–60	64.68	525.71	57.64	800.00	29.63	622.26	100.94	870.44
S7	60–70	250.01	450.00	210.00	614.68	188.66	434.81	107.95	350.00
S8	70–80	55.28	600.00	77.74	307.94	17.71	221.98	20.79	349.00
S9	80–90	236.50	322.53	201.67	241.40	330.36	258.97	143.98	22.20
S10	90–100	1150.00	60.64	1200.00	84.44	368.95	68.95	58.77	84.20
S11	100–110	98.05	57.36	110.20	175.49	47.07	35.35	32.72	0.00
S12	110–120	153.98	228.98	82.24	274.52	68.52	351.28	49.55	452.87
S13	120–130	394.95	267.19	403.19	305.97	367.11	315.33	351.72	315.75
S14	130–140	105.67	99.58	204.29	91.04	228.64	85.87	93.50	166.23
S15	140–150	197.16	88.84	68.01	53.99	85.54	49.33	128.69	33.26
S16	150–160	263.04	226.78	156.51	153.35	170.54	88.67	193.31	170.40
S17	160–170	238.61	511.31	123.30	355.28	102.46	305.72	173.58	197.37
S18	170–180	193.51	476.48	318.91	429.72	164.63	416.97	425.02	389.49
Average erosion (ha)		**217.93**	**359.53**	**220.22**	**293.86**	**164.63**	**257.10**	**130.75**	**220.87**
Maximum erosion (ha)		**1150**	**995.27**	**1200**	**800.00**	**368.95**	**764.88**	**425.02**	**870.44**

Table 3 River bank accretion during the assessment years with respect to base year 1979

Sections (km)		River bank accretion with respect to base year 1979 (ha)							
		1989		1999		2009		2019	
		West	East	West	East	West	East	West	East
S1	0–10	62.19	76.47	67.34	110.38	235.89	116.12	306.84	520.61
S2	10–20	0.13	366.62	9.98	363.43	1.65	594.29	36.87	1104.06
S3	20–30	246.24	300.00	282.79	843.28	364.21	1023.49	513.81	1045.05
S4	30–40	634.41	20.69	948.05	140.16	1248.66	334.75	1062.33	626.11
S5	40–50	404.40	200.00	768.44	392.59	723.12	569.94	873.30	634.96
S6	50–60	418.31	55.14	729.73	100.00	1148.19	121.72	1800.00	200.00
S7	60–70	365.41	108.43	900.00	161.92	1000.43	507.07	1284.40	808.19
S8	70–80	673.64	0.00	786.85	70.51	941.50	192.77	1166.97	135.70
S9	80–90	188.07	270.46	277.86	338.26	302.05	519.54	551.73	769.70
S10	90–100	45.56	377.31	40.24	623.19	506.93	403.19	635.93	340.01
S11	100–110	225.15	195.43	300.62	212.26	567.34	249.95	548.42	504.64
S12	110–120	87.66	8.39	438.94	272.08	620.05	358.20	632.21	677.04
S13	120–130	210.07	68.56	692.87	944.35	809.52	891.53	795.69	882.19
S14	130–140	80.03	202.40	119.74	180.76	372.68	380.75	473.18	385.79
S15	140–150	38.02	5.29	192.38	63.06	245.08	387.44	258.38	460.61
S16	150–160	86.66	2.35	428.09	174.11	573.58	275.57	561.81	273.32
S17	160–170	50.38	4.53	219.66	65.95	283.21	368.35	176.37	161.09
S18	170–180	431.10	55.43	557.46	313.42	567.45	161.08	466.96	575.92
Average accretion (ha)		**235.97**	**128.75**	**431.17**	**298.32**	**583.97**	**414.21**	**674.73**	**561.39**
Maximum accretion (ha)		**673.64**	**377.31**	**948.05**	**944.35**	**1248.66**	**1023.49**	**1800**	**1104.06**
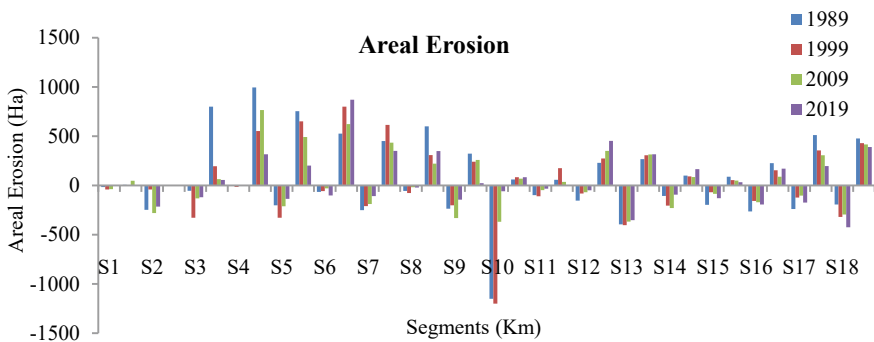
Fig. 4 River bank erosion during assessment years 1989, 1999, 2009, and 2019 with respect to base year 1979
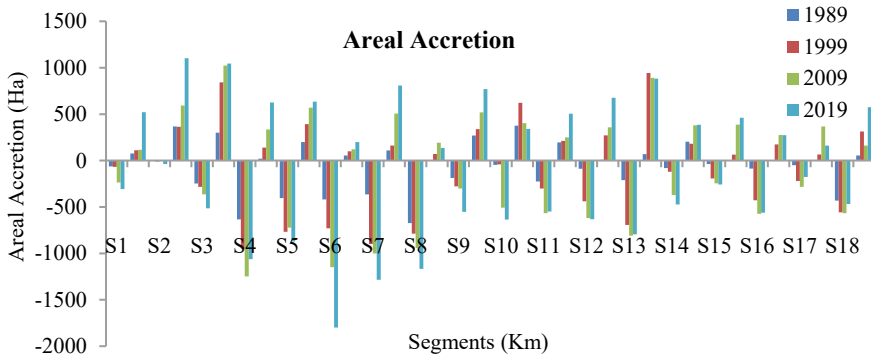
Fig. 5 River bank accretion during assessment years 1989, 1999, 2009, and 2019 with respect to base year 1979

considerably reduced erosion coverage during the successive assessment years, i.e., 2009 and 2019. It was further observed that the maximum areal erosion along the east bank remained almost consistent at sections S4 and S6 during the entire assessment period with erosion coverage of 995.27 ha, 764.88 ha, 800.00 ha, and 870.44 ha, respectively.

Further, Table 3 exhibits the extent of average accretion coverage along west bank to be relatively higher than at the east bank which is also clearly revealed in Fig. 5. Results are also indicative of the fact that the average extent of accretion along both banks exhibits an increasing trend for each successive assessment year. The maximum average accretion coverage was observed during 2019 that covered an aerial extent of 674.73 ha along west bank and 561.39 ha along east bank. Furthermore, the maximum accretion coverage of order 1800 ha was observed at section S6 along the west bank and during the assessment year 2019. Table 4 provides an overall erosion and accretion coverage along both river banks and the annual rate of change with respect to base year 1979.

It can be inferred from Table 4 that there is a continual decrement in overall erosion coverage along both river banks and a continual increase in an overall accretion coverage during the entire assessment period. The overall erosion extent at both banks ranged from 10,394.34 ha to 6329.07 ha from 1979 to 2019, whereas overall accretion at both banks ranged from 6564.94 ha to 22,250.23 ha during the assessment period. However, the annual rate for both erosion and accretion coverage showed a declining trend throughout the assessment years that can be attributed to anthropogenic activities, change in land use practice as well as large variation in flow discharge during monsoon and non-monsoon season.

There are several factors responsible for the erosion and accretion dynamics in the study area. Among these factors, variation in flow discharge, stratigraphy of the river banks, geometry of the channel, and sediment concentration in flow discharge are some of the significant factors affecting the river dynamics. The large variation in flow discharge induces weakening in the cohesive strength of the soil comprising

Fig. 6 River bank erosion and accretion during assessment year **a** 1989 **b** 1999 **c** 2009 and **d** 2019 with respect to base year 1979

(a)

(b)

Fig. 6 (continued)

(c)
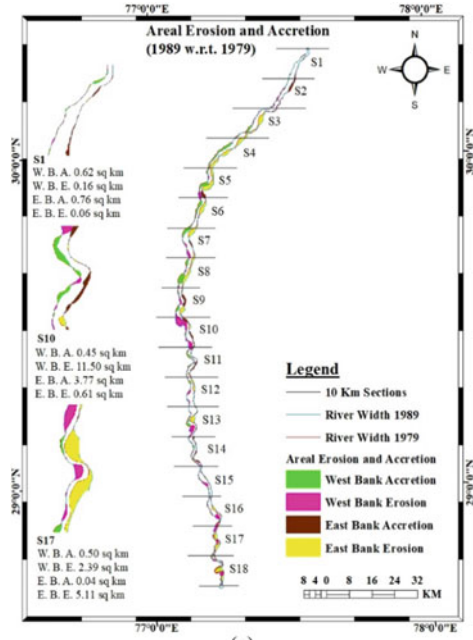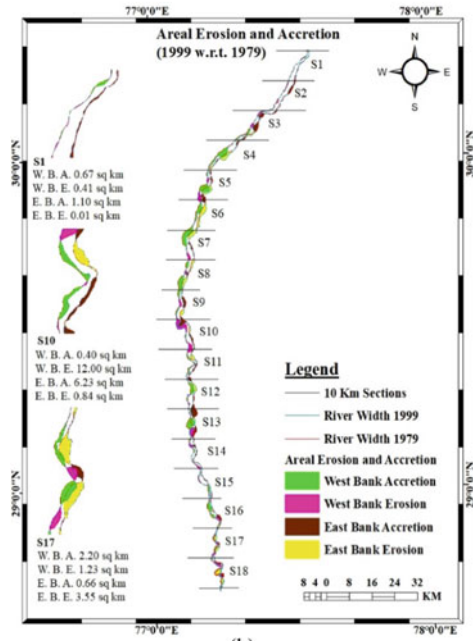
(d)
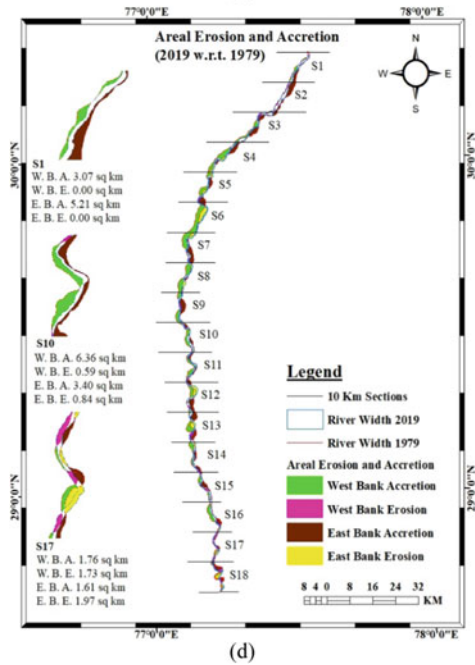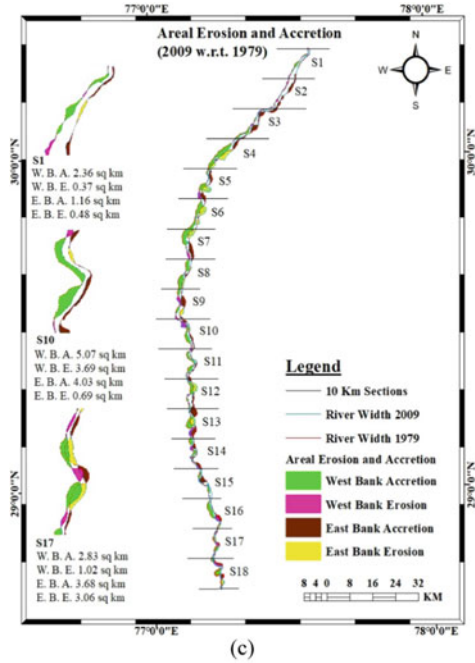
Table 4 Overall and rate of erosion and accretion coverage during the assessment years

Assessment year with respect to 1979	River bank	Erosion		Accretion	
		Overall (Ha)	Rate (Ha/yr)	Overall (Ha)	Rate (Ha/yr)
1989	West	3922.77	392.277	4247.43	424.743
	East	6471.57	647.157	2317.51	231.751
	Entire stretch	10,394.34	1039.434	6564.94	656.494
1999	West	3963.91	198.1955	7761.05	388.0525
	East	5289.55	264.4775	5369.71	268.4855
	Entire stretch	9253.46	462.673	13,130.76	656.538
2009	West	2963.41	98.78033	10,511.54	350.3847
	East	4627.78	154.2593	7455.74	248.5247
	Entire stretch	7591.19	253.0397	17,967.28	598.9093
2019	West	2353.44	58.836	12,145.22	303.6305
	East	3975.63	99.39075	10,105.01	252.6253
	Entire stretch	6329.07	158.2268	22,250.23	556.2558

river banks and eventually causes the undercutting of the banks that leads to erosion. The river bed comprising study area comprises alluvium composed of sand derived from basaltic rocks and also have large proportions silt. The problem of siltation due to the construction of Hathni Kund barrage has increased at the downstream and thereby decreasing the channel depth. During the monsoon season, the shallow depth is less capable of carrying higher discharge which ultimately creates pressure on the banks leading to erosion. Apart from the barrage, long-term land use change toward east and west banks has greatly influenced the magnitude of erosion. The above analysis of results provides a logical justification to conclude river behavior as aggrading type.

4   Conclusions

Spatial analysis of time series river bank erosion and accretion process furnishes framework for implementing efficient flood management and river rejuvenation programs. The present study utilizes five Landsat images covering a decadal period of 40 years (i.e., 1979, 1989, 1999, 2009, and 2019) to evaluate the areal extent erosion and accretion along the upper segment of Yamuna River spanning 180 km between Hathni Kund barrage in Yamuna Nagar, Haryana, and the Wazirabad Barrage in the northern peripheral of Delhi state. The specific conclusions drawn from the study are enumerated as:

- The average erosion coverage along east bank was relatively higher than the erosion coverage witnessed along the west bank.

- The maximum erosion extent of order 1200 ha and 1150 ha was observed at section S10 along the west bank during 1999 and 1989, respectively.
- The maximum extent of accretion was noticed at section S6 of order 1800 ha along the west bank during 2019.
- Throughout the assessment period and for both seasons, the annual rate of erosion and accretion on both river banks exhibited a decreasing trend.
- The overall analysis unveiled river behavior as aggrading type.

The wide range of flow discharge releases from the Hathni Kund barrage, which can be as high as 7079 m^3/s during floods, causes the soil on the riverbanks to lose its ability to hold together, which leads to the erosion of the banks. However, large river training structures along both banks have assisted to protect the banks from erosion. In contrast, the large volumes of sediment carried by flood flows cause sediment deposition downstream along the river segment's bed and banks.

Moreover, the considerable reduction in river discharge during lean season at the downstream of Hathni Kund barrage over last several years in conjunction with unplanned human interventions on the active floodplains has significantly altered the erosion and accretion rates within the river segment. Study outcomes further testify the efficiency and resourcefulness of GIS and remote sensing technique toward time series assessment of the spatial extent of erosion and accretion along the river banks so as to initiate long-term erosion protection measures along the unstable alluvial river banks. In order to predict the future development of the fluvial landscape, further study is needed to integrate fluvial processes with socio-economic aspects.

References

1. Sarkar A, Garg RD, and Sharma N (2012) RS-GIS based assessment of river dynamics of Brahmaputra River in India. J Water Resour Prot 4(2):63–71. https://doi.org/10.4236/jwarp.2012.420082; Kannan S, Ghosh S (2011) Prediction of daily rainfall state in a river basin using statistical downscaling from GCM output. Stochast Environ Res Risk Assess 25(4):457–474

2. Downs PW, Simon A (2001) Fluvial geomorphological analysis of the recruitment of large woody debris in the Yalobusha river network, Central Mississippi, USA. Geomorphology 37(1):65–91. https://doi.org/10.1016/S0169-555X(00)00063-5

3. Thakur PK, Laha C, Aggarwal SP (2012) River bank erosion hazard study of river Ganga, upstream of Farakka barrage using remote sensing and GIS. Nat Hazards 61:967–987. https://doi.org/10.1007/s11069-011-9944-z

4. Debnath J, Das N, Ahmed I, Bhowmik M (2017) Channel migration and its impact on land use/land cover using RS and GIS: a study on Khowai River of Tripura, North–East India. Egypt J Remote Sens Space Sci 20(2):197–210. https://doi.org/10.1016/j.ejrs.2017.01.009

5. Lane SN, Richards KS (1997) Linking river channel form and process: time, space and causality revisited. Earth Surf Proc Land 22(3):249–260. https://doi.org/10.1002/(SICI)1096-9837(199703)22:3<249::AID-ESP... >3.0.CO;2-7

6. Surian N (1999) Channel changes due to river regulation: the case of the Piave River, Italy. Earth Surf Process Land 24(12):1135–1151. https://doi.org/10.1002/(SICI)1096-9837(199911)24:12<1135::AID-ESP40>3.0.CO;2-F

7. Fuller IC, Large ARG, Milan DJ (2003) Quantifying channel development and sediment transfer following chute-off in a wandering gravel-bed river. Geomorphology 54(3–4):307–323. https://doi.org/10.1016/S0169-555X(02)00374-4

8. Dewan A, Corner R, Saleem A, Rahman MM, Haider MR, Rahman MM, Sarker MH (2016) Assessing channel changes of the Ganges-Padma River system in Bangladesh using Landsat and hydrological data. Geomorphology 276:257–279. https://doi.org/10.1016/j.geomorph.2016.10.017

9. Khan NI, Islam A (2003) Quantification of erosion patterns in the Brahmaputra-Jamuna River using geographical information system and remote sensing techniques. Hydrol Process 17(5):959–966. https://doi.org/10.1002/hyp.1173

10. Rinaldi M, Surian N, Comiti F, Bussettini M (2013) A method for the assessment and analysis of the hydromorphological condition of Italian streams: the Morphological Quality Index (MQI). Geomorphology 180–181:96–108. https://doi.org/10.1016/j.geomorph.2012.09.009

11. Langat PK, Kumar L, Koech R (2018) Understanding water and land use within Tana and Athi River Basins in Kenya: opportunities for improvement. Sustain Water Resour Manage 5(3):977–987. https://doi.org/10.1007/s40899-018-0274-0

12. Wang S, Mei Y (2016) Lateral erosion/accretion area and shrinkage rate of the Linhe reach braided channel of the Yellow River between 1977 and 2014. J Geog Sci 26(11):1579–1592. https://doi.org/10.1007/s11442-016-1345-5

13. Wang B, Xu YJ (2018) Dynamics of 30 large channel bars in the lower Mississippi River in response to river engineering from 1985 to 2015. Geomorphology 300:31–44. https://doi.org/10.1016/j.geomorph.2017.09.041

14. Lawler DM (1993) The measurement of riverbank erosion and lateral channel change: a review. Earth Surf Proc Land 18(9):777–821. https://doi.org/10.1002/esp.3290180905

15. Thomas DP, Gupta SC, Bauer ME, Kirchoff CE (2005) Airborne laser scanning for riverbank erosion assessment. Remote Sens Environ 95(4):493–501. https://doi.org/10.1016/j.rse.2005.01.012

16. Wilson GV, Periketi R, Fox GA, Dabney S, Shields D, Cullum RF (2007) Soil properties controlling seepage erosion contributions to river bank failure. Earth Surf Proc Land 32(3):447–459

17. Belmont P, Gran KB, Schottler SP, Wilcock PR, Day SS, Jennings C, Lauer JW, Viparelli OE, Willenbring JK, Engstrom DR, Parker G (2011) Large shift in source of fine sediment in the upper Mississippi River. Environ Sci Technol 45(20):8804–8810. https://doi.org/10.1021/es2019109

18. Kessler AC, Gupta SC, Dolliver HAS, Thomas DP (2012) LIDAR quantification of bank erosion in Blue Earth County, Minnesota. J Environ Qual 41(1):197–207. https://doi.org/10.2134/jeq2011.0181

19. Lovric N, Tosic R (2016) Assessment of bank erosion, accretion and channel shifting using remote sensing and GIS: case study—lower course of the Bosna River. Quaestiones Geographicae 35(1):81–92. https://doi.org/10.1515/quageo-2016-0008

20. Mahmoodzada AB et al (2019) Monitoring of riverbank erosion and shoreline movement at Amu River using remote sensing and GIS: a case study in Jowzjan, Afghanistan. Int J Environ Rural Dev 10(1):140–145. http://iserd.net/ijerd101/10-1-23.pdf

21. Baki ABM, Gan TY (2012) Riverbank migration and island dynamics of the braided Jamuna River of the Ganges Brahmaputra basin using multi-temporal Landsat images. Quatern Int 263:146–161. https://doi.org/10.1016/j.quaint.2012.03.016

22. Hassan MS, Mahmud-ul-islam S (2016) Quantification of river bank erosion and bar deposition in Chowhali Upazila, Sirajganj district of Bangladesh: a remote sensing study. J Geosci Environ Prot 4(1):50–57. https://doi.org/10.4236/gep.2016.41006

23. Ait Mlouk M, Algouti A, Algouti A, Ourhzif Z (2018) Assessment of river bank erosion in semi-arid climate regions using remote sensing and GIS data: a case study of Rdat River, Marrakech, Morocco. Estud Geol 74(2):e081. https://doi.org/10.3989/egeol.43217.493
24. Binh DV, Wietlisbach B, Kantoush S, Loc HH, Park E, Cesare G, Cuong DH, Tung NX, Sumi T (2020) A novel method for river bank detection from Landsat satellite data: a case study in the Vietnamese Mekong delta. Remote Sens (MDPI) 12(20):3298. https://doi.org/10.3390/rs12203298
25. Central Water Commission (CWC) (2009) Yamuna basin organization, 2009. http://www.cwc.nic.in/regional/delhi/welcome.html
26. Sinha R, Jain V, Babu GP, Ghosh S (2005) Geomorphic characterization and diversity of the fluvial systems of the Gangetic plains. Geomorphology 70(3–4):207–225. https://doi.org/10.1016/j.geomorph.2005.02.006
27. Yunus AP, Jie D, Armugha K, Sravanthi N, Liaqat AKR, Chen H (2019) Channel migration characteristics of the Yamuna River from 1954 to 2015 in the vicinity of Agra, India: a case study using remote sensing and GIS. Int J River Basin Manage 17(3):365–375. https://doi.org/10.1080/15715124.2019.1566238

Study of Morphological Changes of River Ganga at the Confluence of River Kosi

Chandan Raj and Vivekanand Singh

Abstract Morphology of the alluvial river changes from time to time due to the natural autogenic processes. Confluence of two alluvial rivers is very sensitive and is more prone to change in its morphology. Formation of fluvial island is an integral part of sediment transfer process to maintain equilibrium. Change in planform, formation of fluvial islands and sandbars, and sinuosity are intensified at the confluence of rivers, which carry heavy sediment load. In present study, temporal changes in morphology of river at confluence zone of river Ganga and Kosi have been investigated using Landsat data from the year 2000 to 2020 at the interval of 5 years. Planform and fluvial islands have been mapped by Normalized Difference Water Index (NDWI) and classification of the satellite image. Accuracy assessment was performed to ensure mapping accuracy. Change in planform and morphological parameters (Sinuosity Index (SI), Braiding Index (BI), and River Network Change Index (RNCI)) has been computed and analyzed. Study reveals that the planform and courses of braided channels have been changed frequently in due course of time. The confluence point has been shifted by 1.5 km toward the left bank. SI has an increasing trend during study period, and it shows meandering at the confluence. BI has also been changed without any specific trend. RNCI shows that the amount of total erosion is almost equal to total deposition in study reach. However, both erosion as well as deposition was more on its left bank side compared to right bank side. The fluvial island at confluence of two highly sediment-loaded rivers is sensitive to spatial change. Monitoring of change in morphology may provide a useful reference for decision-making of flood warning to human settlements present on river island and nearby banks.

Keywords Ganga River · Morphological change · Fluvial Island · NDWI · Confluence of Ganga and Kosi Rivers

C. Raj (✉) · V. Singh
Department of Civil Engineering, National Institute of Technology Patna, Patna, Bihar 800005, India
e-mail: chandan.ce16@nitp.ac.in

V. Singh
e-mail: vsingh@nitp.ac.in

1   Introduction

The river morphology is associated with the physical shape of the river channels and their changes over time [1]. Morphological changes of the river are dependent on various variables such as topography, hydrological condition, vegetation, sediment supply. Stability of river and its response to the changing environment are highly dependent on local circumstances (joining of tributary, type of river, essence of the imposed sediment, vegetation and hydrologic regimes, and effects of natural and anthropogenic disturbances in past). Alluvial rivers are dynamic, and its channel shape and flow pattern change frequently depending upon the local context. River is usually joined by several tributaries at different stages of the river. Confluence of river refers to the point where a tributary joins a major river or mainstream. When tributary of sediment-laden discharge and different hydrological properties join a river, the zone of confluence undergoes more frequent changes. Rate of planform and morphological changes in confluence zone get intensified.

Confluence of river is the key features of the basin, as their hydrological, ecological, and geomorphological nature strongly influences river characteristics in the downstream. Several hydrologists, water resources experts, and researches have studied the morphological changes in different rivers in the world [2–9]. Morphological changes were mostly studied for mapping natural and autogenic geomorphological change [9–11] or to look into changes due to human interventions on its natural flow [12–15]. Study of morphological changes in river due to joining tributary is rare. Bidirectional flow in river near confluence zone and dynamic morphology makes the study of confluences more complex and interesting. Confluence zone of river undergoes frequent morphological changes due to sudden variation of hydrological features in the river. The confluence zone of a tributary in an alluvial river is highly sensitive to planform and morphological changes. In light of its importance, more attention is expected to morphology of river, sediment, and interaction of flow at confluence zone.

Present study demonstrates the changes in morphology at confluence zone of the Kosi River in the Ganga River. Objective of this paper is to compute and analyze planform change in the Ganga River at confluence zone of Kosi River by analyzing Landsat images. Planform of river and morphological parameters such as Sinuosity Index (SI), Braiding Index (BI), and River Network Change Index (RNCI) are computed from year 2000 to 2020 at intervals of 5 years using remote sensing and GIS technique.

2   Study Area

The Ganga is the largest river in Indian subcontinent in terms of water. The river originates from Gaumukh of Himalayan ranges in the state of Uttarakhand and meets Bay of Bengal at Ganga Sagar, West Bengal, flowing a distance 2510 km

through several states (Uttarakhand, Uttar Pradesh, Bihar, Jharkhand, and West Bengal) [16]. Many tributaries meet Ganga on flowing downhill such as Alaknanda, Mandakini, Chambal, Betwa, Yamuna, Ghaghra, Sone, Gandak, Kosi, Fulhar. The Ganga possesses different hydrological and morphological characteristics at different stages on flowing through different types of topography. The stretch of Ganga River at confluence of the Kosi into Ganga River has been considered for this study (Fig. 1).

Study reach has been considered from Kahalgaon to 28.5 km in length when measured along the left channel of the river. The Ganga River flows in curvilinear path flowing along the plateaus of Chhota Nagpur Plateau. The river is flowing in single channel while entering in study reach and leaving the study reach. It is bifurcated into two major channels, and a large island is embedded in between the two channels. Several small sandbars are presented in the stretch. The Kosi River is joining its left channel at Kursela. Kosi River originates from Himalayan range in Nepal. It carries huge discharge and sediment load particularly in Monsoon season. The island between the bifurcated channels is vegetated and permanent, and hence,
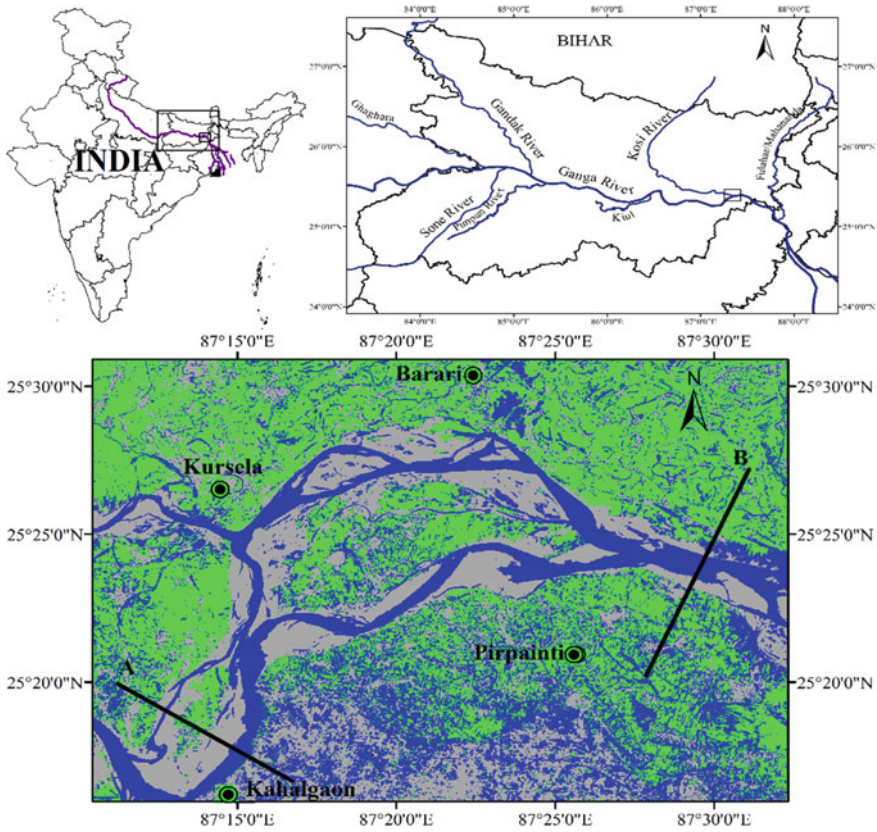
Fig. 1 Study reach: stretch of river Ganga at confluence of the Kosi River

Table 1 Details of multi-temporal Landsat data with date of image, resolution, source, and path/row

Satellite	Date of image	Resolution (m)	Source	Path/row
Landsat 5	21/March/2000	30	USGS	139/042, 139/043
Landsat 5	03/March/2005	30		
Landsat 5	13/March/2010	30		
Landsat 8	15/March/2015	30		
Landsat 8	28/March/2020	30		

it hosts population and agricultural activity. Land is mostly used for agriculture on both sides of the river.

3 Data and Methods

3.1 Data Used

This study used multi-temporal Landsat data form year 2000 to 2020 at an interval of 5 years. These data were collected from website of US Geological Survey (USGS) (http://earthexplorer.usgs.gov/). Only dry season (January–March) images have been selected on the basis of availability and free from clouds. Water remains normal in river, and sky is mostly cloud free in dry season [17]. Details of the data used for study are presented in Table 1.

3.2 Image Processing

Landsat image of year 2000 has been selected as reference image for beginning of study. This image has been checked for positional errors considering Toposheet as the reference. However, Landsat images have already been processed for precision and terrain correction. It is provided with geodetic and radiometric accuracy using Digital Elevation Model (DEM) and Ground Control Points (GCPs) for topographic displacement [18]. Landsat images of all the years were verified for common Geotiff format and common coordinate system WGS_1984_UTM_zone_45N. Finally, area of interest containing study reach was clipped using a rectangular shape file.

3.3 Water Extraction

Extraction of river boundary through the tools of ArcMap (version 10.3) is an automatic process, and it is based upon reflectance of water and other riverine features. Thus, there is possibility of similar reflectance for different features [19]. And hence, riverbank boundary has been digitized manually as suggested by [20–22].

Water present in the river reflects visible range and absorbs Infrared Radiation (IR). IR is reflected more by vegetation and bare soil reflect than open water. Hence, Normalized Difference Water Index (NDWI) has been utilized for the extraction of water feature as proposed by [23]. Water bodies give maximum reflectance to green band and minimum reflectance to Near-Infrared Radiation (NIR). Thus, NDWI may be used to distinguish water and non-water area clearly. NDWI has been computed from Landsat as:

$$NDWI = \frac{Green - NIR}{Green + NIR} \tag{1}$$

where green and NIR are raw Digital Number (DN) values of green and NIR bands. The values of NDWI lies between -1 and 1. The NDWI values are negative for open water, zero for bare soil, and positive for vegetated surfaces in [23]. Water and non-water pixels are produced by this method, which may be counted accurately. Hundred random points in the study reach have been selected for ground truth during accuracy assessment of classified image. An error matrix was formed for the classified image of every year. Overall accuracy has been calculated using formula [24, 25]:

$$Overall\ accuracy\ (\%) = \frac{Number\ of\ correct\ classified\ points}{Total\ number\ of\ selected\ points} \tag{2}$$

Overall accuracy of image classification of all selected years in study reach is presented in Table 2.

Table 2 Overall accuracy of image classification

Years	Overall accuracy (%)
2000	94
2005	91
2010	94
2015	91
2019	92

3.4 Planform

Information about form and structure of the river has been extracted using analysis of planform. All features of the river are observed for changes in due course of time, and the reason behind those changes is discussed in the analysis of planform. These features are changes in the shape of channel, increase or decrease in area of sandbars, increase or decrease in fluvial islands, tendency of erosion or deposition in stretch, effect of confluence of tributaries.

3.5 Sinuosity Index

Sinuosity Index (SI) estimates the deviation in the path of flowing river from a straight-line path. It is redefined in the case of multi-channel river, as "Ratio of mid-channel length of the widest channel to the overall length of the channel reach, measured along straight-line path" [26]. SI is given as:

$$SI = \frac{L_{c\max}}{L_R} \tag{3}$$

where $L_{c\max}$ = midway length of the widest channel and L_R = overall length of the reach in straight-line path.

3.6 Braiding Index

Braiding index (BI) estimates the bifurcations in the mainstream of the river into a number of channels. These bifurcations mainly occur due to the formation of islands and sandbars in between the channels [27]. BI is given as:

$$BI = \frac{2\left(\sum L_i\right)}{L_r} \tag{4}$$

where $\sum L_i$ is the summation of lengths of all islands and sandbars present in the reach. L_r is the total length of the reach measured along midway between the banks of the river.

3.7 River Network Change Index

River Network Change Index is an index that shows the change in river during a given time. It has been computed to investigate the area of erosion or area of deposition in the study reach, that has occurred in due course of the time. It may be considered as spatial and temporal change index for a fluvial system. RNCI is defined by [28] as:

$$\text{RNCI} = \frac{\left(\frac{\sum \text{EA} - \sum \text{DA}}{L}\right)}{Y} \tag{5}$$

where EA is area of erosion, DA is area of deposition, L is straight distance length of sub-reach, and Y is the time period in years.

4 Results and Discussions

4.1 Change in Planform

Planform changed in study period has been analyzed at confluence of Kosi River in Ganga River. Kosi joins river Ganga at Kursela from left side of the river (Fig. 2). This river emerges from the Himalayan Mountain, and it carries massive sediment load during the monsoon season. These sediments are dumped in the Ganga River due to reduction in flow velocity. Sediment carried by Kosi River as well as transported by the Ganga itself contributes to expand islands and sandbars. Flow behavior of the river erratically changes in confluence zone of the rivers. And hence, it is difficult to set a thumb rule for erosion or deposition of sediment in this zone. The area of island at the confluence of Kosi has decreased from 116 to 104 km^2. This decrease may be attributed to the erosion of its right bank and also left bank downstream of the confluence point. The total area of islands and sandbars has increased from 144 to 174 km^2 during study period. Size of islands and sandbars and the vegetation present upon it are prominent factors for their stability [29]. Island has covered large area and became stable. This sediment increases its concentration in the water of the Ganga River, which contributes to expansion of islands and sandbars in the downstream stretch of river. Confluence point of the Kosi has shifted toward left by 1.5 km. Width of the river has also increased near the confluence. Overall width (i.e., from left bank to right bank including island) has increased gradually from 7.4 km in 2000 to 9.2 km in 2020 near confluence of the river. Left channel was major channel in 2000 carrying major part of discharge while right channel was narrow. But as the time progress right channel is getting wider, increasing discharge flowing through it. Left channel of the Ganga River was almost semicircular shaped path in 2000, and right channel was flowing straight with minor curves in path. Width and curves both have increased in its right channel. Width of island has also increased from 4.6 to 8.2 km^2.

Number and area of sandbars are increasing from 2000 to 2020 due to extensive deposition of sediment which is taking place in left stream. Left bank of the island present in between bifurcated streams is shifting further leftward due to deposition of sediment, while its right bank is under erosion shifting leftward. Number and area of sandbars have increased downstream of the confluence point showing deposition of sediments on riverbed. Plan-form change is natural phenomenon in the alluvial river. But, confluence of sediment carrying tributary increases rate of changes in the planform.

4.2 Change in Morphological Parameters

Morphological parameters are the quantifying tools to represent degree of changes in the river. Three parameters (SI, BI, and RNCI) have been computed to analyze the changes at confluence during period of study. Changes in morphological parameters SI, BI, and RNCI have been computed and presented in Table 3.

The values of SI in the study reach have varied from 1.45 to 1.56 (Table 3). Based upon the values of SI, the Ganga River may be considered as meandering river within the study area. SI has increased during 2000–2005 and 2015–2020. SI in this sub-reach has been measured along the left channel of the bifurcated river. Erosion was occurring in the left bankline of the river, and deposition of sediment was going on its right bankline. Sediment carried by the Kosi River also deposited in the Ganga River increasing the rate of aggradation downstream of the confluence. Aggradation of on its left bank is shifting its left channel toward right. And thus, sinuosity of it major left channel has decreased.

BI in the study reach has varied between 1.0 and 2.0 during the study period. BI has decreased gradually from 2000 to 2010 and 2015 to 2020 with an increase in the year 2015. Both Ganga River and Kosi River carry huge sediment load during the monsoon season. High sediment concentration and mild river bed slope lead to deposition of sediment increasing its BI. Sandbars developed in one flood may erode in the next as it is developed by sediment deposition. This led to change in bifurcation of the river also changing values of BI. This shows unstable nature of the river in this stretch.

River Network Change Index (RNCI) shows change in river during a given time [30]. RNCIs have been computed for every sub-reaches and presented in Table 3. RNCI is positive in years 2000–2005 and 2010–2015 showing more erosion than deposition and it is negative during 2005–2010 and 2015–2020 which shows that deposition is more than erosion. However, the values of RNCI are close to 0.0, which shows that the amount of total erosion is almost equal to total deposition in study reach. However, both erosion as well as deposition was more on its left bank side compared to right bank side.

Morphological change is a natural process in the alluvial river. However, confluence of high sediment carrying tributary increased rates of changes in the morphology at its confluence point.
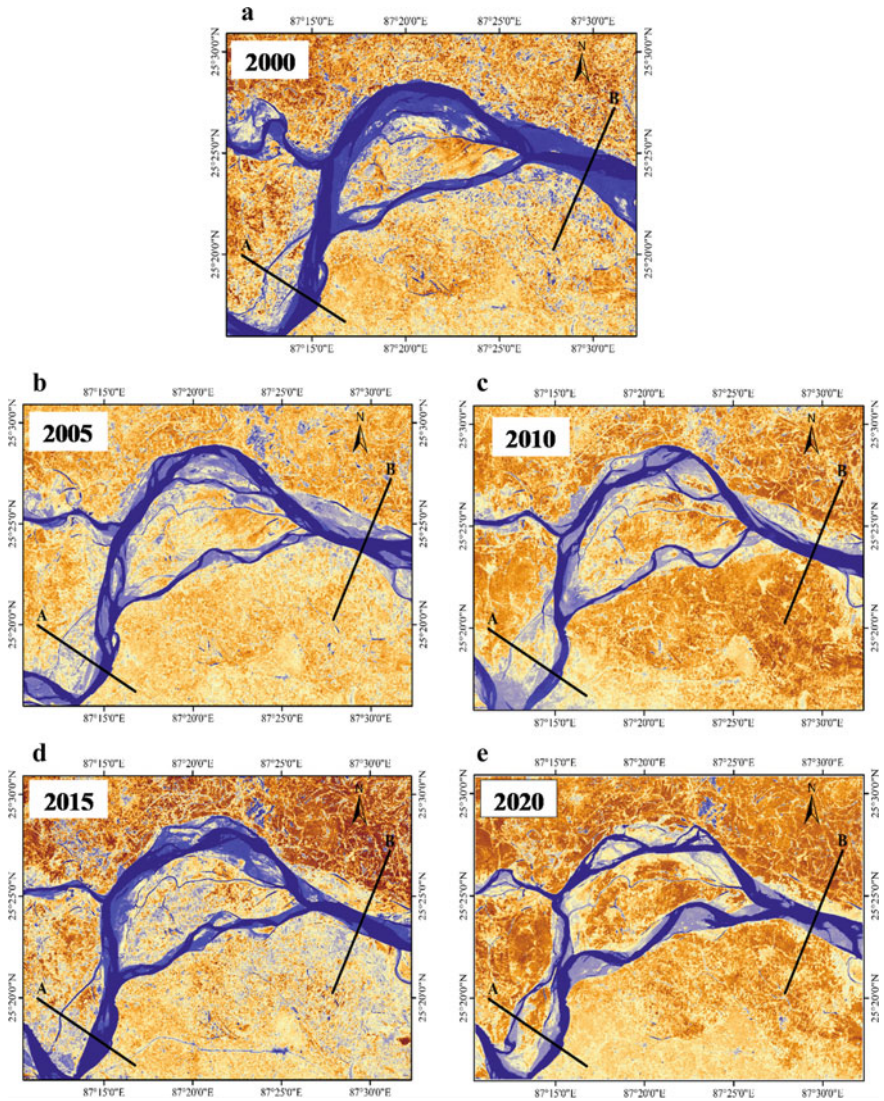
Fig. 2 Planform maps of the study reach (stretch between section lines A and B) of years **a** 2000; **b** 2005; **c** 2010; **d** 2015; and **e** 2020

Table 3 Temporal changes in SI, BI, and RNCI

Years	SI	BI	RNCI
2000	1.45	1.8	
2005	1.50	1.6	0.11
2010	1.49	1.0	−0.11
2015	1.49	2.0	0.02
2020	1.56	1.8	−0.03

5 Conclusions

Significant morphological changes have been experienced under combined action of natural fluvial processes and joining of tributary Kosi in the Ganga River. Accuracy in the quantification of morphological changes is quite challenging. In this study, morphological changes in the Ganga River at confluence of the Kosi River has been quantified and analyzed using remote sensing and GIS technique. Mapping of planform and fluvial islands and sandbar was carried out through computing Normalized Difference Water Index (NDWI) which has a fair overall accuracy above 90%. Planform of the river undergone significant changes during period of study. Confluence of the tributary has significantly changed its planform downstream of the confluence point. Confluence region has faced erosion which has shifted the confluence by 1.5 km. Morphological parameters have also significantly changed during the period of study. SI has an increasing trend, while BI has changed without any specific trend. Computed RNCI computed in the confluence revealed that the amount of total erosion is almost equal to total deposition in study reach. However, both erosion as well as deposition was occurring more on its left bankline compared to right bankline. The fluvial island at confluence of two highly sediment-loaded rivers is sensitive to spatial change. Monitoring of change in morphology may provide a useful reference for decision-making of flood warning to human settlements present on river island and nearby banks.

References

1. Garde RJ (2006) Fluvial morphology. In: Garde RJ (ed) River morphology. New Age International (P) Limited, Publishers, New Delhi, pp 1–10
2. Hickin EJ, Nanson GC (1984) Lateral migration rates of river bends. J Hydraul Eng 110(11). Paper No. 19271:1557–1567
3. Downward SR, Gurnell AM, and Brookes A (1994) A methodology for quantifying river channel planform change using GIS. Variability in stream erosion and sediment transport, proceeding of the Canberra symposium, December 1994. IAHS Publ. No. 224:449–456
4. Salleh KBO (Jan 1997) Channel adjustments and planform changes—part of the upper Linggi River system. Akademika 50:43–55
5. Yeasmin A, Islam N (2011) Changing trends of channel pattern of the Ganges-Padma river. Int J Geomatics Geosci 2(2):2011
6. Hossain MA, Gan TY, Baki ABM (2013) Assessing morphological changes of the Ganges River using satellite images. Quat Int Elsevier Ltd and INQUA, 304(3):142–155. https://doi.org/10.1016/j.quaint.2013.03.028
7. Nabi MR, Rashid S, Hossain MI (2016) Historical Bankline shifting since 1760s: a GIS and remote sensing based case study of Meghna river Plate of Rennell's atlas. Int J Sci Res Publ 6(12):473–483
8. Langat PK, Kumar L, Koech R (2019) Monitoring River channel dynamics using remote sensing and GIS techniques. Geomorphology. https://doi.org/10.1016/j.geomorph.2018.10.007

9. Raj C, Singh V (2022) Assessment of planform changes of the Ganga River from Bhagalpur to Farakka during 1973–2019 using satellite imagery. ISH J Hydraul Eng 28(1):87–97. https://doi.org/10.1080/09715010.2020.1812123

10. Hemmelder S, Marra W, Markies H, Jong SM (2018) Monitoring river morphology and bank erosion using UAV imagery—a case study of the river Buëch, Hautes-Alpes, France. Int J Appl Earth Obs Geoinformation 73(2018):428–437

11. Akhter S, Eibek KU, Islam S, Towfiqul Islam ARM, Chu R, Shuanghe S (2019) Predicting spatiotemporal changes of channel morphology in the reach of Teesta River, Bangladesh using GIS and ARIMA modeling. Quat Int INQUA 513:80–94. https://doi.org/10.1016/j.quaint.2019.01.022

12. Biswas AK, Tortajada C (2012) Impacts of high Aswan dam. In: Biswas AK, Tortajada C (eds) Impacts of large dams: a global assessment. Springer, Berlin Heidelberg, pp 379–395. https://doi.org/10.1007/978-3-642-23571-9_17

13. Rahman MM, Rahaman MM (2018) Impacts of Farakka barrage on hydrological flow of Ganges river and environment in Bangladesh. Sustain Water Res Manage 4(4):767–780. https://doi.org/10.1007/s40899-017-0163-y

14. Resmi SR, Patel PL, Timbadiya PV (2018) Morphological study of upper Tapi river using remote sensing and GIS techniques. ISH J Hydraul Eng 1–9. https://doi.org/10.1080/09715010.2017.1409089

15. Singh P, Patil RG, Singh A (2019) Assessment of recent changes in planform of river Ganga from Mirapur Khadar to Narora Barrage, Uttar Predesh, India. Sustain Water Res Manage 5(2):575–586. https://doi.org/10.1007/s40899-018-0222-z. Springer International Publishing

16. NMCG (2010) River Ganga at a Glance: identification of issues and priority actions for restoration. https://nmcg.nic.in/writereaddata/fileupload/33_43_001_GEN_DAT_01.pdf. Accessed 2 July 202

17. Gurnell AM, Downward S, Jones R (1994) Channel planform change on the river Dee meander 1876–1992. River Res Appl 9(4):187–204

18. USGS (2020) Landsat level of processing. Retrieved from https://www.usgs.gov/land-resources/nli/landsat/landsat-levels-processing

19. Dewan A, Corner R, Saleem A, Rahman MM, Haider MR, Rahman MM, Sarker MH (2017) Assessing channel changes of the Ganges-Padma river system in Bangladesh using Landsat and hydrological data. Geomorphology 276:257–279. https://doi.org/10.1016/j.geomorph.2016.10.017

20. Gupta N, Atkinson PM, Carling PA (2013) Decadal length changes in the fluvial planform of the river Ganga: bringing a mega-river to life with Landsat archives. Remote Sen Lett 4(1):1–9. https://doi.org/10.1080/2150704X.2012.682658

21. Mandarino A, Maerker M, Firpo M (2018) Channel planform changes along the Scrivia river floodplain reach in northwest Italy from 1878 to 2016. Quatern Res 2018:620–637. https://doi.org/10.1017/qua.2018.67

22. Yang X, Damen MC, Van ZRA (1999) Satellite remote sensing and GIS for the analysis of channel migration changes in the active Yellow River Delta, China. Int J Appl Earth Obs Geoinf 1(2):146–157. https://doi.org/10.1016/S0303-2434(99)85007-7

23. Mcfeeters SK (1996) The use of the normalized difference water index (NDWI) in the delineation of open water features. Int J Remote Sens 17(7):1425–1432. https://doi.org/10.1080/01431169608948714

24. Bharatkar PS, Patel R (2013) Approach to accuracy assessment for rs image classification techniques. Int J Sci Eng Res 4(12):79–86

25. Thapa RB, Murayama Y (2009) Urban mapping, accuracy, and image classification: a comparison of multiple approaches in Tsukuba City, Japan. Appl Geogr 29(2009):135–144. https://doi.org/10.1016/j.apgeog.2008.08.001

26. Friend PF, Sinha R (1993) Braiding and meandering parameters. Geol Soc, Lond, Spec Publ 75(1):105–111. https://doi.org/10.1144/GSL.SP.1993.075.01.05

27. Brice JC (1964) Channel patterns and terraces of the Loup Rivers in Nebraska. United States Geological Survey Professional Papers, 422-D

28. Nelson NC, Erwin SO, Schmidt JC (2013) Spatial and temporal patterns in channel change on the Snake River downstream from Jackson Lake dam, Wyoming. Geomorphology. https://doi.org/10.1016/j.geomorph.2013.03.019

29. Leli IT, Stevaux JC, Assine ML (2020) Origin, evolution, and sedimentary records of islands in large anabranching tropical rivers: the case of the Upper Paraná River Brazil. Geomorphology 358(2020):107118. https://doi.org/10.1016/j.geomorph.2020.107118

30. Yousefi S, Moradi HR, Telvari A, Vafakhah M (2015) Monitoring of fluvial systems using RS and GIS (Case study: Talar River, Iran). J Selçuk Univ Nat Appl Sci 4(2):60–72

Estimation of Streambank Erosion Rates Using Jet Apparatus Approach in the Barak River Basin, India

Tinkle Das, Kumar Ashwini, and Briti Sundar Sil

Abstract In the floodplains of alluvial rivers, riverbank erosion is one of the most significant geomorphological problems. The Barak River is one of the critical river basins of Northeast India. The frequent catastrophic flood has exposed the region during monsoon, responsible for the community's suffering. A study is performed to determine the riverbank erosion in a highly dynamic and unstable section of the Barak River in Assam (India). The submerged jet erosion test (JET) is a field method for measuring soil erosion based on impinging jet theory. The average stream bank erosion was calculated for a unit span of riverbank on one sideway of the stream using the surplus shear stress equation, which includes the critical shear stress (τ_c) and erodibility coefficient (K_d). The JET data were evaluated by applying direct parameter optimization to the scouring depth data. To find critical shear stress, the Microsoft Excel Solver method was used to maximize the equilibrium depth value. The results show that the erosion resistance of stream banks varies significantly, with magnitudes of τ_c ranging from 0.55 to 5.99 Pa, whereas K_d ranges from 2.26 to 3.52 cm^3/N s. Streambank erosion rates and quantity estimates for a local stream were calculated using these parameter values. Critical stress and detachment coefficient variation varies widely from location to location. As a result, it must be observed locally to estimate the stream bank erosion at the site.

Keywords Submerged jet erosion · Critical shear stress · Streambank erosion rate · Erodibility coefficient · Barak River basin

T. Das (✉) · K. Ashwini
Department of Civil Engineering, National Institute of Technology Silchar, Silchar 788010, India
e-mail: tinkle_rs@civil.nits.ac.in

K. Ashwini
e-mail: kumara_rs@civil.nits.ac.in

B. S. Sil
Department of Civil Engineering, National Institute of Technology Silchar, Silchar 395007, India
e-mail: bssil@civil.nits.ac.in

1 Introduction

The dislodgment of soil mass causes the soil erosion assessment from the land surface caused by natural phenomena, which is named geological erosion. Geological erosion of soil is driven primarily by the impact of precipitation, runoff, wind velocity, topography, and gravitational forces; so, the capability to correctly predict river-bank erosion is an important challenge for many engineers and researchers globally. Measuring the sediment detachment is one of the considerable challenges because various factors influence the soil's erodibility, such as water content, particle size, clay mineral, swelling potential, and excess pore pressure [1], which are a significant impact on the erodibility factor of fine soil.

Alluvial erosion velocity of the cohesive soil in a stream bank is generally expressed that the rate of alluvial erosion (ε) (m/s) is directly proportional to the excess shear stress. It is also called the detachment particle model [2–4] in Eq. (1):

$$\varepsilon = k_d(\tau_a - \tau_c)^a \tag{1}$$

where ε = erosion rate in meter/second, K_d = detachment coefficient $\left(\mathrm{m^3Ns^{-1}}\right)$, τ_a is the soil boundary shear stress in pascal, τ_c = the critical shear stress in pascal, a = exponent usually taken as unity [2]. One equation has three unknown parameters. To know the surplus stress parameter, critical shear stress (τ_c) and the detachment coefficient (K_d) are to be measured by the submerged JET apparatus test. Before the test, two hydraulic conditions should be checked as per condition given below:

(1) If the $\tau_a < \tau_c \rightarrow n$ o chance of erosion.
(2) If the $\tau_a > \tau_c \rightarrow$ there is a chance of erosion.

The erodibility parameter of cohesive soil is influenced by soil texture, unit weight of soil, water content of the soil, and other soil properties. After investigating various soil parameters, the researcher performed Nemours tests on the erodibility of clayey soil and obtained the K_d and for τ_c Cohesive soil using multiple approaches. It includes Flumes tests, small flumes, hole erosion tests, and submerged jet tests which are also included [5]. The submerged jet erosion test (JET) device is an innovative field and laboratory method for evaluating erodibility characteristics. The JET apparatus includes an impinging jet attached to an adjustable head tank and a point gauge to measure the scour depth and submerge the JET in water to test the soil. Numerous researches have provided a thorough explanation and technique [5–7].

The critical shear stress (τ_c) and detachment coefficient (k_d) are important parameters in the excess shear stress equation. The Microsoft solver technique can be used to calculate the critical shear stress value. The detachment coefficient (k_d) is to be determined, as a function of the critical shear stress. Hanson and Simon [7] derived the experimental relationship between k_d and τ_c which is inversely proportional to each other; the derived relation between k_d and τ_c is given in Eq. (2).

$$k_d = 0.2\frac{1}{\sqrt{\tau_c}} \tag{2}$$

Hanson and Simon [7] suggested the equation based on the total of 83 in situ submerged jet test which was conducted on cohesive soil (silt and clay) with the determination of coefficient $R^2 = 0.64$ and was integrated into stream bank erosion and stability analysis. The limitation of this equation is that it is not valid for non-cohesive soil. Later, Simon et al. [8] again modified the previous model based on the 100 stream bank JETs across the USA and found the relation as Eq. (3).

$$k_d = 1.623\,\tau_c^{-0.839} \tag{3}$$

Wynn et al. [9]used submerged JET apparatus for a total 142 numbers of field experiments conducted in vegetative stream bank with higher roughness coefficient, and 25 field tests were done in the southwest direction and derived the detachment coefficient (k_d) and critical stress (τ_c) with the following relation Eq. (4):

$$k_d = 3.1\tau_c^{-0.376} \tag{4}$$

In addition to these, at the stream bank erosion, the size of soil properties varies from place to place. The main variation of soil particles is the silt–clay content, which is crucial for identifying alluvial erosion and group collapse of soil. The primary drawback of the submerged JET erosion test is that it cannot determine the whole amount of bank erosion. It can perform the jet test from the combined bank of the alluvial rivers at the particular site. The variation of detachment coefficient is different at the different layers, which is essential to understanding the stream bank loss process. The primary purpose of the research was to determine riverbank erosion in a highly dynamic and unstable stretch of Assam's Barak River.

2 Study Area and Data Source

2.1 Barak River Basin

The submerged in situ JET was conducted on a streambed of the Barak River in Northeastern India. The river flows westbound from Lakhipur through the Cachar field district of Assam over a stream length of around 130 km to enter Bangladesh close to Bhanga, as shown in Fig. 1. Various sandbars may be seen in the Barak River's main course. Silty sand is at the top of the layer, while silty clay is at the bottom and toe of the layer in the composite Barak Riverbanks.

[A] - Sonai (24.8333° N, 92.7789° E)
[B] - Sonabari Ghat (24.7650° N, 92.8292° E)
[C] - Tarapur Nathpara (24°51'3.50"N, 92°46'24.46"E)
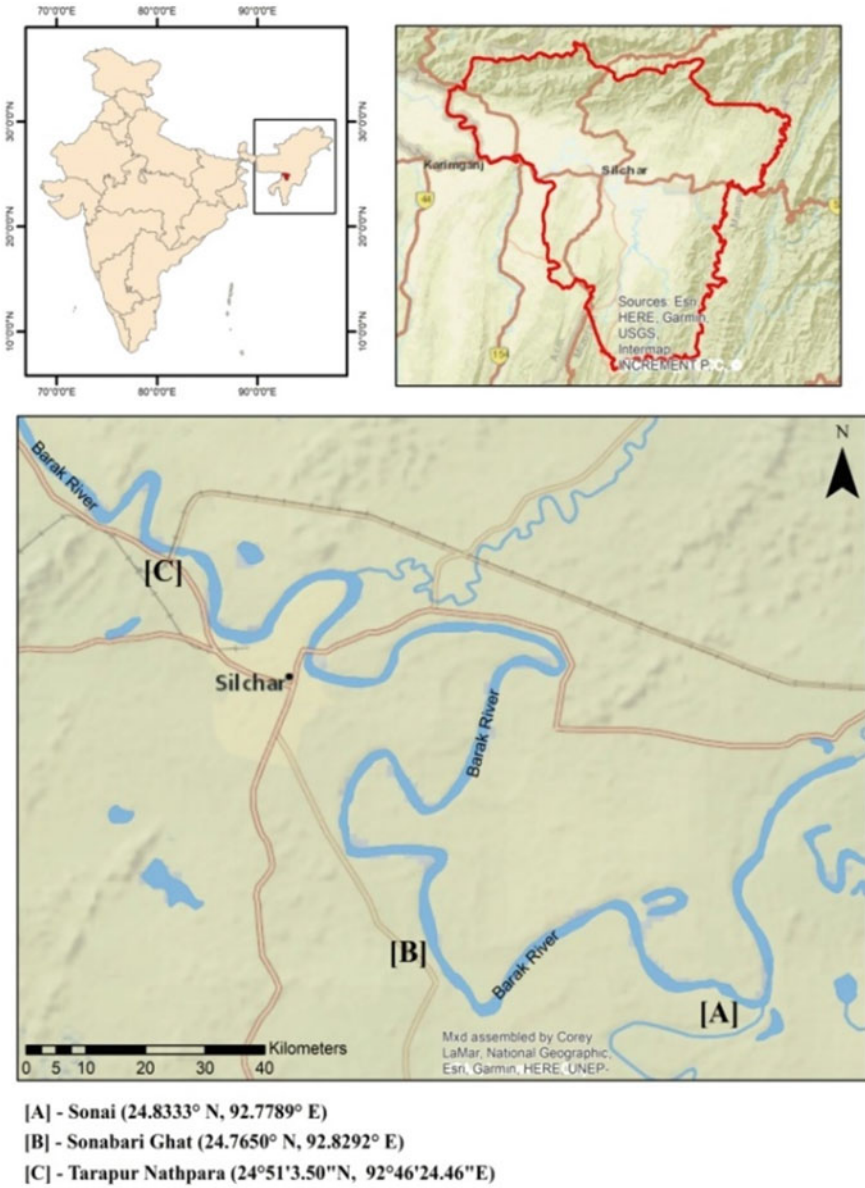
Fig. 1 Index map of the study area

2.2 Data Collection

A total of three field sites are selected for the bank erosion in the Barak River. The required site was chosen, and data were collected based on the most flood-prone regions, critical banks, safety concerns, and easy access. Figure 1 shows a total of six numbers of tests conducted at three different sites of the bank. One of the sites is situated at the upstream part of the Barak River, namely Sonabarighat (24.7650°N, 92.8292°E). The second site is in Sonai (24.7326°N, 92.8889°E) which is situated 7.5 km from Sonabarighat. The last one is at a middle portion of the Barak named Tarapur Nathpara (19.8649°N, 72.6850°E) which is worst affected by the flooded area.

3 Materials and Methods

3.1 Measurement of Erosion Parameters

Hanson and Cook [5, 10] introduced analytical methods for studying the jet, where they assumed that the rate of change in the depth of scour (dJ/dt) was directly proportional to the erosion rate, which, in turn, was dependent on the maximum stress at the boundary. The maximum stress was determined by the diameter of the jet nozzle and the distance from the origin of the jet to the initial channel bed. Thus, the erosion rate equation for jet scour was formulated as presented by Hanson and Cook [5].

$$\frac{\mathrm{d}J_s}{\mathrm{d}t} = k_\mathrm{d}\left[\frac{\tau_0 J_P^2 - J_S^2 \tau_C}{J_S^2}\right] \text{ for } J_S \geq J_P \tag{5}$$

where J_S is the scouring depth in centimeters and J_P is the core length of the jet source. Blaisdell's solution (BL), iterative solution (IT), and scour depth solution (SD) are three methods for analyzing data from JETs and predicting erodibility parameters that have recently been proposed. Reference [11] developed a hyperbolic function to calculate the equilibrium scour depth (J e). As a result, critical shear stress is defined as the maximum scour depth beyond the zero-scour depth (J e).

$$\tau_C = \tau_0 \left(\frac{J_P^2}{J_e^2}\right) \tag{6}$$

$$\tau_0 = c_f \rho_\mathrm{water} U_i^2 \tag{7}$$

$$J_P = C_d d_0 \tag{8}$$

$$U_0 = \sqrt{2gh} \tag{9}$$

τ_0 = It is the maximum shear stress induced at the diameter of the nozzle as a result of jet velocity (its unit is Pa), J_P = length of the core from the jet orifice (cm), and C_d is the diffusion constant, with reported values ranging from 5.8 to 7.4 and a commonly recognized average of 6.2. Reference [12] d_{dia} = The nozzle diameter of the jet, C_f is the local friction coefficient; the typical value of C_f for turbulent flow condition ranges around 0.004165 (e.g., [10, 13]), ρ = density of the fluid, U_0 = the speed at the jet nozzle of the orifice, g = acceleration due to gravity, h = Difference of head measurement. The erodibility coefficient k_d is calculated using the observed scour depth, time, and the non-dimensional time function, as described in [10].

3.2 JET Spreadsheet Tools

The equilibrium scour height (J_e), which is difficult to determine since it is a period dependency necessary to attain zero-depth, is used to predict the rate of erosion of cohesive soil from critical shear stress τ_c [11]. It also created the JET spreadsheet tool to compute the equilibrium scour depth using the graph of times versus jet scour depth. A hyperbolic equation has the following general form:

$$(f - f_0)^2 - A^2 = X^2 \tag{10}$$

The rate of semi-transfer and semi-conjugate of the hyperbola function is A.

$$f = \log\left(\frac{J}{d_0}\right) - x, \tag{11}$$

$$x = \log\left[\frac{U_0 t}{d_0}\right], \text{ and} \tag{12}$$

$$f_0 = \log\left(\frac{J_e}{d_0}\right) \tag{13}$$

$$J_e = d_0 10^{f_0} \tag{14}$$

The Microsoft Excel Solver in the spreadsheet minimizes the difference between the sum of the variation value of x (in the x-axis) based on the observed test value of x and the calculated value. This Excel Solver is used to estimate the equilibrium depth (J_e) by continuously minimizing the search on the spreadsheet with the initial value of coefficient (constraints) $A = 0.5$ and $f_0 = 0.5$. It has the option to choose from different initial values, increase the number of trials, or continue the search once J_e (equilibrium depth) is obtained by the value of f_0 the critical shear stress (τ_c) is then

determined. The spreadsheet tool was again calculated the erodibility coefficient by fitting measured curve line based on the equation [10].

3.3 Development of Shear Stress

According to erosion of fine soil, the rate of stream bank erosion is directly proportional to the surplus shear stress. Reference [14] developed hydraulic stress (Pa) at any height of stream bank, which has calculated by the equation:

$$\tau_a = 0.76 \, \rho g d S \tag{15}$$

where τ_a average hydraulic stress at the midpoint river section (Pa), ρ is the water density (kg/m^3), g is the gravity (m/s^2), d denotes the height of the water from the top of the water level (m), S is the channel slope of the EGL line (energy gradient line).

4 Field Data and Analysis

The submerged JET apparatus was conducted at the Barak River. It is a significant river in the southern part of Assam and the only river flowing through the three districts. During monsoon time, the Barak River exceeds the danger flood level. The small river basin has also exploded its bank and meets the central river stream bank. Generally, it contains silty sand on top of the layer and unconsolidated gravel and stone bottom layer.

Hanson and Cook [10] created a spreadsheet procedure that was used to evaluate the data and record the field data over scour depth over time. The nozzle height, duration, and maximum scour depth are calculated using the first routine sheet. The cumulative time for full scour depth graph based on different times was calculated using the data input and the beginning calculation of the first sheet, as shown in Figs. 2, 3, and 4. The erodibility coefficient for Eq. (1), critical shear stress τ_c, and the erodibility coefficient, k_d, are calculated using the preceding chart and the starting calculation of the first sheet addition sheet.

5 Results and Discussion

A submerged jet apparatus was used to analyze the erosion rate at River Barak by studying the soil property. According to the testing of the soil sample, the soil at the ground surface is only silt and sand layer up to roughly 0.5 m deep. This type of layering is quite common, usually found in the alluvial river bank [15]. The major
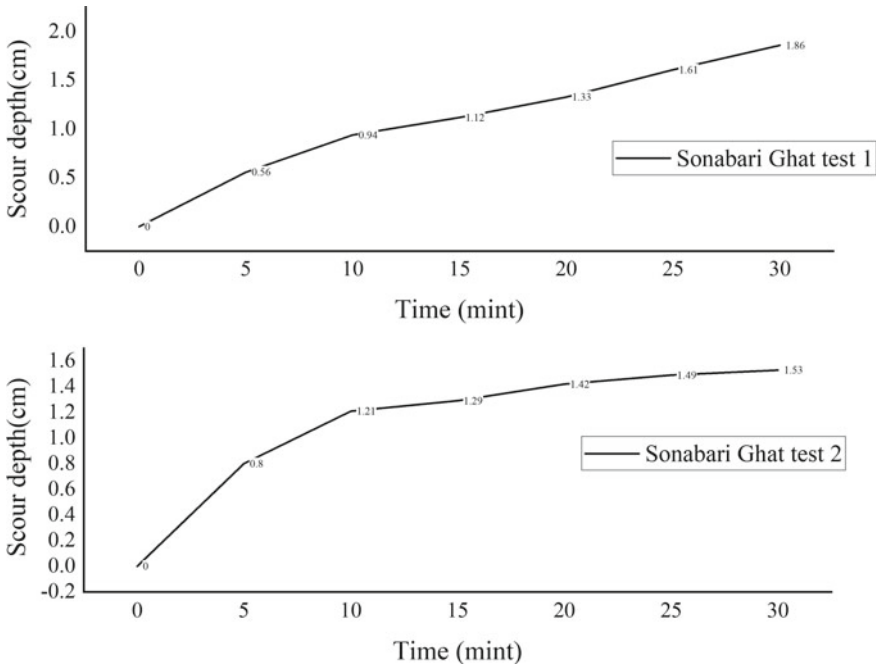
Fig. 2 Scour depth variation over the time at Sonabari Ghat **a** Test-1 **b** Test-2

limitation is that the jet apparatus test is applicable to the cohesive soils only, as the cohesive soil has higher resistance against erosion. We conducted a sieve examination at our research site, and it was discovered to include 25.5% sand, 37.56% clay, and 35.94% silt, with a bulk density of 1.41 gm/cc and a nominal moisture content of 33.10% (NMC), as shown in Table 1 and Fig. 5.

The coefficient of determination R^2 and normalized objective function (NOF) is used to determine the parameters and best fit of statistics of erodibility model and excess shear stress across all erodibility parameter investigations [16]. The erodibility parameter usually fits the data with $R^2 > 0.6$ and NOF > 0.3 across all erodibility studies. As we have seen at our study location Sonabari Ghat site-1 and site-2 (Fig. 6) showing a correlation between observed data and predicted data ($R^2 = 0.97$), which is an excellent result. And, smaller (NOF) normalized objective function value (NOF $= 0$) corresponding to scour depth shows the best goodness of fit model. At Sonai site-1 and site-2, it is $R^2 = 0.98$ and NOF $= 0$ as shown in Fig. 7. It indicates an excellent minimization value. At the third location, the coefficient of determination is $R^2 = 0.92$, there was a slight decrease in the value of R^2 compared to the other two sites, as shown in the graph given below in Fig. 8. The result graphs for the calculated vs. observed erodibility coefficient and scour depth with respect to line of perfect agreement (1:1 line) which is shown in Fig. 9.

The magnitude of erosion parameters τ_c and K_d and the study location along the Barak River are mentioned in Table 2. The erodibility coefficient at the Bark
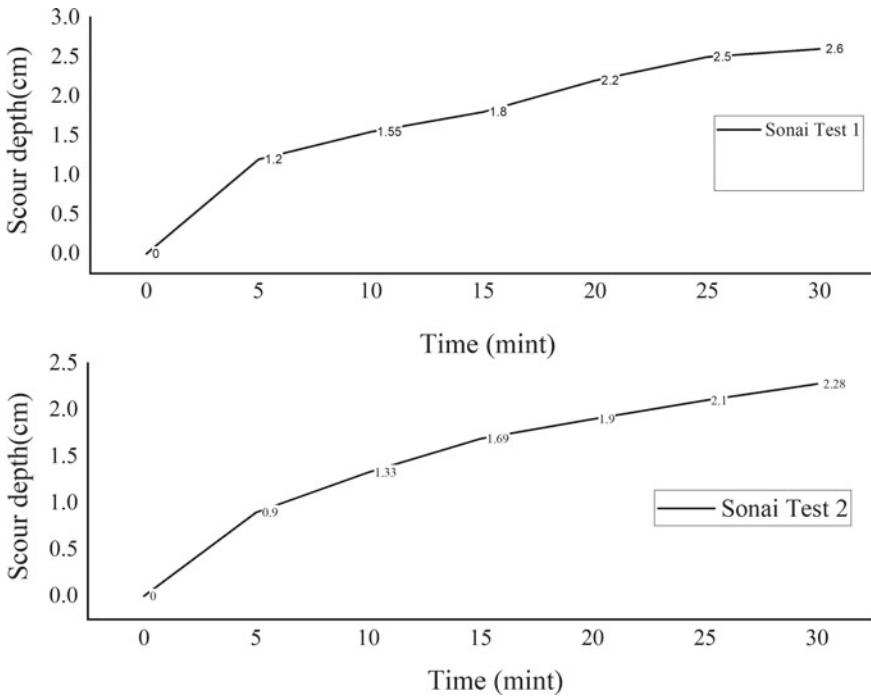
Fig. 3 Scour depth variation over the time at Sonai **a** Test-1 **b** Test-2

Riverbank was calculated using the jet data for the critical shear stress τ_c. It was found to be in between 0.55 and 5.99 Pa. All of the data for the detachment coefficient fall between the limits of (2.26–3.529) $\frac{cm^3}{NS}$. Analysis of results also indicates a broad scope of range in the erosion resistance of the stream bank, as shown in Fig. 10. As we have seen that at the Sonabari Ghat site-1, site-2, the critical shear stress τ_c was 4.98 and 6.0 Pa. Similarly, the critical shear stress range at the Sonai site-1, site-2 is 2.29–3.02 Pa. At the third location, the essential range of shear stress is least among two locations 0.79 and 0.55 Pa, also as observed at the Tarapur Nathpara detachment coefficient K_d. Values are getting (3.30–3.52) cm³/ns, which is higher than among two locations; therefore, location-3 has more erosion in nature. The detachment coefficient K_d ranges from 2.26 to 2.34 cm³/ns, 2.57 to 2.71 cm³/ns, 1.94 to 1.91 cm³/ns for Sonabari Ghat (site-1), (site-2) and Sonai (site-1), (site-2), respectively.

Now for estimation, bank erosion developed shear stress has to be measured. It is due to the hydraulic force exerted at the bank surface by flowing water, which may be calculated using Eq. (15). At three sites where the test was performed, we estimate the rate of erosion. The full bank discharge was assumed to be the channel-forming discharge [17]. The stream banks are mostly stable, with a few localized areas of erosion. We considered a rectangular channel with a homogeneous and broad cross-section area and an average longitudinal gradient of 1 in 6000. The bathymetric
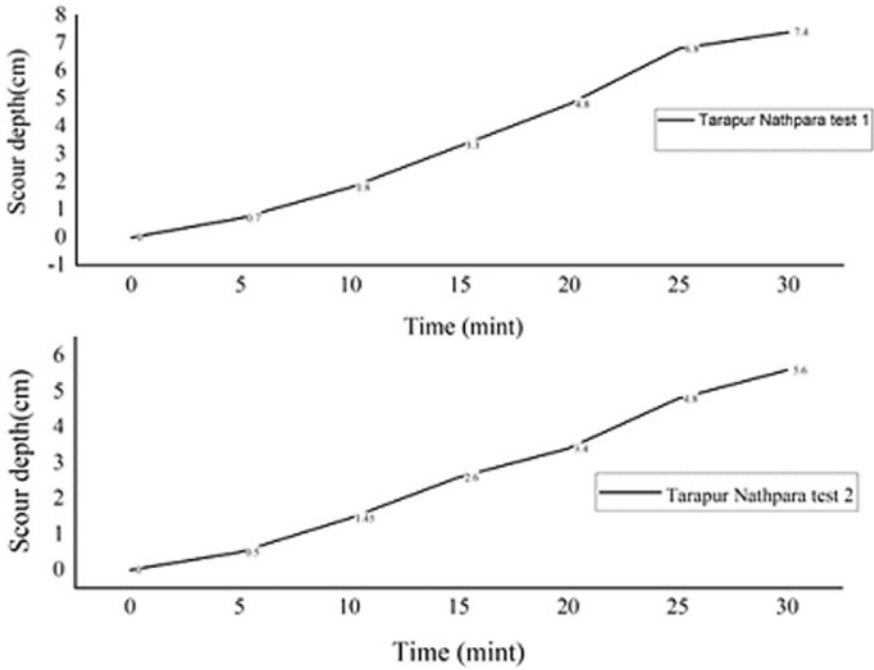
Fig. 4 Scour depth variation over the time at Tarapur Nathpara **a** Test-1 **b** Test-2

Table 1 Sieve analysis test calculation

IS sieve size (micron)	Wt. retained (in gm)	% retained	Cumulative retained	% passing
0.3	0	0	0	100
0.212	1	0.5	0.5	99.5
0.15	3	1.5	2	98
0.075	48	24	26	74
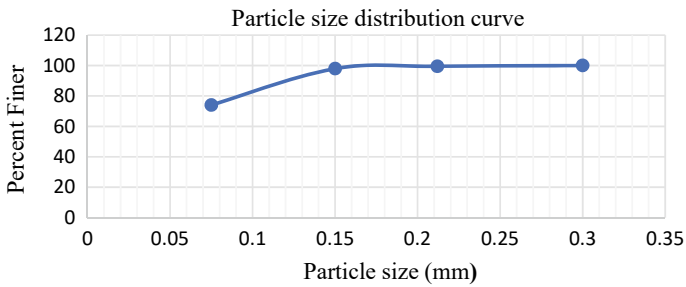
Fig. 5 Particle size distribution curve
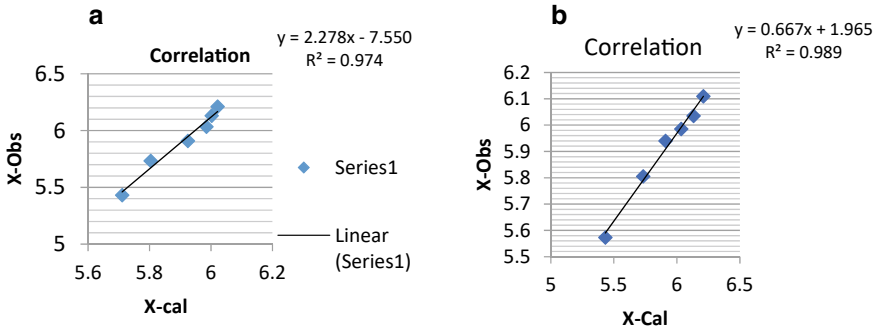
Fig. 6 Showing correlation between observed data and predicted data at Sonabarighat **a** Site-1 **b** Site-2
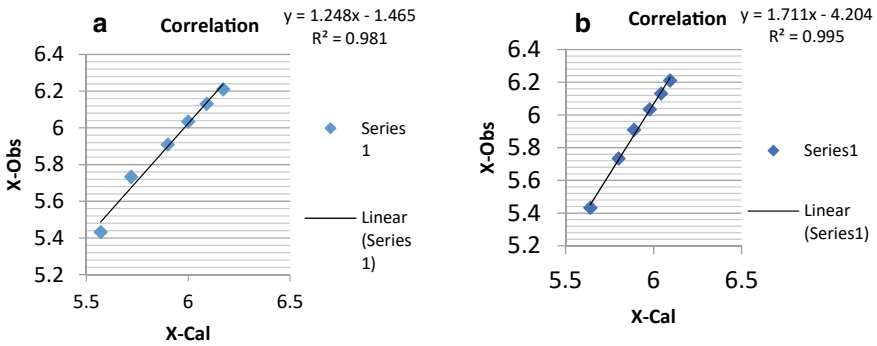
Fig. 7 Showing correlation between observed data and predicted data at Sonai **a** Site-1 **b** Site-2
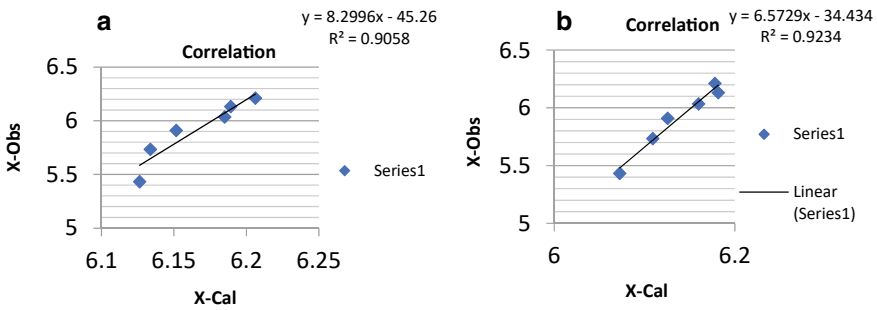
Fig. 8 Showing correlation between observed data and predicted data at Tarapur Nathpara **a** Site1 **b** Site 2

Equation	y = a + b*x
Plot	(Kd) from relationship
Weight	No Weighting
Intercept	-1.21348 ± 0.04264
Slope	1.41356 ± 0.01509
Residual Sum of Squares	0.00123
Pearson's r	0.99977
R-Square (COD)	0.99954
Adj. R-Square	0.99943
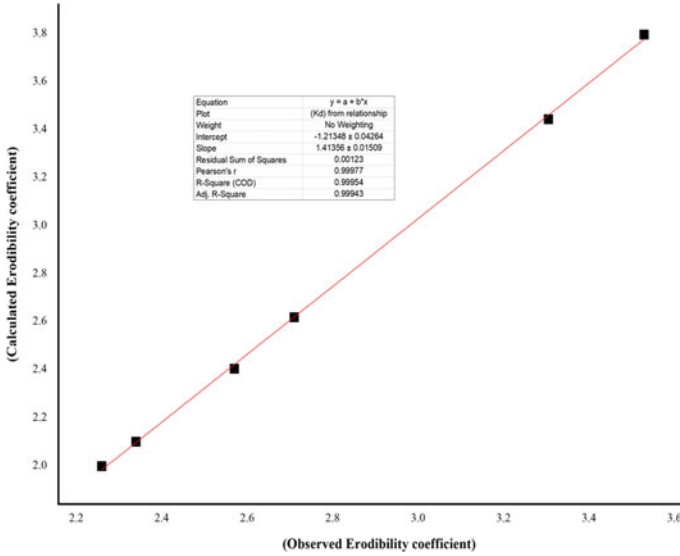
Fig. 9 Result graph of calculated and observed erodibility coefficient

Table 2 Estimation of fluvial erosion in three locations along the Barak River

Sites	Average longitudinal bed slopes (S)	Bank full depth near the bank (d) m	τ_c (Pa)	$k_d \left(\frac{cm^3}{NS}\right)$	τ_a (Pa)	Erosion rate (ε) m
Sonabari ghat site-1	1 in 6000	6	5.99	2.26	6.93	0.12
Sonabari ghat site-2	1 in 6000	6	4.98	2.34	6.93	0.3
Sonai site-1	1 in 6000	6	2.29	2.71	7.456	1.06
Sonai site-2	1 in 6000	6	3.02	2.57	7.456	0.84
Tarapur Nathpara site-1	1 in 6000	6.5	0.79	3.305	8.07	1.2
Tarapur Nathpara site-2	1 in 6000	6.5	0.55	3.529	8.07	1.3

survey calculated full bank depth based on the river's local characteristics and cross-sectional average. The developed shear stress was calculated at the section midpoint by Eq. (15) for each section.

Details of various parameter used for the erosion estimation are given in Table 2. These estimates, however, are based on average soil characteristics and full bank height, which vary from location to location. From Eq. (1), the bank erosion evaluation indicated that site 3 in the Barak River's bank is extremely erodible with the current bank full depth flow. Also, the rate of bank erosion in Sonabari Ghat is low
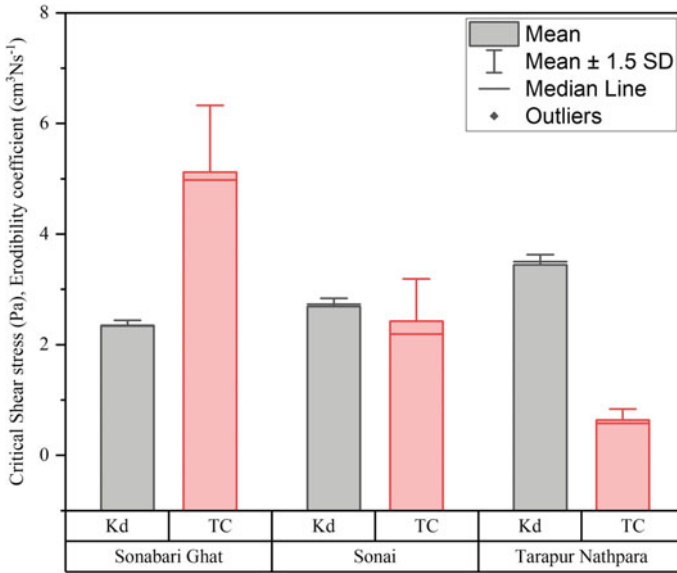
Fig. 10 Erodibility coefficient (K_d) and critical shear stress (τ_c), a bar chart of soil erodibility parameters is shown

erodible. However, the rate of bank erosion in Sonai falls into the moderate erodible group. The results also found that the rate of erosion at Sonabarighat (site-1), (site-2) and Sonai (site-1), (site-2) is 0.12, 0.3, and 1.06, 0.84 m per day, respectively. As a result of this calculation, we may conclude that the river's sediment transport capacity is sufficient to remove the eroded bank material at a full bank depth or peak occurrence.

6 Conclusion

The purpose of this research is to determine Streambank Erosion Rates of clayey soil from the Barak River bank using the submerged JET apparatus in situ, considering Barak River (Assam) as our study area from the upper side to the lower side. The scour function, which anticipated the critical shear stress, was optimized using a new spreadsheet tool Blaisdell's solution which forecasts the scour depth using the corresponding erodibility coefficient. From the field test results, it indicates that the critical shear stress (τ_c) ranges from 0.55 to 5.997 Pa and the detachment coefficient (K_d) value ranges from 2.26 to 3.52 cm^3/(N-s). Critical stress and detachment coefficient variation varies significantly from place to place with the analyzed data. Thus, the estimation of erosion parameters at a site needs to be measured locally. Over prediction of the rate of erosion may be important in the situation such as bridge,

dam construction where a large factor of safety required for an Engineer and Scientist. The excess shear stress measurements from the test may be used to monitor the riverbank's yearly bank erosion. During the peak event, detachment of soil mass is persistent in the Barak River. Using the in situ JET apparatus, we can estimate the erodibility parameter and control the rate of erosion.

References

1. Utley BC, Wynn TM (2008) Cohesive soil erosion: theory and practice. In: World environmental water resources congress 2008 Ahupua'a—Proceedings environmental water resources congress, vol 316, pp 1–10. https://doi.org/10.1061/40976(316)289
2. Partheniades E (1965) Erosion and deposition of cohesive soils. J Hydraul Div 91:105–139. https://doi.org/10.1061/JYCEAJ.0001165
3. Hanson GJ (1990a) Surface erodibility of earthen channels at high stresses: part I. Open channel testing. Trans ASAE 33(1):127–131 https://doi.org/10.13031/2013.31305
4. Hanson GJ (1990b) Surface erodibility of earthen channels at high stresses: part II. Developing an in-situ testing device. Trans ASAE 33(1):132–137. https://doi.org/10.13031/2013.31306
5. Hanson, Cook (1997) Development of excess shear stress parameters for circular jet testing: ASAE. Paper No. 972227. St. Joseph, Mich., ASAE
6. Fox G, Al-Madhhachi A-ST, Miller RB (2013) A scour depth approach for deriving erodibility parameters from jet erosion tests. elibrary.asabe.org. https://doi.org/10.13031/trans.56.10350
7. Hanson GJ, Simon A (2001) Erodibility of cohesive streambeds in the loess area of the midwestern USA. Hydrol Process 15:23–38. https://doi.org/10.1002/HYP.149
8. Simon A, Pollen-Bankhead N, Thomas RE (2011) Development and application of a deterministic bank stability and toe erosion model for stream restoration. In: Stream restoration in dynamic fluvial systems: scientific approaches, analyses, and tools. Geophysical monograph series, vol 194, pp 453–474. American Geophysical Union, Washington, DC
9. Wynn T, Mostaghimi S, Annual EA-2004 A, 2004 undefined the effects of vegetation on stream bank erosion. elibrary.asabe.org
10. Hanson GJ, Cook KR (2004) Apparatus, test procedures, and analytical methods to measure soil erodibility in situ. Appl Eng Agric 20:455–462
11. Blaisdell FW, Hebaus GG, Anderson CL (1981) Ultimate dimensions of local scour. J Hydraul Div 107:327–337. https://doi.org/10.1061/JYCEAJ.0005630
12. Beltaos S, Rajaratnam N (1974) Impinging circular turbulent jets. J Hydraul Div 100:1313–1328. https://doi.org/10.1061/JYCEAJ.0004072
13. Rajaratnam N, Beltaos S (1977) Erosion by impinging circular turbulent jets. ASCE J Hydraul Div 103:1191–1205. https://doi.org/10.1061/JYCEAJ.0004852
14. Leutheusser HJ (1963) Turbulent flow in rectangular ducts. J Hydraul Div 89:1–19. https://doi.org/10.1061/JYCEAJ.0000866
15. Karmaker T, Dutta S (2011) Erodibility of fine soil from the composite river bank of Brahmaputra in India. Hydrol Process 25:104–111. https://doi.org/10.1002/HYP.7826
16. Fox GA, Sabbagh GJ, Chen W, Russell M (2006) Uncalibrated modeling of conservative tracer and pesticide leaching to groundwater: comparison of potential Tier II exposure assessment models. Pest Mgmt Sci 62(6):537–550

17. Chang HH (1988) Fluvial processes in river engineering. Fluv Process river Eng
18. Hanson GJ, Robinson KM, Cook KR (2002) Scour below an overfall: Part II. Prediction. Trans ASAE 45(4):957–964

Study of Data Augmentation Technique for Discharge Prediction Problems Including Meandering Parameters

Tushar Khankhoje and Susmita Ghosh

Abstract For a given river or stream, the most important parameter to know its nature is its discharge. For meandering rivers, the influence of the curved geometry on its discharge is highly pronounced. The Barak River being highly meandering was considered for discharge prediction. A computer-based algorithm known as artificial neural networks was tried to be developed to solve this problem. For the case of limitation of dataset, the training of the ANN is not so accurate. There is a certain minimum number of patterns which are required as a training set. To obtain a sufficient number of training data, the yearly data (sinuosity and slope) were extracted and distributed in the dataset using data augmentation technique. For a given year data, the same sinuosity and slope value is being repeated 12 times, but the head and previous monthly discharge values vary as per the month. In this way, the yearly data have been converted into 12 monthly data, resulting in more number of patterns. This technique had been previously applied in case of image recognition fields for CNN networks where the image is cropped, rotated, resized, use of histogram analysis, etc., to increase the number of training dataset. But, for the normal data type backpropagation network, this is a yet to be properly verified. The results are showing the usefulness of data augmentation technique in our proposed and tested model. So, we can infer that this technique not only benefits in the image (pattern) recognition kind of problems (CNN networks) but also on numerical data-based problems (ANN). Handling and organizing the dataset carefully, the network efficiency can be improved by generating more number of training data points, even if limited number of data points (patterns) is available initially.

Keywords Data augmentation · Discharge prediction · Meandering · Sinuosity · Training dataset

T. Khankhoje (✉) · S. Ghosh
Department of Civil Engineering, National Institute of Technology Silchar, Silchar 788010, India
e-mail: tushark_rs@civil.nits.ac.in

S. Ghosh
e-mail: susmita@civil.nits.ac.in

1 Introduction

The estimation of discharge is done by the rating curve of the given river gauging site [1]. These are established by calculating the discharge using various available methods like Manning's formula, Chezy's formula, Darcy Weisbach formula, etc. The discharge of stream depends upon various factors, i.e., head, bed slope, width, and surface parameters (like roughness), etc. [2]. One can determine the discharge of the stream by knowing these parameters, which are valid only for straight channels [3]. For meandering channels, we cannot simply use the above mentioned formulas for calculating discharge. The roughness parameters for meandering channels include the surface roughness, shape irregularities as well as channel losses due to bends (meanders). Therefore, the extent of meandering (sinuosity index) is a prime factor influencing the roughness and hence discharge of such streams [3]. The conveyance of a compound channel as a function of various geometrical and flow parameters was predicted using ANN technique [4].

ANN is a very powerful tool for establishing input–output relation without even knowing pre-requisite formulas or principles associated with the phenomena. Known as a black-box model, ANN learns from the past data that we feed into it. It makes all the complex unknown relationships simpler using a nonlinear and parallel approach [5]. Karunanithi et al. [5] used the cascade-correlation algorithm to predict the flow of Huron River, Mich., which proved to be more accurate than the power model. One such ANN model was set up for monthly discharge prediction in Barak River using regular arrangements of dataset [6]. But, the number of dataset must be sufficient for accuracy of the network [7]. The sinuosity does not vary in months. Considering yearly data, the number of patterns become too less. A feasible approach was considered, i.e., data augmentation technique [8]. The sinuosity and slope data were repeated 12 times in a year and fed to the network having monthly discharge and head dataset.

2 Study Area and Data Source

2.1 Barak River Basin

The study area is Barak river basin (area $\approx$ 52,000 km^2) which originates in Liyai Kullen village as Mukru River at latitude of 22° 44′ N and longitude of 89° 50′ E in the Manipur, India. The Annapurna Ghat gauging site having 24°49′58″N latitude and 92°47′24″E longitude was considered for study. The index map of the Barak river basin is shown in Fig. 1.
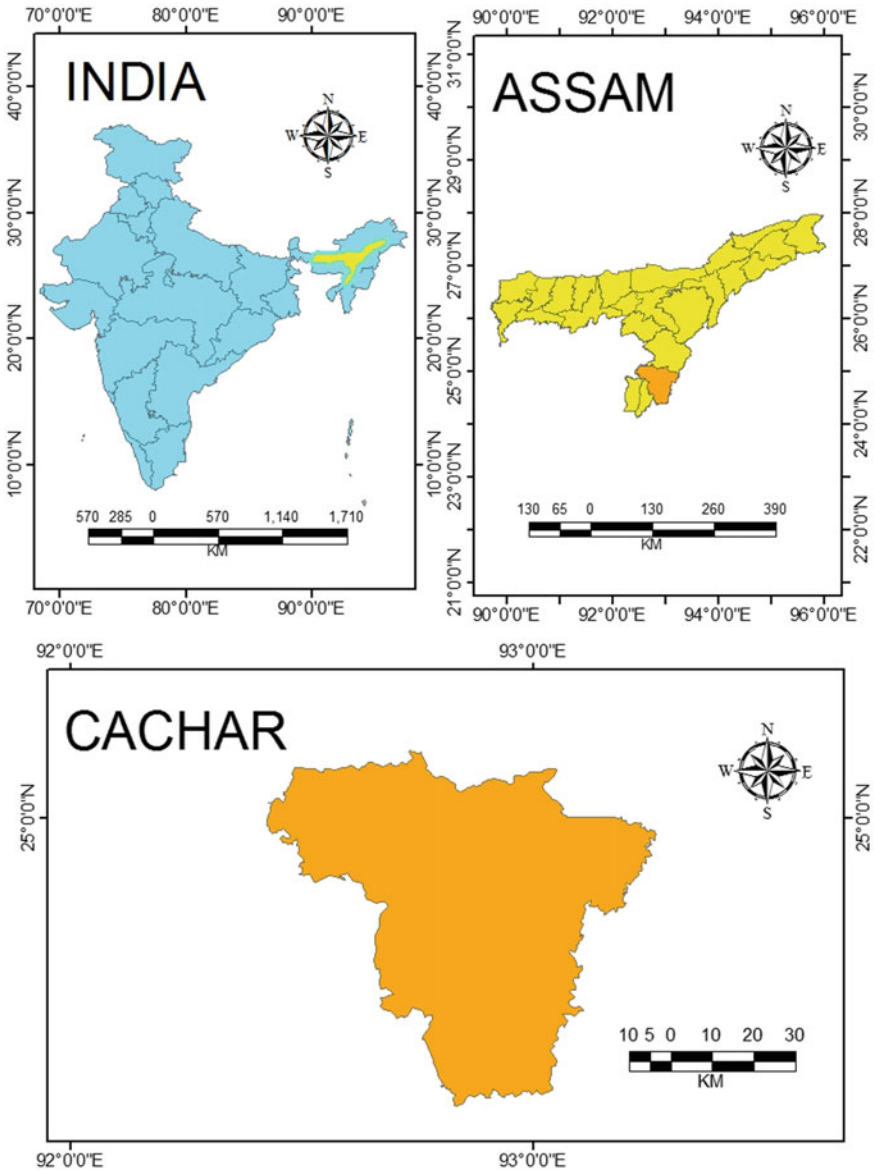
Fig. 1 Index map of study area
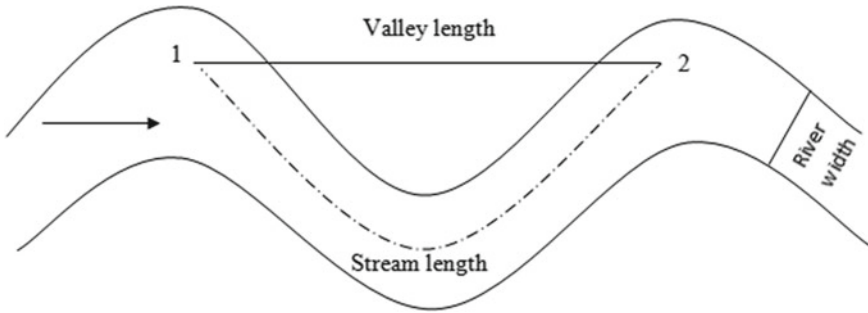
Fig. 2 Simple representation of sinuosity index

2.2 Data Used

The monthly average stage-discharge data for Annapurna Ghat gauging station were collected from Water Resources Department, Silchar division, and the yearly sinuosity and slope data for the same gauging site were obtained from Google Earth software.

There are various expressions for sinuosity index calculation as given by different researchers, according to the type of data being used. Here, it is calculated as the ratio of stream length to valley length as shown in Fig. 2 [9].

2.3 ANN Network Parameters

The major factors which affect the discharge are selected as our input parameters, viz. monthly head, sinuosity, slope, and previous month's discharge. Current month's average discharge was taken as our only output variable.

With four inputs and one output, a hidden layer with three nodes was taken at different learning rates (0.08, 0.09, 0.10, 0.11, 0.12, and 0.13). The number of hidden nodes was also limited due to limited dataset availability. According to Karsoliya [10], it should be between number of input and output nodes and should not exceed twice the input nodes (i.e., $4 \times 2 = 8$). So, we have considered three hidden nodes. Out of total 13 years monthly data, i.e., 152 patterns, 77% was taken for training and rest for testing the network. For hidden and output layers, sigmoid and absolute activation functions, respectively, were taken. The ranges of dataset of all the parameters are shown in Table 1. All the seasons of the year were considered, i.e., 12 months' dataset of 13 years each. So, the monsoon period discharge would be learnt by the model from June to September dataset of each year. Similar trend would be observed for pre-monsoon and post-monsoon periods.

Table 1 Ranges of dataset

Parameter	Minimum value	Maximum value	Range
Discharge (cumecs)	2556	95,094.25	92,538.25
Sinuosity index	1.53012	1.59169	0.06157
Monthly head (m)	8.56	19.15	10.59
Slope (%)	0.3	0.6	0.3

3 Materials and Methods

3.1 ANN Feedforward Backpropagation Algorithm

It consists of the feedforward process, comparison of network and desired output, and the backpropagation process, where the error is transmitted backward to reduce the error proportionately [11].

3.2 Backpropagation Learning Algorithm

Some necessary equations given by Rumelhart et al. [12] were used for this backpropagation neural network as shown in Eqs. (1)–(9).

$$\frac{\partial E}{\partial w_{mn}} = \delta_n * x_m. \tag{1}$$

$$o'_n = o_n * (1 - o_n) \tag{2}$$

$$\emptyset'_n = (1 - \emptyset_n) * (1 + \emptyset_n) \tag{3}$$

$$\emptyset'_n = \emptyset_n * (1 - \emptyset_n) \tag{4}$$

$$e_n = (o_n - t_n) \tag{5}$$

$$\delta_n = e_n * o'_n \tag{6}$$

$$\delta_n = \sum (\delta_n * w_n) * \emptyset'_n \tag{7}$$

$$\Delta w_{mn} = \alpha * \frac{\partial E}{\partial W_{mn}} \tag{8}$$

$$w'_{mn} = w_{mn} + \Delta w_{mn} \tag{9}$$

E represents the sum of squared error for output nodes, w_{mn} is the weight of 'mth' hidden layer node to nth output layer node, δ_n is being a factor for backpropagation error for nth node, x_m is the input signal at 'mth' node, o'_n is the derivative of 'o_n' for 'nth' output layer node, o_n is the output at 'nth' node, $\emptyset'_n$ is the derivative of $\emptyset_n$ for 'nth' hidden node, $\emptyset_n$ is the weighted sum of nodal inputs at the 'nth' hidden node, 'e_n' is the absolute error at 'nth' output node, t_n is being the target output at 'nth' node, w_n is the input signal at 'nth' hidden node, Δw_{mn} is the small change in weight between 'mth' hidden layer node and 'nth' output layer node, α is the learning rate, w'_{mn} is the updated weight between 'mth' hidden node to 'nth' output node.

3.3 Data Augmentation Technique

The data augmentation (DA) is a technique adopted in convolution neural networks that generates additional number of input patterns having common output ranges so as to meet the sufficiency of training dataset in ANN models [8].

For the case of limitation of dataset, the training of the ANN is not so accurate. There is a certain minimum number of patterns which are required as a training set. The minimum number of training data should be 10 times the total number of weights in the network [7]. In this case, we also had a limited number of data for sinuosity and slope. This technique had been previously applied in case of pattern or image recognition fields for convolution networks. But, for our normal data type of backpropagation network, this is still to be tested further for its validation.

Basically, for a given year data, the same sinuosity and slope value is being repeated 12 times, but the head and previous monthly discharge values vary as per the month. In this way, the yearly data have been converted into 12 monthly data, resulting in more number of patterns.

4 Results and Discussions

After collecting all the data and its normalization, it was fed into our network programmed with MATLAB software. With architecture of 4–3–1, the following performance criteria (with 0.11 learning rate), were obtained as shown in Table 2:

The best values were obtained at a learning rate of 0.11 which were the following. Root mean square error comes out to be 1.39194 cumecs, the coefficient of correlation (r) as +0.99998, coefficient of determination (r^2) as 0.99996. The RMSE first

Table 2 Result for different learning rates as obtained by the network

Performance criteria	Validation set						Training set
α	0.08	0.09	0.10	0.11	0.12	0.13	0.11
RMSE	3.659	2.766	2.201	1.391	1.619	2.748	1.436
r	+0.999	+0.999	+0.999	+0.999	+0.999	+0.998	+0.999
r^2	0.998	0.999	0.999	0.999	0.998	0.997	0.999

decreases with α (up to ≈ 0.11) and then rises again rapidly as shown in Fig. 3. The former may be due to overfitting of the data and the later phase due to insufficient number of iterations.

Comparing the measured discharge with the predicted one at different seasons, there is not much difference except during the post-monsoon period. The comparison is shown in Figs. 4, 5, and 6. The discharge is on the higher side during the monsoon period as compared to the pre- and post-monsoon periods.
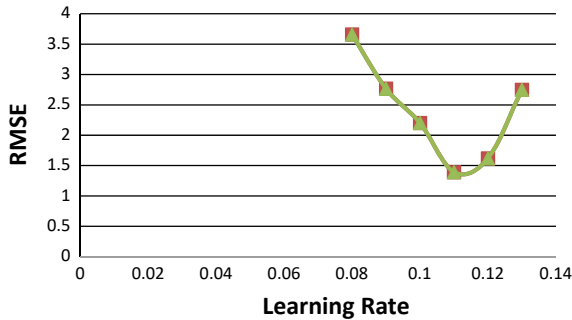
Fig. 3 Variation of RMSE with learning rate
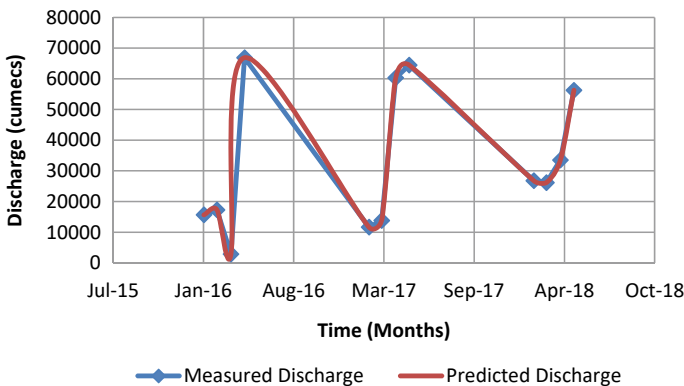
Fig. 4 Discharge comparisons for the pre-monsoon period
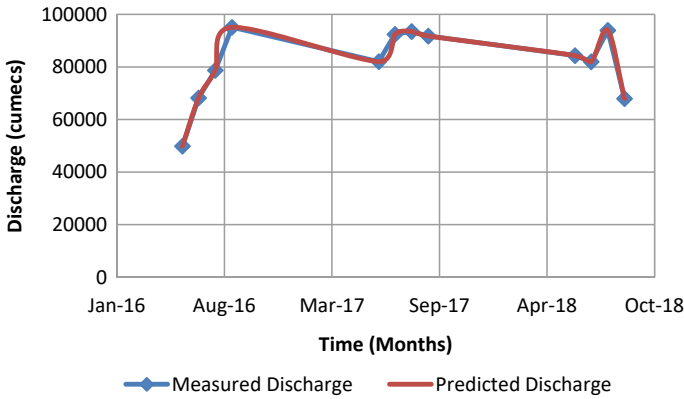
Fig. 5 Discharge comparisons for the monsoon period
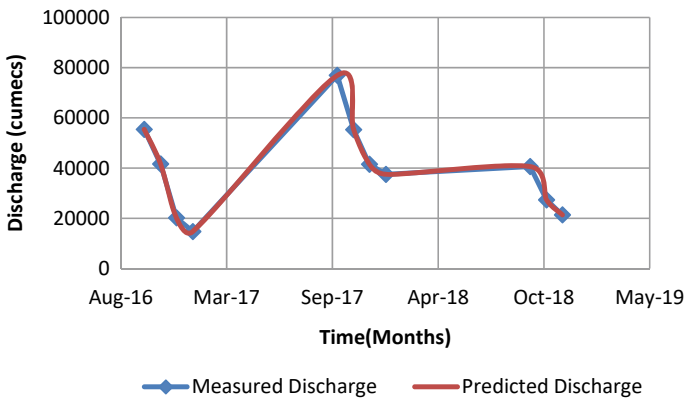
Fig. 6 Discharge comparisons for the post-monsoon period

5 Conclusions

- For a given network, type and number of data available, the data augmentation technique having a specific input, output, and hidden nodes, with an optimal learning rate can be efficiently used. This type of ANN network can be used for similar cases of meandering rivers.
- The result shows the usefulness of data augmentation technique in the proposed and tested model. So, it can be inferred that this technique not only benefits in the image recognition kind of problems but also on numerical data based problems. Handling and organizing the dataset carefully, the network efficiency can be improved by generating more number of training data points, even if limited number of data points (patterns) are available initially.

References

1. Sahoo GB, Ray C (2006) Flow forecasting for a Hawaii stream using rating curves and neural networks. J Hydrol 317(1–2):63–80
2. Sapkale JB (2014) Human interferences and variations in sinuosity index of Tarali channel, Maharashtra, India geography. Indian J Res. Paripex 3(5):36–37
3. Dash SS, Khatua KK (2016) Sinuosity dependency on stage discharge in meandering channels. J Irrig Drainage Eng 142(9)
4. Liu W, James CS (2011) Estimation of discharge capacity in meandering compound channels using artificial neural networks. Can J Civ Eng 27(2):297–308
5. Karunanithi N, Grenney WJ, Whitley D, Bovee K (1994) Neural networks for river flow predictions. J Comput Civil Eng ASCE 8(2):201–220
6. Khankhoje T, Ghosh S (2021) Discharge predictions of meandering river using artificial neural networks. In: Patra KC, Khatua KK, Sahoo SN (ed) Proceedings of HYDRO 2020 international conference (Hydraulics, water resources and coastal engineering) NIT Rourkela, India, 26–28 March 2021, vol 1, pp 507–518
7. Abu-Mostafa YS (1995) Financial market applications of learning from hints. In: Neural networks in the capital markets, pp 411–418
8. Mikolajczyk A, Grochowski M (2018) Data augmentation for improving deep learning in image classification problem. In: IEEE (ed) International interdisciplinary Ph.D workshop (IIPhDW), Swinoujscie, Poland, 9–12 May 2018, pp 117–122
9. Friend PF, Sinha R (1993) Braiding and meandering parameters. Geol Soc London Spec Publ 75(1):105–111
10. Karsoliya S (2012) Approximating number of hidden layer neurons in multiple hidden layer BPNN architecture. Int J Eng Trends Technol 3(6):714–717
11. Kisi O (2004) River flow modelling using artificial neural networks. J Hydrol Eng 9(1):60–63
12. Rumelhart DE, Hinton GE, Williams RJ (1986) Learning representations by back-propagating errors. Nature 323:533–536

Analysis of River Meandering and Morphometric Changes Using GIS Approach: A Case Study of Sub-Basin of the Narmada River

H. S. Lalwani and T. M. V. Suryanarayana

Abstract Morphometric analysis and sinuosity index are important parameters to understand river basin behavior and river pattern. Earlier, measurements of morphometric analysis and sinuosity index were done by traditional methods such as field analysis and topographical maps. With the advancement of Geographical Information System (GIS), these analyses are much easier. The present work is focused for Narmada river sub-basin from Bharuch to Garudeshwar with using Arc GIS software. Sinuosity index has been measured for the different years such as 1988, 1992, 1997, 2000, 2014, and 2018 with the extraction of river from Landsat images: Operational Land Imager (OLI) and Thematic Mapper (TM) (OLI). The extracted river's sinuosity index ranges from 1.60 to 1.69, which is greater than 1.5 and indicates a meandering pattern of the river as well as uneven changes in the river pattern during the analysis period. Morphometric parameters are calculated for 2014 with basin delineation and extraction of stream network process from Digital Elevation Model (DEM) of region using the Arc GIS 10.7 software. Linear and areal aspects of morphometry parameters are calculated from extracted river basin. From the evaluation, the basin is classified as the third order with 69 segment of streams covers an area of 3763.22 km^2 and perimeter of 463.85 km. The total stream length is 591.64 km, and it shows that the first-order streams have the longest total length of stream segments, whereas increasing stream order causes this length to decrease. Mean bifurcation ratio of basin is 1.72 which indicates that the less structural disturbance of drainage pattern. The values for drainage density and texture are 0.148 and 0.16 km/km^2, respectively, and they describe the permeable soil strata with very coarse texture of basin. The elongation ratio, circulatory ratio, and form factors values are 0.410, 0.219, and 0.132, respectively, which indicate very low value and confirm is very elongated type

H. S. Lalwani (✉)
Department of Civil Engineering, C. K. Pithawala College of Engineerimg and Technology, Surat 395007, India
e-mail: honeylalwani1995@gmail.com

T. M. V. Suryanarayana
Water Resources Engineering and Management Institute, The Maharaja Sayajirao University of Baroda, Samiala, Vadodara 391410, India
e-mail: tmvkiran@yahoo.com

basin shape. The study and results can be used for future planning and management of this basin.

Keywords Meandering · Sinuosity index · Morphometric analysis · GIS

1   Introduction

The Büyük Menderes River flows from west-central Turkey to the Aegean Sea east of Milet, the ancient Ionian city of Miletus, is where the word "meander" first appeared. The ancient Greeks called this meandering river Maandros (Latin meander). Since then, the phrase has come to be used to denote anything with a winding form, including ornamental designs in art and architecture. In general, a meander is a curve in a sinuous river. A meander is any of a number of regular sinuous curves, bends, loops, or turns in the channel of a river, stream, or other watercourse. Rivers that are flowing over gently sloping terrain begin to wind around the landscape. These rivers are termed as meandering rivers. Most often found in lowland alluvial plains defined by a dense canopy of plants and cohesive soils, meandering rivers are a frequent platform of rivers. They lack significant longitudinal width changes and have a single, very permanent sinuous channel. River meandering is an inherent characteristic of drainages in an alluvial plain. Straight channels, which have very little sinuosity, are distinguished from braided channel patterns, which include multiple channels or multiple free bars within the course. The process of measuring the outer form and size of landforms, living things, or other objects is known as morphometric. It is the area of study that deals with calculating the quantitative dimensions of any natural shape or form. To describe valley side and channel slopes, relief, area, drainage network type and extent, and other variables, a number of quantitative measures have been developed. Morphometric analysis is the quantitative description and analysis of landforms as applied in geomorphology, and it may be applied to a specific type of landform or to drainage basins. The statistical correlation of variables defining the hydrology and features of drainage basins has produced important findings.

2   Study Area

In research study, river considered for present study is a part of lower Narmada river from Bharuch to Garudeshwar shown in Fig. 1 for determination of sinuosity index and basin considered for study which is in the lower sub-basin of Narmada river shown in Fig. 1 for analysis of morphometric changes of basin. The distance between Bharuch to Garudeshwar is 84.1 km. The study river length is 75.3 km, and area of study river basin is 3763.22 km^2.
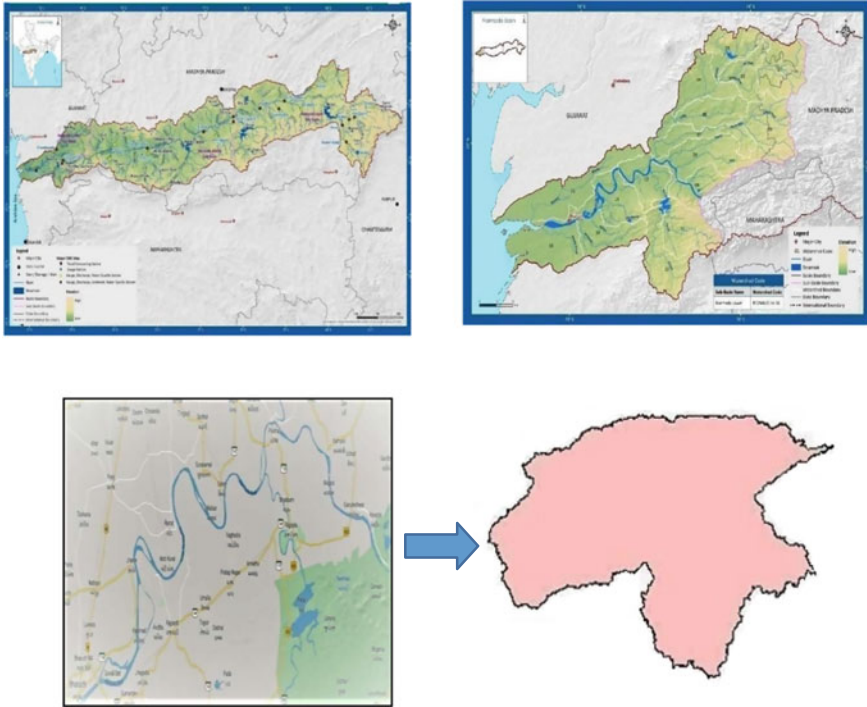
Fig. 1 Index map of study area

3 Data Collection

The study discusses the scenario of river meandering for different years from sinuosity index and basin behavior from morphometric parameters. It derives from satellite images for that particular year. Satellite images can be downloaded from a variety of websites, including the Bhuvan portal and the USGS Earth Resources Observation Systems data center. Here, satellite images such as Landsat images and DEM are downloaded from USGS Earth Resources Observation system data centers.

For research on Landsat, images are a unique resource for global change and applications in regional planning, agriculture, geology, forestry, surveillance, and education.

Raster files called Digital Elevation Models (DEMs) contain elevation information for every raster cell DEMs are widely used for calculations, manipulations, and further analysis of an area, particularly analysis based on elevation.

4　Methodology

The complete flowchart of methodology is given below.
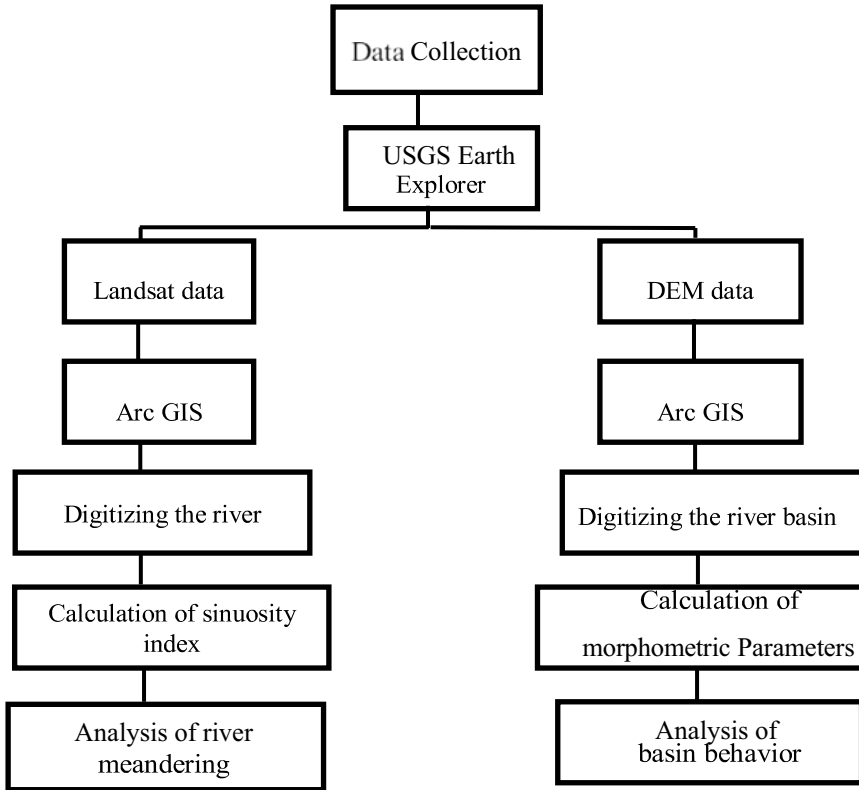
4.1　Methodology for Analysis of Sinuosity Index

GIS was used to investigate river meandering by measuring the sinuosity index for different years. For this study, six sets of imagery were used: Landsat TM and ETM + images acquired in 1988, 1992, 1997, 2000, 2014, and 2018, respectively. For measurement of sinuosity index, extracted river of study area is needed. Then measurements of that river are done by using of Arc GIS 10.7 software.

Steps for extracting the river and measurement of sinuosity index are as follows (Figs. 2, 3, 4, 5, 6 and 7):

Step 1 In Arc GIS, add the satellite image from add data icon.

Step 2 Create a new shape file and start editing by using polygon and select study area portion.

Step 3 Extract selected study area portion by mask process.

Step 4 Classify the extracted portion into iso cluster unsupervised classification.

Step 5 Reclassify the classified image.

Step 6 Convert that image from raster to polygon.

Step 7 From polygon image, copy the river and paste it into new created shape file.

Step 8 Measure the expected river length and observed river length from the measure tool.

Step 9 Calculate the sinuosity index from this analysis by using following formula:

$$\text{Sinuosity index} = \text{Observed length/Expected length}$$

Fig. 2 Add Landsat image
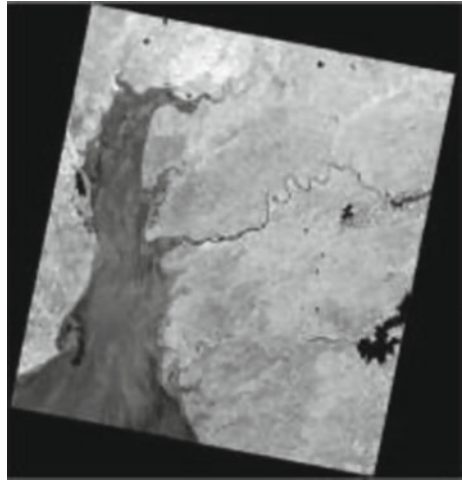
Fig. 3 Extract by mask
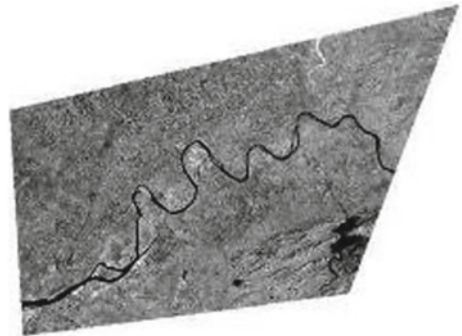
Fig. 4 Unsupervised cluster classification
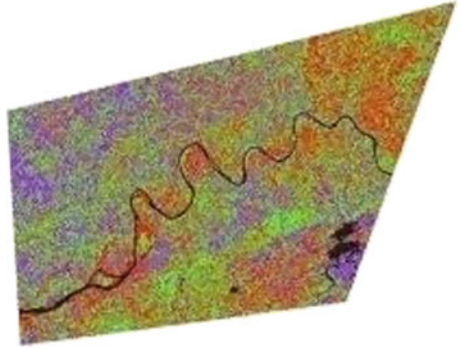
Fig. 5 1reclassificatio of image

Fig. 6 Conversion from raster to polygon

Fig. 7 New created shape

4.2 Methodology for Analysis of Morphometric Parameters

Measurements of several river basin morphometric characteristics have been performed using Arc GIS and mathematical equations. DEM image of study area is acquired for this process. For this analysis, basin delineation process and stream network extraction have been done, and then morphometric parameters have been calculated which are given in Table 1.

Steps for extracting the river basin, basin stream networks, and measurements of morphometric parameters are as follows (Table 1, Figs. 8, 9, 10, 11, 12, 13, 14, 15 and 16):

Step 1 In Arc GIS, add the DEM of area from add data icon.
Step 2 Extract the river basin from DEM image by following procedure.

- Fill the basin DEM image
- Give the flow direction in which water flows
- Create the raster file that shows all drainage basin

Table 1 Morphometric parameters

Morphometric parameter	Method	References
Linear aspects		
Stream order (U)	Hierarchical rank	Strahler [1]
Number of streams (Nu)	$Nu = N1 + N2… + N6$	Horton [2]
Stream length in km (Lu)	$Lu = L1 + L2…. + L6$	Horton [2]
Mean stream length (Lum)	$Lum = Lu/Nu$	Strahler [1]
Bifurcation ratio (Rb)	$Rb = Nu/Nu + 1$	Schumm [3]
Stream length ratio (RL)	$RL = Lu/Lu-1$	Horton [2]
Areal aspects		
Area in km^2 (A)	Area calculation	–
Perimeter in km (P)	Perimeter calculation	–
Length of the basin in km (Lb)	Length calculation	–
Drainage density (Dd)	$Dd = Lu/A$	Horton [4]
Stream frequency (Fs)	$Fs = Nu/A$	Horton [4]
Circulatory ratio (Rc)	$Rc = 12.57*(A/P^2)$	Miller [5]
Elongation ratio (Re)	$Re = 2/Lb*\sqrt{(A/\pi)}$	Schumm [3]
Form factor (Ff)	$Ff = A/Lb^2$	Horton [4]
Drainage texture (T)	$T = Nu/P$	Horton [2]

Fig. 8 Add DEM image

Fig. 9 Fill process

- Convert the raster image into vector polygon
- Select basin from polygon and clip to form the shape file.

Step 3 Create stream network system by following procedure.

Fig. 10 Flow direction

Fig. 11 Raster basin

- Accumulate the flow to the location
- Set the different accumulation rates by trial and error method
- Convert this raster into polyline layer
- Clip the stream network by river basin limits using clip tool.

Fig. 12 Selection of basin

Fig. 13 Extraction of basin
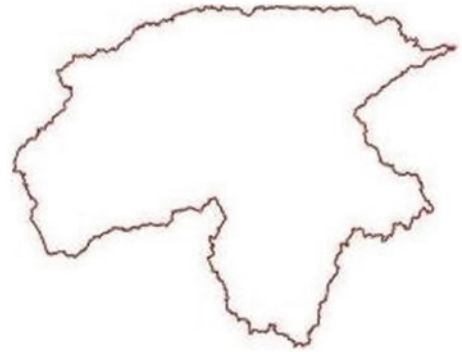
Step 4 Generate the stream orders of stream network. Convert this raster network into polyline network.

Step 5 Show the stream orders, numbers of stream orders, and length of particular stream order from the properties.

Step 6 Measure the area, perimeter, and length of basin using Arc GIS software and other parameters from following formulas.

Fig. 14 Flow accumulation

Fig. 15 Stream feature
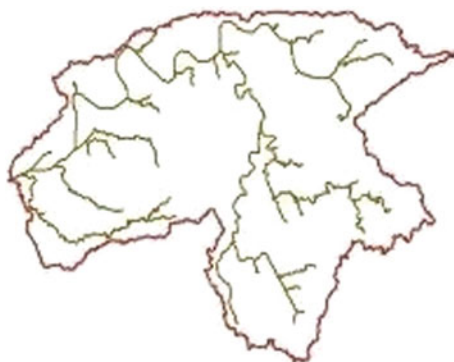
Fig. 16 Stream order
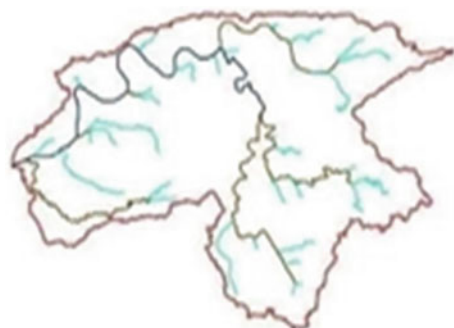
Table 2 Sinuosity index

Years	Expected length (km)	Observed length (km)	Sinuosity index (SI)
1988	75.3	121.27	1.61
1992	75.3	125.42	1.66
1997	75.3	122.69	1.63
2000	75.3	124.63	1.65
2014	75.3	121.99	1.62
2018	75.3	123.58	1.64

5 Results and Discussions

5.1 Sinuosity Index

The sinuosity index of Narmada river from Bharuch to Garudeshwar for different years from 1988 to 2018 is summarized in Table 2.

The Mullar [6] channel sinuosity index is used to analyze the morphology of rivers. No river flows directly from its source to its mouth in real life. A river's path will be straight if the index value is 1. Sinuous rivers have values between 1.0 and 1.5, while meandering rivers have values over 1.5.

Table 2 shows the analyzed values of expected river lengths, observed lengths, and calculated sinuosity index. The sinuosity index value varies from 1.60 to 1.66 in respected years, so clearly it shows the meandering river course.

5.2 Evaluation of Morphometric Parameters

Figure 17 shows the analyzed map of the stream network in the Narmada river sub-basin. For the basin, the linear and areal aspects of the morphometric analysis are carried out. The morphometric parameters of the Narmada river basin have been evaluated. The total study area is 3763.22 km^2 with 463.84 km perimeter.

Fig. 17 Stream network of basin
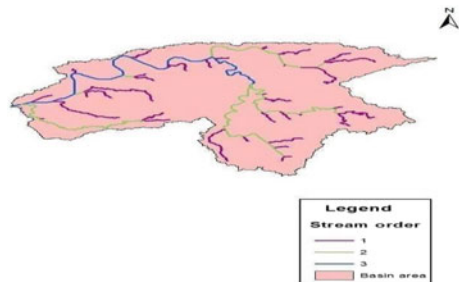
A. Linear aspects

Linear aspects of the basin are characterized by the stream linkages and the nodes. The morphometric parameters stream order, stream number, stream length ratio, and bifurcation ratio make up the linear aspects. The linear aspects of morphometric parameters of the Narmada river sub-basin are discussed further below.

Stream order (U)

In 1964, Strahler developed the idea of stream order. Stream ordering is the first step in morphometric analysis of a drainage basin, a technique for classifying streams in a river basin. With the use of Arc GIS, this basin is classified as the third order.

Stream number (Nu)

The total number of streams in the basin is counted independently using Arc GIS. In general, as stream order rises, the number of streams gradually declines. The size of tributary basins and variance in stream order are strongly influenced by the physiographic and structural conditions of the region. The Narmada river sub-basin has been identified as having 69 stream segments. This analysis has proved the stream segment decreases with the increase in stream order.

Stream length (Lu)

Arc GIS 10.7 software is used to compute the length of a stream (Lu) from a river's mouth to its drainage. The total stream length of the Narmada river sub-basin is 591.64 km. According to this analysis, the first-order streams have the longest overall length of stream segments, and as the stream order increases, this length reduces. Longer stream lengths are typically indicative of low gradients, while comparatively short stream lengths are indicative of regions with steep slopes and finer texture.

Mean stream length (Lum)

The mean stream length (Lum) was calculated by dividing the total length of the stream by the number of stream segments. The Lum values for the Narmada basin vary from 7.86 to 9.095 km. The Lum values differ in relation to various basins since they are inversely proportional to the basin's size and terrain.

Stream length ratio (Rl)

The stream length ratio compares the lengths of streams in one order to the lengths of all streams in the following order. The Rl values for the Narmada river basin are 0.965 to 1.198 which is strongly dependent on the topography and the slope.

Bifurcation ratio (Rb)

The bifurcation ratio is related to the branching pattern of a drainage network and is defined as the ratio of the number of streams in any given order in a drainage basin to the number of streams in the next higher order. Rb indicates a narrow range of fluctuation depending on the location or the environment. The bifurcation ratio for the Narmada sub-basin is with a mean Rb of 1.72. When geological formations

have little impact on the drainage network, the mean bifurcation ratio for a basin is typically between 3.0 and 5.0. Low Rb value denotes minimal structural disruption and stable drainage systems, whereas the low permeability of the terrain and high structural complexity are indicated by the high Rb value. In the current study area, the total bifurcation ratio is 3.42 and the mean is 1.72, indicating a low mean value and fewer structural disturbances in the Narmada sub-basin.

B.   Areal aspects

The areal aspects of a drainage basin show the influence of the basin's denudation history, lithology, climate, and geological structure. The drainage density (Dd), stream frequency (Fs), elongation ratio (Re), circulation ratio (Rc), form factor (Ff), and drainage texture are the morphometric factors that comprise the areal aspects (T).

Basin area (A) and Basin perimeter (P)

In quantitative geomorphology, the area (A) and perimeter (P) of a basin are important parameters. The basin's area is defined as the total area projected onto a horizontal plane, the perimeter of the basin is its entire boundary length, and the size of the basin is its total area projected around on a horizontal plane. The basin area and perimeter of the Narmada river sub-basin are computed 3763.22 km^2 and 463.84 km, respectively, with the help of Arc GIS 10.7.

Basin length (Lb)

There are numerous ways that scientists have defined the length of the basin (Lb). Schumm [3] defines it as the length of the basin parallel to the main drainage line. Using Arc GIS software, the Narmada river sub-basin's length was computed in accordance with this specification and discovered to be 168.60 km.

Drainage density (Dd)

The ratio of the total length of all streams in the basin to the basin area, expressed in terms of km/km^2, is known as the drainage density (Dd).

The Dd of the Narmada sub-basin is found to be 0.16 km/km^2 which is less than 1. According to Table 3, low drainage density and the presence of a highly permeable subsoil are both indicated by the drainage density.

Stream frequency (Fs)

Stream frequency is defined as the number of streams per unit area. Depending on the lithology of the basin, the range of Fs values may range from less than 1 to 6 or

Table 3 Drainage density [4]

Drainage density (km/km^2)	Surface behavior
<1	Highly permeable
1–5	Permeable
>5	Highly impermeable

even more. The basin's stream frequency is 0.75 in this study, and it denotes a low value, the existence of a porous subsurface substance, and low relief.

Circulatory ratio (Rc) and Elongation ratio (Re)

The ratio of the basin's area to the area of a circle with the same diameter as the basin's perimeter is the circulatory ratio, which has no dimensions. According to Miller, geologic materials that are substantially elongated and permeable range in circularity ratios from 0.4 to 0.5. The basin's circular form increases with higher Rc values and vice versa. The circulatory ratio in the study area is 0.219, indicating that the basin is nearly elongated in shape. The elongation ratio was used to show characteristics of basin shape. It is the ratio of the diameter of a circle of the same area as the drainage basin to the basin's maximum length. The elongation ratio can be used to categorize the different river basin shapes. The elongation ratio of the Narmada river sub-basin is 0.410, confirming that the basin is very long (Table 4).

Form factor (Ff)

The form factor is the ratio of the basin area to the square of the basin length. It is a dimensionless number for a completely circular basin. The form factor value would always be greater than 0.78. Smaller the value of form factor, more elongated will be the basin. Form factor value of the Narmada sub-basin is 0.132. Thus, the Narmada sub-basin is the elongated one.

Drainage texture (T)

One of the key elements of geomorphology is the drainage texture, which refers to the distance between drainage lines. The total number of stream segments in all orders per area perimeter makes up the drainage texture. Smith [7] divided drainage texture into five distinct textures, which are represented in Table 5.

Table 4 Elongation ratio range [3]

Elongation ratio	Basin shape
>0.9	Circular
0.8–0.9	Oval
0.7–0.8	Less elongated
0.5–0.7	Elongated
<0.5	Very elongated

Table 5 Drainage texture range [7]

Drainage texture	Basin behavior
<2	Very coarse
2–4	Coarse
4–6	Moderate
6–8	Fine
>8	Very fine

In the present study, the drainage texture of the Narmada sub-basin is 0.148 which is shown in the table, and it indicates a very coarse drainage texture.

6 Conclusions

The results of the current study lead to the following conclusions:

i. The SI of river varies from 1.60 to 1.66. From the analysis, SI value of all selected years is greater than 1.5, which shows the meandering type of river. It also shows very unstable type river, so it concludes that the river has very unstable type of meandering which varies unevenly during this period.

ii. Analysis of morphometric parameters concludes that basin is classified as the third order with the total 69 stream segments having an area and perimeter of 3763.22 km^2 and 463.85 km, respectively. The total stream length is 591.64 km, it shows that the overall length of stream segments in the first-order streams is the longest, and as stream order increases, this length gets shorter. The mean bifurcation ratio is 1.72 which suggests that the basin has less structural disturbance. The drainage density of basin is 0.16 km/km^2, which indicates the permeable subsoil strata with low drainage density. The values of the elongation ratio, circulation ratio, and basin form factor all indicate that the basin shape is very elongated. Stream frequency and drainage texture show the lower value and indicate the presence of a permeable subsurface material and very coarse texture of basin.

References

1. Strahler A (1964) Quantitative geomorphology of drainage basins and channel networks. In: Chow V (ed) Handbook of applied hydrology, McGraw Hill, New York, pp 439–476
2. Horton R (1945) Erosional development of streams and their drainage basins; Hydrophysical approach to quantitative morphology. Geol Soc Am Bull 56:275–370
3. Schumm SA (1956) Evolution of drainage systems & slopes in badlands at Perth, New Jersey. Bull Geol Soc Am 67:597–646
4. Horton RE (1932) Drainage basin characteristics. Trans Amer Geo Phys Union 13:350–361
5. Miller VC (1953) A quantitative geomorphic study of drainage basin characteristics in the Clinch Mountain area. Department of Geology, Columbia University, New York, USA, pp 389–402
6. Mullar JE (1968) An introduction to the hydraulic and topographic sinuosity indexes. Ann Assoc Amerian Geogr 2:371–385
7. Smith K (1950) Standards for grading textures of erosional topography. Am J Sci 248:655–668

Analysis of River Meandering and Morphometric Parameters Using Remote Sensing and GIS

Srushti N. Patel and Falguni Parekh

Abstract In the present study, morphometric analysis on Sabarmati river is carried out using RS and GIS. The study is carried out for Sabarmati river from Dharoi dam to Vasna barrage using TM and OLI-TIRS images of years 1988, 1992, 1996, 2000, (Landsat 4–5) 2014, 2017, and 2021 (Landsat 8). Sinuosity index is calculated for five segments of each 20 km length and one for entire 21.2 km length. The values of sinuosity index for five segment lengths are 1.13 to 1.19, 1.15 to 1.235, 1.547 to 1.7, 1.4 to 1.49, 1.11 to 1.15, and 1.255 to 1.3, respectively. This indicates uneven change in river form over a period of 33 years. From detailed segment analysis, it reveals that behavior of river is braided unstable. It is also observed that for 40–60 km segment (Soja to Vagpur), sinuosity index is the highest. This is the flood prone area, and it needs extra attention at high discharges. Analyses of morphometric parameters are carried out by DEM image. For the study area, linear aspects, like stream order, range from 1 to 4, total stream number is 247, and total stream length is 727.84 km. Mean bifurcation ratio is 1.68, which indicates less structural disturbance. Areal aspect like basin area is of 1667.9 km^2, and perimeter is 408.15 km. Drainage density, stream frequency, drainage texture ratio, circulatory ratio, elongation ratio, and form factor are 0.43 km/km^2, 0.148, 0.6052, 0.1257, 0.298, and 0.069, respectively. Low drainage density indicates highly permeable subsurface material and extensive vegetative cover. Lower elongation ratio, circulatory ratio, and form factor indicate basin is elongated in nature and is more vulnerable to erosion and sediment load. Drainage texture ratio indicates basin is very coarse in nature.

Keywords GIS · Meandering · Morphometric · RS · Sinuosity index

S. N. Patel · F. Parekh (✉)
Faculty of Technology and Engineering, Water Resources Engineering and Management Institute, The Maharaja Sayajirao University of Baroda, Samiala 391410, India
e-mail: fpparekh-wremi@msubaroda.ac.in

© The Author(s), under exclusive license to Springer Nature Singapore Pte Ltd. 2023
P. V. Timbadiya et al. (eds.), *Fluid Mechanics and Hydraulics*, Lecture Notes in Civil Engineering 314, https://doi.org/10.1007/978-981-19-9151-6_26

1 Introduction

The morphology of river describes the shapes of river channels and how they change in shape and direction over time. This change occurs due to sedimentation and erosion. Meandering is a significant way to observe morphometric parameters. Mostly river flows zig-zag manner at flat gradient, which is called meandering of the river. Higher velocity flow erodes the concave bank of the river and deposition on the convex bank due to less energy. The meandering action increases the length of the stream, and river tends to reduce the slope. River shows different plan form characteristics based on which river is classified into three types as follows: straight (SI < 1), braided river (1 < SI > 1.5), and meander river (SI > 1.5).

Morphometric analysis is the measurement and quantitative evaluation of the earth's surface, form, and dimension of landforms. It is important to carry out morphometric analysis of the river and its basin for understanding the geohydrological system like basin's nature which expresses the basin's climate, geological conditions, geomorphology, and structural backdrop. A quantitative assessment of the river basin is required for basin management. Various morphometric parameters are there. Out of these linear parameters like stream order, stream number, bifurcation ratio, strength length, etc., areal parameters like circularity ratio, elongation ratio, drainage density, drainage frequency, etc., and relief parameters which include dissection index, ruggedness index, etc., are significant to understand the river characteristic and basin management.

Prajapati et al. [1] carried out study of meander of Tapi River around Surat city. From the observation and analysis of temporal changes, it is deduced that the channel shifting is more at the ends of meander curvature to the apex of the meander portion of Tapi river. The study also indicates that the flood events and construction of Singapore weir as major factor which causes erosion and sedimentation that ultimately leads to the shift of river banks and changes in the width of the river. Kumar et al. [2] carried out research work which deals with sinuosity index. They determined the meandering and sinuosity of the river Ganga. Remote sensing and Geographical System Information (GIS) analysis, and sinuosity index were used in this study to investigate and classify the river into straight, sinuous, and meander category. Kulkarni [3] suggested that the morphometric analysis of the drainage basin and channel network plays a significant role in comprehension of the geohydrological nature of drainage basin and expresses the prevailing climate, geological setting, geomorphology and structural antecedents of the catchment area. A quantitative evaluation of drainage system is significant aspect of drainage basin. Das [4] carried out the study of a meander in River Barak around Silchar town in Assam using remote sensing and GIS, encompassing a period of thirty-four years between 1976 and 2010. Changes in planform characteristics of River Barak are analysed with the help of six remote sensing images of the years 1976, 1979, 1988, 1999, 2003, and 2010. Khakhlari and Nandy [5] carried out morphometric analysis using Geographical Information System (GIS) techniques to evaluate the different morphometric characteristics by considering three parameters: linear,areal and relief aspects. The basin is characterized by dendritic drainage pattern. Rai et al.

[6] selected Kanhar basin a tributaries of Son River, for detailed morphometric analysis. Seven sub-watersheds are also delineated within this basin to calculate the selected morphometric parameters. Morphometric parameters viz; stream order, stream length, bifurcation ratio, drainage density, stream frequency, form factor, circulatory ratio, etc., are calculated. Saha et al. [7] used Remote Sensing and GIS techniques for the identification of morphological characteristics and analyzing the properties of the Krishni River Watershed in Hindon river basin, which itself is part of the mega Yamuna River in Uttar Pradesh, India. In this study, the Shuttle Radar Topographic Mission (SRTM) Digital Elevation Model (DEM) is used for measurement of morphometric characteristics like areal, linear and relief aspects with the help of ArcGIS software which is an automatic extraction tool was developed by ArcGIS environment to delineate the basin morphometric components. Waikar and Nilawar [8] presented study of Charthana located in Parbhani district of Maharashtra state in India, which deals mainly with the geometry, more emphasis being placed on the evaluation of morphometric parameters such as stream order (Nu), stream length (Lu), bifurcation ratio (Rb), drainage density (D), stream frequency (Fs), texture ratio (T), elongation ratio (Re), circularity ratio (Rc),and form factor ratio (Rf) etc.

2 Study Area and Data Source

2.1 Sabarmati River Basin

The Sabarmati river originates from the Aravalli Mountains range of Udaipur district, Rajasthan, and meets the Gulf of Khambhat. Sabarmati is the non-perennial river of Gujarat. The total catchment area of the Sabarmati basin is 21674 km^2, out of this 4124 km^2 (19.03%) belongs in Rajasthan state and the other 18,550 km^2 (85.60%) lies in Gujarat. The area of the Sabarmati basin lies between east longitude 72°15′ to 73°49′ and north latitude 22°15′ to 24°53′. The major tributaries of Sabarmati river are the Wakal, Hathmati, Harnav, and Watrak rivers.

The study area is in the upper Sabarmati basin from Dharoi dam, Satlasana taluka, and Mehsana district 24°0′16″N 72°51′13″E to Vasna barrage, Ahemdabad district 23.0341367°N 72.5723255°E. River length is almost 166 km considered for sinuosity index and morphometric parameter analysis. Study area is presented in Figs. 1 and 2.

2.2 Data Sources

To analyze the meandering of the Sabarmati river from 1988 to 2021, Landsat images of the years 1988, 1992, 1996, 2000, 2014, 2017, and 2021 were used. The time span of the study is 33 years. For the analysis of morphometric parameters, DEM data were

Fig. 1 Location of Sabarmati river basin (India WRIS)
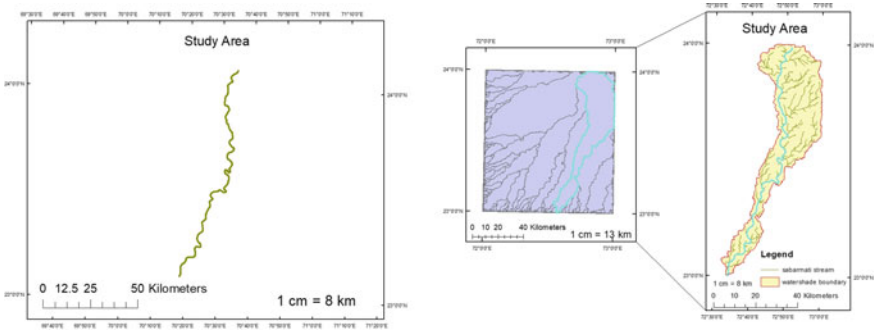
Fig. 2 Location of study area from Dharoi dam to Vasna barrage

used. Remote sensing data were downloaded from USGS earth explorer. Summary of images which were collected for analysis of meandering and morphometric study is presented in Table 1.

Table 1 Summary of images used for meandering and morphometric study

Satellite sensor	Date (dd–mm–yyyy)
Land set 4–5 TM C-1 Level-1	19–Mar–1988
Land set 4–5 TM C-1 Level-1	14–Mar–1992
Land set 4–5 TM C-1 Level-1	25–Feb–1996
Land set 4–5 TM C-1 Level-1	25–Mar–2000
Landsat 8 OLI/TIRS C-1 Level-1	12–Feb–2014
Landsat 8 OLI/TIRS C-1 Level-1	18–Mar–2017
Landsat 8 OLI/TIRS C-1 Level-1	8–Feb–2020
SRTM 1 Arc second global	23–Sept–2014

TM thematic mapper, *OLI* operational land imager, *TIRS* thermal infrared sensor

3 Methodology

3.1 Methodology for Meandering

For the analysis of meandering on the Sabarmati river, the ortho-rectified images of satellites such as Landsat thematic mapper (TM), operational land imager (OLI), and thermal infrared sensor (TIRS) are used for meandering analysis.

Analysis was done by using ArcGIS 10.8. All the Landsat images were georeferenced with the Universal Transverse Mercator (UTM) projection with zone 42N and WRS path 148 and row 44. The satellite images were assured as lesser error images.

For digitization of river and geometrical calculation, GIS software (Arc map) was used. Channel boundaries were digitized as a polygon into an Arc GIS 10.8. After the extraction of the river, Dharoi dam to Vasna barrage river length is divided into different segments (totally six segments in which five segments have a length of 20 km and one segment has a length of 21.2 km) as shown in Fig. 3. The sinuosity index (SI) is calculated using equation: (SI = Observed length (OL)/Expected straight length (EL)).

3.2 Methodology for Meandering

Analysis of morphometric parameters of the Sabarmati river basin is carried out using remote sensing techniques and a Geographical Information System (GIS). The SRTM Digital Elevation Model has been used for delineating water shade. Digitalization of water shade is done by Arc GIS 10.8. The morphometric parameters, linear aspect, areal aspect, and relief aspects are determined. The basin boundary, flow direction, flow accumulation, stream order, stream numbers, stream length, area, and perimeter were find out by Arc GIS 10.8 software. The morphometric parameters like stream length ratio, bifurcation ratio, stream frequency, drainage density, drainage texture

Fig. 3 Extraction of river
with different segments
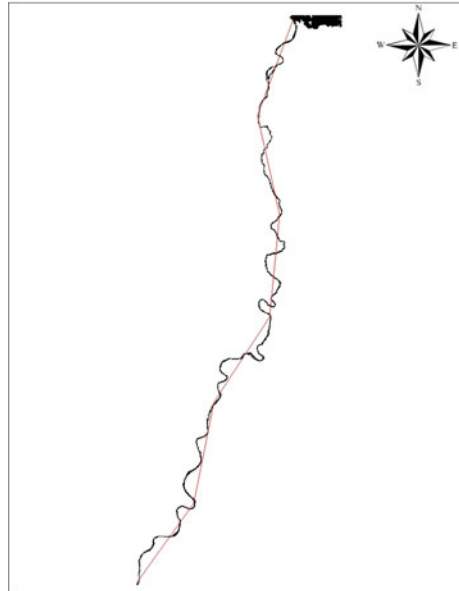
ratio, elongation ratio, circulatory ratio, and form factor are determined based on the
formulas and given in Table2.

4 Results and Discussions

4.1 Sinuosity Index Measurement

Table 3 indicates year wise meander river measured length and straight length of
each segment of study area of Sabarmati river.

There are totally six segments. For the segment lengths 0–20 km, 20–40 km,
40–60 km, 60–80 km,80–100 km, and 100–121.2 km, the value of sinuosity index
ranges from 1.13 to 1.19,1.15 to 1.235,1.547 to 1.7,1.4 to 1.49,1.11 to 1.15, 1.255 to
1.3, respectively, and is presented in Table 4. This indicates uneven change in river
form over a period of 33 years. If SI < 1.2, it is stable river, SI > 1.2 unstable river,
and SI > 1.5 very unstable river.

Table 2 Methodology adopted for computations of morphometric parameters

Morphometric Parameter	Method
Linear Aspects	
Stream order (U)	Hierarchical rank
Number of streams (Nu)	Nu = N1 + N2… + N6
Stream length in km (Lu)	Lu = L1 + L2…. + L6
Stream length ratio (RL)	RL = Lu / Lu-1
Bifurcation ratio (Rb)	Rb = Nu/Nu + 1
Mean bifurcation ratio (Rbm)	Rbm = average of bifurcation ratios of all orders
Rho coefficient (p)	p = RL/Rb
Areal Aspects	
Area in km^2 (A)	Area determination
Perimeter in km (P)	Perimeter determination
Length of the basin in km (Lb)	Length determination
Stream frequency (Fs)	Fs = Nu/A
Drainage texture ratio (Rt)	Rt = Nu/P
Drainage density (Dd)	Dd = Lu/A
Circulatory ratio (Rc)	Rc = 12.57*(A/P^2)
Form factor (Ff)	Ff = A/Lb^2
Elongation ratio (Re)	Re = 2/Lb * $\sqrt{}$(A/π)

Table 3 Measured length of study area of Sabarmati river

Meander river segments length, km							
Year	0–20	20–40	40–60	60–80	80–100	100–121.2	Length of straight segment
2021	23.6	24.5	33.4	29.3	23.1	25.1	20
2017	23.6	24.8	33.8	29.4	23	25.3	20
2014	23.3	24.7	34.4	29.8	22.5	25.3	20
2000	23	24.6	34	29.7	22.9	25.9	20
1996	23.3	24.5	33.6	29.6	22.2	26.3	20
1992	23.8	24.6	33	29.3	23.1	26	20
1988	24	24.4	32.8	29.7	23.9	26.9	21.2

Table 4 Sinuosity index

Sinuosity index (Dharoi dam to Vasna barrage)						
Year	0–20 km	20–40 km	40–60 km	60–80 km	80–100 km	100–121.2 km
2021	1.18	1.225	1.67	1.465	1.155	1.255
2017	1.18	1.24	1.69	1.47	1.15	1.265
2014	1.165	1.235	1.67	1.49	1.125	1.265
2000	1.15	1.23	1.7	1.485	1.145	1.295
1996	1.165	1.225	1.68	1.48	1.11	1.315
1992	1.19	1.23	1.65	1.465	1.155	1.3
1988	1.13	1.15	1.547	1.400	1.127	1.268

4.2 Morphometric Parameter

Linear aspects: The linear aspects of the river basin are related to the channel patterns of the river basin. To analyze the linear aspect of the river basin, the subsequent parameters are calculated.

- Stream order (U): Stream order indicates a measurement of the position of a stream in the hierarchy manner of tributaries. Sabarmati river basin is classified into different stream order as shown in Fig. 4. Totally 247 numbers of streams are identified, out of which 124 are of the first order, 55 are of the second order, 24 are of the third order, and 44 are of the fourth order.
- Stream number (Nu): Stream number is defined as total number of branches present in the basin. The highest number of streams was observed in the first order. The highest number of streams of the first order indicates the less permeability of rocks. The total number of streams in water shade is 247.
- Stream length (Lu): The total length of stream segments is the highest in the first-order streams, and it gets reduced for the higher stream order. Total stream length of study area considered of Sabarmati river water shade is 727.84 km. Stream length of the first-order stream is 385, 85 km, of the second-order stream is 163.66 km, of the third-order stream is 48 km, and of the fourth-order stream is 130 km.
- Mean stream length (Lum): Mean stream length is calculated by dividing the total length of streams of a given order to the total number of streams of such order. The mean stream length values for the study area range from 3.11 km to 2.014 km. The mean stream length values depend upon the size, slope, and topography.
- Stream length ratio (Rl): Stream length ratio is the ratio of the average stream length of the higher order to the next lower order of the stream segments. The stream length ratio has essential relevance with the surface flow, discharge, and erosion stage of the stream. The stream length ratio of study area ranges from 0.296 to 2.689.
- Bifurcation ratio (Rb): The bifurcation ratio may be defined as the ratio between the numbers of stream segments of any given order to the number of stream

Fig. 4 Stream network and stream order of study area
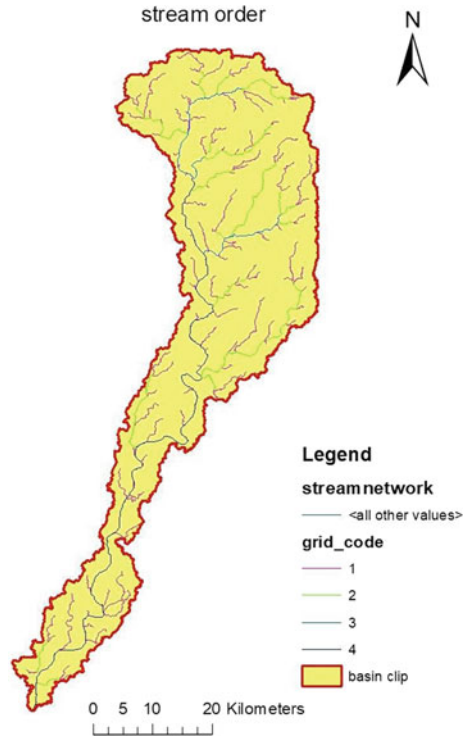
segment of next higher order. The higher Rb value means a drainage pattern is strong, and the lower Rb value indicates the less structural disturbances. For the study area, bifurcation ratio is 0.54 to 2.29. Mean bifurcation ratio is 1.65 which indicates less structural disturbance in water shade as shown in Table 5. Less value of bifurcation ratio indicates that basin is more flat.

Areal aspects: The areal aspects of a drainage basin are influenced by geological structure, lithology, climatic conditions, and denudation history of the basin.

Table 5 Calculated linear aspects

Stream order (U)	Number of streams in each order (Nu)	Total stream length in km (Lu)	Mean stream length in km (Lum)	Stream length ratio (Rl)	Bifurcation ratio (Rb)	Mean bifurcation ratio Rb
1	124	385.84	3.111	0.425	2.25	1.68
2	55	163.66	2.975	0.296	2.29	
3	24	48.338	2.014	2.689	0.54	
4	44	130.00	2.954	–	–	
Total	**247**	**727.838**			**5.04**	

The areal aspects comprise morphometric parameters such as water shade area (A), perimeter (P), and stream length (Ld) (longest stream of water shade), and their values are 1167.9 km^2, 408.14 km, and 154.50 km, respectively.

- Drainage density (Dd): Drainage density is the ratio of total stream length of drainage basin to the total area of that basin. Climatic condition, soil type, land cover, infiltration capacity, and runoff intensity highly affect the drainage density. A high drainage density shows the basin is weak and subsurface material is impermeable, having less vegetation cover and high relief. The low drainage density indicates weak coarse drainage texture, more possibility of runoff, and probability of high erosion of basin area. Also, low drainage density (<1.5) value indicates the lesser relief. The drainage density is also highly affected by the longest basin length. Reference [3] Drainage density (Dd) of the study area is 0.43 km/km^2.
- Stream frequency (Fs): The stream frequency is the total number of streams of all orders per unit area. Stream frequency is dependent on the intensity of the rainfall, temperature, and lithology of the basin. The stream frequency increases with the increase in number of streams in a drainage basin. Reference [3] Stream frequency (Fs) for Sabarmati river water shade is 0.148.
- Circularity ratio (Arc): Circulatory ratio is the ratio of basin area to the area of the circle having the same perimeter as the basin. Arc is affected by slope and relief pattern of the basin. The circulation ratio is related to the duration and frequency of streams, geological structures, land use (land cover), climate, and slope of the basin. Circulatory ratio ranges from 0 to 1. If Rc is nearer to 0, then the basin is circular and near to 1 then the elongated basin. Reference [3] Circulation ratio (Rc) for the study area is 0.1257 which means basin shape is circular.
- Elongation ratio (Re): Elongation ratio is the ratio of the diameter of a circle of the same area as the drainage basin to the maximum length of the basin. Higher values of elongation ratio indicate the high infiltration capacity and low runoff, whereas lower elongation ratio values indicate high susceptibility to erosion and sediment load. Re value is classified as circular (>0.9), oval (0.9–0.8), and less elongated (<0.7) shape of the basin. Reference [3] Elongation ratio of study area is 0.298.
- Form factor (Ff): It is the ratio of basin area to the square of basin length. If Ff > 0.78, it is circular basin and Ff < 0.78 then elongated basin. Higher Ff indicates high peak flows in shorter duration for circular basin and vice versa for elongated basin. Reference [3] Form factor value of the study area is 0.069.
- Drainage texture ratio (Rt): The drainage texture is the total number of stream segments of all orders per perimeter of that area. Rt is affected by infiltration capacity. It depends on the underlying lithology and relief aspects of the terrain. Reference [3] Drainage texture ratio of study area is 0.6052 as shown in Table 6.

Table 6 Calculation of areal aspect

Parameter	Value
Basin area in km^2 (A)	1667.9 km^2
Basin perimeter in km (P)	408.14 km
Length of basin in km (Lb)	154.50 km
Drainage density km/km^2 (Dd)	0.437
Stream frequency (Fs)	0.148
Circulatory ratio (Rc)	0.1257
Elongation ratio (Re)	0.298
Form factor (Ff)	0.069
Drainage texture ratio (Rt)	0.6052

5 Conclusions

The following conclusions are derived from the foregoing study.

- Sinuosity index is calculated for different segments at an interval of 20 km length. There are totally six segments in which five segments have length of 20 km and one segment has a length of 21.2 km. Mostly, SI varies from 1.18 to 1.69.
- For 0–20 km length, SI varies from 1.13 to 1.19 which indicates that this reach is stable braided segment.
- For 20–40 km segment, SI is 1.15 to 1.235 which indicates that this is stable braided segment.
- For 40–60 km segment, SI varies from 1.547 to 1.7 which indicates that river pattern is in meandering form with very unstable behavior and also in the high flood risk zone.
- For 60–80 km segment, SI is 1.4 to 1.49 which indicates braided unstable segment which has moderate flood risk.
- For 80–100 km segment, SI varies from 1.11 to 1.15 which means stable braided segment. For 100–121.2 km segment, SI is 1.255 to 1.3 which means unstable braided river segment. This indicates uneven change in river form over a period of 33 years. From detailed segment analysis, it reveals that behavior of river is braided unstable.
- Also, it is observed that, for 40–60 km segment (Soja to Vagpur), sinuosity index is highest that means meandering of river is detected with unstable behavior. This is the flood prone area, and it needs extra attention at high discharges.

Morphometric parameters like linear and areal aspects include stream order, stream numbers, stream length, bifurcation ratio, stream length ratio, stream frequency, circular ratio and elongation ratio, drainage density, form factor, drainage texture, etc. Morphometric parameters of the basin help to understand various terrain parameters such as nature of the infiltration capacity, surface runoff, bedrock, and subsurface texture.

- The Sabarmati river is having the stream order varying from 1 to 4 with the total of 247 stream segments. A number of stream gradually decrease with increase in stream order. If the stream is mature, then stream number is lesser. Higher stream number and stream length indicate lesser permeability.
- The total stream length is 727.84 km. Bifurcation ratio is between 0.54 and 2.29. Mean bifurcation ratio is 1.27 which indicates less structural distribution in water shade. Also, it indicates the higher possibility of flooding water accumulation rather than spreading out flood.
- Sabarmati river water shade: Area, perimeter, and basin stream length are 1667.9 km^2, 408.15 km, and 154.50 km, respectively. Drainage density is 0.437 km/km^2 which indicates that river is highly permeable due to the course drainage texture.
- Stream frequency for water shade is 0.148 which is very low. It indicates the presence of permeable subsurface material.
- Elongation ratio and form factor are 0.298 and 0.069, respectively, which confirm that water shade is in the elongation shape.
- Circulatory ratio is 0.1257 which is very low which means basin is at a young stage of life cycle and shape of water shade is elongated.
- Drainage texture ratio is 0.6052 which is very low (<2) which means very course drainage texture.

Determination of sinuosity index and analysis of morphometric parameters show the change in length and nature of river basin, respectively. This analysis can be useful for future planning and management of this river basin.

References

1. Prajapati K, Waikhom S, Yadav S (2017) Temporal change study on Tapi river meander using remote sensing and GIS. In: Proceedings of 37th IAHR world congress, Kuala Lumpur, Malaysia. ISSN Online: 2521-716X, ISSN Print: 2521-7119
2. Kumar M, Denis D, Gourav P (2016) Study of meandering of river Ganga near Allahabad (India), using remote sensing and GIS techniques. Asian J Environ Sci 11(1):59–63
3. Kulkarni M (2015) The basic concept to study morphometric analysis of river drainage basin: a review. Int J Sci Res 4(7):2277–2280
4. Das P (2012) Study of Barak River meander and associated hazard around Silchar Town Assam using remote sensing and GIS. E-J Earth Sci India 5(II):0974–835
5. Khakhlari M, Nandy A (2016) Morphometric analysis of Barapani river basin in Karbi Anglong district, Assam. Int J Sci Res Publ 6(10):238–249. ISSN:2250-3153
6. Rai P, Mohan K, Mishra S, Ahmad A, Mishra V (2017) A GIS-based approach in drainage morphometric analysis of Kanhar River Basin India. Appl Water Sci 7(1):217–232
7. Saha A, Tomar S, Rana A, Singh P (2017) Morphometric and hydrological analysis of Krishni River watershed, Uttar Pradesh India: using remote sensing and GIS techniques. 18th ESRI India user conference
8. Waikar M, Nilawar A (2014) Morphometric analysis of a drainage basin using geographical information system: a case study. Int J Multi Curr Res 2:179–184

Empirical Formula for Sequent Depth Ratio (SDR) in Smooth Sloping Rectangular Channels

Mohd Mohsin

Abstract Hydraulic jump is an example of rapidly varied flow (RVF) in which a supercritical flow approaches subcritical flow resulting in the dissipation of energy of the incoming supercritical flow in the form of heat, subsequently protecting the destruction of downstream reach. This property of the hydraulic jump is used to dissipate excess unwanted energy in the design of different types of hydraulic structures such as spillways, straight glacis sloping falls and stilling basins. Despite the requirement of sequent depth in the design of hydraulic jump, entirely formed on the smooth sloping rectangular channel, the exact and easy method to predetermine the value of sequent depth is still undetermined. Therefore, this paper presents an empirical formula to predict the sequent depth ratio (SDR), i.e., y_2/y_1, if the initial Froude number (F_1) and the channel bed slope (S_o) are known in a smooth sloping rectangular channel. The formula is based on the experimental data of Chen (Determining the location of hydraulic jump by model test and hec-2 flow routing, 1995). The formula is simple and better in comparison with the other available methods. The formula has been compared with the available experimental plots, empirical and semi-empirical formulae through a case study (solved numerical problem), which predicts better results. The formula works well for bed slopes ranging from zero to 0.15. The formula will be very useful in the design of a stilling basin where a hydraulic jump is supposed to be entirely formed on a smooth sloping rectangular channel.

Keywords Sequent depth · Sloping · Froude number · Hydraulic jump · Rectangular channel

1 Introduction

A hydraulic jump is an example of rapidly varied flow (RVF) in which a supercritical flow approaches subcritical flow resulting in the dissipation of the energy of the

M. Mohsin (✉)
Civil Engineering Section, University Polytechnic, Aligarh Muslim University, Aligarh, UP 202002, India
e-mail: mmohsin13@hotmail.com

incoming flow in the form of heat. Over the decades, this phenomenon has attracted many researchers not only because of its importance in designing a stilling basin but also for its complexity. Hydraulic jump is mostly used in hydraulic structures such as drops, spillways, gates and increasing the weight of the apron and aerating water for drinking water supplies as well as for the treatment of sewage water. The theory of jump, on horizontal or slightly inclined channels, has little impact of the weight component in the analysis. But, for the sloping channel, this impact becomes so pronounced that it must be considered in the analysis and the same helps in stabilizing the location of the jump [3, 4, 9, 15]. Many investigators have proposed plots, empirical or semi-empirical formulae to calculate sequent depth ratio (SDR) [15, 17, 18] for smooth sloping channels.

In addition, an appreciable number of studies on hydraulic jump upon rough beds have also been done. Probably, Rajaratnam and Subramanya [16] were the first to carry out systematic investigations of hydraulic jumps on rough beds. The studies of hydraulic jump on rough sloping (positive or adverse) beds revealed that the roughness has a remarkable effect on reducing the sequent depth ratio [1, 2, 5–7, 10–14].

Despite the importance of sequent depth in the design of hydraulic jump on the sloping bed, the exact and easy method to predetermine the value of sequent depth is still undetermined for the hydraulic jump entirely formed on the smooth rectangular sloping channel which is classified as a D-jump [8].

Therefore, in the present study, based on the experimental data of Chen [3], the author has tried to develop an empirical formula to calculate the sequent depth ratio for the hydraulic jump entirely formed on the smooth rectangular sloping channel.

2   SDR Prediction Methods

2.1   *Theoretical Method*

Figure 1 shows the definition sketch of the hydraulic jump formed in the sloping channel. For horizontal rectangular channels ($S_o = 0$), the well-known Belanger's equation (1) can be easily applied to calculate SDR, i.e., y_2/y_1.

$$\frac{y_2}{y_1} = \frac{1}{2}\left[-1 + \sqrt{1 + 8F_1^2}\right]$$ (1)

whereas, for sloping channels (Fig. 1), a similar equation, based on conservation of momentum, was presented by Chow [4] as;

$$\frac{y_2}{y_1} = \frac{1}{2}\left[-1 + \sqrt{1 + 8G^2}\right]$$ (2)
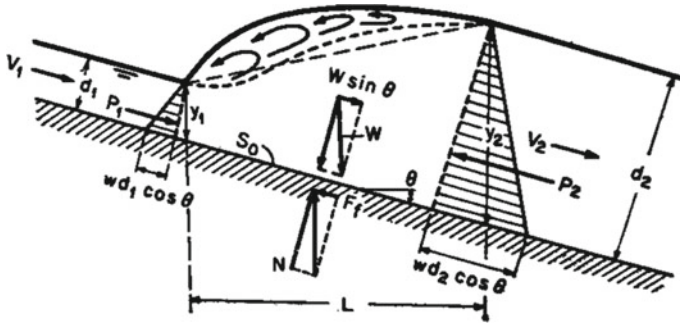
Fig. 1 Definition sketch of hydraulic jump in a sloping channel. *Source* Chow [4]

where

$$G = \frac{F_1}{\sqrt{\cos\theta - \frac{K L_j \sin\theta}{(d_2 - d_1)}}} \tag{3}$$

K = slope correction factor
L_j = length of jump
$d_1 = y_1 \cos\theta$
$d_2 = y_2 \cos\theta$.

Earlier experimental studies have shown that K and $L_j/(d_2 - d_1)$ are a function of F_1.

Therefore,

$$G = f(F_1, \theta)$$

As Eq. (3) involves d_1 and d_2, therefore, Eq. (2) becomes implicit which is difficult to be solved directly but requires a trial and error method along with the value of L_j to be determined experimentally or theoretically.

Therefore, to predict the SDR for the hydraulic jump on sloping channels, the following three methods are available.

2.2 Experimental, Empirical and Semi-Empirical Methods

2.2.1 Method I

Based upon the experimental data of Hickox, Kindsvater, Backmeteff and Matzke and USBR, Chow [4] has presented a plot between y_2/y_1 (or d_2/d_1) and F_1 for S_o
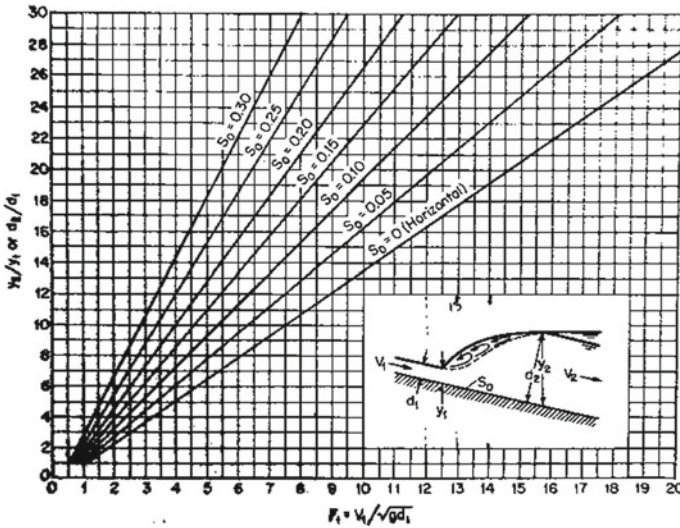
Fig. 2 Experimental relations between F_1 and y_2/y_1 (or d_2/d_1) for jumps. *Source* Chow, Figs. 15–20 [4]

ranging between zero and 0.3 at an interval of 0.05 (Fig. 2). For intermediate slopes, interpolation is required.

2.2.2 Method II

Subramanya [18] presented a plot between y_t/y_2 and $\tan \theta$, (Fig. 3); where y_2 is the equivalent sequent depth corresponding to y_1 in a horizontal floor and can be calculated using Belanger's equation (1). The ratio y_t/y_2 can be obtained using Fig. 3 for the known value of $\tan \theta$. Thereafter, sequent depth for the sloping channel, y_t, can be calculated. Alternatively, he has also presented the best fit formula, Eq. (4), for Fig. 3 to calculate y_t/y_2;

$$y_t/y_2 = 1.0071 \ \exp(3.2386 \ \tan \theta) \tag{4}$$

2.2.3 Method III

Ranga Raju [17] presented an empirical formula to calculate the value of G to be used in Eq. (2).

$$G^2 = K_1^2 F_1^2 \tag{5}$$
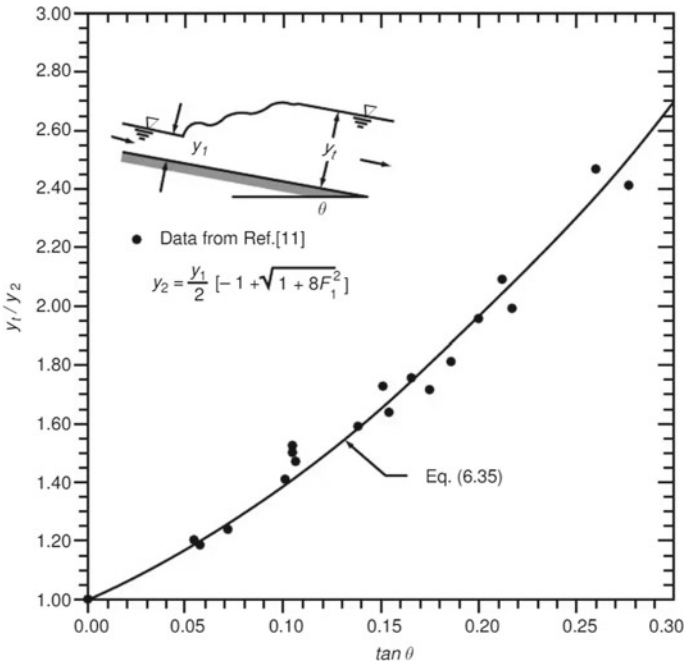
Fig. 3 Variation of y_t/y_2 with $\tan \theta$ (i.e., S_o). Subramanya [18]

where

$$K_1 = 10^{0.027(\theta)} \quad (\theta \text{ in degrees}) \tag{6}$$

To make the solution simpler, the author has developed a single empirical equation based on the experimental data of Chen [3] to predict SDR which can be used without any plot and interpolation.

3 Present Study

3.1 Experimental Data

The experimental data of Chen [3] was used to develop the present empirical formula.

3.2 Present Empirical Formula

Using multiple regression, the empirical formula to calculate the SDR in a smooth sloping rectangular channel has been developed as;

$$y_2/y_1 = d_2/d_1 = 2.1706 F_1 e^{5.961(So)} - (1 + F_1)(12.1 S_o + 0.8) \tag{7}$$

where

$$F_1 = \text{initial Froude number} = \frac{v_1}{\sqrt{gd_1}} = \frac{v_1}{\sqrt{gy_1 \cos\theta}} \tag{8}$$

$$S_o = \text{channel bed slope } (= \tan\theta)$$

Limitations: The formula works well for S_o from zero to 0.15.
For horizontal rectangular channels, $S_o = 0$, Eq. (7) becomes;

$$y_2/y_1 = 1.3706 F_1 - 0.8 \tag{9}$$

4 Comparison

Table 1 compares the predicted SDR from the author's equation (7) with the experimental SDR of Chen [3]. The % errors are mostly in the range of 0 and ±5% which shows that the author's equation is in an excellent agreement with the experimental data.

Table 2 compares the author's equation (7) with the regenerated data of Fig. 2 of [4]. The present formula works well for $F_1 \geq 4$ for bed slope ranging zero and 0.15. But for bed slope 0.05 and 0.10, the % difference is somewhat more. However, the present formula works excellently for the experimental data of Chen [3] for slope 0.05 and 0.09 (Table 1). Hence, more experimental data is required to clarify this contradictory behavior for the same slopes, which should not be observed.

The author's equation (7) has also been tested in Table 3 with Belanger's equation (1). The table gives that the author's equation (7) works well for $F_1 \geq 4$.

Figure 4a–e shows the variation of SDR with F_1 for the experimental data of Chen [3] and the predicted values from the author's empirical formula. The plots show a good agreement of the present author's empirical formula.

Table 1 Comparison of experimental data of Chen [3] and the author's Eq. (7)

S_o	F_1	y_2/y_1 Expt	y_2/y_1 Author's equation (7)	% diff	S_o	F_1	y_2/y_1 Expt	y_2/y_1 Author's equation (7)	% diff
1° or 0.017455	2.41	2.60	2.36	9.36	3° or 0.0524077	3.99	4.81	4.68	2.71
	2.65	2.75	2.69	2.11		4.10	5.06	4.85	4.09
	2.90	2.96	3.04	−2.87		4.36	5.31	5.25	1.26
	3.15	3.23	3.39	−5.06		4.62	5.65	5.65	0.16
	3.39	3.52	3.73	−5.74		4.91	6.06	6.09	−0.46
	3.62	3.90	4.05	−3.85		5.22	6.67	6.57	1.52
	3.82	4.05	4.33	−6.77		5.51	7.03	7.01	0.35
	4.06	4.32	4.66	−7.82		5.90	7.70	7.61	1.25
	4.30	4.61	5.00	−8.38		6.23	8.23	8.11	1.43
	4.57	5.18	5.37	−3.83		6.71	9.13	8.85	3.03
	4.91	5.63	5.85	−4.00		7.09	9.65	9.43	2.29
	5.11	5.87	6.13	−4.40		7.43	10.27	9.95	3.12
	5.34	6.13	6.45	−5.18	4° or 0.0699268	2.93	3.26	3.18	2.49
	5.78	6.71	7.07	−5.24		3.18	3.59	3.59	−0.01
	5.97	6.99	7.33	−4.95		3.35	3.81	3.87	−1.51
	6.32	7.58	7.82	−3.20		3.51	4.24	4.13	2.48
	6.56	8.07	8.16	−1.02		3.55	4.40	4.20	4.53
	6.77	8.33	8.45	−1.39		3.82	4.62	4.65	−0.65
	6.94	8.56	8.69	−1.49		4.04	5.14	5.01	2.48
	7.13	8.96	8.95	0.05		4.32	5.45	5.47	−0.36
2° or 0.034921	2.47	2.68	2.36	11.95		4.63	5.98	5.98	−0.05

(continued)

Table 1 (continued)

S_o	F_1	y_2/y_1 Expt	y_2/y_1 Author's equation (7)	% diff	S_o	F_1	y_2/y_1 Expt	y_2/y_1 Author's equation (7)	% diff
	2.74	2.96	2.75	6.99		5.11	6.75	6.77	−0.25
	3.15	3.45	3.35	3.14		5.47	7.13	7.36	−3.22
	3.23	3.71	3.46	6.79		5.67	7.64	7.69	−0.70
	3.53	4.00	3.90	2.57		6.10	8.30	8.40	−1.26
	3.76	4.21	4.23	-0.61		6.27	8.74	8.68	0.68
	4.01	4.59	4.59	0.03		6.58	9.13	9.19	−0.63
	4.27	5.03	4.97	1.15		7.07	10.00	10.00	0.02
	4.60	5.39	5.45	−1.11		7.54	10.91	10.77	1.25
	4.87	5.75	5.84	−1.58	5° or 0.087489	3.04	3.64	3.61	1.02
	5.11	6.18	6.19	−0.07		3.31	4.05	4.09	−1.14
	5.38	6.49	6.58	−1.45		3.54	4.39	4.51	−2.64
	5.66	6.90	6.99	−1.23		3.80	4.85	4.97	−2.58
	5.87	7.41	7.29	1.57		3.83	5.16	5.03	2.50
	6.12	7.81	7.65	1.97		4.10	5.46	5.51	−0.98
	6.36	8.17	8.00	2.11		4.34	6.00	5.94	0.93
	6.68	8.64	8.47	1.97		4.57	6.29	6.36	−1.02
	6.81	8.98	8.65	3.66		4.91	6.94	6.97	−0.46
	7.33	9.82	9.41	4.17		5.3	7.42	7.67	−3.42
3° or 0.0524077	2.78	2.92	2.83	3.11		5.68	8.10	8.35	−3.15
	3.04	3.29	3.22	1.98		6.20	9.08	9.29	−2.33
	3.30	3.70	3.62	2.18		6.71	10.08	10.21	−1.21
	3.49	4.12	3.91	4.94		7.24	11.27	11.16	1.01

(continued)

Table 1 (continued)

S_o	F_1	y_2/y_1 Expt	y_2/y_1 Author's equation (7)	% diff	S_o	F_1	y_2/y_1 Expt	y_2/y_1 Author's equation (7)	% diff
	3.73	4.53	4.28	5.40		7.97	12.60	12.47	1.02

Table 2 Comparison of author's equation with the plot of Chow [4] for S_o from zero to 0.15

Set no.	Bed slope (S_o)	F_1	SDR or y_2/y_1		% difference (absolute)
			Figure 2 of Chow [4]	Author's equation (7)	
1	0.00	2	2.25	1.94	13.72
		4	5.00	4.68	6.35
		4.5	5.75	5.37	6.65
		6	8.00	7.42	7.21
		8	10.75	10.16	5.44
		10	13.50	12.91	4.40
		12	16.5	15.65	5.17
		20	27.5	26.61	3.23
2	0.05	2	2.5	1.63	34.66
		4	6.00	4.67	22.13
		4.5	7.00	5.43	22.40
		6	9.5	7.71	18.83
		8	13.00	10.75	17.31
		10	16.25	13.79	15.15
		12	19.75	16.83	14.80
		14	23.00	19.87	13.63
3	0.10	2	3.25	1.85	43.10
		4	7.25	5.71	21.26
		4.5	8.25	6.67	19.11
		6	11.50	9.57	16.80
		8	15.50	13.43	13.37
		10	19.50	17.29	11.35
		12	23.50	21.15	10.02
		14	27.50	25.01	9.07
4	0.15	2	4.00	2.77	30.74
		4	8.50	8.16	4.05
		4.5	10.00	9.50	4.98
		6	13.50	13.54	−0.30
		8	18.00	18.93	−5.15
		10	23.00	24.31	−5.70
		12	27.50	29.70	−7.99
		12.5	29.00	31.04	−7.05

Table 3 Comparison of author's equation (7) with Belanger's equation (1)

F_1	SDR or y_2/y_1		% difference
	Belanger's equation (1)	Author's equation (7)	
1	1.00	0.57	42.94
2	2.37	1.94	18.17
3	3.77	3.31	12.20
4	5.18	4.68	9.59
5	6.59	6.05	8.13
6	8.00	7.42	7.21
7	9.41	8.79	6.57
8	10.82	10.16	6.10
9	12.24	11.53	5.74
10	13.65	12.90	5.46
12	16.48	15.64	5.04
14	19.31	18.38	4.75
16	22.13	21.12	4.53
18	24.96	23.86	4.37
20	27.79	26.60	4.23

5 Case Study

To show the easiness in the practical applicability of the author's empirical formula, one solved numerical problem using the four methods has been presented here as a case study.

Problem

[Solved Example 6.10, Subramanya (2008)] [18]

A rectangular channel is laid on a slope of 1 (horizontal): 0.15 (vertical). When a discharge of 11.0 m³/s/m width is passed down the channel at a depth of 0.7 m, a hydraulic jump is known to occur at a section. Calculate the sequent depth.

Solution

Using Method I

Initial velocity,

$$v_1 = q/y_1 = 11.0/0.7 = 15.714 \text{ m/s}$$

Therefore,

$$F_1 = v_1/\sqrt{gy_1} = 15.714/\sqrt{9.81 \times 0.7} = 6.0$$
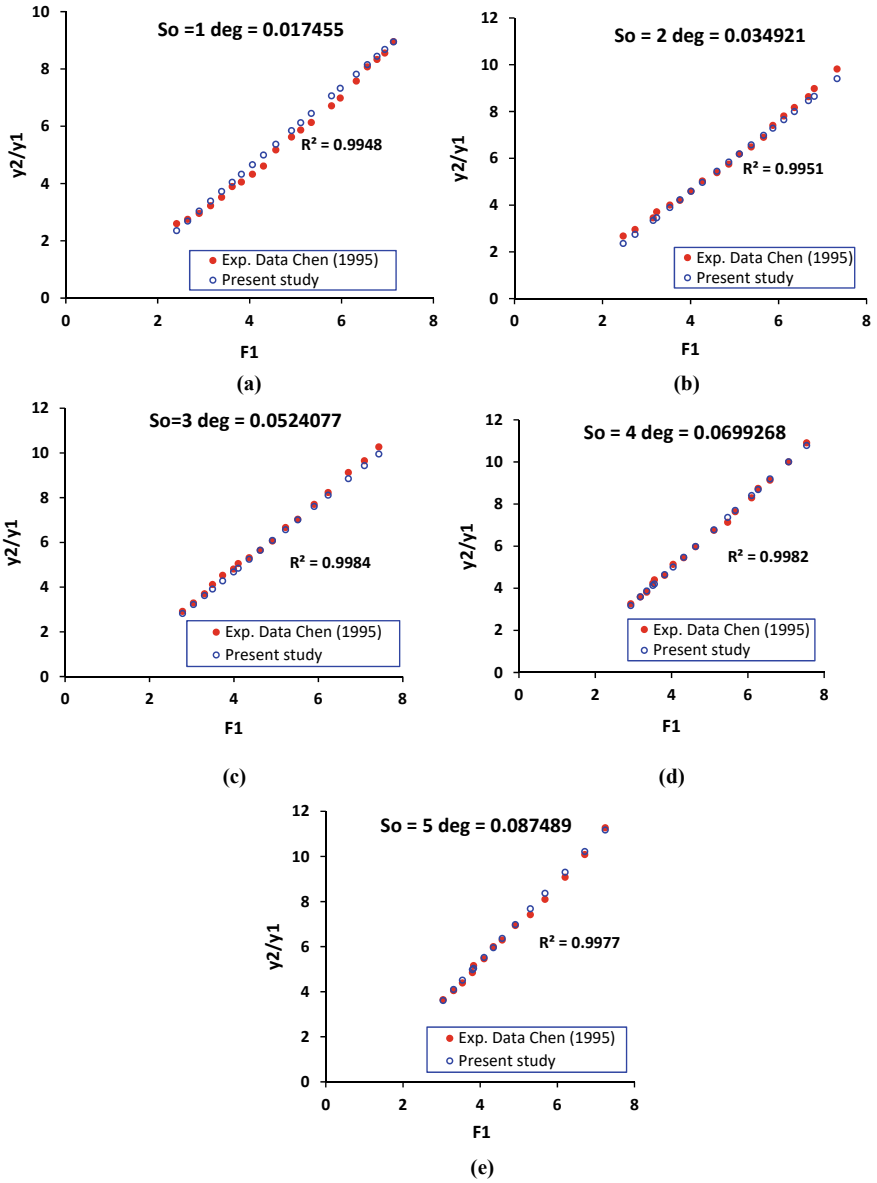
Fig. 4 a–e Variation of SDR (i.e., y_2/y_1) with F_1 for different bed slopes

$$S_o = 0.15 \text{ (given)}$$

From Fig. 2 of [4], y_2/y_1 can be read as 13.4 for $F_1 = 6$ and $S_o = 0.15$. Therefore,

$$\text{sequent depth, } y_2 = 13.4 \times 0.7 = 9.38 \text{ m}$$

Using Method II [18]

y_t/y_2 can be approximately read from Fig. 3 as;

$$y_t/y_2 = 1.63$$

or using the best fit Eq. (4) for Fig. 3;

$$
\begin{aligned}
y_t/y_2 &= 1.0071 \ \exp(3.2386 \ \tan \theta) \\
&= 1.0071 e^{(3.2386 \times 0.15)} \\
&= 1.637
\end{aligned}
$$

and y_2 will be calculated from Belanger's Eq. (1) supposing $S_o = 0$

$$
\begin{aligned}
\frac{y_2}{y_1} &= \frac{1}{2}\left[-1 + \sqrt{1 + 8 F_1^2} \right] \\
&= \frac{1}{2}\left[-1 + \sqrt{1 + 8 \times 6^2} \right] \\
&= 8
\end{aligned}
$$

or,

$$y_2 = 8 \times y_1 = 8 \times 0.7 = 5.6 \text{ m}$$

Therefore, sequent depth for sloping channel,

$$y_t = 1.637 \times y_2$$

Sequent depth,

$$y_t = 1.637 \times 5.6 = 9.17 \text{ m}$$

Using Method III [17]

$$
\begin{aligned}
\theta &= \tan^{-1}(0.15/1) = 8.53° \\
K_1 &= 10^{0.027 \,(8.53)} = 1.6995
\end{aligned}
$$

$$G^2 = K_1^2 F_1^2 = 1.6995^2 \times 6^2 = 103.973$$

$$\frac{y_2}{y_1} = \frac{1}{2}\left[-1 + \sqrt{1 + 8 \times 103.973}\right] = 13.93$$

Therefore,

$$\text{Sequent depth, } y_2 = 13.93 \times 0.7 = 9.75 \text{ m}$$

Method IV

Using author's empirical equation (7):

$$
\begin{aligned}
y_2/y_1 &= 2.1706 F_1 e^{5.961(S_o)} - (1 + F_1)(12.1 S_o + 0.8) \\
&= 2.1706 \times 6 \times e^{(5.961 \times 0.15)} - (1 + 6)(12.1 \times 0.15 + 0.8) \\
&= 13.54 \text{ m}
\end{aligned}
$$

or

$$\text{Sequent depth, } y_2 = 13.54 \times 0.7 = 9.48 \text{ m}$$

As the actual experimental value of the sequent depth is not known for the given problem, the sequent depth from the method I can be assumed as true as the plot is based on experimental data.

The % difference of Method II, III and author's formula to Method I is 2.24, -3.94, -1.07, respectively, which shows that the author's formula is better.

6 Conclusion

It is evident from the comparison and case study that the author's empirical formula works well for the bed slope from 0 to 0.15. The application of the formula is simpler than the available three methods demonstrated in the case study. However, the formula can be further modified using more experimental data particularly for bed slopes greater than 5°.

References

1. Ali HSM (1991) Effect of roughened-bed stilling basin on length of rectangular hydraulic jump. Hydraulic Eng ASCE 117:83–92
2. Carollo FG, Ferro V, Pampalone V (2013) Sequent depth ratio of a B-jump on smooth and rough beds. Agric Eng XLIV(e12):82–86

3. Chen FL (1995) Determining the location of hydraulic jump by model test and hec-2 flow routing. M.Sc. Thesis Faculty of the Fritz J and Dolores H Russ College of Engineering and Technology Ohio University
4. Chow VT (1959) Open channel hydraulics. McGraw-Hill Book Company Inc., New York, USA
5. Ead SA, Rajaratnam N (2002) Hydraulic jumps on corrugated beds. Hydraulic Eng ASCE 128(7):656–663
6. Hughes WC, Flack JE (1984) Hydraulic jump properties over a rough bed. Hydraulic Eng ASCE 110(12):1755–1771
7. Izadjoo F, Shafai-Bejestan M (2007) Corrugated bed hydraulic jump stilling basin. Appl Sci 7(8):1164–1169
8. Kindsvater CE (1944) The hydraulic jump in sloping channels. Trans ASCE 109(1):1107–1120
9. Kumar M, Lodhi AS (2015) Hydraulic jump over sloping rough floors. Hydraulic Eng ISH 22(2):127–134
10. Kumar M, Kumar S, Bidhu S (2019) Determination of sequent depth of hydraulic jump over sloping floor with rounded and crushed aggregates using experimental and ANN model. Water Supply 19(8):2240–2247
11. Mazumder SK (2017) Discussion of Characteristics of hydraulic jump on rough bed with adverse slope. Hydraulic Eng ISH 24(3):345–348
12. Pagliara S, Palermo M (2015) Hydraulic jumps on rough and smooth beds: aggregate approach for horizontal and adverse-sloped beds. Hydraulic Res 53(2):243–252
13. Pagliara S, Lotti I, Palermo M (2008) Hydraulic jump on rough bed of stream rehabilitation structures. Hydro-Environ Res 2(1):29–38
14. Palermo M, Pagliara S (2017) A review of hydraulic jump properties on both smooth and rough beds in sloping and adverse channels. Acta Scientiarum Polonorum Formatio Circumiectus 16(1):91–105
15. Rajaratnam N (1966) The hydraulic jump in sloping channels. Water Energy Int 23(2):137–149
16. Rajaratnam N, Subramanya K (1968) Profile of the hydraulic jump. Hydraulics Div ASCE 94(3):663–674
17. Ranga Raju KG (1993) Flow through open channels. Tata McGraw-Hill, New Delhi, India, pp 196–198
18. Subramanya K (2008) Flow in open channels. Tata McGraw-Hill, New Delhi, India, pp 1296–1311

Prediction of Bed Load Transport Rate in Mountain River by ANN Model

Hitesh Diwakar, Vipinkumar Yadav, and Sanjaykumar M. Yadav

Abstract Bed load transport has a wide range of implications in the design of the hydraulic structure in mountain river and acts as an important factor in fluvial geomorphology. Modeling and predicting bed load transport rate is a significant yet difficult task in river engineering. The available empirical equations provide diverse accuracies with each other and measured data due to their limited application even under similar conditions. In this paper, an artificial neural network (ANN) model was built using MATLAB software for the published data of Little slate Creek River in Idaho, USA, employing five dominant parameters of bed load transport, viz. velocity of flow, slope of water surface, depth of flow, river width and median grain size. By comparing measured and observed bed load values, the deficit of empirical equations for this river was indicated. Compared to that, the developed ANN model presented higher consistency and closer estimation to observed data with 0.94 correlation value. The efficiency of the ANN model was examined by the reliable statistical measures like discrepancy ratio (DR), score percentage, root mean square error (RMSE) and inequality coefficient (U). The performance of the developed ANN model was tested on other published river datasets, and the results were found to be satisfactory.

H. Diwakar
Civil Engineering Department, Dr. S. & S. S. Ghandhy Government Engineering College, Surat 395001, India

V. Yadav (✉) · S. M. Yadav
Department of Civil Engineering, Sardar Vallabhbhai National Institute of Technology Surat, Surat 395007, India
e-mail: vkygecs@gmail.com

S. M. Yadav
e-mail: smy@ced.svnit.ac.in

1 Introduction

The dawn of civilization faced many problems associated with rivers and solved them to the best of their ability. The number of problems is increasing with increase in the population. The river water is being used for multiple purposes like domestic use, drinking, industry operations, hydro-electric power generation, irrigation, navigation, etc., which necessitates changes to be made in the course of water. These problems are getting aggravated due to loose material, sediments, flowing in river and other water courses. Some of this material gets carried by the water flow. Suspending sediment flowing with the water often creates problems in the pump and turbine operations. Furthermore, the significance of accurate sediment movement prediction and extracted information lies in offering more precise interpretation for many purposes such as morphological and sedimentological aspects [1, 2]. Due to nonlinear relationship and complicated interaction of involved parameters, it is difficult to predict sediment transported loads. Many empirical equations for bed load were developed by researchers [3–6].

The nonlinear relationship between flow and sediment loads is difficult to model properly using regression and other statistical techniques owing to absence of proven basic principles of physics which is also affected by some other auxiliary factors [7–9]. The predicted bed load transport rates may differ from observed bed load transport rate by several orders of magnitude [10, 11]. The measured bed load transport rate in gravel-bed rivers and boulder bed streams may vary by several orders of magnitude even for similar (mean) flow conditions [12, 13]. Incorporating slope with bed load measurements [14–16] made it even more complicated and resource consuming than suspended load consequently increasing interest in formulating the predictive models [17]. Nonlinearity among parameters can be simulated to an extent by using the soft computing approach like artificial neural network (ANN) techniques [18, 19]. The literature shows that the ANN techniques have been applied in prediction of suspended sediment loads satisfactorily and much faster than most conventional methods [20–22].

2 Materials and Methods

2.1 *Study Area and Data Source*

Little Slate Creek flows into the Salmon River at the Slate Creek Range Station, about nine miles downstream of Lucile, Idaho. The basic data of Little Slate Creek River were compiled from the published sources which were accessed through direct download and WaterML based web services from the BYU World Water Data Sediment Transport Database portal for selected rivers. The sediment transport data include 133 measurements of bed load transport varying from year 1986 to 1999. Basic geometric details of Little State Creek River are described in Table 1.

Table 1 Summary of hydraulic parameters of Little Slate Creek River

S. No.	Dataset (Source)	Bed load Qb (kg/ms)	Top width (m)	Velocity (m/s)	Discharge at 0.6d (m³/s)	Slope	Depth (m)	d50 (mm)
1	Little Slate Creek	0.0000–0.0077	10.058–15.239	0.2073–1.8257	0.5295–18.318	0.026	0.2347–0.8138	0.4200–17.500

2.2 Methods and Techniques

2.2.1 Statistical/Empirical Formulae

Sediment transport theories can be classified based on approaches or concepts such as the shear stress approach, probabilistic approach, dimensional and regression approach, energy slope approach and other concepts. Bed load transport formulae from different approaches were used for the prediction of transport rates based on their popularity, suitability to gravel-bed rivers, the hydraulic conditions and availability of available data.

Based on shear stress theory, the incipient motion of bed particles will occur when the Shield's parameter θ is greater than the critical value, θ_c which can be expressed as: $\theta = \frac{\tau}{(\gamma_s - \gamma)d}$ and $\theta_c = \frac{\tau_c}{(\gamma_s - \gamma)d}$. Another equation suggested for finding critical shear stress is $\theta_c = \frac{0.273}{1 + 1.2d_*} + 0.046\left(1 - 0.576\,e^{-0.05d_*}\right)$. The critical shear stress value, on the other hand, differs between approaches taken by researchers depending on their experimental research. Summary of the bed load transport equations and their range of applicability is given in Table 2.

2.2.2 Artificial Neural Network

Artificial neural network is used to develop model between input and output variables and processes the information received in the same way as human brain processes. The received inputs at each level of neurons, in the human brain, provide insight, and the knowledge is subsequently passed on to the next upper level. Similar process is imitated by ANNs through multiple linked layers with corresponding weights. The input layer is provided various forms of data which network processes to learn about the underlying phenomenon. The input layer receives a variety of data types that the network will analyze or learn about. The data are subsequently transferred through one or more hidden layers based on weighted connections. The hidden layer is in charge of data processing and transmission to the output unit. Neural networks can be used during the phenomenon in which variables have nonlinear relationships and difficult to develop model using different approaches. For development of model using artificial neural network, MATLAB software is used in the present study. The architecture of the model having five sediment transports input parameters such as velocity, slope, width, diameter of sediment, depth of river and output as bed load transport. The number of layers in ANN architect is 3 and number of neurons in layer 1 (10)-layer 2 (4), and max reverse time 28 as shown in Figs. 1 and 2.

2.2.3 Efficiency Criteria

Discrepancy ratio (DR) compares the distance between the predicted and observed number of cases with the distance between the predicted number and the limit of

Table 2 Selected bed load equations with their range of applicability

Bed load equation	Approach	Proposed equation
Meyer-Peter and Müller [3]	Energy slope	$\emptyset = \begin{cases} 8(\theta - \theta_c)^{\frac{3}{2}} & \theta > \theta_c \\ 0 & \theta < \theta_c \end{cases}$ (1)
Brown [4]	Probabilistic	$\emptyset = \begin{cases} \frac{kexp\left(-\frac{0.391}{\theta}\right)}{0.465}, & \theta < 0.182 \\ 40k\theta^3, & \theta \geq 0.182 \end{cases}$ with $k = \sqrt{\frac{2}{3} + \frac{36}{d*^3}} - \sqrt{\frac{36}{d*^3}}$ (2)
Schoklitsch [5]	Discharge	$qv = \frac{2.5}{\frac{\rho_s}{\rho}} s^{\frac{3}{2}} (q - q_c)$ with $q_c = 0.26(s-1)^{5/3} \frac{D40^{3/2}}{S^{7/6}}$ (3)
Wong and Parker [23]	Shear stress	$\emptyset = 3.97(\theta - 0.0495)^{3/2}$ (4)
Recking [6]	Regression	$\emptyset = 14 \frac{\theta^{2.5}}{1 + \left(\frac{\theta_m}{\theta 84}\right)^4}$ with $\theta_{84} = \frac{SR}{(s-1)d84}$ (5) Also $\theta_m = (5S + 0.06)\left(\frac{D84}{D50}\right)^{4.4\sqrt{S-1.5}}$ for gavel $\theta_m = 0.045$ for sand
Wilcock and Crowe [24]	Equal mobility	$qv = \frac{w^* u_*^3 \rho_s}{(s-1)g}$ $\theta_{50} = \frac{\theta}{\theta_c}, \theta = \frac{u_*^2}{(s-1)gD_x}$ (6) $w^* = \begin{cases} \left(1 - \frac{0.846}{\theta_{50}^{0.5}}\right)^{4.5} & \theta_{50} \geq 1.35 \\ 0.002(\theta_{50})^{7.5}, & \theta_{50} < 1.35 \end{cases}$
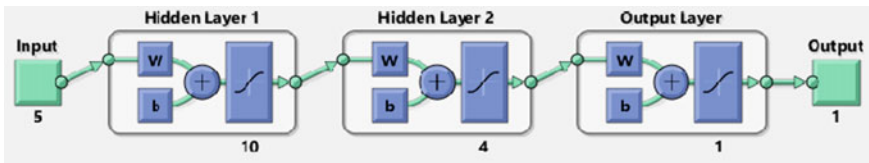
Fig. 1 Layout of ANN architecture

the prediction interval. By simply taking the ratio of predicted results to observed results, the discrepancy ratio can be calculated as presented in Eq. (7). The 100% accuracy is demonstrated by the expected results having a value of discrepancy ratio 1, where the DR values of 0.5 to 2.0 show the satisfactory predicted results.

$$DR = \frac{\text{Predicted results}}{\text{Observed results}} \tag{7}$$
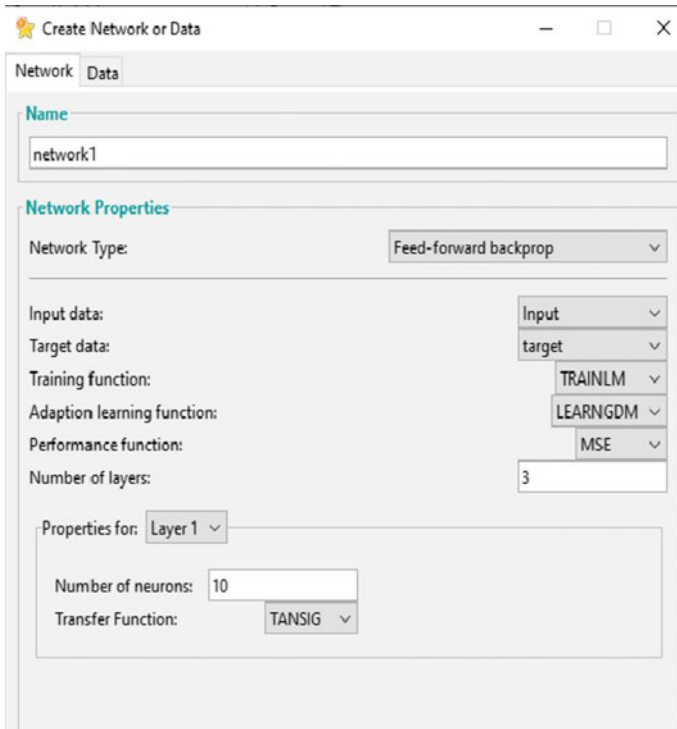
Fig. 2 Functions and algorithm of artificial neural network

If the discrepancy ratio is less than one, the model is underpredicting, and if DR value is greater than one then, the model is overpredicting by more than 100% from the measured value.

Root mean square error (RMSE) is one of the most convenient methods for evaluating simulation models. It measures the deviation between the expected value and those observed. RMSE can be calculated as Eq. (8)

$$\text{RMSE} = \left[\sum_{i=1}^{n} \frac{\left(q_{bo} - q_{bp}\right)^2 i}{n} \right]^{1/2} \tag{8}$$

The ideal value of RMSE is zero, which means that the observed and the expected values match perfectly.

Inequality coefficient (U) is a RMSE-related simulation statistics, formulated as shown in Eq. (9)

$$U = \frac{\text{RMSE}}{\left[\frac{1}{n} \sum_{1}^{n}(q_{bo})i^2\right]^{1/2}\left[\frac{1}{n} \sum_{1}^{n}(q_{bp})i^2\right]^{1/2}} \tag{9}$$

If U = 0, then q_{bp} (bed load predicted) = q_{bo} (bed load observed), indicating a perfect fit in the plot between observed and predicted values. If U = 1, then $q_{bp} \neq q_{bo}$ and model lacks good predictive capability.

3 Results and Discussions

The data of the Little Slate Creek River were randomized for developing the ANN model, in which 70% data were used for training and remaining 30% were used for the testing and validation.

The model was trained and the overall correlation coefficient value was obtained as 0.94, which was considered as satisfactory compared to the empirical formulae. The correlation value for training testing and validation of ANN model is described in Fig. 3.

According to the available data, the sediment prediction with the well-known empirical formulas was taken and compared with the ANN model. Also, from the efficiency criteria, it can be seen that there is too much variation in the discrepancy ratio, RMSE value and inequality coefficient. One of the reasons for over prediction is the effect of nonlinearity in the equation and field observed data. Also, the factor to be kept in mind is the grain size distribution or the grain diameter that plays the major role in sediment prediction. The summary of the statistical measures for empirical and the ANN model is presented in Table 3.

The prediction of empirical equations revealed that accuracy and fit to actual data may not be uniform in similar conditions, and hence, it is expected not to get acceptable outcomes.

4 Conclusions

The underlying processes in any natural phenomena, such as the sediment transport process, can be revealed using ANN models. In the present study, the feed forward backprop network type, tansig transfer functions with 3 layers architecture for the purpose of sediment prediction in Little Slate Creek river Idaho, USA, was successfully developed. The models were optimized utilizing 133 sets of five primary hydraulic and sediment variables in an ordered iterative method based on the variability of internal characteristics (W, V, S, d and D50). In comparison, the ANN models predicted scatters with the R^2 values varying from 0.94 to 0.96, whereas the empirical equations using similar fed data resulted in diverse scatter with R^2 values between 0.08 and 0.53. Overall, the empirical formulas demonstrated an unsatisfactory prediction of the bed loads for a wide range of hydrodynamic and sediment conditions. This can be considered as primary shortcoming of the empirical equations, wherein for a similar condition, the equation exhibits different results. Thus, it can be said that, the performance of such relations was deemed comparatively
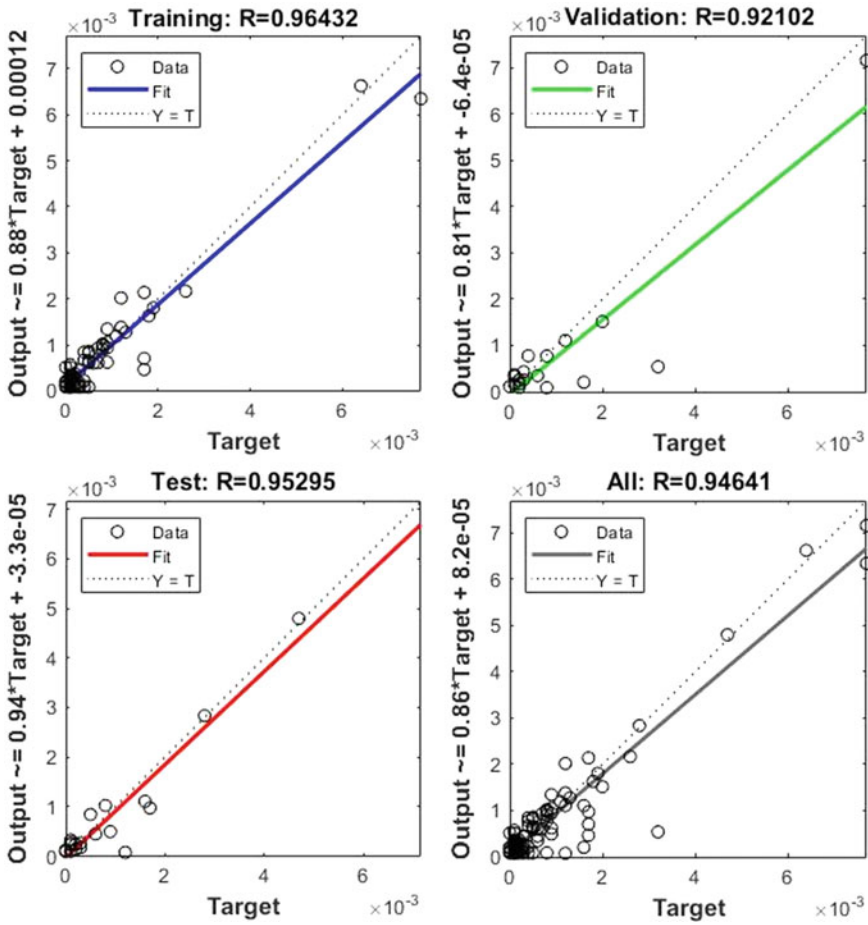
Fig. 3 ANN model correlation coefficient

Table 3 Summary of statistical measures for Little Slate Creek River

Sr. No.	Equation	Summary statistical measures				
		R^2	DR	Score	RMSE	U
1	Rottner [25]	0.53	4978.81	0.00	3.70	0.9993
2	Brown [4]	0.38	501,309.87	0.00	65.68	1.0000
3	Recking [6]	0.08	5,910,357.27	0.00	613.89	1.0000
4	Meyer-Peter and Müller [3]	0.31	889,710.46	0.00	64.63	1.0000
5	Wong and Parker [23]	0.31	429,515.74	0.00	31.26	0.9999
6	Schkotlitsch [26]	0.44	65,930.40	0.00	8.37	0.9997
7	Wilcock and Crowe [24]	0.25	1,942,777,902.45	0.00	159,337.68	1.0000
8	ANN model	0.94	3.68	58.65	0.00	0.15

insufficient. The accuracy performance of the ANN models and empirical equations was assessed using discrepancy ratio, score percentage, root mean square error and inequality coefficient. It was observed that the ANN model with R^2 0.94; DR-3.68; score 58.65; U-0.15 demonstrated more accurate and satisfactory results than the empirical equation in the similar conditions.

Notations

ρ_s	Density of sediment (kg/m³)
ρ	Flow density (kg/m³)
D	Flow depth (m)
d_*	Dimensionless particle parameter: $d_* = [g(s-1)D_x/\vartheta]^{1/3}$
D_x	Grain diameter (subscript denotes % finer) (m)
g	Acceleration due to gravity (m/s²)
$\emptyset$	The dimensionless intensity of the bedload rate: $\emptyset = q_v/[g(s-1)d^3]^{1/3}$
Q_b	Bed load rate in weight per unit width per unit time (kg/m/s)
q_c	Critical discharge at which sediments began to move
q_v	Volumetric bed load transport rate (m³/s/m)
R	Hydraulic radius (m)
S	The slope of the channel
v	Velocity of flow (m/s)
γ	The specific weight of water (N/m³)
γ_s	The specific weight of sediment (N/m³)
τ	Shear stress at the bed (N/m²)
τ_c	Critical shear stress at incipient motion
υ	Kinematic viscosity (m²/s)
u_*	Shear velocity (m/s)
θ	Shield's parameter calculated for diameter d_x: $\theta = \tau/(\gamma_s - \gamma)d_x$
θ_c	Critical Shield's parameter for initiation of motion: $\theta_c = \tau_c/(\gamma_s - \gamma)d$
$s = \frac{\rho_s}{\rho}$	Specific gravity of bed material.

References

1. Francalanci S, Solari L, Toffolon M (2009) Local high-slope effects on sediment transport and fluvial bed form dynamics. Water Resour Res 45(5)
2. Camenen B, Larson M (2008) A general formula for noncohesive suspended sediment transport. J Coastal Res 24(3):615–627
3. Meyer-Peter E, Müller R (1948) Formulas for bed-load transport. In: IAHSR 2nd meeting Stockholm, appendix 2. IAHR. pp 39–64
4. Brown CB (1950) Sediment transportation. Eng Hydraul, Wiley, New York 12:769–857
5. Schoklitsch A (1962) Handbuch des Wasserbaus, 3rd edn. Springer, New York, p 1962
6. Recking A (2013) An analysis of nonlinearity effects on bed load transport prediction. J Geophys Res Earth Surf 118(3):1264–1281
7. Kişi Ö (2010) River suspended sediment concentration modeling using a neural differential evolution approach. J Hydrol 389(1–2):227–235
8. Cao M, Alkayem NF, Pan L, Novák D, Rosa JLG (2016) Advanced methods in neural networks-based sensitivity analysis with their applications in civil engineering. INTECH Press, pp 335–354
9. Melesse AM, Ahmad S, McClain ME, Wang X, Lim YH (2011) Suspended sediment load prediction of river systems: an artificial neural network approach. Agric Water Manag 98(5):855–866
10. Gomez B, Church M (1989) An assessment of bed load sediment transport formulae for gravel bed rivers. Water Resour Res 25:1161–1186
11. Barry KM, Thieke RJ, Mehta AJ (2006) Quasi-hydrodynamic lubrication effect of clay particles on sand grain erosion. Estuar Coast Shelf Sci 67:161–169
12. Reid I, Laronne JB (1995) Bed load sediment transport in an ephemeral stream and a comparison with seasonal and perennial counterparts. Water Resour Res 31(3):773–781
13. Rickenmann D (2001) Comparison of bed load transport in torrents and gravel bed streams. Water Resour Res 37(12):3295–3305
14. Parker G (1984) Discussion of lateral bed load transport on side slopes by Syunsuke Ikeda (November, 1982). J Hydraul Eng 110(2):197–199
15. Sekine M, Parker G (1992) Bed-load transport on transverse slope. I. J Hydraul Eng 118(4):513–535
16. Damgaard JS, Whitehouse RJ, Soulsby RL (1997) Bed-load sediment transport on steep longitudinal slopes. J Hydraul Eng 123(12):1130–1138
17. Yadav SM, Samtani BK (2008) Bed load equation evaluation based on alluvial river data, India. KSCE J Civil Eng 12(6):427–433
18. Hamdia KM, Arafa M, Alqedra M (2018) Structural damage assessment criteria for reinforced concrete buildings by using a Fuzzy analytic hierarchy process. Undergr Space 3(3):243–249
19. Hamdia KM, Lahmer T, Nguyen-Thoi T, Rabczuk T (2015) Predicting the fracture toughness of PNCs: a stochastic approach based on ANN and ANFIS. Comput Mater Sci 102:304–313
20. Sirdari Z, Zangeneh Sirdari N (2015) Bedload transport predictions based on field measurement data by combination of artificial neural network and genetic programming. Pollution 1(1):85–94
21. Bouzeria H, Ghenim AN, Khanchoul K (2017) Using artificial neural network (ANN) for prediction of sediment loads, application to the Mellah catchment, northeast Algeria. J Water Land Dev
22. Kisi O, Dailr AH, Cimen M, Shiri J (2012) Suspended sediment modeling using genetic programming and soft computing techniques. J Hydrol 450:48–58
23. Wong M, Parker G (2006) Reanalysis and correction of bed-load relation of Meyer-Peter and Müller using their own database. J Hydraul Eng 132(11):1159–1168
24. Wilcock PR, Crowe JC (2003) Surface-based transport model for mixed-size sediment. J Hydraul Eng 129(2):120–128
25. Rottner J (1959) A formula for bed load transportation. La Houille Blanche 3 (4):301–307
26. Schoklitsch A (1934) Der Geschiebetrieb und die Geschie -befracht. Wasserkraft und Wasserwirtschaft, 29(4):37–43 (in German)

Model Studies for Assessing Hydrodynamics and Siltation at the Inlet of a Power Plant Intake—A Case Study

B. Krishna, G. A. Rajkumar, M. Karthikeyan, and L. R. Ranganath

Abstract Power plant requires large quantity of cooling water for generating electricity continuously, because of this power plants are mostly located near the water bodies such as rivers, estuary, or sea. The efficiency of the power plant depends on the sand, silt and debris free water available for cooling. In this study, a power plant located in Mumbai estuary which is in operation for more than six decades is facing problem of siltation at the intake due to urbanization, industrialization and sewage disposal into the estuary has resulted in available depth reduction at the intake location leading to decrease in intake volume of water as it affects the performance of power plant. This paper describes in detail the assessment of siltation in the relocated deeper area of the cooling water intake. A 2D MIKE21 hydrodynamic and mud transport models were used to study the hydrodynamics and siltation at the intake location. Existing field measurements are used to calibrate the model for tide, currents and siltation. In the proposed condition, the location of the intake is changed to a location where the required cooling water of about $62 \, m^3$ can be withdrawn to the power plant for cooling purpose. Analysis of the results shows that there is reduction in velocities near the proposed site would apparently result in increase in siltation rates. The annual silt deposition near the proposed intake is found to be of the order of 1.6 m as compared to 0.5 m during the existing condition. Thus, there is significant increase in the siltation owing to the new proposed scheme in the vicinity of intake. Since, siltation being a continuous process, it is suggested that dredging has to be carried out in the shortest possible time with a suitable dredging technique.

Keywords Hydrodynamics · Siltation · Tide · Suspended sediment concentration · Intake

B. Krishna (✉) · G. A. Rajkumar · M. Karthikeyan · L. R. Ranganath
Central Water and Power Research Station, Pune 411024, India
e-mail: krishna07_boora@yahoo.co.in

M. Karthikeyan
e-mail: karthikeyan.m@cwprs.gov.in

1 Introduction

A 1335 MW thermal power station located at Pir Pau in the north-west of Mumbai estuary away from the main flow experienced continual problems with bed sediment swelling at and within the stations intake, which pumps water for cooling purpose [1]. The sediment comprising of clay and silt which hamper the intake pump operations and gets sucked into the station cooling water system. Partial blockage by the sediments blocks the entry of water into the cooling system and reducing efficiency of the power plant resulting increase in the running cost of power plant. In the present circumstances, in order to make available uninterrupted water supply to the power intake, periodical dredging in and around the intake was being carried out.

The present study is to assess the feasibility of shifting the intake of water to deeper contours adjoining Pir Pau. A 2D depth averaged numerical hydraulic model MIKE21 software [2] was used to study the impact of relocation of cooling water (CW) intake on the morphology of the area.

2 Materials and Methods

2.1 Hydrodynamic and Sediment Transport Model

The mathematical model studies were carried out using MIKE 21 software using the Flexible Mesh, which is most suitable for estuaries like Mumbai harbour with meandering coastline. The hydrodynamic studies include simulation of the flow field for the following conditions:

1. With existing intake drawing cooling water of about 55 m^3.
2. For proposed relocation of CW intake at about 500 m away towards south of jetty.

The model simulated to evaluate hydrodynamics would be calibrated with the observed field data. The calibrated model will be used to predict the changes in the flow pattern for the proposed conditions. The results of the hydrodynamic studies are used as basic input for the sediment transport studies. Sediment transport is simulated considering both tide and wave induced currents.

The silt model is calibrated using the pre- and post-dredging information available. Model studies carried out by coupling the flow models with sedimentation models would help in evolving changes in sedimentation pattern, thereby facilitating estimation of siltation or maintenance dredging quantities. These studies predict the probable zone of siltation and zone of erosion. The comprehensive details of the hydrodynamics and siltation studies for both existing and proposed conditions of CW intake are presented in this paper.
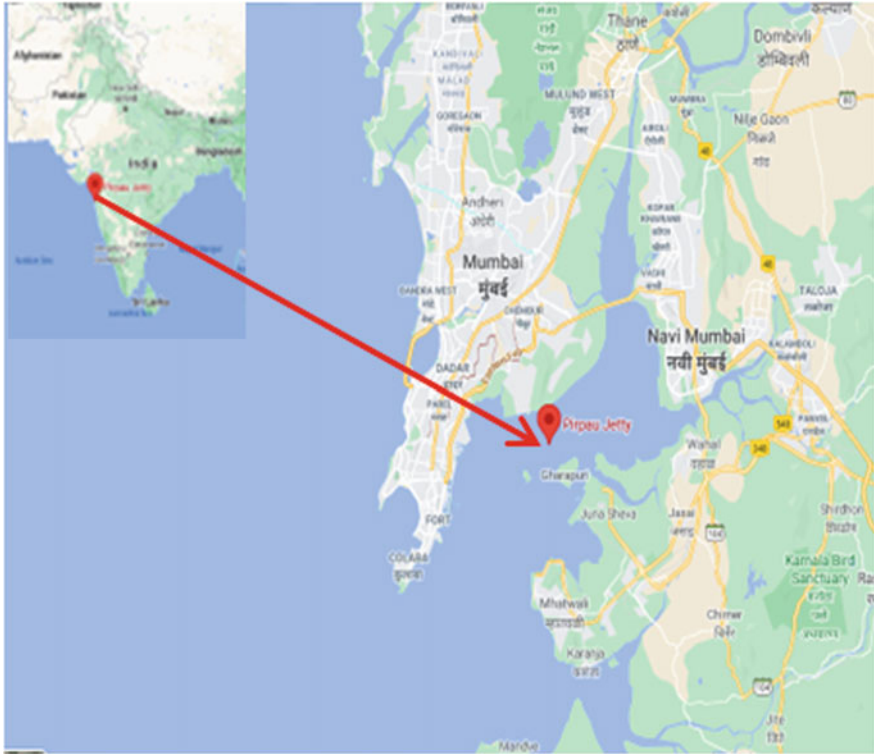
Fig. 1 Location map

3 Study Area and Data Source

3.1 Pir Pau

The water depths near the CW intake are shallow and as a result lot of clay and silt enters the pump chamber along with water affecting performance of sea water handling machinery, pumps and related equipment, screens, etc., and thus increasing the maintenance cost [1]. To obviate this continuous dredging is carried out in front of the CW intake to increase the water depths in the area so as to draw clearer water. Figure 1 shows the location of the study area.

3.2 Data Collection

The data required for the model studies are mainly bathymetry, tide, waves, wind, currents and sediment data. Figure 2 shows the field data collection locations.

Fig. 2 Location of field data collection

The near shore data were taken from the hydrographic survey data and for the offshore region obtained from Admiralty chart. The near shore bathymetry survey near the existing CW intake for an area of about 4.2×2.2 km^2 was carried out. The bathymetry survey for near shore region near the CW jetty is highlighted in Fig. 2.

The tides in the Mumbai region are of the semidiurnal type with diurnal inequality. The tidal data were collected from 08.06.2017 to 28.06.2017 covering both spring and neap tides at two locations, viz. Apollo Bandar and CW Jetty [1]. The tidal plots are shown in Fig. 3.

A large volume of tidal flux gets exchanged in and out of Thane creek during tidal cycle resulting in strong tide induced currents during flood and ebb tide. The velocity data have been collected at three locations, viz. at Apollo Bandar (A), CW Jetty (C) and about 6 km towards east of the CW Jetty (B). The velocity plots showing the magnitude of the current are shown in Fig. 4 (Table 1).

Water samples were collected for all the three locations covering both spring and neap tides. The simultaneous sampling was done at all the three locations on hourly basis for the period from 08.06.2017 to 11.06.2017 during spring tide and 15.06.2017 to 18.06.2017 during the neap tide.

In order to understand nature of the bed material, bed sample was collected at two locations, viz. location A and C and were analysed for grain size distribution. The
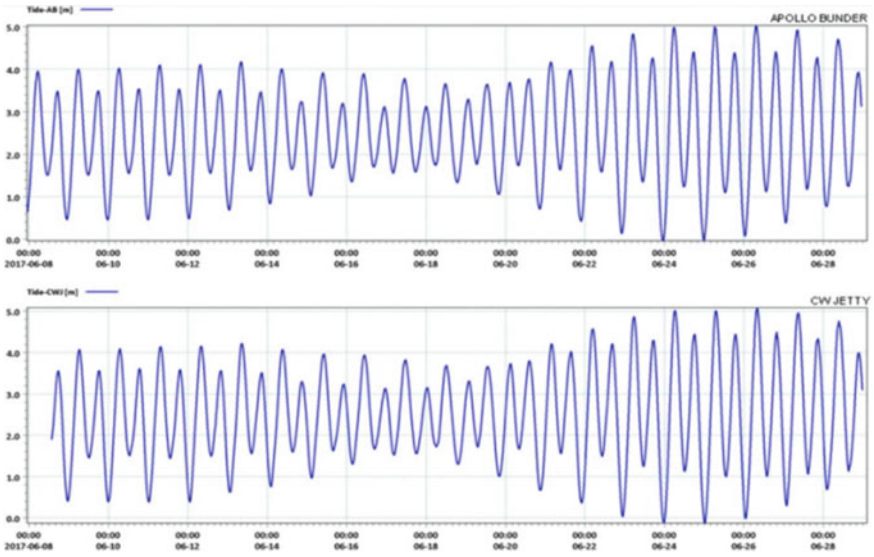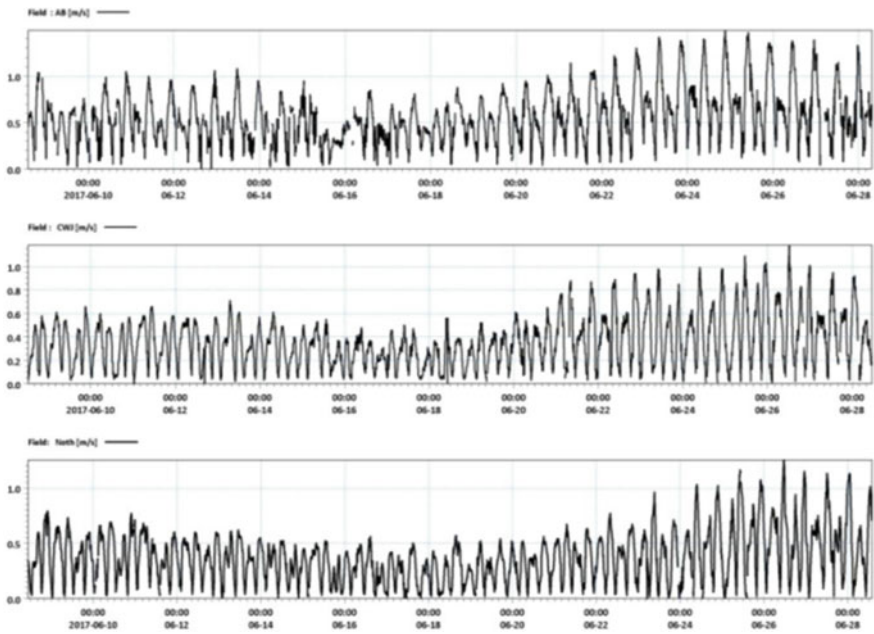
Fig. 3 Observed tide

Fig. 4 Observed current

Table 1 Field data analysis

Location	Maximum tidal range (m)	Maximum Current observed during (m/s)		Average Silt Charge (kg/m3)	
		Flooding	Ebbing	Spring Tide	Neap Tide
Apollo Bandar (A)	5.03	0.90	1.49	1.11–1.72	0.94–1.65
East of CW Jetty (B)	–	0.94	1.25	1.22–1.70	1.21–1.71
CW Jetty (C)	4.91	0.86	1.18	1.13–1.55	1.12–1.50

D50 for the locations for A and C has been found to be 0.0015 mm and 0.001 mm, respectively.

4   Results and Discussions

4.1   Mathematical Model—Existing Conditions

The mathematical model domain developed and considered for the present study extends from Colaba on the South to about 24 km towards North into Thane creek and further up on the east side up to Panvel Creek. The total model domain covers an area of about 24×16 km^2. The mathematical model domain for the existing conditions was discretized by triangular elements consisting about 14,000 elements and 8000 nodes. The area of interest, i.e. near the CW Jetty has been fine meshed for carrying out the studies and visualizing the results more comprehensively. The outcome of flow simulation would be velocity and tidal levels all across the model; the model domain is shown in Fig. 5, while the finer mesh near the CW Jetty is shown in Fig. 6.

The typical flow pattern for the existing conditions near the CW jetty in the model domain during the peak flood and ebb are shown in Fig. 7.

From the above figures, it can be seen that circulations/eddies near the pump intake are aggravated due to intake of pumps, owing to which rate of siltation will be higher thus requiring periodical dredging for maintaining the required depths.

The model thus simulated is calibrated for predicted velocities and water levels by the model with the observed field data at the site. The comparison of currents and water levels are shown in Fig. 8.

From the figures, it can be seen that observed and computed velocities as well as water levels compare well. Thus, it can be inferred that the model is well calibrated with respect to water levels and velocities for the study area under consideration.
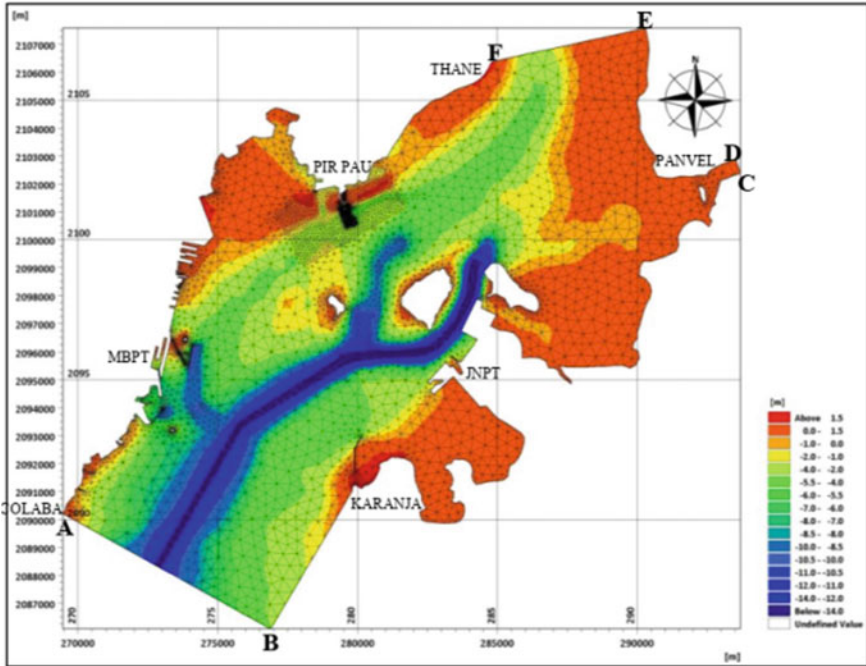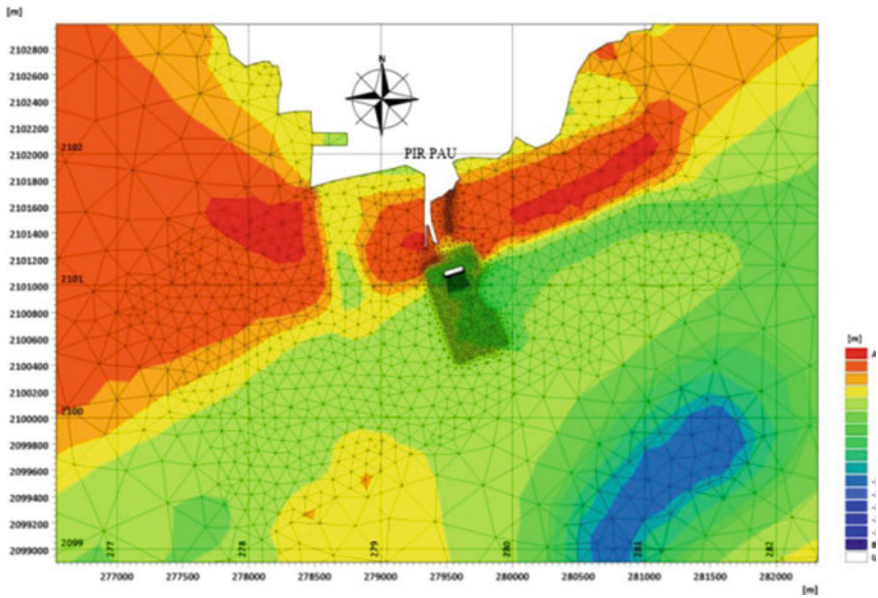
Fig. 5 Bathymetry and Mesh (existing)

Fig. 6 Bathymetry and Mesh (near CW Jetty)

Peak Flood   Peak Ebb
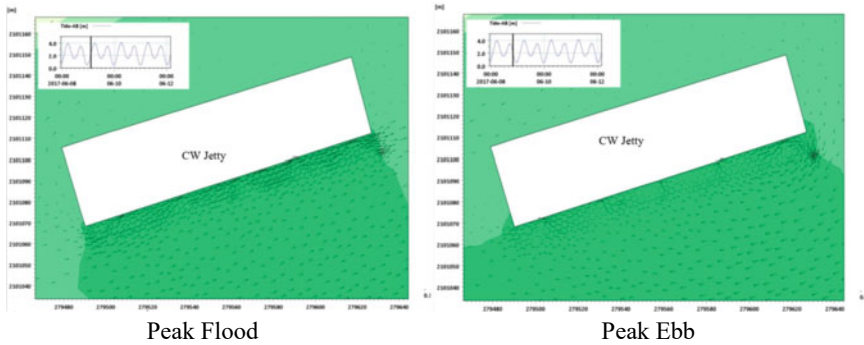
Fig. 7 Flow field in existing condition
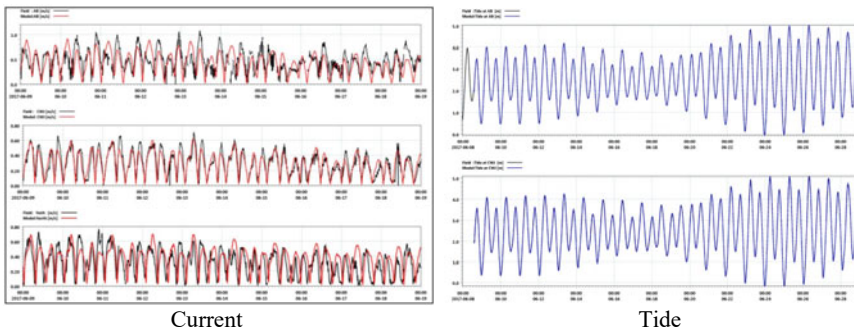
Current   Tide

Fig. 8 Comparison of current and water levels (observed versus computed)

4.2 Sediment Transport Model—Existing Condition

Silt/sediment is being carried by tidal currents and the strength of this current at any instant in space, and time is responsible for siltation in coastal creeks. The morphology study was carried out using MIKE 21 MT module [2]. The above calibrated hydrodynamics model coupled with the silt module will be run to evaluate the probable siltation in the model domain.

The silt model requires silt charge that is prevalent at the site. The water samples have been collected during the field data collection and were analysed for silt charge. The silt charge has been used in the model to simulate the silt model. The sediment model was run for both monsoon and non-monsoon seasons. Figure 9 shows the silt deposition pattern in the model domain as well as near the CW Jetty, as obtained from the silt model.

The silt model predicts an annual silt deposition rate of 3.9 m in front of CW Jetty which compares well with the dredging quantities reported for various years. One important factor which has bearing on siltation taking place at the pump intake

Fig. 9 Silt deposition at different places in the model domain—existing conditions

is topography of the area. A drainage channel traversing from refinery areas meets the intake on its north side. During monsoon, it carries lot of rain water with sediment in suspension. When the channel joins the sea, due to sudden enlargement, the flow velocities reduce, and the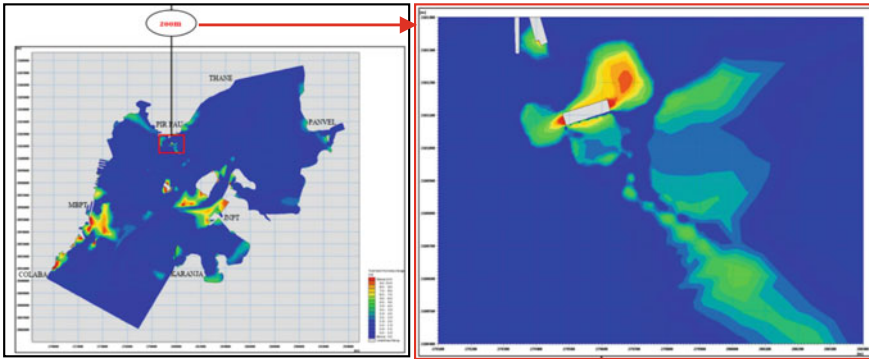refore, the sediment load gets deposited. The point of deposition changes due to change in water level due to tidal variation. Hence, the drainage channel is also contributing to siltation at the pump intake.

4.3 Model Simulation for Proposed Conditions

The model thus calibrated for existing conditions is used for evaluating the hydrodynamics and siltation aspects by incorporating the proposed conditions, wherein three intake structures shall be installed about 500 m south of the jetty, in deeper water depths has been incorporated in the model domain.

The three intake wells with 12 m diameter have been located at about 500 m south of existing CW jetty where the available depths are of the order of 4.3 m w.r.t to CD. The centre to centre spacing between three wells has been kept about 50 m. The bathymetry and grid generated for the proposed conditions by incorporating all the features. The details of the bathymetry at the proposed location is shown in Fig. 10.

The model is then simulated for the proposed conditions with the existing CW Jetty intake being abandoned and by incorporating an intake discharge of 20.83 cumecs each for the proposed three numbers of seawater intake wells. The typical flow pattern for the proposed conditions in the model domain during the peak flood and ebb are shown in Fig. 11, respectively, with the flow pattern for similar conditions near the proposed three intake wells.

In order to assess the changes in the flow conditions due to proposed three intake wells, the velocities for the existing and proposed conditions have been compared at various locations such as in main channel (C1 and C2), channel in front of JN Port (C3), in Trombay channel (C4), at CW Jetty (C5), near the proposed intake wells
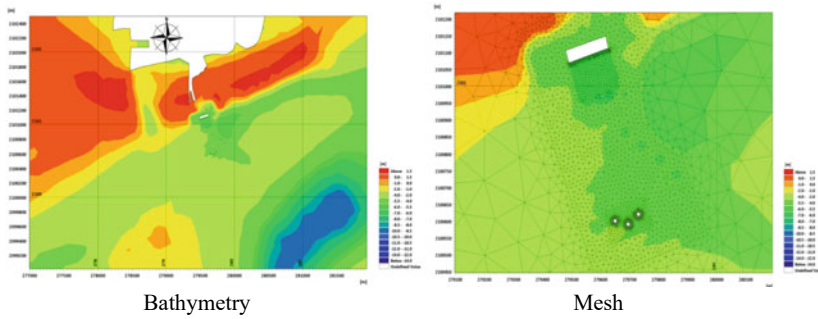
Bathymetry   Mesh

Fig. 10 Bathymetry at the proposed location

Peak Flood   Peak Ebb
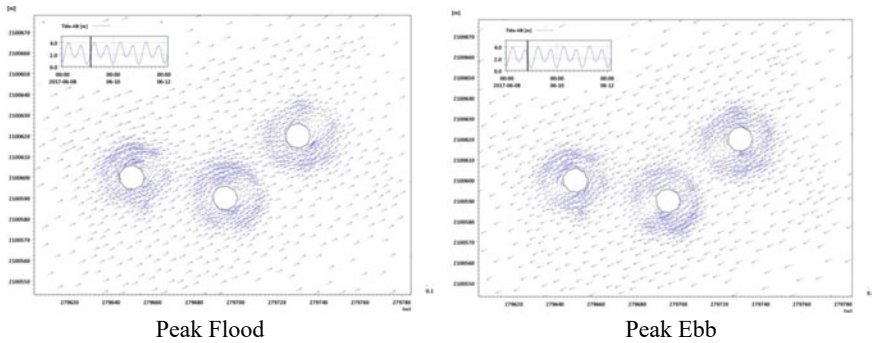
Fig. 11 Flow at the proposed conditions

(C6 and C7) and in the channel in front of Pir Pau Jetty (C8) are shown in Fig. 12 and comparison of currents for existing and proposed conditions for the above locations is shown in Fig. 13. The inference is given in Table 2.

The reduction in velocities near the proposed site would apparently result in increasing in siltation rates.

4.4 Sediment Model—Proposed Conditions

The sediment model is simulated for the proposed conditions. The sedimentation pattern in the model domain as obtained from the simulation is shown in Fig. 14. The annual silt deposition near the proposed intake is found to be of the order of 1.6 m as compared to 0.5 m during the existing conditions. Thus, there is a significant increase in the siltation owing to the new proposed condition.
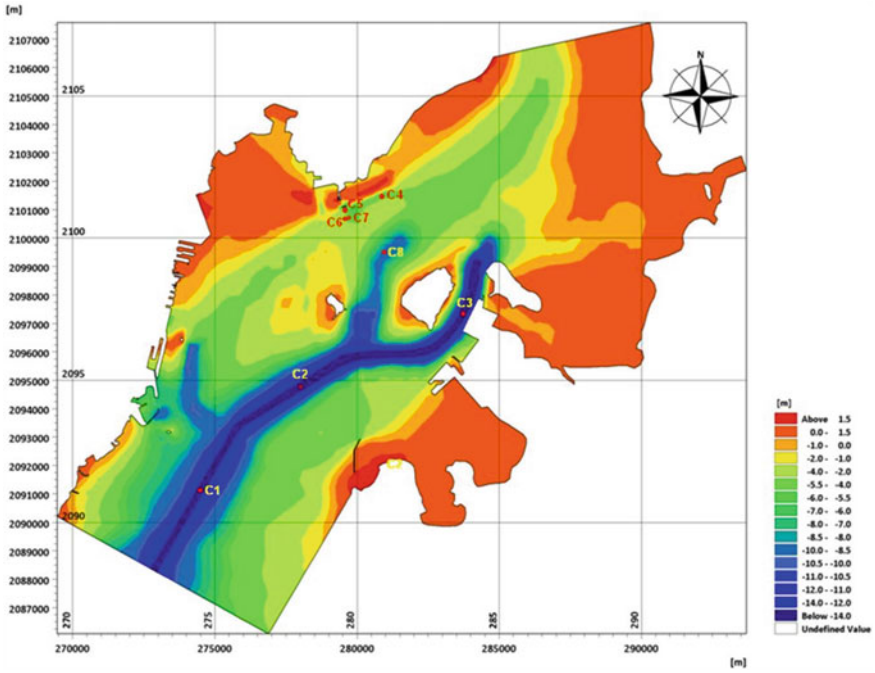
Fig. 12 Location of comparison points—existing and proposed conditions

C1–C4   C5–C8
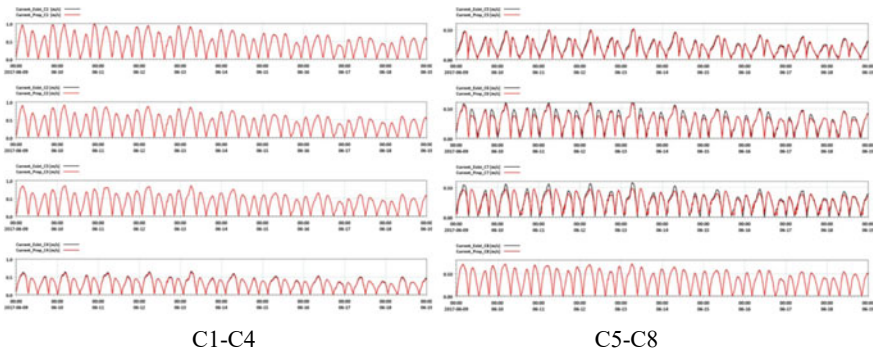
Fig. 13 Comparison of currents—existing and proposed conditions

In the proposed conditions, the siltation near the cooling water jetty is found to increase from 4.0 m/annum to 6.5 m/annum. However, once the bed level regains its original regime, the siltation rate is expected to stabilize.

Table 2 Analysis of currents at various locations during existing and proposed conditions

Location	Inference		Remarks
	Existing	Proposed	
C1 to C4 and C8	No change in velocity		Proposed scheme has no effect on the existing facilities
C5	Slight/negligible change in velocity as compared to existing condition		
C6 and C7	Significant reduction in velocities in proposed condition as compared to existing condition		Reduction is primarily attributed to pumping of sea water from the three intake wells
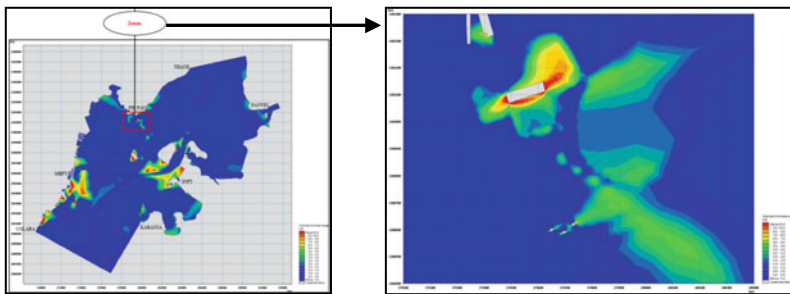
Fig. 14 Silt deposition at different places in the model domain—proposed conditions

5 Conclusions

The following are the main conclusions of the studies:

- The hydrodynamic model for the existing conditions is well calibrated with respect to observed field data. The silt model for the existing conditions predicts an annual silt deposition rate of 3.9 m in front of CW jetty.
- From the hydrodynamic studies for the proposed conditions, it can be inferred that there is no change in the velocities in Main Channel (C1 and C2), channel in front of JN Port (C3), channel in front of Pir Pau Jetty (C8) and Trombay channel (C4). Hence, it can be safely concluded that the proposed scheme has no effect on the prominent facilities in Mumbai Harbour. At CW Jetty (C5), there is slight or negligible change in velocities as compared to existing conditions.
- The cumulative effect of the three intake pumps can be effectively seen near the proposed intake wells (C6 and C7) which is evident from the significant reduction of velocities during the proposed conditions as compared to the existing scenario.
- The reduction in velocities near the proposed site would apparently result in increasing in siltation rates. The annual silt deposition near the proposed intake is found to be of the order of 1.6 m as compared to 0.5 m during the existing

conditions. Thus, there is significant increase in the siltation owing to the new proposed scheme in the vicinity of the three intake wells.

- In the proposed conditions, the siltation near the cooling water jetty is found to increase from 4.0 m/annum to 6.5 m/ annum. However, once the bed level regains its original regime, the siltation rate is expected to stabilize.
- Siltation being a continuous process, the dredging has to be carried out in a shortest possible time with a suitable dredging technique followed by pre- and post-dredging surveys, which will pave way for better understanding of the siltation process of the area.

References

1. CW&PRS Technical Report No. 5591of May 2018 MMS for hydrodynamics and siltation at Trombay, Mumbai
2. User guide of MIKE21—flow model FM for hydrodynamics module and mud transport module, Danish Hydraulic institute 2014

Indispensability of Model Studies in the Design of Settling Basins of Hydropower Projects in River Basins with High Sediment Yield

J. Chandrashekhar Iyer and E. J. James

Abstract A settling basin is provided close to the headwork in a hydropower project to facilitate settlement and exclusion of undesirable sediments in order to minimize the wear and tear of the vulnerable underwater components. The design of settling basin primarily aims at dimensioning of the basin components including the flushing system to achieve the desired sediment settling efficiency. Hydraulic and numerical model studies are ideal tools for ascertaining the water and sediment flow pattern from the inlet to the outlet of the basin for optimizing the geometry of the settling basin, transitions and flushing system. Several model studies for settling basin have been reported from across the world. The paper highlights the importance of model studies in the design of settling basins of hydropower projects in river basins with high sediment yield. The need for further research and importance of performance feedback is discussed.

Keywords Settling basin · Suspended sediment · Model studies · Settling efficiency

1 Introduction

The management and control of sediments in the settling tanks is the major challenges faced by the engineers designing hydropower projects in the river basins with high sediment yield. Large quantity of suspended sediments is to be excluded from entering the water conductor system so as to avoid damage to the vulnerable under water components for durability and trouble-free operation of the power plant. The suspended sediment load in a river and its characteristics such as concentration,

J. Chandrashekhar Iyer (✉)
Polavaram Project Authority, Ministry of Jal Shakti, Hyderabad, Telangana 500004, India
e-mail: jchandra69@gmail.com

E. J. James
Professor, Water Institute, Karunya Institute of Technology and Sciences, Coimbatore, Tamil Nadu 641114, India

grain-size distribution—coarse, medium and fine—and petrography largely decides the scale and complexity of the problem.

The settling basin is also variously known as "desilting basin", "desander" and "sand trap". A settling basin is generally housed close to the headwork to facilitate settlement and exclusion of sediments through the flushing system. The basin can be of open channel or pressure flow type, installed on the surface or underground. The settling basin complex generally comprises an inlet tunnel/channel, inlet transition, main settling basin with a sediment settling-cum-flushing system and outlet transition leading to an outlet tunnel or channel.

2 Dimensioning of Settling Basin

The settling basin is basically designed to meet the stipulated degree of sediment exclusion. Empirical and analytical approaches have been suggested by ref. [1–7] for dimensioning and computing the settling efficiency of settling basin. These empirical and analytical approaches are widely used for design of settling basin world over, and the design approach is constantly evolving. One of the commonly used approaches proposed by ref. [4] is briefly discussed here.

The settling velocity 'w' of a sediment particle of size 'd' is reduced by taking into consideration the retarding effect of turbulence. For a forward velocity 'U' and flow depth 'D', the reduction is given by $w' = \alpha\, U$, where coefficient

$$\alpha = \frac{0.132}{\sqrt{D}} \tag{1}$$

The effective settling velocity 'w_e' of the particle is

$$w_e = w - w' \tag{2}$$

The length of settling basin considering the effective settling velocity of the particle is calculated using the equation $L = \frac{(UD)}{w_e}$.

$$L = \frac{U D\,3/2}{w\sqrt{D} - 0.132U} \tag{3}$$

The settling efficiency 'η' is determined from Velikanov's graph shown in Fig. 1, wherein λ is as under.

$$\lambda = \sqrt{\frac{7.51w^2 L}{U2\left(\sqrt{D} - 0.2\right)2}} \tag{4}$$

Fig. 1 Velikanov–Settling efficiency η versus λ
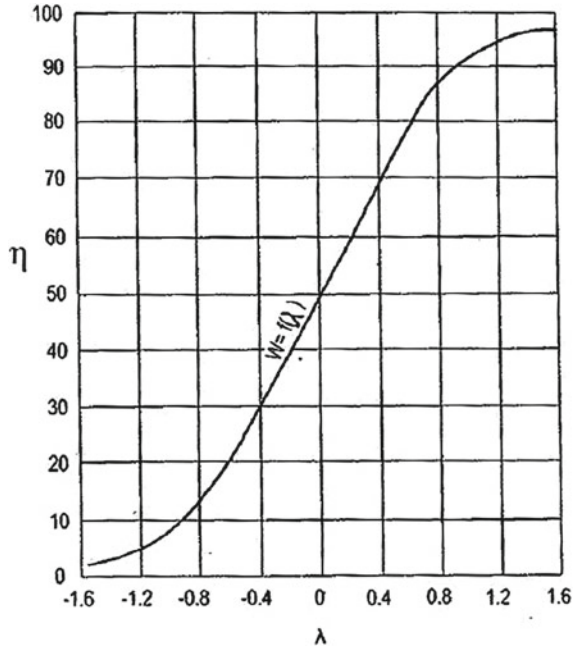
The functional relationship for estimation of settling efficiency based on the different approaches is given in Table 1.

Dobbins [2] has proposed an analytical solution for the design of settling basin from the observations carried out in an open-channel flow, which has been further expressed in graphical form by Camp [1]. The United States Bureau of Reclamation (USBR) [7] developed a basic relationship considering the settling velocity and overflow rate for design of settling basin. The approach proposed by ref. [4] considers

Table 1 Functional relationship for estimation of settling efficiency

S. No.	Approach	Functional relationship for settling efficiency
1	Camp [1], Dobbins [2]	$\eta = f\left[\frac{wL}{UD}, \frac{wD1/6}{Un\sqrt{g}}\right]$
2	USBR [7]	$\eta = 1 - \exp\left(-\frac{wL}{UD}\right)$
3	Sumer [6]	$\eta = 1 - e^{-\left(\frac{\kappa\lambda}{6}\right)\left(\frac{Lu_*}{UD}\right)}$
4	Garde et al. [3]	$\eta = \eta 0\left(1 - e^{\frac{-CL}{D}}\right)$ where η_0 and C are functions of $\frac{w}{u_*}$
5	Ranga Raju et al. [5]	$\eta = f\left[\frac{w}{U}, \frac{LB}{bh}, \frac{D1/6}{n\sqrt{g}}\right]$
		Effect of continuous flushing on the settling efficiency:
		$\frac{\eta d}{\eta} = 1 - 0.12 Q_f^{-0.105} \frac{w^{0.312}}{u_*}$

the retarding effect of turbulence. Sumer [6] has studied sediment settlement in an open-channel flow assuming logarithmic velocity distribution in the basin.

Garde et al. [3] have conducted experiments under steady conditions for subcritical flow in a tilting rectangular flume and observed that the sediment concentration does not seem to have an effect on the efficiency. The paper compares the results from the laboratory experiments with the existing relationships and concludes that the existing approaches are not satisfactory in respect of fine sediments. The paper observes that further theoretical studies should consider the effect of the inlet flow expansion on the vertical diffusion of sediments as well as that of the bottom density current in case of flows with high concentration of bed load. Discussing on this paper, Schrimpf [8] has suggested carrying out numerical simulations with the diffusion–advection equation for the verification exercise.

Ranga Raju [5] based on experimental investigations has concluded that the existing empirical approaches for determination of sediment removal efficiency of settling basins do not give satisfactory results in respect of fine non-cohesive sediments, i.e. when $w/u_* < 0.4$ and developed a new relationship for the entire range of w/u_*. Further, the effect of continuous flushing of a sediment water mixture from the settling basin on its removal efficiency is presented. Sinha and Singh [9] have analysed these empirical and analytical approaches bringing forth the limitations from applicability point of view and suggested modifications in these approaches to account for the varying shape of the basin and for varying rugosity coefficient. Further, the modification, if any, required for applying the approaches originally developed for free flow condition to pressure flow settling basin also need to be addressed.

It is therefore imperative that for design of settling basin, the underlying assumptions and inherent limitations of the empirical approach are well understood and wherever required, modifications are suitably incorporated. As the empirical approaches cannot provide the designers with the water and sediment flow behaviour in the entire domain of the basin, the dimensions and geometry evolved through empirical approach need to be firmed up through model studies.

3   Model Studies

Hydraulic and numerical model studies are indispensable tools for comprehensively ascertaining the water and sediment flow behaviour in the settling basin including the transitions, settling trench and flushing system. Several models have been evolved based on the studies in different river basins with high sediment yield.

3.1 Hydraulic (Physical) Model Studies

The hydraulic model studies primarily focus on optimizing the dimensions of the settling basin, configuring the inlet and outlet transitions and assessing the efficiency of settling basin, duly considering the sediment load and its characteristics. The design process covers optimization of the size of settling trench, spacing as well as the number and size of openings at the bottom of the trench, slope as well as size and other arrangements of sediment flushing tunnel. The presence of turbulence and eddy formation differently affects the settling process in the inlet, central and outlet zones of the basin, which influence the settling efficiency of the basin. The deposition of sediments in the basin or in the flushing tunnel and dune formation between the trench floor openings is mainly the results of improper design or operation of the basin. The overall efficiency of the settling basin is also dependent on the efficacy of the flushing system.

One of the earliest hydraulic model studies for an underground settling basin under pressure flow was carried out by Central Water and Power Research Station (CWPRS), Pune, for Chukha hydropower project on Wangchu river in Bhutan. The model study of the project reported in the Technical Memorandum [10] focussed on the design of inlet transition, settling basin, sediment flushing tunnel and optimization of the size and spacing of the openings on the floor of the settling trench. CWPRS [11] reports on the physical model studies conducted for the world's largest underground settling basin complex of Nathpa Jhakri project involving pressure type flow. The study optimized the geometry of inlet transition. The study, based on an analytical approach, confirmed that the proposed sizing of the settling basin with a length of 525 m is adequate for the given sediment size distribution and concentration of 5000 ppm by volume for settlement of 90% sediments coarser than 0.2 mm diameter. Based on the study, three separate flushing tunnels were proposed beneath the settling trench, first tunnel flushing the sediments from initial 175 m length, second from the next 175 m length and the third from the tail-end length of 175 m length of the settling trench. The hydraulic model study could finalize the size of flushing tunnels for continuous flushing of the settled sediments with 20% discharge, and provided separately the percentage and concentration of sediments flowing into these flushing tunnels. Dune formation observed in the settling trench between the openings below the hopper bottom was not expected to protrude above the top level of the trench. Based on the experience gained through physical model testing of several pressurized underground settling basins in the Himalayas, CWPRS [12] provides the broad guidelines for design of pressure flow type settling basin.

Similarly, the hydraulic model study of the settling basin of Teesta Stage–III hydropower project was carried out at the Hydraulic Research Institute, Roorkee, to assess the hydraulic efficiency of the settling basin and adequacy of flushing system [13]. The dimensioning of the basin was carried out considering the removal of 90% and above sediment sizes coarser than 0.2 mm for an incoming sediment concentration of 2000 ppm. The model study also finalized the size and spacing of the openings in the settling trench connecting the basin with the flushing tunnel.

Based on the model studies on three settling basins for the Alpine region at the Laboratory of Hydraulics, Hydrology and Glaciology, Zurich, the flow field and sediment flux were assessed [14]. Significant turbulent flow conditions were observed in the initial one-third length of the basin, attributed to the non-uniform approach flow conditions. To overcome that, tranquilizing racks were recommended in the inlet transition. Nils [15] based on a physical model study at Alvkarleby Laboratory, Sweden, for a basin with open-channel flow conditions for the Uri hydropower project in India, optimized the flow pattern with modification in the inlet transition design to achieve the desired sediment removal efficiency.

Delft Hydraulics carried out hydraulic model studies for the settling basin of Dul Hasti hydropower project to study pattern of holes and the flushing behaviour during a continuous and discontinuous flushing of sediments. Develay et al. [16] showed that for a continuous flushing, better settling efficiencies were observed in the case of higher concentration. This is due to the fact that the sediment profile had a relatively higher concentration in the lower half of the vertical, resulting in more sediment concentration in the flushing tunnel than that in the head race tunnel. Further, a dune formation was observed near the downstream end of the basin, which could be easily drawn towards the head race tunnel, adversely affecting the efficiency; the need for an additional opening in the invert near the basin end was recognized to overcome this limitation. Jong et al. [17] have shown that in the case of discontinuous or intermittent flushing, the trapping efficiency is progressively reduced during the filling process of the basin due to faster formation and propagation of dunes. Dune formation takes place due to the steep pressure gradient in the sand dunes during the flushing process. The model results helped in assessing the frequency of operation of the sediment flushing system not only during the monsoon period, but also during the non-monsoon period.

Hydraulic model studies [18] carried out for the settling basin of Tala hydropower project in Bhutan shows that the pressure in the flushing tunnel has been always less than the pressure in the settling basin at any section and the difference goes on increasing towards the downstream. This pressure difference was responsible for the flow from the settling basin to the flushing tunnel. The pressure gradient in the flushing tunnel was observed to be steeper than that in the settling basin. However, the study indicated that the velocities through the openings were not proportional to the difference in the head because the total discharge was ultimately controlled by operating the gate at the end of the flushing tunnel.

The hydraulic model studies carried out world over for the design of settling basin demonstrate the significance of this indispensable tool. As seen above, the hydraulic model study provides us vast information on the water and sediment behaviour in the basin and through iterative process and enables firming up the geometry and dimensions of the various individual components of the basin. No two projects are alike as far as the design of settling basin is concerned. Hence, despite broad guidelines in place, designers cannot dispense with project-specific hydraulic model studies. The hydraulic model studies suffer from limitations due to scale effects which also affects simulation of finer sediment fractions. Keeping in view the several variables

associated with water flow and sediment transport processes, the design of various components of the basin shall continue to be a grey area for researchers.

3.2 Numerical Model Studies

Several computational fluid dynamic (CFD) models exist today for simulation of water and sediment flow. The hydrodynamic and sediment transport models involve the numerical solution of one or more of the governing differential equations of continuity, momentum and energy of fluid, along with the differential equation for sediment continuity. The review by Papanicolaou et al. [19] brings out the capabilities of selected 1D, 2D and 3D sediment transport models and discusses their strengths and limitations. A comparison therein of select features of few of the 2D and 3D models is given at Table 2.

CFD models are widely used world over in hydraulic engineering, wherein design of settling basin is no exception and the algorithms are constantly evolving. Olsen [20] discusses the CFD model SSIIM, which is an abbreviation for "*Sediment Simulation In Intakes with Multiblock option*". The computational programme solves the continuity equation together with the Reynolds-averaged Navier–Stokes (RANS) equations in three dimensions to compute the water motion for turbulent flow.

$$\frac{\partial U_i}{\partial x_i} = 0 \tag{5}$$

$$\frac{\partial U_i}{\partial t} + U_j \frac{\partial U_i}{\partial x_j} = \frac{1}{\rho} \frac{\partial}{\partial x_j} \left(-P\delta_{ij} - \rho \overline{u_i u_j} \right) \tag{6}$$

where $i = 1, 2, 3$; where U_j is the averaged velocity, x is the spatial geometrical scale, ρ is the water density, P is the dynamic pressure, δ_{ij} is the Kronecker delta and $-\rho \overline{u_i u_j}$ is the turbulent Reynolds stresses. The model uses an unstructured and non-orthogonal grid made of a mixture of tetrahedral and hexahedral cells. The finite-volume method is applied as discretization scheme and standard k–ε turbulence model is used to solve the Reynold's stress term. The grid is adaptive and moves with the changes in the bed and water levels. The computation of the sediment transport for modelling the hydro-morphological changes in the bed is divided into suspended and bed load transport. The suspended sediment transport is calculated by solving the following transient convection–diffusion equation, while the bed load transport is simulated by Van Rijn's formula.

$$\frac{\partial c}{\partial t} + U_j \frac{\partial c}{\partial x_j} + w \frac{\partial c}{\partial z} = \frac{\partial}{\partial x_j} \left(\Gamma \frac{\partial c}{\partial x_j} \right) + S \tag{7}$$

where U is the water velocity, w is the fall velocity of the sediment, Γ is the turbulent diffusivity, c is the sediment concentration over time and over the spatial geometrical

Table 2 Comparison of select features of few 2D and 3D models

Model	Bed sediment transport	Suspended sediment transport	Sediment mixtures	Cohesive sediment	Sediment exchange processes
Two-dimensional (2D) models					
TABS2	Yes[a]	Yes[a]	No	Yes	Entrainment and deposition
MIKE 21	Yes[a]	Yes[a]	No	Yes	Entrainment and deposition
MOBED2	Yes	Yes	Yes	No	Entrainment and deposition
USTARS	Yes	Yes	Yes	No	Entrainment and deposition
FAST2D	Yes	Yes	No	No	Entrainment and deposition
FLUVIAL 12	Yes	Yes	Yes	No	Entrainment and deposition
DELFT 2D	Yes	Yes	No	Yes	Advection–diffusion
CCHE2D	Yes	Yes	Yes	No	Advection–diffusion
Three-dimensional (3D) models					
CH3D-SED	Yes	Yes	Yes	Yes	Entrainment and deposition
MIKE 3	Yes[a]	Yes[a]	No	Yes	Entrainment and deposition
SSIIM	Yes	Yes	Yes	No	Advection–diffusion
FAST3D	Yes	Yes	No	No	Entrainment and deposition
DELFT 3D	Yes	Yes	No	Yes	Entrainment and deposition
TELEMAC3D	Yes[a]	Yes[a]	No	Yes	Entrainment and deposition
ECOMSED	Yes[a]	Yes[a]	No	Yes	Entrainment and deposition

[a] Treated as a total load without separation

scales x and z and S is the source term for taking the inflowing sediments at the boundary into account. The computational model predicts the sediment deposition pattern and trap efficiency.

Olsen et al. [21] showed that the calculations of water and sediment flow in a 3D settling basin using the SSIIM model compared well with the experimental procedures. SSIIM has been used for modelling one unit of settling basin for calculating the water and sediment flow in the settling basin of Nathpa Jhakri hydropower project [22]. The study showed that the settling efficiency from the numerical study and that from the physical model study is in good agreement, except for a recirculation

zone observed in the inlet zone based on the numerical model. The numerical model could provide settling efficiency of finer fractions also which could not be simulated in the physical model study conducted at CWPRS, Pune, due to limitations of scale. The results from a three-dimensional numerical modelling of bed changes in a pressure flow settling basin by applying SSIIM model [23] compared well with the measurements made in a physical model.

The applicability of the numerical model TELEMAC-2D has been studied [24] to simulate the water and sediment flow process in the open-channel flow type multi-basin desander of Chavimochic irrigation and hydroelectric project in Peru. The reduced scale physical model study carried out at the Hydraulics Institute of the Piura University in Peru demonstrated that in spite of the discrepancies in flow distribution predicted by the numerical model and observed in the physical model, the sediment settling efficiency for each basin and overall settling efficiency obtained by these two types of models compared well. For the sediment flushing system, numerical simulation is carried out for an existing settling basin with two software packages ANSYS CFX and FLOW-3D [25], to investigate the flow dynamics and the required sediment flushing discharge after introducing improvements. A good agreement between the results of the numerical simulations using both software packages is reported.

CFD model studies have been conducted for many projects for simulation of sediment transport processes and predicting settling efficiency. The numerical model is less costly and can be adapted to different physical domains more easily than physical model. Further, these models do not suffer from distorted scale effects. However, one needs to be aware of the common errors and uncertainties in computational fluid dynamics that include errors in numerical approximations, modelling, input data, boundary conditions and errors in programming. Some of the grey areas for future research include the study of model limitations, role of grid sensitivity, mobile bed model calibration and verification.

4 Discussions

The wealth of information generated on the water flow and sediment transport in a basin, from the many hydraulic and numerical model studies conducted, needs to be analysed and inferences drawn for future use. Further, with future investigations and flow of more information, the empirical approaches and broad guidelines could also be revisited and bettered. While there are several aspects related to the settling basin components for discussion and future research, this paper would focus only on two aspects, viz. sizing of the settling basin and significance of performance evaluation and feedback on operational settling basins.

4.1 Sizing of Settling Basin

The sizing of settling basin primarily aims at determination of optimum length, width and depth of the basin. The sizing of the pressure flow type settling basins, mean velocity and sediment removal criteria in the case of a few underground hydropower projects under operation is given in Table 3, wherein the design has been finalized after conducting hydraulic model studies. Though the basin shape, inflowing discharge and sediment characteristics, etc., are not mentioned, the limited information given in the table deserves introspection.

CWPRS [12] recommends maximum forward velocity in the main basin as 0.15 m/s, 0.30 m/s and 0.35 m/s for effective settlement of 0.1 mm, 0.2 mm and 0.3 mm sediment size, respectively, which is seen exceeding in certain projects. The feedback on basin performance vis-à-vis higher flow velocity, from these projects and in particular Chukha and Dul Hasti, could be of interest to study. Sensitivity analysis of forward velocity on settling efficiency could be studied on models. It is seen from the table that the sediment removal criteria commonly stipulated by the power plant are removal of 90% and above sediments coarser than 0.2 mm. The criterion does not stipulate any restriction on the permissible concentration of the

Table 3 Sizing of settling basin in select hydropower projects under operation

Hydropower project	Mean forward velocity (m/s)	Length (m)	Maximum width (m)	Maximum depth (m)	Sediment removal criteria
Dul Hasti	0.640	240	15.00	14.50	Above 90%, > 0.3 mm
Parbati-III	0.415	250	12.20	22.35	Above 90%, > 0.3 mm
Chamera-III	0.400	200	13.00	17.00	Above 90%, > 0.3 mm
Chamera-II	0.262	375	16.00	21.75	Above 90%, > 0.2 mm
Nathpa Jhakri	0.320	525	16.31	27.50	Above 90%, > 0.2 mm
Teesta–III	0.250	320	17.00	23.00	Above 90%, > 0.2 mm
Teesta–V	0.317	250	20.00	24.50	Above 90%, > 0.2 mm
Tala	0.263	250	13.90	18.50	Above 90%, > 0.2 mm
Chukha	0.630	348	8.50	11.70	Above 90%, > 0.2 mm
Dhauli Ganga	0.310	300	13.00	16.20	Above 90%, > 0.2 mm

remaining sediment sizes. In fact, the advancements made over the years in the field of metallurgy, anti-abrasive materials and coatings relating to power plant machinery, if factored in, could possibly relax the sediment removal criteria, thereby effecting economy in settling basin. Rather than a general prescription, the stipulation of sediment control and exclusion expected in the settling basin should be project-specific and after duly considering the sediment load in the river, sediment size distribution and petrography, head, discharge and related features of the vulnerable components of the power plant. The dimensions of the settling basin optimized through hydraulic model studies in the listed projects could well be a reference for comparison with the results of the empirical and analytical approaches.

Based on the method developed [3] for the settling performance of the basin, equations have been developed [26] for the estimation of optimum length, width and depth, considering the cost factor. Monograph has been developed [27] for arriving at the best optimized dimension of settling basin by comparing the result obtained by different analytical and empirical approaches for practical range of depth of settling basins and the data commonly considered for estimation of sizing of basins. The length required for 90% efficiency with respect to the depth of the basin has been presented. Mishra et al. [28] have carried out analysis to develop correlations for sizing of the settling basin of small hydropower projects.

Numerical model studies should preferably be used to optimize the combination of length, width and depth to maximize the performance of the basin and simultaneously effecting economy. Few best combinations could then be tested on hydraulic model.

4.2 Performance Evaluation and Feedback

The performance evaluation study for a number of settling basins of small hydropower projects in the State of Himachal Pradesh in India carried out [29] concludes that the observed efficiency of settling basin was found to be less, attributing to the turbulence in flow causing re-suspension of sediments and inadequate sediment flushing arrangement. Performance evaluation findings [29] confirm that non-operation of continuous flushing has resulted in choking the flushing system and decreasing the basin efficiency. Based on analysis of experimental data [5], it is concluded that continuous sediment flushing from basin bottom improves the sediment removal efficiency. The post-commissioning sediment measurements carried out at different locations in Nathpa Jhakri project by SJVN Ltd. have been analysed [30] for a broad comparison of the settling efficiency of the prototype and estimation of the physical and numerical model studies as given in Table 4.

It is necessary that the hydraulic performance of the vital components of the settling basin of commissioned hydropower projects is measured by the project proponents, evaluated with respect to the predicted performance and documented for future use.

Table 4 Comparison of settling efficiency in the prototype and model studies

Sediment size (mm)	Physical model (%)	Numerical model (SSIIM) (%)	Prototype (%)
Greater than 0.2 mm	90	94	90–100
Overall	36	37	40–60

5 Conclusions

In order to minimize the wear and tear of the vulnerable underwater components of the power plant, settling basin is provided at huge cost to settle and flush out undesirable sediments. The following conclusions are drawn from the present review:

(i)   The empirical and analytical approaches discussed in the paper are widely used for dimensioning and computing settling efficiency of settling basin. Review points out the inherent limitations in these relationships, restricting their wider applicability.

(ii) The information and results flowing from the laboratory experiments on sediment transport in a settling basin as well as from related hydraulic and numerical model studies should help better the existing empirical and analytical approaches and development of new design aids.

(iii) The stand-alone design evolved through the empirical and analytical approaches is in no way complete for taking up execution. The design should essentially be followed up by studies on a hydraulic model and/or CFD model before grounding. The water and sediment flow behaviour along the transitions, in the main basin, settling trench as well as in the flushing system needs to be ascertained before firming up the dimensions and geometry of the basin components.

(iv) Hydraulic and numerical models are widely used indispensable tools for the design of settling basin. The inherent limitations of the hydraulic model studies due to scale effects and the uncertainties in numerical model studies due to errors and approximations in programming and modelling should be kept in view and suitably addressed.

(v)   The stipulation of sediment control and exclusion expected in the settling basin should be project-specific and after duly considering the sediment load in the river, sediment size distribution and petrography, head, discharge and related features of the vulnerable components of the power plant instead of a general prescription. The advancements made over the years in the field of metallurgy, anti-abrasive materials and coatings relating to power plant machinery, if factored in, could possibly relax the sediment removal criteria, thereby effecting economy in settling basin.

(vi) Numerical model studies should preferably be used to optimize the combination of length, width and depth to maximize the performance of the basin

and simultaneously effecting economy. Few best combinations could then be tested on hydraulic model.

(vii) The hydraulic performance of the vital components of the settling basin of commissioned hydropower projects should be measured by the project proponents, evaluated with respect to the predicted performance and documented for future use.

Notations

A	Settling basin cross-sectional area (m^2)
B	Width of settling basin (m)
b	Approach channel width (m)
D	Depth of flow (m)
d	Sediment particle size (mm)
g	Acceleration due to gravity ($m\ s^{-2}$)
h	Flow depth in approach channel (m)
κ	Von Karman universal constant
L	Length of settling basin (m)
n	Manning's rugosity coefficient ($s\ m^{-1/3}$)
η	Efficiency of settling basin (%)
η_d	Efficiency of settling basin with flushing
Q	Design discharge in settling basin ($m^3\ s^{-1}$)
Q_f	Flushing discharge ($m^3\ s^{-1}$)
U	Average forward velocity ($m\ s^{-1}$)
u_*	Shear velocity ($m\ s^{-1}$)
w	Settling velocity ($m\ s^{-1}$)
w_e	Effective fall velocity ($m\ s^{-1}$)
w'	Reduction in fall velocity ($m\ s^{-1}$)

References

1. Camp TR (1946) Sedimentation and the design of Settling tanks. Trans Am Soc Civ Eng 111:895–936. https://doi.org/10.1061/taceat.0005912
2. Dobbins WE (1943) Effect of turbulence on sedimentation. Trans ASCE 69:235–262
3. Garde RJ, Raju KGR, Sujudi AWR (1990) Design of settling basins. J Hydraul Res 28:81–91. https://doi.org/10.1080/00221689009499148

4. Mosonyi E (1991) Water power development high head power plants, vol IIB. Akademiai kiado, Budapest, Hungary
5. Ranga Raju KG, Kothyari UC, Srivastav S, Saxena M (1999) Sediment removal efficiency of settling basins. J Irrig Drain Eng 125:308–314. https://doi.org/10.1061/(asce)0733-9437(1999)125:5(308)
6. Sumer BM (1977) Settlement of solid particles in open-channel flow. ASCE J Hydraul Div 103:1323–1337. https://doi.org/10.1061/jyceaj.0004874
7. Vanoni VA (1975) Sedimentation engineering. American Society of Civil Engineers (ASCE)
8. Schrimpf W (1991) Design of settling basins. J Hydraul Res 29
9. Sinha S, Singh AP (2018) Sediment removal efficiency estimation criteria for modern day desilting basins. ISH J Hydraul Eng 25:104–117. https://doi.org/10.1080/09715010.2018.1426057
10. CWPRS (1992) Technical memorandum on desilting basins. Pune, India
11. CWPRS (1990) Specific note on model studies for desilting basin for Nathpa Jhakri project. Himachal Pradesh, India
12. CWPRS (2005) Guidelines for design of desilting basins (Pressure flow). Pune, India
13. Ojha BK (2014) Sediment management at Teesta III—a case study. Int J Technol Res Eng 2:171–175
14. Paschmann C, Fernandes JN, Vetsch DF, Boes RM (2017) Assessment of flow field and sediment flux at alpine desanding facilities. Int J River Basin Manag 15:287–295. https://doi.org/10.1080/15715124.2017.1280814
15. Johansson Nils (1992) Model tests for Uri hydroelectric power project desilting basin in Northern India. In: Proceeding 5th international sysmposium on river sedimentation. Karlsruhe, pp 503–508
16. Develay D, Binquet J, Divatia E, Venkatesha CR (1996) Desilting basin system of the Dul Hasti hydroelectric project. J Hydraul Eng 122:565–572. https://doi.org/10.1061/(asce)0733-9429(1996)122:10(565)
17. Jong RJ de, Perdijk HWR, Develay D, Gautier JBJ (1992) Hydraulic model studies of settling basin of a hydroelectric project. In: Proceeding 5th international symposium on river sedimentation. Karlsruhe
18. CWPRS (2001) Hydraulic model studies for desilting basin of Tala hydroelectric project, Bhutan
19. Papanicolaou ATN, Elhakeem M, Krallis G, Prakash S, Edinger J (2008) Sediment transport modeling review—current and future developments. J Hydraul Eng 134:1–14. https://doi.org/10.1061/(asce)0733-9429(2008)134:1(1)
20. Olsen NRB (1994) SSIIM—a three-dimensional numerical model for simulation of water and sediment flow. In: International conference on hydraulic engineering software, hydrosoft, proceedings, pp 227–234
21. Olsen NRB, Skoglund M (1994) Three-dimensional numerical modeling of water and sediment flow in a sand trap. J Hydraul Res 32:833–844. https://doi.org/10.1080/00221689409498693
22. Olsen NRB, Chandrashekhar J (1995) Calculation of water and sediment flow in desilting basins. In: Proceeding 6th international symposium on river sedimentation. New Delhi
23. Olsen NRB, Kjellesvig HM (1999) Three-dimensional numerical modelling of bed changes in a sand trap. J Hydraul Res 37:189–198. https://doi.org/10.1080/00221689909498305
24. Estigoni MV, Vasquez JA, Robb DM, Wang E, Mauad FF (2015) 2D numerical modelling of sediment trap efficiency in a multi-basin desander. In: 22nd Canadian hydrotechnical conference
25. Daneshvari M, Münch-Alligné C, de Cesare G (2012) Numerical simulation of a new sand trap flushing system. In: 4th IAHR international symposium on hydraulic structures
26. Vittal N, Raghav MS (1997) Design of single-chamber settling basins. J Hydraul Eng 123:469–471
27. Sinha S (2019) Monograph on desilting basins sizes estimation for hydropower projects. Int J Green Energy 16:317–332. https://doi.org/10.1080/15435075.2019.1566136

28. Mishra S, Singal SK, Khatod DK (2013) Sizing and quantity estimation for desilting tank of small hydropower projects—an analytical approach. Int J Green Energy 10:574–587. https://doi.org/10.1080/15435075.2012.668864
29. Singh G, Kumar A (2016) Performance evaluation of desilting basins of small hydropower projects. ISH J Hydraul Eng 22:135–141. https://doi.org/10.1080/09715010.2015.1094750
30. Singh TP, Chandrashekhar J, Agrawal AK (2007) Analysis of water and sediment flow in desilting basin of a run-of-river hydroelectric project. In: International conference on small hydropower. Hydro SriLanka

Field Data Collection and Analysis for Siltation Studies at New Mangalore Port, Panambur, Karnataka

Banwari Lal Meena, H. B. Jagadeesh, and Prabhat Chandra

Abstract The annual maintenance dredging at New Mangalore port (NMP) is one of the major recurring expenses for the port. With the stage-wise development of the port, the maintenance dredging cost also has increased substantially over the last six decades. Even though the littoral drift is minimal, considerable siltation takes place in the approach channel and the port basin during southwest monsoon due to deposition of suspended sediments while crossing the approach channel. CWPRS has proposed to carry out mathematical model studies for prediction of siltation in the port approach channel and port basin. It is difficult to predict siltation pattern extent and quantity without site specific extensive field data collection, analysis and model studies for assessment of dredging requirements for maintaining a clear draft of -15.4 m in the NMP channel throughout the year, hence, field studies were carried out by CWPRS for data collection in respect of tides, currents, bed samples, beach surveys, sediment concentrations during non-monsoon and monsoon seasons during the year 2020. The observed tide data and available tide table data are matching well. The current observations using Acoustic Doppler Current Profiler (ADCP) were carried out at selected salient locations. In the present paper, the details of field data collected and its analysis will be presented.

Keywords Field data · Mathematical model · Siltation · Beach survey · Soil sampling · Water sampling and tide and current data

B. L. Meena (✉) · H. B. Jagadeesh · P. Chandra
Central Water and Power Research Station, Pune 411024, India
e-mail: meena.banwarilal@gmail.com

H. B. Jagadeesh
e-mail: jagadeeshhb@yahoo.co.in

P. Chandra
e-mail: pchandra_2003@yahoo.co.in

1   Introduction

New Mangalore Port located on the west coast of India is an artificially created lagoon type of port. The port facilities have been developed in stages over the past five decades. The required tranquility has been achieved by constructing two breakwaters of length 770 m each, which were extended in three stages flanking the entrance. The present length of the approach channel is 7.5 km from the port lagoon entrance and the channel is dredged to a depth of -15.4 m below CD, while the lagoon is dredged to -15.1 m. Even though the port basin was developed on sandy beach, the major portion of the channel is located on silty bed. Though the littoral drift from adjacent beaches is minimal, considerable siltation takes place in the approach channel and the port basin during southwest monsoon season due to deposition of suspended sediments while crossing the channel, with the coastal and tidal currents. The long-term effects on the siltation pattern in different areas in and around the port, formation of hard patch in the approach channel, siltation in front of approach channel and on the north and the south sides of breakwaters, etc., have been observed.

Siltation in harbor is a complex problem phenomena. The maintenance dredging quantity increased progressively with the increase in drafts.

It is difficult to predict siltation pattern extent and quantity without site specific extensive field data collection, analysis and model studies. Regular dredging in the harbor and approach channel area is required to maintain the draft for safe navigation of the vessels throughout the year. Dredging in the coastal waters being very expensive, generally dredging quantity and frequency influences considerably the efficiency of the harbor and needs to be considered for the port planning.

CWPRS has proposed to carry out mathematical model studies for assessment of dredging requirements for maintaining a clear draft of -15 m in the NMP channel throughout the year. Since the field data were not available for the mathematical model studies, field studies were carried out by CWPRS for required data collection in respect of tides, currents, bed samples, beach surveys, sediment concentrations during non-monsoon and monsoon seasons during the year 2020.

2   Study Area and Data Source

2.1   New Mangalore Port

New Mangalore Port, an artificial lagoon type of all weather major port, is located on the open coast in the west coast of India, in Karnataka State is shown in Fig. 1. During 1960s, initial efforts were made to develop the existing old Mangalore Port located at the confluence of Rivers Nethravati and Gurupur into a major all weather port. But due to complex nature of salinity mixing process, large fresh water discharges, shallow water, limited space for major port development and large siltation in estuary, it was differed and a site near Panambur, about 10 km north of the river outfall on an open sandy beach, was selected for the development.
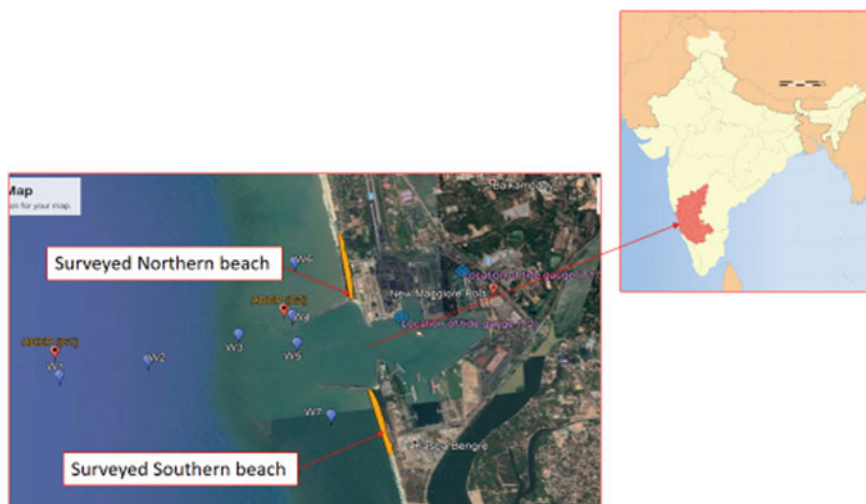
Fig. 1 Location plan of New Mangalore Port

2.2 Survey Schedules, Equipments and Resources

The following data were collected during 18.02.2020 to 25.02.2020 for non-monsoon season; tidal data at two locations, current data at two locations, beach survey to an extent of 1.5 km on north side and 2 km on south side of the port, water sample at seven locations, soil sampling and beach sampling at salient locations as shown in Fig. 1. During 09.09.2020 to 12.09.2020 corresponding to the monsoon season, the following observations were made, beach survey to an extent of 1.5 km on north and 2 km south side of the port, beach sampling at salient locations, water samples were taken at 15 locations in the Gurupur river and at 4 locations at northern and southern beaches as shown in Fig. 1.

Beach survey on Panambur beach (northern beach) was conducted with respect to bench mark in front of main administrative building established in 1964 as + 8.397 datum (12°56′31.11″N, 74°48′43.43″E), and beach survey on Tannirbavi beach (southern beach) was conducted with respect to bench mark M15 (12°54′16.1″N, 74°48′45.7″E) as +4.202 m with respect to chart datum. Beach survey profile lines spaced at an interval of 50 m and 100 m as per topography of the beach.

At NMP, two tide measuring locations were selected; one at Eastern Dock Arm near berth number three (T1) and the second one at western face of berth number 16 (T2), as shown in Fig. 1. The tide data sampling were recorded at every 15 min time interval around the clock from February 18, 2020 to February 25, 2020.

The current observations using Acoustic Doppler Current Profiler (ADCP) were carried out at the following two locations; C1 at the tip of the northern breakwater at a depth of −7 m other, C2 at a depth of −10 m adjacent the approach channel

Fig. 2 Fly leveling of benchmark from NMPT main building to northern beach and eroded profile lines (Blue) in monsoon season

near north breakwater as shown in Fig. 1. Current data sampling were taken at every 15 min round the clock during the period of observation.

2.3 Beach Survey

Prior to the start of the survey, reconnaissance of the site was made. Established benchmarks were shown by the NMPT officials both at the north and south side of the port. Fly leveling was carried out from these locations to the beaches to establish bench marks for the beach surveying works as shown in Figs. 2 and 3.

2.4 Tidal Observation

At NMP, two tide measuring locations were selected; one at Eastern Dock Arm near berth number three (T1) and the second one at western face of berth number 16 (T2), as shown in Fig. 1. The tide data sampling were recorded at every 15 min time interval around the clock from February 18, 2020 to 25, 2020 (Fig. 4).

Fig. 3 Eroded profile lines in monsoon season at Tannirbavi beach (southern beach)
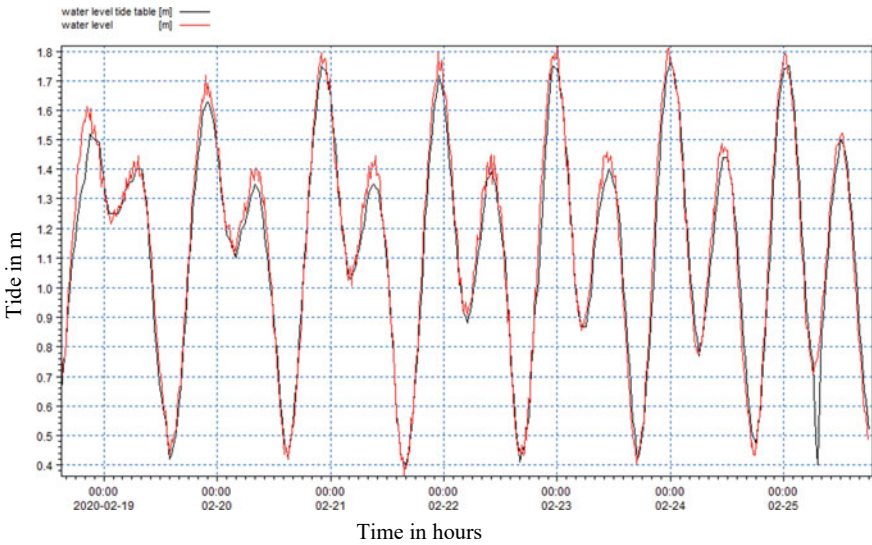

Fig. 4 Comparison of tide at tide gauge No. 20667 (N-12° 56′08.73″ E-74° 49′03.80″) from 18/02/2020 to 25/02/2020

2.5   Current Observations

The current observations using Acoustic Doppler Current Profiler (ADCP) were carried out at the following two locations, C1 at the tip of the northern breakwater at a depth of −7 m other, C2 at a depth of −10 m adjacent to the approach channel
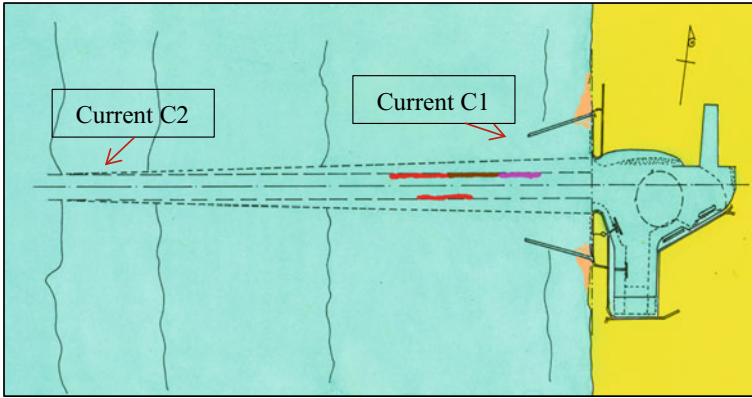
Fig. 5 Location plan of observed currents C1 and C2

near north breakwater (Fig. 5). Current data sampling were taken at every 15 min round the clock during the period of observation.

The current meter observations (at C1 and C2) were taken along the beam light of current meter covering whole depth of water at specified location from the current meter face. But for analysis three depths, 0.2d, 0.6d and 0.8d depths have been considered (Figs. 6 and 7).

Fig. 6 Current speed at ADCP No.1826 (C1) (N-12° 55′44.54″ E-74° 47′53.89″) from 21/02/2020 to 25/02/2020
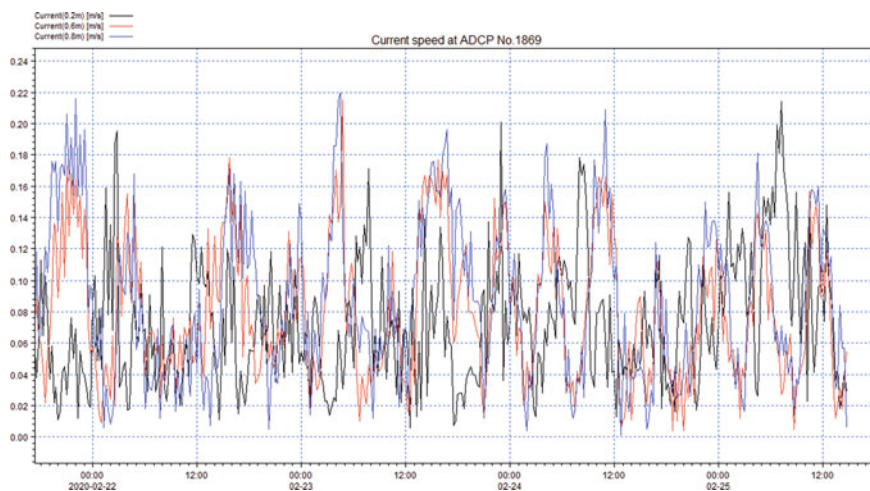
Fig. 7 Current speed at ADCP No.1869 (C2) (N-12° 55′16.29 E-74°18.32″) from 21/02/2020 to 25/02/2020
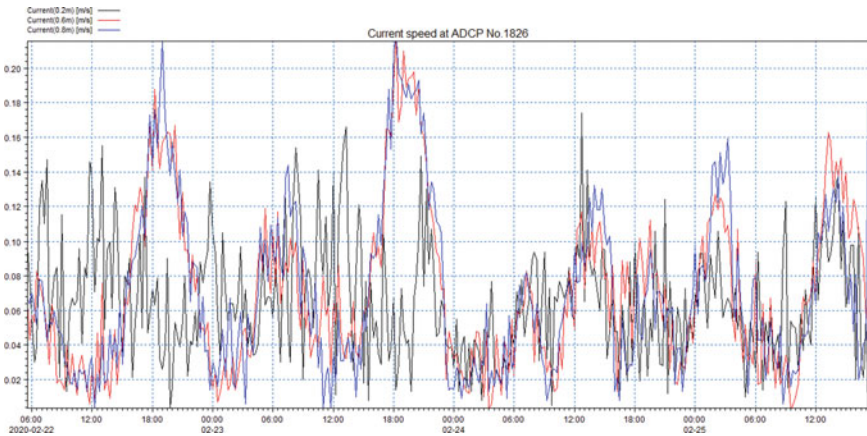

Fig. 8 Comparison of erosion near security post in February 2020 and September 2020

2.6 Water and Bed Sampling

Soil/water samples were collected in mid of flooding, mid of ebbing, low water slag and high water slag at different locations. Total soil samples (11 Nos) and water samples (37 Nos) were collected. Bed samples were analyzed in CWPRS laboratory for grain size distribution (D_{50} size). During non-monsoon season, sediment samples and water samples were collected at salient locations from February 18, 2020 to February 25, 2020. It was observed that sediment samples collected near coast mostly lie in sand fractions (coarse, medium and fine sand) and sediment

samples collected from inside (offshore region) are mainly having silt, and clay fractions up to 80%, were also observed during earlier data collected at NMP. Suspended sediment concentration in non-monsoon season varies from 50 mg/l to 550 mg/l at different locations.

3 Conclusions

The main observations during field data collection are as below:

 (i) The tide data sampling were recorded at every 15 min time interval around the clock from February 18, 2020 to February 25, 2020. The tidal range observed at New Mangalore Port was 1.8 m during the period of data collection, and highest tide was observed on February 23, 2020. At Tide gauge No. T1 (located at Eastern dock arm) tide data well matched with tide table data. At tide gauge No. 2 near the entrance of the harbor (berth No.16) (T2), even though tide is matching well with the tide table, there is a small error, and this error is almost constant over the period of measurement. This error in tide may be attributed to reference datum error taken at the top of the berthing structure. However, this will not affect the tidal range measured, and accordingly, it can be used in mathematical modeling for siltation studies.

 (ii) The current observations using Acoustic Doppler Current Profiler (ADCP) were carried out at the following two locations one, C1 at the tip of the northern breakwater at a depth of − 7 m other C2 at a depth of − 10 m adjacent to the approach channel near north breakwater. Current data sampling were taken at every 15 min round the clock during the period of observation. Minimum observed current was 0.00 m/s, maximum observed current was 0.288 m/s and average current was 0.074 at location C1. At location C2, minimum current was 0.001 m/s, maximum current was 0.238 m/s and average current was 0.08 m/s.

 (iii) During beach survey on northern side beach, it was observed that there is a considerable erosion up to 400 m chainage from the root of northern break water (zero chainage). It was also seen that a nearby water body observed only during monsoon season at 1000 m also joined to the sea in monsoon season. The quantum of erosion was about 0.97 MCM on the Panambur beach (northern beach). On southern side beach, the severe erosion was observed from zero chainage (N-12°55′14.1″, E-74°48′24.6″) to 1375 m chainage. The quantum of erosion was about 1.87 MCM on the Tannirbavi beach (southern beach). It was also observed that this erosion was different at different locations and may vary in other years. In general, erosion was observed both on the north and south side of the port.

 (iv) Collected bed samples were analyzed for grain size distribution (D_{50} size) and percentage composition in CWPRS laboratory. It was observed that sediment samples collected during non-monsoon season near coast mostly lie in sand fractions (coarse, medium and fine sand) and sediment samples collected from

inside (offshore region) are mainly having silt, and clay fractions up to 80% were also observed during earlier data collected at NMP.

(v) Suspended sediment concentration in non-monsoon season varies from 50 to 550 mg/l at different locations. In monsoon season, it was not possible to collect samples from inside area due to heavy weather conditions and warnings from local fishing authorities, however, data have been collected from accessible point in monsoon season. Sediment samples were collected from very near to coast, hence, showing mainly sand fractions (coarse, medium and fine sand). Suspended sediment concentration of water samples collected from Gurupur river varies from 45 to 145 mg/l.

References

1. Jagadeesh HB, Joshi VB, Purandare UV (2003) Long term effects on siltation patterns due to developments at New Mangalore Port, conference on hydraulics and water resources—HYDRO
2. Jagadeesh HB, Joshi VB, Purandare UV (2004) Analysis of formation of hard patches along the approach channel at New Mangalore Port, proceeding of the Indian national conference on harbour and ocean engineering

Comparison of Methods for Determining Sediment Distribution of a Reservoir—A Case Study

Anjana Khamari and Anil Kumar Kar

Abstract Sediment deposition and its distribution along a reservoir bed take a major role in reduction of precious reservoir storage. During recent times, due to growth in urbanization, infrastructure development and mining activities leads to deforestation. Further, the variations in climatic parameters, changes in cultivation style and similar phenomena help in loosening of top soil leading to large-scale sediment generation, which ultimately gets carried into the downstream reservoir. Further, the pattern of deposition depends on number of factors like slope, reservoir length, size of sediment, inflow capacity, sediment load and volume and many other factors. As the reservoir storage space between dead storage to maximum water level has particular significance at individual levels, the distribution of sediment needs to be estimated for individual levels. The methods like area increment method, trigonometric method, elevation of sediment accumulation method and area reduction method are being applied in this study. This study makes a comparison of different processes and methods for estimating sediment distribution over a temporal period taking Hirakud reservoir as a case study. The results signify importance of estimation of distribution pattern and very useful for reservoir managers and planners. This also leads for taking preventive steps for sediment generation and its probable entry into reservoir.

Keywords Sediment distribution · Sediment load · Area reduction method · Sediment-accumulation method · Trigonometric method · Area increment method

1 Introduction

In water resources systems, the dam reservoirs are the most important and economical design. The sedimentation on dam reservoirs is the reduction of volume and other damages. Maximum methods for the predicting of sediment yields are measure

A. Khamari (✉) · A. K. Kar
Civil Engineering Department, VSSUT, Burla, India
e-mail: anjanakhamari357@gmail.com

directly or indirectly based on the results. The direct measurements of yield sediment are measured the most dependable method for the calculation of yield sediment. These are proficient by either surveying of reservoirs or sampling the sediment load of the river. Both methods are defined in following sections of the guidelines. Another method for the prediction of sediment yields depends on measurements to derive empirical relationships and to checked measures. The sediment yield rates the Universal Soil Loss Equation or increment factors [1].

For the determination of sediment yield of the watershed, there are various types of factors used, i.e.,

a. Geologic formation and type of soil
b. Ground cover
c. Land use
d. Topography
e. Upland erosion (nature of drainage network density, slope, shape, size and alignment of channels)
f. Runoff
g. Sediment characteristics—mineralogy and grain size
h. Hydraulic channel characteristics
i. Intensity and rainfall amount.

In this study four types of methods i.e., elevation of sediment accumulation method, area increment method, trigonometric method and area reduction method are used. From these four methods, the most useable and less error method is area reduction method, because it is an experimental method to measure the sediment in a reservoir. For these methods to use many software and optimize the data, Thomas [2], to estimate the sedimentation to provide the list value of data and in short time period the value can be find out. Vemu and Pinnamaneni [3], to estimate the sediment loss of a watershed area by using remote sensing and GIS. Estigoni and Mauad [4], to present the two different modeling techniques to estimate the assess sedimentation single beam bathymetric data and a case study of Peruvian reservoir. In the both methods to put same data in traditional method and insertion pf mesh points (IMP). By diffracting both the above two methods in IMP case provides the lower sedimentation. Fendreski and Abdeveis [5], to describe that both the methods between have little difference to estimate the sedimentation. Gharaghezlou et al. [6], to put the exact data in the area reduction method and the results are less error. Jahangrzadeh [7], to estimate in loss of needed capacity of reservoir. If the storage capacity is provided sufficient, then the design of the storage capacity is more economical. Torabi and Yonesi [8], to estimate the sediment distribution in the dam, i.e., Ekbatan reservoir by using area reduction method and to optimize the parameters with algorithms to reduce the sediment error. Tukaram et al. [9], to conclude that the storage capacity of the reservoir generally increased by the sedimentation day by day. Jaiswal et al. [10], the estimation of reservoir sediment and its profiles is most important to design the Water Resources Engineering. The operation and modification of the reservoir data can be generated. Sadeghian and Daneshkah [11], to estimate the area increment method has 12 m and 15 m error is in Latian Dam and Amirkabir Dam, respectively.

In this method, the data cannot found accurately. Foteh and Garg [12], this study to describe the deposition of sedimentation by through remote sensing. Mahadik et al. [13], to analyze the area reduction accurately. Ion methods for calculation the sedimentation on a reservoir were for the years 2019 to 2026, i.e., 50% of the volume of NraDevghar dam will be full by silt in 2026. Salinas [14], here to design before and after the dam construction the previous 10 years data can be recorded. Talukdar [15], to optimize the sedimentation data and design the reservoir.

Rathore et al. [16] have done the study on Hirakud using remote sensing for the year 1999–2001. They found the loss in total storage is around 984Mcum (16.9% of live storage).

Tobgay [17] found Hirakud dam reservoir capacity at full reservoir level was found that 5768.63 MCM during year 2012, related to 8136 MCM at time, when it first performed. In between 55 years, the total decrease is 2368 MCM.

2 Study Area

Hirakud reservoir is having a hues potential water reserve for meeting the various demand of Odisha state. Number of reservoirs constructed on Chhattisgarh at upstream of Hirakud dam restrict the entry of flow to the reservoir. Thus, the available water during monsoon is becoming facetious for its utility during non-monsoon periods. Further, the larger anthropogenic activities at upstream generally lot of sediments which is gently stored at Hirakud reservoir, thus reducing the live storage capacity. Hirakud dam is a one of the most important and world longest earthen dams. It is situated in Sambalpur district of the state Odisha in India on the Mahanadi River. The dam construction started at 1947 and ended 1957. It is a composite dam and reservoir. It is situated 16.6 km from Sambalpur district, Odisha. The main dam length is 4.8 km and entire earthen dam length is 25.8 km. There are 64 sluice gates and 34 crest gates. The capacity of spillway is 42,450 m^3/s. The total capacity of the reservoir 5,896 million cubic meters and the catchment area is 83,400 km^2. It is a composite structure of concrete, masonry and earth dam. The Hirakud Dam reservoir built across the Mahanadi River. It located at Sambalpur district in Odisha (India). The Hirakud dam is the longest earthen dam in the world. The total dam length is 25.79 km and the length of main dam is 4.8 km. Crop and irrigated area is 2355 km^2. F.R.L/M.W.L is RL 192.024 m and the catchment area is 83,400 km^2. It is a composite structure used concrete, earth and masonry. The upper drainage Hirakud dam basin of the Mahanadi River is centered on the state Chhattisgarh (Fig. 1).
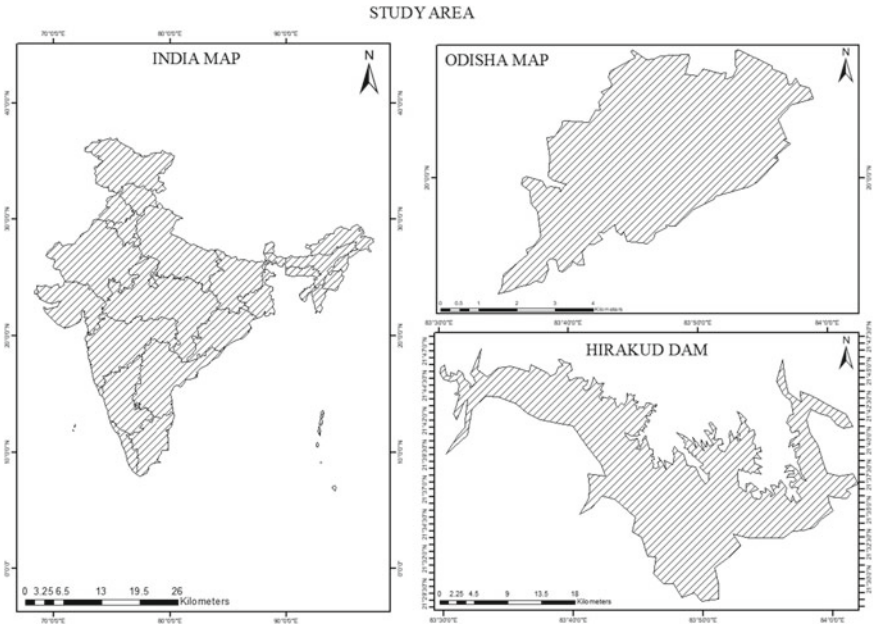
Fig. 1 Location map of Hirakud catchment

3 Methodology

There are four types of methods about the sedimentation, i.e.,

I. Area increment method
II. Area reduction method
III. Elevation of sediment accumulation method
IV. Trigonometric method.

3.1 Area Increment Method

The principle of sedimentation forecasting deposit in the reservoirs by area increment method is based upon the calculation of reduction of area in each height as a result of exact quantity of accumulation of sedimentation. To determine the distribution in Hirakud dam reservoir under the area increment method, the used formula is:

$$V_s = A_0 * (H - h_0) + V_0 \tag{1}$$

where

V_s Volume of sediment deposited in the reservoir (ha.m).

A_0 Area correction factor (ha), (It is equal to the original reservoir area at new zero elevation).

H Reservoir depth near Hirakud dam in meter, i. e., measured from the stream bed to the full reservoir level (FRL).

h_0 Sedimentation depth in meter.

V_0 Volume of sediment deposited below new zero elevation (ha.m).

3.2   Area Reduction Method

In case of dam reservoirs, the sedimentation is one of critical phenomena which leads to the reduction of useful volume. Area reduction method was developed based on the analysis of distribution of sediment data formed by several data.

$$A_p = C_p^m (1 - P)^n \tag{2}$$

where

A_p Dimensionless relative area at the distance 'P' above the stream bed.

C_p, m and n Dimensionless constant.

     Area reduction method is more suitable for area increment method.

     In case of time scales, the sediment level changes may imitate the variety of procedures. Vertical sediment accumulation occurs increasing the thickness of sediment form and produced by the addition of the material on the upper surface. In the primary flux of elements, the accumulation can be separated for the first time. We study the different types of reservoir and basic things about the distribution of sediment accumulation takes place immediately at upstream side of the dam, then the equation should be:

$$Y = 22.6 + 0.886 * D - 81.2 * b - 0.175 * C + 0.494 * W \tag{3}$$

where

Y   Original depth filled with sediment (%)

D   Depletion in original stage at the end of design period (%)

B   Slope of curve drawn between depth and capacity of the reservoir on log-log paper

C   Storage capacity remained at the end of design period (acre-ft.)

W   Specific weight of the sediment (fb/ft^3)

4   Trigonometric Method

It is a method of rewrite a subjective sum of cosines and sines as a single instance of cosine or sine. The basic trigonometric function is easy to work with multiple functions. It is a graphical method for calculation of the sediment distribution. In a small capacity i.e 300 MCM reservoir consider and the original capacity curve and final capacity curve compare.

Universal Soil Loss Equation (USLE):

By using USLE, calculate the loss of soil over the years. In this equation, calculate average annual soil loss.

Average annual soil loss,

$$A = R * K * L * S * C * P \tag{4}$$

where

A Average annual soil loss in tons per acre.
R Rainfall-runoff factor (MJ/ha.mm/h) (The greater the intensity and duration of the rain storm, the higher the erosion potential).
K Soil erodibility factor (t.ha.h/ha/MJ/mm).
L Slope length factor.
S Slope degree factor.
P Factor for supporting conservation practices.
C Cover factor.

Rainfall-Runoff Factor (*K*):

It is determined from rainfall intensity. But maximum time to collect the daily rainfall intensity is very difficult. So, for the calculation of R by using mean annual rainfall data, the equation is:

$$R = 0.5 * P \tag{5}$$

where

R Rainfall-runoff factor (MJ/ha.mm/h).
P Mean annual rainfall (mm).

By using inverse distance method, calculate the rainfall-runoff factor effective weighted and very fast, average interpolation method in LLWIS. To derive the spatial distribution by using this factor of rainfall-runoff in Hirakud dam reservoir.

Soil Erodibility Factor (*K*):

Soil erodibility factor represents susceptibility of the soil to the rate of runoff and erosion. Here, soil map cannot represent accurately in the large scale. So, for preparation of soil erodibility factor by using 1:2 million scale.

Slope Length Factor (*L*):

$$L = (\lambda/22.1)^m$$

where,

L Slope length factor.
λ Slope field length (m).
m Slope steepness (dimensionless parameter).

Slope Steepness Factor (S):
By using different methods or equation to calculate the values of S.
Cover Factor (C):
By using Landsat images to derive the cover factor.
Conservation Practices Factor (P):
In the Hirakud dam, very small area has conservation practices.
Sediment Yield Estimation:
Annual sediment yield of a watershed is defined as ratio of sediment delivered at given area.

$$SY = A * SDR \tag{6}$$

where

SY   Annual sediment yield.
A Total gross area.
SDR   Sediment delivered ratio.

It is calculated on 20 years average rainfall erosivity factor and other parameters.

5   Results and Discussion

After analyzing the data, the result can be obtained and discussed in this section. The average annual rainfall-runoff factors value varies. The soil erodibility factors were less than 1. In case of the combined spatial distribution, slope length gradient factor is calculated by using DEM at Hirakud dam. But in water resources systems, the dam sedimentation reservoirs are the most destructive phenomena. It leads to the reduction of sedimentation on reservoir. Most common experimental method is area reduction method. In area reduction method, various types of parameters can be calculated. Empirical area reduction method is based on principle on distribution. Sediment in a reservoir at the different levels depends on the shape of the catchment area. In reservoir sediments, particles are gravel, silt, sad, etc. In a river, water flowing through upstream to downstream. The sediment particles carry flow through the downstream level. Due to obstruction, the velocity of water decreases then the sediment particle settles down in the reservoir, i.e., called sediment reservoir.

6 Conclusion

1. As the reservoir is the life line of the state Odisha, the live storage estimation at least should be made annually.
2. The remote sensing-based techniques are highly recommendable as it considers the land use land cover changes more usefully.
3. The physical measurement of sediments inflow is to be continued as a regular practice.
4. The live storage reduction as established from different studies is to be considered as a caution for stake holders and planner at Hirakud dam reservoir.
5. Ample step may be taken for catchment treatment in order to decrease the deposition of sediment.

References

1. Wischmeier WH, Smith DD (1965) Predicting rainfall erosion losses from cropland east of the rocky mountains. Agricultural handbook 282, U.S. Agriculture research service, 1965
2. Thomas S (2004) Review of method to measure short time scale sediment accumulation. J Marine Geol 114
3. Vemu S, Pinnamaneni B (2012) Sediment yield estimation and prioritization of watershed using remote sensing and GIS. Int Arch Photogrammetry, Remote Sens Spat Inf Sci XXXIX-B8
4. Estigoni MV, Mauad FF (2014) Comparison of method to assess reservoir volume and sedimentation based on bathymetric surveys. J IAHR Eur Congr
5. Fendreski N, Abdeveis S (2014) Investigation and Calibration of area-reduction and area-increment empirical methods in sediment distribution type of maroon reservoir dam in Khuzestan, Iran. J URL (3)
6. Gharaghezlou M, Masoudian M, Fendereski R (2014) Calibration the experimental area reduction method in assessing the distribution of sediment in Droodzan reservior dam in Iran. J Civil Eng Urbanism
7. Jahangrzadeh A (2014) Reservoir sedimentation based on uncertainty analysis J Eng Hydrol
8. Torabi S, Yonesi H (2015) Calibration the area—reduction method in sediment distribution of Ekbatan reservoir dam using genetic algorithm's. J Springer Int Publishing Switz 7
9. Tukaram S, PT N, MR G (2016) Comparison of area reduction method and area increment method for reservoir sedimentation distribution-case study of Ujjani dam. Int J Res Adv Eng Technol 2:108–111
10. Jaiswal RK, Nayal TR, Jain SK, Lohani AK (2017) Application of RS data for reservoir sediment profiling using Latin hypercube one at time (LH-OAT) technique. Int J Adv Agric Sci Technol 4:10–17
11. Sadeghian M, Daneshkah I (2017) A comparison between the amount of reservior sediment load prediction during design period and the operational period. Int J Ground Sediment Water 6
12. Foteh R, Garg V (2018) Reservoir sedimentation assessment through remote sensing and hydrological modelling. J Indian Soc Remote Sens 46
13. Mahadik PP, Nimbalkar PT, Jadhav RH (2019) Distribution of sediment in the reservoir by area reduction method. J Int Eng Adv Technol 8
14. Salinas E (2021) Understanding sedimentation at the El Molinito reservoir (NW Mexico) before and after dam construction using physical sediment analyses. J South Am Earth Sci 111

15. Talukdar G (2021) Sediment analysis and modelling based approach for optimal allocation of riverine sandbar for socio economic benefits. J Ecol Eng 173
16. Rathore DS, Anju C, Agarwal PK (2006) Assessment of sedimentation in Hirakud reservoir using digital remote sensing technique. J Indian Soc Remote Sens 34(4):377–383
17. Tobgay S (2014) Temporal analysis of area-capacity curve of Hirakud reservoir, M. Tech Thesis, NIT, Rourkela
18. Iqabal J, Shah M (2015) Distribution, source identification and risk assessment of selected metals in sediments from freshwater lake. J Sediment Res 241
19. Kavehk K, Hosseini K (2015) New proposed method for prediction of reservoir sedimentation distribution. J Int Sediment Res 235

Impact of Sand Mining on River Channel and Its Inundation Pattern

Vaibhav Garg and Rahul M. Kapurkar

Abstract In the present study, the effects of sand mining on river channel geometry, its hydraulics, and the inundation pattern in the surrounding of the channel have been studied. A sand mining dominant stretch of the Krishna River has been selected for the study. For the analysis, the hydrological modeling technique has been adopted. The Hydrologic Engineering Center (HEC)-Hydrologic Modeling System (HMS) and River Analysis System (RAS) tools were used for estimating discharge, channel hydraulics, and inundation pattern analysis. However, Cartosat 30 m digital elevation model has been used for topographic parameters. Land use land cover (LULC) data has been procured from the Indian Space Research Organization (ISRO) and Geosphere-Biosphere Program (GBP) LULC project. The discharge data for calibration and validation of the model was taken from India Water Resources Information System Portal. The discharge data has been analyzed for the highest peak flood observed. It was found that in the selected region, the highest flood has come in the year 2006. The channel bank line, center line, and cross section were delineated using geospatial tools. A slight change in the inundation pattern for designated high discharge has been observed. However, it was concluded that if an event with more discharge occurs in the region, the inundation pattern may change. The average discharge of the after mining scenario was 2559.48 cm which was slightly more than the before mining scenario discharge of 2553.95 cm. It was also found that velocity in the channel has increased. The average velocity of the before mining scenario was 1.41 m/s and after the mining scenario was 1.66 m/s. This might have been attributed

V. Garg (✉)
Water Resources Department, Indian Institute of Remote Sensing, 4, Kalidas Road, Dehradun, Uttarakhand 248 001, India
e-mail: vaibhav@iirs.gov.in

R. M. Kapurkar
Department of Geography, Savitribai Phule Pune University, Pune, Maharashtra 411007, India

due to the contraction or reaming of banks by the quarry or other remaining. High discharge with increased velocity may result in cutting of river banks, more siltation, and floods in surroundings.

1 Introduction

Each river and tributary has its individual unique set of hydrologic, geologic, anthropogenic, and climatic physical characteristics. Further, they have associated specific environmental impacts. River sand is widely used in the construction industry, and its mining is a major issue in developing countries [1]. Day-by-day requirements of sand for the construction and development sector are increasing. The river channels get modified into different forms according to the change in flow and deposition of sediments attributing to river sand mining. It also disturbs the sediment-supply-transport balance of the rivers, aggravating the widespread instability in the river flow system [2–4].

In India, monitoring dig-out sand does not have strong rules or guidelines. At present, the river sand is considered as the material with a low value which is available in abundance. With India's development, there is a remarkable requirement of sand to build skyscrapers, factories, building apartments, residences, schools and colleges, commercial offices, and basic transportation such as roads, national highways, state highways, air runways, and vehicles parking buildings.

The mining of sand and gravel from the river and stream terraces, channels and floodplains, frequently interests' attention because in some situations extraction of sand and gravel may conflict with other resources such as esthetic, fisheries, and leisure tasks, or with the essentials of stable river channels [5]. It is acceptable to mine sand and gravel from sources situated in the river or river channels within suitable environment-friendly limits provided that appropriate precautions are applied. However, the proper safeguards and practices are generally not followed.

River sand mining impacts on stream's physical characteristics, such as channel geometry, in-stream roughness of the bed, bed elevation, discharge capacity, flow velocity, and the capacity of sediment transportation [6–8]. Sand mining is now a regular practice and is the current problem for river characteristics and maintenance of natural flow. Due to river sand mining, river bank lines are being modified at greater extent. After in-stream sand mining, usable sand gets transported to the sites but not so useful sand-like pebbles, boulders, gravel, pea gravel, small stone, or larger size sand is left at the bankside and bank line edges. At some places, the sand quarry forms huge sand piles. The size of sand piles is approximately 30–40 m wide and 6–8 m high. The width and height of sand piles vary from place to place. These sand piles decrease the river width as the number of sand piles is inside the bank line. This activity is not at all ignorable; the disturbed or modified width affects the flow of

the river. The riverside sand piles are also barriers to water in the flood time period. These left-back unusable sand piles can change the flood inundation pattern along the river channel. The flooded river may be very destructive for the riverside villages, cities, crops, bridges, etc. There is an urgent need for a scientific approach to monitor these changes in the river channel and analyze their impact on river characteristics and flood inundation patterns.

A very few studies, particularly in India, have been carried out to study the impact of sand mining on river hydraulics and inundation pattern. Earth observation satellites provide synoptic coverage of the earth's surface at regular intervals. Using the temporal remote sensing data, the changes in river width and location of sand piles along the river channel may easily be identified. Further, through a suitable hydrological-hydrodynamic modeling approach, incorporating these geospatial inputs, the impact of river sand mining on channel hydraulics may be attempted [9]. With this aim, the impact of sand mining on the hydraulics of the Krishna River stretch (Karad to Arjunwad) was studied using the most widely used Hydrologic Engineering Center (HEC)-Hydrologic Modeling System (HMS) and River Analysis System (RAS) models.

2 Study Area and Data Source

2.1 Krishna River Basin

The Krishna River, Godavari River, Tapi River, and the West flowing rivers of Western *Ghats* are the major river basins/system of the Maharashtra state of India, whereas the Krishna Basin covers an area of about 2,58,948 km^2 which is around 8% of the total geographical area of the country. This large basin lies in the states of Maharashtra (69,425 km^2), Karnataka (113,271 km^2), and Andhra Pradesh, Telangana (76,252 km^2). The Krishna River originates in the Western *Ghats*, at an elevation of about 1340 m in the north of Mahabaleshwar. It flows for about 1400 km and outfalls the Bay of Bengal. The principal tributaries joining Krishna are Koyna, Ghataprabha, Warna, Malaprabha, Bhima, Tungabhadra, and Musi. Approximately 127 km of sand mining-affected Krishna River stretch from Karad gauging station (Satara District) to Arjunwad gauging station (Kolhapur District) was selected for this present study, as shown in Fig. 1. It covers a 12,753 km^2 area which is spread over Satara, Sangli, and Kolhapur districts of Maharashtra state. It lies between 73° 33′ 11″ E to 74° 50′ 17.62″ E longitudes and 16° 40′ 57.82″ N to 18° 2′ 58.15″N latitudes. The basin is bounded by the Western *Ghats* (Sahyadri Range) in the west, the Deccan Plateau to the north, south, and east.
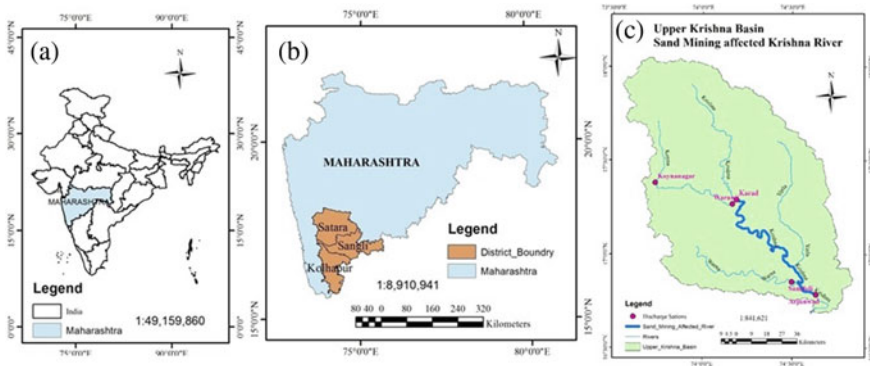
Fig. 1 Location of the study area: the sand mining-affected stretch of Krishna River

2.2 Climate

Maharashtra state receives precipitation from both the northeast and southwest monsoon. The state has very highly variable precipitation ranging from 6200 mm in upper catchments to 400 mm in shadow areas of lower catchments. The Upper Krishna Basin is in a semi-arid environment. The annual average of precipitation in the Upper Krishna Basin is 1300 mm. Maximum precipitation mostly occurs in 4 months between June and September with the sum of rainy days varying between 40 and 100 days. For example, Satara, Sangli, and Kolhapur districts in the Upper Krishna Basin have experienced floods numerous times throughout the recent decade. In the Upper Krishna Basin, there is a great variation in terms of temperature and rainfall. Sub-tropical monsoon type of climate is seen in most parts of the sub-basin. The heaviest rainfall with the most humid climate was also recorded in the basin. In the part of the Western *Ghats*, the Upper Krishna Basin receives heavy rainfall, but, on eastern part, it has very low rainfall. The drought condition also prevails mostly in Upper Krishna Basin during the summers. The annual precipitation of the Upper Krishna Sub-Basin differs between 400 and 6200 mm [10]. The high precipitation occurs in Mahabaleshwar and Patan tehsil of Satara district and Shahuwadi tehsil in Kolhapur district, and the least precipitation occurs in Koregaon and Khatav (Vaduj) tehsil of Satara district and Vita and Tasgaon tehsil of Sangli district. In this study area basin, the minimum temperature observed was 6 °C and maximum temperature was 43 °C, and the annual average temperature is 28 °C. The temperature of the area comprises in sub-basin varies between 14 °C in the winter and 38 °C in the summer.
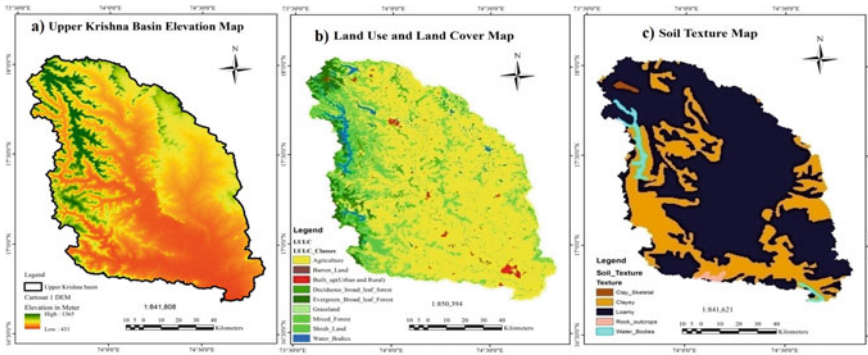
Fig. 2 **a** Elevation map, **b** LULC map, **c** soil texture map of the study area

2.3 Topography

The Western *Ghats*, altitude range from 600 to 2100 m, make western edge of the Krishna River Basin. About 50–60 km away from the *Ghats* in the east, there are undulating plains of the Deccan. These hill ranges run from north to south separating Deccan Plateau and the Arabian Sea through narrow coastal plain, named as Konkan. The Upper Krishna Basin is entirely covered by Deccan trap lava flows. Mostly the central part, elevation range between 450 and 1400 m, of the Upper Krishna Basin falls in the plateau. The general slope of the basin tends eastward. The average height of this section of the *Ghats* is 1200 m above mean sea level, but some peaks attain more heights like Mahabaleshwar (1438 m). The Cartosat digital elevation model (CartoDEM) available at 1 arc sec, approximately 30 m (http://bhuvan.nrsc.gov.in/data/download/) of the selected region, is shown in Fig. 2a. The elevation varies from 431 to 1365 m in the selected sub-basin of the Krishna River.

2.4 Land Use and Land Cover

In the Upper Krishna Basin, the maximum area is under agriculture. The western part of the basin finds huge natural vegetation cover. In the vegetation types, there is an evergreen, deciduous, and mixed type of forest. In agriculture practices, sugarcane is taken throughout the year, rice in monsoon, and wheat in the winter season. In the present study, the land use land cover (LULC) of the year 2005 generated under the Indian Space Research Organization (ISRO) Geosphere-Biosphere Program project entitled "Land use/Land cover Dynamics and Impacts of Human Dimension in Indian River Basins" at 1: 2, 50,000 scale was used. In the given land use and land cover map (Fig. 2b), the major part of the Upper Krishna Basin (70.55%) is covered with the agricultural area. Nearly about 12.35% of the basin area is covered by forest, wasteland covers around 7.56% of the total basin area, approximately 4.50% of

the basin area is covered by water bodies, and nearly about 1.2% is covered by the settlement. The same LULC map has been used for extracting the Manning's n values for the HEC-GeoRAS model setup.

2.5 *Soil*

The soil properties are also considered essential in hydrological simulation of the basin. In the Krishna River Basin mainly the red soils, black soils (regur), lateritic and laterite soil, alluvium, mixed soil (black and red, yellow and red), and saline soils and alkaline soils are found. It is reported that the typical lateritic soils are generally found in Kolhapur and Satara districts, which extends down the *Ghats* in Konkan region. The soils are poor in organic matter; frequently covered with forests or plantations. In the Kolhapur district, the cashew nut orchards develop well in this type of soil. The main soil classification is based on soil texture, soil erosion, soil slope, and soil productivity, respectively. Soil texture plays a vital role in determining crops and productivity cropping systems. It has also a great influence on the structure of the soil, density, infiltration rate, porosity, and hydraulic conductivity. The soil map provided by the National Bureau of Soil Survey and Land Utilization Planning (NBSSLUP) at scale 1:2, 50,000 was used, in the present study. The soil texture map (Fig. 2c) shows the distribution of soil texture in the basin. Most areas of the basin have a loamy texture of soil. Based on texture, the major part falls under the loamy texture category (70.70%) with clayey texture (27.01%). The rock outcrops and water bodies accounting for the minimum of (1.99%) and clay skeletal texture (0.30%) are also found in some areas of the basin.

2.6 *Discharge Data*

The discharge data available at India WRIS for Karad, Shamdoli, and Arjunwad gauging stations is used in this study. The high discharge data from June 30, 2006, to August 30, 2006, period is used for model calibration and validation with the model output results.

3   Methodology

In the present study, 1-D HEC-RAS hydrodynamic model was set up for sand mining-affected Krishna River from Karad to Arjunwad. In HEC-RAS hydrodynamic modeling, stream centerline, banks, the flow path centerline, the cross-section cut lines, and polygon layer of land use land cover to estimate Manning's value are required. The generation of these parameters is described in the subsequent sections.

Firstly, flow path of the river and its banks were delineated on the Google Earth from upstream toward the downstream direction. After assigning the river reach name, the remaining attributes of the river feature class were populated by stream centerline attributes option. It created a 3D stream centerline layer from the 2D layer using elevations from DEM. The bank lines were delineated for the time period before the sand mining initiation. Further, for the after mining condition, it has been modified at the locations of the sand piles or mining.

Cross sections are created as shown in Fig. 3 with the help of the editor toolbox in HEC-RAS. Each cross section should be drawn from the left overbank to the right overbank. The cross section should be delineated from upstream toward downstream. Cross sections must cross the main channel only once, and two cross sections may not intersect each other. It should be perpendicular to the flow path line. After creating the cross sections, the geometric attributes to each cross-section were assigned. Along with it, the river/reach name, river station, bank station, and downstream reach length information were added automatically to each of the cross-section cut line. To complete the cross-sectional data, station elevation information needs to be extracted from the DEM. This elevation data created a 3D cross-sectional surface line layer from the cross-sectional cut line.

Land use and land cover data was used to extract the Manning's n values for each cross-section (XS) cut line. Manning's n value option of the RAS menu helped to determine the horizontal variation in Manning's n values along each cross section. It represents the resistance of surface flow used by the land surface and taken from LULC shown in Table 1. After verifying, all hydro-preprocessing layers and tables are exported. Exported RAS data is used for next processing in HEC-RAS.

At the upstream boundary condition, input flow hydrograph of Karad gauging station discharge data and at the confluence of Warna river input lateral inflow hydrograph of Shamdoli gauging station discharge data were provided for the period of June 30–August 30, 2006. The model was run in unsteady flow mode. With the help of these conditions, the model provided the simulated discharge at downstream Arjunwad gauging station. In this selected discharge period, the highest flood peak event occurred, i.e., on July 30, 2006. Then the model was calibrated and validated against the observed discharge data at the Arjunwad gauging station. After successful hydraulic computation, the data was exported in GIS for RAS mapping. As the model results in different hydraulic characteristics of the river, the change in velocity, discharge, stress, and stream power were analyzed for both pre-and post-sand mining scenarios. Along with this, the spatial pattern change in flood inundation in-and-around the river channel was also analyzed. In post-processing, four flood inundation profiles were created for different flood events of July 05, July 15, July 30, and August 15, 2006, for both before and after sand mining conditions.
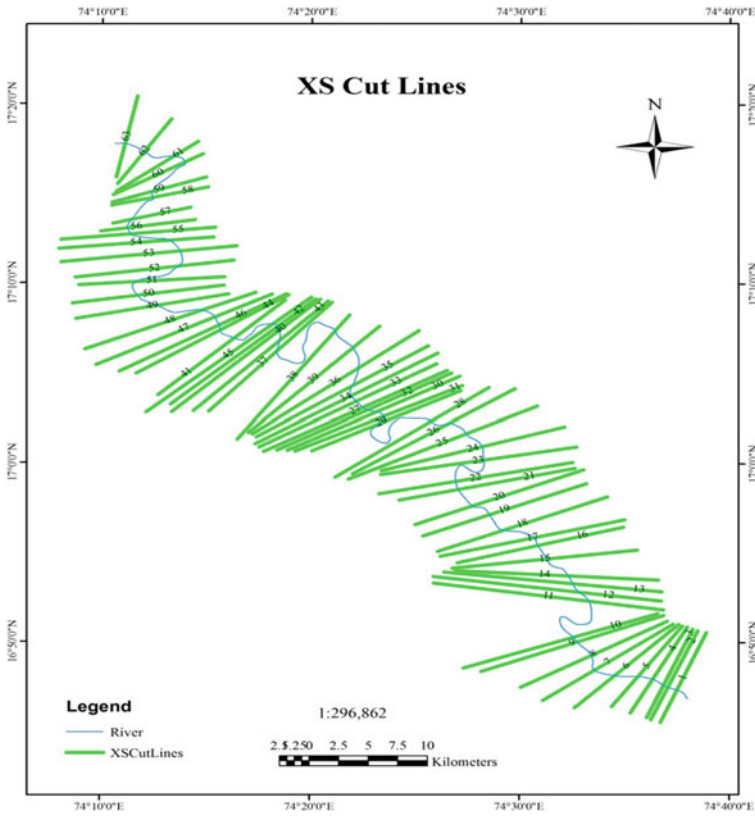
Fig. 3 Cross-section XS cut lines map

Table 1 Manning's *n* value corresponds to each LULC Class (based on Chow et al. [11])

LULC class	*n* value
Waterbodies	0.030
Evergreen broad leaf forest	0.125
Deciduous broad leaf forest	0.100
Mixed forest	0.070
Shrub land	0.060
Grassland	0.030
Agriculture	0.045
Built-up (Urban and rural)	0.200
Barren land	0.035

4 Results and Discussion

With the development and boom in the construction industry, the requirement for sand is huge. It forced to excessive mining of sand from the river. It has been seen that river reaches of the Upper Krishna River under consideration are impacted due to local sand mining as shown in Fig. 4. There is a need to study the impact of these changes.

To investigate the impacts of sand mining on flood inundation, a flood event of 50-year return period was considered. Flood event on dated July 30, 2006, is the highest flood event recorded in Karad gauging station of Upper Krishna Basin. As per the objective of the study, the Upper Krishna Basin was delineated from CartoDEM with the help of the HEC-GeoHMS model. After basin delineation, the hydrodynamic model was set up for the Upper Krishna Basin for flood inundation mapping using the most widely used HEC-RAS. For the HEC-RAS model, inputs of hydro-preprocessing layers are created with the help of HEC-GeoRAS as described in the methodology section. The period from June 30, 2006, to August 30, 2006, was used to simulate the model in unsteady conditions. The simulated discharge at the downstream station "Arjunwad" was compared with the observed data of the said period, as shown in Fig. 5. A high value of the coefficient of determination, 0.93, was estimated between simulated and observed discharge.

Later, the well-calibrated HEC-RAS model was used to study the impact of sand mining on river hydraulics. For this analysis, two scenarios were created, i.e., before mining and after mining. Due to sand mining, the cross-section, depth, or channel geometry has changed. This change in channel geometry may change inundation patterns in the surrounding/hydraulics of the river channel. The results with respect to inundation patterns and changes in the hydraulics of the channel are discussed in the subsequent sections.

4.1 Change in Flood Inundation Pattern

Initially, the investigation of the impact of sand mining on flood inundation was carried out for both scenarios (before and after mining). From the whole simulation period, July 5, 2006, July 15, 2006, July 30, 2006, and August 18, 2006, flood profile was created for both scenarios as shown in Fig. 6. It is to be noted that for different scenarios (pre-and post-mining), the discharge or the initial boundary conditions were kept constant. The flood inundation map before and after mining conditions shown very marginal change as shown in Fig. 6. It is also shown that the slight changes in after mining flood conditions are mainly at the river meandering.
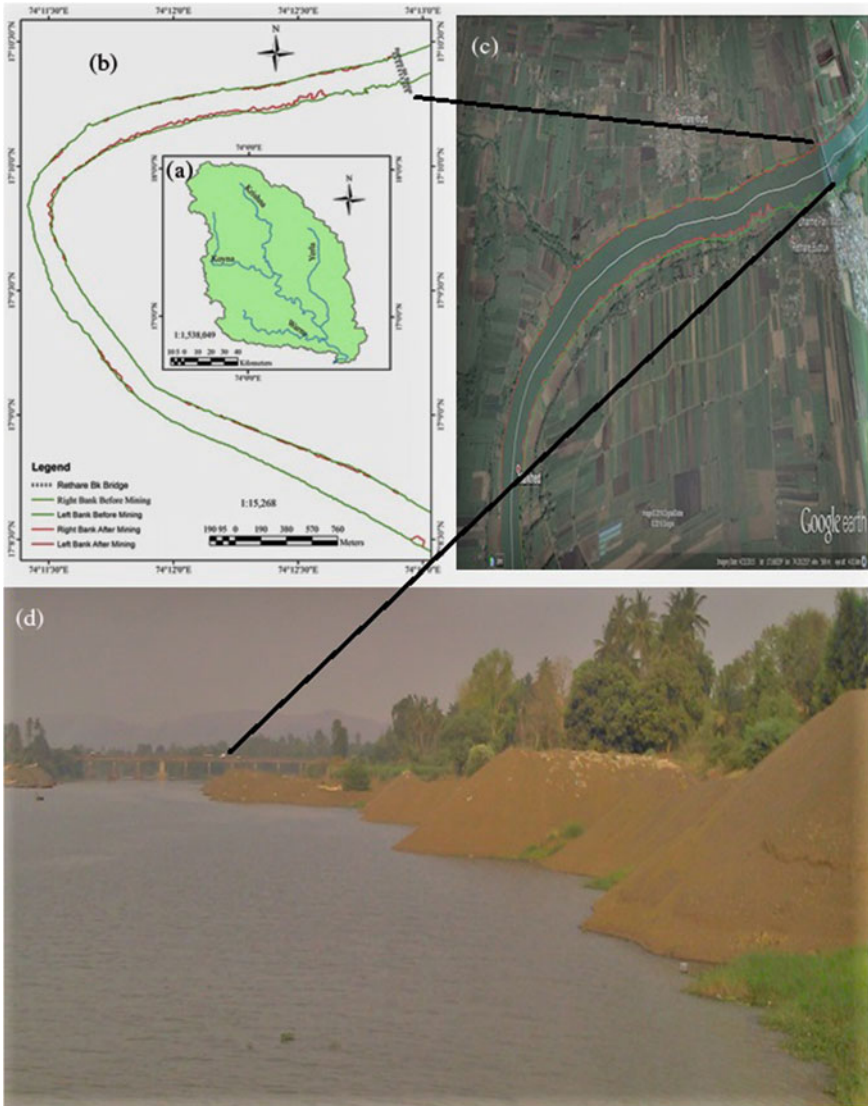
Fig. 4 **a** Selected upper Krishna Basin, **b** sand mining-affected bank line view, **c** sand mining-affected bank line view on Google Earth—(Red—after mining and Green—before mining), **d** field photo (Near Rethare Bk Bridge, Karad Tehsil)

4.2   *Change in Hydraulics of River Channel*

The estimated velocity at different cross sections is shown in Fig. 7. The velocity of flow seems to be increased after mining as compared to before mining conditions.
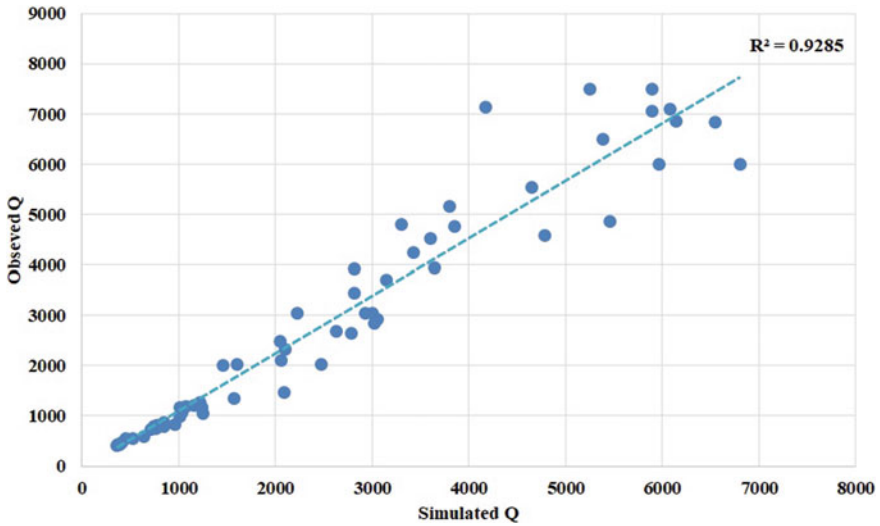
Fig. 5 Comparison of simulated and observed discharge (Q), in cumec, at Arjunwad station

This may be attributed due to the contraction of channel width. Increased velocity of water is not only harmful to carrying silt which sometimes leads to reservoir sedimentation but also causes severe soil/bank erosion. The increased velocity of the river cuts the river bank curves. In the future channel, geometry may change due to these changes. Further, the useful land may lose due to cutting or erosion. Increased velocity may affect steam power and shear stress. In the future, the formation of oxbow lakes at high curve meander is also possible.

As mentioned earlier, the model has been run in unsteady flow with constant initial boundary conditions (flood hydrograph) at Karad Station for both scenarios. The comparison of simulated discharge under both before and after mining conditions is shown in Fig. 8. A very slight change in discharge was observed, and the maximum change was observed for the highest peak of the July 30, 2006, flood event.

Any liquid moving along a solid boundary will incur a shear stress on that boundary. High shear stress of flow is destructive to river boundary. The following graph (Fig. 9) shows the shear stress of river flow. It shows that the shear stress is increased after the mining took place.

5 Conclusions

Hydrological and hydraulic processes of the Upper Krishna Basin part are investigated using HEC-HMS and HEC-RAS models. Simulated discharge was validated for a period from June 30, 2006, to August 30, 2006, against the observed. Discharge simulated at Arjunwad by the HEC-RAS model shows a slight increase after mining.
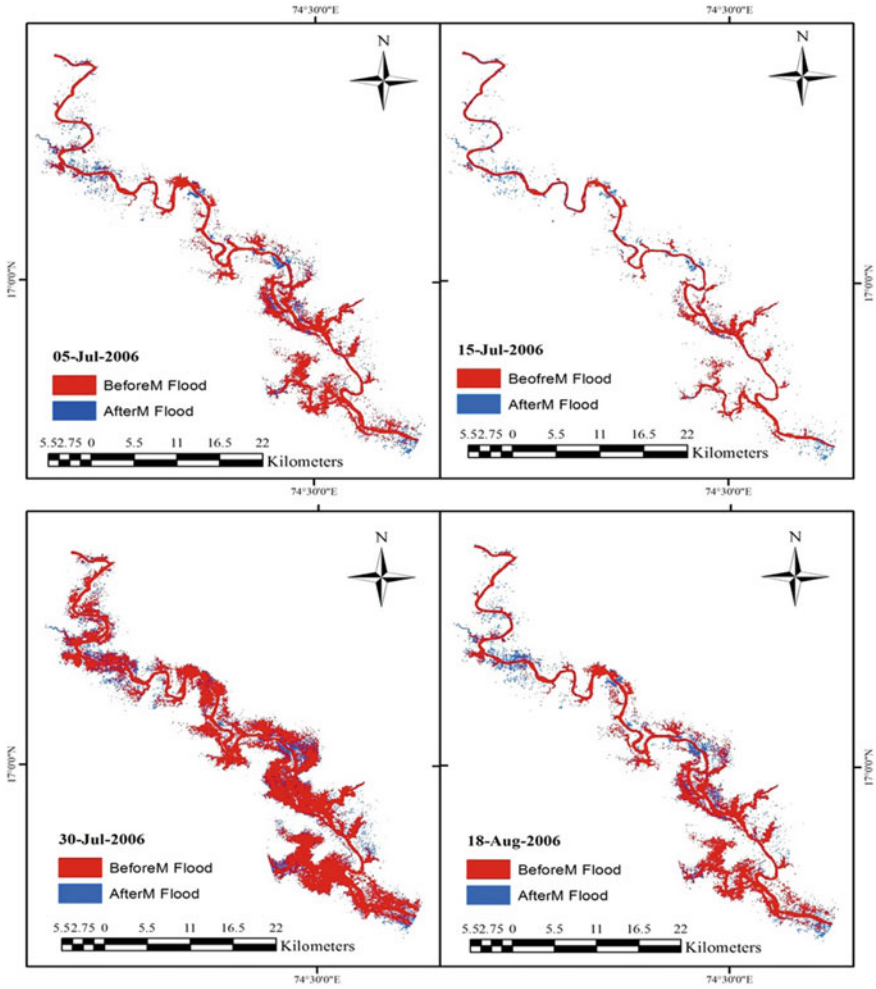
Fig. 6 Flood inundation maps (before versus after mining)

In the after mining scenario, the major change in discharge was found at the highest peak as compared to before mining. In case of more future intense rains, more discharge will be generated and more areas may get inundated which may affect more life and property. Therefore, the flood inundation pattern for four profiles, i.e., July 5, July 15, July 30, and August 18, 2006, was studied for both scenarios. To investigate the impacts of sand mining on flood inundation, a flood event of 50-year return period was considered. Flood event dated July 30, 2006, is the highest flood event recorded in Karad gauging station of Upper Krishna Basin. In the flood inundation patterns, little changes at some places (locations of the meandering) in after mining scenario were observed. This may be due to DEM used (30 m) as river width

Fig. 7 Simulated velocity (m/s) under both pre- and post-mining scenarios
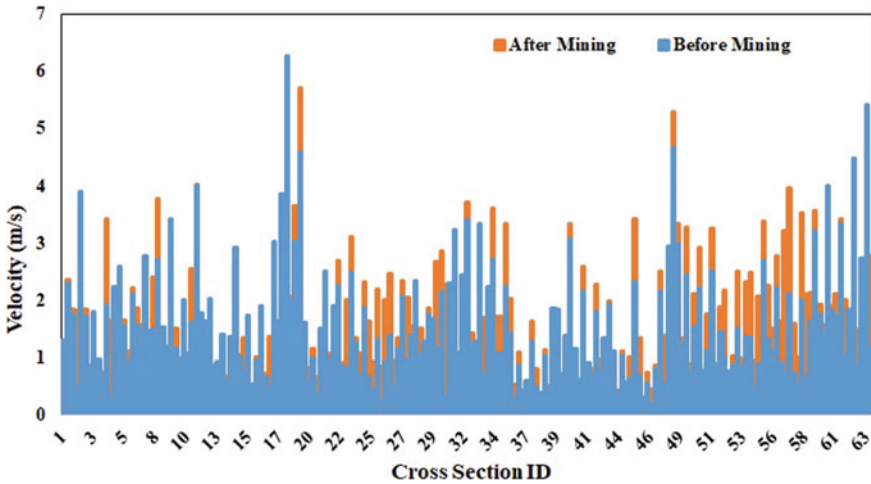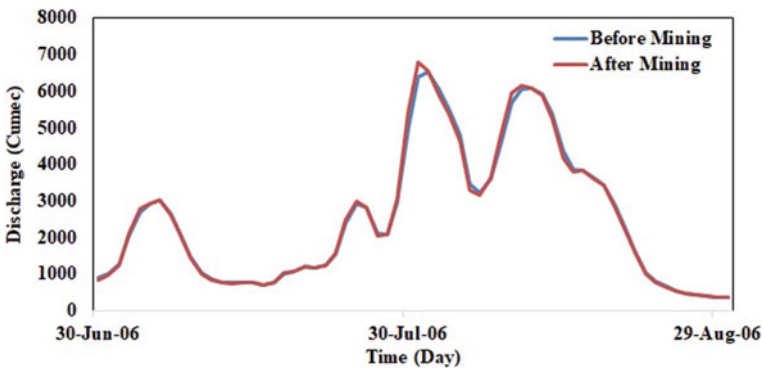

Fig. 8 Simulated discharge for the entire period of both the scenarios (before and after mining)

is around 150 m. So proper channel characteristics are not delineated with help of DEM. All these changes are observed due to changes in the geometry of the river. This may also affect/change hydraulics of the channel, i.e., velocity, discharge, and shear stress. In after mining condition, results show velocity, shear stress, and stream power increased as compared to before mining results. Contraction of the channel might have resulted in a high rate of velocity and shear stress. Channel contraction can cause bank line cut. Due to changes in the hydraulics of the channel, erosion, side cutting of banks may increase and loss of agricultural land would be there. In the future, high intense rainfall with a short duration is predicted by IPCC, so more discharge is expected, resulting in inundation pattern change under future conditions. It is recommended that for more accurate results, high-resolution DEM is required. A large amount of field survey data is needed for channel geometry. It is to be noted

Fig. 9 Estimated channel shear stress before and after mining conditions

that the ground survey requires highly accurate equipment for acquiring channel geometry, cross section, etc.
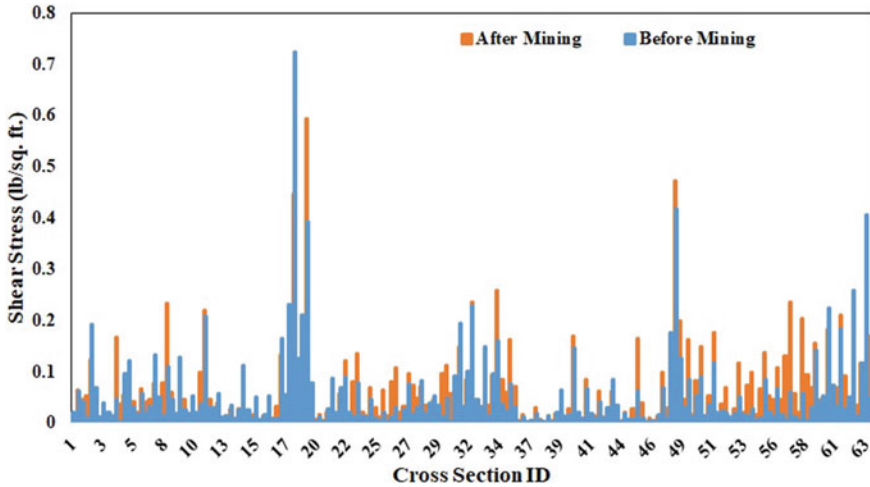
References

1. Martin-Vide JP, Ferrer-Boix C, Ollero A (2010) Incision due to gravel mining: modeling a case study from the Gallego River, Spain. Geomorphology 117:261–271
2. Knighton AD (1984) Fluvial forms and process. Arnold Publishers, London
3. Knighton AD (1989) River adjustment to changes in sediment load: the effects of tin mining on the Ringarooma River, Tasmania, 1875–1984. Earth Surf Proc Land 14:333–359
4. Wishart D, Warburton J, Bracken L (2008) Gravel extraction and planform change in a wandering gravel-bed river: the river wear, Northern England. Geomorphology 94:131–152
5. Padmalal D, Maya K, Sreebha S, Sreeja R (2008) Environmental effects of river sand mining: a case from the river catchments of Vembanad lake, Southwest coast of India. Environ Geol 54:879–889
6. Rinaldi M, Wyzga B, Surian N (2005) Sediment mining in alluvial channels: physical effects and management perspectives. River Res Appl 21:805–828
7. Luo X-L, Zeng EY, Ji R-Y, Wang C-P (2007) Effects of in-channel sand excavation on the hydrology of the Peral river delta, China. J Hydrol 343:230–239
8. Ako TA, Onoduku US, Oke SA et al (2014) Environmental effects of sand and gravel mining on land and soil in Luku, Minna, Niger State, North Central Nigeria. J Geosci Geomatics 2(2):42–29

  9. Salimi S, Ghanbarpour MR, Solaimani K, Ahmadi MZ (2008) Floodplain mapping using hydraulic simulation model in GIS. J Appl Sci 8(4):660–665
10. Water Resources Department (2015) Integrated state water plan for upper Krishna (K-1) sub-basin. Upper Krishna (K-1) sub-basin division, Water Resources Department, Government of Maharashtra, Satara, India
11. Chow VT, Maidment DR, Mays LW (1988) Applied hydrology. McGraw-Hill International Editions, Singapore

Field Study on the Coastal Dynamics and Sediment Transport Along the Visakhapatnam Coast

D. Hari Prasad, M. G. Muni Reddy, and N. Darga Kumar

Abstract Coastal erosion is a major setback for any country with a great coastline and a major crisis that impacts both coastal population and the ecological balance. The geographical modifications in the shoreline are primarily linked to the natural factors such as tides, storms, sea waves, change in the sea level, winds and the weathering, erosion, accretion, and anthropogenic effects along the shore. This study has made an eminence attempt in quantitative assessment of coastal erosion along the Visakhapatnam coast. Recent episode of severe beach erosion toppled the beach and the adjoining beach pressure and cyclone in the Bay of Bengal from Oct 2014 to the end of the month. Post-Hudhud cyclone beach survey is carried out at different locations at regular intervals along the coastline. Beach profile dynamics are studied in detail based on the three seasons—NE, fair weather period, and SW monsoon. Field survey of beach profiling was conducted from the benchmarks up to -1.0 m in the surf zone. From the survey data, sediment transport volumes were computed using the 3D modeling methods. Beach erosion has been changing dynamically every year. Annual sediment volume variation pattern was presented along with the potential erosion locations in the study area. Digital elevation model (DEM) is prepared from the survey data. All the data is categorized based on the monsoon seasons. Continuous erosion trend was observed at locations where wave actions causing direct effect. Fair weather period showed a trend of maximum deposition along the coast. At certain locations, maximum erosion was observed during pre-monsoon period.

Keywords Coastal erosion · Beach profile survey · Sediment movement · DEM

D. Hari Prasad (✉)
Aarvee Associates Architects Engineers and Consultants Pvt. Ltd., Hyderabad 500082, India
e-mail: hari.jntuh@gmail.com

M. G. Muni Reddy
Department of Civil Engineering, Andhra University, Visakhapatnam 530003, India

N. Darga Kumar
Department of Civil Engineering, JNTU College of Engineering, Manthani, Ramagundam, Telangana 505212, India

1 Introduction

Visakhapatnam City is situated on the east bank of India, in 17°04′2″ North scope and 82°00′2″ East scope of slopes. In view of geographical conditions, the city and its environs can be partitioned into four classifications, viz. hilly district, upland tracks, rolling fields, and plains. The tropical twisters influence this area in two seasons amid a year: pre-storm (April–May) and post-rainstorm (October-December). Hegde and Akshaya [1] discussed on shoreline transformation study of Karnataka coast: geospatial approach. In this review, an endeavor has been made to explore the shoreline change along the Karnataka drift.

The pinnacle recurrence is observed to be in the months of June, November, and December between the years 1877 and 2013, and the Vizag City has experienced. Erosion of Visakhapatnam coastline began way back in the year 1933 when the island breakwater was built for the improvement of inward harbor. Kumar et al. [2] discussed on coastal processes along the Indian Coastline. In this review, the deliberate information, wave height, and current speed at a couple of areas are introduced alongside the evaluated silt transport rates. In the beginning, the erosion is not important and completely restrained by occasionally pumping sand that is dredged in the entry channel to the northern shore. It is noticed that the sea made rapid inroads eroding the adjoining roads, the shore as well as some nearby houses. Kumar et al. [3] has discussed on coastal vulnerability assessment for Orissa State, East Coast of India. The present review is an endeavor to build up a coastal defenseless file for the sea condition of Visakhapatnam. The erosion of the coastline north of entry channel, close to the coastal battery has been alarming the authorities to take immediate protective measures. A sea wall is built and to this further substantial amounts of concrete, and stone blocks are placed in the region as a coastal erosion measure. Still the coastal erosion is prevailing along the coast of Vizag.

Cherian et al. [4] discussed on coastal erosion assessment along the southern Tamil Nadu Coast, India. Coastal zone is an exceptionally multifaceted, vigorous, and delicate environment. The Visakhapatnam (Vizag) shoreline has been experiencing seasonal erosion and deposition during SW monsoon and NE monsoon at several places. Erosion continues to be monitored Hari Prasad et al. [5]; Panigrahi et al. [6] during harsh season which get turned during calm periods toward north of these rugged outcrops and promontories. E and ESE waves influence the most of shore areas Vizag City. Thus, the sediment transport is mainly directed toward the north as well as the building of any constructions like breakwaters intercept the littoral drift coming from the northern shores as well as the south are eroded.

In these shores, erosion happens while finishing of the SW monsoon (Aug–Sept) and the shore is reformed on account of deposition during NE monsoon (Oct–Nov). Figure 1 shows the erosion that happened in the month of August 2007 and beach reformation near Ramakrishna Beach (RK Beach) in the month of October 2007. Again the same process can be noticed every year by May erosion starts, and by end of August, the beach reformation takes place. However, this cycle is disturbed when any cyclone strikes the shore and erosion may happen during NE monsoon

Fig. 1 Beaches changes observed in the year 2007

Fig. 2 Beaches changes observed in the year 2010

season. Acute beach erosion at RK Beach, Kurusura Submarine Museum and close to YMCA during 2007–2008 is largely due to the increased amount of erosion over Bay of Bengal. Figure 2 shows the disintegration at the Kurusura Submarine between May 13 and 26, 2010, which is additionally because of a violent wind. From these reviews, it gives an idea that the extension of shoreline at submarine exhibition hall is very defenseless for disintegration because of wave merging amid cyclonic periods.

2 Method Adopted

Shoreline profile study is carried out at 33 locations for duration of 15 months from August 2015 to October 2016 along the RK Beach of Visakhapatnam Coast. Temporary benchmarks (TBM) were established by National Institute of Ocean Technology (NIOT) along the review range. Dumpy levels and 5 m [IS: 1779(1961)] leveling staffs are utilized to quantify the diminished levels to build up shoreline profile from landside to low tide line. Shoreline profiling is carried out at each 100 m interims in the 4 km of RK Beach.

Fig. 3 BM–12

Fig. 4 BM–09

Information recorded in the field is exchanged to exceed expectation sheets and diagrams are prepared taking separation from TBM to LTL on X-pivot and RL's on Y-hub. Date and time of estimation are noted to make recordings of high tide level (HTL) and low tide level (LTL). At a few areas, profiling was done up to −1.50 m. Figures 3 and 4 show the benchmark placed by NIOT of location P-09 in the RK Beach near the Gokul Park.

2.1 Study Area and Data Source

In the study area shown in Fig. 5, coastline is appeared to have already been controlled and determined by the prevailing monsoonal wind directions of both SW and NE. For shaping the shoreline, long shore currents and waves also have played a significant part. Study area covers 33 transects in RK Beach Point No. P01-P34. Introduction of manmade structures like breakwaters, groins, and bulkheads cause erosion on the down-drift side and accretion on the up-drift side.
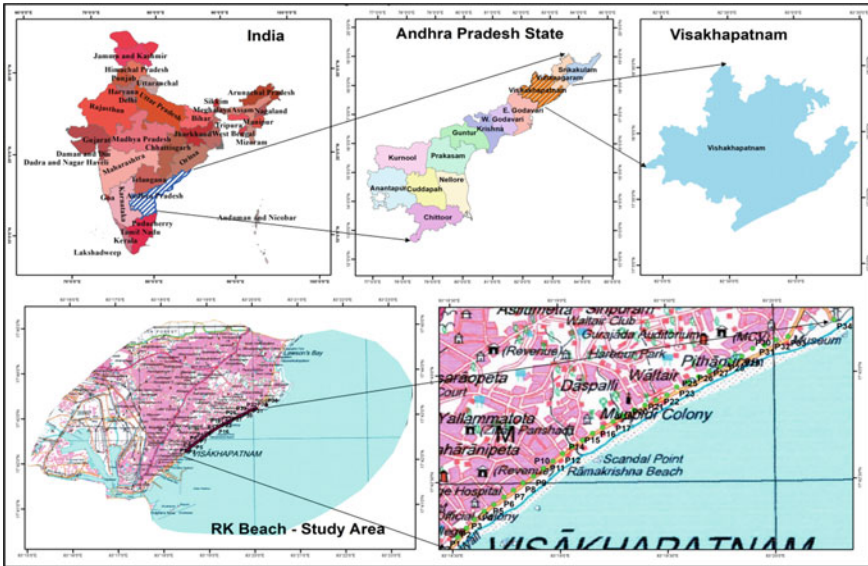
Fig. 5 Key map

Waves hitting the coast obliquely can cause erosion. Extreme events like cyclones, tsunamis, depressions that generate high energy waves are likely to cause damage to the shoreline requiring long time to recover. Long term causes like damming of rivers which trap silt behind, thereby limiting silt influx into the sea. Events on geologic timescale such as land subsidence and sea level rise also cause erosion. Along the east coast of India, littoral drift occurs in the northerly direction for 8 to 9 in months in a year, with the waves approaching the coast from southeast direction. Due to this, there is a southerly littoral drift for 3 to 4 months due to North–East monsoon waves.

2.1.1 Data Collection

The data collected from different sources are presented in Table 1.

2.2 Beach Profiles

Beach profiles are taken at 100 m interval using auto level from the temporary benchmarks placed by the NIOT. These beach profiles are linear stretches. It covers RK Beach till lighthouse.

Figure 6 presents the beach profiles of the point P-10 (17°42′33.6960″N, 83°18′55.2954″E) near the Novotel Hotel in RK Beach Vizag City. Erosion is

Table 1 Data collection and sources

S. No.	Type of data	Source of data
1	Topo sheets-65O2NW, 6502SE, 65O2SW, 65O2NW, 65O2SW, 65O3NW, 65O5NE, 65O5NW, 65O5SE, 65O6NW, 65O9NW)–1:25,000	Survey of India, Hyderabad
2	Land use, drainage, soil, and slope map	Satellite data, SRTM & Topo sheet
3	Vizag city maps	GVMC
4	Cyclone data	IMD

observed in the month of September when compared to August 2015. October, November, and December 2015 three months follow the same trend, i.e., deposition.

Figure 7 presents the beach profiles of the point P-20 (17°42′51.1200″N, 83°19′23.8440″E) located in the RK Beach. At this location, beach profiles were remained stable during the months of August, September, October, and November 2015. It is observed that sediment deposition about 40 m wide is happening in the month of January 2016 at LTL.

Figure 8 presents the beach profiles of the location P-25 which is near to Kurusura Sub-Museum (17°42′58.9320″N 83°19′38.8920″E) along the RK Beach. It is observed that in the month of January 2016 a berm of 20 m width is formed seaward at a distance of 110 m from TBM. This location witnesses 65 m width beach erosion at LTL.

Figure 9 presents the beach profiles of the point P-10 (17°42′33.6960″N, 83°18′55.2954″E) near the Novotel Hotel. In these locations, beach is uniformly
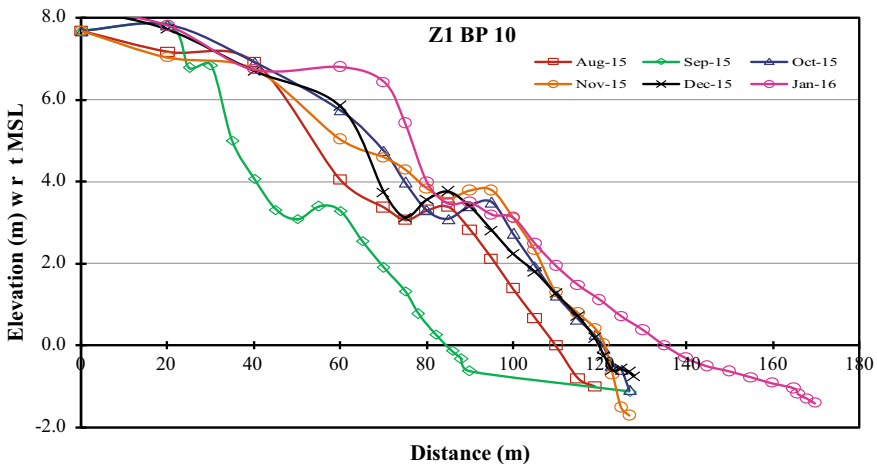
Fig. 6 Beach profiles of P-10–Aug 2015 to Jan 2016
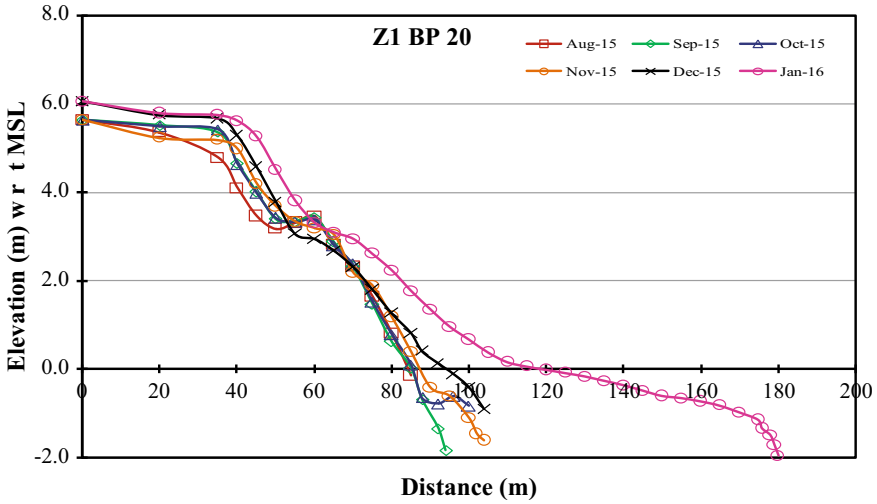
Fig. 7 Beach profiles of P-20–Aug 2015 to Jan 2016
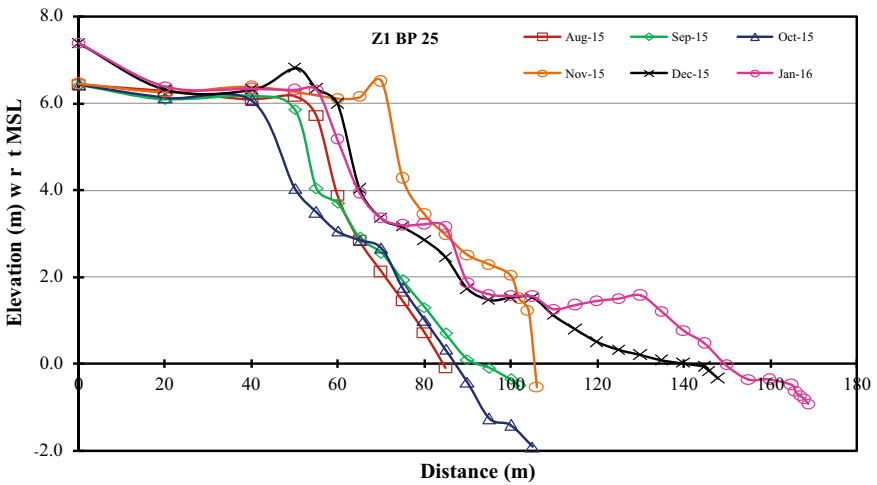
Fig. 8 Beach profiles of P-25–Aug 2015 to Jan 2016

same. A mild slope beach of width 20 m is formed at distance of 120 m from TBM in the months of April and May. Beach witnesses erosion of width 20 m at LTL.

Figure 10 presents the beach profile of the point P-19 (17°42′49.7880″N, 83°19′20.7840″E) along the RK Beach. It is clearly visible that mild steep beach slope of width 20 m is formed below water.

Figure 11 presents the beach profiles of the location P-25 which near to Kurusura Sub-Museum (17°42′58.9320″N, 83°19′38.8920″E) along the RK Beach. It is
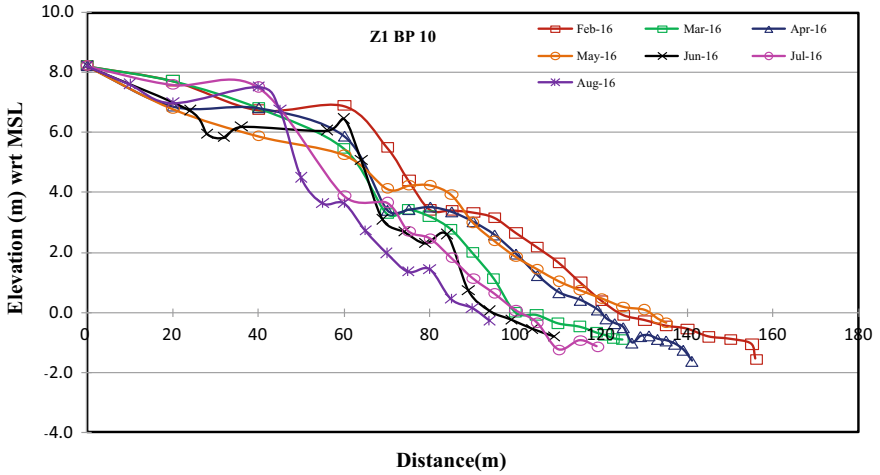
Fig. 9 Beach profiles of P-10–Feb 2016 to Aug 2016
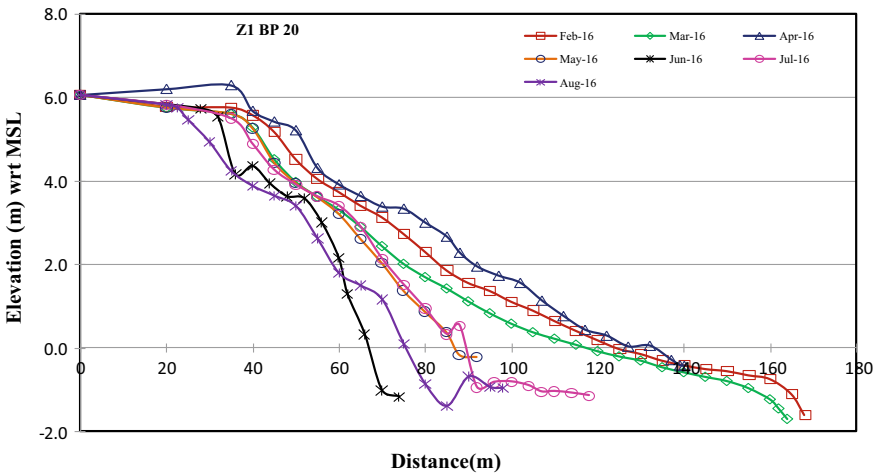
Fig. 10 Beach profiles of P-20–Feb 2016 to Aug 2016

observed that berm of width 30 m is formed at a distance 110 m from TBM. Mild steep slope of width 40 m is visible at LTL. Beach erosion of 20 m is visible at a distance of 80 m from the benchmark.
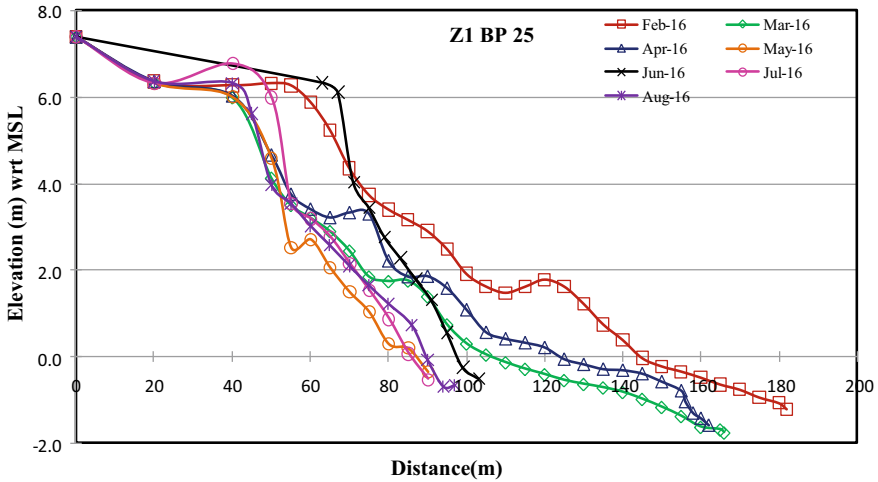
Fig. 11 Beach profiles of P-25–Feb 2016 to Aug 2016

2.3 Field Survey—Sediment Transport Computation

Thirty-three transects are surveyed every month to estimate the sediment transport along the shore. The volume of sand subjected to erosion/accretion is computed in CAD software by considering two beach profiles data as one section of the beach.

Initially, all the beach profiles are arranged in (a, b) format with 'a' as the distance offset (Chainage) from BM to the water line and 'b' indicates the RL on the beach. Levels along the transect are calculated by raise and fall method of dumpy level.

Two beach profiles are joined using the loft command and volume can be computed with mass properties commands. Slope of the beach as shown in Fig. 12 is computed from these profiles by measuring the angle between the baseline to beach inclination.

Figure 13 shows the 3D model of the beach profiles along the RK Beach. Sediment transport volume is computed by taking two profiles on each end of one beach section as shown in the figure.

Fig. 12 Beach slope (m)

Fig. 13 Beach section view
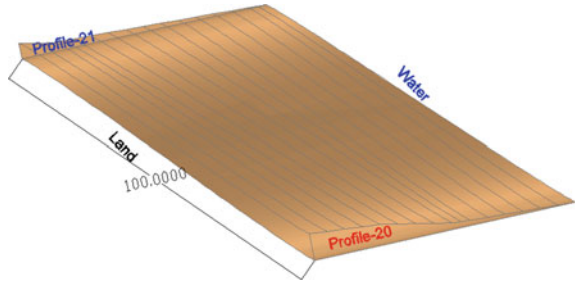
3 Results and Discussions

The sediment transport computation is carried out for 12 profiles as they are linear by nature. The sections selected are as follows: P07-10, P10-11, P11-12, P17-18, P18-19, P19-20, P20-21, P21-22, P22-23, P23-24, P24-25, P25-26.The field survey is carried out from August 2015. Every month 33 transects of beach profiles are recorded using dumpy level. Figures 14 and 15 present the monthly frequency of data so that detailed erosion and accretion trends can be assessed.

In Fig. 14, the locations P10-11 and P11-12 show the erosion trend of 33,771.28 m³/month and 32,012.98 m³/month, respectively, in the months of February, April, July, and October 2016. Profile P17-18 shows the erosion patches of 33,355.059 m³/month in the months of March, April, July, and October 2016. These locations witnessed the highest deposition during pre-monsoon months of April and May 2016.

Fig. 14 Fieldwork volume—P10-11, P11-12, P17-18
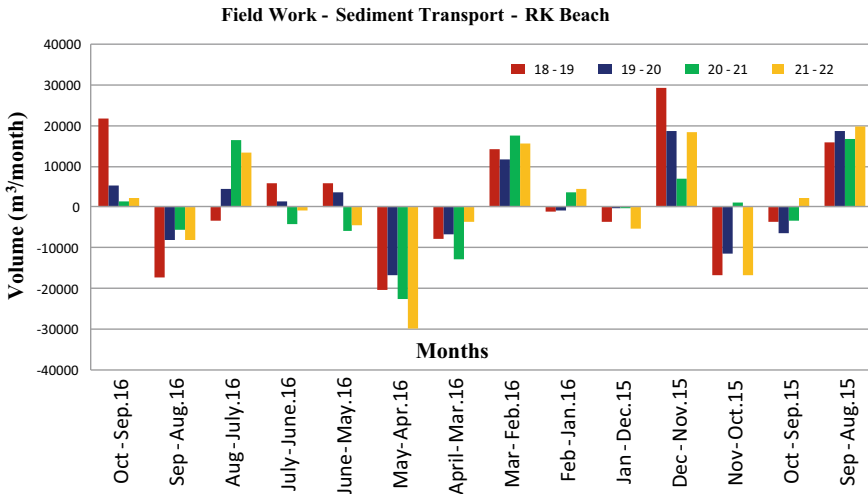
Fig. 15 Fieldwork volume—P18-19, P19-20, P20-21, P21-22

During the monsoon, these locations experience erosion trend and this can be attributed to the increased wave action along the coast. During the monsoons with increased wave action and surface currents are causing more suspended sediment load and offshore movement of the sediments. During the monsoon receding in the months of August and September, accretion is witnessed at these locations. This location is near to Novotel Hotel where in the past dredging has been done by Dredging Corporation of India (DCI). From Fig. 15, it is visible that all the four profiles P18-19, P19-20, P20-21, and P21-22 show maximum the erosion of 29,906.64 m³/month trend from the month March 16 onwards. These locations witnessed the highest deposition during post-monsoon months of August and November 2016.

During the monsoon, these locations move toward erosion trend with increased wave action along the coast. During monsoons, the wave behavior is dynamic and the surface currents are so high causing more suspended sediment load and offshore movement of the sediments. During the monsoon receding trend in the months of August and September, accretion was witnessed at these locations.

From Fig. 16, it is visible that initially there is erosion trend in the months of April and May 2016. Particularly, profile P24-25 near Kurusura Submarine shows erosion patches of 33,612.795 m³/month in the months of March, June, and September 2016. These locations witnessed the highest deposition during NE monsoon months of April and May 2016.

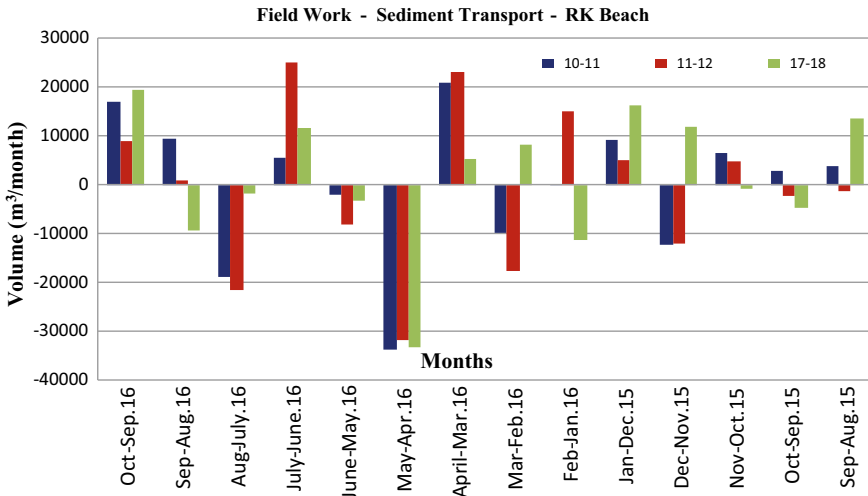During the monsoon, these locations are subjected to erosion trend with increased wave action along the coast. During the monsoon, receding trend in accretion is witnessed at these locations, especially in the months of August and September.
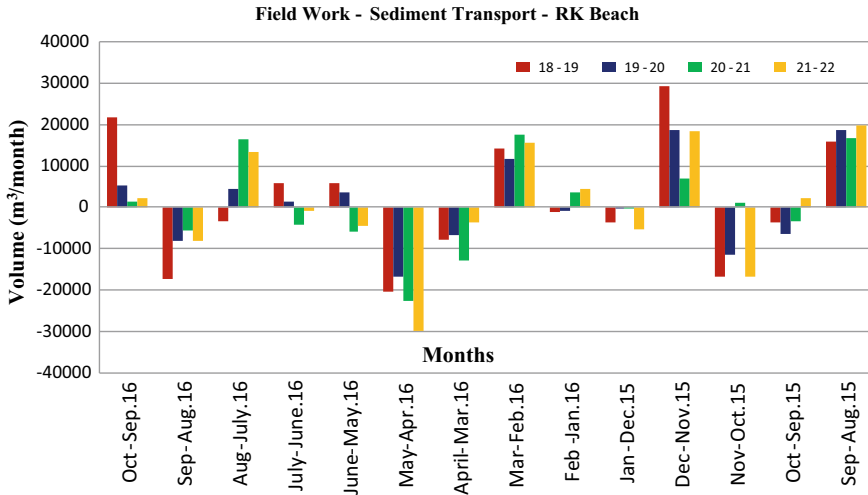
Fig. 16 Fieldwork volume—P22-23, P23-24, P24-25, P25-26

4   Conclusions

Along the RK Beach, the location points such as Kaali temple and Kurusura Museum are affected by erosion. The net sediment transport of 396,270.864 m^3/yr is observed toward the north of the study area. From the field data, also it is witnessed that the maximum erosion is taken place at Museum place in the RK Beach.

References

1. Hegde AV, Akshaya BJ (2015) Shoreline transformation study of Karnataka coast: geospatial approach. International conference on water resources, coastal and ocean engineering (ICWRCOE 2015), Aquatic Procedia, vol 4, pp 151–156
2. Sanil Kumar KC, Pathak P, Pednekar P, Raju NSN, Gowthaman R (2006) Coastal processes along the Indian coastline. Curr Sci 91(4):25
3. Srinivasa Kumar T, Mahendra RS, Nayak S, Radhakrishnan K, Sahu KC (2010) Coastal vulnerability assessment for Orissa state, east coast of India. J Coast Res 26:523–534
4. Anil Cherian N, Chandrasekar ARG, Rajamanickam GV (2012) Coastal erosion assessment along the Southern Tamilndu coast, India. Int J Earth Sci Eng 05:352–357
5. Hari Prasad D, Muni Reddy MG, Darga Kumar N (2015) A study on coastal erosion modeling using GIS and remote sensing technologies, case study: Andhra Pradesh coast. Int J Earth Sci Eng, Caffet-Innova 8(2):208–211. ISSN 0974-5904
6. Panigrahi JK, Sathish Kumar V, Tripathy JK (2010) Littoral drift by alongshore flow at Visakhapatnam e East coast of India. J Hydro-Environ Res 4:317–327

A Capacity Loss and Silt Assessment of Khuga Reservoir, Manipur, Using Bathymetry Survey Technique—A Case Study'

M. S. Bist, Ajay Sonavane, Ajit Singh, J. K. Singh, and M. Selva Balan

Abstract The Khuga Dam is an irrigation project constructed across the Khuga River situated 10 km from Churachandpur Town, Imphal City, Manipur State in India. The project is providing drinking water and water supply for irrigation to most parts of Churachandpur Town and its nearby villages. The dam construction was started in the year 1983–84 and completed in 2010. More than 10 years after operation, the project authority decided to evaluate the existing storage capacity and estimation of silt deposited in the reservoir by conducting bathymetry survey. The purpose of the bathymetry survey was to find the present storage capacity of the reservoir so the proper distribution of water supply for irrigation and drinking purpose can be planned by the project authority. This study also included to find out the possible methods for increasing the reservoir storage capacity by removal of silt deposited in the reservoir. Under National Hydrology Project (NHP), CWPRS, Pune, conducted the bathymetry survey of Khuga reservoir. The survey was done by using the bathymetry survey equipment consisting of echo sounder, DGPS with antenna mounted on a motorized boat and data acquisition system for survey data logging. The survey equipment had accuracy in submeters and in cms for position. The survey was carried out at reservoir EL 844.0 m. The analysis was carried out using software such as Hypack, Surfer, Eiva, Global Mapper, Google Earth, and AutoCAD (AutoCAD manual, source: www.autodesk.com, [1]) for fixing survey area reservoir boundary during data collection can be planned. After the analysis, the gross loss in reservoir volume was calculated; it was calculated, and there was a reduction of 26.72% in the dead storage reservoir capacity.

Keywords Hypack · NAVISOFT · Bathymetry · DGPS · Echo sounder

M. S. Bist (✉) · A. Sonavane · A. Singh · J. K. Singh · M. Selva Balan
Central Water and Power Research Station (CWPRS), Pune 411024, India
e-mail: msbist1974@cwprs.gov.in

A. Sonavane
e-mail: ajay.sonavane@cwprs.gov.in

1 Introduction

The Executive Engineer, Water Resources Department, Government of Manipur had requested CWPRS, Pune, to conduct bathymetry survey of Khuga Dam, Manipur. Subsequently after accepting the proposal, CWPRS took the study under National Hydrology Project and carried out bathymetry survey of Khuga reservoir [2] from January 24th to 27th, 2020.

The construction of the Khuga Dam started in the year 1983–84 and completed in the year 2010 with a project cost of Rs.381.28 crores. The Khuga Dam is shown in Fig. 1, and the reservoir boundary on Google Earth map is shown in Fig. 2. The CWPRS conducted the bathymetric survey by deploying integrated bathymetry system (IBS) consisting of dual frequency echo sounder (210 kHz and 33 kHz) for measuring the water depth and a Global Positioning System (GPS) for finding the accurate location of boat moving on the predefined grid lines preloaded on the software in laptop. The data (depth and position) collected at site was logged in real-time mode in laptop with survey software. Processing and calculations were done later by processing software such as Hypack and surfer at CWPRS.

Sedimentation in reservoirs is a serious problem as it reduces the utility period of the reservoir, which is also termed at its useful life. Dam and storage reservoirs are built-up at enormous cost for augmentation of water resources, and these play a vital role in the development of nation. A design capacity of water storage in dam at minimum cost will give rise to maximum output and in turn better return for capital invested on the reservoir project. The life of the reservoir cannot be forecasted precisely as the process of sedimentation is a complex phenomenon which also cannot be so precisely estimated. The rate of sedimentation depends on the various

Fig. 1 Khuga dam and spillway

Fig. 2 Google image of Khuga reservoir boundary

factors including geographical features of the terrain, rainfall, deforestation, etc. The complexity of various parameters in the process of reservoir such as the space and position occupied by sediment, lack of knowledge regarding contribution of sediment by water from each of the tributaries, the variability of sediment flow from year to year, season to season, the inability to evaluate accurately suspended sediment and bed load, all prevent the hydraulic engineer from forming definite conclusions regarding useful life of reservoir. It is therefore essential to monitor the actual rate of sediment deposition in the reservoir and redefines the volume–elevation–capacity curves.

Thus, the sedimentation survey studies are useful in

1. Ascertaining useful life of reservoir.
2. Revised the capacity curve for more efficient operation of the reservoir.
3. In enforcing better watershed management and understanding climate factors on the rate of sedimentation.
4. Assessing regional silt indices for developing design data for planning of new reservoir.
5. In bringing efficiency and economy in control measures.
6. Forecasting hydropower generating capacity year to year.

2 Components and Methodology

The bathymetry survey was carried out with a boat equipped with single beam dual frequency echo sounder [3] Mobile GPS system with beacon correction and a laptop for logging the data in real time. The IBS system used during survey consists of the following components:

(i) Single beam dual frequency echo sounder (210 kHz, 33 kHz) Knudsen make.
(ii) GPS makes Trimble using beacon correction (GPS manual, Trimble make) [4].
(iii) Data collection laptop with Hypack software (Hypack manual) used for real-time data acquisition.

A motorized boat was used for deploying the survey equipment during survey. The echo sounder sensor with special fixture was fitted on one side of the boat, and the GPS antenna was mounted on boat for receiving the satellite signal. The Hypack survey software was used for fixing of grid lines and interfacing of echo sounder and GPS equipment. The survey software logged the boat position longitude, latitude (x, y) data, and water depth (z) values at required interval/grid. The depth and position data is logged in real-time mode in laptop with survey software. Figure 3 shows GPS equipment with antenna fixed in boat, and Fig. 4 shows echo sounder recorder with sensor, whereas Fig. 5 shows laptop screen with data logging points. The echo sounder was calibrated for its accuracy before using it. The GPS accuracy for boat location was achieved in submeter with beacon correction from near seashore reference station.

The CWPRS survey team in boat while conducting survey is shown in Fig. 6. The survey boat was equipped with survey equipments like echo sounder, GPS, antenna, and battery for power up the instruments. The survey was carried out by running the boat on the predefined straight grid line based on the pre-survey process. This included loading the survey boundary, assigning the proper coordinate system for the GPS, setting the data logging protocol, zone, coordinate system, etc. Similarly,

Fig. 3 GPS equipment with antenna

Fig. 4 Echo sounder recorder with sensor
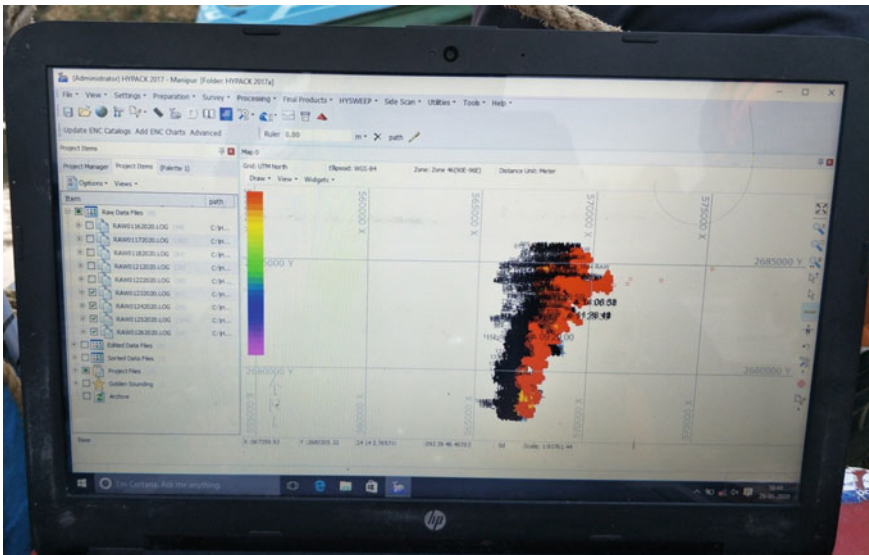
Fig. 5 Laptop screen showing data logging points

the echo sounder needs to be calibrated for the sound velocity before actual depth data logging on every day before start of survey work.

Boat navigation was also controlled by the software, so that boat tracks the grid line accurately while logging the data. The bathymetric survey was carried out during the month of January 2020 at the EL of 844.0 m. The boundary profile was extracted from Google Earth at CWPRS prior to the site visit. The same has been verified by running the boat on the actual cross section at site. After confirmation, the actual survey lines were carried out on the required cross section. The bathymetry data collection was completed.

3 Analysis and Results

After completing the survey, the data were filtered and noised and were removed using
software such as Hypack [5]/Surfer [6]. During analyzing the data, the bathymetry
raw data were converted into excel/XYZ format. The grids were made using Kriging
method, and volume and corresponding area were calculated at survey EL of 844.0 m
using Simpson 1/3 method and Simpson 1/6 method. The different volume value was
calculated below survey level with an interval of 1 m up to reservoir bottom. The
elevation–volume–capacity, elevation–area curve, Digital Elevation Model (DEM)
was plotted. The volumes at survey level and at dead storage level were calcu-
lated and compared. Figure 7 shows surface map of Khuga reservoir. Figures 8
and 9 show elevation–capacity curve and elevation–area–capacity curve of Khuga
reservoir, respectively [2].
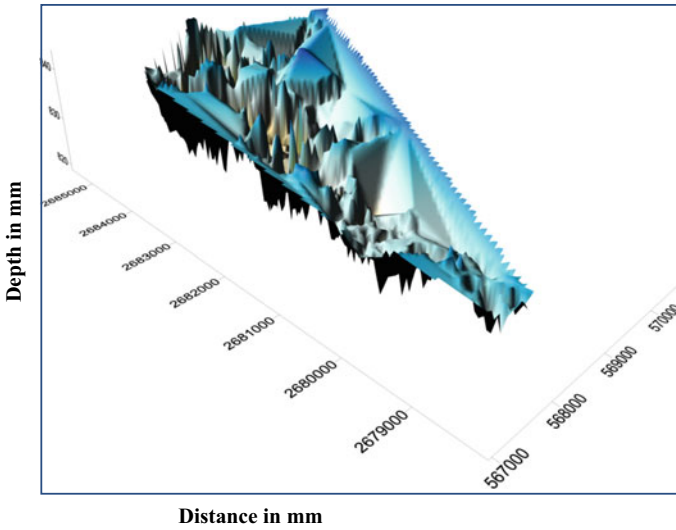
Fig. 7 Surface map of Khuga reservoir
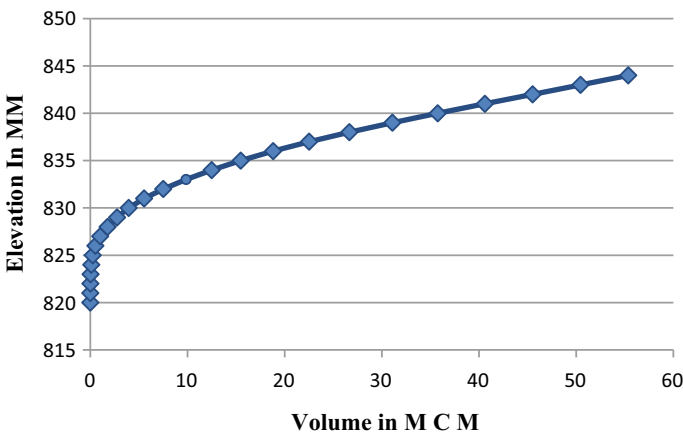
Fig. 8 Elevation–capacity curve of Khuga reservoir

4　Conclusions

The collected data was edited and filtered and analyzed using Hypack, Surfer. The volume–capacity curves, DEM, surface map, depth profile were drawn.

- The reservoir gross storage capacity calculated was 55.361 M.CM for reservoir water spread area of 5.625 sq. km at survey level 844.0 m RL
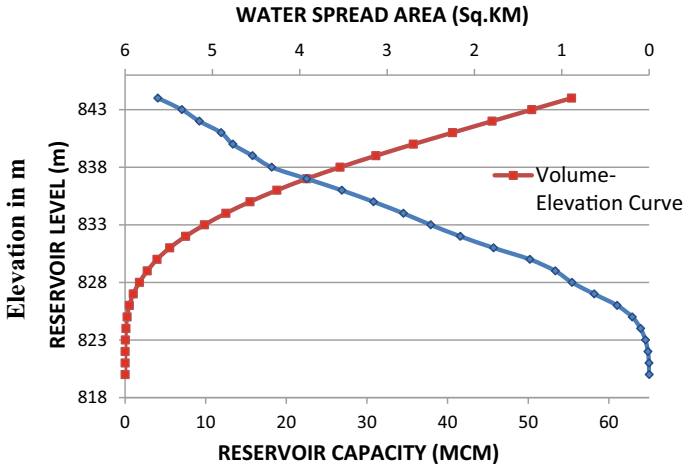
Fig. 9 Elevation–area–capacity curve of Khuga reservoir

- After comparing with the original data, it was concluded that there was a substantial reduction of 26.72% in the dead storage capacity of the reservoir.

References

1. AutoCAD manual, source: www.autodesk.com
2. CWPRS, Pune technical report no. 5877, (Dec 2020). Bathymetry survey of Khuga Reservoir in Manipur state under national hydrology project (NHP)
3. GPS manual, Trimble make, source: http://www.trimble.com
4. Single beam echo sounder manual, Knudsen makes. Source: https://www.knudseneng.co
5. Hypack manual, source: https://www.hypack.com
6. Surfer manual source: https://www.goldensoftware.com

Rain-On-Grid Local-Inertial Formulation to Model Within Grid Topography

N. Nithila Devi and Soumendra Nath Kuiry

Abstract Flood inundation can be simulated using externally coupled hydrology and hydraulic models (decoupled models), large-scale hydrological models and rain-on-grid or direct run off models. External coupling can only simulate the fluvial (river) flooding in the hydraulic domain. The large-scale hydrological models transfer the overland flow component to the downstream point based on simplified hydrological routing methods that are not accurate especially when backwater, flood-plain reach interaction processes are involved, as in the case of low-lying terrains of deltas. To overcome the aforementioned issues, the rain-on-grid models incorporate the effective rainfall as a source term in the continuity equation of the two-dimensional (2D) shallow water equations (SWEs). This represents the pluvial flooding that is typical of urban areas. Owing to the improved computational efficiency and similar accuracy in comparison with the full 2D SWEs, local-inertial approximations have been widely used for flood forecasting, especially in large basins. However, the availability of very high-resolution data from LiDAR that can resolve smaller urban landscape features demands more computational cost. Therefore, to further increase computational efficiency without compromising on the accuracy, a bathymetry-based sub-grid approach is introduced into the local-inertial rain-on-grid model. Though sub-grid formulation operates at a coarser grid, the fluxes through the cell interfaces are estimated based on pre-stored hydraulic properties, thus capturing the within grid topographic features. To illustrate the advantage of the sub-grid-based local-inertial rain-on-grid formulation, the Adyar basin comprising the Chennai city in Tamil Nadu, India, is chosen as a case study. The study shows that the proposed sub-grid-based local-inertial model can simulate flood flow through the urban features with improved accuracy.

Keywords Rain-on-grid · Local-inertial formulation · Sub-grid model · Urban flooding

N. N. Devi · S. N. Kuiry (✉)
Department of Civil Engineering, Indian Institute of Technology Madras, Chennai 600036, India
e-mail: snkuiry@civil.iitm.ac.in

1 Introduction

Reasonable accuracy and less computational cost are important in real-time flood simulation, flood early warning, and post-disaster economic loss assessments. Flood inundation can be simulated using externally coupled hydrology and hydraulic models (decoupled models), large-scale hydrological models and overland flow models. External coupling is done by providing the run off hydrograph that is obtained from hydrological model as an input boundary condition to the hydraulic model. It is only in the hydraulic domain one could simulate the fluvial (river) flooding. However, this methodology becomes complicated when the river reach is sufficiently long and has significant lateral inflows.

In large-scale hydrological models, the large basin is divided into a number of sub-basins using Geographical Information System (GIS). The large-scale hydrological models then budget the rainfall into evapotranspiration, infiltration, ground water and overland flow for the hydrological response groups (HRG) that have similar run off generation characteristics, within a sub-basin. The overland flow component of HRGs is transferred to the downstream point determined based on the topology of the basin and reach definition. This process accumulates mass till the reach, and then the flow is routed from the reach to the outlet of the basin using Muskingham-Cunge (continuity), kinematic or diffused routing methods [1]. These routing methods are simplified and not accurate especially when backwater, flood-plain reach interaction processes are involved as in low-lying terrains of deltas. It is in that regard, MGB-IPH model [2] employed local-inertial equation. It is also available as a plugin to be used in the open-source GIS—Map Window. This further facilitates the use of remotely sensed data both as inputs and for validation. However, the large-scale hydrological models simulate flood depths caused by riverine flooding alone and not in the upper catchment areas.

The overland flow models solve continuity and momentum equations on each cell throughout the domain and hence are computationally expensive compared to the large-scale hydrological models, especially in the context of large basins. To cut down the cost, instead of using full two-dimensional (2D) shallow water equations (SWEs), diffusive-wave approximations are widely used. The computationally efficient kinematic wave models that simulate flow based on channel bed slope and friction cannot accurately simulate the flow dynamics in low-relief areas. Explicit schemes are observed to more convenient in grid-based routing than implicit schemes. In explicit diffusive numerical schemes, generally time constraints are imposed to ensure stability: CFL condition [3] to preserve the validity of explicit scheme in flood wave propagation and Hunter [4] to avoid overshooting or excessive volume leaving the cell in one time step in non-staggered grids. In the latter case, the time step is dictated by square of the grid size. Bates et al. [5] came up with a new formulation in that regard to include local acceleration term, so that the time step is subjected to only CFL that is inversely proportional to the grid size. This allowed for larger time steps, and hence, the local-inertial models are faster than diffusive models. Further, Huang and Lee [6] proposed a digital elevation model (DEM)-based overland flow

model that determined the flow direction in each time step based on the water stage rather than considering all the neighbours. In order to relax the time step, Bates et al. [5] formulation was implemented in the momentum equation and also a quasi-2D approach was implemented to alleviate the CFL criteria.

Computationally, efficient models are in demand for the following reasons:

- Availability of very high-resolution data with the advancement of technologies such as LiDAR that could resolve various minute features of the urban landscape. Implementation of such high-precision data causes a lot of computational cost [7].
- Uncertainty analysis requires running of the model with large number of several hundreds of random parameter sets to ascertain uncertainty quantiles for overland flow models that simulate flooding in the entire catchment [8].
- Real-time forecasting for large basins/global and country wise forecasts require the flood to be simulated as early as possible. This is due to the fact that rainfall predictions from various models and ensemble members are to be utilized in real-time forecasting.

In order to make the overland flow models more effective, concept of sub-grid is becoming increasingly popular. The sub-grid approaches allow for the usage of coarser numerical grids, while still accounting for the variability within the grid. These techniques ensure accuracy comparable to finer grid models. There are three different ways in which the sub-grid concept can be implemented: (i) quadtrees [9, 10], (ii) hydraulic geometry relationships [11] and (iii) bathymetry approach [12]. In the quadtree approach of discretization, the coarser grids are multiples of finer grid size; therefore, at the faces of discretization, the fluxes are factored or summed accordingly. This method requires the knowledge of the hydrodynamics of the domain, so that one can use finer grids at the places where the flow dynamics is strong. The hydraulic geometry relationships represent any channel below the adopted grid resolution, using relationship between channel depth and width. The cell faces are regarded as separate one-dimensional (1D) models with different widths and bed elevations. To circumvent the instability in water surface when the water flows from a large to small channel, the smallest width is considered. Also, in order to save computational cost, the flow width is estimated at each face a priori. However, this method is generally applied in larger data-scarce regions that approximate the channel to be rectangular. In the bathymetry approach, hydraulic properties tables like elevation versus area are calculated for each face, and the corresponding values are used in the calculations. Hence, the bathymetry-based approach is advantageous over quadtree and hydraulic geometry theory models as it does not require user intervention in grid generation and is applicable to smaller areas. This is of greater importance in urban areas [13, 14], where the intervention of small-scale terrain features like buildings, roads, etc. govern flood dynamics. Therefore, in this study due to the aforementioned reasons, a novel computationally efficient sub-grid-based overland flow model is proposed to simulate fluvial floods, especially urban floods.

2 Materials and Methods

2.1 Sub-grid Formulation

Effective rainfall is added as a source term in the continuity equation of the local-inertial model [15]. The generalized continuity and momentum equations for local-inertial overland flow model are as follows:

$$\frac{\partial h}{\partial t} + \frac{\partial q_x}{\partial x} + \frac{\partial q_y}{\partial y} = R - f \tag{1}$$

$$\underbrace{\frac{\partial q_x}{\partial t}}_{\substack{\text{local} \\ \text{acceleration}}} + \underbrace{gh\frac{\partial(h+z)}{\partial x}}_{\substack{\text{pressure}+ \\ \text{bed gradients}}} + \underbrace{\frac{gn^2 q_x^2}{h^{\frac{7}{3}}}}_{\text{friction}} = 0 \tag{2}$$

$$\underbrace{\frac{\partial q_y}{\partial t}}_{\substack{\text{local} \\ \text{acceleration}}} + \underbrace{gh\frac{\partial(h+z)}{\partial y}}_{\substack{\text{pressure}+ \\ \text{bed gradients}}} + \underbrace{\frac{gn^2 q_y^2}{h^{\frac{7}{3}}}}_{\text{friction}} = 0 \tag{3}$$

where q_x and q_y are the unit width discharges in the x- and y-directions, respectively; h is the flow depth, z is the bed elevation, g is the acceleration due to gravity, n is the Manning's roughness coefficient and t is the time. Equation (1) is the continuity equation containing rainfall (R) and infiltration (f) terms too. Equations (2) and (3) are momentum conservation equations in x- and y-directions, respectively.

The continuity and momentum equations are discretized using a staggered grid approach in which the water depth is updated at the cell's centre, while the mass fluxes or the discharges are updated along the cell edges. Bates et al. [5] discretized the momentum and continuity equations as follows:

$$q_{t+\Delta t} = \frac{q_t - gh_t\Delta t\frac{\partial(h_t+z)}{\partial x}}{(1 + gh_t\Delta tn^2 q_t/h_t^{10/3})} \tag{4}$$

$$h_{t+\Delta t} = h_t + R - f + \text{area}(q_{\text{up}} + q_{\text{down}} + q_{\text{right}} + q_{\text{left}})_t \tag{5}$$

where t represents the values at previous time step and Δt represents the values at the new time step; $q_{\text{up}}, q_{\text{down}}, q_{\text{left}}$ and q_{right} represent the unit discharge values along the four edges of the cell.

The sub-grid approach is formulated for the aforementioned inertial model. Following are the pre-processing steps that are to be performed before running a sub-grid model:
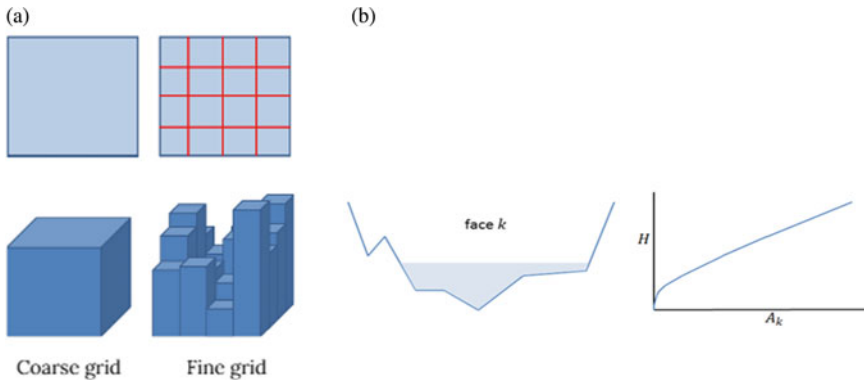
Fig. 1 Bathymetry-based sub-grid approach: **a** coarser and finer cell representation and **b** variation of face area with water depth along a coarse cell's edge *Source*: Casuilli 2009

- Extract the sub-grid elevations within the coarser grid for the entire domain.
- Construction of a common edge along the cell interfaces by considering the maximum or mean of bed elevation on either side of the edge on a finer level. The common edge will be further used in wetted face area calculations.
- Estimate wetted volume in the cell and face area along the edges for each incremental elevation.
- Fit suitable curves of elevation and hydraulic properties for each coarse cell (Fig. 1).

The novelty lies in the fact that the proposed sub-grid inertial formulation is employed on a raster/square grid and uses a common edge for finding out wetted face area, which is then used in discharge estimation. This is due to the fact that the square grid directly employs the DEM data's elevation values, the grid edges will have different elevation on its either side. Another change is that instead of depth based equation, a volume-based continuity equation is used.

2.2 Study Area

The Adyar River basin comprising Chennai city in Tamil Nadu, India, is chosen as the study area, as shown in Fig. 2, occupies an area of about 724 km^2. The upper part of the basin, lying in Kancheepuram and Thiruvallur districts, consists of a vast expanse of rural agricultural area and 163 water bodies that are locally referred to as tanks, of considerable capacity [16]. The lower part of the basin constitutes the southern portion of Chennai Metropolitan Area (CMA). The city being a business hub has witnessed steep growth in manufacturing, health care, retail and IT sectors in the past few decades [17]. It houses a number of schools, colleges, shopping malls, pilgrim sites, historical landmarks and commercial sites. The Chennai International
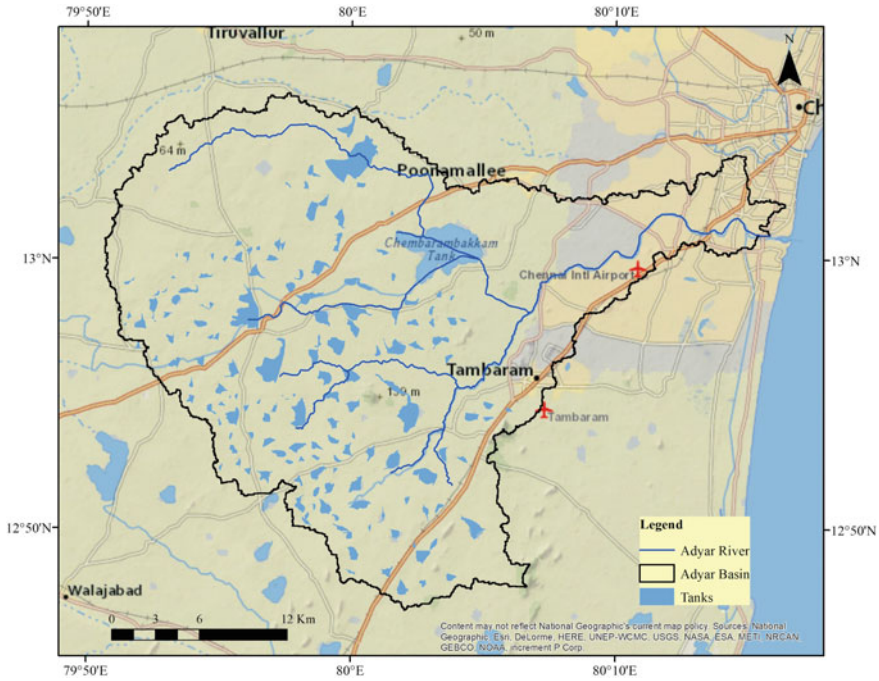
Fig. 2 Study area map

Airport has its secondary runway built over the Adyar River. In addition to that, the population is expected to grow in leaps and bounds to around 10 million by 2025 [18]. On the downside, rapid urbanization has culminated into unregulated settlements in the flood plains of the city's rivers, wetlands and tanks [17, 19–22].

The city of Chennai had witnessed flooding during 1943, 1976, 1985, 1996, 1998, 2005, 2008, 2015 and 2017. The heavy rainfall is a recurring phenomenon during the North-East (NE) monsoon season (mid-October to mid-December) due to deep depressions and cyclones. Being a coastal city with low-lying terrain (average elevation is around ~6 m), Chennai suffers from frequent inundation even for a short precipitation spell. Ill-conceived and maintained storm drains, encroached macro-drainage systems (rivers and canals), sand bars at the river mouths further escalate this issue. Apart from this, urban sprawl and climate change are expected to increase the flood magnitude in the coming years. In this study, we attempt to formulate flood mitigation measures for the Adyar River basin under changing climate and urbanization.

(a)

(b)
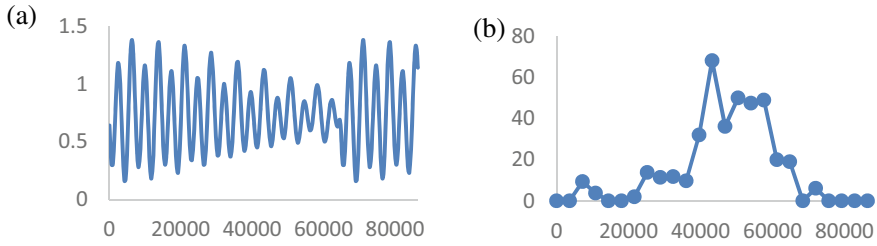
Fig. 3 Times series of **a** tide elevation and **b** rainfall for 100-year return period. The x-axis represents simulation time in seconds. The y-axis represents **a** tidal elevation in m and **b** rainfall in mm

Table 1 Scenarios description

Scenarios	Algorithm	Numerical grid size	DEM resolution
Full2d_45m	HEC-RAS full 2D SWE	45 m × 45 m	10 m
Inertial_90m	Local-inertial 2D SWE	90 m × 90 m	90 m
Sub-Inertial_90m	Sub-grid implementation in local-inertial 2D SWE	90 m × 90 m	10 m

2.3 Scenarios Used

The rainfall corresponding to 100-year return period and tidal boundary condition is used for all the model runs (Fig. 3). The return period rainfall data is obtained by performing Gumbel distribution analysis on the Indian Meteorological Department (IMD) rainfall data [16]. Table 1 describes the various scenarios used in the study.

3 Results and Discussions

Figure 4 shows the maximum inundation extents simulated by the Inertial_90 m and Sub-Inertial_90 m models. It can be seen in the enlarged areas that the street level flooding can be better captured by the model with the proposed sub-grid implementation. In order to further drive home the point, Fig. 5 presents an even more expanded view of the downstream urban area of the Adyar basin. Various finer topographical features of the Chennai city like Buckingham canal, Mambalam drain, Chennai International Airport have been better represented with the use of sub-grid algorithm. Hence, it is evident that the implementation of sub-grid on a coarser inertial grid model can effectively resolve the within the grid topographic details, such as canals, streets, highways and buildings.

In order to quantify the accuracy, the Full2d_45 m is taken as a reference as the 100-year return period scenario is hypothetical. The maximum flood inundation
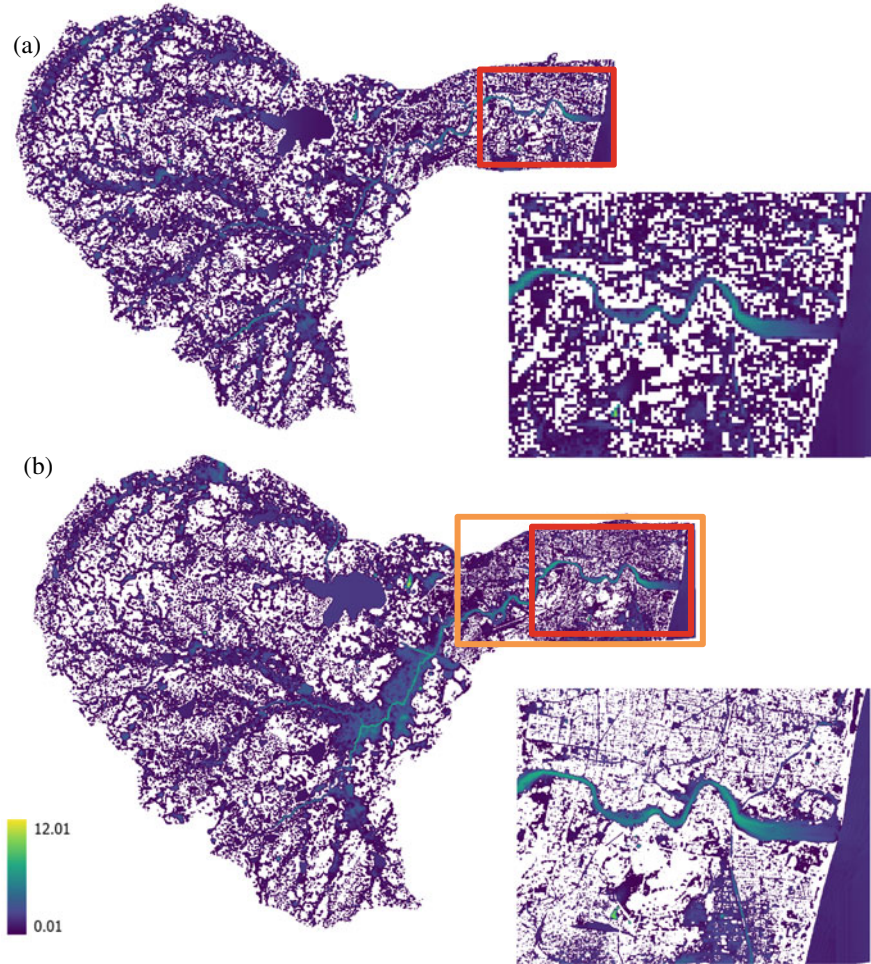
Fig. 4 Maximum inundation extents of **a** inertial_90 m and **b** sub-Inertial_90m models. The enlarged view of the region within the red box is presented by the side

depth values at various points from all the model simulations were extracted and the performance statistics were calculated. Table 2 shows the calculated values of the performance indices of the models. The Root Mean Squared Error (RMSE) of Sub-Inertial_90 m is around 27% lesser than that of Inertial_90 m model (Table 2). It is noteworthy to mention that the improved accuracy is achieved only with 2.81 times more computational cost of that of the Inertial_90 m model.

Fig. 5 Enlarged view of the area within the green box in Fig. 4b. The places within boxes labelled as 1, 2, 3 and 4 represent central and southern Buckingham canals, Mambalam drain and Chennai International Airport, respectively

Table 2 Validation of simulated maximum flood depths with that from Full2d_45 m

Scenarios	R^2	RMSE (m)	Relative time taken
Inertial_90 m	0.79	0.86	1
Sub-Inertial_90 m	0.85	0.59	2.81

4 Conclusions

From the proposed study, the following are the key conclusions:

- The sub-grid inertial formulation can effectively resolve the smaller topographic features like streets, buildings, highways and storm drain canals. It is accomplished at around 2.81 times the computational cost of the coarser inertial model without sub-grid implementation.
- The overland flow inertial formulation with sub-grid implementation can simulate flood depth throughout the entire catchment with more accuracy than that of the model without sub-grid implementation. Thus, it has promising deployment in a flood forecasting framework for the entire catchment.

References

1. Kauffeldt A, Wetterhall F, Pappenberger F, Salamon P, Thielen J (2016) Technical review of large-scale hydrological models for implementation in operational flood forecasting schemes on continental level. Environ Model Softw 75:68–76
2. Pontes PRM, Fan FM, Fleischmann AS, de Paiva RCD, Buarque DC, Siqueira VA, Jardim PF, Sorribas MV, Collischonn W (2017) MGB-IPH model for hydrological and hydraulic simulation of large floodplain river systems coupled with open source GIS. Environ Model Softw 94:1–20
3. Courant R, Friedrichs K, Lewy H (1967) On the partial difference equations of mathematical physics. IBM Journal 11:215–234
4. Bates PD, De Roo APJ (2000) A simple raster-based model for flood inundation simulation. J Hydrol 236:54–77
5. Bates PD, Horritt MS, Fewtrell TJ (2010) A simple inertial formulation of the shallow water equations for efficient two-dimensional flood inundation modelling. J Hydrol 387(1–2):33–45
6. Huang PC, Lee KT (2017) Efficient DEM-based overland flow routing using integrated recursive algorithms. Hydrol Process 31(5):1007–1017
7. Li Z, Hodges BR (2019) Modeling subgrid-scale topographic effects on shallow marsh hydrodynamics and salinity transport. Adv Water Resour 129:1–15
8. Try S, Lee G, Yu W, Oeurng C, Jang C (2018) Large-scale flood-inundation modeling in the Mekong River Basin. J Hydrol Eng 23(7):05018011
9. Liang Q, Du G, Hall JW, Borthwick AG (2008) Flood inundation modeling with an adaptive quadtree grid shallow water equation solver. J Hydraul Eng 134(11):1603–1610
10. Stelling GS (2012) Quadtree flood simulations with sub-grid digital elevation models. Proc Inst Civ Eng 165(10):567
11. Neal J, Schumann G, Bates P (2012) A subgrid channel model for simulating river hydraulics and floodplain inundation over large and data sparse areas. Water Resour Res 48(11)
12. Casulli V (2009) A high-resolution wetting and drying algorithm for free-surface hydrodynamics. Int J Numer Meth Fluids 60(4):391–408
13. Costabile P, Costanzo C, Ferraro D, Barca P (2021) Is HEC-RAS 2D accurate enough for storm-event hazard assessment? Lessons learnt from a benchmarking study based on rain-on-grid modelling. J Hydrol 603:126962
14. Zeiger SJ, Hubbart JA (2021) Measuring and modeling event-based environmental flows: an assessment of HEC-RAS 2D rain-on-grid simulations. J Environ Manage 285:112125
15. Sridharan B, Gurivindapalli D, Kuiry SN, Mali, VK, Nithila Devi N, Bates PD, Sen D (2020) Explicit expression of weighting factor for improved estimation of numerical flux in Local Inertial models. Water Resour Res 56(7):e2020WR027357
16. Nithila Devi N, Sridharan B, Bindhu VM, Narasimhan B, Bhallamudi SM, Bhatt CM, Kuiry SN et al (2020) Investigation of role of retention storage in tanks (small water bodies) on future urban flooding: a case study of Chennai City. India. Water 12(10):2875
17. Gupta AK, Nair SS (2010) Flood risk and context of land-uses: Chennai city case. J Geogr Regional Plann 3(12):365–372
18. Sekar SP, Kanchanamala S (2011) An analysis of growth dynamics in Chennai Metropolitan area. Inst Town Planners India J 8:31–57
19. Bunch MJ (2000) An adaptive ecosystem approach to rehabilitation and management of the Cooum River environmental system in Chennai, India. [dissertation]. Univ of Waterloo, Ontario, Canada

20. Suriya S, Mudgal BV, Nelliyat P (2012) Flood damage assessment of an urban area in Chennai, India, part I: methodology. Nat Hazards 62(2):149–167
21. Singh R, Arrighi J (2017) Report: rapidly growing Chennai submerged by rare extreme rainfall event. Raising Risk Awareness Initiative. Climate and Development Knowledge Network (CDKN). https://cdkn.org/resource/report-rapidly-growing-chennai-submerged-rare-extreme-rainfall-event/?loclang=en_gb Accessed on 16 Oct 2017
22. Nithila Devi N, Sridharan B, Kuiry SN (2019) Impact of urban sprawl on future flooding in Chennai city, India. J Hydrol 574:486–496

Design of Smart Geo-Sensor for Detection of Fluoride in Water Resources

Tanmay Sardar, Shivani Pandey, Satanand Mishra, and H. L. Tiwari

Abstract Water quality monitoring is a very important factor for sustainable life. In this developing world, the concentration of fluoride is increasing day by day due to urbanization, industrialization, and heavy population. Nearly 120 million communities in India have estimated the risk of fluorosis as an effect of exposure to aquas fluoride. Increased fluoride in drinkable water is a nationwide concern. About 64% of California's population on community water system receive fluorides' water. Fluoride is also detrimental to the robustness of humans. The World Health Organization (WHO) reports permissible range as 0.5–1.5 mg/L. Going beyond, this range is hazardous and treacherous. Sensing the parameter on a real-time on-field basis is an essential thing. The concept of an intelligent sensor can sense these parameters and collectively helps to monitor water resources. In this study, we have proposed the design of a smart geo-sensor for sensing the fluoride in the water. The proposed design is portable, independent, selective for fluoride and technically sound. The proposed design is simulated and optimized after designing. Smart sensor has five main components as sensing node, controlling node, alarming node, connecting node, and power node which is discussed in detail.

Keywords Smart sensor · Water quality monitoring · Fluoride · Real-time geo-sensor · Permissible range

T. Sardar
Mechanical Engineering Department, Motilal Nehru National Institute of Technology, Allahabad 211004, India

S. Pandey
Academy of Scientific and Innovative Research (AcSIR), AMPRI, Bhopal 462026, India

S. Mishra (✉)
CSIR-Advanced Materials and Processes Research Institute (AMPRI), Bhopal 462026, India
e-mail: snmishra07@gmai.com

H. L. Tiwari
Civil Engineering Department, Maulana Azad National Institute of Technology, Bhopal 462003, India

1   Introduction

Earth is a blue planet covering three-fourth of the surface by essential elements, i.e., water. About 844 million people are dealing with the scarcity of clean water [1] and 1.8 billion rely on groundwater [1–6]. Monitoring the contaminating parameters of water is one of the prime step nowadays. Water quality determines its suitability for crucial events and needs. Fluoride is a universal grave issue due its to its toxicity [6–11]. Sixty-six million Indians are at fluoride risk due to long exposure [6, 12–15]. Fluoride can cause hypersalivation, cardiac failure, nausea, convulsion, tooth decay, skeletal weakness, acne, seizures, high blood pressure, neurological problems, thyroid dysfunction, abdominal pain, and many more [9, 11, 16–20]. Removing fluoride entirely is also not a solution because fluoride under the limit prevents dental caries [21]. Keeping the fluoride in limit is a significant part of the study. The allowable limit for fluoride is 1.5 mg/L (1.5 ppm), whereas rock salt comprises 157 ppm and groundwater carries 48 ppm [20]. It is critical and essential to detect fluoride in real time.

Purification of the water is very much necessary, and so, detection of such hazardous elements is crucial. A portable real-time smart sensor has proved its valuable success in WQM by sensing the target molecules and sharing the data with the cyber world and user very effectively at the point of care. The smart sensing module splits into five nodes as shown in Fig. 1 and discussed in this section.

- Sensing node: The most varying and important part of the sensor is the sensing node. It consists of sensor, as a transducer and signal conditioning for quality signals.
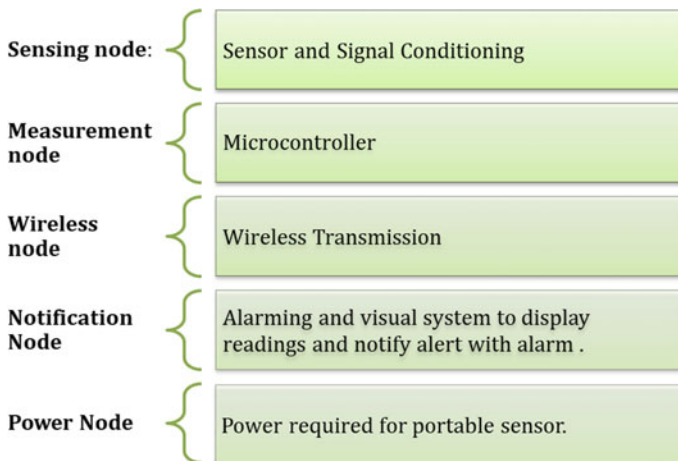
Fig. 1   Architecture of smart sensing module

- Measurement node: Sensed parameters are converted into measurable values with the help of a microcontroller. The microcontroller is also used to control the flow of the sensing procedure.
- Wireless node: Networking tools like WIFI, Bluetooth, UWB are popular for communication nowadays. The proposed design uses Bluetooth module tool.
- Notification node: It is an alarming node for a quantitative study, and it also shows calculated parameters on screen.

This paper is about the design of a smart and real-time portable optical sensor for the detection of fluoride in drinking water. The proposed design is the combination of different nodes for point of care.

2 Methodology

In Fig. 2, explanation of different steps required to complete the study is shown, which includes material, phenomenon, different parts, designing, and simulation. The target molecule was fixed as fluoride (F). Different parts of the intelligent sensor have been studied according to our needs. This design selected modified carbon quantum dots (CQDs) based on the selectivity for fluoride.

Based on receptor material, the fluorescence quenching phenomenon was selected and found perfect [22]. All other parts and components are selected accordingly, and modeling is done with the help of SolidWorks. STL file was ready to print in a 3D printer after slicing. Microcontroller Arduino Nano is chosen for the process of parameters' calculations of the sensing units and control them. In the alarm and notification node, LCD panel and Bluetooth module are placed appropriately in the
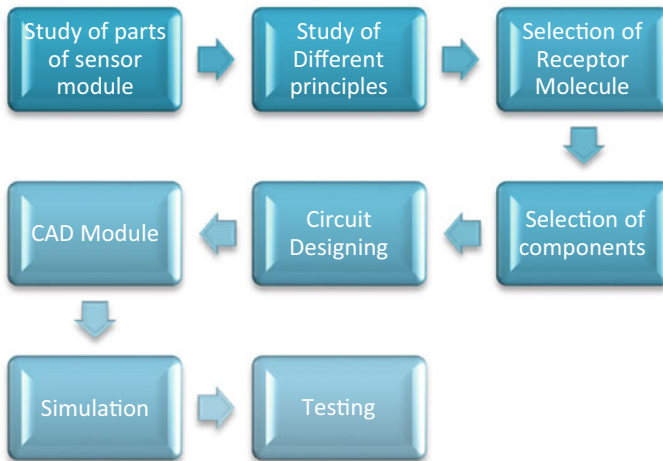
Fig. 2 Methodology chart

structure for display and communication, respectively. This assembly required 7–12 V and 150 mA according to the calculation. So, we have attached 5 AA batteries as a power source. The design is simulated before the 3D print.

3 Sensing Module Modeling

The module is a combination of five parts and their interface. The design is modeled with the help of "SolidWorks-2016" software. Different parts are designed separately and then assembled. The total structure is made up of fused deposition modeling (FDM) 3D printer.

3.1 Receptor Material

For more sensitivity for sensors, we have moved toward the quantum world. Selective receptor means molecules that attract the selected target molecule. Carbon quantum dots (CQDs) are selected for the process after reviewing different researchers [22–24]. Quantum dots are nanocrystals that inherently give fluorescence at specific wavelengths in the visible spectrum enabling sensing applications. CQD can be synthesized in a variety of ways. The importance of glucose, HCL, coffee bean, graphite, carbon fibers, and other biological sources is growing for many applications [25]. Receptor material for the proposed design is synthesized from the waste material of the crop that is wheat straw. Waste material management was one of the objectives for a green environment. The designed structure is highly selective for the fluoride compound. Figure 3a shows the fluorescence quenching effect of the receptor at different concentrations of fluoride. Figure 3b show a correlation value of 0.994, and a good linear connection was established in the spectrum of 0–1.5 mM. The detection limit (LOD) was calculated to be around 49 μM.

3.2 Components of the Sensing Node

The sensing node can be divided into three main sections that are a source, cuvette, and detector units. The sensing node section consists of the light emitting diode emitting violet band, cuvette (20 × 20 mm), and light detector as main components. The light from the point source is converged using lenses with a focal length of 1.6 cm. The light is absorbed by the receptor within the cuvette and utilized to induce excitation. Further, the receptor emits light with a higher wavelength which is detected by the detector. The detector detects and transfers the induced signal data to a microcontroller for further process.
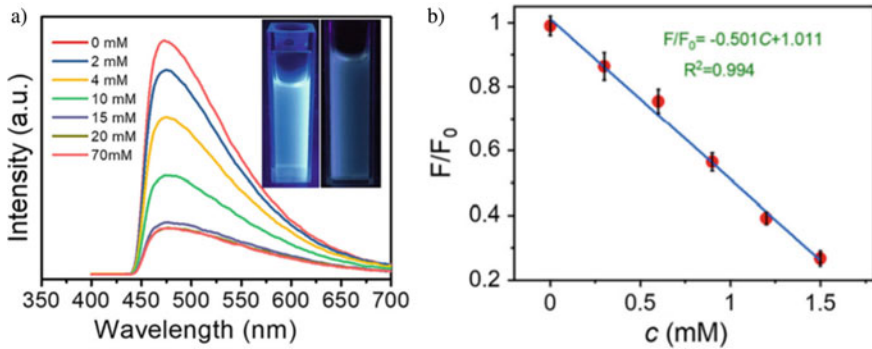
Fig. 3 **a** Fluorescent emission spectra of receptor CDs **b** relationship between F/F0 and concentrations of F—from 0 to 1.5 mM [22]

The geo-based real-time sensor has huge potential to monitor and maintain different water resources [26–28]. Once the recent contamination level of the water is sensed and stored securely on cloud referring to specific latitude and longitude, that can be useful data for the community. The Global Positioning System (GPS) has revolutionized global communication. For a wide range of applications, GPS is the quickest and most precise approach [27, 29–32]. Inbuilt GPS can be used with the help of smartphone-based applications (SBAs), and external GPS modules also can be connected to the proposed sensor [27, 33, 34].

3.3 Measurement Node

The microcontroller is placed below the above setup and powered by a battery after calculations. Arduino Nano works on 5v, and I/P volt is 7.5 V with 32 KB flash memory and ATmega328 processor. The signal from the photo-sensing node is between 0 and 40 mA [35–37]. The signal is converted to measuring values of fluoride in water and further process to share. The flow of the process is controlled and instructed by coding, which is uploaded with Arduino software IDE (1.8.13) via micro-USB.

3.4 Wireless Node

The concept of wireless networking system (WNS) is resolved with Bluetooth module HC-05. On the opposite facet of the display unit, the design has triggered Bluetooth (HC-05) for communication purposes with the mobile. The cellphone-based network helps the sensor to connect with the cyber world and share the required parameters [38–40].

	RED	Above 1.5 ppm	Non Drinkable water	Super Danger Zone
	GREEN	0.5 to 1.5 ppm	Drinkable water under the limit given by WHO	Neutral Zone
	YELLOW	0 TO 0.5 ppm	Drinkable water in absence of alternative source	Avoiding Zone

Fig. 4 Graphical abstract for alarming zones

3.5 *Alarming Node*

LCD display (16 × 2 LCD display module no.ADM1602K-NSW-FBS/3.3 V) [41, 42] is placed on one of the longest faces. I2C interface module (I2C product code: EC-2114 LCD module) is connected for simplicity [43, 44]. It will convert 16 pins to 4 pins and helps for compact wire designing. According to the human health parameters, the contamination range is divided into three parts. The permissible range is 0.5–1.5 ppm for a healthy community. Figure 4 shows the graphical abstract of the alarming node, which express different zones according to the contamination limit. The green zone is a safe and neutral zone best for potable water.

4 Result

In this study, an accurate design of the optical sensing device is given. The proposed design is modeled in SolidWorks and simulated on different platforms. Figure 5 shows the proposed design. The proposed design has its sensing node on the top of the model and the power node as the base. Microcontroller, communication, and display nodes are the supporting pillar for the design.

Drop test is a simulation for the most dominant failure of portable products [45, 46]. For the long life of the product, it is necessary to ensure the safety of the device and the different parts in it. While working, the falling of devices from the table or hands is commonly observed [45–49]. According to ergonomics, standing elbow height is 100 cm on average. Height for drop test-I is ensured 3.28 ft. Components like lenses, LED, light detectors are very sensitive components. It is important to ensure the safety of these components. The device is impacted on this critical side of design for testing purposes. The device is impacted on a rigid target with a deacceleration of 9.81 m/s^2. ABS material was available and compatible for the print in Creality Ender 3. ABS material is used for printing the device with a strength 35 MPa. From Fig. 6,
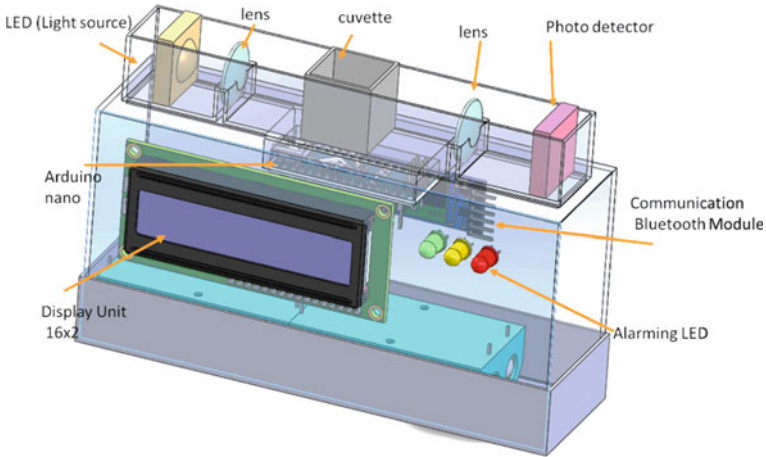
Fig. 5 CAD of a proposed design

it can be concluded that the device is safe for the impact test. Drop test-II is also conducted with the same setup and from the height of 5 ft. Test-II is also observed safe.

The proposed opto-chemical design is effective with the help of electrical components like Arduino, LED, Detector, LCD panel, external GPS, and Bluetooth module. The interfacing of the components with each other is the important part. The final simulation with all parts is shown in Fig. 7. The circuit simulation is performed on different platforms.
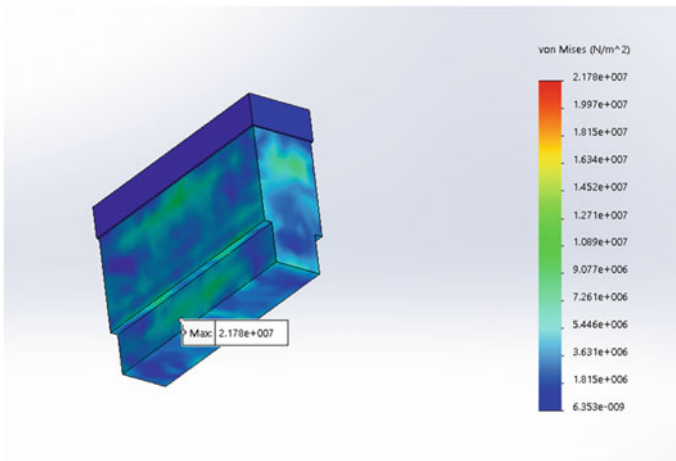
Fig. 6 Drop test simulation for a proposed design
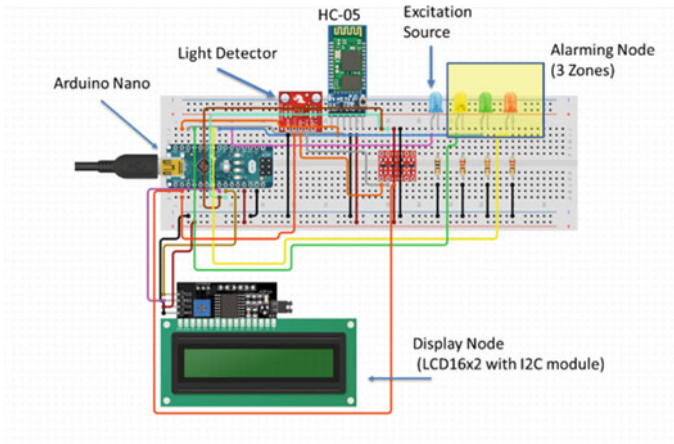
Fig. 7 Circuit simulation for proposed sensor

5 Conclusion

The proposed design fulfills the prime objective to sense the aquas fluoride for WQM. The proposed design is found to be safe in the drop test for 5ft. The interfacing of the different components is done accurately. The proposed sensor is selective for fluoride. The proposed design is a cost-effective, sensitive, portable Opto-biosensor in a range of 0–70 mM with LOD of 49 μM. The sensing probe is reusable so the device is valued for one-time money. In order with portability, the proposed design is light weighted and compact in nature for real-time field use. The proposed design is optimized and simulated for the drop test. The proposed design is simulated for ABS and PLA material. The designed circuit is also simulated with codding with different platforms.

6 Future Work

The sensor development field is moving to the next level. We plan to develop the design and introduce optical fiber modeling based on the fluorescence phenomenon. For the future, we are also planning to develop a special mobile application to carry out the process smoothly and record appropriately.

References

1. Cerro C, Developing solutions for dealing with water and food scarcity: atmospheric water generator and urban farm tower. In: 2018 advances in science and engineering technology international conferences, Aset, pp 1–6. https://doi.org/10.1109/Icaset.2018.8376754
2. Hartley K, Biswas AK, From evidence to policy in India's groundwater crisis
3. Egeruoh-Adindu I, Anozie I (2018) Water scarcity and underground water pollution in Africa. Nigerian Law J 21
4. Panwar M, Panwar AM, Antil MS (2015) Issues, challenges and prospects of water supply in urban India. Iosr J Human Soc Sci 20(5):68. https://doi.org/10.9790/0837-20526873
5. Khanna A (2020) Int J Soc Sci Econ Res Overview Technol Driven Solut Water Crisis Devel Nations. https://doi.org/10.46609/Ijsser.2020.V05i05.013
6. Mukherjee I, Singh UK (2018) Groundwater fluoride contamination, probable release, and containment mechanisms: a review on Indian context. Environ Geochem Health 40(6):2259–2301. https://doi.org/10.1007/S10653-018-0096-X
7. Ranjan R, Ranjan A (2015) Fluoride toxicity in animals. https://doi.org/10.1007/978-3-319-17512-6
8. Ranjan R, Ranjan A (2015) Sources of fluoride toxicity 11–20. https://doi.org/10.1007/978-3-319-17512-6_2
9. Mcivor ME (2012) Acute fluoride toxicity. Drug Saf 5(2):79–85. https://doi.org/10.2165/00002018-199005020-00001
10. Rao N (2003) Fluoride and environment-a review, 15–17
11. Kanduti D, Sterbenk P, Artnik B (2016) Fluoride: a review of use and effects on health. Materia Socio-Medica 28(2):133. https://doi.org/10.5455/Msm.2016.28.133-137
12. Vennila S, Soorya V (2012) Fluoride contamination in drinking water in Palacode Region, Tamil Nadu. Int J Res Chem Environ 2:116–123
13. Chakraborti D et al (2016) Fate of over 480 million inhabitants living in arsenic and fluoride endemic Indian Districts: magnitude, health, socio-economic effects and mitigation approaches. J Trace Elements Med Biol 38:33–45. https://doi.org/10.1016/J.Jtemb.2016.05.001
14. Adimalla N, Li P, Qian H (2018) Evaluation of groundwater contamination for fluoride and nitrate in semi-arid region of Nirmal Province, South India: a special emphasis on human health risk assessment (Hhra) 25(5):1107–1124. https://doi.org/10.1080/10807039.2018.1460579
15. Kisku GC, Sahu P (2020) Fluoride contamination and health effects: an Indian scenario. Environ Concerns Sustain Develop 213–233. https://doi.org/10.1007/978-981-13-5889-0_11
16. Ozsvath DL (2008) Fluoride and environmental health: a review. Rev Environ Sci Bio/Technol 8(1):59–79. https://doi.org/10.1007/S11157-008-9136-9
17. Shaik N, Shanbhog R, Nandlal B, Tippeswamy HM (2019) Fluoride and thyroid function in children resident of naturally fluoridated areas consuming different levels of fluoride in drinking water: an observational study. Contemp Clin Dentistry 10(1):24. https://doi.org/10.4103/Ccd.Ccd_108_18
18. Denbesten P, Li W (2011) Chronic fluoride toxicity: dental fluorosis. Monographs Oral Sci 22:81–96. https://doi.org/10.1159/000327028
19. Unde MP, Patil RU, Dastoor PP (2018) The untold story of fluoridation: revisiting the changing perspectives. Indian J Occupational Environ Med 22(3):121. https://doi.org/10.4103/Ijoem.Ijoem_124_18
20. Del Bello L (2020) Fluorosis: an ongoing challenge for India. Lancet Planetary Health 4(3):E94–E95. https://doi.org/10.1016/S2542-5196(20)30060-7
21. Štepec D, Ponikvar-Svet M (2019) Fluoride in human health and nutrition. Acta Chimica Slovenica 66(2):255–275. https://doi.org/10.17344/Acsi.2019.4932
22. Liu S et al (2021) Facile synthesis of carbon dots from wheat straw for colorimetric and fluorescent detection of fluoride and cellular imaging 246:118964. https://doi.org/10.1016/J.Saa.2020.118964

23. Udhayakumari D (2020) Detection of toxic fluoride ion via chromogenic and fluorogenic sensing. A comprehensive review of the year 2015–2019. Spectrochimica Acta - Part A: Molecular and Biomolecular Spectroscopy, 228. https://doi.org/10.1016/J.Saa.2019.117817

24. Li ZY et al (2018) Calix[4]Arene containing thiourea and coumarin functionality as highly selective fluorescent and colorimetric chemosensor for fluoride ion. Spectrochimica Acta—Part A: Molecular Biomolecular Spectroscopy 200:307–312. https://doi.org/10.1016/J.Saa.2018.04.040

25. Huang C, Dong H, Su Y, Wu Y, Narron R, Yong Q (2019) Synthesis of carbon quantum dot nanoparticles derived from byproducts in bio-refinery process for cell imaging and in vivo bioimaging. Nanomaterials 9(3):387. https://doi.org/10.3390/Nano9030387

26. Sicard C et al (2015) Tools for water quality monitoring and mapping using paper-based sensors and cell phones. Water Res 70:360–369. https://doi.org/10.1016/J.Watres.2014.12.005

27. Gao X, Wu N (2016) Smartphone-based sensors. Electrochem Soc Interface 25(4):79–81. https://doi.org/10.1149/2.F07164if

28. Vikesland PJ (2018) Nanosensors for water quality monitoring. Nat Nanotechnol 13(8):651–660. https://doi.org/10.1038/S41565-018-0209-9

29. Radoglou-Grammatikis P, Sarigiannidis P, Lagkas T, Moscholios I (2020) A compilation of uav applications for precision agriculture. Comput Netw 172:107148. https://doi.org/10.1016/J.Comnet.2020.107148

30. Norasma CYN, Fadzilah MA, Roslin NA, Zanariah ZWN, Tarmidi Z, Candra FS (2019) Unmanned aerial vehicle applications in agriculture. Iop Conf Series: Mater Sci Eng 506(1):012063. https://doi.org/10.1088/1757-899x/506/1/012063

31. Sahu B, Chandra B, Viswavidyalaya K, Chatterjee S, Mukherjee S, Sharma C (2019) Centre for advanced agricultural science and technology (Caast) on conservation agriculture (Icar-Nahep) view project

32. Pule M, Yahya A, Chuma J (2017) Wireless sensor networks: a survey on monitoring water quality. J Appl Res Technol 15(6):562–570. https://doi.org/10.1016/J.Jart.2017.07.004

33. You M et al (2017) Household fluorescent lateral flow strip platform for sensitive and quantitative prognosis of heart failure using dual-color upconversion nanoparticles. ACS Nano 11(6):6261–6270. https://doi.org/10.1021/Acsnano.7b02466

34. L Z et al (2017) A 3d printed smartphone optosensing platform for point-of-need food safety inspection. Anal Chim Acta 966:81–89. https://doi.org/10.1016/J.Aca.2017.02.022

35. Sharma V (2020) Arduino based smart water management. Int J Eng Res V9(08). https://doi.org/10.17577/Ijertv9is080239

36. Gokulanathan S, Manivasagam P, Prabu N, Vidya S, Gsm based water quality monitoring system using arduino a gsm based water quality monitoring system using Arduino. https://doi.org/10.34293/Sijash.V6i4.341

37. Leela Vathi V, Aravind V (2021) Solar power and water quality monitoring using wireless sensor network with zigbee. Lecture Notes Electric Eng 673:737–746. https://doi.org/10.1007/978-981-15-5546-6_61

38. (Pdf) A Comparative Study Of Wireless Protocols: Bluetooth, Uwb, Zigbee, And Wi-Fi. https://www.researchgate.net/publication/312471356_a_comparative_study_of_wireless_protocols_bluetooth_uwb_zigbee_and_wi-fi. Accessed 15 Sep 2021

39. Hc-05 Bluetooth Module Hc-05-Bluetooth To Serial Port Module (2010)

40. Bhat M, Chawla A, Bangera T, Kolwalkar C, Engineering T, Mumbai U (2015) Bluetooth based weather station article. Int J Eng Trends Technol 28(2). https://doi.org/10.14445/22315381/Ijett-V28p219

41. (Pdf) Adm1602k-Nsw-Fbs Datasheet—Lcd Module. http://www.datasheet.es/pdf/905645/adm1602k-nsw-fbs-pdf.html. Accessed 30 Sep 2021

42. Bott R (2014) Specification of lcd module. Igarss 2014(1):1–5

43. Interface I2c 16x2 Lcd With Arduino Uno (Just 4 Wires)—Arduino Project Hub. https://create.arduino.cc/projecthub/akshayjoseph666/interface-i2c-16x2-lcd-with-arduino-uno-just-4-wires-273b24. Accessed 30 Sep 2021.

44. I2c Module For 16x2 (1602) Character Lcd Buy Online At Low Price In India—Electronic-scomp.Com. https://www.electronicscomp.com/i2c-module-16x2-lcd-India. Accessed 30 Sep 2021
45. Josserand C, Thoroddsen ST (2016) Drop impact on a solid surface. Ann Rev Fluid Mech 48:365–391. https://doi.org/10.1146/Annurev-Fluid-122414-034401
46. Wu J, Song G, Pin Yeh C, Wyatt K (1998) Drop/impact simulation and test validation of telecommunication products. Thermomechanical phenomena in electronic systems -proceedings of the intersociety conference, 330–336. https://doi.org/10.1109/Itherm.1998.689582
47. Blanken N, Saleem MS, Thoraval MJ, Antonini C (2021) Impact of compound drops: a perspective. Curr Opin Colloid Interface Sci 51:101389. https://doi.org/10.1016/J.Cocis.2020.09.002
48. Arriaga A, Pagaldai R, Zaldua AM, Chrysostomou A, O'brien M (2010) Impact testing and simulation of a polypropylene component. Correlation with strain rate sensitive constitutive models in ansys and ls-Dyna. Polymer Testing 29(2):170–180. https://doi.org/10.1016/J.Polymertesting.2009.10.007
49. González EV et al (2018) Simulating Drop-weight impact and compression after impact tests on composite laminates using conventional shell finite elements. Int J Solids Struct 144–145:230–247. https://doi.org/10.1016/J.Ijsolstr.2018.05.005

Understanding the Impact of Agricultural Fertilizer Application Over Inflows into Nagarjuna Sagar Reservoir

K. Tarun Teja and K. S. Rajan

Abstract Excessive nutrient loading into the inland water bodies and resulting algal blooms have been a major threat to the water quality of the inland water bodies such as lakes and reservoirs where the water is relatively stagnant for longer duration. To improve the conditions, it is essential to study and understand the role of the contributing factors in increasing the nutrient load coming into the water body from the watershed. In general, the excessive usage of inorganic (NPK) fertilizers are considered to be the spearhead behind the increasing nutrient output from the watershed, but their impact has not been well evaluated due to several constraints. So, this study tries to evaluate the role of the fertilizer application on the nutrient yield from the watershed into an inland water body. Nagarjuna Sagar reservoir and its contributing watershed were modelled and analysed using the Soil and Water Assessment Tool (SWAT) model. The temporal land use data from NRSC (2005 to 2017) and fertilizer application data for the same duration have been used to evaluate the role of fertilizers on the nutrient output from the watershed. Total nitrogen (TN) output from the watershed was used as proxy to understand the relationship between the contributing factors and the nutrient yield. This research used two land use conditions, namely business as usual with fertilizers (BAUF) and business as usual without fertilizers (BAUNF) to simulate the effect of the fertilizer application on TN yield effectively. The assessment showed that the usage of fertilizer from 2005 to 2017 has increased manifold and has had a deteriorating impact on the water body through an increase in the TN yield output by several times. From the SWAT model, the maximum annual TN output from NS contributing watershed under BAUNF and BAUF conditions were 247 and 759 tonnes, respectively, a nearly 204% increase. This indicates that uncontrolled use of the inorganic fertilizer combined with changing land use can have a negative impact on the water quality by increasing nutrient output from the contributing watershed.

K. T. Teja (✉) · K. S. Rajan
Lab for Spatial Informatics, IIIT-Hyderabad, Hyderabad 500032, India

K. S. Rajan
e-mail: rajan@iiit.ac.in

Keywords SWAT model · Inland water body water quality · Fertilizer application · Nagarjuna Sagar

1 Introduction

Freshwater resource is an extremely scarce resource and have to be managed and utilized properly to have sustained growth. Recent trends in water usage points out to over exploitation of these resources by various sectors resulting in the aggravated water scarcity [11, 19]. In addition, increasing inland water body contamination due to the mismanagement of untreated water from these sources has turned out to be a major reason for limiting freshwater availability towards various applications resulting in various socio-economic problems [11]. Recent studies by [1–3, 7, 12, 20] have observed rapid decline in the water quality of several water bodies spread across the world and pointed out that the nutrient contamination is a major threat to the fresh water bodies. Nutrient contamination is a natural phenomenon, but excess amount of nutrients or nutrient rich water accelerate the growth of photosynthetic algae, phytoplankton and cyanobacteria (AP) and under supportive conditions could result in harmful algal blooms [17]. These AP blooms could cause severe damage to the water quality, flora and fauna of the water bodies especially in lakes and reservoirs as they are more susceptible due to stagnation of water for longer durations [9]. So to improve water availability by improving water quality, it is important to regulate contamination levels in the water body and one way to achieve this is by reducing the incoming nutrient content from the contributing watershed.

To manage the incoming contamination flow, it is vital to understand the contributing factors for the contamination. Works from [6, 8, 10, 12, 16, 21, 22] showed that there are several causes of nutrient contamination in the water bodies, including the land use and indicated that the agricultural land use is one the most prominent factor. Though these works were crucial, they fail to bring forth the role of individual processes of agricultural land use such as crop management and agricultural inputs like fertilizers on the production of nutrient content in the watershed. This is important because the agricultural land use and practices remained from several centuries and the water bodies copped with the contamination levels in the water, but it is only in the recent decades that water bodies started showing adverse effects of the nutrient contaminants. It is important to find out what is causing these changes, this analysis could prove vital as it will improve the current understanding on the role of each underlying process on contaminant production and help in controlling their output in future. An earlier study by the authors [11] studied the role of increasing agricultural land use and fertilizer application on the nutrient contamination in Nagarjuna Sagar (NS) a large inland multipurpose reservoir and identified that fertilizer may be a major contributor to the nutrient production in the contributing watershed. Though this is helpful, this comparison was done more on a qualitative perspective and needs further quantitative assessment to understand the relationship in a better way.

To understand this relationship better, it is important to assess two things. First it is necessary to analyse the impact of fertilizer application on nutrient production in the contributing watershed of NS, and the second is to study how much of the excess nutrient content is being carried into the waterbody by various processes happening in the watershed. While the second segment is very important, it is very hard to control all the processes that lead to nutrient movement from the watershed to the water body. So, studying the first segment is extremely vital as it can be easily assessed and regulated. Further, if it is assumed that most of the nutrient yield from the NS watershed ends up in the water body, then understanding the correlation between fertilizer application and nutrient output is even more important. So, the fertilizer induced nutrient generation in the watershed can be directly used to assess the impact of fertilizer on inland water quality. Hence, the current study focused on analysing the influence of fertilizers and used sensitivity analysis by estimating and comparing the nutrient yield from the contributing watershed in the presence and absence of the fertilizers under the same land use and other pan watershed conditions.

Since the study involves sensitivity analysis that needs accurate replication of all the processes happening across the watershed, a multitude of calculations and simulations must be run several times over and over. So, applying process-based hydrological models would be beneficial. These models could precisely simulate various underlying interactions between several feature and parameter of the watershed and accurately predict the nutrient output from the watershed. In addition, once the model is setup, it can also be extended to run further simulations under diverse conditions that could arise in future to simulate their impact on water quality. Works from [4, 5, 8, 13–15, 18, 23–25] suggested that Soil and Water Assessment Tool (SWAT) is one of the best hydrological models for studying the nutrient production and movement in the watershed. In this work, total nitrogen (TN) was used as a reference for studying the nutrient production from the NS watershed at various conditions. This is due to the reason that all gauging stations in the Krishna basin where water quality is checked, report only the in-stream nitrate (NO_3) content and only this parameter can be used to calibrate the model. So, using the TN values where NO_3 plays a major role is the best practice. Hence, this study used the SWAT model to estimate the TN yield from the NS watershed in the presence and absence of fertilizer usage under same land use and other watershed conditions to understand the impact of fertilizer on water body contamination.

2 Study Area

Krishna River is one of the most important rivers in India, and it originates in the Mahadev range (1337 m elevation) of the Western Ghats. The river moves from west to east direction passing through four states, Maharashtra Karnataka, Telangana and Andhra Pradesh. Krishna River has two main tributaries namely Bhima and Tungabhadra and 11 smaller tributaries with total water potential of 78,120 million cubic metres (MCM). Krishna River with all its tributaries hosts around a collection

of 33 large, medium and small reservoirs along its path as of 2018 bringing the live
storage capacity to 50,117 MCM and soon add another 4287 MCM after completion
of projects that are under construction. Out of these reservoirs, Nagarjuna Sagar
reservoir is one of the biggest reservoirs.

Figure 1 shows the Krishna basin along with the Nagarjuna Sagar basin. Nagarjuna
Sagar (NS) reservoir is a multipurpose reservoir constructed in 1972. NS reservoir is
used for providing irrigation water, drinking water and for generating hydropower. NS
has a maximum water spread area of 285 Km^2 holding up to 2208 m^3 of water which
is used to provide the necessary water for a catchment year of 215,000 km^2. NS has
two major inflowing rivers namely Pedda Vagu and River Krishna. NS also has two
irrigation canals connected to it from neighbouring water bodies. Agriculture land
use in the Northwest upstream direction has become a primary land use around this
reservoir. Hydroelectricity generation is another important service that this reservoir
provides along with tourism. NS is surrounded by deciduous forest in the South and
Southwest direction where Krishna River joins NS.

3 Methods

The Krishna River has many in situ monitoring stations along the river, but most of
these points do not record water quality. The water quality data from these monitoring
stations is important as they provide the NO_3 concentration data in the river stream
which is essential for the SWAT model calibration. Only a limited number of locations
have these facilities, and the closest one to the NS is Wadenapally gauge station (See
Fig. 1) which is outside the NS watershed. So, instead of NS watershed the SWAT
model was setup for the entire Krishna basin and after calibration, the same model
was used study the NS watershed TN output. So, all the necessary datasets for the
Krishna River basin were collected from various sources.

SWAT model is semi-distributed hydrological model that is dependent on preci-
sion datasets to simulate various watershed parameters accurately. Further, SWAT
model needs run in periods, calibration and validation process to setup the model
before using it for predicting the TN yield. Table 1 shows the input files used in
the work along with their sources. SWAT mainly needs weather data to simulate
the hydrological cycle; in this work, the precipitation and temperature datasets from
Indian Meteorological Department (IMD) were used at the scale of 0.25 degree
and 1 degree, respectively. In addition, the model also requires land use data, soil
data and terrain slope data to model the percolation and movement of the water on
the surface. Land use data at 1:250,000 scale was collected from National Remote
Sensing Centre (NRSC), and the major classes of the data are agriculture land, fallow
land, deciduous forests, degraded forests, built up area, wasteland and water bodies.
World soil data was collected from Food and Agricultural Organization of United
Nations (FAO). Slope of the terrain was calculated using the 30 m digital elevation
model (DEM) data from ASTER satellite. The DEM is one of the most important
input data that SWAT needs for delineating the boundary of the Krishna basin and NS
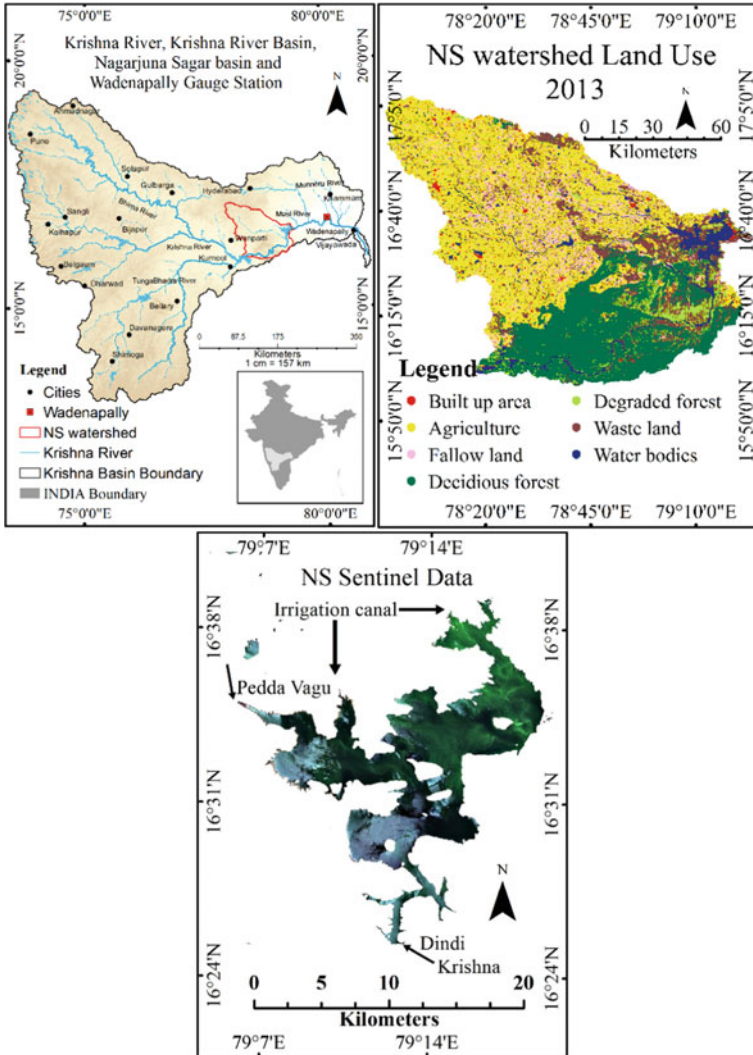
Fig. 1 Krishna River, Krishna River basin (left) along with the Wadenapally gauge station and major cities locations, land use in Nagarjuna Sagar watershed (centre) and Nagarjuna Sagar water spread (NS)(right)

watershed. In addition to these essential datasets, the model used in this study was incorporated with water usage, land use intensity information like crop and fertilizer usage details collected from literature and Central Research Institute for Dryland Agriculture (CRIDA), respectively, to improve the nitrate and TN simulation efficiency. The fertilizer data was collected at district level. Nagarjuna Sagar watershed comprises of Mahbubnagar and Nalgonda districts so in this the fertilizer application

Table 1 Information about the input files used in the work along with their sources

SWAT model set up and TN yield estimation

Input data for SWAT model

Data used	Source	Link	Resolution
1. Weather data	IMD	https://imdpune.gov.in/clim_pred_lrf_new/grided_data_download.html	PCP 0.25 and Temp 1 degree
2. Land use data	NRSC	https://imdpune.gov.in/clim_pred_lrf_new/grided_data_download.html	1:250,000 scale
3. Soil data	FAO-UNESCO	http://www.fao.org/soils-portal/data-hub/soil-maps-and-databases/harmonized-world-soil-database-v12/en/	1: 5,000,000 scale
4. Basin water usage	Literature		
5. Reservoir data	India-WRIS	https://indiawris.gov.in/wris/#/	Monthly scale
6. Crop management	CRIDA	http://icar-crida.res.in/	Monthly scale
7. Fertilizer management	CRIDA	http://icar-crida.res.in/	Monthly scale
8. Digital elevation model (DEM)	ASTER	http://www.earthexplorer.usgs.gov	30 m

from these two districts was to understand the impact of fertilizer on water quality. Urea was considered as a proxy for inorganic fertilizer application as it is mostly widely used fertilizer for agricultural purposes.

Figure 2 shows the flow of the study. Using the input datasets, the initial model was established. Since the river flow is a major component of the hydrological cycle and because it has the capacity to represent the hydrological process happening in the watershed quite accurately, the model must be fine-tuned so that the simulated flow will match with the observed flow. So, the flow simulated from the model was calibrated and validated and later the nutrient concentration in the river network at Wadenapally was also calibrated using the observed nitrate concentration. SWAT CUP was used to calibrate the flow and in-stream nitrate concentrations simulated by the SWAT model. Since the flow and in-stream nitrate concentration of the entire Krishna basin is calibrated, it can also be considered that the output of these parameter from various watersheds inside the basin can also be considered as calibrated. So, the output from these parameters from NS watershed can also be considered as calibrated and this TN output from this watershed can be used for further analysis.

After calibration and validation, the TN yield from NS watershed was estimated under business as usual (BAU) conditions from 2005 to 2017 using the corresponding land use data. The land use data is available for every alternative year, so the study analysed TN output from Nagarjuna Sagar watershed for every alternative year from

Fig. 2 Shows the process
followed by the study

SWAT model initial setup

Flow calibration and Validation

In stream Nitrate (No^3) concentration

Compare TN yield from 2013 and 2017 with and without fertilizer usage

Study the impact of fertilizers on TN yield
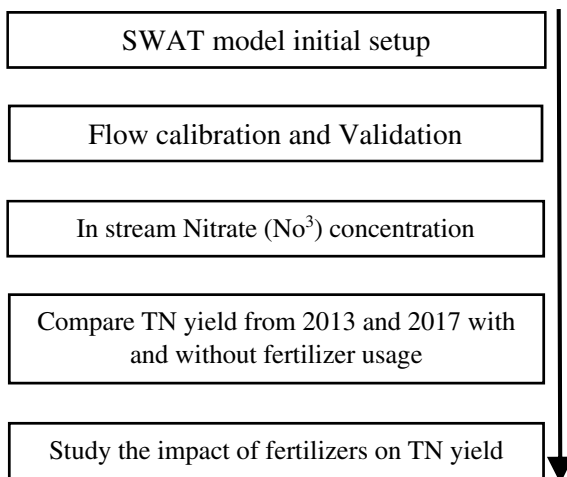
2005 to 2017. In BAU condition which is the current land use conditions, some agricultural field may apply fertilizer, and some may not. Since the data at field scale not available, it was assumed that all an average fertilizer amount is used across the watershed and hereafter this scenario will be noted as BAU with fertilizer application (BAUF). In the second scenario, it is assumed that there is no application of inorganic fertilizers, and hereafter, this condition will be called as BAU without fertilizer applications (BAUNF). In the BAUF scenario, the model simulated TN output using BAU land use data with the respective fertilizer application intensity and crop management data. In the BAUNF scenario, the same simulation was carried out with same setting but without fertilizer data and the TN output was recorded. Later, the TN production from NS watershed under these two conditions were compared to understand the impact of fertilizers on the TN production. The results of this analysis are presented below.

4   Results and Discussion

From the initial setup of the model, the simulated flow in the Krishna River from 2007 to 2017 was compared against the observed flow at Wadenapally gauge station. The initial results had an R^2 of 0.2 and highlighted that there is a need to calibrate the model for improving the flow estimates. Hence, the model was calibrated and validated using SWAT CUP which resulted in R^2 value of 0.71 (See Fig. 3). The model was then calibrated for the in-stream nitrate concentration so that the model predicts the TN output from the watershed with better accuracy. So, the study calibrated nitrate concentration simulated at Wadenapally from 2013 to 2016 against the observed data using the SWAT CUP tool. The R^2 for in-stream nitrate concentration has come to 0.70 (See Fig. 3). The parameters used for the flow calibration using SWAT CUP are

mainly concerned with increasing ground flow, reducing the surface flow either by increasing evapotranspiration or percolation and manipulating surface lag. Similarly, the parameter used for nitrate calibration deal with regulating the de-nitrification and nutrient uptake by the crops. The results of the calibration of the model are shown in Fig. 4.

This calibrated model was used to simulate the TN yield from NS watershed in BAUF and BAUNF conditions and were compared against each other. The results of this analysis are shown in Fig. 4. Form the figure, the contaminants output under the BAUF land use scenario with the current land use and fertilizer application
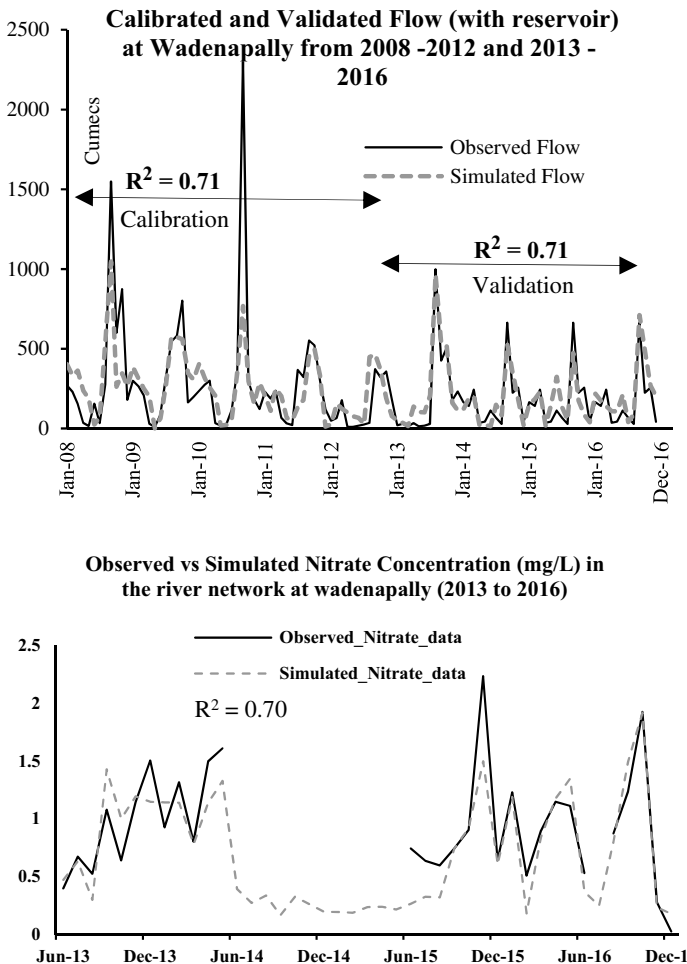
Fig. 3 Calibration and validation of simulated flow against observed flow at Wadenapally from 2008 to 2012 and 2013 to 2016, respectively, (top) and it also shows the comparison (bottom) between observed and simulated nitrate concentration at Wadenapally

Simulated Total Nitrate output from the NS contributing watershed under various land use scenarios (2005 to 2017)
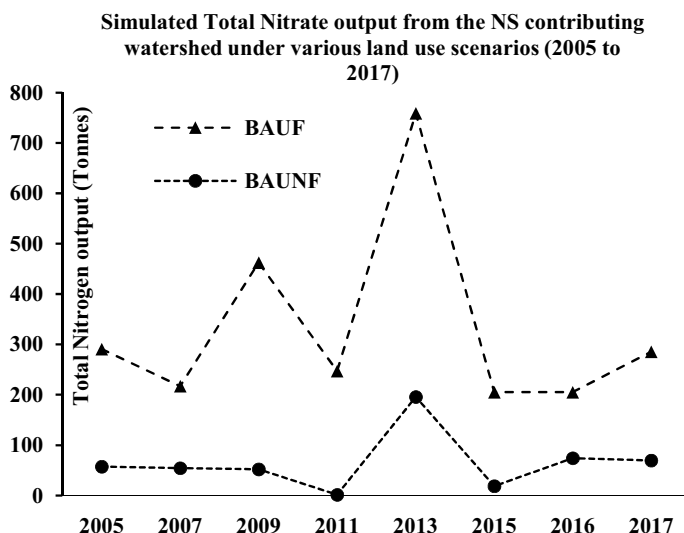
Fig. 4 Simulated TN yield from NS watershed during the presence and absence of fertilizer

conditions showed that that the maximum yield of TN was around 759 Tonnes. Similarly, the maximum TN output in the BAUNF scenario, where the agricultural land use remained same, but application of the fertilizers was limited to only minimal organic fertilizers, was 247 tonnes. This shows that TN output has decreased by three times due the effect of the non-application of the fertilizers. This analysis shows that along with the agricultural land use, the application of fertilizers has a major impact on the inland water body's water quality as it influences the production of the contaminants from the watershed. This increase in the TN production would negatively impact water quality in the NS water body as the nutrient input to the water body is directly proportional to the nutrient production in the contributing watershed. Hence, it is essential to regulate the fertilizer usage and control the contaminant production.

5 Conclusion

The study analysed the impact of the fertilizer application on the TN output from the NS watershed in Krishna River basin using calibrated SWAT model. To achieve this, the SWAT model was calibrated for the river flow and in-stream nitrate content in the river across the entire Krishna basin using the observed data collected at the Wadenapally gauge station. The R^2 value achieved during the calibration process for the flow and nitrates is 0.71 and 0.70, respectively. This calibrated model was used to simulate TN production from NS watershed under two conditions—business as usual with fertilizer application (BAUF) and business as usual with no inorganic

fertilizer application (BAUNF) from 2004 to 2017. The results showed that for the similar conditions of land use, weather and other inputs, change in fertilizer intensity levels could increase the TN output by over three times from 247 tonnes without fertilizer to 759 tonnes with fertilizers. This could directly impact the nutrient content reaching the NS reservoir and cause devastating algal blooms impact water quality drastically. Hence, there is a necessity for controlled usage of the artificial fertilizers in the contributing watershed.

References

1. Arto I, Andreoni V, Rueda-Cantuche JM (2016) Global use of water resources: a multiregional analysis of water use, water footprint and water trade balance. Water Resour Econ 15:1–14. https://doi.org/10.1016/j.wre.2016.04.002
2. Bhagowati B, Ahamad KU (2018) A review on lake eutrophication dynamics and recent developments in lake modeling. Ecohydrol Hydrobiol. https://doi.org/10.1016/j.ecohyd.2018.03.002
3. Bhateria R, Jain D (2016) Water quality assessment of lake water: a review. Sustain Water Resour Manage 2(2):161–173. https://doi.org/10.1007/s40899-015-0014-7
4. Daniel EB, Camp JV, LeBoeuf EJ, Penrod JR, Dobbins JP, Abkowitz MD (2011) Watershed modeling and its applications: a state-of-the-art review. Open Hydrol J 5(1)
5. Fares A (2008) Overview of the hydrological modeling of small coastal watersheds on tropical islands. In: Coastal watershed management, pp 1–35
6. Foley JA, DeFries R, Asner GP, Barford C, Bonan G, Carpenter SR, Snyder PK et al (2005) Global consequences of land use. Science 309(5734):570–574. https://doi.org/10.1126/science.1111772
7. Glibert PM (2017) Eutrophication, harmful algae and biodiversity—challenging paradigms in a world of complex nutrient changes. Mar Pollut Bull 124(2):591–606. https://doi.org/10.1016/j.marpolbul.2017.04.027
8. Golmohammadi G, Prasher S, Madani A, Rudra R (2014) Evaluating three hydrological distributed watershed models: MIKE-SHE, APEX, SWAT. Hydrology 1:20–39. https://doi.org/10.3390/hydrology1010020
9. Jørgensen SE, Williams WD, Centre UIET, Committee ILE (2001) Lakes and reservoirs: water quality: the impact of eutrophication: UNEP-international environment technology centre
10. Kavian A, Mohammadi M, Gholami L, Rodrigo-Comino J (2018) Assessment of the spatiotemporal effects of land use changes on runoff and nitrate loads in the Talar River. Water 10. https://doi.org/10.3390/w10040445
11. Kondraju TT, Rajan KS (2019) Water quality in inland water bodies: hostage to the intensification of anthropogenic land uses. J Indian Soc Remote Sens. https://doi.org/10.1007/s12524-019-01033-2
12. Le Moal M, Gascuel-Odoux C, Ménesguen A, Souchon Y, Étrillard C, Levain A, Pinay G et al (2019) Eutrophication: a new wine in an old bottle? Sci Total Environ 651:1–11. https://doi.org/10.1016/j.scitotenv.2018.09.139
13. Malago A, Bouraoui F, Vigiak O, Grizzetti B, Pastori M (2017) Modelling water and nutrient fluxes in the Danube River Basin with SWAT. Sci Total Environ 603–604:196–218. https://doi.org/10.1016/j.scitotenv.2017.05.242
14. Marcinkowski P, Piniewski M, Kardel I, Giełczewski M, Okruszko T (2013) Modelling of discharge, nitrate and phosphate loads from the Reda catchment to the Puck Lagoon using SWAT. Annals of Warsaw Univ Life Sci—SGGW Land Reclamation 45:125–141. https://doi.org/10.2478/sggw-2013-0011

15. Narasimhan B, Srinivasan R, Bednarz ST, Ernst M, Allen P (2010) A comprehensive modeling approach for reservoir water quality assessment and management due to point and nonpoint source pollution. Trans ASABE, 53. https://doi.org/10.13031/2013.34908
16. Rodriguez W, August PV, Wang Y, Paul JF, Gold A, Rubinstein N (2007) Empirical relationships between land use/cover and estuarine condition in the Northeastern United States. Landscape Ecol 22(3):403–417. https://doi.org/10.1007/s10980-006-9036-8
17. Rouse JD, Bishop CA, Struger J (1999) Nitrogen pollution: an assessment of its threat to amphibian survival. Environ Health Perspect 107(10):799–803
18. Saleh A, Du B (2002) Evaluation of SWAT and HSPF within BASINS program for the upper North Bosque River watershed in central Texas. Trans Am Soc Agricult Eng 47. https://doi.org/10.13031/2013.10387
19. Sharma RK, Yadav M, Gupta R (2017) Chapter five—water quality and sustainability in india: challenges and opportunities. In: Ahuja S (ed) Chemistry and water. Elsevier, pp 183–205
20. Tan W, Liu P, Liu Y, Yang S, Feng S (2017) A 30-year assessment of phytoplankton blooms in Erhai lake using landsat imagery: 1987–2016. Remote Sens 9(12):1265
21. Tong STY, Chen W (2002) Modeling the relationship between land use and surface water quality. J Environ Manage 66(4):377–393. https://doi.org/10.1006/jema.2002.0593
22. Wan R, Cai S, Li H, Yang G, Li Z, Nie X (2014) Inferring land use and land cover impact on stream water quality using a Bayesian hierarchical modeling approach in the Xitiaoxi River Watershed, China. J Environ Manage 133:1–11
23. Wang G, Jager HI, Baskaran LM, Baker TF, Brandt CC (2016) SWAT modeling of water quantity and quality in the Tennessee River Basin: spatiotemporal calibration and validation. Hydrol Earth Syst Sci Discuss 1–33. https://doi.org/10.5194/hess-2016-34
24. White JD, Prochnow SJ, Filstrup CT, Scott JT, Byars BW, Zygo-Flynn L (2010) A combined watershed–water quality modeling analysis of the Lake Waco reservoir: I. Calibration and confirmation of predicted water quality. Lake Reservoir Manage 26(2):147–158. https://doi.org/10.1080/07438141.2010.495315
25. Yasin H, Clemente R (2013) Application of SWAT model for hydrologic and water quality modeling in Thachin River Basin, Thailand. Arab J Sci Eng 39:1671–1684. https://doi.org/10.1007/s13369-013-0770-3

Application of Pollution Indices for the Assessment of Chambal River Water Quality at Kota City, Rajasthan

Porush Kumar, Kuldeep, and Anil K. Mathur

Abstract Chambal River is the largest perennial river in Rajasthan, flowing in the northeast direction. More than 20 lac population of Kota city is dependent on the Chambal river for all water demands like potable, agricultural, industrial and commercial. The water quality of the Chambal River is deteriorating due to the continuous flow of polluted water through anthropogenic activities downstream of the Kota barrage at Kota, Rajasthan (India). The primary aim of this research is to analyze the water quality of Chambal River for potable use with the help of different water quality indices such as Water quality index (WQI), Comprehensive pollution index (CPI), Organic pollution index OPI), and Eutrophication index (EI). Twenty-four water quality parameters have been selected to evaluate these indices, and thirty-six samples have been collected during the study period from four sampling sites, namely, Akelgarh, Rangpur, Shri Raj Rajeshwar Temple (SRRT), and Keshoraipatan. Seasonal variations in selected water quality parameters have also been computed, and the influencing factors have been identified. This study reveals that WQI, CPI, and OPI values were not under the category of safe limits after crossing Kota Dam at Kota (Rajasthan), indicating the rising levels of pollution due to manmade activities and there is significant availability of nutrients in the river that causes eutrophication as per evaluated EI. A correlation study identifies a significant relationship between different water quality parameters. The present study provides an earlier sign of detected pollution to stakeholders for taking necessary actions and designing a proper management plan to reduce pollution levels in the downstream of Kota barrage at Kota city.

P. Kumar · Kuldeep (✉) · A. K. Mathur
Department of Civil Engineering, University Department, Rajasthan Technical University, Kota, Rajasthan 324010, India
e-mail: kuldeep.kamboj44@rtu.ac.in

P. Kumar
e-mail: porushverma46@gmail.com

A. K. Mathur
e-mail: akmathur@rtu.ac.in

1   Introduction

The deterioration in surface water quality has become a global environmental concern due to its impact on humans and the environment. The degradation of surface water quality at different levels has increased substantially during the last century [1]. Polluted water contains many diseases causing organisms such as viruses, bacteria, protozoa, and helminths, which are harmful to human health [2]. Rivers are an essential source of water on the earth which contribute significantly to the development of any nation and the livelihood of the nation's citizens [3].

The accumulation of harmful pollutants in water bodies by anthropogenic activities has become a susceptive and significant issue across the world [4]. Water quality is directly related to food productivity, human health, reduction of poverty, gender equality, sustainable development, economic growth, and social development of communities. These issues seriously affect water resources management and planning [5]. Both natural and anthropogenic activities are accountable for worsening surface water quality. But, anthropogenic activities are immensely liable for the poor water quality of surface water [6]. Increased pollution levels ensure the greater availability of nutrients loading to eutrophication, which is harmful to human beings and the biotic component of the freshwater ecosystem [7].

Kota, the industrial and educational metropolis of Rajasthan, is a fast-growing city in India located on the bank of the Chambal River. It is tremendously dependent on the Chambal river for its total water demand for all purposes (e.g., domestic, agricultural, industrial, commercial, and fire) [8, 9]. More significant employment opportunities, better education facilities, industrialization, commercialization, rapid urbanization, superior medical facilities, modernization, and public social and personal benefits are accountable for unexpected population growth of the city leading to improper town planning and management [10, 11].

Several studies suggest that the factors mentioned earlier negatively impact water quality [12, 13]. Hence, the primary aim of this research is to analyze the water quality of Chambal River for potable use with the help of different water quality indices such as Water quality index (WQI), Comprehensive pollution index (CPI), Organic pollution index (OPI), and Eutrophication index (EI).

2   Study Area and Research Methodology

The city of education Kota is situated in the southeast part of Rajasthan (India), widely known as Hadoti. The city of Kota is famous worldwide for coaching institutes for preparing entrance exams in engineering and medical institutions in India [14]. It is

Table 1 Sampling points with GPS coordinates

Sampling points	Sampling points code	Sampling points position	Latitude	Longitude	Total sampling
Akelgarh	S-1	Upstream	25.15122	75.80984	6
Rangpur	S-2	Downstream	25.26765	75.95587	8
SRRT	S-3	Downstream	25.28666	75.93032	11
Keshoraipatan	S-4	Downstream	25.26073	76.00514	11

situated on the banks of the Chambal River, about 240 km from Jaipur, the capital of the state of Rajasthan [15]. The population of Kota city has crossed 1.2 million as per the census of India, 2011 [16].

Four sampling sites have been selected for study: Akelgarh, Rangpur, Shri Raj Rajeshwar Temple (SRRT), and Keshoraipatan. Only one sampling point is selected for water quality monitoring in upstream of Kota barrage, and the rest are all selected from downstream because the river flows through a deep gorge before it. Hence, limited/negligible sources of water pollution are present in upstream of Chambal Dam. The GPS coordinates of sampling points are mentioned in Table 1.

Thirty-six samples have been collected from all sampling points to analyse 24 water quality parameters, viz., Biochemical Oxygen Demand (BOD), Boron Dissolved (B^{3+}), Calcium (Ca^{2+}), Ammonia Nitrogen (NH_3-N), Chloride (Cl^-), Conductivity (K), Dissolved Oxygen (DO), Chemical Oxygen Demand (COD), Fecal Coliform (FC), Magnesium (Mg^{2+}), Nitrite (NO_2^-), Fluoride (F^-), pH, Nitrate (NO_3^-), Phosphate (PO_4^{3-}), Sodium (Na^+), Temperature (T), Potassium (K^+), Sulfate (SO_4^{2-}), Bicarbonate Alkalinity (HCO_3^-), Total Coliform (TC), Total Dissolved Solids (TDS), Total Hardness (TH), and Turbidity. The sampling and testing were carried out in the laboratory of the Regional Office, RSPCB, Kota, as per IS-3025 prescribed by BIS [14]. The study area with sampling points and the research methodology are shown in Figs. 1 and 2.

3 Pollution Indices

The water quality status is determined by various water quality indices such as WQI, CPI, OPI, and EI. The governing equations of these indices are described in this section. The index range and associated water quality status are tabulated in Table 2.

3.1 Water Quality Index (WQI)

Following is the procedure for the calculation of the Water Quality Index (WQI) to ascertain the quality of drinking water [8, 15, 16]:
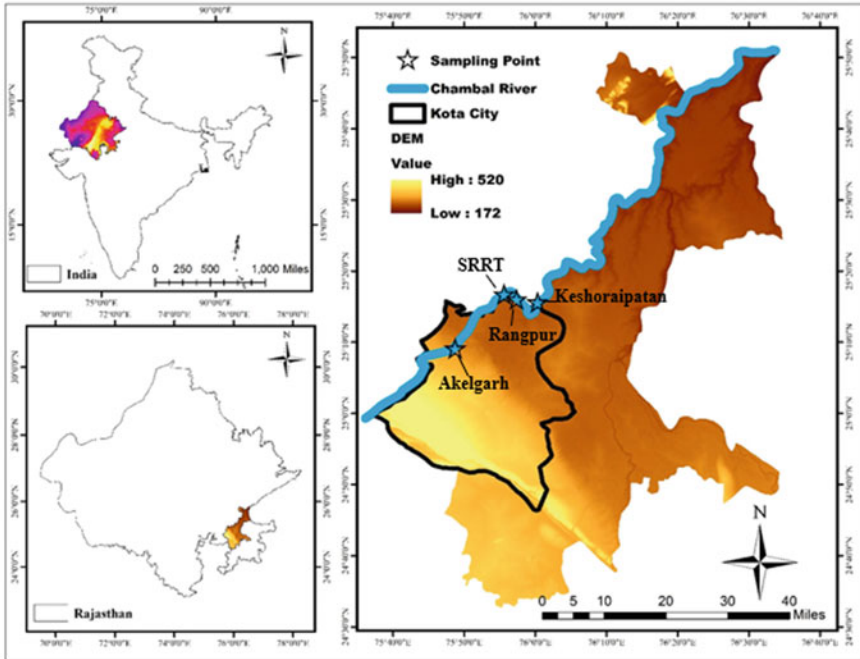
Fig. 1 Sampling point position at Kota City
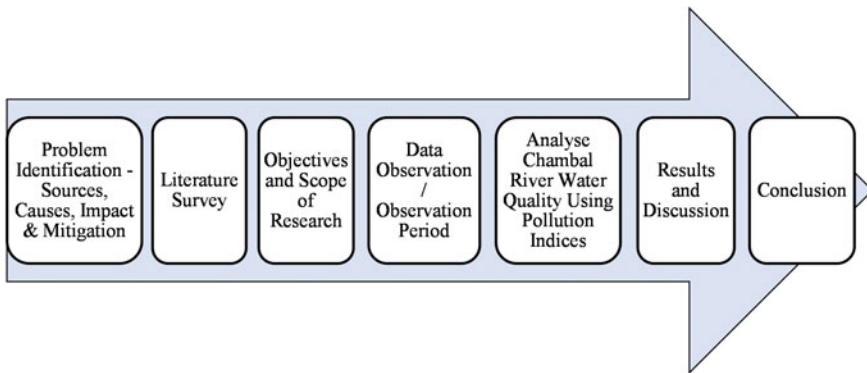
Fig. 2 Methodology adopted for research work

Table 2 Water quality indices with index values and corresponding status

S. no.	Index	Index value	Water quality status
1	Water quality index (WQI)	0–50	Excellent
		50–100	Good
		100–200	Poor
		200–300	Very poor
		300–400	Unsuitable
2	Comprehensive pollution index (CPI)	< 0.8	Qualified
		0.8–1.0	Basically quantified
		1.0–2.0	Polluted
		> 2.0	Seriously polluted
3	Organic pollution index (OPI)	4.0–5.0	Heavily polluted
		3.0–4.0	Moderately polluted
		2.0- 3.0	Lightly polluted
		1.0–2.0	Being to be contaminated
		0–1.0	Good
		< 0	Excellent
4	Eutrophication index (EI)	< 0	Zero eutrophication
		> 0	Eutrophication

1. Different weights (W_i)—All parameters are assigned different weights (W_i) based on their importance. The limit of assigned weight is from 1 to 5. Relative weight (RW$_i$) is calculated by the following formula [17]:

$$RW_i = \frac{W_i}{\sum_i^n W_{ii}} \qquad (1)$$

2. Quality Rating Scale (q_i)—It is calculated with the following formula [18]:

$$q_i = \frac{e_i - v_i}{b_i - v_i} * 100 \qquad (2)$$

vi Base value for each variable (zero (0) for all except pH 7)
bi standard value set by IS-10500
ei observed values.

3. Sub-index (SI$_i$)—The sub-index for each water quality parameter is calculated by the following formula [19]:

$$Sl_i = RW_i \times q_i \qquad (3)$$

4. Water quality index (WQI)—The water quality index for drinking water is determined by the following formula:

$$WQI = \sum_{i}^{n} Sl_i \qquad (4)$$

3.2 Comprehensive Pollution Index (CPI)

The comprehensive pollution index (CPI) identifies the pollution level in a precise water body [1, 7, 12].

1. The following formula calculates the CPI:

$$CPI = \frac{1}{n} \sum_{i=1}^{n} PI_i \qquad (5)$$

PI_i Pollution index of i number parameter
n Number of parameters.

2. PI_i is calculated by the formula as follows:

$$PI_i = \frac{C_i}{S_i} \qquad (6)$$

C_i Measured concentration of the parameter
S_i Standard limit of the parameter.

3.3 Organic Pollution Index (OPI)

The Organic Pollution Index (OPI) is calculated by the following formula [20]:

$$OPI = \frac{COD}{CODs} + \frac{DIN}{DINs} + \frac{DIP}{DIPs} + \frac{DO}{DOs} \qquad (7)$$

COD: Chemical Oxygen Demand, DIN: Dissolved Inorganic Nitrogen, DIP: Dissolved Inorganic Phosphorus, and DO: Dissolved Oxygen.

3.4 Eutrophication Index (EI)

The eutrophication index for the water body is calculated by the three parameters as follows [21]:

$$EI = \frac{COD + DIP + DIN}{4500} \times 10^6 \qquad (8)$$

DIP: Dissolved Inorganic Phosphate, COD: Chemical Oxygen Demand, and DIN: Dissolved Inorganic Nitrogen.

4 Results and Discussions

The water quality of the Chambal river is determined by various pollution indices like WQI, CPI, OPI, and EI in summer, winter, rainy, and annual periods. The annual and seasonal evaluated values of WQI, CPI, OPI, and EI are exhibited in Tables 3 and 4. The value of WQI at Akelgarh (upstream) of Kota Barrage varies between 73.26 and 95.04 in the summer, winter, and rainy seasons, which is a clear sign of "good water quality" during the whole observation period. The annual value of WQI at Akelgarh was 84.71, which is in the safe range and suitable for human consumption for drinking purposes. On the other hand, the scenario of sampling sites in downstream of the Chambal river is quite different.

Table 3 Calculated values of WQI and CPI

Sampling points	WQI				CPI			
	Annual	Winter	Summer	Rainy	Annual	Winter	Summer	Rainy
S-1	84.7	73.2	85.83	95.0	0.58	0.56	0.55	0.65
S-2	200.5	189.2	167.1	222.8	1.38	1.23	1.18	1.56
S-3	203.8	182.0	187.7	237.6	1.30	1.18	1.24	1.48
S-4	256.8	245.4	227.7	290.1	1.65	1.64	1.46	1.81

Table 4 Calculated values of OPI and EI

Sampling points	OPI				EI			
	Annual	Winter	Summer	Rainy	Annual	Winter	Summer	Rainy
S-1	1.84	1.84	1.82	1.85	0.0005	0.0004	0.0004	0.0004
S-2	2.04	2.41	1.56	2.10	0.0027	0.0026	0.0022	0.0029
S-3	2.44	2.63	2.14	2.49	0.0042	0.0029	0.0065	0.0041
S-4	2.77	2.90	2.35	2.95	0.0102	0.0102	0.0129	0.0083
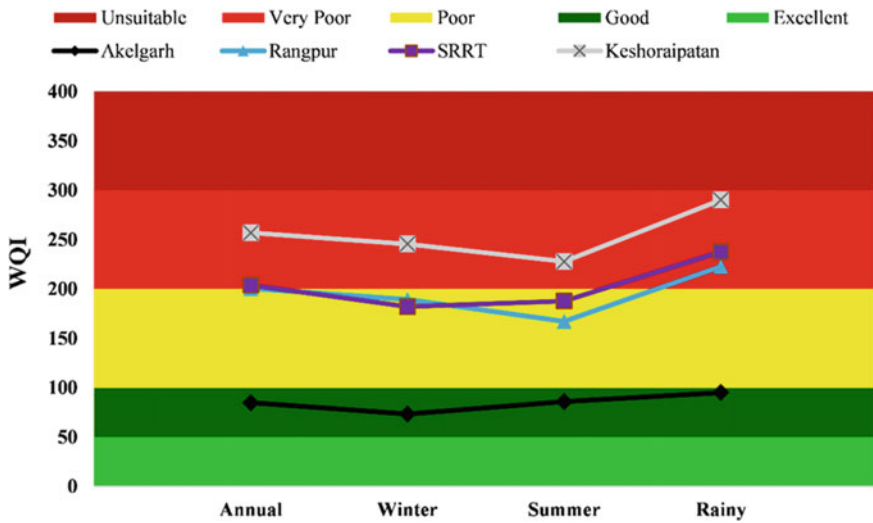
Fig. 3 WQI variation in each season for the year 2020

The WQI values at Rangpur and Sri Raj Rajeshwar Temple (SRRT) varied between 167.1–222.81 and 182–237.66, respectively, in summer, winter, and rainy periods, indicating that the quality at these sampling points varies from "poor to very poor" category of water quality as mentioned in Table 2. The situation worsened for Keshoraipatan as water quality remained "very poor" during all seasons, with WQI values between 227.71 and 290.16. Even water quality approaches to almost "unsuitable category" throughout the rainy period, suggesting the prohibition of river water for drinking purposes. The annual and seasonal variations in WQI are exhibited in Fig. 3.

The CPI values varied between 0.55 and 0.65 in summer, winter, and rainy seasons at upstream (Akelgarh) of the Kota barrage showing the water quality status are "Qualified" at the Akelgarh. The CPI values at Rangpur, SRRT, and Keshoraipatan varied between 1.18 and 1.56, 1.18–1.48, and 1.46–1.81, respectively, indicating the Chambal River water condition was "Polluted" at these sampling points. The annual and seasonal evaluated values of CPI are exhibited in Table 3. The pollution level in the downstream (Rangpur, SRRT, and Keshoraipatan) is exceptionally high in the rainy season, as shown in Fig. 4.

The organic pollution level at Akelgarh is in the position of "Being to be Contaminated," and values vary between 1.82 and 1.85 in summer, winter, and rainy seasons, while OPI values at Rangpur, SRRT, and Keshoraipatan vary in between 1.56–2.41, 2.14–2.63, and 2.35–2.95, respectively, indicating the downstream of Chambal Dam is "Lightly Polluted" due to the presence of organic matter to a smaller extent. The level of organic pollution at all sampling points of the Chambal River is low, indicating that the quality of organic matter is minimal in the river water. The annual and seasonal variations of OPI are exhibited in Fig. 5.
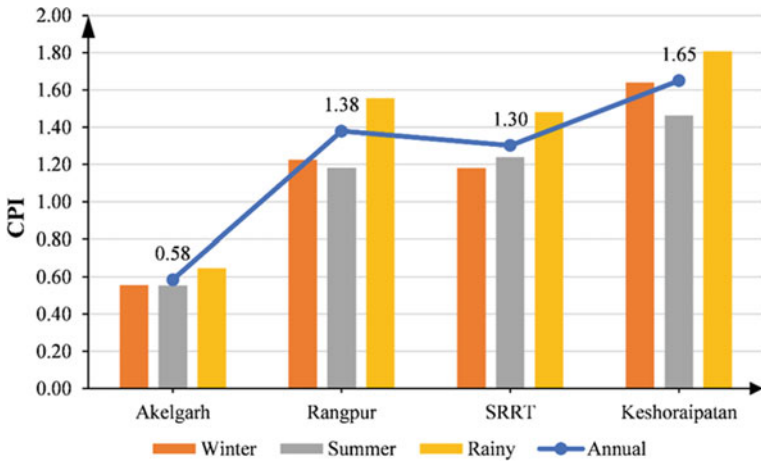
Fig. 4 CPI variation in each season for the year 2020
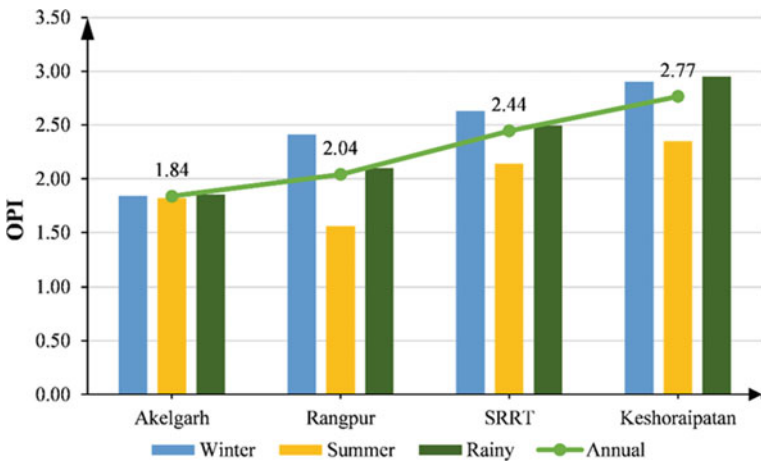
Fig. 5 OPI variation in each season for the year 2020

The Eutrophication Index at Akelgarh was lower than 0.005 at all seasons during the observation period. The lower value of the Eutrophication Index shows the lower availability of nutrients in the upstream of Kota barrage. The EI values at Rangpur, SRRT, and Keshoraipatan are evaluated between 0.0022–0.0029, 0.0029–0.0065, and 0.0089–0.0129, respectively, ensuring the availability of nutrients to a greater extent in each season. The max value of EI is 0.0129, obtained at Keshoraipatan in the summer season. The annual and seasonal variations of OPI is exhibited in Fig. 6.

The correlation matrix was performed using MS Excel 2021 software to exhibit the relationship between the water quality parameters as presented in Fig. 7. The
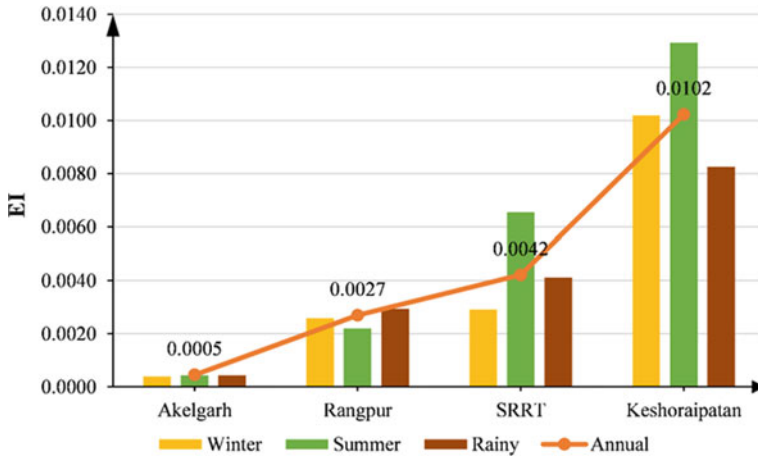
Fig. 6 EI variation in each season for the year 2020

correlation values lie between +1 to -1 here -1 stands for perfect negative correlation while +1 stands for perfect positive correlation. There is a positive correlation between multivalent ions and TDS Correlation analysis suggests an increase in Sodium, Boron, Calcium, Magnesium, Bicarbonates, Potassium, Nitrate, Nitrite, Phosphate, Sulphate, and Fluoride ions leads to an increase in TDS and Turbidity. TDS determines Electrical Conductivity. Hence, as TDS increases, the values of EC increase. Total hardness can also be associated with TDS, as the concentration of multivalent metallic ions (commonly Calcium and Magnesium) determines the water's hardness. BOD and COD are inversely proportional to DO, and a positive correlation exists between TC and FC.

This study reveals significant variation in water quality as the Chambal River flows from Akelgarh to Keshoraipatan. Different water quality indices indicate that water quality upstream of Kota barrage is within safe limits in all seasons (except rainy) due to the less/negligible pollution sources. Hence, river water can be used to complete all the city's water demands. However, primary treatment becomes necessary for drinking in the rainy season due to high Turbidity due to surface runoff and soil erosion caused by precipitation during this season. The water quality of the Chambal River in downstream of Kota Barrage is at intolerable limits during all seasons. The primary cause of unacceptable limits of different water quality indices is the direct discharge of more than two dozen wastewater streams into the Chambal River by drains, solid waste runoff, surface runoff, agricultural runoff, industrial waste effluents, and soil erosion.

Variable	NH₃-N	BOD	B	COD	Ca	Cl⁻	k	DO	FC	F	Mg	NO₃⁻	NO₂⁻	pH	PO₄³⁻	K	Na	SO₄²⁻	Temp	TA	TC	TDS	TH	Turb
NH₃-N	1.0																							
BOD	0.2	1.0																						
B	0.7	0.2	1.0																					
COD	0.0	0.9	0.0	1.0																				
Ca	-0.5	-0.1	-0.5	0.3	1.0																			
Cl⁻	0.5	0.4	0.8	0.2	-0.4	1.0																		
k	0.5	0.1	0.7	0.0	-0.2	0.7	1.0																	
DO	0.1	-0.6	-0.4	-0.4	0.4	-0.7	-0.4	1.0																
FC	-0.2	-0.4	-0.5	-0.4	0.0	-0.7	-0.8	0.5	1.0															
F	0.7	0.5	0.8	0.3	-0.3	0.8	0.6	-0.4	-0.4	1.0														
Mg	0.1	0.4	0.6	0.3	-0.1	0.7	0.6	-0.8	-0.7	0.6	1.0													
NO₃⁻	0.7	0.4	0.6	0.2	-0.2	0.6	0.2	0.0	-0.1	0.8	0.2	1.0												
NO₂⁻	0.5	0.5	0.7	0.4	0.1	0.7	0.4	-0.2	-0.5	0.8	0.5	0.8	1.0											
pH	-0.3	0.1	-0.1	0.1	-0.2	0.1	0.2	-0.7	-0.3	-0.1	0.3	-0.6	-0.3	1.0										
PO₄³⁻	0.8	0.6	0.7	0.4	-0.5	0.6	0.6	-0.4	-0.4	0.8	0.6	0.6	0.6	-0.1	1.0									
K	0.0	0.6	0.3	0.5	0.0	0.3	0.0	-0.5	0.0	0.6	0.5	0.4	0.5	0.1	0.3	1.0								
Na	0.1	0.0	0.3	0.1	0.0	0.6	0.9	-0.5	-0.8	0.3	0.6	-0.1	0.3	0.5	0.3	-0.1	1.0							
SO₄²⁻	0.8	0.3	0.9	-0.1	-0.7	0.7	0.7	-0.3	-0.5	0.7	0.4	0.5	0.5	0.0	0.8	0.1	0.3	1.0						
Temp	-0.3	0.3	-0.1	0.3	-0.1	0.1	-0.1	-0.4	-0.1	-0.2	0.1	-0.1	-0.1	0.1	-0.1	-0.3	0.0	-0.1	1.0					
TA	-0.4	-0.1	-0.2	0.2	0.8	-0.1	0.1	0.0	-0.4	-0.2	0.3	-0.4	0.2	0.2	-0.3	0.1	0.3	-0.4	-0.3	1.0				
TC	-0.3	-0.3	-0.5	-0.3	0.1	-0.8	-0.9	0.7	0.9	-0.5	-0.8	-0.1	-0.4	-0.5	-0.5	-0.1	-0.9	-0.5	-0.1	-0.2	1.0			
TDS	0.4	0.2	0.7	0.1	-0.3	0.9	0.9	-0.7	-0.8	0.6	0.8	0.2	0.5	0.4	0.5	0.1	0.9	0.7	0.0	0.1	-0.9	1.0		
TH	-0.4	0.1	-0.2	0.4	0.8	0.0	0.1	-0.1	-0.4	0.0	0.4	-0.1	0.4	0.0	-0.2	0.2	0.3	-0.5	0.0	0.9	-0.3	0.1	1.0	
Turb	0.0	-0.2	-0.1	-0.2	0.1	-0.1	-0.1	0.0	0.2	0.1	0.0	-0.1	-0.1	0.4	-0.2	0.4	0.1	-0.1	-0.8	0.3	0.1	0.0	0.1	1.0

Fig. 7 Correlation between each water quality parameter for the year 2020

5 Conclusions

The city's sudden growth significantly adversely affects the Chambal River's water quality due to lacking proper river pollution control and management plan. Chambal river is the "Lifeline" of the citizens of Kota city because it satisfies all the water demands for all purposes. Results of different water quality indices (WQI, CPI, OPI, and EI) indicate that water quality upstream of Kota Dam is within safe limits in all seasons (except rainy) due to the less/negligible pollution sources.

The WQI, CPI, and OPI values in SRRT, Rangpur, and Keshoraipatan indicate that the water quality is in the "polluted" state. A significant amount of organic material entered downstream through various paths, leading to a heavy organic pollution load in the river. The Eutrophication Index identifies the presence of nutrient enrichment in the Chambal River. Discharge of effluent from sanitary sewage (domestic and industrial) without treatment, direct dumping of refuse (e.g., garbage, rubbish, and sullage), agricultural runoff, surface runoff, and deforestation are blameworthy for Chambal River water pollution in the downstream of Kota barrage at Kota City, Rajasthan, India. Water quality was highly polluted in the rainy season, followed by the winter and summer. Awareness should be created among the general public to reduce water pollution, and environmental agencies should treat wastewater streams before they are released into the river. Stakeholders should develop proper water management and pollution mitigation strategies to provide high-quality water to the city of Kota.

References

1. Yadav NS, Kumar A, Mishra S, Singhal S (2018) Assessment of water quality using Pollution-Index in the study stretch of River Chambal India. Integr Res Adv 5(1):20–25
2. Wu Z, Zhang D, Cai Y, Wang X, Zhang L, Chen Y (2017) Water quality assessment based on the water quality index method in Lake Poyang: the largest freshwater lake in China. Sci Rep 7(17999):1–10
3. Gangwar RK, Singh J, Singh AP, Singh DP (2013) Assessment of water quality index: a case study of river Ramganga at Bareilly U.P. India. Int J Sci Eng Res 4(9):2325–2329
4. Şener Ş, Şener E, Davraz A (2017) Evaluation of water quality using water quality index (WQI) method and GIS in Aksu River (SW-Turkey). Sci Total Environ J 584–585:131–144
5. Akhtar N, Ishak MIS, Ahmad MI, Umar K, Yusuff MS, Anees MT, Qadir A, Almanasir YK (2021) Modification of the water quality index (WQI) process for simple calculation using the multi-criteria decision-making (MCDM) method: a review. Water 13(905):1–34
6. Singh UK, Kumar B (2017) Pathways of heavy metals contamination and associated human health risk in Ajay River basin, India. Chemosphere 174:183–199
7. Sukanya S, Joseph S (2020) Water quality assessment using environmetrics and pollution indices in a Tropical River, Kerala, SW Coast of India. Curr World Environ 15(1):11–23
8. Kumar P, Yadav D, Kuldeep MAK (2022) Drinking and irrigation water quality analysis for Chambal River at Kota. ECS Trans 107(1):3049–3059
9. Kuldeep SS, Mathur AK (2021) An assessment of water quality indices of Chambal river in Kota City for drinking and irrigation Purposes. Weentech Proc Energy 7(1):118–133
10. Kuldeep SS, Mathur AK (2022) Assessment of the Chambal River Quality at Kota Metropolis through the drinking water quality index and irrigation water quality index. Adv Mater Manuf Energy Eng 1:559–573
11. Kumar P, Kuldeep, Mathur AK (2021) Irrigation water quality indices for Chambal River at Kota City. SPAST Abstracts
12. Kumar P, Kuldeep KP, Mathur AK (2022) Analysis of irrigation water quality indices for Chambal River at Kota. ECS Trans 107(1):10797–10810
13. Kumar N, Choudhary MP (2017) Effect on water quality of Chambal river due to discharge of open drains in Kota City. Int Res J Eng Technol 4(11):890–894
14. Kumar P, Kuldeep GN (2021) An assessment of ambient air quality using AQI and exceedance factor for Udaipur City, Rajasthan (India). Weentech Proc Energy 7(1):94–106
15. Kumar P, Yadav D, Kuldeep, Mathur AK (2021) Chambal River water quality for drinking and irrigation at Kota city, Rajasthan (India). SPAST Abstracts
16. Handbook DC (2011) District census handbook Kota, village and town wise primary census abstract (PCA). Census of India
17. Sisodiya S, Mehar RK, Mathur AK (2020) Statistical analysis for Urban lakes of Hadoti Region, Rajasthan. Int J Lakes Rivers 13(1):35–42
18. Sisodiya S, Mehar RK, Mathur AK (2020) Datasets for assessment of water quality indices for irrigation and drinking for Hadoti Lakes, Rajasthan. Internat J Lakes Rivers 13(2):121–130
19. Son CT, Giang NTH, Thao TP, Nui NH, Lam NT, Cong VH (2020) Assessment of Cau River water quality assessment using a combination of water quality and pollution indices. J Water Supply: Res Technol—AQUA 69(2):160–172.
20. Liu S, Lou S, Kuang C, Huang W, Chen W, Zhang J, Zhong G (2011) Water quality assessment by pollution-index method in the coastal waters of Hebei Province in Western Bohai Sea China. Marine Pollut Bull 62(10):2220–2229

21. Katarzyna W, Zdechlik R (2021) Application of water quality indices to the assessment of the effect of geothermal water discharge on river water quality—case study from the Podhale region (Southern Poland). Ecol Ind 121:1–14

Water Quality Modelling Using QUAL-2K at Bray Marina, UK

Dinesh Sahoo and Ratnakar Swain

Abstract One of the most crucial aspects for a healthy environment is water quality. A wide range of animals and plants rely on clean water. Pollutants, fertilizers, and excess fluids from sediments are commonly transferred by spillage from towns and agricultural regions to nearby lakes and rivers, affecting water quality. We have to measure a variety of properties to determine water quality, such as conductivity, DO, NH4-nitrogen, pH, organic and inorganic phosphorus content. Water quality modelling includes water quality-based data using mathematical simulation techniques. Water quality modelling assists individuals in understanding the significance of water quality concerns, and the model gives evidence for policymakers to make choices on how to effectively mitigate water. Water quality simulation can also assist uncover information gaps and assess the relationship between freshwater resources and water quality. Water quality modelling is especially important at both local and global levels due to the increasing use of freshwater by humans. Understand and predict changes in water resources over time due to water shortages, climate change and economic factors. In this study, we are using the steady-state model QUAL-2K. The model will use the following data: conductivity, DO, NH4-nitrogen, pH, organic and inorganic phosphorus content.

Keywords QUAL-2K · Water quality modelling · Pollution · Bray Marina · Thames River

1 Introduction

The United Kingdom receives moderate amount of the annual rainfall, within the average rainfall of around 3677 mm which results in high surface runoff and forms

D. Sahoo (✉) · R. Swain
Department of Civil Engineering, National Institute of Technology, Rourkela 395007, India
e-mail: sahoodinesh1@gmail.com

R. Swain
e-mail: swainrk@nitrkl.ac.in

an extensive stream network, i.e. 1500 discrete rivers, with a total of about 200,000 km of water sources. We all know, however, that groundwater is particularly sensitive to contamination, particularly in densely populated and heavily developed metropolitan catchment regions. Pollution of surface waters and rivers is mainly due to human activities, in particular industry, development, and agriculture. Many incidents related to the pollution of the river have been reported over the years [1].

In the United Kingdom, studies on contamination have primarily focussed on a specific kind of pollutant, such as untreated hazardous and chemical effluent, release from land fill, e.g. leachate, silt, and discharge from sewage treatment facilities. In the United Kingdom, there have been few research on the evaluation of river basin using QUAL-2K technology, and the water quality criteria addressed have been extremely limited, notably amount of oxygen (DO), biological oxygen (BOD), and ammonia. But in this study, we will use data such as conductivity, DO, NH4-nitrogen, pH, organic and inorganic phosphorus content. The state of the water quality of rivers, especially in urban areas, requires close and frequent monitoring due to the constant population growth and the extensive development activities in these areas.

1.1 Water Quality Modelling

Water quality modelling is a valuable method for forecasting and simulating pollution amount, distribution, and risk in a specific body of water. Water quality modelling entails analysing water quality data using mathematical simulation approaches [3]. Water quality modelling assists individuals in comprehending the significance of water quality concerns, and the model gives evidence for policymakers to make choices in order to appropriately mitigate water. Water quality simulation can also assist uncover information gaps and assess the relationship between waterbodies and water quality. Water quality modelling is especially important at both local and global levels due to the increasing use of freshwater by humans [6]. The findings of these models' modelling under numerous environmental scenarios are a critical component of eia process and may give the basis and engineering services for environmental stewardship authorities to make sound judgements.

Dissolved oxygen (DO): The amount of oxygen dissolved in water is referred to as dissolved oxygen (DO). The quantity of free, semi oxygen contained in moisture is referred to as dissolved oxygen. It is a critical criterion in determining water quality since it impacts the creatures that reside in the waterbody. Dissolved oxygen levels that are too high or too low can harm aquatic species and degrade water quality [2].

Conductivity: Conductivity is a measure of the ability of a solution to conduct electricity and, therefore, a measure of ionic activity and water content. The more dissolved salt in water, the higher its ion content or its conductivity [4]. Conductivity is an excellent measure for reflecting the amount of dissolved solids (total dissolved solids, or TDS) or salinity of a water source. Conductivity data can determine the concentration of a solution, detect contaminants, and determine the purity of water.

pH: The pH value of water indicates its acidity or alkalinity. It is determined as the ratio of the concentration of hydrogen ions. This is a non-dimensional integer that shows the acidic or basic strength of a solution. In truth, the pH of water is a measure of how acidic or basic the water is. Additional hydrogen ions (H^+) are present in acidic water, while extra hydroxyl (OH) ions are present in basic water. For home usage and the demands of living organisms, safe pH values for drinking water vary from 6.5 to 8.5 [13].

NH_4-Nitrogen: Ammoniacal-nitrogen measurement is an important water quality parameter used to indicate water pollution and the presence of untreated sewage. High NH4-N levels in water supplies lead to unpleasant odours and tastes [15]. These high concentrations are the main reason for the reduction of the disinfecting effect of chlorine and other halogens and the increased risk of pathogen contamination during water treatment and distribution [5]. Therefore, the NH4-N content in groundwater should be reduced before it is consumed.

Phosphorus: Phosphorus is understood to be a crucial contributor to eutrophication of aquatic systems. There are many natural and human sources of phosphorus. Soil and rocks, sewer treatment facilities, runoff from fertilised lawns and farms, malfunctioning septic systems, animal manure storage places, disturbed land regions, drowned wetlands, water purification, and property maintenance preparations are examples [14]. Because phosphorus is an uncommon nutrient in most aqueous locations, even a small increase in phosphorus can cause a cascade of consequences, including rapid plant growth, algal blooms, low chemical oxygen demand, and the death of some fish, snails, and other aquatic creatures [9].

2 Literature Review

At the beginning of the phase (1925–1955), a simple nonlinear BOD-DO system model that successfully predicted water quality was constructed, for a one model was used to handle river and estuary waste concerns. Following that, most scholars updated and expanded on the Streeter-Phelps theories (S-P models). To the Thomas equation, Dobbins-Camp has made additional coefficients: the rate of change in BOD owing to silt release and surface runoff, as well as the rate of change in oxide controlled by algal photosynthesis and respiration [11].

From 1965 to 1970, surface water models were divided into six linear systems, and independent research on the multivariate coefficient estimate of the BOD-DO model made quick progress.

The one-dimensional model has been modified to a two-dimensional model that may be used to simulate lake and golf water quality simulations. The number of federal variables in the model has grown dramatically since 1975, and three-dimensional systems were established during this time. The models, including MIKE11, QUAL, OTIS, and WASP models, were created and used at this stage [13].

Besides the aforementioned common models, different water quality models were created after 1995 to mimic complex water environmental circumstances. Whitehead et al., created a semi-distributed comprehensive nitrogen model (INCA) that takes into account the impacts of environmental and soil N sources, land use, and hydrologic [10]. To simulate the influence of tidal impacts on water quality modelling, water quality modelling, and HEC-RAS models were developed. Kannel et al. recently found that these freely accessible models (e.g., WASP7, QUAL2EU, and QUASAR) are the best for modelling dissolved oxygen along rivers and streams. But in this study, we will use QUAL-2K for water quality modelling [12].

3   Methodology

3.1   QUAL-2K

The model assumes that chemical, physical, and biological qualities (model input parameters) are continuous along a reach in the subdividing parts of the river, and starting with the headwaters of the river's main stem, the reaches are numbered in increasing order. For these components, concentration flow and temperature are used to maintain heat balance, hydrological balance and material balance, respectively. Nonpoint and point inputs, as well as nonpoint and point outflows (abstractions), can be put at any point along the channel's length [16].

Q2K's most fundamental unit is the element. A steady-state flow balance is implemented for each model element.

$$Q_i = Q_{i-1} + Q_{in,i} - Q_{out,i} - Q_{evap,i}$$

where $Q_{in, i}$ is the total input of point and nonpoint sources into the reach [m^3/d], $Q_{ab, i}$ is the total outflow from the reach owing to point and nonpoint abstractions [m^3/d], Q_i = abstraction from reach i to reach $i + 1$ [m^3/d] and Q_{i-1} = source from the up-reach $i - 1$ [m^3/d] (Fig. 1).

Thus, the downstream outflow is simply the difference between inflow and source gains minus withdrawal and evaporative losses.

Fig. 1 Reach flow balance [7]
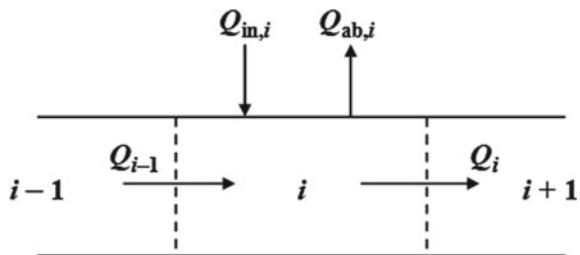
The power equations used to relate mean velocity and depth to flow for the elements in the reach are:

$U = aQ^b$

$H = \alpha Q^\beta$

Where a, b, α, and β are empirical coefficients calculated from velocity-discharge and stage-discharge rating curves. The velocity and depth measurements may then be used to calculate the cross-sectional area and breadth [8].

4 Study Area and Data Source

4.1 Bray Marina, Berkshire, UK

Bray Marina with longitude -0.834930 and latitude 51.410969, in its country park, offers dockers a delightful quiet anchorage. Marina 400berth has an active marine club as well as boat training courses.

4.2 Data Collection

The Thames River is the longest river in England and the 2nd largest in the United Kingdom after the River Severn, with a total length of 346 kms. The river begins in Gloucestershire and runs across the Thames Estuary to the North Sea near Essex, Tilbury, Gravesend, and Kent. The Thames is also the drainage system for the whole Greater London area. The Tideway refers to the river's lower portions, which are named for its lengthy tidal stretch up to Teddington Lock. The developed QUAL-2K model for Thames River is divided into 8 segments (as shown in Fig. 2), which equals 100 km length and uses uniform hydraulic characteristics to simulate the water quality. A 100 km stretch of the river was selected for undertaking our aforesaid study. The monitoring stations along Thames River were Station 1 (Toplow, chainage 0 km) at Bray lock, Toplow. Station 2 (Dorney, chainage 10 km) adjacent to Trumper's Field, Dorney. Station 3 (Slough, chainage 20 km) at wastewater treatment plant near Merican Way, Station 4 (Slough, chainage 35 km) at the Tamblyn Field, Station 5 (Staines, chainage 45 km) near the Reeds Motors, Station 6 (Windsor, chainage 65 km) at the Boat House, Station 7 (Egham, chainage 80 km) at the Runnymede Boatyard, and Station 8 (Staines, chainage 90 km) near the Thames side brewery and Tap Room.

From May 2010 to February 2012, this data collection contains hourly physical and nutritional monitoring data from the cut at Bray Marina in Berkshire, UK. Total reactive phosphorus, total phosphorus, temperature, DO, ammonium, conductivity, pH, and the chlorophyll are among the parameters assessed. Hourly averaged flow
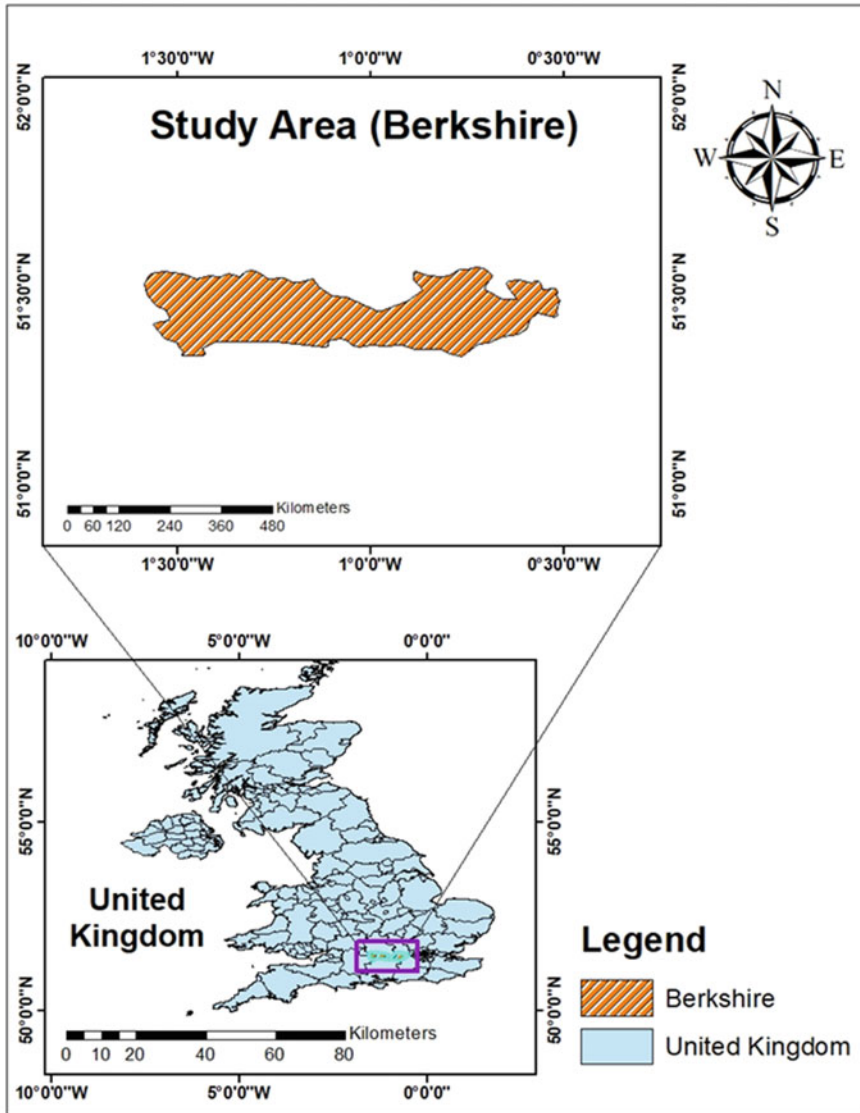
Fig. 2 Index map of study area

data (from the EA flow measuring station on The Cut at Binfield) is also available. The instrumentation was located 5 m from the riverside in a trailer unit.

A submersible pump was utilised to continuously pump water from river's middle towards a flow cytometer in the trailer unit, which housed the YSI sounde and the Hach Lanuge Sigmatax sampling probe. The Sigmatax unit transfers a 10 ml thread to the Phosphax Sigma after homogenising the sample in a glass chamber with an

ultrasonic probe. The Phosphax Sigma is an in place, elevated device that analyses total phosphorus and total reactive phosphorus using colorimetric and digestive techniques. TP was measured measuring the absorbance using an acid per-sulphate decomposition using a procedure based on Eisenreich et al. After boiling to 140 °C and applying a tension of 359 kPa (1975). The phosphomolybdenum blue complexation procedure was used to quantify TRP. The instrument was tested using standard solutions.

5   Results and Discussion

After all the testing and input of values was done, the model was run and the values were predicted by the model for a stretch of 100 km. The predicted results and the comparison studies have been shown in this chapter.

5.1   Comparison of Results

Comparison for Conductivity
From the graph of conductivity, it can be shown that, the values are within the permissible limit as prescribed by WHO. Initially the values are high as 1112 mho/cm at upstream and gradually decreases towards the downstream. The r^2, RMSE, NSE values come out to be 0.83, 7.79, and 83.26, respectively. Which is quite good (Fig. 3).

Comparison for Dissolved Oxygen
From the graph of dissolved oxygen, it can be shown that, the values are within the permissible limit as prescribed by WHO. Initially the values are low at upstream and gradually increases and then decreases towards the downstream. The r^2, RMSE, NSE values come out to be 0.88, 3.45, and 94.21, respectively. The NSE value is higher among all the parameter (Fig. 4).

Fig. 3 The observed and simulated graph for conductivity of Thames River
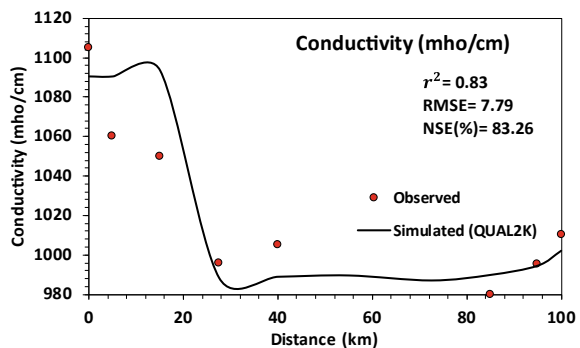
Fig. 4 The observed and
simulated graph for
dissolved oxygen of Thames
River
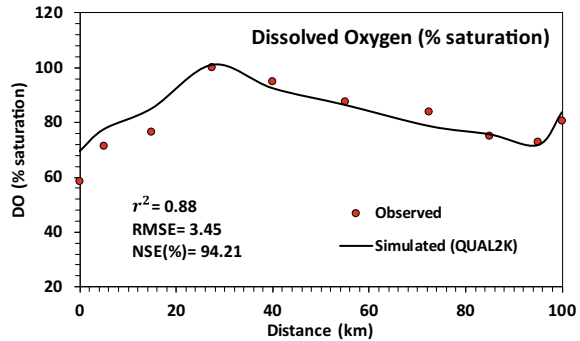
Fig. 5 The observed and
simulated graph for
temperature of Thames River
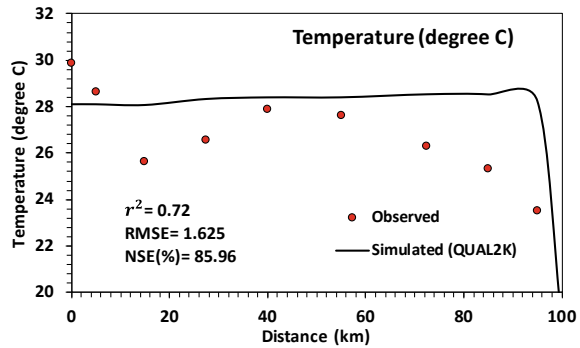
Comparison for Temperature

From the plot of temperature, initially the values are high at upstream, then remain
constant throughout and then suddenly decreases at the downstream. The r^2, RMSE,
NSE values come out to be 0.72, 1.62, and 85.96, respectively. The RMSE value is
lower among all the parameters, which is quite impressive (Fig. 5).

Comparison for Organic Phosphorus

From the plot of organic phosphorus, initially the values are low at upstream, then
remain constant throughout and then suddenly increases at the downstream. The r^2,
RMSE, NSE values come out to be 0.79, 11.25, and 76.37, respectively. Which is
quite good (Fig. 6).

Comparison for Turbidity

From the plot of turbidity, initially the values are high at upstream, then remain
constant throughout and then suddenly decreases at the downstream. The r^2, RMSE,
NSE values come out to be 0.75, 8.65, and 80.24, respectively. Which is quite good
(Fig. 7).

Comparison for pH

From the plot of pH, initially the values are high at upstream, then decreases at
the downstream. The r^2, RMSE, NSE values come out to be 0.93, 2.24, and 91.21,

Fig. 6 The observed and simulated graph for organic phosphorus of Thames River
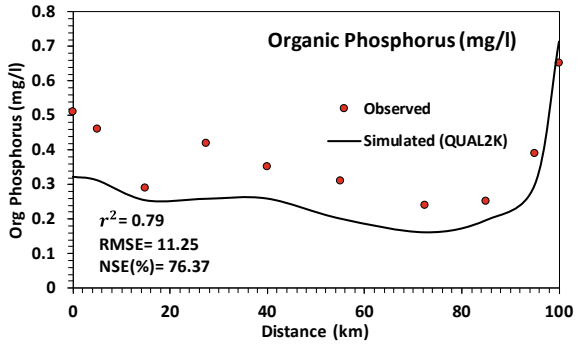
Fig. 7 The observed and simulated graph for turbidity of Thames River
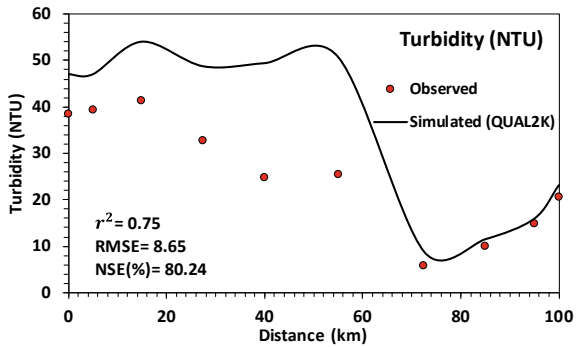
respectively. The r^2 value came highest, which shows that the model simulated pH quite well (Fig. 8).

Fig. 8 The observed and simulated graph for pH of Thames River
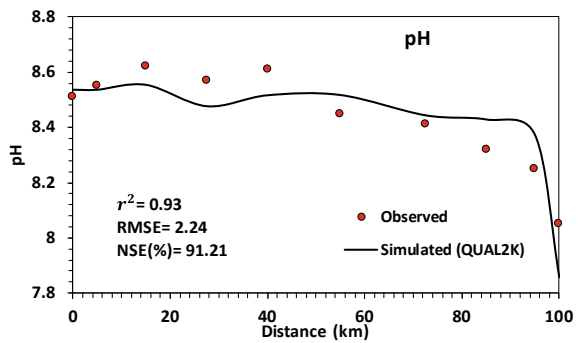
6   Conclusions

Deterioration of water quality is widespread all over the world, especially in rural parts of Berkshire, UK. Water pollution countermeasures and preventative actions should typically be based on a thorough assessment of the sources of pollution and their respective contributions to water degradation. To evaluate conductivity, DO, NH4-nitrogen, pH, and abiotic phosphorus content in the river, this study used a hybrid method using an empirical export factor model and a practise river water quality model. Calibration and validation applied using field measurement data indicates that this flow is in poor condition and requires management options. The main causes of water pollution in the study area were the large number of animal feedlots, overuse of fertilizers, and weak water treatment ability. However, QUAL-2K has shown that this model is absolutely reliable in stream modelling when detailed and complex data is not available during the calibration and validation process due to acceptable match with the measured data.

References

1. Ashwani S, Vivek B, Ratnoji S, Jayakumar P, Jainet PJ (2017) Application of QUAL2K model for prediction of water quality in a selected stretch of Pamba River. Int J Civil Eng Technol 8(6):75–84
2. Chapra S (1997) Surface water quality modeling. The McGraw-Hill Companies, Inc. Intl. Edn. Bangkok
3. Bui HH, Ha NH, Nguyen TN, Nguyen AT, Pham TT, Kandasamy J, Nguyen TV (2019) Integration of SWAT and QUAL2K for water quality modeling in a data scarce basin of Cau River basin in Vietnam. Ecohydrol Hydrobiol 19(2):210–223
4. Jou CJ, Lee CL, Fu YT, Kao CM (2012) Simulation of a long narrow type constructed wetland using the stream model QUAL2K. Sustain Environ Res 22(4):255–260
5. Xin Z, Ye L, Zhang C (2019) Application of export coefficient model and QUAL2K for water environmental management in a Rural Watershed. Sustainability 11(21):6022
6. Ismail HA, Abed AG (2013) BOD and DO modeling for Tigris River at Baghdad city portion using QUAL2K model. J Kerbala Univ 9(1):257–273
7. Chapra SC, Pelletier GJ, Tao H (2008) QUAL2K: a modeling framework for simulating river and stream water quality, version 2.11. USA: Documentation and User's Manual. Civil and Environmental Engineering Department, Tufts University, Medford
8. Brown LC, Barnwell TO (1987) The enhanced stream water quality models QUAL2E and QUAL2E-UNCAS (EPA/600/3-87-007). US Environmental Protection Agency, Athens
9. Kalburgi PB, Shivayogimath CB, Purandara BK (2010) Application of QUAL2K for water quality modeling of River Ghataprabha (India). J Environ Sci Eng 4:6–11
10. Zhang RB, Qian X, Yuan XC, Ye R, Xia BS, Wang YL (2012) Simulation of water environmental capacity and pollution load reduction using QUAL2K for water environmental management. Int J Environ Res Public Health 9:4504–4521

11. Wright RM, Mcdoneii AJ (1979) In-stream deoxygenation rate prediction. J Environ Eng Div 105:323–333
12. Ying T (2011) Application of QUAL2K model in water resources management and protection of Daling river basin. Water Resour Hydropower Northeast China 05:52–53
13. Ye C (1993) Progress of studies on water environmental mathematical model. Adv Environ Sci 01:74–81
14. Donnert D, Salecker M (1999) Elimination of phosphorus from municipal and industrial waste water. Water Sci Technol 40:195–202
15. Chen D, Yang K, Wang H (2014) Nitrate removal from groundwater by hydrogen-fed autotrophic denitrification in a bio-ceramsite reactor. Water Sci Technol 69:2417–2422
16. Pelletier GJ, Chapra SC, Tao H (2006) QUAL2Kw—a framework for modeling water quality in streams and rivers using a genetic algorithm for calibration. Environ Modell Software 21:419–425

Emanation of Radon from Coastal and Inland Groundwater of Northern Kerala, India

P. Arjun, N. P. Jesiya, Girish Gopinath, and T. R. Resmi

Abstract The radiogenic isotope radon (^{222}Rn) is an excellent tracer for monitoring and identifying several hydrogeological processes because of having a short half-life and considerably presence of large concentration in groundwater relative to the surface water. The groundwater radon distribution in various geological formation of coastal and inland regime in Kasaragod district was carried out using a RAD7 detector and RAD H$_2$O accessory to determine the correlation amongst the geology of the study area and radon concentrations of groundwater. The study area is classified into five lithological groups that differ in groundwater occurrence in space and time. About 70 measurements of ^{222}Rn from monitored open wells in the study area were analyzed. The ^{222}Rn of the coastal alluvium region is ranged from 77.1 to 832 Bq/m^3 and average radon concentration of 408 Bq/m^3. In fluvial alluvium region, it is ranged from 39.6 to 479 Bq/m^3 and average radon concentration of 440 Bq/m^3. Gneiss /Khondalite/ Charnockite region is ranged from 117.5 to 2343 Bq/m^3 and average radon concentration of 782 Bq/m^3. In laterite region is ranged from 436 to 1114 Bq/m^3 and average radon concentration of 636 Bq/m^3 and in tertiary alluvium

P. Arjun (✉)
Land and Water Management Research Group, Centre for Water Resources Development and Management (CWRDM), Kunnamangalam, Kozhikode 673571, India
e-mail: arjun130591@gmail.com

School of Environmental Studies, Cochin University of Science and Technology (CUSAT), Kochi 682022, India

N. P. Jesiya
Department of Civil Engineering, National Institute of Technology (NIT), Kozhikode 673601, India
e-mail: jesynp@gmail.com

G. Gopinath
Department of Climate Variability and Aquatic Ecosystems, Kerala University of Fisheries and Ocean Studies (KUFOS), Kochi 682508, India
e-mail: ggcwrdm@gmail.com

T. R. Resmi
Ecology and Environment Research Group, Centre for Water Resources Development and Management (CWRDM), Kunnamangalam, Kozhikode 673571, India
e-mail: rtr@cwrdm.org

region, it is ranged from 37.8 to 1135 Bq/m^3 and average concentration of 346 Bq/m^3. High radon actions were primarily found in Gneiss /Khondalite /Charnockite rocks and Lateritic regions. Radon values were compared with the maximum contaminant levels (MCL) for potable water range good for human consumption proposed by USEPA which is 11.3 Bq L^{-1} and WHO is 100 Bq L^{-1} and it was determined that the groundwater radon concentration values were well within the safe limit.

1 Introduction

Radon is a noble gas and is present everywhere in nature; its activity in groundwater is quite complicated and is controlled by a number of variables. As a result, there are geographical differences in radon activity in groundwater. In general, the concentration of uranium and radium in the parent rocks has a major role in regulating the radon activity in groundwater. It is formed naturally after radionuclides as ^{238}U, ^{235}U, and ^{232}Th decay [1]. The decay of uranium, thorium, and actinium series produces three naturally occurring isotopes of radon: radon (^{222}Rn), thoron (^{220}Rn), and actinon (^{219}Rn). A radon isotope has a 3.8 day half-life and could be present for a while in water and air, which may possibly cause serious medical issues in individuals [2]. Its occurrence in soil and waters has significantly aided our society in identifying and predicting the incidence of earthquakes, volcano eruptions, and other various hydrogeological events [3]. But on the other hand, its existence at significant concentrations in the enclosed environment and water supplies creates a health threat for humanity for its carcinogenic potential [4]. It is predicted that groundwater will have a large concentration of radon gas when it filters down via uranium-rich rocks. The radon emission and escaping into the surface is enhanced as once groundwater is exposed to environment [5].

In a geological environment, radon concentrations can differ significantly between different types of rocks and even within the same lithological groups. Radon may dissolve into groundwater when infiltrating fractures and voids in soils. Surface water infiltrates through aquifers, therefore radon can be used as a natural tracer for qualitative study [6]. Public health studies involve regular monitoring of drinking water quality, including radon levels. Many studies have been carried out around the world to detect and collect preliminary findings on radon concentration levels [7], but no such studies has been carried out in the coastal belt of Kasaragod district in northern Kerala, India. Several hydrological research in the field of isotopic signature studies has been carried out in Northern Kerala using deuterium and tritium [8–10], but not much studies was done using radon isotopes. The present study was conducted to estimate the radon concentration from Coastal and Inland groundwater aquifers of the study area and to understand various factors that influence its distribution in different geological formations.

2 Study Area

The study area includes the coastal stretch of about 845.9 km^2 of Kasaragod district, Kerala state Area (Fig. 1). The study area bounded in the north by Dakshina Kannada district of Karnataka State, in the south by Kannur District of Kerala, and in the west by the Arabian Sea, located in 74° 51′ 54.87" to 75° 13′ 41.16" E Longitude 12° 2′ 35.49" to 12° 47′ 0.59" N Latitude. The coast is drained by a large number of west-flowing rivers. Nine rivers drain through the study area with annual stream flow ranging from 307 to 4000 mm^3 [11]. The important of them are Manjeshwaram, Shiriya, Chandragiri, Nileshwar, and Kariangode. The minimum temperature varies from 19.7 °C to 25 °C, while the monthly average high temperature is from 29.2 °C to 33.4 °C. [11]. The area is subjected to a humid tropical climate with an average annual rainfall is around 3000 mm. Dry weather starts in February and ends in May. The Kasaragod coast experiences two monsoons. The southwest monsoon is the dominant monsoon, it opens in the coast around June and continues till September, and northeast monsoon is witnessed in October and November. In this particular study the radon samples were collected during post-monsoon 2018 December.

Geologically, Kasaragod area mainly contains crystalline rocks and is broadly lateralized. In the Physiographical bases, the district can be alienated into three distinct units (a) coastal plains (b) Midlands, and (3) Eastern high land region [12]. The study area of the Kasaragod coast is broadly divided into five geological belts (i) Coastal Alluvium (ii) Fluvial Alluvium (iii) Gneiss/Charnockite /Khondalite (iv) Laterite (v) Tertiary Alluvium. Coastal Alluvium exists as thin strips parallel to Kasaragod's southern coastal plain. The area of the alluvium expands to the southward of the district and exceeds 5–7 km toward Trikaripur area [12]. They were formed by the action of the movement and deposition of sediments from adjacent hilly terrain. The alluvial deposit occurs in isolated pockets near to the shoreline of northern Kasaragod and has a confined thickness. The coastal plains are distinguished with secondary soils that are sandy and barren, with little water retention capacity. Even though the alluvium width is larger in the Kanhangad and Nileshwar blocks, possible fracture zones are observed in the upper section, preceded with tertiary sediments in lower depths that do not contain potential fracture zones. The surface geological features of the coastal belt mainly consist of sand, sand dunes, and estuarine deposits. The midlands and highlands are characterized by laterites and rocks (gneisses, granites, khondalite, and charnockite) [13].

3 Methodology

In this current study, the radon (^{222}Rn) concentrations in groundwater samples were measured from 70 open wells in different depths as well as from various lithological units such as coastal alluvial (9 samples), fluvial alluvial (18 samples),
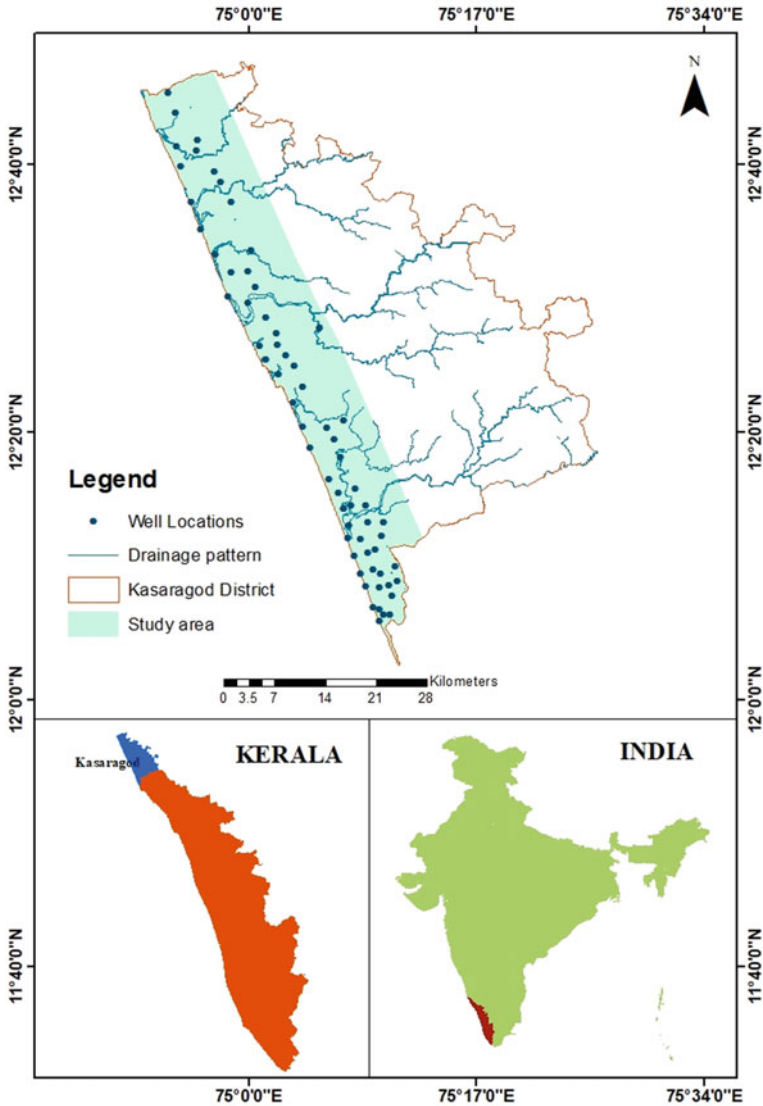
Fig. 1 Study area map of coastal and inland areas of Kasaragod district with radon sample locations

Gneiss/Charnockite/Khondalite (22 samples), laterite (4 samples), and tertiary alluvium (13 samples) during post-monsoon season from the coastal areas of Kasaragod district, Northern Kerala, India. The sampling points were determined and demarcated by detailed field visit using handheld Garmin GPS device, GIS software, and SOI topographic maps. A detailed questionnaire for well inventory was prepared for gathering information relevant to the current hydrogeological status of the study

area. In situ measurements such as total depth of the open well, depth to water level, sample collection time, and other geological and geomorphological characteristics were recorded. Further, in situ measurement of physical parameters of groundwater such as temperature, pH, EC, TDS, and salinity was done in the study area using Eutech multi-parameter tester (PCS Testr 35).

The groundwater samples from variously identified observatory wells were collected without any contact with the atmospheric air in 250-ml vials by using the Ruttner water sampler. The sampling was done in the month of December (Post-monsoon) of 2018. The collected samples were analyzed after taking it to laboratory and it radon activity is expressed in Bq/m^{-3}. The time difference between taking the sampling time was few hours, so radioactive decay of radon are corrected in the water sample data with the error calculation formula with respect to the sampling time. Radon concentration of sample is measured in situ using RAD7 instrument, an electronic radon detector.

The RAD7 is mainly composed of an air pump that extracts radon from the samples and a silicon semiconductor alpha detector that converts alpha radiation straight to an electrical signal. The silicon semiconductor alpha detector has been fitted to convert the alpha radiation directly into an electrical signal. The operation of this RAD7 equipment is based on following principle: (i) radon is expelled from groundwater sample by using a bubbling kit, (ii) expelled radon will enters into a hemisphere chamber by air circulation, (iii) polonium decayed from radon is collected onto a silicon solid state detector by an electric field, and (iv) radon concentration were calculated from the count rate of polonium [14].

RAD7 is fitted with a desiccant ($CaSO_4$) tube used to eliminate moisture and keep the relative humidity under 10% because the sensitivity of the instrument reduces with high humidity. The purging process is carried out for 10 min at first because relative humidity of the instrument should be maintained around RH 6% and the trapped radon inside the system should be removed after each sample analysis is completed. The equipment was calibrated in accordance with the recommendations of the Environmental Protection Agency (EPA). The RAD7 H_2O is an accessory to RAD7 that helps in the measurement of radon concentration ranges from < 10 pCi/l to > 4 × 105 pCi/l in groundwater [15]. It is expressed in Becquerel per cubic meter (Bq/m3). One Becquerel is equivalent to single radioactive disintegration per second. Curie is a unit of radioactivity equivalent to 1 g of radium and the prefix 'pico' means trillionth 4 pCi/L equals to 148 Bq/m3. Radon concentration in water is generally expressed in Becquerel per liter (Bq/l).

4   Results and Discussion

4.1   Radon Concentration in Groundwater of Study Area

Radon (^{222}Rn) is a geogenic diffusive gas and the investigations on the relationship between the radon anomaly and factors viz. physiographic, geologic, and hydrogeological aspects of the study area will enable to understand the variation of radon distribution in groundwater. The groundwater samples collected from five lithological formations were measured for radon concentration. The ^{222}Rn of the coastal alluvium region is ranged from 77.1 Bq/m^3 to 832 Bq/m^3 and average concentration of 408 Bq/m^3. In fluvial alluvium region, the minimum radon concentration is 39.6 Bq/m^3 and the maximum is 479 Bq/m^3 and average concentration of 440 Bq/m^3 (Fig. 2).

In Gneiss/ Khondalite/ Charnockite region the radon ranged from 117.5 Bq/m^3 to 2343 Bq/m^3 and average concentration of 782 Bq/m^3. The ^{222}Rn in laterite region is ranged from 436 Bq/m^3 to 1114 Bq/m^3 and average concentration of 636 Bq/m^3 and in tertiary alluvium region, it is ranged from 37.8 Bq/m^3 to 1135 Bq/m^3 and average concentration of 346 Bq/m^3. Higher radon concentrations were primarily noted in the Gneiss /Khondalite/ Charnockite rocks and lateritic region.

The controlling factors such as electrical conductivity, temperature, water table depth, geology, and geomorphological features of the study area were analyzed. The groundwater temperature varied from 24.2 ℃ to 30 ℃ and average value of 26.4 ℃, so the temperature ranges are indicative of non-thermal water in the area [16]. The radon gas having a diffusive nature, during the higher temperature its solubility decreases in water, so very quickly the gas escapes from it. Therefore, the temperature of groundwater is a key significant factor which influences the extent of radon dissolution in the groundwater [17–19].

The average groundwater level in coastal alluvium is 2.4 m and that in fluvial alluvium is 1.8 m. In Gneiss/Charnockite/Khondalite, the groundwater comparatively deep, i.e., 9.8 m. Laterite formations have minimum water table depth of 5.1 m and maximum water table depth of 10.8 m and its average water table depth 8.3 m and in tertiary alluvium, the average water table depth is 4.3 m. The water table depth of different aquifers in various geological formations in the study area has shown not much significant correlation between radon concentration levels and water table depth.

While measuring the physio-chemical parameters on groundwater, coastal alluvium groundwater sample having minimum pH is 6.1, maximum pH is 7.7, and average pH is 6.9. In fluvial alluvium, pH of groundwater ranges from 4.5 to 7.4 with average value of pH is 6.1. The average pH value of groundwater in Gneiss/Charnockite/ Khondalite is 5.5 and which has a minimum pH of 4.6 and maximum pH is 7.5. The pH value of groundwater in laterite formations ranges from 4.6 to 6.5 and average value is 5.6. Also, in tertiary alluvium minimum pH is 4.9 and maximum pH is 7.3 with average pH of groundwater is 6.3. The pH values depict the
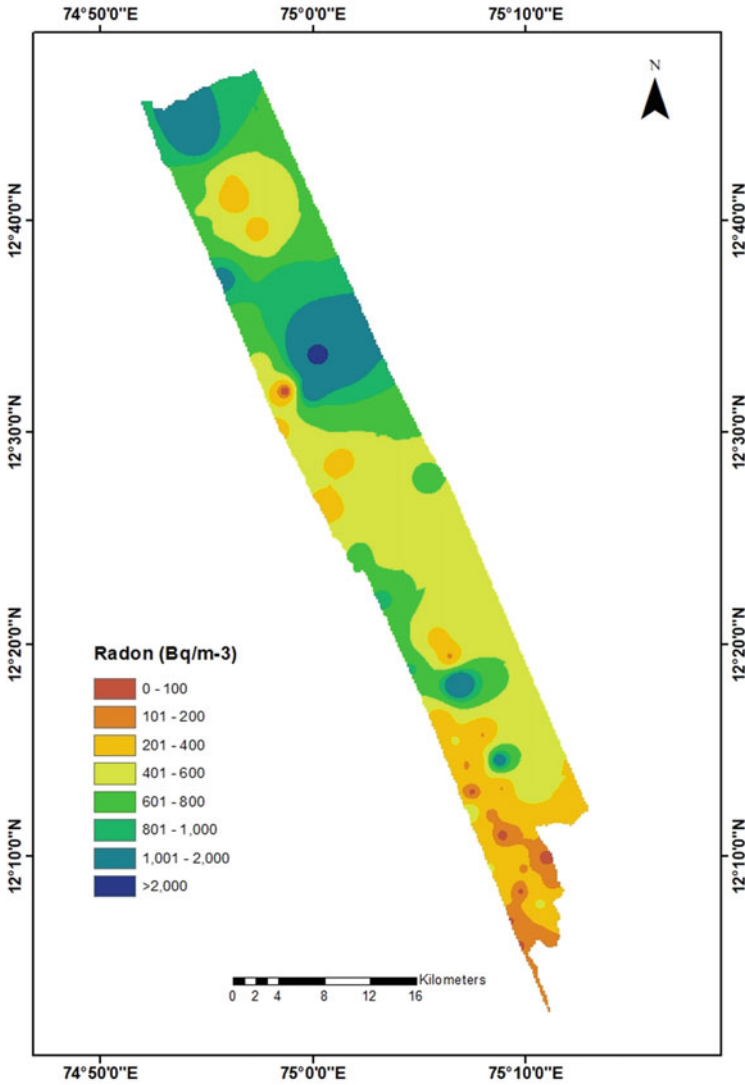
Fig. 2 Spatial distribution of ^{222}Radon (Bq/m^3) of groundwater sample during post-monsoon (December) 2018 in coastal and inland aquifers of the study area

slightly acidic behavior of the groundwater which can be assessed as low rock-water interactions of acidic rainwater infiltrated into coastal aquifer acidic [20].

Electrical conductivity (EC) is a good indicator of mineralization of the groundwater. Groundwater sample collected from coastal alluvium having an average EC of 931 µS/cm and that of fluvial alluvium formation have 286 µS/cm. The average

EC of groundwater in Gneiss/Charnockite/Khondalite is 139 µS and laterite formations have an average EC of 80 µS/cm. The groundwater in tertiary alluvium have an average EC is of 230.5 µS/cm. Groundwater samples in all geological formation were having lower EC values indicating that these are comparatively least mineralized and is a fresh groundwater, it is because of low extent of rock-water interactions in the aquifer [20]. So, no much significant correlations were observed between the radon concentration and electrical conductivity.

The Coastal alluvium groundwater samples having a total dissolved solids (TDS) of range from 121 mg/L-3120 µS and average TDS is 656 mg/L. In fluvial alluvium, TDS value ranges from 40 mg/L-630 mg/L and average value of 203 mg/L. Gneiss/Charnockite/Khondalite shows TDS value of 29 mg/L-312 mg/L and average value of 99 mg/L. Laterite formations also have an average TDS value of 57 mg/L in groundwater and in tertiary alluvium, the TDS in groundwater ranges from 46 mg/L–326 mg/L and average value of 168 mg/L (Fig. 3). Higher total dissolved solids concentration were observed in groundwater samples from coastal alluvium formation. The present study area confined in shallow aquifers (<18 m in Gneiss/Charnokite/Khondalite formation) and the possibility of groundwater mixing with other geological components is low within the shallow circulation zone. Therefore, the physio-chemical parameters are showing no significant influence on radon activity in groundwater of the study area.

5   Conclusions

The groundwater radon distribution in the various geological formations of the coastal and inland regimes in Kasaragod district was carried out using a RAD7 detector and RAD H_2O accessory and the study pointed out that there was no significant correlation between radon concentration and electrical conductivity, temperature, and depth to the water level within various geological formations of the study area. The physio-chemical parameters show the least influence on the ^{222}Rn activity of groundwater because in shallow aquifers the possibility of groundwater mixing with other geological components is comparatively low within the shallow circulation zone.
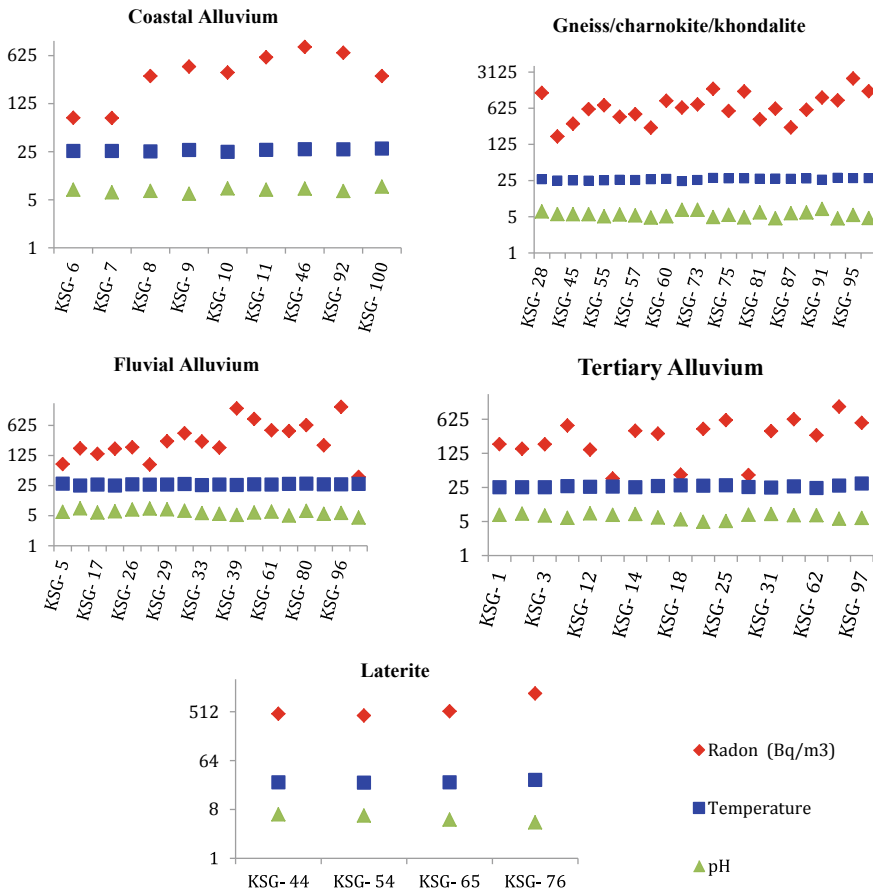
Fig. 3 Radon (^{222}Rn) concentration in groundwater in various geological formations of the study area is compared with temperature and pH

References

1. Duggal V, Mehra R, Rani A (2013) Determination of 222rn level in groundwater using A Rad7 detector in the Bathinda district of Punjab, India. Radiat Prot Dosimetry 156(2):239–245. https://doi.org/10.1093/rpd/nct054

2. Donkor NKA, Poku PA, Kotei Addison CD, Wemengah DD, Adimado AA (2018) Measurement of radon concentration in groundwater in the Ashanti region of Ghana. J Radioanalytical Nuclear Chem https://doi.org/10.1007/s10967-018-5930-1

3. Krishan G, Rao MS, Kumar CP, Semwal P (2015) Radon concentration in groundwater of east coast of West Bengal, India. J Radioanal Nucl Chem 303:2221–2225. https://doi.org/10.1007/s10967-014-3808-4

4. WHO (World Health Organization) (1993) Guidelines for drinking water quality, vol 1, 2nd edition. WHO, Geneva

5. Hunse TM, Najeeb KM, Rajarajan K, Muthukkannan M (2010) Presence of radon in groundwater in Parts of Bangalore. J Geol Soc India 75:704–708

6. Choubey VM, Bartarya SK, Ramola RC (2003) Radon in groundwater of eastern Doon valley, Outer Himalaya. Radiat Meas 36(2003):401–405

7. Nalukudiparambil J, Gopinath G, Resmi TR, Anil Kumar KS (2021) Groundwater radon (^{222}Rn) assessment of a coastal city in the high background radiation area (HBRA), India. Arab J Geosci Springer 14:724. https://doi.org/10.1007/s12517-021-07082-7

8. Gopinath G, Resmi TR, Pragath M, Jesiya NP, Shahul Hameed A, Deshpande RD (2021) Isotopic differentiation of groundwater recharge processes in a semi-arid region of southern India. Environ Earth Sci Springer 80(16). https://doi.org/10.1007/s12665-021-09816-y

9. Jesiya NP, Gopinath G, Resmi TR (2021) Comprehending the groundwater recharge of a coastal city in humid tropical setting using stable isotopes. J Environ Manage Elsevier 287:112260. https://doi.org/10.1016/j.jenvman.2021.112260

10. Swetha TV, Gopinath G, Reshmi TR (2020) Isotope mass balance estimation of groundwater recharge in a hard rock tropical river basin in Kerala, India. J: Groundwater Sustain Develop Elsevier. https://doi.org/10.1016/j.gsd.2020.100422

11. Ground water information booklet of Kasaragod district (2013) Kerala State, Central ground water board (CGWB)

12. Basak P, Nizimuddin M (1985) Groundwater in the coastal belt of Kasaragod district. (Report), Groundwater division, CWRDM, Kozhikode GW/R-127/85

13. District survey report of Minor minerals of Kasaragod district (2016) Department of Mining and Geology, Govt. of Kerala

14. Basak P, Nizimuddin M, Latha P (1985) Salt water intrusion in coastal aquifers of Kasaragod district (Report) Groundwater division, CWRDM, Kozhikode GW/R-128/85

15. Durridge Company Inc (2015) RAD7 Radon Detector. User Manual

16. Gopinath G, Seralathan P (2006) Chemistry of groundwater in lateritic terrains of the Muvattupuzha river basin, Kerala, India. J Geol Soc India, Springer 68:705–714. ISSN: 0974–6889

17. Durridge Company Inc (2016) RAD7 RADH2O Radon in Water Accessory. Owner's Manual

18. Wilhelm E, Battino R, Wilcock RJ (1977) Low-pressure solubility of gases in liquid water. ACS Publication. https://doi.org/10.1021/cr60306a003

19. Cothern CR, Smith JE (1987) Environmental Radon book chapter, Environmental science research, vol 35, Springer Science

20. Sukanya S, Noble J, Joseph S (2021) Factors controlling the distribution of radon (222Rn) in groundwater of a tropical mountainous river Basin in Southwest India. Chemosphere 263:128096

Groundwater Quality Assessment and Water Quality Index (WQI) Mapping of Phreatic Aquifer, Palakkad District, Kerala

T. V. Swetha, R. Remitha, and Gopinath Girish

Abstract The secondary data of 12 physico-chemical parameters from 50 sampling locations was collected from the CGWB, 2018 report for groundwater quality assessment and water quality index (WQI) mapping of phreatic aquifer in Palakkad district, Kerala. pH, electrical conductivity, total dissolved solids, Ca^{2+}, Mg^{2+}, Na^+, K^+, NO_3^{2-}, $SO4^{2-}$, F^-, Cl^-, HCO_3^- were considered for the assessment. The results were compared with WHO and BIS standards to interpret the permissible water samples. Using the analytical data, spatial distribution maps displaying concentrations of each parameter were prepared using Arc GIS 10 software in order to evaluate the water quality. The quality of water for drinking purposes was evaluated based on the water quality index map considering five parameters such as calcium, magnesium, bicarbonate, fluoride and nitrate. Gibbs diagram indicates that the rock-water interaction is the dominant process controlling the groundwater chemistry in the study area. WQI map shows that groundwater from eight locations are unsuitable for drinking. Quality of water for irrigational activities was determined by evaluating Sodium Adsorption Ratio (SAR), Residual Sodium Carbonate (RSC), Sodium Percentage and USSL diagram. From these studies, it was concluded that most of the samples are suitable for drinking and irrigation purposes except a few locations which exceeds the permissible limits. Ion-exchange processes and silicate weathering along with anthropogenic activities are mainly controlling the groundwater chemistry of the phreatic aquifer system of this study region.

Keywords WQI · SAR · USSL · Gibbs · Piper trilinear diagram

T. V. Swetha (✉) · R. Remitha
Department of Geology and Environmental Science, Christ College, Irinjalakuda, Thrissur, Kerala 680125, India
e-mail: tvthulasy@gmail.com; swetha.geology@gmail.com

G. Girish
Department of Climate Variability and Aquatic Ecosystems, Kerala University of Fisheries and Ocean Studies, Kochi, Kerala 682508, India

1 Introduction

Water being the basic human entity is known to be the major natural resource for the existence of life. Drinking, agricultural, industrial, household, recreational, environmental activities are various purposes for which water resources are harnessed. Compared to surface water, groundwater is less vulnerable to contamination as it is highly mineralized in its natural state. When water penetrates slowly through the subsurface porous media, it gets saturated with dissolved solids from these minerals as it had been in contact with minerals in soil and bedrock for a prolonged period of time. Natural factors that control chemistry of water include precipitation pattern, precipitation amount, geological features of watershed and aquifer and when the quantity and quality of the groundwater is assessed, the water can be optimally used and sustained. According to Babiker et al. [2], the chemistry of groundwater is related to lithology of the area, the residence time (i.e., time the water is in contact with rock material), the inputs from atmosphere, soil and weathering. It also depends on various pollutant sources such as mining, land clearance, saline water intrusion, industrial and domestic wastes. Conducting geochemical studies of groundwater provides a better understanding about the possible changes in quality of water as development progresses. Total dissolved solids (TDS) defines the inorganic salts and small amounts of organic matter present in water and Calcium, Magnesium, Sodium, and Potassium cations and carbonate, hydrogen carbonate, chloride, sulphate and nitrate anions are the principle constituents in water.

In this study, the spatio-temporal variation of physical and chemical parameters, hydrogeochemical process involved and the water type of the groundwater regime of Palakkad district is carefully identified to reveal the status of groundwater quality for drinking and irrigation purposes in the present scenario.

2 Study Area and Data Source

2.1 Palakkad District

Palakkad district, known as the "Gateway of Kerala" lies between 10.7867 °N latitude and 76.6548 °E longitude. It is 92 m above sea level and has no coastal line. The average annual temperature in Palakkad is 25.9 °C/78.6 °F. Physiographical division of the study area is the high land and mid land and the elevation varies from 20 to 2386 m amsl (Central Ground Water Board, Kerala Region). One of the important physiographic features of the district is the Palakkad Gap. Laterite soil, virgin forest soil, black cotton soil and alluvial soil are the major kind of soil types found in the district.
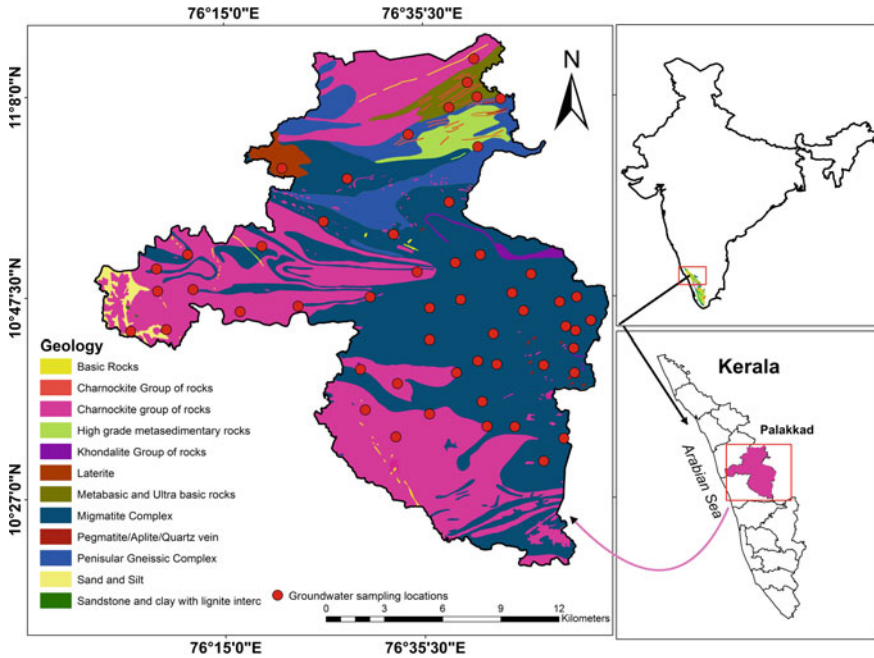
Fig. 1 Study area map with geology and groundwater sampling locations

2.2 Geological Setting and Hydrogeology

The district is broadly divided into 5 geological terrain: (1) Lowland of Charnockite in the west, (2) Migmatite complex in the East, (3) Khondalite group which occurs as linear bodies in the Northeastern hill region, (4) Waynad group which occurs as high hills in the north Attapady area and (5) Peninsular Gneissic Complex (PGC) confined to the north of Bharathapuzha [8]. The entire district is divided into three hydrogeological units (a) Valley fills/Alluvium (b) Laterite terrain and (c) Crystallines. Groundwater occurs in phreatic condition in the laterite and alluvium hydrogeological units and it is in semi confined to confined condition in weathered crystallines (Fig. 1).

2.3 Data Used

Data used in the present study for the analysis of groundwater quality is the secondary data collected from Groundwater year book of Kerala, (GWYB 2017–2018). The physico-chemical parameters such as pH, Electrical conductivity, Total dissolved solids and the major ions (Calcium, Magnesium, Sodium, Potassium, Carbonates, Sulphates, Chlorine, Fluoride and Nitrate) were considered for the assessment of

Table 1 Standard values of physico-chemical water quality parameters

Chemical parameters	BIS standards (2012)	WHO Standards (2011)
PH	6.5–8.5	6.5–8.5
E.C (μS/cm)	–	500
TDS (mg/l)	500	500
$HCO_3 + CO_3$ (mg/l)	500	
Cl (mg/l)	250	250
SO_4 (mg/l)	200	250
Ca (mg/l)	75	75
Mg (mg/l)	30	50
Na (mg/l)	–	200
K (mg/l)	–	200
F^-	1	1.5
NO3-	45	50

water quality in the area. Water samples from 50 locations were taken into consideration for evaluating water quality of the area, covering the entire Palakkad district. The various physico-chemical parameters and their standard limit [3, 18] is given in the following Table 1.

Using the Gibbs diagram, the major mechanism controlling the groundwater chemistry in the area was determined and the Piper trilinear diagram has been plotted using AquaChem 2014.2 version for the identification of the major water type of the area.

The irrigation quality was evaluated using SAR ratio, RSC, Sodium percentage and USSL diagram [16]. The permeability of soil get reduced when the sodium reacts with soil and thus making the soil infertile for plant growth. The evaluation of sodium concentration is important in determining quality of groundwater for irrigational purposes (Todd 1980), which is given by the equation:

$$\%\text{Na} = (\text{Na} + K)100\,\text{Ca} + \text{Mg} + \text{Na} + K \tag{1}$$

Sodium Adsorption Ratio (SAR) measures the relative concentration of sodium to calcium and magnesium and it expresses the relative activity of sodium ions in the exchange reactions with the soil. Water having SAR values less than 10 are considered excellent, 10–18 is good, 18–26 is fair, and above 26 are unsuitable for irrigational uses (USDA 1954).

SAR is defined by:

$$\text{SAR} = \text{Na}\sqrt{(\text{Ca} + \text{Mg})/2} \tag{2}$$

Residual Sodium Carbonate is an alternative measure of the sodium content in relation with magnesium and calcium (Muhammad Arshad et al., 2017). RSC is defined by the following equation:

$$RSC = (CO_3^- + HCO_3^-) - (Ca^2 + Mg^2) \tag{3}$$

The United States Salinity Laboratory (USSL) (1954) proposed standards for irrigation water quality classification. The combined effect of sodium hazard and salinity hazard in the irrigation quality of water could be interpreted from this plot.

The quality for drinking purposes was determined using water quality index (WQI) mapping.

2.4 Water quality index (WQI) mapping

Water quality index (WQI) is an important and most effective tool for determining quality of water for drinking purposes. For calculating WQI, weight is assigned for the physico-chemical parameters according to the parameters relative importance in the overall quality of water for drinking purposes based on WHO drinking water standards (Table 2) [17]. The assigned weight ranges from 1 to 5. The maximum weight of 5 is assigned for Ca^{2+}, 4 for Mg^{2+}, 3 for HCO_3^-, 2 for F^- and 1 for NO_3^{2-}.The relative weight is given by the equation:

$$W_i = w_i / \sum w_i n_i = 1 \tag{4}$$

where

W_i relative weight
w_i weight of each parameter
n *number of parameters.*

The quality rating scale for each parameter is calculated by dividing its concentration in each water sample by its respective standards (WHO) and multiplying the results by 100.

$$q_i = (C_i / S_i) \times 100$$

where

q_i is the quality rating
C_i is the concentration of each chemical parameter in each sample in milligrams per litre
S_i is the WHO standard for each chemical parameter.

Table 2 Physico-chemical water quality parameters of study area

Location name	PH	E.C	TDS	Ca	Mg	Na	K	Hco3+Co3	So4	Cl	F	NO_3
Agali	6.99	790	505.6	49.3	13.70	83.2	2.3	230.00	44	71.9	0.2	27.3
Alanallur	7.03	220	140.8	13.6	5.50	23	7.1	28.00	12.03	29.3	0.6	12.1
Alathur	7.85	930	595.2	52.6	42.80	53.6	5.3	140.00	24	182.8	0.2	6.1
Athipetta	8.2	570	364.8	38.2	19.60	41.5	16.9	155.00	14.1	71.0	0.1	1.7
Chalissery	7.64	172	110.08	9.5	3.70	18	5.2	12.00	1.8	27.3	0.5	22.6
Chavadiyur	7.6	770	492.8	34.6	48.30	51.9	3.20	310.00	23.2	29.2	0.4	40.8
Chemmanampathy	7.36	1770	1132.8	102.3	64.90	129.9	25.9	240.00	131.25	241.0	0.5	183.0
Cherpulassery	7.59	420	268.8	22.8	10.16	38.7	20.58	45.00	24.5	46.4	0.2	64.0
Chittur	7.72	510	326.4	45.7	16.80	37.9	4.99	195.00	18	24.5	0.6	10.0
Gopalapuram	7.59	940	601.6	41.0	14.00	117	2	230.00	14.5	81.0	0.0	102.0
Kalladikkode	3.55	174	111.36	5.2	1.70	28.2	1.5	1.00	2.3	29.0	0.0	23.0
Kanjikkode	8	1200	768	42.2	25.70	133.5	75.2	240.00	58	164.0	0.1	54.0
Karimpuzha	7.86	135	86.4	18.2	3.50	15.7	3.2	48.00	8	15.3	0.3	5.3
Koduvayur	7.76	220	140.8	9.3	6.80	30.4	1.6	62.00	9.2	19.4	0.6	2.2
Kollengode	8.27	770	492.8	26.1	40.50	65.3	3.3	245.00	46.8	63.2	0.3	1.3
Koppam	8.2	250	160	11.0	7.00	35.71	3.85	46.00	4.5	42.9	1.0	18.0
Kozhinjampara	7.17	1000	640	62.3	27.10	74.8	3.9	165.00	44	144.8	0.3	35.0
Kuzhalmannom	7.59	840	537.6	48.6	29.00	65	8.6	230.00	44	91.5	0.5	4.0
Mankara	9.07	270	172.8	12.0	6.30	27	5.12	34.00	15.64	34.8	0.5	0.2
Mannarkkad	8.02	430	275.2	24.2	7.20	36.2	16.6	80.00	15.7	53.6	0.2	4.4
Meenakshipuram	7.71	830	531.2	41.1	26.6	64.7	9.3	195.00	30.8	61.0	0.0	78.1

(continued)

Table 2 (continued)

Location name	PH	E.C	TDS	Ca	Mg	Na	K	Hco3+Co3	So4	Cl	F	NO₃
Meenkara	7.64	1180	755.2	69.1	32.6	73	9.1	300.00	55	130.0	0.6	10.8
Mundur	7.67	280	179.2	21	10.3	24.5	3.8	96.00	8.8	23.8	0.1	3.1
Nadupuni	7.53	1950	1248	86.6	76.5	227	12.7	310.00	462	180.4	1.2	21.7
Nenmara	7.93	560	358.4	41	16.5	52	7.5	110.00	45	65.1	0.1	21.0
Ottapalam	7.72	390	249.6	18	6.1	54.2	1.5	65.00	3	66.8	0.0	10.1
Palakkad	7.92	730	467.2	40.6	32	60	2.5	215.00	27	68.0	0.4	15.0
Pattambi	7.55	330	211.2	20.3	8.5	15	5.2	20.00	17.9	38.0	0.2	14.7
Pudunagaram	7.97	960	614.4	59	24.7	82.5	31.7	300.00	30.7	75.0	0.2	24.5
Shoranur	7.62	230	147.2	24	7.5	26	7.5	64.00	10	30.0	0.8	5.1
Thavalam	7.56	380	243.2	28.9	14	31.4	2.1	88.00	7.2	40.5	4.1	25.1
Tirthala	7.9	640	409.6	54.7	17.1	42.8	3.21	190.00	24	61.3	0.2	2.4
Vadakkanchery	8.34	760	486.4	59.6	26.5	63.5	5.6	175.00	36.5	92.7	0.1	31.9
Vattalakki	7.45	1200	768	32.8	55.20	156.8	8.56	463.60	51.7	110.8	1.8	28.9
Kottathara	7.56	2500	1600	51.3	136.40	278.8	8.06	585.60	31.2	571.6	2.0	24.9
Naikarapadi	7.35	880	563.2	38.5	58.40	56.9	7.2	384.30	10.9	66.1	0.0	34.8
Kollengode-I	7.6	1560	998.4	71.9	42.70	221.1	11.90	500.20	90.3	221.1	1.5	4.6
Kollengode-II	7.35	730	467.2	38.2	39.10	63.2	3.3	305.00	45.3	49.8	0.6	2.9
Parayur	7.55	510	326.4	61.9	14.30	23.4	3.2	238.00	20.6	25.9	0.4	7.1
Koduvayur	7.1	210	134.4	7.9	6.30	27.9	1.3	76.00	7.5	16.6	0.0	1.0
Koduthirapally	7.5	660	422.4	59.1	18.70	56.4	2.7	238.00	46.9	53.8	0.8	3.0
Vannamada	7.53	1060	678.4	78.3	34.40	108.1	3.1	329.00	59.6	80.3	0.0	102.1

(continued)

T. V. Swetha et al.

Table 2 (continued)

Location name	PH	E.C	TDS	Ca	Mg	Na	K	Hco3+Co3	So4	Cl	F	NO3
Gopalapuram	7.23	750	480	41.9	8.83	119.5	1.3	262.00	29.8	47.7	1.3	62.0
Muthalamada	7.56	1050	672	49.4	61.50	95.4	2.1	378.00	26.3	152.1	1.6	11.5
Eruthenpathy	7.73	1300	832	34.1	22.70	259.5	2.5	488.00	142.7	99.6	1.6	12.7
Erattakulum	7.29	350	224	35.0	10.60	22.4	3.3	164.00	14.9	19.3	0.4	0.0
Koppanur	8.18	2500	1600	14.7	37.00	559	3.3	1000.00	55	317.9	4.6	26.1
Kozhipara	7.53	1670	1068.8	71.1	79.50	179.1	2.7	281.00	57.7	418.7	1.2	12.4
Athikode	7.73	1100	704	59.0	32.00	164	3.04	427.00	82.6	112.0	0.9	3.5
Velanthavalam	7.49	740	473.6	52.4	27.3	76.4	3.9	244.00	62.8	59.5	0.2	29.9
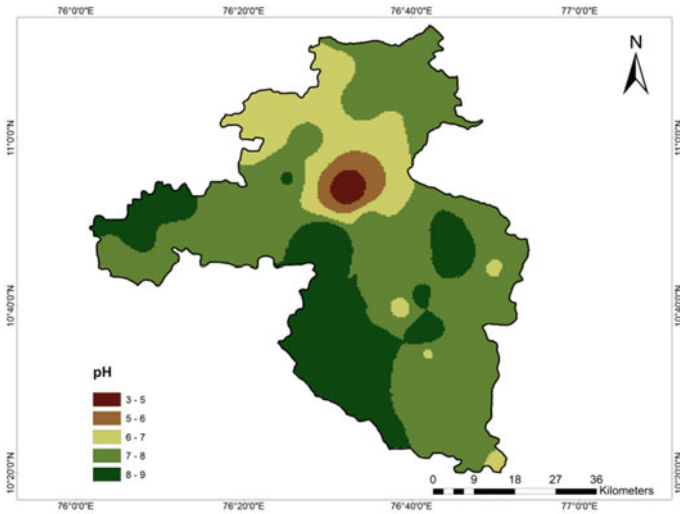
Fig. 2 pH

For calculating final WQI, SI is determined for each parameter and the sum of SI values gives the water quality index of each sample.

$$SI_i = W_i \times q_i$$
$$WQI = \Sigma SI_i$$

where

SI_i is the sub-index of i th parameter
q_i is the rating based on concentration of i th parameter
n is the number of parameters.

The Arc GIS tools, inverse distance weight (IDW) and overlay analyst function 'overlay' used to prepare spatial distribution maps of physical and chemical water quality parameters (Figs. 2, 3, 4, 5, 6, 7, 8, 9, 10) and water quality index map (Fig. 15) of the study area.

3   Results and Discussion

3.1   Physical Characteristics of Groundwater

The statistical summary of groundwater chemistry parameters of the study area is given in the Table 1. According to the results, majority of the area has pH ranging
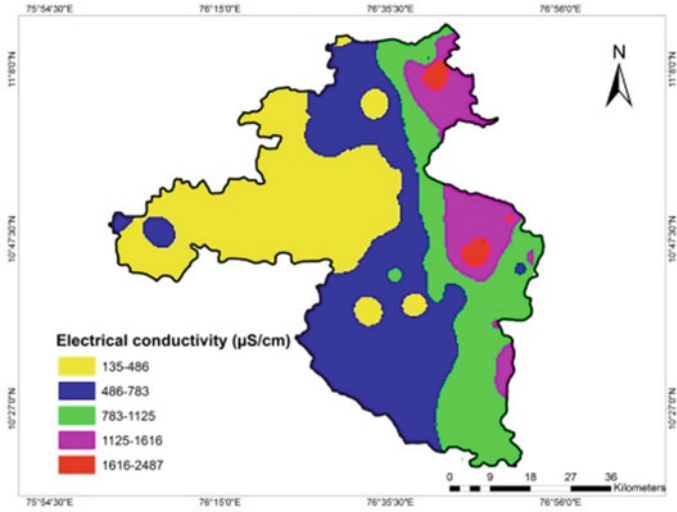
Fig. 3 EC
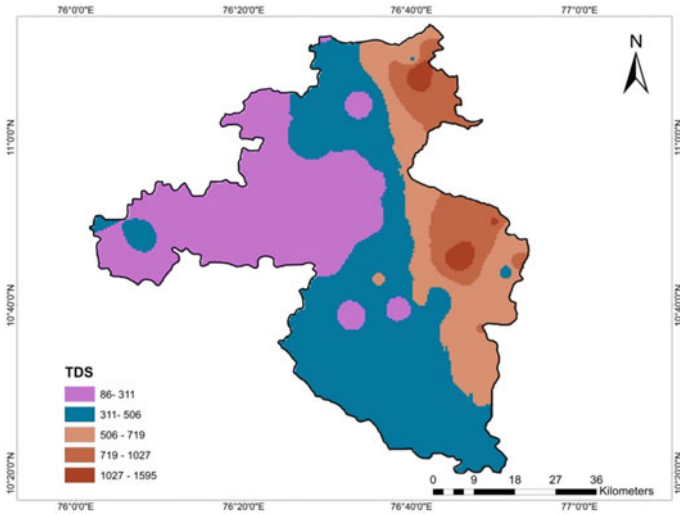
Fig. 4 TDS

between 7 and 8 that is alkaline in nature indicating permissible limit. Only location Kalladikode has pH values between 3 and 5. Most of the samples in the study area shows EC values less than 1500 μS/cm and falls under Type I category that indicates low enrichment of salts in groundwater. Three locations (Kottathara, Koppanur and Kollengode I) having EC values between 1500 and 3000 exceeds the permissible limit which falls under the category II that is medium enrichment of salts. None of
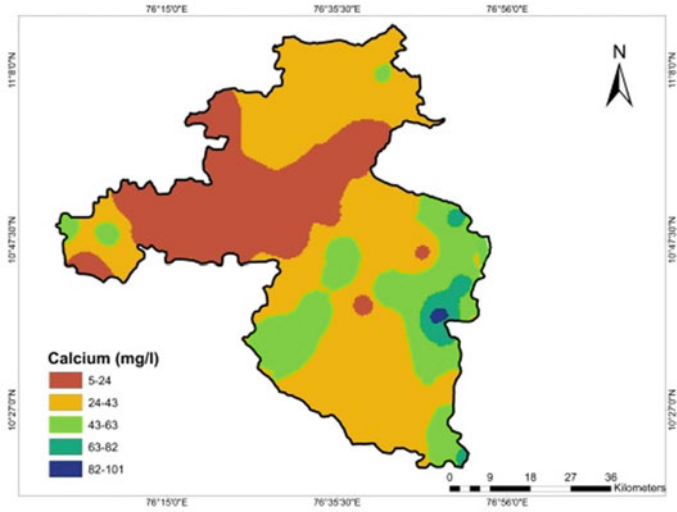
Fig. 5 Calcium (Ca)
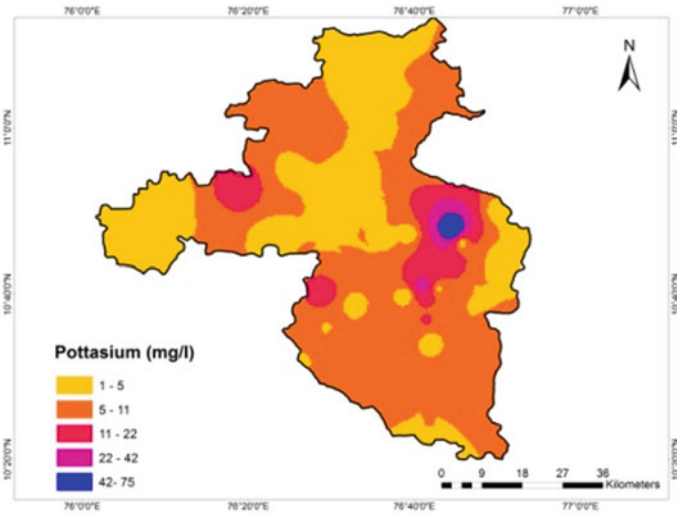
Fig. 6 Pottasium (K)

the collected samples exceeds 3000 μS/cm and thus the entire study area falls under Type I and Type II category.

The TDS values of the study area ranges from 86 to 1595 mg/litre. Majority of the samples (15 samples) have TDS value ranging between 300 and 600 mg/litre, thereby indicating good quality. TDS values of 9 locations range between 600 and 900 mg/litre which indicates fair quality of groundwater. Three samples show TDS
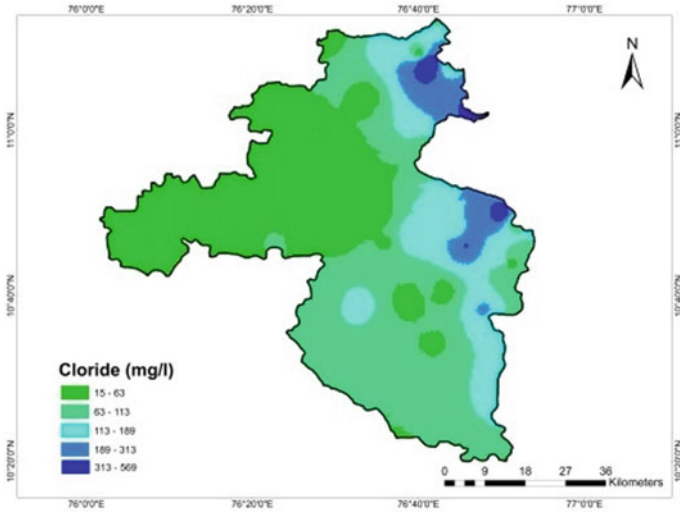
Fig. 7 Chloride (Cl)
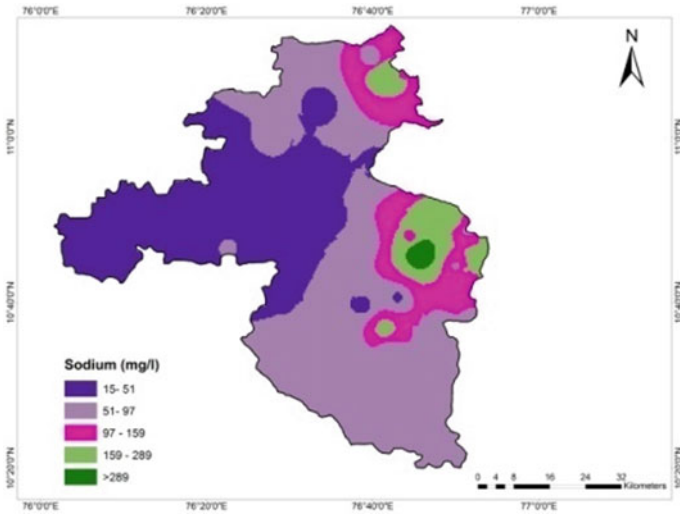
Fig. 8 Sodium (Na)

levels ranging from 900 to 1200, thus indicating poor quality. The samples collected from locations Nadupuni, Kottathara and Koppanur have TDS level exceeding 1200 mg/litre and suggest that the water is unsuitable.
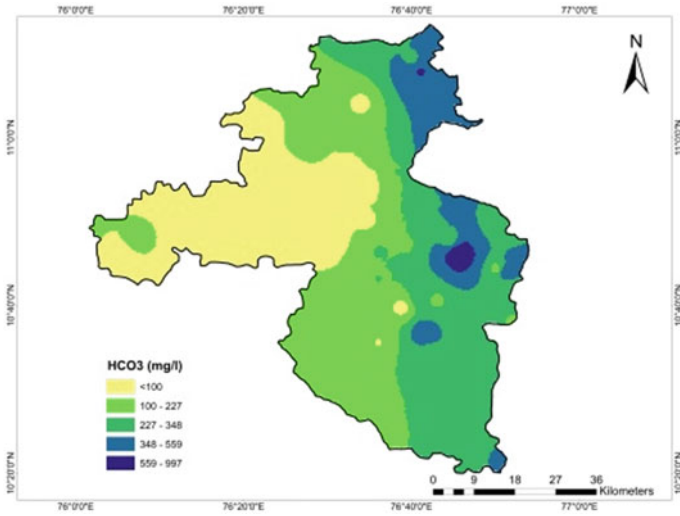
Fig. 9 Bicarbonate (HCO_3^-)
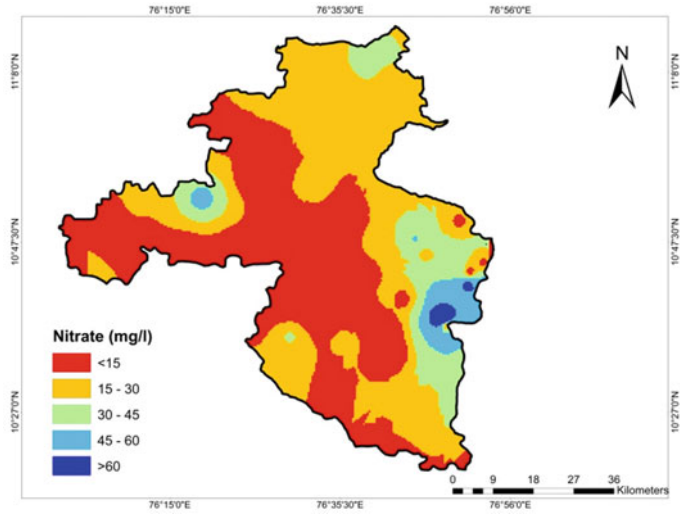
Fig. 10 Nitrate (NO_3)

3.2 Major Ion Chemistry

Calcium and magnesium ions accounts for most of hardness in groundwater. The desirable limit of calcium concentration is given as 100 mg/l (WHO 2017) and can be extended up to 200 mg/l. All the samples in the study area lie within the
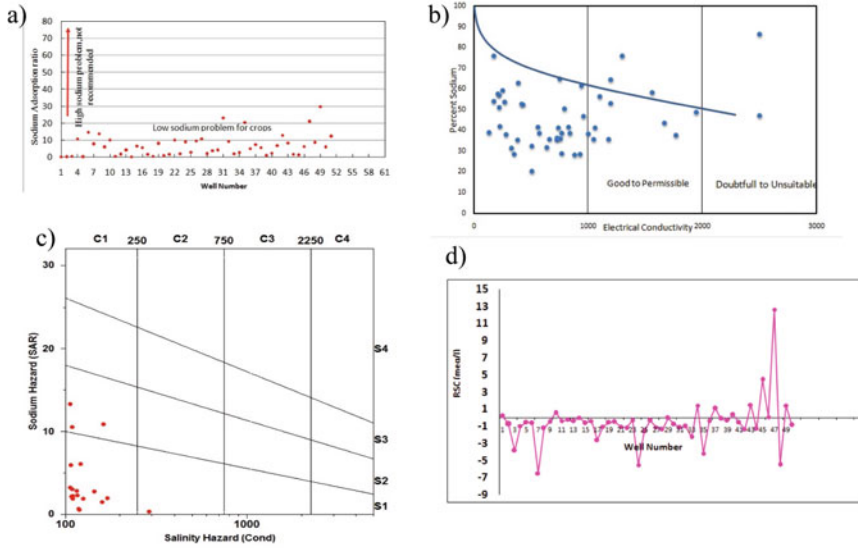
Fig. 11 Various ratio plots to verify groundwater quality for irrigation **a)** SAR **b)** Na% **c)** USSL **d)** RSC

Water types
I.Ca^{2+}-Mg^{2+}- Cl^--SO_4^{2-}
II.Ca^{2+}-Mg^{2+}- HCO_3^-,
III. Na^+- K^+-Cl^--SO_4^-
IV. Na^+- K^+ HCO_3^-type

Fig. 12 Piper plot showing water types of study area

Fig. 13 Gibbs diagram showing rock dominance in groundwater chemistry
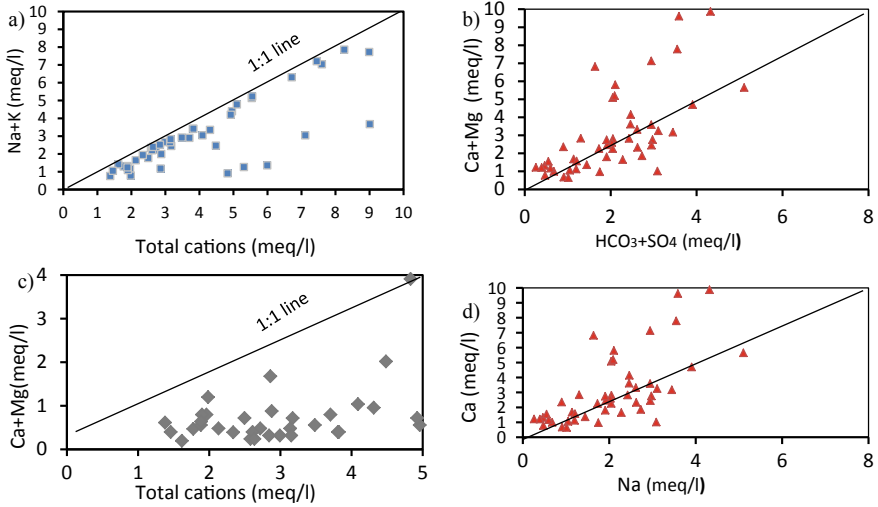
Fig. 14 Scatter plots showing Stoichiometric relations between major ions **a** Na + K/Total cations **b** Ca + Mg/HCO$_3$ + SO$_4$ **c** Ca + Mg/Total cations **d** Ca versus Na

permissible limit and thus indicate suitable quality. The desirable limit for magnesium concentration in water is specified as 50 mg/l by WHO. Majority of the samples falls with the permissible limits of Mg concentrations. Six locations exceeds the limit (>50) and the water sample from Kottathara location shows magnesium concentration of 136 mg/l which indicates higher concentrations.

According to WHO, the permissible limit of Na concentration is 200 mg/l. All the water samples falls within the permissible limit except two (Kottathara and Kollengode I). Kottathara and Kollengode have concentrations of 278.8 mg/l and 221.1 mg/l, respectively. The desirable limit for potassium concentrations is specified as 20 mg/l as and the concentrations of potassium in the study area lies between 1 mg/l and 75 mg/l. Majority of the samples shows potassium content that is within the permissible limit. Out of 50 locations, only 3 areas exceed the desirable limits (Pudunagaram, Kanjikode and Cherpulassery).

The bicarbonate concentration ranges from as 125 to 350 mg/l and 8 water samples of present study area have values exceeding the above limit. The location Koppanur shows the highest value of 1000 mg/l and Kalladikode have the least concentration of 1 mg/l. The higher concentration of HCO3 in the water indicates dominance of mineral dissolution.

High concentrations of chloride may give a salty taste to water and may cause physiological damages. In the study area, the concentration of chloride is between 15 mg/l and 569 mg/l. The permissible limit for chloride concentration is 250 mg/l and majority of the water samples lies within the proposed permissible limit and 3 locations shows higher concentrations (Kottathara-571.6 mg/l, Kozhipara-418.7 mg/l and Koppanur-317.9 mg/l). Sulphate is one of the major anions present in groundwater and its concentration in all the samples lies within the permissible limit.

Studies indicate that high fluoride groundwater occur in the hard rock aquifers in Palakkad district mostly in the eastern part. Major sources of fluoride are from fluorite (CaF2) which is a common accessory mineral in granite, granite-gneisses and pegmatite. According to WHO, 1.5 mg/l is the maximum permissible limit and 1.0 mg/l. is the highest desirable limit of fluoride in drinking water. Palakkad district have registered relatively higher concentrations of fluoride over a decade. In the present study, 10 locations have recorded fluoride concentrations higher than the permissible limit. Rest of t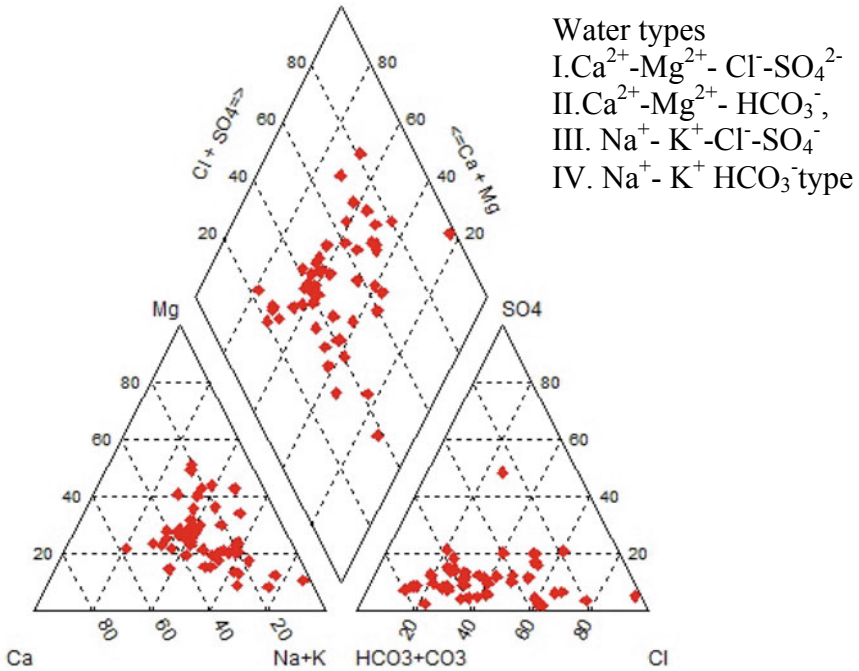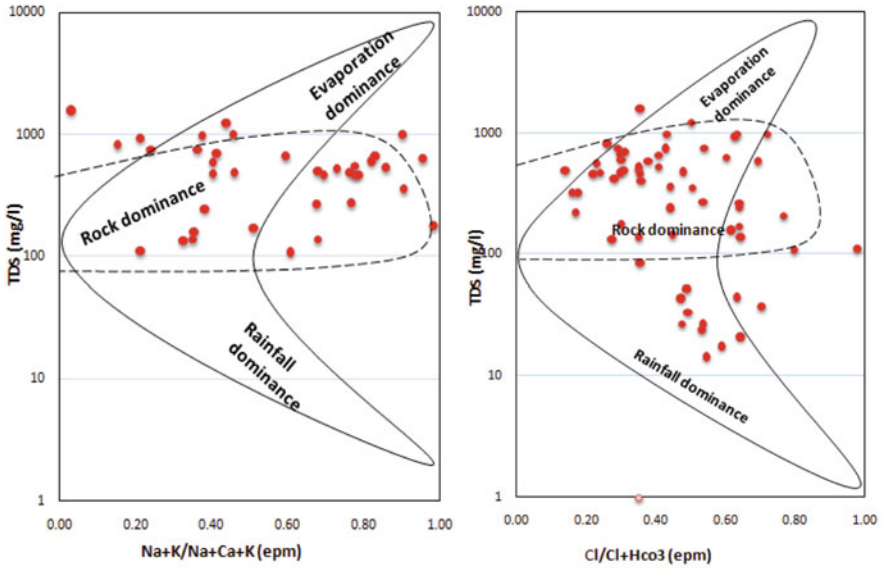he samples is within the permissible limit. Thavalam and Koppanur have concentrations of 4.1 mg/l and 4.58 mg/l, respectively.

Nitrate is a key parameter in the evaluation of groundwater quality, the present study shows that out of 50 locations, 5 areas reported nitrate concentration above the mentioned limits of WHO.

3.3   Irrigation Quality Assessment

Sodium Adsorption Ratio (SAR) in most of the areas is excellent, i.e. less than 10. Seven locations fall under good water quality (10–18). The water samples that graded as excellent and good can be used for irrigation. The location Athikode has

Table 3 Classification of water based on SAR

SAR range	Water class	Number of samples
< 10	Excellent	39
10–18	Good	7
18–26	Doubtful	3
> 26	Unsuitable	1

Table 4 Sodium percentage and respective water categories

% Na range	Water class	Number of samples
< 20	Excellent	0
20–40	Good	22
40–60	Permissible	21
60–80	Doubtful	6
> 80	Unsuitable	1

SAR ratio greater than 26, thus is unsuitable for irrigation purposes. Classification of water based on SAR range is given in the Table 3 and Fig. 11a.

The evaluation of water quality for irrigation purposes based on Na % reveals that none of the samples fall in excellent category. Forty-three samples show good to permissible water quality and only one location (Koppanur) has Na % of 86.6 which indicates that the water is unsuitable. The classification based on Na % is given in the following Table 4 and Fig. 11b.

It is observed that, Residual Sodium Carbonate (RSC) of 45 samples fall in safe category (Fig. 11d). Three samples (Vattalakki, Gopalapuram and Athikode) has RSC values between 1.25 and 2.5 epm, thus is categorized as marginally suitable for irrigation. The samples from locations Koppanur and Eruthenpathy is unsuitable for irrigation (Table 5).

According to the obtained USSL plot (Fig. 11c), majority of the samples lies in the field C1-S1 which indicates low salinity water and sodium content and thus it can be used in each type of soil. Few samples fall in C2-S2 field indicating medium salinity and sodium content and may require special soil management such as adding gypsum and organic matters to the soil. One sample lies in C4-S4 field indicating very high salinity and very high sodium content water. Thus it is generally unsuitable for irrigation (Table 6).

Table 5 Range of residual sodium carbonate and corresponding water classes

RSC (epm)	Water category	Number of samples
< 1.25	Safe	45
1.25–2.5	Marginally suitable	3
> 2.5	Unsuitable	2

Table 6 Classification of irrigation quality of water based on SAR and EC

Sodium hazard	Salinity hazard	Extent
S1	C1	Low
S2	C2	Medium
S3	C3	High
S4	C4	Very high

3.4 Major Water Type and Mechanism Controlling Groundwater Chemistry

Groundwater aquifer hydrochemistry in the study area is determined using piper trilinear diagram (Piper AM 1944). The water samples from present study area falls in four facies, therefore major water types of study area are $Ca^{2+} - Mg^{2+} - Cl^- - SO_4^{2-}$, $Ca^{2+} - Mg^{2+} - HCO_3^-$, $Na^+ - K^+ - Cl^- - SO_4^-$ and $Na^+ - K^+ HCO_3^-$ type (Fig. 12).

The groundwater chemistry shows alterations from its entry to exit from an aquifer due to various factors such as soil textures, structures, weathering, contamination, mining and other activities. Gibbs diagram is used to demonstrate the control of groundwater chemistry. It is obtained by plotting TDS against $Na/(Na + Ca)$ and $Cl/(Cl + HCO_3)$. In the present study, the predominant samples fall in rock dominance field (Fig. 13). Rock dominance of most of the samples is caused by the interaction between the aquifer rocks and groundwater that is influenced by rock-forming minerals existing in metamorphic rocks of the area. The subsurface water chemistry indicates the dominance of interaction and chemistry between rock and the percolation waters [14].

3.5 Hydrogeochemical Process Involved

The hydrogeochemical processes help to understand the changes in water quality due to rock-water interactions. The geochemical properties of groundwater also depend on the chemistry of water in the recharge area as well as the different geochemical processes occurring in the subsurface. The higher concentrations of cation and anion can be attributed to ion exchange process and evaporation (Girish Gopinath et al. 2013). The $Na^+ + K^+$ to total cations ratio (Fig. 14a) reveals the involvement of silicate weathering which is responsible for increased concentrations of sodium and potassium ions in the groundwater.

The binary plot of $Ca^{2+} + Mg^{2+}/HCO_3^- + SO_4^{2-}$ was examined (Fig. 14b) and it shows the dispersion of most of the points above the 1:1 line which indicates that excess of Ca^{2+} and Mg_2 in water over $HCO_3^- + SO_4^{2-}$. From the known lithology of study area with Gneissic, Migmatite and Khondalite the excess $HCO_3^- + SO_4^{2-}$ occurs in few samples that reflects its input to water may be from silicate weathering

and then ion exchange process can be the extra source for excess Ca^{2+} and Mg^{2+} in groundwater.

The Na^+ K v/s Total cations scatter diagram (Fig. 14a) of the study area shows sample points falling both along and below the 1:1 line. This suggests that the cations in the groundwater might have been derived from silicate weathering. The Ca^{2+} + Mg^{2+}/ Total cations (TZ^+) plot (Fig. 14 c) indicate ion exchange process is the key geochemical processes contributing Ca^{2+} and Mg^{2+} ions to groundwater in different hydrogeology units (coastal alluvium, lateritic terrain and crystallines) of study area. The longer residence time of groundwater in aquifer caused the Ca^{2+}/Na^+ (Fig. 14d) ion exchange process between groundwater and aquifer material and it increased the concentration of sodium in groundwater. The higher concentration of HCO_3^- than Na^+ validate that silicate weathering is the probable source which increased the HCO_3^- concentration because of the reaction of feldspar minerals with carbonic acid occurs in the water.

3.6 Water Quality Index Map

The water quality index indicates the quality of water with reference to an index number which reflects the overall status of groundwater quality for drinking purposes. The WQI was calculates for groundwater samples by taking into consideration five parameters, namely Calcium, Magnesium, Bicarbonate, Fluoride and Nitrate. The weighted arithmetic WQI was calculated and given in Table 7. WQI of the study area is classified as excellent (<50), good (50–100), poor (100–200), very poor (200–300) and water unsuitable for drinking (WQI > 300). Majority of the water samples lies within the range of 50–200 indicating good to poor quality of water. It is noted that groundwater from eight locations are unsuitable for drinking purpose. The higher values of WQI in these areas may be due to presence of mining areas, dumping solid wastes and improper use of fertilizers. The spatial distribution map of WQI is shown in the Fig. 15.

Table 7 Water quality index levels

Water quality index	Description	No. of samples
0–50	Excellent	4
51–100	Good	10
101–200	Poor	19
201–300	Very poor	9
> 300	Unfit for drinking	8
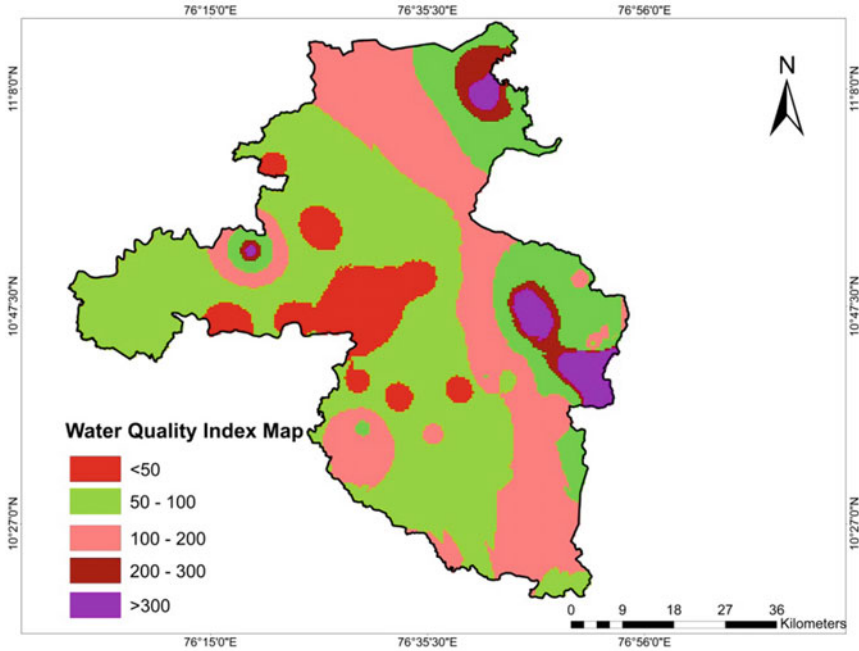
Fig. 15 Water quality index map of KRB

4 Conclusions

The present study reveals that the concentrations of major ion and minor ions are within the permissible limits for drinking quality except a few samples. The mean abundance of major cations is $Ca^{2+} > Na^+ > Mg^{2+} > K^+$ and the major anions is HCO_3^- $> Cl^- > NO_3^- > SO_4^2$. Among the cations Ca^{2+} is the dominant cation followed by Na^+ and HCO_3^- is the dominant anion. Since the eastern parts are covered mainly by hornblende–biotite gneiss and migmatites, the geological influence on the concentrations of cations is well understood. The high sodium concentration may be attributed to weathering of plagioclase feldspar, i.e. Silicate weathering which was revealed from the hydrogeochemical analysis of the study area. Majority of the samples have desirable range of pH, EC and TDS. Location Kottathara have higher Mg concentrations exceeding the limit. Koppanur shows highest value of bicarbonate concentration. The higher concentrations of fluoride are noticed in 10 locations and nitrate in 5 locations of the study area, respectively. The higher concentrations of water quality parameters in these locations can be attributed to intense usage of fertilizers during agricultural activities and along with geogenic influences. The suitability of water for irrigational purposes was evaluated on the basis of SAR, RSC and Na percentage in few locations such as Koppanur and Athikode exhibits higher ranges of irrigation

water quality limits and thus is unfit for irrigation. The area falls under rock dominance field indicating rock weathering as the dominant process controlling water quality and the various ion ratio plots such as $Na^+ + K^+$ versus Total cations, $Ca^{2+} + Mg^{2+}$ v/s Total cations, Na^+ versus Ca^{2+}, HCO_3^- versus $Ca^{2+} + Mg^{2+}$ validates the probability of weathering and ion exchange processes. The water type of the area was concluded as $Ca^{2+} – Mg^{2+} Cl^- – SO_4^{2-}$, $Ca^{2+} – Mg^{2+} – HCO_3^-$, $Na^+ – K^+ – Cl^- – SO_4^-$ and $Ca^{2+} – Mg^{2+} – Cl^- – SO_4^{2-}$ type from the Piper Trilinear Diagram. The water quality index map indicates that in some regions towards western part of the study area are unsuitable for drinking purpose since it has WQI > 300.

References

1. Arshad M, Shakoor A (2017) Irrigation water quality
2. Babiker IS, Mohamed AM, Hiyama T (2007) Assessing groundwater quality using GIS. Water Resour Manage 21(4):699–715
3. BIS (1991) Specifications for drinking water, Bureau of Indian Standards, New Delhi
4. Central Ground Water Board, Report on Mapping of hard rock aquifer system and aquifer management plan, Palakkad district, Kerala
5. Gibbs RJ (1970) Mechanisms controlling world water chemistry. Science 170:795–840
6. Girish G, Resmi TR, Seralathan P (2013) Assessment of groundwater quality in Kavaratti Island in the Lakshadweep Archipelagos India. Chem Ecol 29(4):309–319. https://doi.org/10.1080/02757540.2012.760546
7. Gopinath G, Seralathan P (2006) Chemistry of groundwater in lateritic terrains of the Muvattupuzha river basin, Kerala, India. J Geol Soc India Springer 68:705–714, ISSN: 0974–6889
8. Groundwater Year Book of Kerala, CGWB (2018) Kerala region, Thiruvanathpuram
9. Groundwater Year Book of Kerala, CGWB (2020) Kerala region, Thiruvanathpuram
10. Laluraj CM, Girish Gopinath, Dinesh Kumar PK, Seralathan P (2006) Seasonal variation in groundwater chemistry and quality of phreatic coastal and crystalline terrine aquifers of central Kerala, India. Environmental forensic. Taylor and Francis, vol 7, pp 335–344. https://doi.org/10.1080/15275920600996305
11. Laluraj CM, Gopinath G (2006) Assessment on seasonal variation of groundwater quality of phreatic aquifers–a river basin system. Environ Monit Assess 117(1):45–57. https://doi.org/10.1007/s10661-006-7675-5
12. Piper AM (1944) A graphical interpretation of water analysis. Trans Am Geophys Union 25:914–928
13. Sathish Kumar V, Amarendar B, Ratnakar Dhakate, Sankaran, S, Raj Kumar K (2012) Assessment of groundwater quality for drinking and irrigation use in shallow hard rock aquifer of Pudunagaram, Palakkad district:149–165
14. Satish Kumar V, Amarender B, Dhakate R, Sankaran S, Raj Kumar K (2016) Assessment of groundwater quality for drinking and irrigation use in shallow hard rock aquifer of Pudunagaram, Palakkad District Kerala. Appl Water Sci 6:149–167. https://doi.org/10.1007/s13201-014-0214-6

15. Todd DK (ed) (2005). Wiley, New York
16. U.S. Salinity Laboratory (USSL) (1954) Diagnosis and Improvement of Saline and Alkaline Soils, U.S. Dept. Agriculture Handbook, Washington DC, 160
17. Vasanthavigar M, Srinivasamoorthy K (2010) Application of water quality index for groundwater quality assessement: Thirumanimuttar sub-basin, Tamil Nadu. Environ Monitor Assess 171(1–4):595–609
18. WHO (World Health Organization) (2008) Guidelines for drinking water quality 1, Geneva WHO

Increasing Efficiency of Oxygen Separation from Air Through Ceramic Membranes—A Review

Mohammad Adnan Iqbal, Shivendra Kumar Jaiswal, and Adbur Rahman Quaff

Abstract Oxygen is one of the most crucial gas for life as well as for human economic activity. It is the third largest gas present in the environment. The boom in the modern technology (energy sector, environment, chemical as well as petrochemical industries) has surge forward the need of low cost oxygen with ultra-high purity (>99.9%). The potential of continuous separation and delivery of 100% pure oxygen from air in dense ceramic membranes has grabbed recognition. However, operating temperature, stability in CO_2 containing environment, mechanical strength and cost are some bottleneck parameters for oxygen permeation flux. Therefore, it becomes challenging to design and optimize membrane material having better stability toward CO_2 containing environment for its practical application. So, perovskite-type cubic oxides (generalized chemical formula ABO_3, A—rare alkaline-earth metal; B—Co, Fe, Mn; O—oxygen) have analyzed in terms of its oxygen permeation capacity. This present work is based on the review performed and focuses on methods achieving higher efficiency of oxygen in terms of production as well as energy consumption.

Keywords Oxygen separation · MIEC membrane · Oxygen flux · Perovskite

1 Introduction

Oxygen is an eminent gas and a major chemical used in several industrial operations worldwide [1]. The production of industrial oxygen is mainly based on cryogenic distillation and pressure swing adsorption (PSA) requiring more investments and operation costs [2]. High purity oxygen (>99%) is obtained in cryogenic distillation,

M. A. Iqbal (✉) · S. K. Jaiswal · A. R. Quaff
Department of Civil Engineering, National Institute of Technology Patna, Patna 800005, India
e-mail: mdi.phd20.ce@nitp.ac.in

S. K. Jaiswal
e-mail: skj@nitp.ac.in

A. R. Quaff
e-mail: arquaff@nitp.ac.in

unlike PSA which produce pure oxygen around 95% [3, 4]. However, these conventional methods are also a significant cause for emission of greenhouse gases bringing international attention in accordance with the latest energy policies. Membrane-based oxygen separation technique involves less energy involvement [5] and thus reduce emission of greenhouse gases related with chemical industries. Researchers have elaborated two major types of ceramic membranes for oxygen separation from atmospheric air. Pure oxygen conducting membrane in which oxygen transport takes place through membrane while electron is transported through electrodes. In such type of ceramic membrane, generation of oxygen depends on the current supplied. Another type is mixed ionic electronic membrane (MIEC), and in this membrane, ions and electrons both are transported through membrane.

Transport of oxygen through membrane occurs due to difference in partial pressure/chemical potential of oxygen on the two sides [6]. Membrane technology exhibits better efficiency in terms of energy and is superior in selectivity of oxygen, giving highly pure oxygen.

2 Materials used for MIEC-Based Oxygen Membranes

Researchers have reported single-phase ionic transport materials (such as fluorites and perovskites) as membranes for permeation of oxygen. Both these single-phase membrane have been well explored in the area of various strategies of doping and also in terms of membranes with self-support and membranes with different thicknesses of supporting selective layers. However, nowadays dual-phase membranes have attracted attention because of its high permeation along with thermal stability. The schematic representation of permeation of oxygen through dense ceramic membrane is shown in Fig. 1 [7].

2.1 Single-Phase Ionic Transport Material

Dense ceramic membranes for permeation of oxygen can be made of various structures such as perovskites (ABO3), fluorites (AO2), brownmillerites (A2B2O5), pyrochlores (A2B2O7) and Ruddlesden-Popper series (An+1BnO3n+1). All of these materials have ability to transport oxygen via its lattice; however, fluorite and perovskites are most explored for its oxygen permeation ability. Perovskites materials are able to conduct both electrons and oxygen ions [8]. However, fluorites attain high conductivity for oxygen ions but low for electrons.
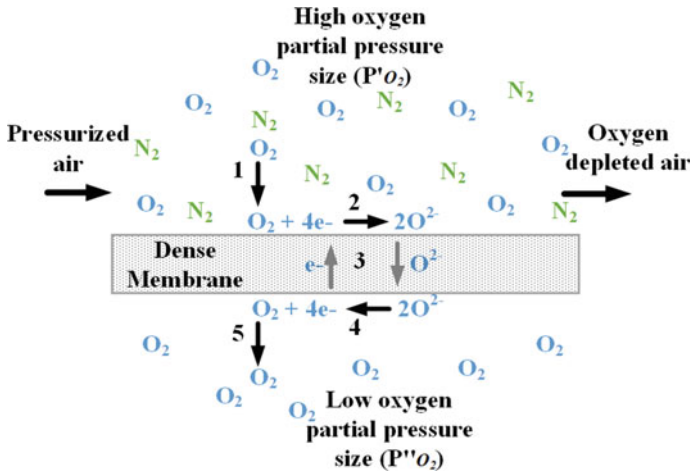
Fig. 1 Schematic view of oxygen permeation through dense ceramic membrane [7]

2.1.1 Fluorites

The structure for oxide of fluorite represented as AO2, where A is the cation with valency four (Zr^{4+} or Ce^{4+}) and is having larger size [9]. The electronic conductivity through fluorite membranes is very poor. Therefore, it requires conduction of electrons externally to work as a membrane for oxygen transport.

The merits of fluorites are its minimum chemical expansion and stability of its phase in CO2 and reducing gas containing environment, in comparison with perovskites [10–13].

2.1.2 Perovskites

Perovskite represents cubic structure having formula ABO3, where A and B are cation sites for alkali and rare earth metals, respectively.

The transport of oxygen ions at temperature above 700 °C is dominated by the vacancy sites of oxygen which gets increased with increase in temperature [5]. The rate of transport of oxygen is given by Arrhenius equation (positive activation energy) and increases when temperature is increased. Yasutake et al. [14] reported a remarkable work showing that the vacancy concentration (δ) of oxygen, and subsequently, the diffusion rate of ions can be improved by doping of cation sites with different sizes and valences cation.

The most explored materials in perovskite are SCFO (Sr(Co, Fe)O3-δ) [15] and BSCF (Ba0.5Sr0.5Co0.8Fe0.2O3-δ). These show extraordinary permeation rate, due to higher exchange rate at surface [5]. The major drawback of cobalt-based membranes are there instability in some gases containing environment such as CO2,

limiting its application for separation of gases [16]. Further, SCFO perovskites also show unstable behavior when low temperature and low oxygen partial pressure are present.

Metal ions substitution also contributes to enhancement of permeation of oxygen. Cheng et al. [17] analyzed various doped BCFO perovskites. Among all analyzed perovskites, they reported that the Zr-doped, BaCo0.7Fe0.2Zr0.1O3-δ, shows highest permeation of oxygen. However, BaCo0.7Fe0.2Ta0.1O3-δ exhibits best stability in structure. The doping of membrane with Ta increases the stability of membrane as earlier reported by Liu et al. [18]. Further, similar effect of Zr has been found by Yao et al. [19]. As discussed before, BSCF perovskites exhibit maximum permeation of oxygen [20]. Moreover, the oxygen permeation can further be increased by doping the Fe-ions B-site with Al, Ce and Ni, as observed by Babakhani et al. [21]. Below 850 °C, the cubic perovskite changes its phase to an orthorhombic phase (brownmillerite), decreasing the permeation of oxygen [22]. Some of the perovskite oxygen permeation data is listed in Table 1.

2.2   Dual-Phase Ionic-Electronic Transport Materials

Researchers found it tough to find a single material showing better electronic and ionic conductivity both. Therefore, dual-phase membrane comes out to be optimistic contender for mixed ionic electronic conducting membrane. In dual-phase membrane, one phase conducts electrons, while other phase conducts oxygen ions [5]. The concept for dual-phase membrane was introduced first by Mazanec et al. [23]. The merit for dual-phase membrane is better chemical and mechanical stability with respect to single-phase membrane [24]. A schematic view of dual-phase ceramic membrane is shown in Fig 2.

2.2.1   Dual-Phase Based on Ceramic-Metallic Mixtures

In dual-phase membranes, the preferred metals for conduction of electrons are noble metals, and for ionic transport ceramic materials such as fluorite and perovskite materials are used. The oxygen permeation flux data for some of the ceramic-metallic dual-phase membranes are listed in Table 2. Mazanec et al. [23] developed and analyzed dual-phase membranes for the first time which consisted of YSZ with Pd, Pt, In90Pr10 and In95Pr2.5Zr2.5. An increase in permeation flux of oxygen is obtained by increasing percentage of metal (in volume) higher that the value required to get percolative composite. However, best oxygen flux was with a 50 vol.% of In95Pr2.5Zr2.5 [23]. It has been found that 30 vol. % of metal is needed in the mixture to get a percolated network [35].

Table 1 Perovskite single-phase membrane oxygen permeation data

Membrane	Temperature (°C)	Thickness (mm)	Oxygen flux (mol cm^{-2} s^{-1})	P'O2 (Pa)	P''O2 (Pa)	References
BaBi0.5Co0.2Fe0.3O3-δ	800–925	1.5	2.789×10^{-7} to 5.589×10^{-7}	0.21	–	[25]
BaBi0.4Co0.2Fe0.4O3-δ	800–925	1.5	3.064×10^{-7} to 5.985×10^{-7}	0.21	–	[25]
BaBi0.2Co0.2Fe0.6O3-δ	800–925	1.5	1.984×10^{-7} to 5.589×10^{-7}	0.21	–	[26]
BaCe0.4Fe0.6O3-δ	800–950	1–1.5	7.440×10^{-8} to 1.786×10^{-7}	0.21	–	[27]
BaCe0.2Fe0.8O3-δ	800–950	1–1.5	9.449×10^{-8} to 2.902×10^{-7}	0.21	–	[27]
BaCe0.15Fe0.85O3-δ	800–950	1–1.5	1.689×10^{-7} to 3.891×10^{-7}	0.21	–	[27]
Ba0.5Sr0.5Co0.8Fe0.2O3-δ	850–900	1.8	8.929×10^{-8} to 1.563×10^{-6}	0.01 − 1	–	[26]
	800–900	1.5	7.068×10^{-7} to 2.307×10^{-6}	0.09 − 1	9.3×10^{-3} to 0.1147	[28]
	850–950	0.22	1.406×10^{-6} to 3.266×10^{-6}	0.21	–	[29]
SrCo0.8Fe0.2O3-δ	850–950	1.5	6.510×10^{-7} to 9.300×10^{-7}	0.01 − 1	–	[25]
SrCo0.89Fe0.1Cr0.01O3-δ	880	1.4	4.700×10^{-7}	0.21	0.084	[30]

(continued)

Table 1 (continued)

Membrane	Temperature (ºC)	Thickness (mm)	Oxygen flux (mol $cm^{-2} s^{-1}$)	P'O2 (Pa)	P"O2 (Pa)	References
SrCo0.85Fe0.1Cr0.05O3-δ	880	1.4	5.200×10^{-7}	0.21	0.084	[30]
SrCo0.95Ti0.05O3-δ	880	1.4	4.500×10^{-7}	0.21	0.084	[30]
SrCo0.8Ti0.2O3-δ	880	1.4	4.800×10^{-7}	0.21	0.084	[30]

Fig. 2 Schematic view of dual-phase ceramic membrane [7]
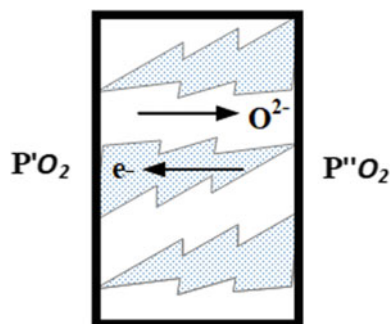
2.2.2 Dual-Phase on Mixed Ceramics

An alternative to improve transport of electrons with reduced price in comparison with novel metals is to utilize ceramic phase such as spinel and perovskite material along with ceramic phase for ionic conduction. For this ceramic-ceramic systems, certain aspects such as stability of membranes both phase in temperature and CO2 environment as well as thermal chemical expansion need to be addressed.

Spinel and perovskite material depicts better conductivity for electron than other ceramics, so these are used for electronic conduction phase. Fluorites are utilized for oxygen conducting phase [36]. Moreover, fluorites are more stable in CO2 and reduce environment and also show lesser thermal expansion in comparison with perovskites [12].

3 Factors Affecting Permeation and Stability

As per the discussion in previous sections, the major drawback of MIEC membrane employed for permeation of oxygen is its thermal, chemical and phase stability. Membrane material selection is a difficult task as it requires many properties to be fulfilled. MIEC membranes requires material with high ionic and electronic transport

Table 2 Ceramic metallic dual-phase membranes oxygen permeation flux data

Membrane	Temperature (°C)	Thickness (μm)	Oxygen flux (mol cm^{-2} s^{-1})	P'O2 (atm)	P''O2 (atm)	References
(YSZ)0.7-(Pd)0.3	1100	2000	10−10	0.209	1.4×10^{-3}	[31]
(YSZ)0.6-(Pd)0.4	1100	2000	4.3×10^{-8}	0.209	0.014	[32]
(YSZ)0.6-(Pd)0.4	800	1720	1.6×10^{-8}	0.209	0.026	[23]
(YSZ)0.5-(Pd)0.5	1100	800	1.56×10^{-6}	0.209	–	[23]
(YSZ)0.5-(Pt)0.5	1100	800	1.34×10^{-6}	0.209	–	[23]
(YSZ)0.5-(In90Pr10)0.5	1100	800	1.71×10^{-6}	0.209	–	[23]
(YSZ)0.5-(In90Pr10)0.5	1100	300	4.09×10^{-6}	0.209	–	[23]
(YSZ)0.5-(In95Pr2.5Zr2.5)0.5	1100	300	5.80×10^{-6}	0.209	–	[23]
[(Bi2O3)0.74(SrO)0.26]0.6-Ag0.4	680	1000	5×10^{-8}	0.209	0.0024	[33]
[(Bi2O3)0.75(Er2O3)0.25]0.6-Ag0.4	852	230	3.08×10^{-7}	0.209	0.046	[34]
[(Bi2O3)0.75(Er2O3)0.25]0.6-Ag0.4	680	129	1.79×10^{-7}	1	2×10^{-6}	[24]

with appreciable value at high temperatures (>800–850 °C). The change is phase of perovskite material at these temperatures need special doping techniques to tackle this. Further, stability under operating environment is needed. The material selected for membrane should be chemically resistant to CO2 and H2S environment. Further, doping strategies are explored to enhance chemical resistance. The sintering step in membrane preparation specifies the grain size and composition of membrane. Oxygen permeation can be improved by controlling the temperature and time of sintering.

3.1 Chemical and Thermal Expansion

Thermal expansion is an important factor that affects MIEC membrane performance, mainly in sealing and co-sintering of various layers in asymmetric membranes. In engineering, generally the coefficient of thermal expansion coefficient is taken as linear. However, some MIEC oxides like Co-containing or Fe-containing perovskites exhibit oxygen loss mostly for temperature above 400–600 °C, thus resulting to increased coefficient of thermal expansion for these temperature ranges.

Except thermal expansion, some MIEC materials like La1-xSrxCo1-yFeyO3-δ (LSCF) also exhibit chemical expansion. This means that vacancies are formed while ionic transport because of metal cation reduction leading to lattice expansion due to positive charged oxygen vacancies steric effect. It leads to modification in radius of cation [37]. This chemical expansion occurs because of high temperature as well as due to fluctuation of oxygen partial pressure on both side of membrane, i.e., permeate and feed side. With decrease in oxygen partial pressure and increase in temperature, considerable increase in oxygen vacancies occurs leading to chemical expansion causing stress in the membrane and membrane failure [38].

3.2 Phase Transformation

As discussed, perovskite exhibits high oxygen flux as they are mainly alkaline-earth compounds. Among all phases perovskite material can adopt, the most favorable is cubic structure in terms of permeation of oxygen. For example, Ba0.5Sr0.5Co0.8Fe0.2O3-δ (BSCF) and SrCo0.8Fe0.2O3-δ (SCF) present high permeation rates because of cubic phase which is relatively stable at high temperatures (>850 °C). Below 850 °C, these cubic perovskite gets converted into orthorhombic brownmillerite phase [39], leading to dramatic fall in permeation rate of oxygen. The oxygen vacancies in brownmillerite structure exist in ordered arrangement, where one out of six sites for oxygen are vacant, thus minimizes flux of oxygen. Further, the expansion of lattice due to this change in phase results in mechanical instability issue [40]. While transformation of phase from perovskite (ABO3) to brownmillerite (A2B2O5), there exists two phase region for low partial pressure of

oxygen (<0.1 atm) and low temperature [41]. However, with increase in temperature, the brownmillerite phase can again transform into a perovskite phase [42].

4 Oxygen Permeation Improvement

4.1 Modification of membrane surface

The flux of oxygen through membrane depends on the chemical reaction leading to oxygen exchange which can be further improved by modification in both the surfaces "flat" of membrane. Simply roughening the surfaces of membrane leads to increase in surface/volume ratio and thus improves oxygen permeation [43]. Moreover, further oxygen permeation improvement can be done with layered structure, a dense membrane and supporting porous top layer [44].

4.2 Combination of thin film and porous substrate

It has been reported that the flux of oxygen permeation is inversely dependent on thickness of membrane, thus decrease in the membrane thickness will increase the flux of permeation of oxygen. However, this statement holds good only if permeation of oxygen is due to bulk diffusion. In perovskite membrane, the limiting species for permeation of oxygen is oxygen vacancies. Thus, synthesis of thin film above porous substrate layer is utilized to improve oxygen permeation flux. This is also utilized for membranes where transport of electrons is limited by bulk diffusion.

5 Conclusions

Oxygen is vital for several processes of industrial application, which is formed by energy intensive and expensive fractional distillation. The evolution of ceramic membranes with dense mixed ionic electronic membranes allows energy efficient supply of pure oxygen with cost effectiveness. In past decades, various research has been done to improvise the permeation of oxygen and stability of MIEC membranes.

Perovskite-based materials show better transport for both ions and electrons but lags in terms of chemical stability in operating environment. However, fluorite is more chemically stable in environment containing CO_2, SO_2 and H_2O but lags in its permeation ability. Combining two phases may improve performance of membrane. However, compatibility of both materials for sintering and operation process needs to be explored.

References

1. Bose AC (ed) (2008). Inorganic membranes for energy and environmental applications. Springer Science and Business Media
2. Baker RW (2002) Future directions of membrane gas separation technology. Ind Eng Chem Res 41(6):1393–1411
3. Banaszkiewicz T (2021) The possible coupling of lng regasification process with the TSA method of oxygen separation from atmospheric air. Entropy 23(3):350
4. Belaissaoui B, le Moullec Y, Hagi H, Favre E (2014) Energy efficiency of oxygen enriched air production technologies: cryogeny vs membranes. Sep Purif Technol 125:142–150
5. Sunarso J, Baumann S, Serra JM, Meulenberg WA, Liu S, Lin YS, da Costa JCD (2008) Mixed ionic–electronic conducting (MIEC) ceramic-based membranes for oxygen separation. J Membr Sci 320:13–41
6. Bouwmeester HJM, Burggraaf AJ (1996) Dense ceramic membranes for oxygen separation. In Fundamentals of inorganic membrane science and technology. Elsevier, pp 435–528
7. Arratibel Plazaola A, Cruellas Labella A, Liu Y, Badiola Porras N, Pacheco Tanaka DA, Sint Annaland MV, Gallucci F (2019) Mixed ionic-electronic conducting membranes (MIEC) for their application in membrane reactors: a review. Processes 7(3):128
8. Wei Y, Yang W, Caro J, Wang H (2013) Dense ceramic oxygen permeable membranes and catalytic membrane reactors. Chem Eng J 220:185–203
9. Jiang Q, Faraji S, Slade DA, Stagg-williams SM (2011) A review of mixed ionic and electronic conducting ceramic membranes as oxygen sources for high-temperature reactors. In: Elsevier BV (ed) Inorganic polymeric and composite membranes: structure, function and other correlations, 1st edn. Amsterdam, The, Netherlands, pp 235–273
10. Deronzier E, Chartier T, Geffroy PM (2021) Oxygen semi-permeation properties of Ba1-xSrxFeO3-δ perovskite membranes. Solid State Ionics 361:115560
11. Han N, Guo X, Cheng J, Liu P, Zhang S, Huang S, Rowles MR, Fransaer J, Liu S (2021) Inhibiting in situ phase transition in Ruddlesden-Popper perovskite via tailoring bond hybridization and its application in oxygen permeation. Matter 4(5):1720–1734
12. Hoon J, Sook G, Yoo C, Haeng J (2013) Contribution of the surface exchange kinetics to the oxygen transport properties in Gd0.1Ce0.9O2−δ-La0.6Sr0.4Co0.2Fe0.8O3−δ dual-phase membrane. Solid State Ion 253:64–69
13. Lu H, Zhang Q, Liu R, Gui J (2021) Oxidative coupling of methane over SrO/La2O3 catalyst in an oxygen-permeable separation membrane reactor. Catal Lett 151(6):1805–1809
14. Yasutake T, Zhang HM, Furukawa S, Yamazoe N (1985) Oxygen permeation through perovskite-type oxides. Chem Lett 14:1743–1746
15. Jia T, Popczun EJ, Lekse JW, Duan Y (2021) Effective Ca^{2+}-doping in Sr1-xCaxFeO3-δ oxygen carriers for chemical looping air separation: a theoretical and experimental investigation. Appl Energy 281:116040
16. Zhu X, Yang W (2011) Critical factors affecting oxygen permeation through dual-phase membranes. In: Elsevier BV (ed) Inorganic polymeric and composite membranes: structure, function and other correlations, 1st edn. Amsterdam, The, Netherlands, pp 275–293
17. Cheng H, Yao W, Lu X, Zhou Z, Li C, Liu J (2015) Structural stability and oxygen permeability of BaCo0.7Fe0.2M0.1O3−δ (M = Ta, Nb, Zr) ceramic membranes for producing hydrogen from coke oven gas Hongwei. Fuel Process Technol 131:36–44
18. Liu J, Cheng H, Jiang B, Lu X, Ding W (2013) Effects of tantalum content on the structure stability and oxygen permeability of BaCo0.7Fe0.3−xTaxO3−δ ceramic membrane. Int J Hydrog Energy 38:11090–11096
19. Yao W, Cheng H, Zhao H, Lu X, Zou X, Li S, Li C (2016) Synthesis, oxygen permeability, and structural stability of BaCo0.7Fe0.3-xZrxO3−δ ceramic membranes. J Membr Sci 504:251–262
20. Ganji E, Towfighi J, Shirazi L, Nakhaei A (2011) Order–disorder transition and phase stability of BaxSr1−xCo0.8Fe0.2O3−δ oxides. J Membr Sci 376:78–82

21. Babakhani EG, Towfighi J, Shirazi L, Nakhaeipour A, Zamaniyan A, Shafiei Z (2012) Structure stability and oxygen permeability of perovskite-type oxides of Ba0.5Sr0.5Co0.8Fe0.1R0.1O3−δ (R = Al, Mn, Fe, Ce, Cr, Ni, Co). J Mater Sci Technol 28:177–183

22. Niedrig C, Taufall S, Burriel M, Menesklou W, Wagner SF, Baumann S, Ivers-Tiffée E (2011) Thermal stability of the cubic phase in Ba0.5Sr0.5Co0.8Fe0.2O3−δ (BSCF)1. Solid State Ion 197:25–31

23. Mazanec TJ, Cable TL, Frye JG (1992) Electrocatalytic cells for chemical reaction. Solid State Ion 56:111–118

24. Kim J, Lin YS (2000) Synthesis and oxygen permeation properties of ceramic-metal dual-phase membranes. J Membr Sci 167:123–133

25. Shao Z, Yang W, Cong Y, Dong H, Tong J, Xiong G (2000) Investigation of the permeation behavior and stability of a Ba0.5 Sr$_{0.5}$ Co$_{0.8}$ Fe$_{0.2}$ O$_{3-\delta}$ oxygen membrane. J Membr Sci 172, 177

26. Shao Z, Xiong G, Cong Y, Yang W (2000) Synthesis and oxygen permeation study of novel perovskite-type BaBix Co0.2 Fe$_{0.8\,x}$ O$_{3-\delta}$ ceramic membranes. J Membr Sci 164, 167

27. Zhu X, Wang H, Yang W (2004) Novel cobalt-free oxygen permeable membrane. Chem Commun 1130

28. Wang H, Cong Y, Yang W (2002) Oxygen permeation study in a tubular Ba0.5 Sr0.5 Co0.8 Fe0.2 O3-δ oxygen permeable membrane. J Membr Sci 210, 259

29. Liu S, Gavalas GR (2005) Oxygen selective ceramic hollow fiber membranes. J Membr Sci 246:103

30. Kharton VV, Yaremchenko AA, Kovalevsky AV, Viskup AP, Naumovich EN, Kerko PF (1999) Perovskite-type oxides for high-temperature oxygen separation membranes. J Membr Sci 163(2):307

31. Chen CS, Boukamp BA, Bouwmeester HJM, Cao GZ, Kruidhof H, Winnubst AJA, Burggraaf AJ (1995) Microstructural development, electrical properties and oxygen permeation of zirconia-palladium composites. Solis State Ion. 76:23–28

32. Chena CS, Kruidhof H, Verweij H, Burggraaf AJ (1996) Oxygen permeation through oxygen ion oxide-noble metal dual phase composites. Solid State Ion 88:569–572

33. Wu K, Xie S, Jiang GS, Liu W, Chen CS (2001) Oxygen permeation through (Bi2O3)0.74(SrO)0.26- Ag (40%v/o) composite. J Membr Sci 188:189–193

34. Chen AJBCS, Kruidhof H, Bouwmeester HJM, Verweij H (1997) Thickness dependence of oxygen permeation through Erbia-stabilized oxide-silver composites. Solid State Ion 99:215–219

35. Shaula AL, Kharton VV, Marques FMB, Kovalevsky AV, Viskup AP, Naumovich EN (2005) Oxygen permeability of mixed-conducting composite membranes: effects of phase interaction. J Solid State Electrochem 10:28–40

36. Balager M, Garcia-Fayos J, Solis C, Serra JM (2013) Fast oxygen separation through SO$_2$- and CO$_2$-stable dual-phase membrane membrane based on NiFe2O4–Ce0.8Tb0.2O2−δ. Chem Mater 25:4986–4993

37. Marrocchelli D, Bishop SR, Tuller HL, Yildiz B (2012) Understanding chemical expansion in non-stoichiometric oxides: ceria and zirconia case studies. Adv Funct Mater 22:1958–1965

38. Omar S, Nino JC (2013) Consistency in the chemical expansion of fluorites: a thermal revision of the doped ceria. Acta Mater 61:5406–5413

39. Bouwmeester HJM (2003) Dense ceramic membranes for methane conversion. Catal Today 82:141–150

40. Švarcová S, Wiik K, Tolchard J, Bouwmeester HJM, Grande T (2008) Structural instability of cubic perovskite BaxSr1−xCo1−yFeyO3−δ. Solid State Ion 178:1787–1791

41. Pei S, Kleefisch MS, Kobylinski TP, Faber J, Udovich CA, Zhang-McCoy V, Dabrowski B, Balachandran U, Mieville RL, Poeppel RB (1995) Failure mechanisms of ceramic membrane reactors in partial oxidation of methane to synthesis gas. Catal Lett 30:201–212

42. Balachandran U, Dusek JT, Maiya PS, Ma B, Mieville RL, Kleefisch MS, Udovich CA (1997) Ceramic membrane reactor for converting methane to syngas. Catal Today 36:265–272

43. Haag S, van Veen AC, Mirodatos C (2007) Influence of oxygen supply rates on performances of catalytic membrane reactors. Catal Today 127:157–164
44. York APE, Xiao T, Green MLH (2003) Brief overview of the partial oxidation of methane to synthesis gas. Top Catal 22:345–358

Water Quality Index Assessment for Upper Ganga Riverine Wetland

Alka Yadav and Mitthan Lal Kansal

Abstract Riverine wetland plays an integral role in maintaining a healthy environment besides providing various socio-economic benefits. However, the water of the riverine ecosystem is susceptible to pollution and contamination due to various anthropogenic activities, e.g., sewage discharge, agricultural runoff, and religious activities at ghats along the river stretch. Therefore, studying the water quality index of riverine wetlands is imperative. The study assesses water quality by Water Quality Index (WQI). The WQI is evaluated based on historical water quality data for the past five years, i.e., 2016–2020. The present study includes the seasonal variations of water quality parameters. The secondary data forming the basis of this work was collected from Uttar Pradesh Pollution Control Board (UPPCB). The study findings reveal an increasing trend in fecal and total coliform count at numerous sites. These sites fall into class C, i.e., unfit for drinking due to higher bacterial count and anthropogenic inputs in water. Also, the WQI value at all the study area sites in the year 2020 indicates a moderate level of water pollution.

Keywords Riverine wetland · Water quality · Water pollution · Water quality index · Water quality standards

1 Introduction

Wetlands are highly fragile, dynamic ecosystems comprising marshes, lakes, mangroves, floodplains, and peatlands, which remain continually or periodically inundated with flowing or still, fresh, brackish, or salty water [1].

Wetlands are usually found along the shorelines of lakes, rivers, and oceans, as well as in isolated depressions. Natural wetlands get their water from lakes, flooded

A. Yadav (✉) · M. L. Kansal
Department of Water Resources Development and Management, Indian Institute of Technology Roorkee, Roorkee 247667, India
e-mail: ayadav@wr.iitr.ac.in

M. L. Kansal
e-mail: mlk@wr.iitr.ac.in

rivers, tidal flows, or groundwater connections. These biodiversity hotspots offer the most productive ecosystems providing vital support for primary productivity and livelihood of dependent livestock, flora, and fauna. Riverine wetlands, which serve as significant freshwater reserves, are prone to pollution from natural and anthropogenic sources [2]. They serve as a sink for industrial and biological waste, such as sewage, agricultural runoff containing nutrient-rich fertilizers and agrochemicals, and pathogens from untreated wastewater [3]. As different aquatic species possess varying tolerances to various parameters such as chemical concentrations, temperature, pH, and dissolved oxygen (DO) levels, the water quality directly affects the ecology of the river and hence the biodiversity.

There is a need for sustainable development to maintain both health of natural resources and check their exploitation, especially in developing countries. Wetland as an engineered ecosystem can treat wastewater from sewage, agricultural land, or industrial streams, ensuring future water and environmental sustainability and resiliency. Wetland sustainability is a direct function of its hydrologic, environmental, socio-economic, and policy factors (see Fig. 1).

River health assessments are significant because they provide policymakers with vital information for river governance and conservation. For this purpose, the Pressure-State-Response subsets have been taken and modified from the PSR model of Cheng [4] (see Fig. 2). PSR model studies "Pressure" or impact of human activities (both direct and indirect) on wetland water quality (state). Response to the pressure-state interaction leads to management measures like economic and environmental policies aimed at improving the quality of wetland services. The hydrological aspects of wetland sustainability can be determined through water quantity and quality.

Monitoring river water quality is essential as it has a tremendous impact on other three aspects, i.e., environment, life, and policy associated with the riverine wetland. Over the years, Water Quality Index (WQI) has emerged as an important tool for carrying out water quality assessments to gage the impact of pollutants, analyze intervention scenarios, and devise effective water resource management plans in
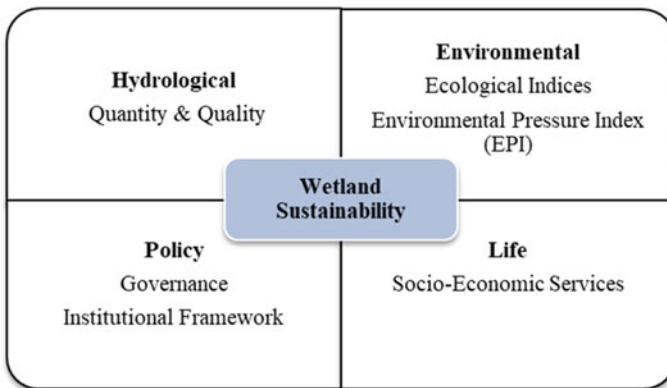
Fig. 1 Components of wetland sustainability
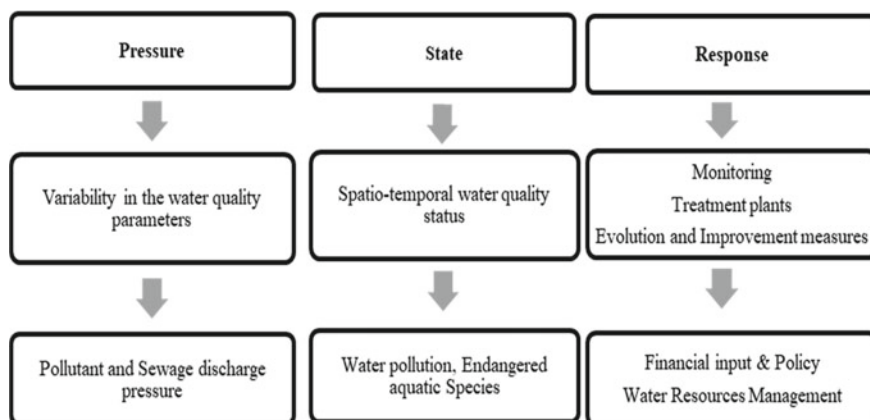
Fig. 2 Pressure-state-response (PSR) model (modified from Cheng 2007)

the basin areas [5, 6]. In this context, numerous studies have been undertaken to determine WQI by various researchers. Various WQI models have been developed to ascertain the usability of water resources for potential applications ranging from domestic uses like drinking to industrial uses, etc. [7–9]. Ichwana and Nelly [10], Khadse et al. [11], Bora and Goswami [12], Verma et al. [13], and Akukumtoshi et al. [14] have computed WQI for several rivers.

2 Study Area

River Ganga, part of the Hindu holy trinity, originates from Gangotri, situated in the northernmost part of Uttarakhand at an altitude of 7010 m. The river spans Uttar Pradesh, Bihar, Jharkhand, and West Bengal, covering 2525 km before merging into the Bay of Bengal. The entire river stretch of the Ramsar site from Brijghat to Narora (see Fig. 3.) has a total water spread area of about 26,590 ha. It serves as a natural habitat for IUCN Red-listed species like Ganges River Dolphin, Crocodile, Gharial, and various species of turtles, otters, and fish, besides catering to the needs of more than 20,000 water birds. In the wet season, its depth ranges from 300 to 362 cm, whereas in the dry season, it ranges from 50 to 150 cm. The river is marked by irregular flow caused by uneven water flow from the higher reaches and variable precipitation along the stretch [15].

This stretch has gained immense international recognition and is accorded protected status. However, over the years, the area has faced a high risk of adverse change driven by natural factors and anthropogenic pressures such as hydropower and construction projects, widening of highways and roads along with the river, unplanned urbanization and construction activities, mixing of untreated sewage, open defecation along river banks, and dumping solid wastes and muck directly
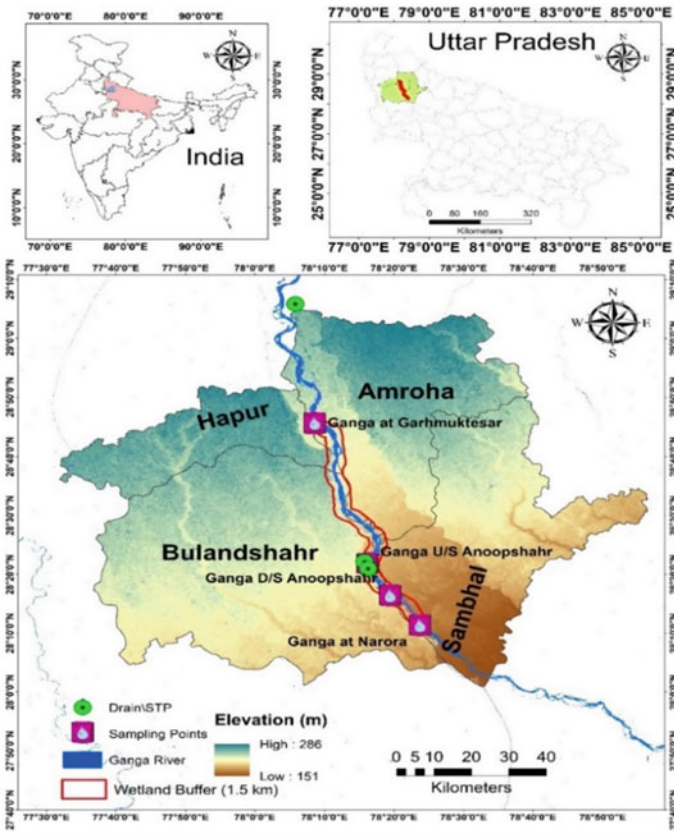
Fig. 3 Study area map

in the river. Besides, religious activities include mass bathing, submerging *pujasam-agri*, flowers, *jalsamadhi* by sadhus, saints, and seers, and *asthivisarjan* (immersion of funerary ashes) also contribute to the deterioration of water quality.

2.1 Monitoring Stations of the Study Area

The historical data of water quality parameters used for Water Quality Index (WQI) measurement is obtained for the four stations, i.e., Garhmuktesar (Upstream Brijghat), Upstream (U/S) Anoopshahar, Downstream (D/S) Anoopshahar, and Narora (Bulandshahar) courtesy Uttar Pradesh Pollution Control Board, India (UPPCB). The description regarding coordinates, discharge, and activities related to stations (see Table 1).

Table 1 Monitoring stations of the study area

Stations	Coordinates		Discharges	Activities
	Latitude	Longitude		
Garhmuktesar	28°45.42	78°08.31	Choiyaan drain upstream of the station	Bathing, boating, fishing, religious activity
U/S of Anoopshahar	28°21.53	78°16.19	–	Bathing, boating, cattle grazing
D/S of Anoopshahar	28°20.37	78°16.23	Anoopshahar STP Outlet just upstream of the station	Cremation, defecation, religious activity, etc
Narora Barrage (Narora Ghat)	28°11.42	78°24.11	Origin of lower River Ganga Canal	Bathing, boating, religious activity

3 Methodology

3.1 Water Quality Indexing

The procedure comprises developing a Water Quality Index to determine water quality at four Ganga River locations. The Water Quality Index model in the present study involves the following five steps:

1. Parameters selection for water quality measurement,
2. Development of parameters rating scale (Qi),
3. Assigning unit weight to each indicator parameter (Wi) based on their importance,
4. Subindex value determination by multiplying the unit weight with the quality rating (Wi × Qi),
5. Calculation of the total WQI by combining the sub-indices as given by Eq. (1).

$$\text{WQI} = \sum_{i=1}^{n} Q_i W_i \qquad (1)$$

where Q_i = sub-index for ith water quality parameter; W_i = Unit weight of ith water quality parameter;

3.1.1 Parameter Selection for Water Quality Measurement

For the evaluation of WQI, critical parameters such as pH, dissolved oxygen (DO), biochemical oxygen demand (BOD), total coliform (TC), and fecal coliform (FC), based on the evidence of excessive organic pollution in the Ganga river basin were chosen. These parameters are used to classify the Indian rivers based on the designated best use. Central Pollution Control Board [16] (http://cpcbenvis.nic.in/waterpollution/criteria.htm) has defined parameters values for classes A, B, C, and D, respectively (see Table 2). The data was collected on a seasonal basis, i.e., pre-monsoon

(May), monsoon (September), and post-monsoon (December) w.r.t four parameters for each site.

Microbiological parameters (Total Coliform and Fecal Coliform, MPN/100 ml) total coliform are bacteria present in the soil, surface water, and human and animal feces. These bacteria do not generally cause significant sickness, but their presence in water indicates the presence of other fecal pathogenic organisms. The presence of fecal coliform in aquatic habitats could mean that human or animal feces have contaminated the water. By direct discharging human sewage, fecal coliform bacteria can infiltrate waterways.

Physico-Chemical Parameters (pH, DO, BOD) pH determines the acidic or alkaline status of the water. A human body comprises 50–60% water on average; thus, the pH of potable water directly affects human health and metabolic activities. Similarly, pH has a significant bearing on aquatic ecosystems. Low pH values in the 3.5–4.5 are associated with the deteriorating fish reproduction system [17]. In contrast, pH greater than 11 can damage their skin and other vital organs and even cause death.

Dissolved oxygen (DO, mg/L) determines whether aerobic or anaerobic organisms cause biological changes, and its monitoring is thus critical for aerobic wastewater treatment operations. A significant drop in DO implies a vast amount of organic contamination in the river. About 4–6 mg/l of DO is optimum for sustaining aquatic lifeforms [18, 19]. Water temperature, altitude, salinity, and turbulence influence the quantity of DO present in surface waters. Biological Oxygen Demand (BOD, mg/L) is used as a parameter to determine the strength of domestic and industrial waste in terms of oxygen. A minimum DO of 2–7 mg/l is necessary for laboratory tests or should be present in water to break down oxidizable organic material [20].

Table 2 Water quality standards for River (CPCBENVIS, 2021)

Category of water best usage	Class A	Class B	Class C	Class D	Class E
pH	6.5–8.5	6.5–8.5	6–9	6.5–8.5	6.0–8.5
DO (mg/l), min	6.0	5.0	4.0	4.0	–
BOD (mg/l), max	2.0	3	3	–	–
Total Coliform (MPN/ml), max	50	500	5000	–	–
Fecal Coliform (MPN/ml), max	20	200	2000	–	–
Free Ammonia N(mg/l), min	–	–	–	1.2	
Electrical Conductivity, max (micromhos/cm)	–	–	–	–	2250
Sodium Absorption Ratio, max	–	–	–	–	26
Boron (mg/l), max	–	–	–	–	2

A = Drinking water source without conventional treatment, but after disinfection, B = Outdoor bathing (organized), C = Public water supply with conventional treatment and disinfection, D = Propagation of wildlife and fisheries, E = Irrigation, Industrial cooling, controlled waste disposal, Below E = Not meeting A, B, C, D and E Criteria * MPN: Most Probable Number

Table 3 Weights and ratings assigned to the parameters according to the UWQI

Category	Parameters	Weight factors
Microbiological/Health hazard	Fecal coliform (MPN/100 ml), min	0.28
	Total coliform (MPN/100 ml), min	0.25
Chemical parameters	DO (mg/l), max	0.22
	BOD (mg/l), min	0.11
Physical parameters	pH	0.14

3.1.2 Weightage

The following factors were considered while assigning weights to the water quality variables:

- Microbiological parameters were assigned more weightage than physical and chemical parameters as they have the most significant health impact.
- The parameters related to known health risks were given higher weight.
- The weightage and rating assigned as per the modification of Universal Water Quality Index (UWQI) [21] (see Table 3).

3.1.3 Development of a Rating *Scale to Obtain the Rating (Qi)*

Qi was determined according to the range of values in each class through a rating scale. The scale is marked from 0 to 100, and the scores are further categorized into five classes. This scale is a modified version of Tiwari and Mishra's rating system [22] (see Table 4).

Table 4 Rating scale (modified Tiwari and Mishra [22])

Parameters	Range of parameters				
pH	7–8.5	8.5–8.6	8.6–8.8	8.8–9.0	9.0
		6.8–6.9	6.7–6.8	6.5–6.7	< 6.5
DO (mg/l)	> 6	5.1–6	4.1–5	3.0–4	< 3
BOD (mg/l)	0–3	3.0–6	6.0–80	80–125	>125
Total coliform (MPN/100 ml)	0–5	5.0–50	50–500	500–10,000	> 10,000
Fecal coliform (MPN/100 ml)	0–1	1–25	25–250	250–2500	> 2500
Qi	100	80	60	40	0
Extent of pollution	Clean water	Slightly polluted	Moderately polluted	Excessively polluted	Severely polluted

3.1.4 Determining the Sub-index Value (Wi × Qi)

The sub-index value is calculated by multiplying the unit weight by the rating obtained by combining the sub-indices to produce the overall water quality index (WQI). The WQI is the product of all the parameters' ratings (Qi) and unit weights (Wi) as shown in Eq. 1.

3.2 Data Collection

The data was collected as per season, i.e., pre-monsoon, monsoon, and post-monsoon for the month's May, September, and December, respectively, from Uttar Pradesh Pollution Control Board [23] (http://www.uppcb.com/river_quality.htm.) (see Table 5).

4 Result and Discussions

4.1 Spatio-Temporal Variation in Physico-Chemical Parameters

For this study, pH lies in the range of 6.7–8.6. A slight pH variation observes for all stations (see Fig. 4), which may depict the low variation of free CO_2 [24].

DO varies from 6.3 to 11.2 mg/l. As seen in Fig. 5, the average DO value meets the criterion at all monitoring stations. There is no marked change in the level of DO (mg/l) from 2016 to 2020, except for the year 2020, when there is an increase in oxygen level at some sites. At all monitoring stations, an increasing trend has been observed in DO levels post-monsoon (December).

In the case of BOD, there is decreasing trend from 2016 to 2020. It varies from 0.6 to 4.3 mg/l over five years. The COVID-19 lockdown imposed for a few months in 2020 improved the DO and decrease the BOD level in Ganga.

4.2 Spatio-Temporal Variation in Total Coliform and Fecal Coliform Count

The total coliform value lies in 350–2700 MPN/100 ml, while the Fecal Coliform value range is 110–1400 MPN/100 ml. All monitoring locations do not match the category "A" criteria of the designated best use concept. An increasing trend has been observed in both fecal and total coliform count. Anoopshahar STP 1 and STP 2 outlet at site Ganga downstream (d/s) Anoopshahar resulted in a high fecal and

Table 5 Ganga River water quality data (UPPCB, 2021)

Year	Month	pH	DO (mg/l)	BOD (mg/l)	Total coliform (MPN/100 ml)	Fecal coliform (MPN/100 ml)
Ganga at Garhmuktesar						
2020	May	7.8	9	0.6	540	320
	September	7.7	8	1.2	1600	540
	December	6.9	11.2	1.4	1400	790
2019	May	7.6	8.2	1.5	350	170
	September	8.1	7.6	1.7	540	220
	December	7	8.7	0.6	540	220
2018	May	7.4	7.6	2.1	430	250
	September	8.5	8.2	3	450	230
	December	6.8	8.1	2	390	110
2017	May	7.7	7.6	2.4	410	210
	September	8.1	7.5	2.5	450	250
	December	6.9	8.8	3.1	550	270
2016	May	7.6	8.7	2.2	1000	630
	September	8.5	7.3	2.4	1200	610
	December	6.7	8.4	1.9	900	370
Ganga upstream Anoopshahar						
2020	May	7.6	8.4	1.1	1500	750
	September	7.7	7.9	1	2000	930
	December	6.9	8.5	1.1	1700	780
2019	May	7.4	7.4	1.2	530	220
	September	7.8	7.4	1.3	540	250
	December	6.7	10.1	1.1	350	140
2018	May	7.6	7.2	1.6	550	270
	September	8.3	7.6	2.4	430	350
	December	6.9	9.7	2.6	410	250
2017	May	7.2	6.3	4.3	610	270
	September	8	7.4	2.2	630	230
	December	6.9	9.2	1.4	450	230
2016	May	7.6	8.2	2.5	700	320
	September	8.5	7.3	2.3	550	370
	December	6.8	9.4	3.1	610	250
Ganga downstream Anoopshahar						
2020	May	7.6	8.6	1.2	2700	1400
	September	8.6	8	1.3	2300	1300

Table 5 (continued)

Year	Month	pH	DO (mg/l)	BOD (mg/l)	Total coliform (MPN/100 ml)	Fecal coliform (MPN/100 ml)
	December	6.8	8.6	1.3	2600	1300
2019	May	7.6	7.2	1.4	530	220
	September	8.5	7.3	1.4	920	430
	December	7.1	10.3	0.8	430	210
2018	May	7.6	7.2	1.4	430	310
	September	8.2	7.6	2.2	450	230
	December	6.8	10.3	3	430	220
2017	May	7.5	7.1	4	430	210
	September	8.5	7.2	2.4	450	220
	December	6.9	9	1.6	420	220
2016	May	7.6	8.5	2.5	550	220
	September	8.6	7.5	2.1	410	350
	December	6.7	9.2	3.2	430	140
Ganga at Narora						
2020	May	7.7	8.9	1.3	2400	1300
	September	8.6	8.1	1.2	2700	1400
	December	6.9	8.8	0.9	2200	1100
2019	May	7.6	7.3	1.5	750	510
	September	8.1	7.5	1.1	1600	280
	December	7.1	10	1	1600	920
2018	May	7.7	7	1.8	550	290
	September	7.9	7.6	2	650	410
	December	6.9	9	3	610	450
2017	May	7.5	6.9	3.8	630	250
	September	7.8	7.5	2	610	280
	December	7.1	8.7	1.2	550	250
2016	May	7.6	8.3	3.5	710	430
	September	8.3	7.2	3.4	900	550
	December	6.8	8.8	3.8	550	200

total coliform count. It was significantly higher in the year 2020, during the period of Covid lockdown, as shown in Fig. 6.

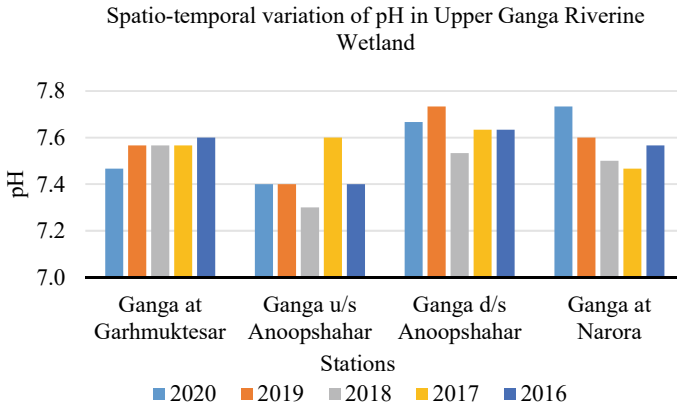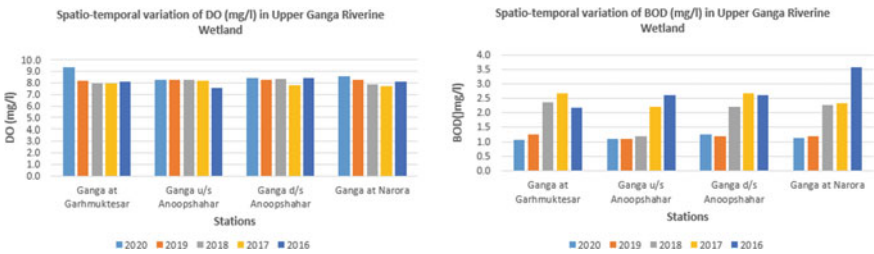Fig. 4 Spatio-temporal variation of pH

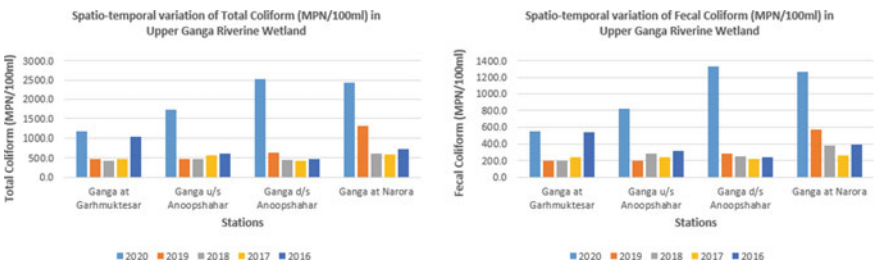Fig. 5 Spatio-temporal variation of DO (mg/l) and BOD (mg/l)

Fig. 6 Spatio-temporal variation of total coliform (MPN/100 ml) and fecal coliform count (MPN/100 ml)

4.3 Water Quality Index (WQI)

The water quality is classified from very poor to excellent based on the WQI data [22]. WQI ranges have been given below concerning pollution and water quality

Table 6 WQI-based scale of water quality

WQI range	Water quality status	Extent of pollution
90–100	Excellent (**E**)	Clean
70–90	Good (**G**)	Slightly polluted
50–70	Moderate (**M**)	Moderately polluted
25–50	Poor (**P**)	Excessively polluted
0–25	Very Poor (**VP**)	Severely polluted

status (see Table 6). The water quality indices have been obtained by taking the average of months representing each season (see Table 7 and Fig. 7).

Table 7 shows the average values of WQI corresponding to the four stations. Station Garhmuktesar has an average WQI ranging from 63.56 to 75.56; upstream and downstream of Anoopshahar have WQI ranging from 65.74 to 72.78 and 65.56 to 75.37, respectively; and Narora has an average WQI ranging from 64.63 to 68.33. The spatiotemporal variation of WQIs is shown in Fig. 8.

Table 7 WQI matrix for study area from year 2016 to 2020

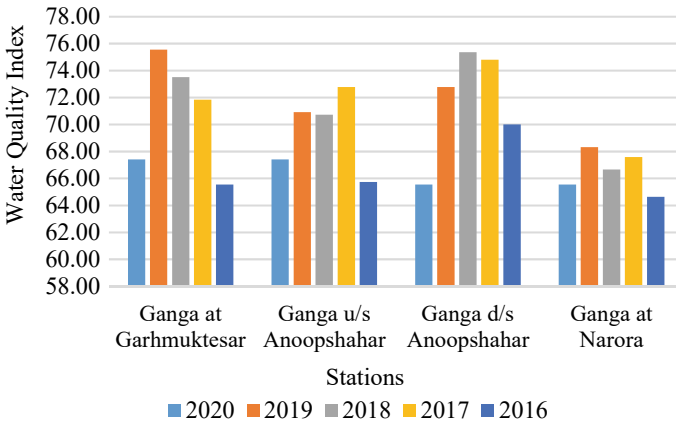| Stations	2020	2019	2018	2017	2016
Ganga at Garhmuktesar	67.41 (M)	75.56 (G)	73.52 (G)	71.85 (G)	63.56 (M)
Ganga u/s Anoopshahar	67.41 (M)	70.93 (G)	70.74 (G)	72.78 (G)	65.74 (M)
Ganga d/s Anoopshahar	65.56 (M)	72.78 (G)	75.37 (G)	74.81 (G)	70.0 (G)
Ganga at Narora	65.56 (M)	68.33 (M)	66.67 (M)	67.59 (M)	64.63 (M)

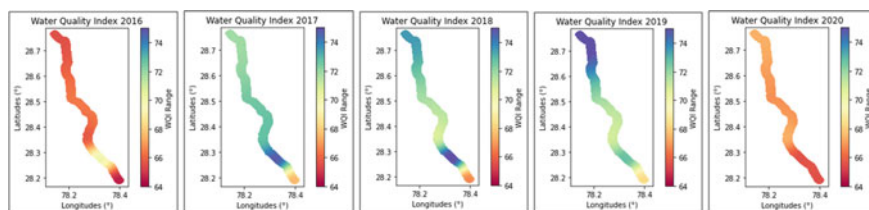**Fig. 7** Water quality index (average) for the stations

Fig. 8 Water quality index (average) spatial map of the study area (2016–2020)

5 Conclusion

In this study water quality of the Upper Ganga Riverine Wetland, stretching from Brijghat to Narora, was evaluated. Despite the implementation of intervention schemes and regulatory mechanisms by authorities, the water quality analysis of routinely monitored parameters (pH, DO, BOD, total and fecal coliform) at selected sites in the Upper Ganga Riverine Wetland suggests that the river is subjected to increasing microbial pollution. The above analysis indicates that the increase in sewage discharge along the river degrades the water quality. The computed WQI values in the study area range between 65 and 76 that fall under the moderate water quality (or moderately polluted)/good water quality (or slightly polluted) category of WQI. It can downgrade to the poor class shortly if the continual disposal of water pollutants in the river remains unchecked in the wake of poorly implemented monitoring measures.

For the prevention of any health issues, this study suggests proper sewage conveyance infrastructure coupled with the strict application of rules and legislation to check and manage sewage disposal prior to the intake of river water for drinking and other purposes. In addition, it is necessary to examine if goals such as pollution regulatory compliance or the execution of effective pollution control methods are being achieved. Besides, a minimum ecological flow is also required for the subsistence of a healthy riverine wetland.

References

1. Syphard AD, Garcia MW (2001) Human-and beaver-induced wetland changes in the Chickahominy River watershed from 1953 to 1994. Wetlands 21(3):342–353
2. Singh KP, Malik A, Mohan D, Sinha S (2004) Multivariate statistical techniques for the evaluation of spatial and temporal variations in water quality of Gomti River (India)—a case study. Water Res 38(18):3980–3992
3. Paul D (2017) Research on heavy metal pollution of river Ganga: a review. Ann Agrarian Sci 15(2):278–286
4. Cheng S (2007) Study on integrative assessment for conservation and sustainable utilization of wetlands resources. Chinese Academy of Forestry
5. Kumar B, Singh UK, Ojha SN (2019) Evaluation of geochemical data of Yamuna River using WQI and multivariate statistical analyses: a case study. Int J River Basin Manage 17(2):143–155

6. Leong WC, Bahadori A, Zhang J, Ahmad Z (2021) Prediction of water quality index (WQI) using support vector machine (SVM) and least square-support vector machine (LS-SVM). Int J River Basin Manage 19(2):149–156
7. Horton RK (1965) An index number system for rating water quality. J Water Pollut Control Fed 37:300–305
8. Tyagi S, Sharma B, Singh P, Dobhal R (2013) Water quality assessment in terms of water quality index. Am J Water Resour 1(3):34–38
9. Sutadian AD, Muttil N, Yilmaz AG, Perera BJC (2016) Development of river water quality indices—a review. Environ Monit Assess 188(1):58
10. Ichwana I, Syahrul S, Nelly W (2016) Water quality index by using national sanitation foundation-Water quality index (NSF-WQI) method at Krueng tamiang aceh, Paper presented at international conference on technology, innovation and society Universitas Syiah Kuala, Indonesia
11. Khadse GK, Patni PM, Labhasetwar PK (2016) Water quality assessment of Chenab river and its tributaries in Jammu Kashmir (India) based on WQI. Sustain Water Resour Manage 2(2):121–126
12. Bora M, Goswami DC (2017) Water quality assessment in terms of water quality index (WQI): case study of the Kolong River, Assam India. Appl Water Sci 7(6):3125–3135
13. Verma RK, Murthy S, Tiwary RK, Verma S (2019) Development of simplified WQIs for assessment of spatial and temporal variations of surface water quality in upper Damodar river Basin, Eastern India. Appl Water Sci 9(1):21
14. Lkr A, Singh MR, Puro N (2020) Assessment of water quality status of Doyang river, Nagaland, India, using water quality index. Appl Water Sci 10(1):1–13
15. Garg A, Joshi B (2015) Ecosystem sustenance of Upper Ganga Ramsar site through phytoremediation. Geohydrology 45(2):175–180
16. CPCBENVIS (2021) http://cpcbenvis.nic.in/waterpollution/criteria.htm. Accessed 1 Sept 2021
17. Leo ML, Dekkar M (2000) Hand book of water analysis. Marcel Dekker, New York
18. Sawyer CN, McCarty PL, Parkin GF (1994) Chemistry for environmental engineering, vol 4. McGraw-Hill, New York
19. Burden FR, Mc Kelvie I, Forstner U, Guenther A (2002) Environmental monitoring handbook. Mc graw-Hill Handbooks, New York, pp 3.1–3.21
20. De AK (2003) Environmental chemistry, 5th edn. New Age International Publisher, New Delhi, p 284
21. Boyacioglu H (2007) Development of a water quality index based on a European classification scheme. Water S.A 33(1)
22. Tiwari TN, Mishra MA (1985) A preliminary assignment of water quality index of major Indian rivers. Indian J Environ Prot 5(4):276–279
23. UPPCB (2021), http://www.uppcb.com/river_quality.htm. Accessed 10 Sept 2021
24. Jayaprakash RI (1988) A study of the environmental biology of Netravathi river system. Dissertation, Mangalore University

Review of Pollutant Release and Its Mobility Due to Sediment Erosion in the River Bed

Ranjit Kurmi, Ashwini Iangrai, and Anurag Sharma

Abstract A huge quantity of sediment is present in rivers, and sedimentation is a prime factor that influences the broad use of rivers. Sedimentation and resuspension are the major practices affecting the river morphology and water quality. During non-flood period, the flow discharge reduces, and ultimately, a huge amount of polluted sediment is stored at the riverbed. In previous study, the contribution of the pollution released from sediments into the river was assessed in relation to 16 metal (loid)s, three non-metals, and the ions PO_43 and NH_4^+. The methods used here included the segments of sampling area, analytical methods, and data processing. Methods based on the total contaminant concentration are still often used to quantify the environmental risk presented by polluted soils and sediments. The pollutant or contaminant present in the river bed may be phosphorus (P) and heavy metals such as plutonium (Pu) and nickel (Ni). Hence, the research on the pollutant mobility in the river is significant, and its chemical and sediment dynamics must be included for the maintenance of the river health. Therefore, more research is needed to quantify the release of pollutant mobility due to sediment resuspension in a river. Results will enable to calculate the pollutant mobility with sediment transport in the small scale or in the field environment. There is still much to learn about the crucial mechanisms that determine the fates of metallic elements in the watershed; thus, further research may be done to examine the impact of geochemical characteristics on the distribution of metallic elements in this watershed.

Keywords Sedimentation · Resuspension · Pollutant mobility · Watershed

R. Kurmi (✉) · A. Iangrai
Department of Civil Engineering, Central Institute of Technology Kokrajhar, Kokrajhar 783370, India
e-mail: ranjitkurmi08@gmail.com

A. Sharma
Department of Civil Engineering, National Institute of Technology Rourkela, Rourkela, Odisha 769008, India
e-mail: sharmaan@nitrkl.ac.in

1   Introduction

Practical knowledge is necessary for improving and executing technical problem solutions and for substantiating sediment-related quality objectives, which needed a broad range of models and simulation methods in various spatial along with temporal appraise. To quantify the environmental risk caused by contaminated or polluted soils and sediments, approaches based on the total contaminant content are applied. Due to specific chemical properties and prevailing environmental parameters, many elements are only partly bioavailable. The possible long-term negative effects of heavy metal contamination on the environment and health of humans are of grave concern. The hazardous elements in terrestrial and aquatic environments are related especially to the mining activities. Metals including Cu, Pb, As, Cd, Cr, and Zn are abundant in the mining waste dump, which is typically acidic.

2   Literature Review

Dvořák [2] says that specialize in risk component, an organic waste product, nutrient levels, bioaccessibility, and bioavailability within the sediment of a dam reservoir. Estimation of sample of sediment for organic impurities indicated low grades of polycyclic aromatic hydrocarbons, and residing elevated PCB content because of the in-depth exploitation of those compounds; nonetheless, these organic impurities don't formulate any severe environmental hazard. Increased As, Cd, and Zn content was predicted when high mobility of Zn, and particularly, Cd, together with high bioaccumulation potential, highlights a possible environmental risk. The outcomes showed fluctuations in pollutant weights in sediment on the basin and an entirely diverse intake of contaminants via the individual tributaries (Fig. 1).

Tansel and Rafiuddin [7] was concerned about areas far from possible sources that may be affected by contaminants carried by river currents and deposited in Miami River sediments. The impurities are metals like As, Cd, Hg, Zn, Pb within the surface sediments are analyzed to a grain size of less than 0.075 mm to 6.3 mm and organic content. The samples were gathered in the bay waters and along the riverbank.

Chen [1] highlighted the examination of acid mine drainage, the fate of metallic elements, their method of emigration in a waste mud containment, and their fallout downstream. Here, the result showed that the waste in the mud confinement had been severely acidified and weathered. Metallic components demonstrated a significant degree of activity and mobility, with an order of Cd > Zn > Mn > Cu ≈ Cr > As ≈ Pb causing these massive metals to become dangerously contaminated in the catchment basin. In the downstream alluvium, the proportions of dissoluble, substitutable, and organic Pb, Cu, and Zn were rather low. The most important pouring force employed for the immigration of metallic elements was hydraulic expatriation caused by elevation change. The most crucial course of action for the reduction of metallic elements in river water was designated as the precipitation of iron oxyhydroxides. Some of
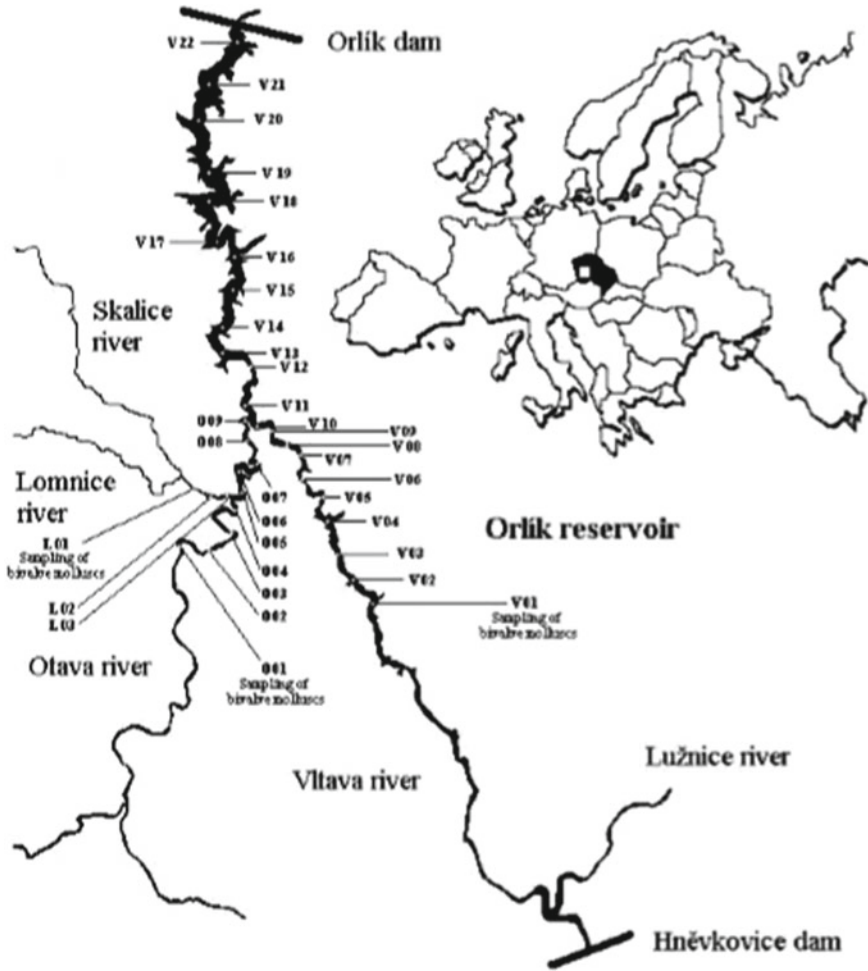
Fig. 1 Location of the various sampling points are shown on schematic maps [2]

the following processes, including diffusion, precipitation, resuspension, adsorption, and desorption, among others, can have an impact on the mobilization and percentage of metallic elements in aquatic systems. The bulk of these processes are dependent on the watershed's hydropower variables, which are virtually always connected to variations in riverbed elevation.

Förstner [2] was related with the topics like dynamic traits of the outlines of sediment-related techniques in rivers which constituted spectacular impacts of stormwater incidents on particle transport, timely and comprehensive outcomes of sulfide oxidation throughout resuspension, and biological accretion and possible discharge of harmful chemicals. Pollutant mobility is a result of the stabilizing and mobilizing actions in the chemical and hydraulic fields. Organic materials react

violently. Degradation of organic materials will result in an oxygen shortage and might improve floc and biofilm configuration. The analysis of variations in pH and redox state, competition between dissolved ions, and techniques like complexation by organic entities should all be included in the survey of residue and water chemistry aberrations. It is necessary to study the whole effects of contaminants on aquatic ecosystems since the complete process will have an impact on the solution or solid stability situations (Fig. 2).

Schroeder [5] finalized their research on the availability and discharge of impurities from deposited and suspended sediments. The grant of the pollutant discharge will occur from sediments to the comprehensive waterway. Sixteen metals, three non-metals, and the ions were taken into consideration while evaluating the journey budget. Ex-situ suction-based pore water sampling, in-situ dialyzes-based pore water sampling, suspension experiments, chronological extraction analysis, statistics, and graphs are some of the techniques and materials employed in this investigation. Researchers studying pore water emphasize that profiling and pepper-based surveys are equivalent and urge that organisms that reside in the sediment be subjected to high levels of metal (loid) concentrations. Only, a few metals (loid) surpass the predetermined approach levels during resuspension. The largest quantities discharged per ton of ceased residue were between 10–5 and 10–1% of the usual daily load of the river Trave. Taking everything into consideration, the most pristine sediments inside
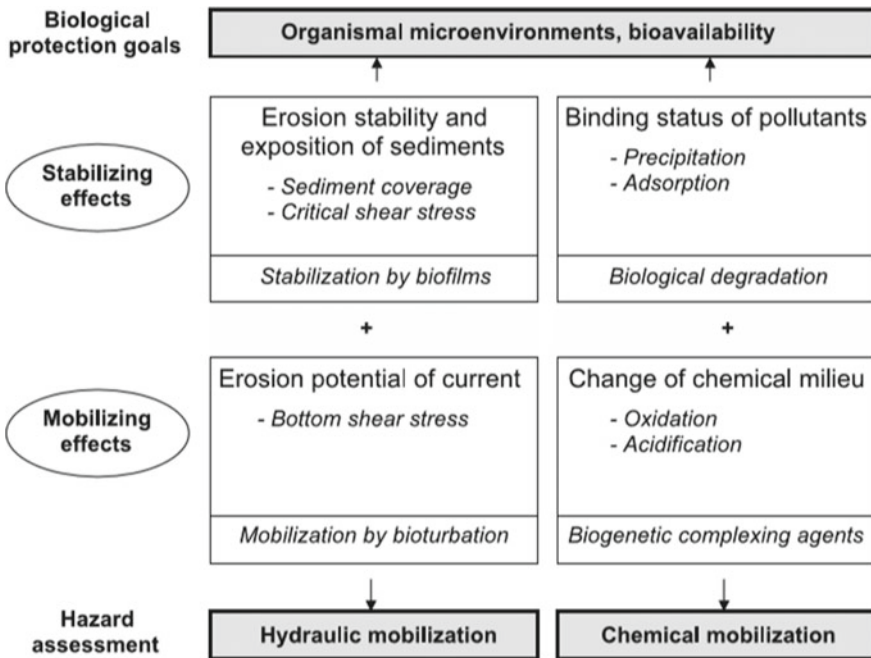

Fig. 2 Biological protection objectives, hydraulic and chemical hazard evaluation, and the stabilizing and mobilizing impacts on pollutants. Modified from Westrich and Kern (1996) [3]

the research area—rather than any potentially hazardous materials—are discovered to be the source of the greatest concern. The recommendations support requests to include fractionation and speciation laws in sediment legal evaluations.

Sturm [4] has executed their research project on the survey of the mobilization and objective of inorganic pollutants due to resuspension of cohesive sediments in streams and estuaries throughout storm incidents or dredging activities. It integrated the flume and column researches of sediment resuspension with bench-scale surveys of the effect of heavy metals on the sediments. Resuspension percentages of cohesive sediment were measured in flume and column studies as a part of shear stress, humics, and sediment pH using kaolinite infected by heavy metals and several other polluted field sediments. The impacts were understood in terms of a theoretical model of interparticle forces. Evidence from the bench-scale, flume, and column experiments were given rise to the effective usage to formulate a model of metal mobilization associated with a sediment resuspension relationship during a numerical transport model. The trials conducted on the Etowah River sediments ended with a sign that there was a rapid boost in sediment erosion with the increased inflow (Fig. 3).

Ingvertsen [3] examined the aggregate heavy metal concentrations in the To Lich River sediments and found out that heavy metals like Cd were the high-priority pollutant of these sediments as compared to Pb and Ni. Substitutions that were done in the chemical equilibrium state of the sediment caused by an anthropogenic disorder such as dredging and land disposition, or further agitation was proven to be significant for Cd and smaller in Pb, but Ni was especially get in the residual amount and was assessed less accessible to mobilization. They concluded that the experiment showed that, despite the possibility that oxidation could increase the concentrations of heavy metals in sedimentary pore water at equilibrium, other sediment mineral fractions appeared to be effective at immobilizing heavy metals that could have been released from the oxidizable fraction (Fig. 4).
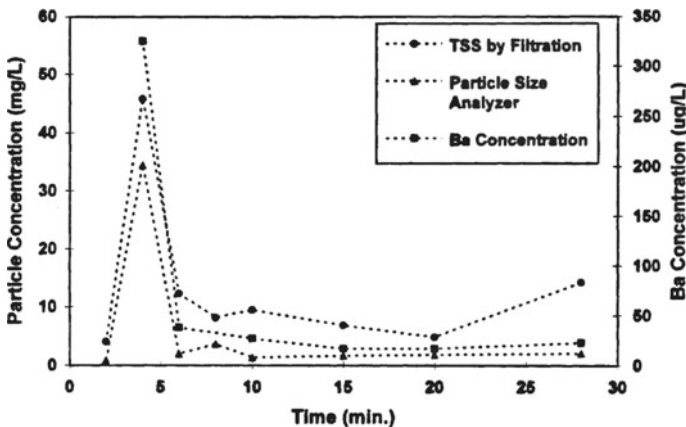

Fig. 3 Variation with time of resuspended particle and barium concentration in flume test with constant shear stress [6]
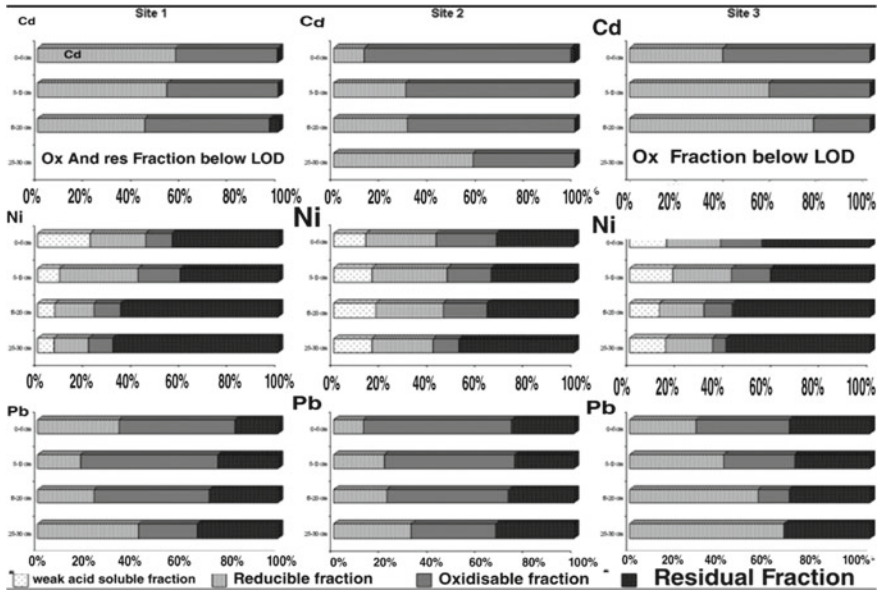
Fig. 4 Here, the relative distributions of Cd, Ni, and Pb among the BCR fractions in one core sample from each of the three sampling sites in the To Lich River are shown in three columns of graphs are shown. Each bar on the graphs depicts the relative distribution for a single depth region [4]

3 Research Gap

Most of the research work related to the resuspension of sediments shows the potential and activity of elements with river currents. In some cases, tests conducted showed signs of instantaneous increase in sediment erosion with the increase in flow. To understand the pollutant mobility due to resuspension of sediment in riverbed, multiple experiments and statistical tests were conducted.

Future research may be done to determine how geochemical resources or qualities impact the distribution of metallic elements in this watershed, as well as to gain knowledge of the key strategy that will determine how metallic elements fare in the riverbed.

The incorporation of biological data was required due to the anticipated increase of process studies and models. Few of their exopolymers, meanwhile, would work well as complex agents for the mobilization or evolution of heavy metals. Once deterioration or abasement has reached its conclusion with regard to organic contaminants, biological abasement might be seen as a stabilizing effect. However, it is feasible that metabolic processes will produce intermediates that are both more mobile and hazardous than the initial pollution.

Since it may be used to assess possible dangers of the sources of pollution near the reservoirs, evaluating the findings of organic and inorganic pollutants can be

beneficial for the aquatic environment. There hasn't been much research done on the mobility and distribution of heavy metals in anoxic sediments in some rivers that receive wastewater. When biological breakdown of organic contaminants reaches its culmination, it might be viewed as a stabilizing effect. Therefore, it is absolutely necessary to include biological knowledge in future process research and model building. Additionally, very little is currently understood about how shifting flow conditions may affect how lowland river banks respond to linked resuspension occurrences.

4 Results and Discussions

Similar outcomes were recorded alongside the sampling region, with the majority of the sediment samples performing fairly acidic and having a pH value between 5.2 and 5.8. The minor set of samples had pH values that were somewhat higher, ranging from 6.1 to 6.5. Similar results are shown for the sorption capacity of the alluvium or sediment, with values varying between 160 and 220 mmol/kg and reaching as high as 320 mmol/kg in the deposit or sediment. By calculating the MBC, the biological activity of the deposit was projected, and it was found that the values next to lakes and tributaries had a higher degree of changeability and indeterminate allocation without any obvious pattern. Therefore, it was not anticipated that modifying physicochemical qualities would result in significant changes in contaminant mobility.

The Hg concentration of the sediments has received remarkably notable attention in recent decades. Sediment Hg level in their research area exceeded 1 mg/kg in 1994 and 1995. The mean Hg level of 0.32 mg/kg during the past 20 years shows that the Hg level has significantly decreased. The highest Hg levels were found in deposits or silt from the Otava river, in line with the bulk of the risk factors identified.

The bioavailability of organic matter and the volume of organic matter in sediments both manage to increase the biological activity of the sediment, which in turn causes a greater discharge of ammonium and orthophosphates into the water.

5 Conclusions

Transport and erosion in indivisible catchment regions cause sedimentation, which is a continual and natural process. Any hazard assessment in this area will be built on the physical characteristics and sediment assessment methods. When river flow or currents are reduced, fine particles may be mobilized, collected, or be taken out to the bay. Metals migration was shown to be influenced by a number of factors, including damming stoppage, hydraulic transfer, and benthic processes. There have been instances where testing indicates that sediment erosion increases instantly as flow increases. While some sediment crystals effectively immobilized heavy metals

released from the oxidizable portion, other studies also demonstrated that oxidation increased the equilibrium pore water concentration of heavy or hefty metal in the sediments. The results of academic study conducted globally vary from region to region. Therefore, a number of experiments and statistical analyses were carried out to better understand the pollutant mobility caused by the resuspension of silt in riverbed.

Sediments are intermittently deposited and mobilized. Alluvium-bound pollutants may undergo extensive dissipation of contaminants during floods in flood plains, dike foreshores, and polder regions. Because of the failure of dams and excessive rainfall in recent years, there were catastrophic floods in addition to seasonal floods. Events like breakdown of tailing dams in mining districts in extremely infected areas generate an immense environmental risk. The result causes long-lasting contamination of river residue and flooded soils. Extensively diversified contamination sources having greater catchment areas create a pollutants mixture, which is tougher to treat than industrial waste. Because of the greater amount of polluted materials to be treated, traditional remediation techniques are often economically unacceptable. In these situations, the concept of "geochemical engineering" can provide affordable and long-lasting solutions.

References

1. Chen M (2018) Migration and fate of metallic elements in a waste mud impoundment and affected river downstream: a case study in Dabaoshan Mine, South China. Ecotoxicol Environ Saf
2. Dvořák T (2017) Content of inorganic and organic pollutants and their mobility in bottom sediment from the Orlík water reservoir (Vltava river, Czech Republic). Soil Sediment Contam Int J, 1–41
3. Förstner U (2004). Sediment dynamics and pollutant mobility in rivers: an interdisciplinary approach. Lakes Reservoirs Res Manag, 1
4. Ingvertsen ST (2013) Pollution and potential mobility of Cd, Ni and Pb in the sediments of a wastewater- receiving river in Hano, Vietnam. Springer Science + Business Media Dordrecht, p 1
5. Schroeder HL-L (2020) Sediment water (interface) mobility of metal(loid)s and nutrients under undisturbed conditions and during resuspension. J Hazardous Mater
6. Sturm T, Amirtharajah A, Tiller C (1996) Mobilization and fate of Inorganic contaminants due to resuspension of cohesive sediment. Hazardous Substance Research Centre, p 1
7. Tansel B, Rafiuddin S (2016) Heavy metal content in relation to particle size and organic content of surficial. Elsevier

Application of QUAL2K Model for Water Quality Modeling of Bhadra River Stretch, India

Satish Kumar Mummidivarapu, S. Rehana, and Himanshi Singh

Abstract This research was carried out along the Bhadra River, which is one of the tributaries of the Tungabhadra and originates near Gangamula in Karnataka's the Western Ghats. The study stretch is around 27 km divided into three reaches with elements of 1 km as 3, 4, and 20 for each reach, respectively. The objectives of the study are to assess the effects of wastewater discharges on the water quality of the Bhadra River stretch and to simulate the dissolved oxygen (DO) by varying the biochemical oxygen demand (BOD) loads coming from different pollutant sources within the study stretch using the QUAL2K river water quality model. The study period considered is about 24 months (April 2014–March 2016) for the simulation of temperature, pH, DO, and nitrate parameters with the help of observed data at three monitoring stations. The investigation period was separated into two parts: the model was calibrated using monthly average data from April 2014 to March 2015 (12 months), and the model was validated using monthly average data from April 2015 to March 2016 (12 months). The R-square (R^2) value for temperature and pH ranges from 0.87–0.56 to 0.64–0.62, respectively. The Root Mean Square Error (RMSE) for nitrate and DO ranges from 0.06–0.02 to 0.47–0.34, respectively. The results revealed that the Bhadra river stretch was highly polluted due to effluents coming from the industries present in the study stretch. It was also discovered that river flow rate, point source discharge, fast Carbonaceous Biochemical oxygen demand (CBOD) oxidation rate, and nitrification rate as the highly sensitive quality parameters defining the Bhadra river water quality. There must be a reduction of 25% of BOD effluent to reach the minimum standards set by the Central Pollution Control Board (CPCB). It is noted that a 75% reduction of BOD effluent from point sources will lead to an increase of 15% average DO throughout the study stretch.

S. K. Mummidivarapu · S. Rehana (✉) · H. Singh
Hydroclimatic Research Group, Lab for Spatial Informatics, International Institute of Information Technology, Gachibowli, Hyderabad, Telangana 500032, India
e-mail: rehana.s@iiit.ac.in

S. K. Mummidivarapu
e-mail: mummidivarapu.satish@research.iiit.ac.in

H. Singh
e-mail: Himanshi.singh@research.iiit.ac.in

1 Introduction

In many poor and developing nations, wastewater originating from municipal and industrial sources is discharged with little to no treatment. This practice has persisted throughout human history, but significant water quality issues have become prevalent due to population expansion and increased industrialization. It is vital to formulate the complicated connections between waste loads from diverse sources and the consequent water quality of receiving waterways. Mathematical models are the most effective approaches to describing these interactions [1]. Surface water management now incorporates specific mathematical models for assessing the pollution effect. Bottino et al. [2] expressed that water quality models are essential for water management because they anticipate long- and short-term changes in water quality parameters. The United States Environmental Protection Agency (US-EPA) defines water quality models as "tools for modeling the flow of contaminants and precipitation from the ground surface via pipe and network channels, storage treatment units, and finally to receiving waterways". There are various water quality models, each requiring a different level of confidence in the model's output. Among the water quality models, QUAL2E was the most widely utilized mathematical model for assessing the traditional pollution impact in river and stream water quality. This model was created by the US Environmental Protection Agency (US-EPA), and it has certain limitations [3]. Park and Lee [4] updated it due to several limitations and created QUAL2K 2000, which featured new water quality interactions. Chapra and Pelletier [9] refined it further in 2003 under the moniker QUAL2K 2003. Pelletier et al. [5] created QUAL2Kw, an updated version of QUAL2E, by altering the QUAL2K 2003. QUAL2K is a widely used technique for estimating the quality of river water [6–8].

The QUAL2K is a one-dimensional, time-variable model that simulates temperature, carbonaceous BOD, DO, phytoplankton, phosphorus, and nitrogen in each specified reach of the stream. It may also imitate river stream pH, alkalinity, inorganic suspended particles, pathogenic bacteria, and bottom algae. The ability to add hourly data into the QUAL2K model is a big plus. It may model a system stream with multiple tributaries and the main branch. This one-dimensional model simulates the effects of point and non-point pollution loading and is based on the principle that the channel is well mixed in both vertical and lateral directions. All hydraulic parameters are modeled as a one-dimensional, steady-state flow with non-uniform flow, meaning water depth, and velocity vary depending on channel location (Fig. 1).

Because the dial heat budget calculations are dynamic, the model incorporates dial changes as water quality dynamics, and the heat budget is calculated on a dial time scale. QUAL2K divides a river stream into reaches, which are then separated into elements, which are the fundamental computing units. The present study goals are
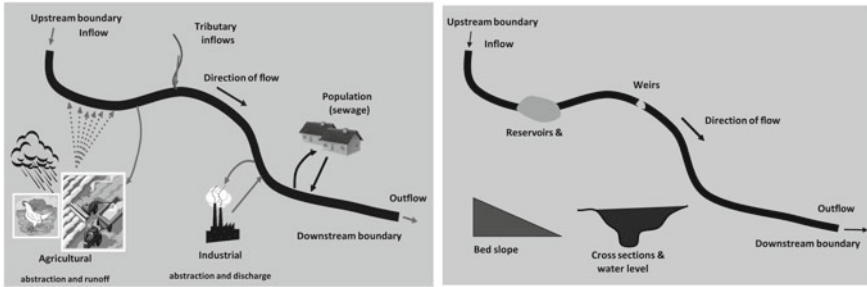
Fig. 1 Typical inflows, outflows, and hydraulics data required for a one-dimensional model

to use the QUAL2K model to simulate temperature, dissolved oxygen, nitrate, and pH parameters to assess the influence of wastewater discharges on the water quality of the Bhadra river stretch. To evaluate the model's performance using statistical measures such as the Root Mean Square Error (RMSE), Mean Bias Error (MBE), and R-square (R^2). To simulate dissolved oxygen for various probable contamination scenarios and compare the predicted DO to baseline values.

2 Study Area and Source of Data

2.1 Bhadra River (Bhadravathi Stretch)

The Bhadra River begins at Gangamula in Karnataka's Western Ghats and flows for 190 km till it reaches Koodli, Karnataka, where it meets the Tungha River to form the Tungabhadra River. The flow of the Bhadra River, which is downstream of the reservoir, is considered in this research and is influenced by the outflow of the Bhadra reservoir. The river stretch is under investigation, and the location of the Bhadra reservoir, discharge stations, and water quality monitoring stations are depicted in Fig. 2. The current study length of the Bhadra River is approximately 27 km long, and the Mysore Paper Mill (MPM), the Visveshvarya Industrial Steel Limited (VISL), and the Bhadravathi city are the two industries and municipal effluents that pollute it the most. Non-point sources such as overland flow from surrounding towns and farmland contaminate the 27 km study area and these drains [6]. The CPCB has recognized this river length as one of India's most polluted river stretch [11].

2.2 Data Collection

The hydraulic and hydrological data, climate data, and water quality data are all required by the QUAL2K model. In terms of discharge statistics, the Bhadra river
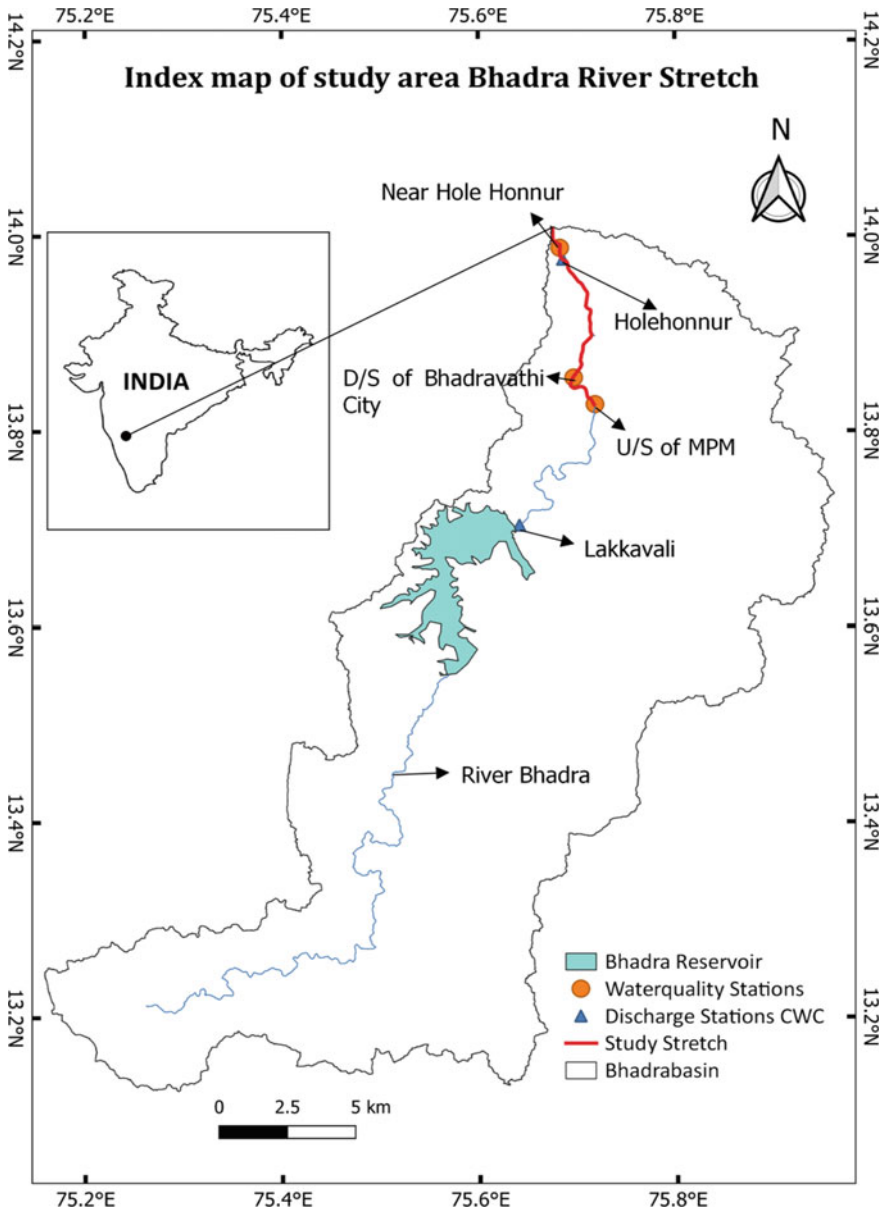
Fig. 2 Index map of the study area describing about the reservoir, water quality monitoring stations, and downstream study stretch

Table 1 Average water quality data at different monitoring stations

WQ Stations	Latitude	Longitude	Duration	Water quality parameters			
				Temp (°C)	DO	NO$_3$	pH
U/S of MPM	13.827 N	75.718 E	Apr14–Mar15	29.67	6.63	0.27	7.78
			Apr15–Mar16	27.67	6.96	0.12	7.39
D/S/ of Bhadravathi city	13.854 N	75.696 E	Apr14–Mar15	29.08	5.90	0.36	7.57
			Apr15–Mar16	27.58	6.58	0.17	7.26
Near Holehonnur	13.987 N	75.682 E	Apr14–Mar15	27.75	5.08	0.24	7.35
			Apr15–Mar16	28.00	6.68	0.17	7.24

has two discharge monitoring stations (one at Lakkavali and the other at Holehonnur), both of which are managed by the Central Water Commission (CWC). The data at Lakkavali station (upstream of the study element) is unavailable. As a result, the discharge data is computed using Bhadra reservoir outflow data, set to 10.36 m^3/s. The model climatic data taken from the India Meteorological Department (IMD) includes air temperature, wind speed, and dew point temperatures. There are three water quality monitoring stations in the study stretch, all maintained by the CPCB and KSPCB's national water quality monitoring program. The observed water quality data applied in this research comes from the Karnataka state government's Advanced Center for Integrated Water Resource Management (ACIWRM). The Table 1 below displays the average water quality data for a specific time period and the coordinates of the monitoring stations used in the simulation of the specified quality parameters.

Based on morphology, the current research stretch of the Bhadra River was split into three reaches, each of which was further divided into 3, 4, 20 elements. Rehana and Mujumdar [8] provided information on the hydraulic features of the river's headwaters and lengths. The average bed width was 61.85 m, the longitudinal slope was 0.00161, manning's coefficient was 0.0492, and the side slope was 0.50. The headwater's temperature, NO$_3$, pH, and DO were acquired from ACIWRM. Rehana and Mujumdar [8] and Sumithra and Narayana [10] provided data on water quality, including DO and BOD, and flow rates for the point sources. The three point sources in the study stretch (Mysore paper mills, Bhadravathi city, VISL) had BOD loads of 399 mg/L, 15 mg/L, and 279 mg/L, respectively. However, the CPCB has set a minimum BOD effluent limit for paper mills of about 30 mg/L.

3 Methodology

The establishment of a water quality model is a crucial stage in achieving the study's objectives. Water quality models are incredibly effective for replicating the natural state of a river system and, as a result, forecasting changes in the natural state under different situations. Most prior research in this field has focused chiefly on point source-based variables such as DO and BOD; however, in this work, four parameters

are examined for simulation: temperature, DO, NO_3, and pH. River water quality variables are influenced by (1) point and non-point pollution sources merging in a river length, (2) climatic circumstances, and (3) water quality and quantity at the river's headwater. Various pollutant load scenarios are explored for the modeling of DO to find the influence of wastewater loadings on the river health of the study stretch. The steps involved in the current methodology are schematically depicted in Fig. 3.
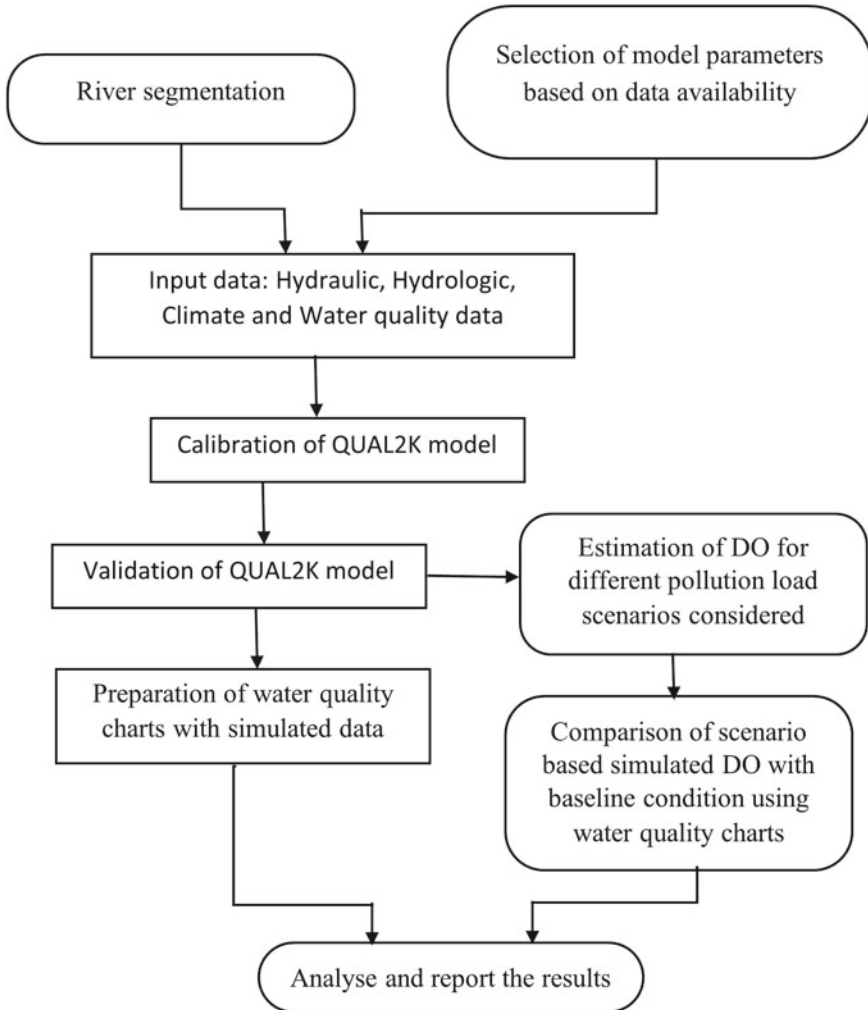

Fig. 3 Flowchart of the proposed methodology in the present study

3.1 Development of QUAL2K Model

The QUAL2K (or Q2K) model is an updated version of the QUAL2E model for river and stream water quality. The following are the characteristics of the QUAL2K: (i) Diurnal water quality kinetics and heat balance (the model simulates all water quality variables, temperature, and heat budget on a diurnal time scale); (ii) Mass and heat input (the model can simulate the point and diffuse loads and abstractions). The QUAL2K model divides the study river into multiple reaches (Fig. 4), each of which is split into elements. These elements are the model's shortest simulation portions. For each model element, a steady-state flow equity is performed as follows:

$$Q_i = Q_{i-1} + Q_{in,i} - Q_{ab,i} \tag{1}$$

Here, Q_i is the outflow from element i into element $i + 1$ (m³/d), Q_{i-1} is inflow from the upstream element $i - 1$ (m³/d), $Q_{in,i}$ is the total inflow into the element i from point and non-point sources (m³/d) and $Q_{ab,\,i}$ is the total outflow from the element i due to point and non-point abstractions (m³/d).

Each element's outflow is computed, and the velocity and depth are determined using one of three methods: rating curves, weirs, and manning equations. A trapezoidal channel is ideal for each section. The manning equation was used to represent the connection between depth and flow under steady flow circumstances as:

$$Q = \frac{S_o^{1/2} A_c^{5/3}}{n\,P^{2/3}} \tag{2}$$

Here, Q is flow (m³/d), $n =$ the Manning roughness coefficient, S_o is the bottom slope (m/m), A_c is the cross-sectional area (m²), and P is the wetted perimeter (m), Chapra and Pelletier [9].

The governing equation of QUAL2K is a one-dimensional advection–dispersion equation.

$$V\frac{\partial c}{\partial t} = \frac{\partial\left(A_c E \frac{\partial c}{\partial x}\right)}{\partial x}\,\mathrm{d}x - \frac{\partial(A_c U C)}{\partial x}\,\mathrm{d}x + V\frac{\mathrm{d}c}{\mathrm{d}t} + S \tag{3}$$

Here, U is averaged velocity (m/d), A_c is cross-sectional area (m²), E is longitudinal dispersion coefficient (m²/d), c is the concentration (g/m³), V is the volume (m³), x is the distance (m), and S is the sources and sinks of the constituent due to reactions and mass transfer mechanisms (g/m³/d).

The QUAL2K model provides a standard mass balance Eq. (4) for all water quality concentrations in the water column of elements i (Fig. 5) is as follows:

$$\frac{\mathrm{d}C_i}{\mathrm{d}t} = \frac{Q_{i-1}}{V_i}C_{i-1} - \frac{Q_i}{V_i}C_i - \frac{Q_{ab,i}}{V_i}C_i + \frac{E_{i-1}}{V_i}(C_{i-1} - C_i)$$
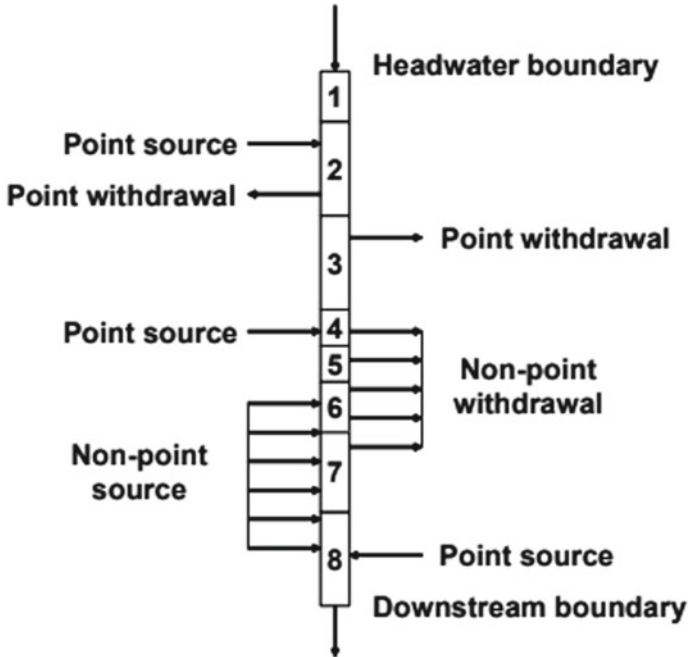
Fig. 4 QUAL2K segmentation scheme for a river with no tributaries (*Source* QUAL2K manual [5])

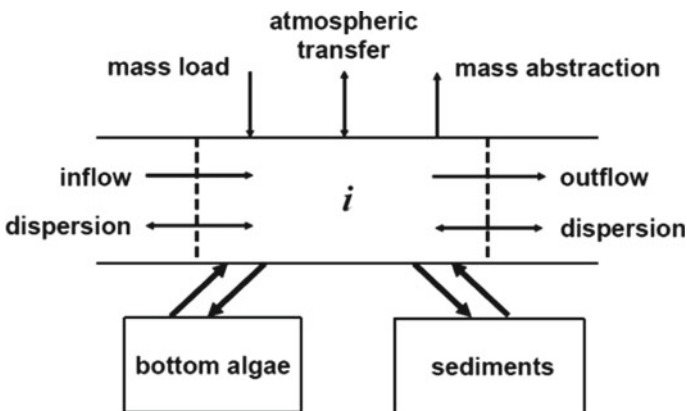$$+ \frac{E_i}{V_i}(C_{i+1} - C_i) + \frac{W_i}{V_i} + S_i \tag{4}$$

Fig. 5 Processes involved in the modeling of QUAL2K's general mass balance (*Source* QUAL2K manual [5])

Here, C_i is the variable concentration for element i (g/m^3), V_i is the volume of the element i (m^3), W_i is external loading of the constituent to element i (g/d or mg/d), t is time (d), Q_i is the outflow from element i into element $i + 1$ (m^3/d), and E_i is the bulk dispersion coefficient between elements i and $i + 1$ (m^3/d).

The model user's handbook contains a detailed description of the processes and mathematical representations of the interacting water quality model parameters and sources and sinks of constituents due to reactions and mass transfer mechanisms. Based on the hydraulics of the channel, the QUAL2K used a hydraulics-based formula to internally compute the longitudinal dispersion for a border between two elements:

$$E_{p,i} = 0.011 \frac{U_i^2}{H_i} \frac{B_i^2}{U_i^*} \tag{5}$$

Here, $E_{p,i}$ is the longitudinal dispersion coefficient between elements i and $i + 1$ (m^2/d), U_i is velocity (m/d), B_i is the width (m), H_i is mean depth (m), and U_i^* is the shear velocity (m/d), and this, in turn, is linked to more basic features by:

$$U_i^* = \sqrt{g H_i S_i} \tag{6}$$

Here, g is the acceleration due to gravity, and S_i is the channel slope.

Modeling was carried out for 24 months (April 2014-March 2016), with the QUAL2K model being calibrated for 12 months (Apr-14 to Mar-15) and validated for 12 months (Apr-15 to Mar-16) for temperature, DO, NO$_3$, and pH simulations. The impact of point source BOD loadings on study stretch is considerable. The MPM and VISL's BOD effluents aren't even close to meeting CPCB requirements. Pollution scenarios (25%, 50%, 75%, and 100% effluent BOD) were constructed based on effluent BOD loads to simulate the DO of the study stretch. Water quality charts depict the simulated DO based on pollution scenarios compared to the effluent BOD baseline condition of 100%.

4 Results and Discussions

4.1 QUAL2K Model Calibration and Validation

Figure 6 depicts the QUAL2K model calibration and validation results for various parameters and the distance of the Bhadra river stretch. Temperature, pH, and DO findings exhibit close fits to actual data over the calibration period. Three statistical error metrics (RMSE, MBE, and R^2) must be established to assess the model's performance. R^2 values for temperature, pH, and DO during model calibration are obtained as 0.87, 0.50, and 0.62, respectively, while RMSE values for temperature, nitrate, and pH are obtained as 0.23, 0.06, and 0.08, respectively. R^2 values for

temperature, nitrate, and pH during the validation period are 0.56, 0.90, and 0.64, respectively, while RMSE for temperature, DO, nitrate, and pH are 0.42, 0.47, 0.02, and 0.03, respectively.

The calibration parameters, reaction rates, and coefficients of the water quality model are more important for the model's performance during calibration. The ISS settling velocity was 0.35 m/day for all three reaches. The DO simulation is influenced by the fast CBOD oxidation rate, which varies from 0.0126 to 0.136 per day. Organic nitrogen hydrolysis rate (1.25–1.58 per day), organic nitrogen settling velocity (0.65–1.96 m/day), ammonium nitrification (0.09–0.32 per day), nitrate denitrification rate (0.19–1.9 m/day), and sediment-denitrification transfer coefficient (1.03–3.14 m/day) were the calibration parameters used in the model. The calibration variable ranges are constructed using the maximum and minimum values of the model. The exact values of the calibration parameters used in the respective reaches of the study stretch are given in Table 2. As mentioned above, the model performance was evaluated using some statistical error parameters. The RMSE, MBE, and R^2 values for the calculated and measured data during the calibration and validation phase are given in Table 3.

4.2 Estimation of DO from Pollution Load Scenarios

Pollution scenarios are created based on the availability of point source data. The BOD effluent from point sources (MPM and VISL-399 mg/l and 279 mg/l, respectively) is obsolete, obtained from Rehana and Mujumdar [8]. Because BOD load is one of the influencing factors for the overall DO condition of the stretch, the pollution scenarios of 25%, 50%, 75%, and 100% BOD effluent were investigated for DO modeling. Figure 7 compares and illustrates the fluctuation in DO throughout the study stretch for various pollution scenarios. Based on the examination of the simulated DO, it was revealed that a decrease of 25% BOD effluent results in an increase of 8% average DO across the study stretch. Similarly, during the investigation process, 11.5% of average DO increase for a 50% reduction in BOD effluent and 15% of average DO increase for a 75% drop in BOD effluent.

5 Conclusions

The following conclusions can be drawn from the preceding research:

(i) The QUAL2K model was used to simulate temperature, nitrate, pH, and DO parameters for the Bhadra River stretch, and the model's calibration and validation for a period of 24 months were successfully completed.

(ii) The model performance was evaluated using statistical error parameters, i.e., RMSE, MBE, and R^2. It has been observed that the RMSE for Nitrate and pH
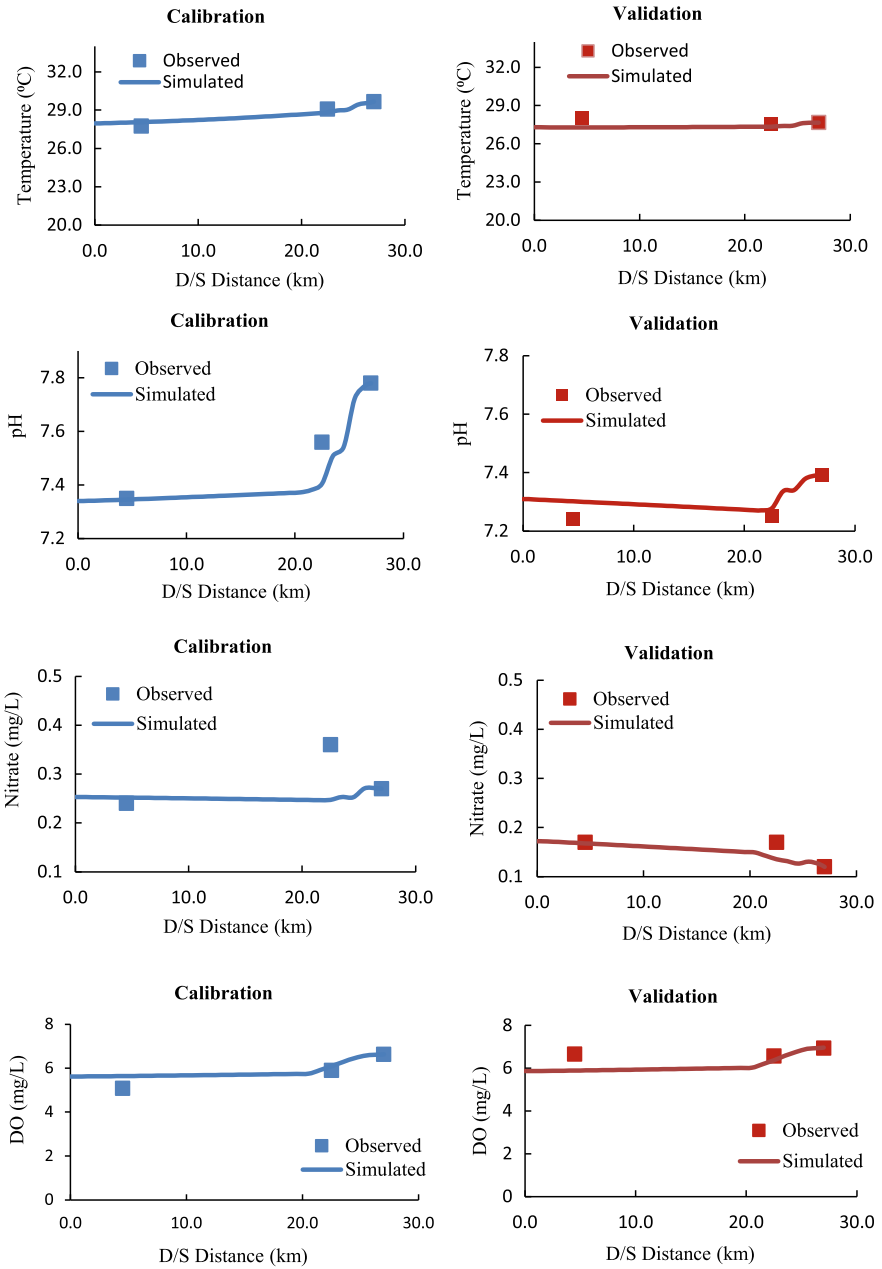
Fig. 6 Calibration and validation results of temperature, pH, nitrate, and dissolved oxygen

Table 2 Calibration parameters for the Bhadra River stretch water quality modeling

Parameters	Units	Values		
		Reach 1	Reach 2	Reach 3
ISS settling velocity	m/day	0.35	0.35	0.35
Fast CBOD oxidation rate	/day	0.1260	0.1360	0.01260
Organic N hydrolysis rate	/day	1.5300	1.5800	1.2500
Organic N settling velocity	m/day	0.6500	0.6600	1.9600
Ammonium nitrification	/day	0.3256	0.1530	0.0921
Nitrate denitrification rate	m/day	1.9000	0.9213	0.1950
Sed- denitrification transfer coefficient	m/day	3.1410	2.0000	1.0350

Table 3 Root mean square error (RMSE), Mean bias error (MBE), and R^2 for the simulated and observed water quality parameters; (C—Calibration and V—Validation)

Parameters	RMSE		MBE		R^2	
	C	V	C	V	C	V
Temperature	0.23	0.42	−0.02	0.29	0.87	0.56
DO	0.34	0.47	−0.25	0.32	0.50	0.12
Nitrate	0.06	0.02	0.03	0.01	0.11	0.90
pH	0.08	0.03	0.05	−0.03	0.62	0.64

Fig. 7 Variation of DO for different pollution scenarios of BOD loads
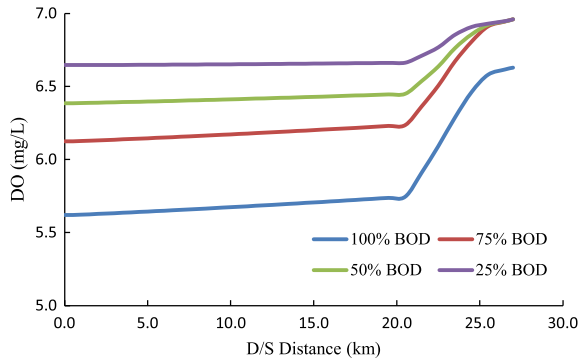
parameters is very satisfactory, while for temperature and DO parameters is good.

(iii) The results revealed that the Bhadra river stretch was highly polluted due to effluents coming from the industries, mostly MPM and VISL present in the study stretch. There must be a reduction of 25% of BOD effluent to reach the minimum standards set by the CPCB.

(iv) Under diverse contamination scenarios, the validated QUAL2K river water quality model is successfully employed to forecast DO. There is a 15% rise in

average DO throughout the study stretch due to a 75% drop in BOD effluent from point sources.

(v)   The water quality model, QUAL2K, was the most sensitive to BOD effluent load, rapid CBOD oxidation rate, and nitrification rate for modeling dissolved oxygen.

(vi) The QUAL2K can be used to successfully mimic various management scenarios with reduced trash loading, allowing the river's DO to be restored to levels above the permitted limit with minimal effort.

References

1. Mustafa A, Sulaiman S, Shahooth S (2017) Application of QUAL2K for water quality modeling and management in the lower reach of the Diyala river. Iraqi J Civil Eng 11:66–80
2. Bottino F, Ferraz IC, Mendiondo EM, do Carmo Calijuri M (2010) Calibration of QUAL2K model in Brazilian micro watershed: effects of the land use on water quality. Acta Limnologica Brasiliensia 22:474–485
3. Hossain MA, Sujaul IM, Nasly MA (2014) Application of QUAL2Kw for water quality modeling in the Tunggak River, Kuantan, Pahang, Malaysia. Res J Recent Sci 3:6–14
4. Park S, Lee YS (2002) A water quality modeling study of the Nakdong River, Korea. Ecol Model 152:65–75. https://doi.org/10.1016/S0304-3800(01)00489-6
5. Pelletier GJ, Chapra SC, Tao H (2006) QUAL2Kw—a framework for modeling water quality in streams and rivers using a genetic algorithm for calibration. Environ Model Softw 21:419–425
6. Chaudhary S, Dhanya CT, Kumar A, Shaik R (2019) Water quality-based environmental flow under plausible temperature and pollution scenarios. J Hydrol Eng 24:05019007. https://doi.org/10.1061/(ASCE)HE.1943-5584.0001780
7. Cox BA (2003) A review of currently available in-stream water-quality models and their applicability for simulating dissolved oxygen in lowland rivers. Sci Total Environ 314–316:335–377. https://doi.org/10.1016/S0048-9697(03)00063-9
8. Rehana S, Mujumdar PP (2011) River water quality response under hypothetical climate change scenarios in Tunga-Bhadra river, India. Hydrol Process 25:3373–3386. https://doi.org/10.1002/hyp.8057
9. Chapra, SC, Pelletier, GJ (2003) QUAL2K: a modeling framework for simulating river and stream water quality (beta version): documentation and user's manual. Civil and Environmental Engineering Department, Tufts University
10. Sumithra S, Narayana J (2003) Municipal and industrial waste characteristics and management in Bhadravathi City. In: Aquatic ecosystems. APH Publishing Corporation, New Delhi, India
11. CPCB (Central Pollution Control Board) (2011) Polluted river stretches in India: criteria and status. CPCB, Delhi, India

Environmental Impact Assessment of Water Resource Projects

Jitesh N. Vyas, Supriya Nath, Dudekula Nikhil Kumar, R. B. Deogade, and Prabhat Chandra

Abstract Environmental impact assessment (EIA) is a tool to ensure sustainable development by assessing the impact of activities or projects on the environment. The goal of an EIA is to anticipate and address any potential environmental issues that may occur as a result of the proposed development during the planning and design phase of the project. EIA is used to predict and suggest ways to reduce adverse impacts of the project for maximum social and economic benefit with minimum environmental impact due to the project. EIA plays a significant role in determining the sustainability of the proposed project and helps decision-makers accept or reject the proposed project based on the EIA report. In this paper, EIAs conducted on various water resource projects across India in recent years were studied. The methodology followed for the EIA study in India has been discussed, and the findings of various projects were analysed by comparing them with the guidelines by MoEF. The reports on water resource projects were reviewed, and the findings have been discussed in the context of physicochemical analysis and biological parameters.

Keywords Sustainable development · Environmental impact · EIA methodology · Physicochemical analysis · Biological parameter

J. N. Vyas (✉) · S. Nath · D. N. Kumar · R. B. Deogade · P. Chandra
Central Water and Power Research Station, Ministry of Jal Shakti, Government of India, Pune 411024, India
e-mail: jiteshvyas33@gmail.com

D. N. Kumar
e-mail: nikhil.dk@cwprs.gov.in

R. B. Deogade
e-mail: deogade_rb@cwprs.gov.in

1   Introduction

Environmental impact assessment (EIA) is a systematic scrutiny of all environmental impacts caused due to any developmental projects. It helps decision-makers to anticipate probable consequences of the project on the environment [1]. EIA is a preventative, participatory, and methodical process that relies on multidisciplinary contributions from experts of various fields. The process involves assessing the current situation of the environment where the project will be conducted and predicting the potential consequences of the project in the future. The purpose of an EIA is to identify and evaluate the environmental and social impacts of any planned major activity before it is executed. It provides both environmental and economic benefits as it helps in the reduction of cost and time of project completion by avoiding treatment expenses and costs that may have been incurred to meet the environmental laws and regulations.

In India, EIA was introduced in 1994 by the Ministry of Environment and Forests (MoEF) through a notification under the Environmental Protection Act (EPA) 1986. In 1994, EIA became mandatory for 29 highly polluting activities (project, plan, program, or policy). In 2006, 32 new activities were added to the list of requirements in the Environmental impact Assessment notification (2006) [2].

1.1   Objectives of EIA

The objective of an EIA is to predict the possible environmental problems that will arise as a result of the intended project and to resolve them during the planning and design stages. The ultimate goal is to achieve or sustain environmental protection and sustainable development, as well as propose ways to mitigate adverse impacts [2]. It allows us to carry out an Environmental Cost–Benefit Analysis of projects at an early stage. The study enables us to recognize the legislative measures that need to be taken and the role that concerned agencies should assume to ensure a more efficient environmental management process. As a result, it is easier to identify types and extents of impacts and how to minimize them through good engineering practices [1]. An EIA therefore is a systematic procedure that helps identify and mitigate impacts on individuals or society in consultation with those affected. For impacts that cannot be reduced during the planning stage, efforts are made to mitigate those impacts [1].

1.2 EIA Has Two Roles [3]

1. The legal role of EIA is to ensure that development projects have minimal environmental impacts throughout their 'lifecycle', i.e., during planning, construction, use, maintenance, and demolition.
2. The educational role–EIA is instrumental in educating everyone concerned about the probable environmental impacts of the project.

2 Methodology of EIA in Water Resource Projects

During the EIA process, a preliminary screening is undertaken to make sure that the time and resources are allocated to proposals that are of concern. The EIA process consists of eight steps that have varying significance while evaluating the overall impact of the project. In the end, there is a post-monitoring of the project to ensure that the decisions and actions taken in accordance with the EIA report are implemented. The MoEF introduced the current EIA notification on 14th September 2006.

The EIA process is divided into eight parts (as illustrated in Fig. 1):

1. **Screening**: The first stage primarily identifies projects that require assessment of State Environment Impact Assessment Authority (SEIAA) and those that do not. EIAs are conducted in two stages, the first to determine if a project requires an EIA and second to determine the level of assessment required.
2. **Scoping**: This stage identifies and summarizes the key impacts and issues that should be further examined, as well as the scope and limitation of the investigation. It also specifies the various aspects of the assessment that must be examined in the EIA report.
3. **Impact analysis**: In this stage of the EIA, the environmental impact and social implications are identified and predicted, and significance is evaluated.
4. **Mitigation**: This part of the EIA process suggests steps to mitigate and minimize the potential negative environmental effects of development activities.
5. **Reporting**: This stage provides the EIA results to the decision-making body and other interested parties in the form of a report.
6. **Review of EIA**: It assesses the adequacy and efficacy of the EIA report and provides decision-making information.
7. **Decision-making**: It determines if the proposal should be rejected, authorized, or modified further.
8. **Post monitoring**: After the project has been approved, this stage begins. It verifies that the project's consequences do not exceed regulatory limits and that mitigation measures are implemented in accordance with the EIA report's recommendations.

Public Consultation: This step of the EIA process has two components: a public hearing process in which only local residents affected by the project are allowed to speak, and a method for collecting written comments from other concerned citizens.
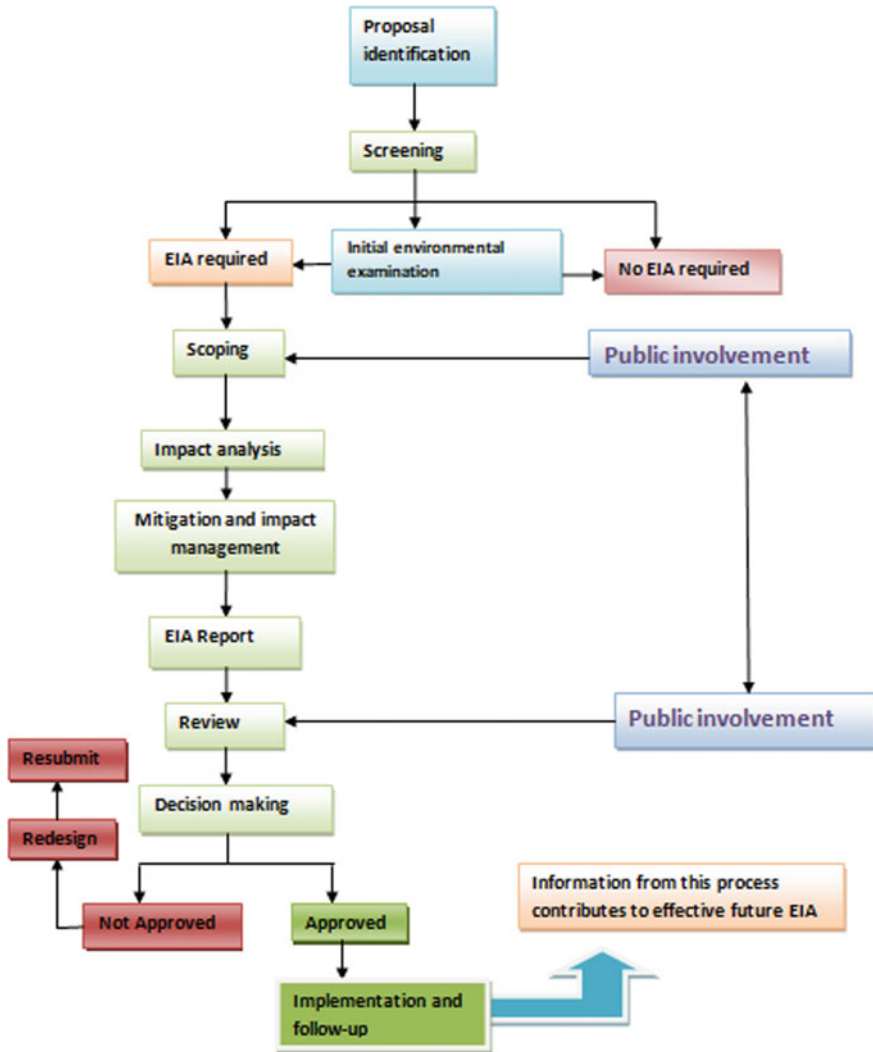
Fig. 1 Steps involved in environmental impact assessment (EIA) process

3 Results and Analysis

3.1 Physicochemical Analysis for EIA in Water Resource Projects in India

The physicochemical analysis to determine the baseline status was conducted for various parameters by different agencies for EIA on several marine projects. Selected

projects were studied, and some of them were compared with BIS Standards or CPCB Standards. The result of this comparison has been provided in Table 1. Most of the parameters showed complete compliance; however, few of them showed deviation towards the higher end. Dissolved oxygen (DO) was slightly less, and total suspended solids (TSS) were found higher than permissible limits at Ennore SEZ and NCTPS Stage III Thermal Power Projects. Dissolved oxygen was slightly less, and pH and TSS were more than acceptable limits at Construction of Groyne at Periyathalai. Ions like sulphate, chloride, and calcium were more than acceptable limits at Beach Resort Project, Sindhudurg, Maharashtra. Conductivity and Iron were greater than the permissible limits at the Indian Coast Guard, West Bengal. Biological oxygen demand (BOD), TSS, Iron (Fe), Copper (Cu), zinc (Zn), and lead (Pb) were higher than permissible limits at Kutchh Power Generation Limited during Post-monsoon, while TSS, Fe, Cu, Zn, and Pb were found higher than permissible during Pre-monsoon.

The physicochemical analysis to determine the baseline status was conducted for various parameters by different agencies for EIA on several projects on various rivers of India, and three of them were compared with BIS Standards or CPCB Standards. The result of this comparison has been given in Table 2. Most of the parameters showed complete compliance; however, few of them showed deviation towards the higher end compared to BIS Standard/CPCB Standards. BOD, total hardness, TSS, and iron were greater than permissible limits at Ganga River [9]. DO was lesser, while BOD and total hardness were greater than acceptable limits at the Cauvery river [10]. Conductivity, sulphate, fluoride, chloride, and calcium were greater than acceptable limits at River Adyar during pre-monsoon, while during post-monsoon conductivity, nitrate, chloride, and calcium were greater than permissible limits. These deviations found in the baseline studies indicate that some of the parameters did not meet the standards even before the project was started. It may be due to any previous contaminant present in those sites or any other anthropogenic disturbance associated with any former work on those sites in these rivers.

3.2 Biological Analysis for EIA in Water Resource Projects in India

The biological analysis to determine the baseline status was conducted for various parameters by different agencies for EIA on several marine projects was studied. The result of this comparison has been given in Table 3. The agencies studied the biological parameters like total viable counts (TVC), total coliforms, primary productivity (PP), Chlorophyll 'a', Phytoplanktons, Zooplankton, Benthic Community (Macrobenthos), fisheries, flora, and fauna. They found biodiverse and ecologically productive regions in these water project areas. However, they did not find any endangered species or vulnerable groups which would negatively impact ecology significantly. Only the Indian Coast Guard at West Bengal needs to consider the mangrove species which were found to be abundant (17 species) at the proposed site

Table 1 Physicochemical analysis for EIA in water resource projects (marine) in India

Parameters	BIS Standard/CPCB Standards	Ennore SEZ and NCTPS Stage III Thermal Power Projects [4]	Construction of Groyne at Periyathalai[5]	Beach Resort Project, Sindhudurg[6]	Indian Coast Guard, West Bengal [7]	Kutchh Power Generation Limited [8]	
						Post monsoon	Pre monsoon
pH	6.5–8.5	8.0 to 8.2	8.3–8.6	7.89	7.79–8.4	7–7.15	7.35–7.92
Conductivity	< 2000 μmhos/cm	NA	NA	NA	2067–17,440 μS/cm	NA	NA
Turbidity	<50 NTU	7.6–21 NTU	4.6–8.6 NTU	NA	NA	NA	NA
Temperature (°C)	NA	29.1–37.2	25.0–27.5	30.5	31.2–32.6	28.2–28.6C	30–31
Salinity	NA	34–36‰	34–40 psu	37,000	NA	34–41‰	33.71–40.94
Dissolved Oxygen (DO)	> 6 mg/l	4.837–5.816 mg/l	3.8–5.2 mg/l	NA	NA		6.8–7.9 mg/l
BOD	< 5 mg/l(<2 mg/l desirable)	0.288–1.056 mg/l	0.524–0.86 mg/l	NA	NA	14.4–20 mg/l	0.2–2 mg/l
Total Hardness as $CaCO_3$	< 50 mg/l	NA	NA	6750 mg/l	1200–5800 mg/l	NA	NA
Total Alkalinity	< 200 mg/l	NA	NA	200 mg/l	NA	NA	NA
Total Suspended Solids	< 50 mg/l	57.6–112.8 mg/l	46.4–97.2 ppm	NA	NA	38–110 mg/l	1304–2378 mg/l

(continued)

Table 1 (continued)

Parameters	BIS Standard/CPCB Standards	Ennore SEZ and NCTPS Stage III Thermal Power Projects [4]	Construction of Groyne at Periyathalai[5]	Beach Resort Project, Sindhudurg[6]	Indian Coast Guard, West Bengal [7]	Kutchh Power Generation Limited [8]	
						Post monsoon	Pre monsoon
Sulphate as SO_4^{2-}	< 200 mg/l	NA	NA	**3976 mg/l**	18.4–29.6 mg/l	17.3–19.6 mg/l	0.8–3.2 mg/l
Nitrate as NO_3^-	< 50 mg/l	5.128–9.602 μmol/l	7.0–8.7 μmol/l	1.18 mg/l	19–29 mg/l	NA	NA
Nitrite as NO_2^-	NA	0.575–0.900 μmol/l	0.056–0.245 μmol/l	NA	0.18–0.41 mg/l	NA	NA
Ammonia	< 1 mg/l	0.003–0.158 μmol/l	0.017–0.091 μmol/l	NA	NA	2.8–14 mg/l	2.8–16.8 mg/l
Total Nitrogen	NA	12.127–15.398 μmol/l	NA	10.24 mg/l	NA	NA	NA
Fluoride as F^-	< 1.5 mg/l	NA	NA	2.56 mg/l	NA	NA	NA
Chloride as Cl^-	< 250 mg/l	NA	NA	**22,000 mg/l**	NA	NA	NA
Inorganic Phosphate as PO_4^{2-}	< 1 mg/l	0.227 to 0.868 μmol/l	NA	NA	0.12–1.32 mg/l	BDL	BDL
Total Phosphorous	NA	0.869–1.784 μmol/l	2.05–3.65 μmol/l	0.34 mg/l	NA	NA	NA
Sodium as Na^+	NA	NA	NA	9000 mg/l	NA	NA	NA

(continued)

Table 1 (continued)

Parameters	BIS Standard/CPCB Standards	Ennore SEZ and NCTPS Stage III Thermal Power Projects [4]	Construction of Groyne at Periyathalai[5]	Beach Resort Project, Sindhudurg[6]	Indian Coast Guard, West Bengal [7]	Kutchh Power Generation Limited [8]	
						Post monsoon	Pre monsoon
Potassium as K^+	NA	NA	NA	248.6 mg/l	NA	NA	NA
Calcium as Ca^{2+}	< 75 mg/l	NA	NA	**720 mg/l**	240.48–360.72 mg/l	NA	NA
Magnesium as Mg^{2+}	NA	NA	NA	1208.32 mg/l	145.8–1190.7 mg/l	NA	NA
Iron	< 0.5 mg/l	33.534 - 80.12 µg/l	NA	NA	**2.028–9.324 mg/l**	**64.28–285.72 mg/l**	**2.85–277.14 mg/l**
Copper	< 1 mg/l	3.140 to 6.515 µg/l	NA	NA	NA	**5.5–19 mg/l**	**4–17.5 mg/l**
Cadmium as Cd	< 0.005 mg/l	0.558 to 3.925 µg/l	NA	BDL	NA	**0.17–1.25 mg/l**	**0.17–0.89 mg/l**
Zinc	< 5 mg/l	22.310–34.652 µg/	NA	NA	NA	**3.71–9.71 mg/l**	**1.14–8.28 mg/l**
Lead as Pb	< 0.05 mg/l	1.985–4.120 µg/	NA	BDL	NA	**6.66–46.66 mg/l**	**6.66–53.33 mg/l**
Remarks		DO was slightly less and TSS was found higher than permissible limits	DO was slightly less and pH, TSS were found higher than permissible limits	SO_4^{2-}, Cl^- and Ca^{2+} were found higher than permissible limits	Conductivity and Iron were found higher than permissible limits	BOD, TSS, Fe, Cu, Zn, Pb were found higher than permissible limits	TSS, Fe, Cu, Zn, and Pb were found higher than permissible limits

Bold values indicate these values do not meet the BIS Standard/CPCB Standards

Table 2 Physicochemical analysis for EIA in water resource projects on rivers in India

Parameters	BIS Standard/CPCB Standards	Ganga River [9]	Cauvery River [10]	River Adyar[11]	
				Pre-monsoon	Post-monsoon
pH	6.5–8.5	7.31–7.65	7.12–7.81	5.95–6.73	**7.48–8.96**
Conductivity	< 2000 μmhos/cm	NA	404–1223.33	**1679.69–5120.31**	**656.25–13,759.38**
Dissolved oxygen (DO)	> 6 mg/l	6.4–7.9	**3.6–6.89**	NA	NA
BOD	< 5 mg/l(<2 mg/l desirable)	**2.1–12.9**	**2.92–13.8**	NA	NA
Total hardness as $CaCO_3$	< 50 mg/l	88.32–213.4	**119.33–322.93**	NA	NA
Total alkalinity	< 200 mg/l	99.4–187.2	110–159.01	NA	NA
Total suspended solids	< 50 mg/l	**157–1279**	NA	NA	NA
Sulphate as SO_4^{2-}	< 200 mg/l	1.71–56.9	NA	**204–292**	32.42–272
Nitrate as NO_3^-	< 50 mg/l	2.7–12.6	NA	4.21–45.93	**1.02–75.91**
Nitrite as NO_2^-	NA	NA	NA	0.01–1.07	0.09–3.61
Total nitrogen	NA	NA	0.012–0.123	NA	NA
Fluoride as F^-	< 1.5 mg/l	< 0.1	NA	**0.48–2.03**	0.15–0.91
Chloride as Cl^-	< 250 mg/l	15.83–42.2	NA	**110–1210**	**150–3470**
Inorganic phosphate as PO_4^{2-}	< 1 mg/l	NA	NA	0.24–4.67	0–0.13
Total phosphorous	NA	NA	0.002–0.03	NA	NA
Sodium as Na^+	NA	NA	NA	136.3–795	31.82–1120
Potassium as K^+	NA	NA	NA	0–44.17	0–64.8
Calcium as Ca^{2+}	<75 mg/l	23.04–49.66	NA	**56–208**	**48–424**
Magnesium as Mg^{2+}	NA	3.68–21.42	NA	16.4–120.6	12–686

(continued)

Table 2 (continued)

Parameters	BIS Standard/CPCB Standards	Ganga River [9]	Cauvery River [10]	River Adyar[11] Pre-monsoon	Post-monsoon
Iron	< 0.5 mg/l	**1.69–4.12**	NA	NA	NA
Zinc	< 5 mg/l	0.01–2.7	NA	NA	NA
Remarks		BOD, Total Hardness, TSS and Iron are greater than permissible limits	DO is lesser while BOD, Total Hardness are greater than permissible limits	Conductivity, SO_4^{2-}, F^-, Cl^- and Ca^{2+} are greater than permissible limits	Conductivity, NO_3^-, Cl^- and Ca^{2+} are greater than permissible limits

Bold values indicate these values do not meet the BIS Standard/CPCB Standards

while designing the project to minimize the adverse impact on the mangroves. Project Report for Indian Coast Guard evaluated and found that 6 species of amphibians and 11 species of reptiles were recorded from the study area in which eight species were in Schedule II category, and the rests were in schedule IV category. In the case of the International Union for Conservation of Nature (IUCN) status, only one species Ophiophagus Hannah was under the threatened category [7].

3.3 Impact Analysis on Water Quality of Marine EIA Projects

The EIA for the Ennore SEZ and NCTPS Stage III Thermal Power Projects found that the project had a minor or insignificant impact on temperature and salinity [4].

According to the EIA studies for the construction of a Groyne at Periyathalai, the installation of a Groyne could have temporary localized effects on ambient water quality near the construction regions. Effects on water quality that are expected during and immediately after the building of a Groyne may also have short-term consequences [5].

According to an EIA conducted for the Beach Resort Project in Sindhudurg in 2015, improperly managed surface runoff, oil, and waste spills inside the premises, as well as improper debris disposal and sewage discharge, could have a significant short-term negative impact on the water quality of nearby seawater. The report also states that the proposed project will have no impact on the area's water quality because it has committed not to discharge any effluents outside of the developed area and has ensured zero effluent discharge by fully utilizing treated effluent on-site through landscaping and flushing [6].

Project Report for Indian Coast Guard evaluated potential adverse and beneficial impacts due to contamination and overuse of water resources which are proposed to be managed by effective water management strategies during the construction stage. For long-term water management, suggestions like rainwater harvesting were suggested for optimum utilization of rainwater and also to recharge the groundwater level. They suggested that the pipeline for the collection of sewage should be properly sealed to avoid the leakage of wastewater of sewage that may contribute to contamination of the groundwater quality of the locality. Groundwater quality was proposed to be periodically monitored [7].

According to the Marine EIA Report of Kutchh Power Generation Limited, no discharge of liquid waste to other public borders is planned for the proposed power station because the majority of wastewater generated by the facility, such as demineralization, is treated before being discharged. The plant's effluent would be processed at a wastewater treatment plant before being recycled for plant usage and green belt development [8].

Table 3 Biological analysis for EIA in water resource projects (marine) in India

Parameters	Ennore SEZ and NCTPS Stage III Thermal Power Projects [4]	Construction of Groyne at Periyathalai [5]	Beach Resort Project, Sindhudurg [6]	Indian Coast Guard, West Bengal [7]	Kutchh Power Generation Limited [8]	
					Post monsoon	Premonsoon
Total viable counts (TVC)	NA	7 to 11×10^2	NA	NA	NA	NA
Total coliforms	NA	12 and 20×10^5	NA	NA	NA	NA
Primary productivity (PP)	10.08 to 22.64 (mgC/m³/hr)	NA	NA	NA	0.36–0.96 mg/m³	0.01–0.03 mg/m³
Chlorophyll 'a'	0.120 to 0.260 mg/m³	0.175 to 0.351 mg/m³	NA	NA	NA	NA
Phytoplanktons	703–3398 sp	Density of phytoplankton varied from $4,228$ to $6,264$cells/l	NA	19 sp.	11–32 sp.	8-23 sp
Zooplankton	NA	$3,445$–$5,405$ nos/m³	NA	33 sp.	$83.88 \times 10^3/100$ m³ to $141.59 \times 103/100$ m³	NA
Benthic Community (Macrobenthos)	425–525 No./m²	275–1150 Nos/m²	NA	NA	65–988 No./m²	NA
Fisheries	NA	NA	Nil	75 fish species	22 groups	NA
Flora	NA	NA	45 sp.	**17 mangrove species**	NA	NA
Fauna	NA	NA	56 birds, 10 reptiles,	45 species of birds, 11 species of mammals, 6 species of amphibians and 11 species of reptiles	NA	NA

3.4 Impact on Biological Environment by Marine EIA Projects

The area is devoid of mangrove vegetation, seaweeds, and coral reefs, according to the EIA report for the Ennore SEZ and NCTPS Stage III Thermal Power Projects, and no uncommon, endangered, or vulnerable marine species were found during the maritime survey. The planned project's output would have no effect on the quality of the current natural coastal environment [4].

Most larval fish could be negatively affected if turbidity levels rise sufficiently, and there is a chance of a decline in the benthic population during the building phase, according to EIA studies for the construction of Groyne at Periyathalai. But it also stated that the effects of the building will only be temporary. Invertebrates, young/larval fish, and birds would have a new habitat type as rocky, hard bottom material would take the place of these ecosystems that would be lost [5].

According to the Beach Resort Project, Sindhudurg, dumping wastewater into surface water bodies would have a minor negative impact on flora and fauna. This could be avoided by taking proper precautions during the construction and operation phases to prevent any disruption to the local ecology, and by incorporating the existing trees in the green belt development [6].

Project Report for Indian Coast Guard found that the initial disturbances to benthic organisms would cause death at the dredging site, but they would regenerate after completion of capital dredging [7].

Marine EIA Report of Kutchh Power Generation Limited reported that there would not be an effect on marine reptiles and mammals due to construction activities as they migrate temporarily from such sites. It also mentioned that the area does not sustain corals although fringing corals occur in patches that were at least 25–30 km away from the proposed site. The nature of circulation in the Gulf would not affect these corals [8].

4 Conclusions

In this paper, the reports on water resource projects were reviewed and found that most of the parameters showed compliance to the set standards for physicochemical analysis for EIA in water resource projects (marine) as well as water resource projects on rivers in India, but few of them showed deviation in some of the parameters which indicate the presence of previous contaminants in those sites or any other anthropogenic disturbance associated with any former work on those sites. The biological parameters were also studied that were reported in EIA in water resource projects (marine) in India as part of the baseline study. None of them mentioned any endangered species or corals present in these sites except the Indian Coast Guard at West Bengal had abundant mangrove species. The impacts predicted by various reports on water quality and the biological environment by EIA conducted on marine projects

have been discussed. Most of them found that the impacts could be minimized by the adoption of proper mitigation measures.

References

1. Pandey KM, Ajoy D, Hirakjyoti D, Amitava R, Writuparna N (2013) Environmental impact assessment and management: protecting ecology in North-East India. J Environ Res Dev 7:1459
2. Agrawal DK, Lodhi MS, Panwar S (2010) Are EIA studies sufficient for projected hydropower development in the Indian Himalayan region? Curr Sci, 154–161
3. EPA W (2008) Environmental impact assessment (EIA). Environ Sci Stud Companion, 375
4. WAPCOS Limited (TANGEDCO) (2014) Comprehensive Marine EIA Study for Outfall of the proposed Ennore SEZ and NCTPS Stage III Thermal Power Projects of the NCTPS Complex. https://coastalresourcecentre.files.wordpress.com/2014/11/comprehensive-marine-report-of-nctps.pdf
5. WAPCOS Centre for Environment (2014) EIA Studies for Construction of Groyne at Periyathalai, Tiruchendur Taluk, Thoothukudi District, Water Resources Organisation, Public Works Department, Government of Tamil Nadu. http://environmentclearance.nic.in/writereaddata/online/RiskAssessment/03072015U75Z1TSRRiskAssessmentandDMP.pdf
6. SENES Consultants India Pvt. Ltd (2015) Environmental impact assessment study for "Beach Resort Project" At Sagartirath Village, Dist. Sindhudurg, Maharashtra. http://environmentclearance.nic.in/writereaddata/EIA/07082015N3HKPSNAEIAEMPReport.pdf
7. Centre for Envotech and Management Consultancy Pvt. Ltd (2017) EIA Report for CRZ clearance for proposed defence projects under Indian Coast Guard Station, for Indian Coast Guard Frazerganj, District- South 24 Parganas, West Bengal. http://www.environmentclearance.nic.in/writereaddata/FormB/EC/FORM_1/02092017KMXFGDOSNewForm-I.pdf
8. Cholamandalam MS Risk Services Limited (2013) Marine EIA study for seawater intake and marine outfall of 5×660 MW coal based thermal power plant Village Bhadreswar, Taluka Mundra, Kutch Submitted to Kutchh Power Generation Limited. https://fdocuments.in/document/marine-eia-study-for-seawater-intake-and-marine-outfall-of-marine-eia-study.html?page=1
9. Sen and Lall Consultants Pvt. Ltd (2013) Environmental Impact Assessment Study for proposed river front development of 20 Ghats along river Ganga in Patna, Bihar. https://nmcg.nic.in/writereaddata/fileupload/27_FinalEnvironmentImpactAssessment%20Patna_RFD.pdf
10. Venkatachalapathy R, Karthikeyan P (2012) Environmental impact assessment of Cauvery river with diatoms at Bhavani, Tamil Nadu, India. Int J Geol Earth Environ Sci 2:36–42
11. Venugopal T, Giridharan L, Jayaprakash M, Periakali P (2009) Environmental impact assessment and seasonal variation study of the groundwater in the vicinity of River Adyar, Chennai, India. Environ Monit Assess 149:81–97

Advanced Sensor for Arsenic and Fluoride Detection

Shivani Pandey, Satanand Mishra, Vijay Kumar Dwivedi, Tanmay Sardar, Archana Singh, and Hari Narayan Bhargav

Abstract Arsenic and Fluoride on the top of hazardous contaminants in water that has been exposed to root substantial effects in individuals through drinking water. It affects more than 200 million individuals spread over 50 countries and could enter the human body through the absorption of nutrient, drinking water system, inhalation, and dermic interaction. To ensure safety, it is critical not only to detect but also precisely quantify aqueous Arsenic and Fluoride. The urgent need is to develop a smart water quality testing systems that are capable of collecting real-time geolocated water quality data without the requirement for professional experience using. Synthesized nanoparticles and carbon quantum dots materials for a fluorometric detection and quick quantification of Arsenic and Fluoride in drinking water. The quantum dots mechanism has been completely defined, and the sensing mechanism has been systematically implemented. FTIR and XPS techniques are used for specific functional group determination and TEM for morphological and structural detection. Developed materials are extremely selective for Arsenic and Fluoride both, based on functional group selectivity. Synthetic Arsenic and Fluoride standards and water samples from impacted regions were used to test the sensing material's consistency in performance. The proposed sensor detects Arsenic and Fluoride in common applications for non-expert users, especially in rural locations. The Artificial Intelligence is used for water quality monitoring.

S. Pandey · S. Mishra (✉) · A. Singh
Department of CARS & GM, AcSIR—CSIR-Advanced Materials and Processes Research Institute, Bhopal, Madhya Pradesh 462026, India
e-mail: snmishra07@gmail.com

V. K. Dwivedi
Department of Civil Engineering, National Institute of Technology Durgapur, Durgapur, India

T. Sardar
Mechanical Engineering Department, Motilal Nehru National Institute of Technology, Allahabad 211004, India

H. N. Bhargav
Department of Intelligent Materials and Advanced Processes, AcSIR—CSIR-Advanced Materials and Processes Research Institute,, Bhopal, Madhya Pradesh 462026, India

1 Introduction

Recently, the wellspring of fresh water supply is persistently lessening referable to groundwater decrease consumption, environmental consequences, helpless asset the executives, and ecological contamination. Also, the expanding pace of the total populace, ~80 million every year, brings developing interest for the source of water in quantity of 64 billion cubic meters yearly [1]. The significant toxins in water system consist of natural colors, radio-active metallic, weighty metallic, and oxyanions of metals (CrO_3^{2-} AsO_3^- SeO_4^{2-}, and so forth). Among the contaminations, the harmfulness of Arsenic oxyanions and Fluoride cations are intense and one of a kind begin into the water body system referable for normal wonders—due to regular sources of soil or through anthropogenetic root refer to cancer-causing. Resulting in utilization for Arsenic- and Fluoride-tainted consuming water has developed the significant well-being perils as of late. High grouping of (As) and Fluoride in drinking water may at first reason skin illness and ultimately go toward malignancy as well as very pinnacle of worry to public well-being [2]. The administrative offices all throughout the planet like (WHO) [3] US Environmental Protection Agency (USEPA) [4] Health Canada, and European Union (EU) [5] have drawn most extreme lines on Arsenic and Fluoride in consumption water up to 0.01 mg/L to guarantee protected utilization for Arsenic- and Fluoride-polluted consumption water to shield individuals as of illnesses.

In the direction to ensure the safe feeding of Arsenic- and Fluoride-contaminated drinking water and safeguard individuals since ailments, maximum limits on Arsenic in drinking water have been set at 0.01 mg/L and Fluoride have maximum limit of 1.5 mg/l. People from Bangladesh, West Bengal [6], and other parts of India [7], Cambodia [8], and Inner Mongolia of China El Salvador, Peru, China [9], Iran Kurdistan [10], Thailand, Eastern Croatia [11], Mexico [12], Nicaragua [13], northern Afghanistan, northern Mali, and Zambia in Africa [14], and Vietnam [13] are among the countries where people live. Arsenic and Fluoride poisoning is a serious threat [15]. Figure 1 shows different mechanism for Arsenic and Fluoride Detection like Adsorption, Coagulation, Oxidation, Ion-exchange, Membrane Filtration, and Electrocoagulation.

Numerous manageable and normally plentiful materials including waste rice husk [16] for example oxy-hydroxides, carboxylic and amine doped initiated carbon, and oxy-hydroxides, carboxylic and amine doped graphene oxide [17] what's more, enacted carbon [18] have been inspected as productive adsorbents for As and Fluoride based on functional group selectivity. As of late, some book materials including cellulose-based filaments [19], metal natural structure (MOF) [20], and hydrogel [21] have additionally been investigated. A few of these As expulsion materials and procedures have likewise been executed essentially in the influenced provincial
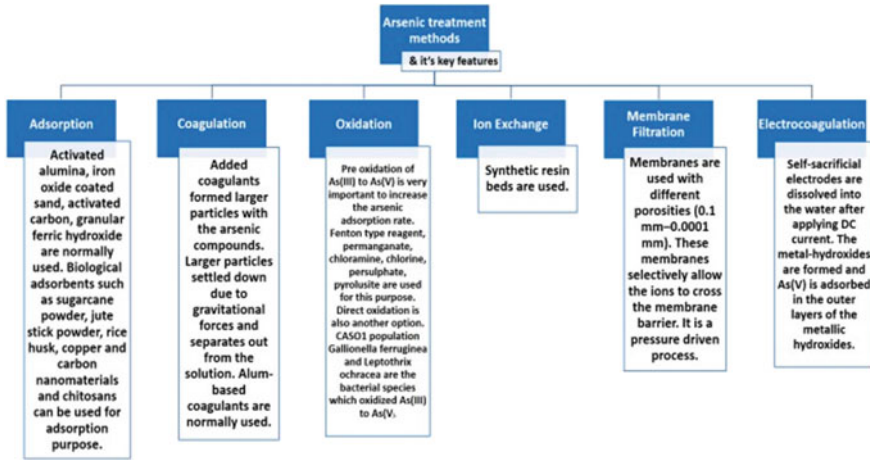
Fig. 1 Different mechanism for Arsenic and Fluoride Detection [32]

regions. The primary worry of the multitude of compelling cycles is mostly identified with cost, both beginning and functional, as the Arsenic and Fluoride issue is generally in creating or immature nations and regions. According to a World Bank report, low-paying countries (US$ 1025), lower-medium-paying countries (US$ 1026–4035), and upper-medium-paying countries (US$ 4036–12,475) are the most vulnerable and confronting difficulties for diminishing As and Fluoride beneath rule esteems because of their restricted financial limits. In this manner, there is a drive for ceaseless improvement in the current evacuation strategy just as presenting new advances. Table 1 shows advantage and disadvantage of different mechanism. Oxidation, Coagulation, Adsorption, Ion-exchange, membrane-filtration, and electrocoagulation are different mechanism with their removal efficiency, adsorption shows maximum removal efficiency.

In carbon dot synthesis method rice husk or other sources such as coffee beans are used as material. Microwave digestion system is used for synthesis. Fluorescence, wavelength, function group, reaction time, and reaction rate are detected by this method. Fluorescence, reaction time is short, response time is less, ultrasensitive, reliable, non-destructive, fast, simple, and reproducible are properties obtained by this method.

Effective parameters for sensors are basically divided into two parts: static and dynamic. Both characteristics are having certain parameters.

Table 1 Advantage and disadvantage of different mechanism

Arsenic removal technology	Advantages	Disadvantages	Removal Efficiency of As$^{(v)}$ (%)
Oxidation	– Low operating cost – Works over a wide pH range	– Very slow process – Drinking water has bad smell and color in addition of chlorine, permanganate, etc. – Sludge formation	>95
Coagulation	– It can be operated within a wide range of pH	– Pre-oxidation of arsenite required – High arsenic contaminated sludge production – Expensive process – Additional filtration required	>90
Adsorption	– Low cost – Ease of operation	– pH, effective surface area, and the nature of the adsorbent need to be maintained – Arsenite cannot be removed very well – Post-filtration required – Organic matter, other salts in water decreases the efficiency of the process – Removal of the generated heavy flocs are difficult	100
Ion exchange process	– pH independent process – Only efficient for the arsenite removal	– Only efficient for the arsenite removal -Expensive process – Low capacity – Sludge disposal problem – Resin needs to be replaced again and again	95
Electrocoagulation	– Less area requirement – Sustainable technology	– Sludge production – High investment cost – High energy consumption	>99

Table 1 (continued)

Arsenic removal technology	Advantages	Disadvantages	Removal Efficiency of As$^{(v)}$ (%)
Membrane Filtration	-Easy operational – Technique – High arsenate removal efficiency – No sludge production	– Membrane fouling – High investment cost	>99

2 Working Principle

The CQDs' surface functional groups improve their optical characteristics, targeting capabilities, and biocompatibility. The CQDs, like other QDs, have normal or down-converted PL. They might, however, show up-converted PL, which is useful in some applications like photodynamic therapy. The PL emission spectra of CQDs is approximately symmetrical in terms of wavelength. Dynamic quenching, static quenching, fluorescence resonance energy transfer (FRET), inner filter effect (IFE), and photoinduced electron transfer are the quenching mechanisms in CQDs. Analytical Methods (PET). An increase in temperature could boost the dynamic quenching impact in dynamic quenching [22]. Dynamic quenching is a quenching technique in which the excited state of CQDs returns to its ground state as a result of a collision between the CQDs and the quencher via charge transfer or energy transfer. Fluorescence quenching of CQDs at concentrations is ranging from 0.5 to 10 M and a LOD of 0.25 mM [23]. Figure 2 shows fluorescence quenching effect on CQD. CQD in absence of analyte emit emission and CQD in presence of the analytes shows fluorescence quenching.

To determine if the fluorescence quenching mechanism of CQDs is IFE, the fluorescence spectra should be corrected. The deviation of IFE is calculated using Eq. 1 as follows:

$$I_{\text{corr}}/I_{\text{absd}} = 10\left(A_{\text{ex}}x_1 + A_{\text{em}}y_1\right) \tag{1}$$

The absorbance (per cm) at the excitation and emission wavelengths, respectively, is denoted by A_{ex} and A_{em}. The optical path lengths of the excitation and emission beams are the parameters x_1 and y_1. Figure 3 shows sensor process flow diagram in which distilled water is used in cuvette through Bluetooth module via microcontroller and display through LCD.
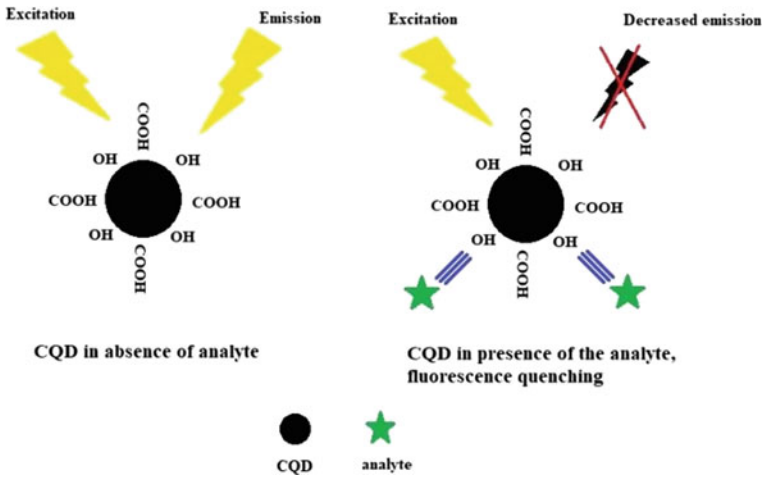
Fig. 2 Fluorescence quenching effect on CQD [33]

3 Methodology

The whole methodology is divided into three parts: material development, sensor development, and material and sensor connectivity.

3.1 Material Development

Besides, the easy surface variety of carbon quantum dots (CQDs) utilizing broad scope of basic practical gatherings (e.g., carboxyl, epoxy, and hydroxyl) has allowed agents for pairing of the ideal specific their surface receptors to overhauling or acclimate new objective selectivity [24] Their effortless and very much perceived blend techniques (counting pyrolysis, aqueous union, microwave amalgamation, and so on alongside cost-viability are likewise valuable for increase from a business point of view [25]. The essential detecting component for the utilization of CQDs as tactile tests depends on analyte-initiated extinguishing or upgraded fluorescence of an all-around extinguished CQD-quencher complex (through an electron/energy transport mechanism with an electron drawing out or tolerating analyte) [26].

The latest innovation of CQDs has greatly aided magnify the choice of sensing media toward the detection of heavy metals. To adapt the optical and surface properties of CQDs, surface functionalization, surface passivation, or atomic doping are normally favored to gain the preferred spectral properties for enriched or indiscriminate sensing features.

Material development is divided into two parts. First is preparation of rice husk carbon (RHC) in which rice husk powder (5 g) is made by washing rice husk with
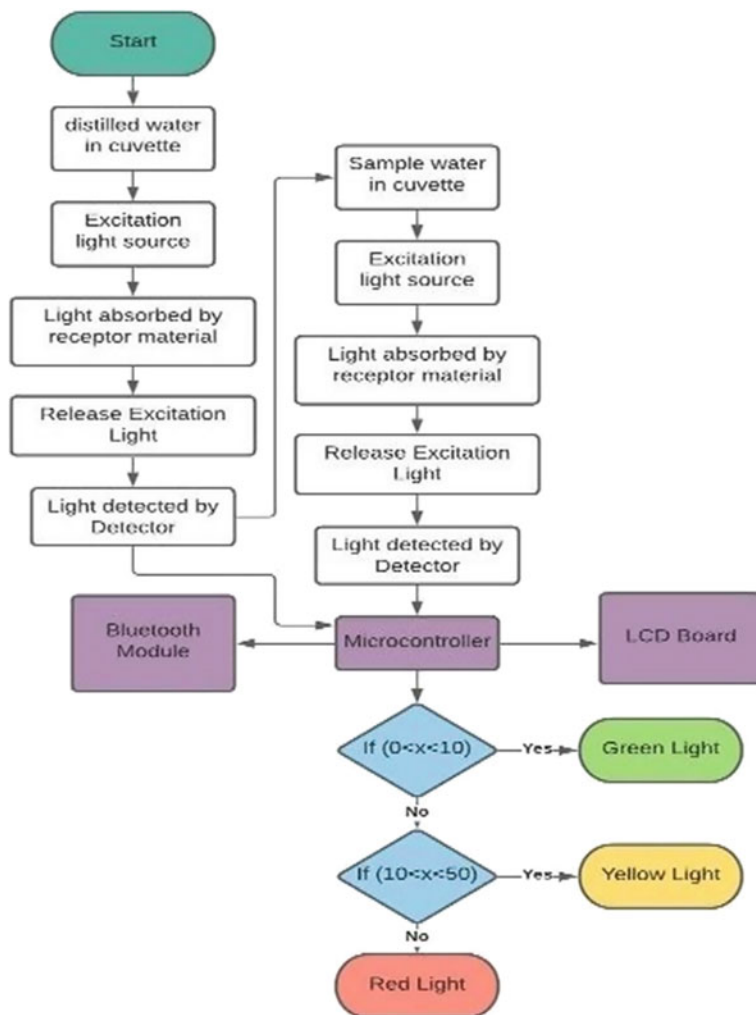
Fig. 3 Sensor process flow diagram

DI water then drying and meshing (100) then furnace heating in N2 atmosphere at 750 °C for two hours then obtained rice husk ash (RHA) treated with NaOH (99.9%) at 900 °C for N_2 atm as a result obtained rice husk carbon is washed with DI water then vacuum filtered and dried at 90 °C for 12 h. Figure 4 shows Synthesis of carbon quantum dots (CQD) the source material is rice husk ash which is converted into rice husk carbon via ultrasonicator treatment and vacuum filtration as a result CQD is obtained.

Second part is preparation of carbon quantum dots (CQDs) in which 50 mg rice husk carbon (RHC) mixed with 10 ml H_2SO_4 (98%) and 3 ml DI water after that

Fig. 4 Work flow of CQD synthesis
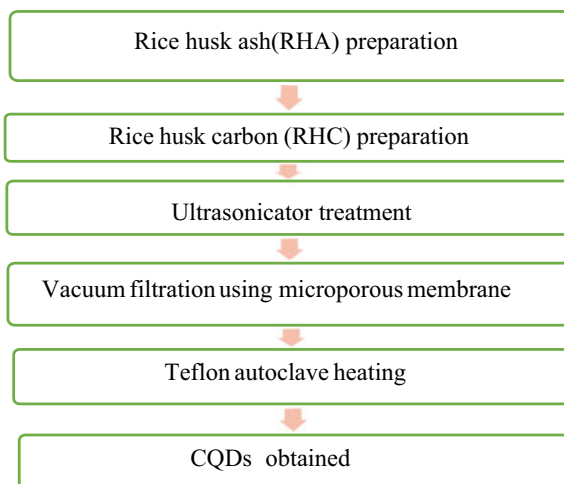
it is treated with ultrasonicator for 5 h. In this 20 ml HNO_3 (70%) is added after that ultrasonicated for 10 h then vacuum filtered using (0.22 μm) membrane. Then, this black sample obtained is treated with 30 ml DI water and pH 8 is maintained by 1 M NaOH solution. After that heated in 100 ml Teflon autoclave at 200 °C for 10 h. Then, vacuum filtration (0.22 μm) is done to obtain resultant rice husk derived CQDs.

Further treatment is required to store obtained CQD. Obtained CQDs are preserved in 100 ml ethanol solution. Then, 5 ml sample is taken with 45 ml DI water ultrasonicated for 5 h. After that centrifugation is done at 10,000 rpm for 30 min. So obtained small particles is collected from above part of vessel. Table 2 gives the summery of the CQD synthesis in which rice husk is used as raw material through conventional method, the effective parameters are fluorescence, functional group, reaction time, and reaction rate.

Table 2 Summery of CQD synthesis

| Measures	Explanations
Materials	Rice husk or (coffee beans, ashes or even waste, orange juice), eggshell membrane CA, L-cysteine, dextrin Lactose, HCl, glucose, H_3PO_4, BSA, urea, citric acid, and amine
Instrumentation	Microwave digestion system for C dot synthesis or by conventional method
Effective Parameters	Fluorescence, wavelength, functional group, reaction time, and reaction rate
Properties	Physical and optical properties, high quantum yields, good chemical stability coupled with the ability to tune their surface chemistry. Fluorescence, reaction time is short, response time is less, ultrasensitive, reliable, nondestructive, fast, simple, and reproducible
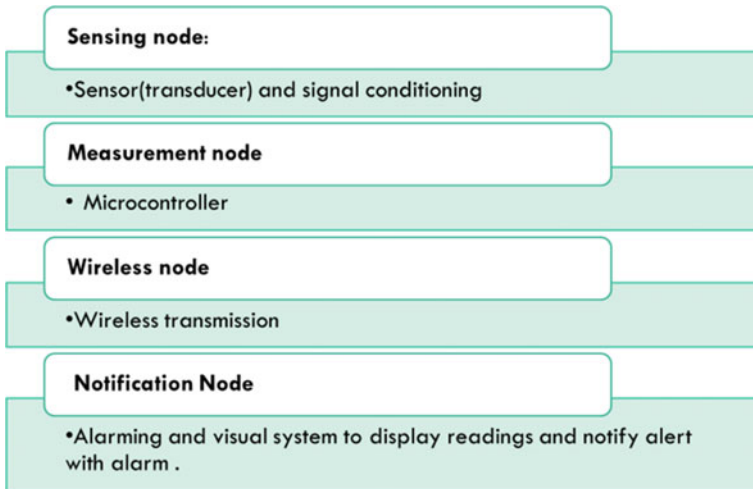
Fig. 5 Sensor module

3.2 Sensor Development

Sensor development is majorly divided into four main nodes. Sensing node mainly includes sensors and signal conditioning, measurement node includes microcontroller, wireless node includes wireless transmission and notification node includes alarming and visual system to display readings and notify alert with alarm. Figure 5 shows architecture of sensing module which consist of sensing node, measurement node, wireless node, notification node.

3.3 Material–Sensor Connectivity and Artificial Intelligence Monitoring

The goal of this is to develop AI-based algorithms based on observed correlated changes in many water-quality metrics such as free chlorine concentration, pH, alkalinity, and TOC in WDSs as a result of E. coli blending and diffusion. In reality, an AI algorithm properly trained on a system's standard conditions can detect departures from the typical conditions that are obvious enough to be considered anomalies [27]. In particular, allows for the integration of datasets obtained for each parameter via pattern recognition techniques based on Artificial Intelligence for automatic detection and correct visualization of Arsenic and Fluoride in WDS. Both characteristics are crucial. Both of these aspects improve water-quality conditions: False alarms are reduced by correctly recognizing the pollution cause as well as accurately predicting the contamination period associated with each conceivable pollution cause, even

when dealing with huge and complex WDS [28, 29]. As a result, the system's efficiency is improved, and public health threats are reduced in advance. The Support Vector Machines (SVMs) and the Artificial Neural Network (ANN) are examined and compared among the available supervised learning methods [30].The feasibility of early detection of Arsenic and Fluoride in drinking water distribution systems is demonstrated through the use of decay trend monitoring and data notified, and the accuracy of anomaly detection is demonstrated through the use of SVMs learning and ANN analysis, leading to the conclusion that demonstrated via the use of advanced pattern recognizer [31].

3.4 Overview of the System Architecture

Figure 6 shows the system architecture of the sensing systems. In the figure, different sensors are connected and interfaced with microcontroller. The signals are manipulated and optimized before sending to the microcontroller. The microcontroller sends the measured signals to the cyber world with different ways. The sensing system is powered with the powering node of the module.

4 Factors Affecting Sensitivity

Three factors are mainly responsible for affecting sensitivity. Chemical factors such as concentration, substrate-absorbing capacity, particle shape, solvent binding property effect sensitivity. Dimensional factors such as response time, structural dimension, intensity, area, and wavelength effect sensitivity. Properties such as thermal,
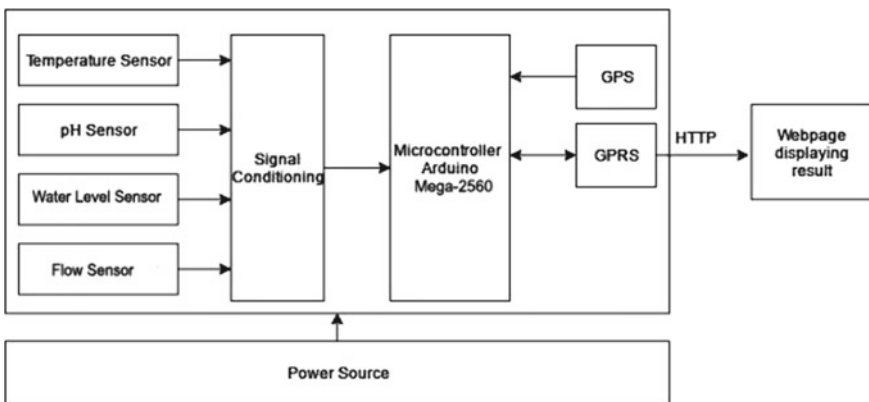

Fig. 6 System architecture [34]

Table 3 Different factors for sensitivity

Chemical Factors	Dimensional Factors	Other Properties
Concentration	Response time	Thermal
Solvent binding properties	Structural dimension	Optical
Chemical properties	Structural arrangement	Magnetic
substrate-absorbing capacity	Directional properties	Electrical properties
Particle shape	Drinking water monitoring	Electrochemical properties
	Intensity	
	Area	
	Wavelength	

Table 4 Sensor characteristics

Sensor characteristics	
Static	Dynamic
Accuracy	Dynamic error response
Distortion hysteresis	Instability and drift noise
Minimum detectable signal	Operating range
Nonlinearity	Repeatability
Selectivity/specificity	Step response
Sensitivity	
Threshold	

optical, magnetic, electrical and electrochemical effect sensitivity. Table 3 shows different factors for sensitivity chemical, dimensional, and other factors as well.

5 Sensor Characteristics

Effective parameters for sensors are basically divided into two parts: static and dynamic. Both characteristics parameters are described below. Table 4 shows sensor characteristics in which static and dynamic characteristics are shown.

6 Results and Discussions

In this study, we have done characterization of developed material for quantitative and qualitative analysis.
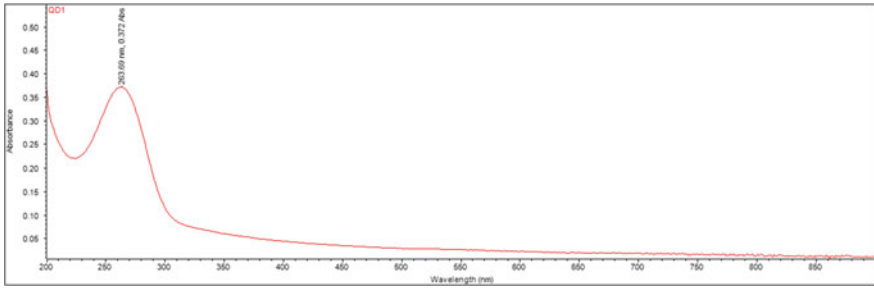
Fig. 7 UV—visible characterization for carbon quantum dots

6.1 UV—Visible Characterization

UV—visible characterization for carbon quantum dots is done. Figure 7 shows the observed peak on 263 nm for developed CQDs.

6.2 Transmission Electron Microscope (TEM)

TEM images of carbon dot derived from rice husk are given in Fig. 8a–c. TEM image of carbon quantum dots shows the presence of particle size in nano-range and their dispersion and fringe width and their type of structure.
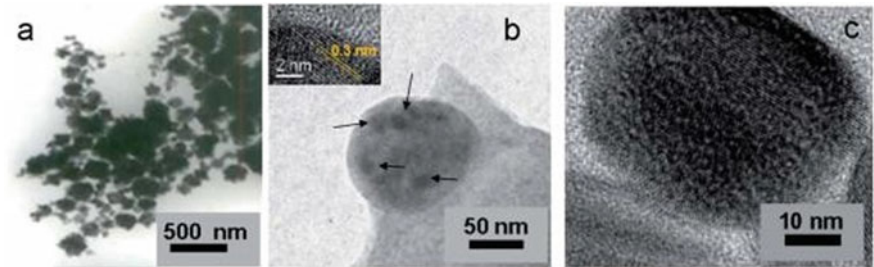

Fig. 8 **a** HRTEM of C-dots with porous structure with C-dots adsorbed onto them, **b** enlarged TEM image of selective C-dots embedded in particles with highlighted spots being carbon-dots adhered particles and the inset shows a HRTEM snapshot of a representative C-dot particle with a fringe width of 0.3 nm, **c** HRTEM of C-dots with porous structure with C-dots [35]
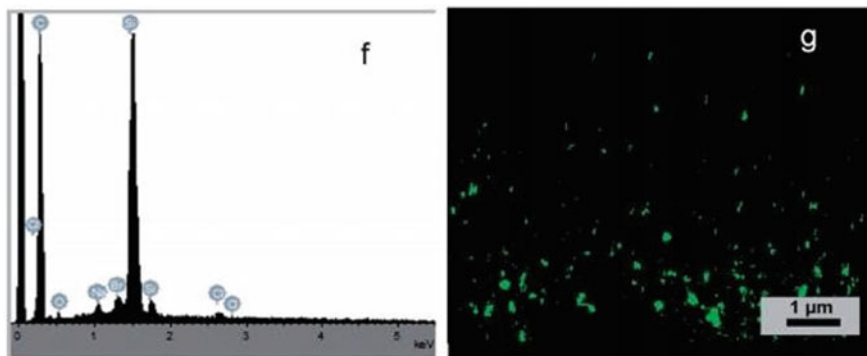
Fig. 9 Complex's EDAX depicts the key elemental composition and shows the fluorescent image of the complex [36]

Table 5 Elemental composition of CQDs

Element	Weight (%)	Atom (%)
C	56.14	68.49
O	21.96	11.46
H	21.9	20.05

6.3 Energy Dispersive X-Ray Analysis (EDAX)

Figure 9 shows the elemental composition of fluorescent carbon dots given by the EDAX. In Table 3, we have given the observed result of the EDAX analysis.

Table 5 shows elemental composition of CQD in which C, H, O.

7 Alarming System

Water level selection using Artificial Intelligence (AI) is done by using Artificial Neural Network (ANN) are examined and compared among the available supervised learning methods allows for the integration of datasets obtained for each parameter via automated identification and accurate visualization using AI-based pattern recognition algorithms for Arsenic and Fluoride in alarming zone. Figure 10 shows the alarming zones using AI.
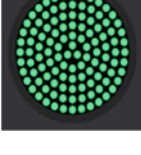
	RED	Above 50 ppb	Non Drinkable water	Super Danger Zone
	YELLOW	10 to 50 ppb	Drinkable water in absence of alternative source guided by Govt.	Danger Zone
	GREEN	0 TO 10 ppb	Drinkable water under the limit given by WHO	Neutral Zone

50 ppb

10 ppb

0 ppb

Fig. 10 Water level selection using Artificial Intelligence

8 Conclusions

Apart from selectivity, most sensors have a detection limit that is well below WHO/EPA limits. There is a lot of opportunity for development in the domain of As(III) detection in terms of sensor planning and development. There is a huge need for highly selective and sensitive sensors for an extra usable toolset for As(III) detection. Greater development of polymeric sensors for As(III) detection is necessary for device production to give a permanent solution for societies that are significantly plagued by arsenic poisoning. Carbon dots-based fluorescence sensors are useful tools for sensing or imaging heavy metals of interest, owing to their main advantages over fluorescent dyes or noble metal/metal oxide nanomaterials. Many carbon dots-based fluorescence sensors have been shown to have outstanding performance in the detection of heavy metals, with "turn-on" and ratio-metric measurement being particularly useful [37, 38]. Increased energies are being completed in zones such as multiple-heavy metal recognition to improve finding quantity, heavy metal speciation for high toxic species, fabrication of gel/solid sensor platforms such as paper-based devices, sensor arrays, hydrogel or polymer films, and IIPs for cost-effective detection, and fabrication of gel/solid sensor platforms such as paper-based devices, sensor arrays, hydrogel or polymer films, and IIPs for cost-effective detection, smart visual detection, and on-site analysis, and fabrication of gel/solid sensor platforms such as paper-based devices, and sensor arrays, hydrogel or polymer films.

9 Future Study

We'll create an AI-powered mobile application platform that can capture sensor images with a smartphone's built-in camera, identify the presence of sensing parameters, and classify the extent of sensing parameter supported color intensity identified within the training sets on the captured image using a deep CNN algorithm. This technology of sensor will create an early warning system that can help people in getting Arsenic and Fluoride-free water.

References

1. Grafton RQ, Horne J (2014) Water markets in the murray-darling basin. Agric Water Manag 145:61–71
2. Bagla P, Kaiser J (1996) India's spreading health crisis draws global arsenic experts. Science 274:174–175
3. World Health Organization (2017) Guidelines for drinking-water quality: fourth edition incorporating first addendum. https://apps.who.int/iris/handle/10665/254637
4. Adler RW (2015) US Environmental Protection Agency's new waters of the United States Rule: Connecting law and science. Freshw Sci 34:1595–1600. https://doi.org/10.1086/684002
5. Vézina A (2014) Guidelines for Canadian drinking water quality—summary table. Water and Air Quality Bureau, Healthy Environments and Consumer Safety Branch; Health Canada, Ottawa, ON, Canada
6. Von Ehrenstein O, Guha Mazumder D, Hira-Smith M, Ghosh N, Yuan Y, Windham G, Ghosh A, Haque R, Lahir (2006) Drinking water arsenic and adverse reproductive outcomes in men and women: asystematic PRISMA review
7. Krishna AK, Satyanarayanan M, Govil PK (2009) Assessment of heavy metal pollution in water using multivariate statistical techniques in an industrial area: a case study from patancheru, medak district, Andhra Pradesh, India. J Hazard Mater 167:366–373
8. Buschmann J, Berg M, Stengel C, Winkel L, Sampson ML, Trang PTK, Viet PH (2008) Contamination of drinking water resources in the mekong delta floodplains: Arsenic and other trace metals pose serious health risks to population. Environ Int 34:756–764
9. Wade T, Xia Y, Wu K, Li Y, Ning Z, Le XC, Lu X, Feng Y, He X, Mumford J (2009) Increased mortality associated with well-water arsenic exposure in inner Mongolia, china. Int J Environ Res Pub Health 6:1107–1123
10. Mosaferi M, Yunesian M, Dastgiri S, Mesdaghinia A, Esmailnasab N (2008) Prevalence of skin lesions and exposure to arsenic in drinking water in Iran. Sci Total Environ 390:69–76
11. Cavar S, Klapec T, Grubešic RJ, Valek M (2005) High exposure to arsenic from drinking water at several localities in Eastern Croatia. Sci Total Environ 339:277–282
12. Armienta M, Segovia N (2008) Arsenic and fluoride in the groundwater of Mexico. Environ Geochem Health 30:345–353
13. Bundschuh J, García M (2008) Rural Latin America—a forgotten part of the global groundwater arsenic problem. Groundwater for sustainable development: problems, perspectives and Challenges. Leiden Balkema Publisher, London, UK, pp 311–321
14. Amini M, Abbaspour KC, Berg M, Winkel L, Hug SJ, Hoehn E, Yang H, Johnson CA (2008) Statistical modeling of global geogenic arsenic contamination in groundwater. Environ Sci Technol 42:3669–3675

15. Chakraborti D, Sengupta MK, Rahman MM, Ahamed S, Chowdhury UK, Hossain A, Mukherjee SC, Pati S, Saha KC, Dutta R (2004) Groundwater arsenic contamination and its health effects in the ganga-meghna brahmaputra plain. J Environ Monit 6:74

16. Amin MN, Kaneco S, Kitagawa T, Begum A, Katsumata H, Suzuki T, Ohta K (2006) Removal of arsenic in aqueous solutions by adsorption onto waste rice husk. Ind Eng Chem Res 45:8105–8110

17. Hao L, Liu M, Wang N, Li G (2018) A critical review on arsenic removal from water using iron-based adsorbents. RSC Adv 8:39545–39560

18. Budinova T, Petrov N, Razvigorova M, Parra J, Galiatsatou P (2006) Removal of arsenic (iii) from aqueous solution by activated carbons prepared from solvent extracted olive pulp and olive stones. Ind Eng Chem Res 45:1896–1901

19. Chen H, Sharma SK, Sharma PR, Yeh H, Johnson K, Hsiao BS (2019) Arsenic (iii) removal by nanostructured dialdehyde cellulose–cysteine microscale and nanoscale fibres. ACS Omega 4:22008–22020

20. Liu T, Zhang Z, Wang Z, Wang Z-L, Bush R (2019) Highly efficient and rapid removal of arsenic (iii) from aqueous solutions by nanoscale zero-valent iron supported on a zirconium 1,4-dicarboxybenzene metal–organic framework (bio-66 mof). RSC Adv 9:39475–39487

21. Maity S, Naskar N, Lahiri S, Ganguly J (2019) Polysaccharide-derived hydrogel water filter for the rapid and selective removal of arsenic. Environ Sci Water Res Technol 5:1318–1327

22. Zu F et al (2017) The quenching of the fluorescence of carbon dots: a review on mechanisms and applications. Microchemical Acta 184(7):1899–1914

23. Zhang QQ et al (2018) Inner filter with carbon quantum dots: a selective sensing platform for detection of hematin in human red cells. Biosens Bioelectron 100:148–154

24. Wang H, Wang (2006) Quantum-sized carbon dots for bright and colorful photoluminescence. J Am Chem Soc 128:7756

25. Shang F, Uber JG, Rossman LA (2008) Modeling reaction and transport of multiple species in water distribution systems. Environ Sci Technol 42(3):808–814

26. Derfus AM, Chan WC, Bhatia SN (2004) Probing the cytotoxicity of semiconductor quantum dots. Nano Lett 4:11–18. https://doi.org/10.1021/nl0347334

27. Perelman L, Arad J, Housh M, Ostfeld A (2012) Event detection in water distribution systems from multivariate water quality time series. Environ Sci Technol 46(15):8212–8219

28. Smola AJ, Schölkopf B (2004) A tutorial on support vector regression. Stat Comput 14(3):199–222

29. Tinelli S (2018) Monitoring, Early Detection & Warning Systems for Contamination Events in Water Distribution Networks. PhD thesis, Pavia University, Pavia, Italy, in collaboration with NYU Tandon School of Engineering – Urban Infrastructure Institute.

30. Tinelli S, Juran I (2017) Numerical modeling of early bio-contamination in a water distribution system and comparison with laboratory experiments. In: Proceedings of ASCE international conference on sustainable infrastructure (Soibelman L. & Peña-More)

31. Van Thienen P, de Graaf B, Hoogterp J, van Summeren J, Vogelaar A (2018) Bounds on water quality sensor network performance from design choices and practical considerations. Water Pract Technol 13(2):328–334

32. Chowdhury S, Mazumder MJ, Al-Attas O, Husain T (2016) Heavy metals in drinking water: occurrences, implications, and future needs in developing countries. Sci Total Environ 569:476–488

33. Tinelli S, Juran I, Cantos WP (2018) Development of risk assessment tools for early detection of bio-contamination in water distribution systems. Water Sci Technol Water Supply 18(6):2151–2161

34. Sigdel A, Lim J, Park J, Kwak H, Min S, Kim K, Lee H, Nahm CH, Park P-K (2018) Immobilization of hydrous iron oxides in porous alginate beads for arsenic removal from water. Environ Sci Water Res Technol 4:1114–1123

35. Sharma PR, Sharma SK, Antoine R, Hsiao BS (2019) Efficient removal of arsenic using zinc oxide nanocrystal-decorated regenerated micro fibrillated cellulose scaffolds. ACS Sustain Chem Eng 7:6140–6151

36. Xia Y, Wade T, Wu K, Li Y, Ning Z, Le XC, Chen B, Feng Y, Mumford J, He X (2009) Well water arsenic exposure, arsenic induced skin-lesions and self-reported morbidity in inner mongolia. Int J Environ Res Pub Health 6:1010–1025; Nanomaterials 2020(10)1323: 27 of 37
37. Van Thienen P, Pieterse-Quirijns I, Vreeburg JHG, Vangeel K, Kapelan Z (2019) Artificial intelligence-based monitoring system of water quality parameters for early detection of non-specific bio-contamination in water distribution systems. Water Supply 19(6):1785–1792. https://doi.org/10.2166/ws.2019.0572013
38. Kalman D et al (2006) Pregnancy outcomes, infant mortality, and arsenic in drinking water in West Bengal, India. Am J Epidemiol 163:662–669